

Graduate Texts in Physics

Bogdan Povh  
Klaus Rith  
Christoph Scholz  
Frank Zetsche  
Werner Rodejohann

# Particles and Nuclei

An Introduction to the Physical Concepts

*Seventh Edition*

 Springer

# Graduate Texts in Physics

## Series Editors

Sadri Hassani  
Illinois, USA

W.J. Munro  
Kanagawa, Japan

Richard Needs  
Cambridge, UK

William T. Rhodes  
Florida, USA

Martin Stutzmann  
Garching, Germany

Andreas Wipf  
Jena, Germany

## **Graduate Texts in Physics**

Graduate Texts in Physics publishes core learning/teaching material for graduate and advanced-level undergraduate courses on topics of current and emerging fields within physics, both pure and applied. These textbooks serve students at the MS- or PhD-level and their instructors as comprehensive sources of principles, definitions, derivations, experiments and applications (as relevant) for their mastery and teaching, respectively. International in scope and relevance, the textbooks correspond to course syllabi sufficiently to serve as required reading. Their didactic style, comprehensiveness and coverage of fundamental material also make them suitable as introductions or references for scientists entering, or requiring timely knowledge of, a research field.

More information about this series at  
[www.springer.com/series/8431](http://www.springer.com/series/8431)

Bogdan Povh • Klaus Rith • Christoph Scholz •  
Frank Zetsche • Werner Rodejohann

# Particles and Nuclei

An Introduction to the Physical Concepts

Seventh Edition

 Springer

Bogdan Povh  
Max-Planck-Institut für Kernphysik  
Heidelberg, Germany

Klaus Rith  
Department Physik  
Universität Erlangen-Nürnberg  
Erlangen, Germany

Christoph Scholz  
SAP AG  
Walldorf, Germany

Frank Zetsche  
DFS Deutsche Flugsicherung GmbH  
Langen, Germany

Werner Rodejohann  
Max-Planck-Institut für Kernphysik  
Heidelberg, Germany

The first edition was translated by Dr. Martin Lavelle

Title of the original German Edition:

B. Povh, K. Rith, C. Scholz, F. Zetsche: Teilchen und Kerne  
Eine Einführung in die physikalischen Konzepte. (9. Auflage)  
(c) Springer 1993, 1994, 1995, 1997, 1999, 2004, 2006, 2009 und 2014

ISSN 1868-4513

Graduate Texts in Physics

ISBN 978-3-662-46320-8

DOI 10.1007/978-3-662-46321-5

ISSN 1868-4521 (electronic)

ISBN 978-3-662-46321-5 (eBook)

Library of Congress Control Number: 2015942913

Springer Heidelberg New York Dordrecht London

© Springer-Verlag Berlin Heidelberg 1995, 1999, 2002, 2004, 2006, 2008, 2015

This work is subject to copyright. All rights are reserved by the Publisher, whether the whole or part of the material is concerned, specifically the rights of translation, reprinting, reuse of illustrations, recitation, broadcasting, reproduction on microfilms or in any other physical way, and transmission or information storage and retrieval, electronic adaptation, computer software, or by similar or dissimilar methodology now known or hereafter developed.

The use of general descriptive names, registered names, trademarks, service marks, etc. in this publication does not imply, even in the absence of a specific statement, that such names are exempt from the relevant protective laws and regulations and therefore free for general use.

The publisher, the authors and the editors are safe to assume that the advice and information in this book are believed to be true and accurate at the date of publication. Neither the publisher nor the authors or the editors give a warranty, express or implied, with respect to the material contained herein or for any errors or omissions that may have been made.

Printed on acid-free paper

Springer-Verlag GmbH Berlin Heidelberg is part of Springer Science+Business Media ([www.springer.com](http://www.springer.com))

# Preface

Since the first German edition of this textbook in 1993, many extensions and corrections of the text have been added in every further edition. For the present seventh English edition, the text of several chapters and also many figures have been thoroughly revised and updated, and plenty of additional information has been added.

Werner Rodejohann joined the team of authors. He mainly cared about the chapters that deal with neutrinos and the Higgs particle. A new Chap. 11 has been added with the focus on neutrino properties, neutrino oscillations and Majorana neutrinos; additional aspects of the latter topic are summarised in Chap. 18. Chapter 12 has been extended by a discussion on spontaneous symmetry breaking, the Higgs potential and the experimental observation of the Higgs particle at the LHC.

Updates on experimental results include new information about the elastic form factors of proton and neutron, in particular from JLab experiments (Chap. 6) and the final results for the proton structure function  $F_2^p$  and charged-current cross-sections obtained by the experiments H1 and ZEUS at the HERA electron/positron-proton collider HERA (Chaps. 8, 10, 12). Chapter 15 has been substantially extended by a discussion of CP violation in the decay of neutral K- and B-mesons and its detailed investigation by fixed-target experiments with high-energy kaon beams at CERN and FNAL and the two B-factory experiments BaBar and BELLE. A section on the investigation of the nucleon's spin structure in deep-inelastic lepton-nucleon scattering with polarised beams and targets has been added to Chap. 16.

We would like to thank Lara de Nardo, Markus Diefenthaler and Friedrich Stinzing for producing some of the new figures and Armine Rostomyan and Morgan Murray for carefully reading and correcting the translations of several newly written paragraphs.

Heidelberg, Germany  
March 2015

The authors

# Preface to the First Edition

The aim of *PARTICLES AND NUCLEI* is to give a unified description of nuclear and particle physics because the experiments which have uncovered the substructure of atomic nuclei and nucleons are conceptually similar. With the progress of experimental and theoretical methods, atoms, nuclei, nucleons and finally quarks have been analysed during the course of this century. The intuitive assumption that our world is composed of a few constituents – an idea which seems attractive, but could not be taken for granted – appears to be confirmed. Moreover, the interactions between these constituents of matter can be formulated elegantly and are well understood conceptually, within the so-called standard model.

Once we have arrived at this underlying theory, we are immediately faced with the question of how the complex structures around us are produced by it. On the way from elementary particles to nucleons and nuclei, we learn that the “fundamental” laws of the interaction between elementary particles are less and less recognisable in composite systems because many-body interactions cause greater and greater complexity for larger systems.

This book is therefore divided into two parts. In the first part we deal with the reduction of matter in all its complication to a few elementary constituents and interactions, while the second part is devoted to the composition of hadrons and nuclei from their constituents.

We put special emphasis on the description of the experimental concepts, but we mostly refrain from explaining technical details. The appendix contains a short description of the principles of accelerators and detectors. The exercises predominantly aim at giving the students a feeling for the sizes of the phenomena of nuclear and particle physics.

Wherever possible, we refer to the similarities between atoms, nuclei and hadrons, because applying analogies has not only turned out to be a very effective research tool but is also very helpful for understanding the character of the underlying physics.

We have aimed at a concise description but have taken care that all the fundamental concepts are clearly described. Regarding our selection of topics, we were guided by pedagogical considerations. This is why we describe experiments



which – from today’s point of view – can be interpreted in a straightforward way. Many historically significant experiments, whose results can nowadays be much more simply obtained, were deliberately omitted.

PARTICLES AND NUCLEI (TEILCHEN UND KERNE) is based on lectures on nuclear and particle physics given at the University of Heidelberg to students in their 6th semester and conveys the fundamental knowledge in this area, which is required of a student majoring in physics. On traditional grounds these lectures, and therefore this book, strongly emphasise the physical concepts.

We are particularly grateful to J. Hüfner (Heidelberg) and M. Rosina (Ljubljana) for their valuable contributions to the nuclear physics part of the book. We would like to thank D. Dubbers (Heidelberg), A. Fäßler (Tübingen), G. Garvey (Los Alamos), H. Koch (Bochum), K. Königsmann (Freiburg), U. Lynen (GSI Darmstadt), G. Mairle (Mannheim), O. Nachtmann (Heidelberg), H.J. Pirner (Heidelberg), B. Stech (Heidelberg) and Th. Walcher (Mainz) for their critical reading and helpful comments on some sections. Many students who attended our lecture in the 1991 and 1992 summer semesters helped us through their criticism to correct mistakes and improve unclear passages. We owe special thanks to M. Beck, Ch. Büscher, S. Fabian, Th. Haller, A. Laser, A. Mücklich, W. Wander and E. Wittmann.

M. Lavelle (Barcelona) has translated the major part of the book and put it in the present linguistic form. We much appreciated his close collaboration with us. The English translation of this book was started by H. Hahn and M. Moinester (Tel Aviv) whom we greatly thank.

Numerous figures from the German text have been adapted for the English edition by J. Bockholt, V. Träumer and G. Vogt of the Max-Planck-Institut für Kernphysik in Heidelberg.

We would like to extend our thanks to Springer-Verlag, in particular W. Beiglböck for his support and advice during the preparation of the German and, later on, the English editions of this book.

Heidelberg, Germany  
May 1995

Bogdan Povh  
Klaus Rith  
Christoph Scholz  
Frank Zetsche

# Contents

<b>1</b>	<b>Hors d'œuvre</b> .....	1
1.1	Fundamental Constituents of Matter .....	1
1.2	Fundamental Interactions .....	3
1.3	Symmetries and Conservation Laws .....	4
1.4	Experiments .....	5
1.5	Units .....	6
	Reference.....	7
 <b>Part I Analysis: The Building Blocks of Matter</b>		
<b>2</b>	<b>Global Properties of Nuclei</b> .....	11
2.1	The Atom and Its Constituents .....	11
2.2	Nuclides.....	13
2.3	Parametrisation of Binding Energies .....	19
2.4	Charge Independence of the Nuclear Force and Isospin .....	21
	Problem.....	23
	References.....	23
<b>3</b>	<b>Nuclear Stability</b> .....	25
3.1	Beta Decay.....	27
3.2	Alpha Decay.....	31
3.3	Nuclear Fission .....	34
3.4	Decay of Excited Nuclear States .....	36
	Problems .....	38
	References.....	40
<b>4</b>	<b>Scattering</b> .....	41
4.1	General Observations About Scattering Processes .....	41
4.2	Cross-Sections.....	44
4.3	The “Golden Rule” .....	48
4.4	Feynman Diagrams.....	50
	Problems .....	52
	References.....	53

<b>5</b>	<b>Geometric Shapes of Nuclei</b> .....	55
5.1	Kinematics of Electron Scattering .....	55
5.2	The Rutherford Cross-Section .....	58
5.3	The Mott Cross-Section .....	63
5.4	Nuclear Form Factors .....	64
5.5	Inelastic Nuclear Excitations .....	72
	Problems .....	73
	References .....	74
<b>6</b>	<b>Elastic Scattering Off Nucleons</b> .....	75
6.1	Form Factors of the Nucleons .....	75
6.2	Quasi-elastic Scattering .....	82
6.3	Charge Radii of Pions and Kaons .....	85
	Problems .....	86
	References .....	86
<b>7</b>	<b>Deep-Inelastic Scattering</b> .....	87
7.1	Excited States of the Nucleons .....	88
7.2	Structure Functions .....	90
7.3	The Parton Model .....	92
7.4	The Quark Structure of Nucleons .....	95
7.5	Interpretation of Structure Functions in the Parton Model .....	96
	Problems .....	101
	References .....	101
<b>8</b>	<b>Quarks, Gluons, and the Strong Interaction</b> .....	103
8.1	Quarks in Hadrons .....	103
8.2	The Quark-Gluon Interaction .....	104
8.3	Scaling Violations of the Structure Functions .....	110
8.4	Flavour-separated Parton Distributions .....	116
8.5	Nuclear Effects in Deep-Inelastic Scattering .....	117
	Problems .....	121
	References .....	122
<b>9</b>	<b>Particle Production in <math>e^+e^-</math> Collisions</b> .....	123
9.1	Lepton Pair Production .....	125
9.2	Resonances .....	129
9.3	Non-resonant Hadron Production .....	133
9.4	Gluon Emission .....	135
	Problems .....	137
	References .....	138
<b>10</b>	<b>Phenomenology of the Weak Interaction</b> .....	139
10.1	Properties of Leptons .....	139
10.2	The Types of Weak Interactions .....	143
10.3	Coupling Strength of the Weak Interaction .....	146
10.4	The Quark Families .....	151

10.5	Parity Violation .....	154
10.6	Deep-Inelastic Scattering with Charged Currents .....	157
	Problems .....	163
	References .....	165
<b>11</b>	<b>Neutrino Oscillations and Neutrino Mass</b> .....	167
11.1	Lepton Families .....	168
11.2	Neutrino Oscillations .....	168
11.3	Neutrino Oscillation Experiments .....	171
11.4	Majorana Neutrinos? .....	180
	Problems .....	182
	References .....	183
<b>12</b>	<b>Exchange Bosons of the Weak Interaction and the Higgs Boson</b> .....	185
12.1	Real W and Z Bosons .....	185
12.2	Electroweak Unification .....	191
12.3	Width of the $Z^0$ and the Number of Neutrinos .....	194
12.4	Symmetry Breaking .....	196
12.5	The Higgs Boson .....	200
12.6	Grand Unification .....	204
	Problem .....	204
	References .....	205
<b>13</b>	<b>The Standard Model</b> .....	207
	Reference .....	211
 <b>Part II Synthesis: Composite Systems</b>		
<b>14</b>	<b>Quarkonia</b> .....	215
14.1	The Hydrogen Atom and Positronium Analogues .....	215
14.2	Charmonium .....	218
14.3	Quark-Antiquark Potential .....	221
14.4	The Chromomagnetic Interaction .....	224
14.5	Bottonium and Toponium .....	226
14.6	The Decay Channels of Heavy Quarkonia .....	227
14.7	Decay Widths as a Test of QCD .....	230
	Problems .....	232
	References .....	232
<b>15</b>	<b>Mesons</b> .....	233
15.1	Meson Multiplets .....	233
15.2	Meson Masses .....	237
15.3	Decay Channels .....	239
15.4	Neutral-Kaon Decay .....	241
15.5	CP Violation and the CKM Matrix .....	246
	Problems .....	250
	References .....	251

<b>16</b>	<b>Baryons</b> .....	253
	16.1 The Production and Detection of Baryons .....	254
	16.2 Baryon Multiplets .....	260
	16.3 Baryon Masses .....	263
	16.4 Magnetic Moments .....	266
	16.5 Spin Structure of the Nucleon .....	270
	16.6 Semileptonic Baryon Decays .....	274
	16.7 How Good Is the Constituent-Quark Concept? .....	282
	Problems .....	283
	References .....	285
<b>17</b>	<b>The Nuclear Force</b> .....	287
	17.1 Nucleon-Nucleon Scattering .....	288
	17.2 The Deuteron .....	292
	17.3 Nature of the Nuclear Force .....	295
	Problems .....	301
	References .....	301
<b>18</b>	<b>The Structure of Nuclei</b> .....	303
	18.1 The Fermi Gas Model .....	303
	18.2 Hypernuclei .....	308
	18.3 The Shell Model .....	312
	18.4 Deformed Nuclei .....	320
	18.5 Spectroscopy Through Nuclear Reactions .....	324
	18.6 Beta Decay of the Nucleus .....	330
	18.7 Double Beta Decay .....	338
	Problems .....	343
	References .....	344
<b>19</b>	<b>Collective Nuclear Excitations</b> .....	347
	19.1 Electromagnetic Transitions .....	348
	19.2 Dipole Oscillations .....	351
	19.3 Shape Oscillations .....	360
	19.4 Rotational States .....	363
	Problems .....	371
	References .....	372
<b>20</b>	<b>Nuclear Thermodynamics</b> .....	373
	20.1 Thermodynamical Description of Nuclei .....	374
	20.2 Compound Nuclei and Quantum Chaos .....	376
	20.3 The Phases of Nuclear Matter .....	379
	20.4 Particle Physics and Thermodynamics in the Early Universe .....	384
	20.5 Stellar Evolution and Element Synthesis .....	393
	Problems .....	399
	References .....	400

- 21 Many-Body Systems in the Strong Interaction** ..... 401
- Reference ..... 404
  
- Appendix A** ..... 405
- A.1 Accelerators ..... 405
- A.2 Detectors ..... 411
- A.3 Combining Angular Momenta ..... 421
- A.4 Physical Constants ..... 422
  
- Solutions to Problems** ..... 425
- References ..... 451
  
- Index** ..... 453

# Chapter 1

## Hors d'œuvre

*Nicht allein in Rechnungssachen  
Soll der Mensch sich Mühe machen;  
Sondern auch der Weisheit Lehren  
Muß man mit Vergnügen hören.*

Wilhelm Busch  
Max und Moritz (4. Streich)

### 1.1 Fundamental Constituents of Matter

In their search for the fundamental building blocks of matter, physicists have found smaller and smaller constituents that have proven to be themselves composite systems. By the end of the nineteenth century, it was known that all matter is composed of atoms. However, the existence of close to 100 elements showing periodically recurring properties was a clear indication that atoms themselves have an internal structure, and are not indivisible.

The modern concept of the atom emerged at the beginning of the twentieth century, in particular as a result of the experiments by Rutherford and co-workers. An atom is composed of a dense nucleus surrounded by an electron cloud. The nucleus itself can be decomposed into smaller particles. After the discovery of the neutron in 1932, there was no longer any doubt that the building blocks of nuclei are protons and neutrons (collectively called nucleons). The electron, neutron and proton were later joined by a fourth particle, the neutrino, which was postulated in 1930 in order to reconcile the description of  $\beta$ -decay with the fundamental laws of conservation of energy, momentum and angular momentum.

Thus, by the mid-thirties, these four particles could describe all the then known phenomena of atomic and nuclear physics. Today, these particles are still considered to be the main constituents of matter. But this simple, closed picture turned out in fact to be incapable of describing other phenomena.

Experiments at particle accelerators in the 1950s and 1960s showed that protons and neutrons are merely representatives of a large family of particles now called *hadrons*. More than 200 hadrons, sometimes called the “hadronic zoo”, have thus far been detected. These hadrons, like atoms, can be classified in groups with similar properties. It was therefore assumed that they cannot be understood as fundamental

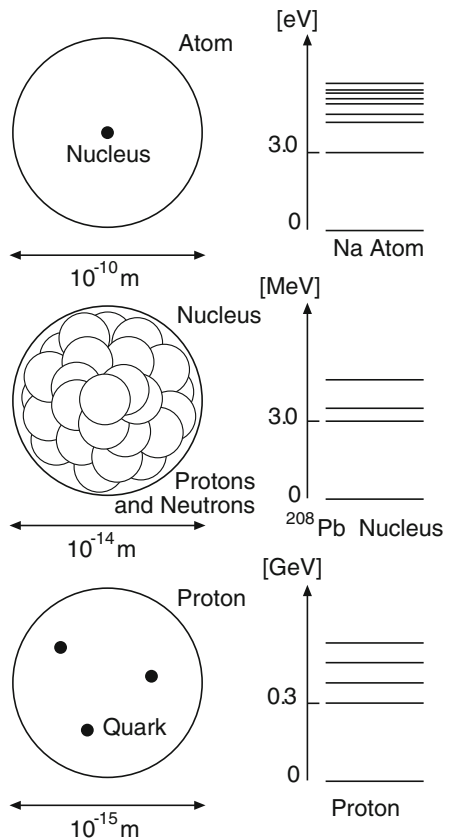
constituents of matter. In the late 1960s, the quark model established order in the hadronic zoo. All known hadrons could be described as combinations of two or three quarks.

Figure 1.1 shows different scales in the hierarchy of the structure of matter. As we probe the atom with increasing magnification, smaller and smaller structures become visible: the nucleus, the nucleons, and finally the quarks.

**Leptons and quarks** The two fundamental types of building blocks are the *leptons*, which include the electron and the neutrino, and the *quarks*. In scattering experiments, these were found to be smaller than  $10^{-18}$  m. They are possibly point-like particles. For comparison, protons are as large as  $\approx 10^{-15}$  m. Leptons and quarks have spin  $1/2$ , i.e., they are fermions. In contrast to atoms, nuclei and hadrons, no excited states of quarks or leptons have so far been observed. Thus, they appear to be elementary particles.

Today, however, we know of six leptons and six quarks as well as their antiparticles. These can be grouped into so-called “generations” or “families”, according to certain characteristics. Thus, the number of leptons and quarks is relatively large;

**Fig. 1.1** Length scales and structural hierarchy in atomic structure. To the right, typical excitation energies and spectra are shown. Smaller bound systems possess larger excitation energies





furthermore, their properties recur in each generation. Some physicists believe these two facts are a hint that leptons and quarks are not elementary building blocks of matter. Only experiment will teach us the truth.

## 1.2 Fundamental Interactions

Together with our changing conception of elementary particles, our understanding of the basic forces of nature and so of the fundamental interactions between elementary particles has evolved. Around the year 1800, four forces were considered to be basic: *gravitation*, *electricity*, *magnetism* and the barely comprehended forces between atoms and molecules. By the end of the nineteenth century, electricity and magnetism were understood to be manifestations of the same force: *electromagnetism*. Later it was shown that atoms have a structure and are composed of a positively charged nucleus and an electron cloud; the whole held together by the electromagnetic interaction. Overall, atoms are electrically neutral. At short distances, however, the electric fields between atoms do not cancel out completely, and neighbouring atoms and molecules influence each other. The different kinds of “chemical forces” (e.g., the Van der Waals force) are thus expressions of the electromagnetic force.

When nuclear physics developed, two new short-ranged forces joined the ranks. These are the *nuclear force*, which acts between nucleons, and the *weak force*, which manifests itself in nuclear  $\beta$ -decay. Today, we know that the nuclear force is not fundamental. In analogy to the forces acting between atoms being effects of the electromagnetic interaction, the nuclear force is a result of the *strong force* binding quarks to form protons and neutrons. These strong and weak forces lead to the corresponding fundamental interactions between the elementary particles.

**Intermediate bosons** The four fundamental interactions on which all physical phenomena are based are gravitation, the electromagnetic interaction, the strong interaction and the weak interaction.

Gravitation is important for the existence of stars, galaxies, and planetary systems (and for our daily life), it is of no significance in subatomic physics, being far too weak to noticeably influence the interaction between elementary particles. We mention it only for completeness.

According to today’s conceptions, interactions are mediated by the exchange of vector bosons, i.e., particles with spin 1. These are *photons* in electromagnetic interactions, *gluons* in strong interactions and the  $W^+$ ,  $W^-$  and  $Z^0$  bosons in weak interactions. The diagrams in Fig. 1.2 show examples of interactions between two particles by the exchange of vector bosons: In our diagrams we depict leptons and quarks by straight lines, photons by wavy lines, gluons by spirals, and  $W^\pm$  and  $Z^0$  bosons by dashed lines.

Each of these three interactions is associated with a charge: electric charge, weak charge and strong charge. The strong charge is also called *colour charge* or

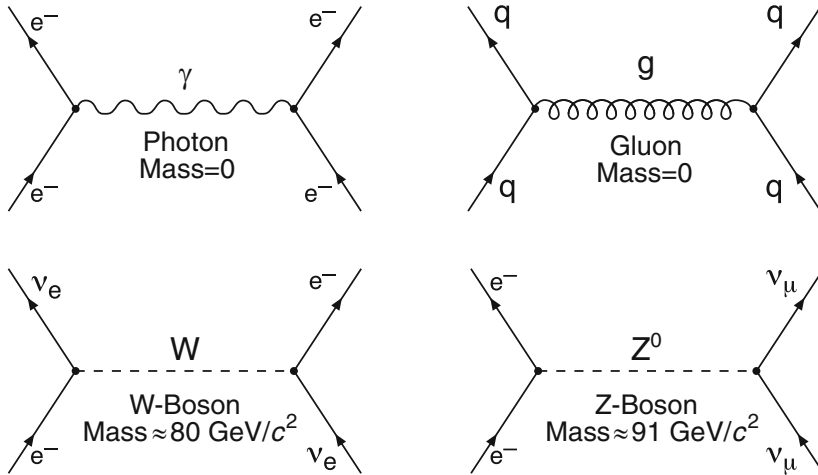


**Fig. 1.2** Diagrams for fundamental interactions between particles by the exchange of vector bosons

*colour* for short. A particle is subject to an interaction if and only if it carries the corresponding charge:

- Leptons and quarks carry weak charge.
- Quarks are electrically charged, so are some of the leptons (e.g., electrons).
- Colour charge is only carried by quarks (not by leptons).

The W and Z bosons, masses  $M_W \approx 80 \text{ GeV}/c^2$  and  $M_Z \approx 91 \text{ GeV}/c^2$ , are very heavy particles. According to the Heisenberg uncertainty principle, they can only be produced as virtual, intermediate particles in scattering processes for extremely short times. Therefore, the weak interaction is of very short range. The rest mass of the photon is zero. Therefore, the range of the electromagnetic interaction is infinite.

The gluons, like the photons, have zero rest mass. Whereas photons, however, have no electrical charge, gluons carry colour charge. Hence they can interact with each other. As we will see, this causes the strong interaction to be also very short ranged.

### 1.3 Symmetries and Conservation Laws

Symmetries are of great importance in physics. The conservation laws of classical physics (energy, momentum, angular momentum) are a consequence of the fact that the interactions are invariant with respect to their canonically conjugate quantities (time, space, angles). In other words, physical laws are independent of the time, the location and the orientation in space under which they take place.

An additional important property in non-relativistic quantum mechanics is reflection symmetry.<sup>1</sup> Depending on whether the sign of the wave function changes under reflection or not, the system is said to have negative or positive *parity* ( $P$ ), respectively. For example, the spatial wave function of a bound system with angular momentum  $\ell\hbar$  has parity  $P = (-1)^\ell$ . For those laws of nature with left-right symmetry, i.e., invariant under a reflection in space  $\mathcal{P}$ , the parity quantum number  $P$  of the system is conserved. Conservation of parity leads, e.g., in atomic physics to selection rules for electromagnetic transitions.

The concept of parity has been generalised in relativistic quantum mechanics. One has to ascribe an *intrinsic parity*  $P$  to particles and antiparticles. Bosons and antibosons have the same intrinsic parity, fermions and antifermions have opposite parities. An additional important symmetry relates particles and antiparticles. An operator  $\mathcal{C}$  is introduced which changes particles into antiparticles and vice versa. Since the charge reverses its sign under this operation, it is called *charge conjugation*. Eigenstates of  $\mathcal{C}$  have a quantum number  $\mathcal{C}$ -*parity* which is conserved whenever the interaction is symmetric with respect to  $\mathcal{C}$ .

Another symmetry derives from the fact that certain groups (“multiplets”) of particles behave practically identically with respect to the strong or the weak interaction. Particles belonging to such a multiplet may be described as different states of the same particle. These states are characterised by a quantum number referred to as strong or weak *isospin*. Conservation laws are also applicable to these quantities.

## 1.4 Experiments

Experiments in nuclear and elementary particle physics have, with very few exceptions, to be carried out using particle accelerators. The development and construction of accelerators with ever greater energies and beam intensities has made it possible to discover more and more elementary particles. A short description of the most important types of accelerators can be found in the appendix. The experiments can be classified as *scattering* or *spectroscopic* experiments.

**Scattering** In scattering experiments, a beam of particles with known energy and momentum is directed towards the object to be studied (the *target*). The beam particles then interact with the object. From the changes in the kinematical quantities caused by this process, we may learn about the properties both of the target and of the interaction.

Consider, as an example, elastic electron scattering which has proven to be a reliable method for measuring radii in nuclear physics. The structure of the target

---

<sup>1</sup>As is well known, reflection around a point is equivalent to reflection in a plane with simultaneous rotation about an axis perpendicular to that plane.

becomes visible via diffraction only when the de Broglie wavelength  $\lambda = h/p$  of the electron is comparable to the target's size. The resulting diffraction pattern of the scattered particles yields the size of the nucleus rather precisely.

Figure 1.1 shows the geometrical dimensions of various targets. To determine the size of an atom, X-rays with an energy of  $\approx 10^4$  eV suffice. Nuclear radii are measured with electron beams of about  $10^8$  eV, proton radii with electron beams of some  $10^8$ – $10^9$  eV. Even with today's energies,  $10^{11}$  eV for electrons and  $4 \cdot 10^{12}$  eV for protons, there is no sign of a substructure in either quarks or leptons.

**Spectroscopy** The term “spectroscopy” is used to describe those experiments which determine the decay products of excited states. In this way, one can study the properties of the excited states as well as the interactions between the constituents.

From Fig. 1.1 we see that the excitation energies of a system increase as its size decreases. To produce these excited states high energy particles are needed. Scattering experiments to determine the size of a system and to produce excited states require similar beam energies.

**Detectors** Charged particles interact with gases, liquids, amorphous solids, and crystals. These interactions produce electrical or optical signals in these materials which betray the passage of the particles. Neutral particles are detected indirectly through secondary particles: photons produce free electrons or electron-positron pairs, by the photoelectric or Compton effects, and pair production, respectively. Neutrons and neutrinos produce charged particles through reactions with nuclei.

Particle detectors can be divided into the following categories:

- Scintillators provide fast time information, but have only moderate spatial resolution.
- Gaseous counters covering large areas (wire chambers) provide good spatial resolution, and are used in combination with magnetic fields to measure momentum.
- Semiconductor counters have a very good energy and spatial resolution.
- Cherenkov counters and counters based on transition radiation are used for particle identification.
- Calorimeters measure the total energy at very high energies.

The basic types of counters for the detection of charged particles are compiled in Appendix A.2.

## 1.5 Units

The common units for length and energy in nuclear and elementary particle physics are the *femtometre* (fm, or *Fermi*) and the *electron volt* (eV). The Fermi is a standard SI-unit, defined as  $10^{-15}$  m, and corresponds approximately to the size of a proton.

An electron volt is the energy gained by a particle with charge  $1e$  by traversing a potential difference of 1 V:

$$1 \text{ eV} = 1.602 \cdot 10^{-19} \text{ J}. \quad (1.1)$$

For the decimal multiples of this unit, the usual prefixes are employed: keV, MeV, GeV, etc. Usually, one uses units of  $\text{MeV}/c^2$  or  $\text{GeV}/c^2$  for particle masses, according to the mass-energy equivalence  $E = mc^2$ .

Length and energy scales are connected in subatomic physics by the uncertainty principle. The Planck constant is especially easily remembered in the form

$$\hbar \cdot c \approx 200 \text{ MeV} \cdot \text{fm}. \quad (1.2)$$

Another quantity which will be used frequently is the coupling constant for electromagnetic interactions. It is defined by:

$$\alpha = \frac{e^2}{4\pi\epsilon_0\hbar c} \approx \frac{1}{137}. \quad (1.3)$$

For historical reasons, it is also called the *fine structure constant*.

A system of physical quantities which is frequently used in elementary particle physics has identical dimensions for mass, momentum, energy, inverse length and inverse time. In this system, the units may be chosen such that  $\hbar = c = 1$ . In atomic physics, it is common to define  $4\pi\epsilon_0 = 1$  and therefore  $\alpha = e^2$  (Gauss system). In particle physics,  $\epsilon_0 = 1$  and  $\alpha = e^2/4\pi$  is more commonly used (Heavyside-Lorentz system). However, we will utilise the SI-system [1] used in all other fields of physics and so retain the constants everywhere.

## Reference

1. S.U.N. Commission, Symbols, units and nomenclature in physics. *Physica* **93A**, 1 (1978)

**Part I**  
**Analysis:**  
**The Building Blocks of Matter**

*Mens agitat molem.*

Vergil  
Aeneid 6, 727

## Chapter 2

# Global Properties of Nuclei

The discovery of the electron and of radioactivity marked the beginning of a new era in the investigation of matter. At that time, some signs of the atomic structure of matter were already clearly visible: e.g. the integer stoichiometric proportions of chemistry, the thermodynamics of gases, the periodic system of the elements or Brownian motion. However, the existence of atoms was not yet generally accepted. The reason was simple: nobody was able to really picture these building blocks of matter, the atoms. The new discoveries showed for the first time “particles” emerging from matter which had to be interpreted as its constituents.

It now became possible to use the particles produced by radioactive decay to bombard other elements in order to study the constituents of the latter. This experimental ansatz is the basis of modern nuclear and particle physics. Systematic studies of nuclei became possible by the late 1930s with the availability of modern particle accelerators. But the fundamental building blocks of atoms – the electron, proton and neutron – were detected beforehand. A pre-condition for these discoveries were important technical developments in vacuum techniques and in particle detection. Before we turn to the global properties of nuclei from a modern viewpoint, we will briefly discuss these historical experiments.

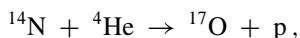
### 2.1 The Atom and Its Constituents

**The electron** The first building block of the atom to be identified was the electron. In 1897 Thomson was able to produce electrons as beams of free particles in discharge tubes. By deflecting them in electric and magnetic fields, he could determine their velocity and the ratio of their mass and charge. The results turned out to be independent of the kind of cathode and gas used. He had in other words found a universal constituent of matter. He then measured the charge of the electron

independently – using a method that was in 1910 significantly refined by Millikan (the drop method) – this of course also fixed the electron mass.

**The atomic nucleus** Subsequently, different models of the atom were discussed, one of them being the model of Thomson. In this model, the electrons, and an equivalent number of positively charged particles are uniformly distributed throughout the atom. The resulting atom is electrically neutral. Rutherford, Geiger and Marsden succeeded in disproving this picture. In their famous experiments, where they scattered  $\alpha$ -particles off heavy atoms, they were able to show that the positively charged particles are closely packed together. They reached this conclusion from the angular distribution of the scattered  $\alpha$ -particles. The angular distribution showed  $\alpha$ -particle scattering at large scattering angles which was incompatible with a homogeneous charge distribution. The explanation of the scattering data was a central Coulomb field caused by a massive, positively charged nucleus. The method of extracting the properties of the scattering potential from the angular distribution of the scattered projectiles is still of great importance in nuclear and particle physics, and we will encounter it repeatedly in the following chapters. These experiments established the existence of the atom as a positively charged, small, massive nucleus with negatively charged electrons orbiting it.

**The proton** Rutherford also bombarded light nuclei with  $\alpha$ -particles which themselves were identified as ionised helium atoms. In these reactions, he was looking for a conversion of elements, i.e., for a sort of inverse reaction to radioactive  $\alpha$ -decay, which itself is a conversion of elements. While bombarding nitrogen with  $\alpha$ -particles, he observed positively charged particles with an unusually long range, which must have been ejected from the atom as well. From this he concluded that the nitrogen atom had been destroyed in these reactions, and a light constituent of the nucleus had been ejected. He had already discovered similar long-ranged particles when bombarding hydrogen. From this he concluded that these particles were hydrogen nuclei which, therefore, had to be constituents of nitrogen as well. He had indeed observed the reaction



in which the nitrogen nucleus is converted into an oxygen nucleus, by the loss of a proton. The hydrogen nucleus could therefore be regarded as an elementary constituent of atomic nuclei. Rutherford also assumed that it would be possible to disintegrate additional atomic nuclei by using  $\alpha$ -particles with higher energies than those available to him. He so paved the way for modern nuclear physics.

**The neutron** The neutron was also detected by bombarding nuclei with  $\alpha$ -particles. Rutherford's method of visually detecting and counting particles by their scintillation on a zinc sulphide screen is not applicable to neutral particles. The development of ionisation and cloud chambers significantly simplified the detection of charged particles, but did not help here. Neutral particles could only be detected indirectly. Chadwick in 1932 found an appropriate experimental approach. He used



the irradiation of beryllium with  $\alpha$ -particles from a polonium source, and thereby established the neutron as a fundamental constituent of nuclei. Previously, a “neutral radiation” had been observed in similar experiments, but its origin and identity was not understood. Chadwick arranged for this neutral radiation to collide with hydrogen, helium and nitrogen, and measured the recoil energies of these nuclei in a ionisation chamber. He deduced from the laws of collision that the mass of the neutral radiation particle was similar to that of the proton. Chadwick named this particle the “neutron”.

**Nuclear force and binding** With these discoveries, the building blocks of the atom had been found. The development of ion sources and mass spectrographs now permitted the investigation of the forces binding the nuclear constituents, i.e., the proton and the neutron. These forces were evidently much stronger than the electromagnetic forces holding the atom together, since atomic nuclei could only be broken up by bombarding them with highly energetic  $\alpha$ -particles.

The binding energy of a system gives information about its binding and stability. This energy is the difference between the mass of a system and the sum of the masses of its constituents. It turns out that for nuclei this difference is close to 1 % of the nuclear mass. This phenomenon, historically called the mass defect, was one of the first experimental proofs of the mass-energy relation  $E = mc^2$ . The mass defect is of fundamental importance in the study of strongly interacting bound systems. We will therefore describe nuclear masses and their systematics in this chapter at some length.

## 2.2 Nuclides

**The atomic number** The atomic number  $Z$  gives the number of protons in the nucleus. The charge of the nucleus is, therefore,  $Q = Ze$ , the elementary charge being  $e = 1.6 \cdot 10^{-19}$  C. In a neutral atom, there are  $Z$  electrons, which balance the charge of the nucleus, in the electron cloud. The atomic number of a given nucleus determines its chemical properties.

The classical method of determining the charge of the nucleus is the measurement of the characteristic X-rays of the atom to be studied. For this purpose the atom is excited by electrons, protons or synchrotron radiation. Moseley’s law says that the energy of the  $K_\alpha$ -line is proportional to  $(Z - 1)^2$ . Nowadays, the detection of these characteristic X-rays is used to identify elements in material analysis.

Atoms are electrically neutral, which shows the equality of the absolute values of the positive charge of the proton and the negative charge of the electron. Experiments measuring the deflection of molecular beams in electric fields yield an upper limit for the difference between the proton and electron charges [4]:

$$|e_p + e_e| \leq 10^{-21} e . \quad (2.1)$$

Today's cosmological estimates give an even smaller upper limit for any difference between these charges.

**The mass number** In addition to the  $Z$  protons,  $N$  neutrons are found in the nucleus. The mass number  $A$  gives the number of nucleons in the nucleus, where  $A = Z + N$ . Different combinations of  $Z$  and  $N$  (or  $Z$  and  $A$ ) are called *nuclides*.

- Nuclides with the same mass number  $A$  are called *isobars*.
- Nuclides with the same atomic number  $Z$  are called *isotopes*.
- Nuclides with the same neutron number  $N$  are called *isotones*.

The binding energy  $B$  is usually determined from atomic masses [1], since they can be measured to a considerably higher precision than nuclear masses. We have:

$$B(Z, A) = [ZM(^1\text{H}) + (A - Z)M_n - M(A, Z)] \cdot c^2. \quad (2.2)$$

Here,  $M(^1\text{H}) = M_p + m_e$  is the mass of the hydrogen atom (the 13.6 eV binding energy of the H-atom is negligible),  $M_n$  is the mass of the neutron and  $M(A, Z)$  is the mass of an atom with  $Z$  electrons whose nucleus contains  $A$  nucleons. The rest masses of these particles are:

$$\begin{aligned} M_p &= 938.272 \text{ MeV}/c^2 = 1,836.153 m_e \\ M_n &= 939.565 \text{ MeV}/c^2 = 1,838.684 m_e \\ m_e &= 0.511 \text{ MeV}/c^2. \end{aligned}$$

The conversion factor into SI units is  $1.783 \cdot 10^{-30} \text{ kg}/(\text{MeV}/c^2)$ .

In nuclear physics, nuclides are denoted by  ${}^A\text{X}$ , X being the chemical symbol of the element. For example, the stable carbon isotopes are labelled  ${}^{12}\text{C}$  and  ${}^{13}\text{C}$ ; while the radioactive carbon isotope frequently used for isotopic dating is labelled  ${}^{14}\text{C}$ . Sometimes the notations  ${}^A_Z\text{X}$  or  ${}^A_Z\text{X}_N$  are used, whereby the atomic number  $Z$  and possibly the neutron number  $N$  are explicitly added.

**Determining masses from mass spectroscopy** The binding energy of an atomic nucleus can be calculated if the atomic mass is accurately known. At the start of the twentieth century, the method of mass spectrometry was developed for precision determinations of atomic masses (and nucleon binding energies). The deflection of an ion with charge  $Q$  in an electric and magnetic field allows the simultaneous measurement of its momentum  $p = Mv$  and its kinetic energy  $E_{\text{kin}} = Mv^2/2$ . From these, its mass can be determined. This is how most mass spectrometers work.

While the radius of curvature  $r_E$  of the ionic path in an electrical sector field is proportional to the energy,

$$r_E = \frac{M}{Q} \cdot \frac{v^2}{E}, \quad (2.3)$$

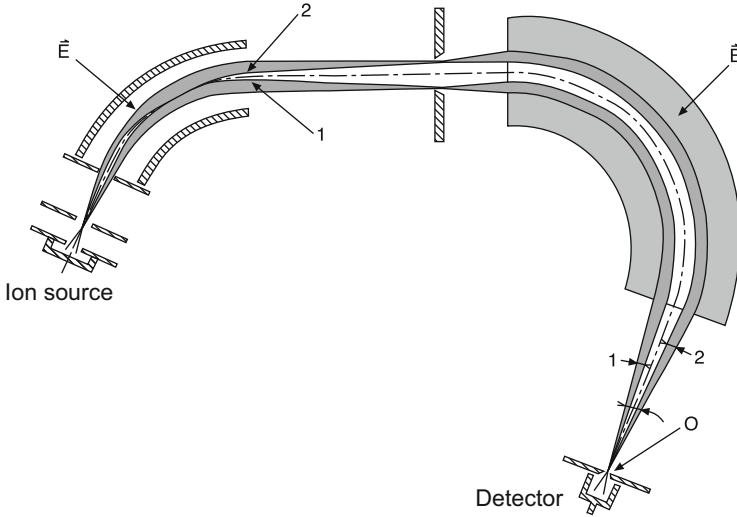


**Fig. 2.1** Doubly focusing mass spectrometer [5]. The spectrometer focuses ions of a certain specific charge to mass ratio  $Q/M$ . For clarity, only the trajectories of particles at the edges of the beam are drawn (*1 and 2*). The electric and magnetic sector fields draw the ions from the ion source into the collector. Ions with a different  $Q/M$  ratio are separated from the beam in the magnetic field and do not pass through the slit *O*

in a magnetic field  $B$  the radius of curvature  $r_M$  of the ion is proportional to its momentum:

$$r_M = \frac{M}{Q} \cdot \frac{v}{B}. \quad (2.4)$$

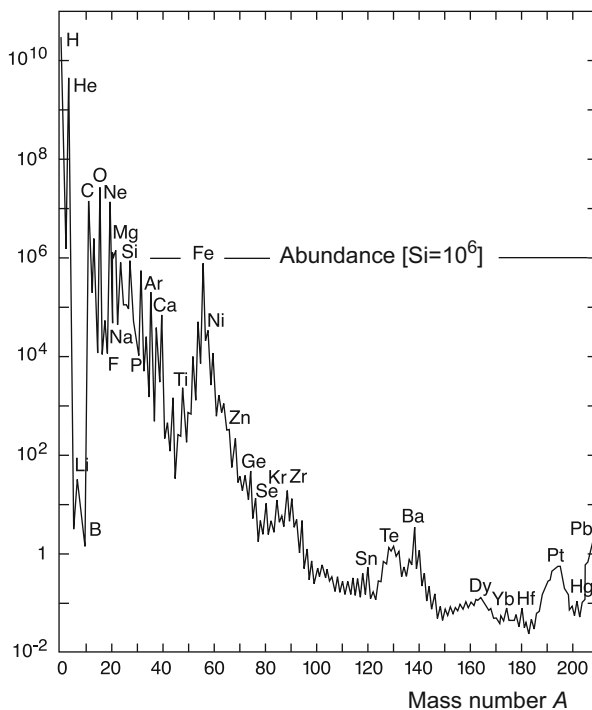
Figure 2.1 shows a common spectrometer design. After leaving the ion source, the ions are accelerated in an electric field to about 40 keV. In an electric field, they are then separated according to their energy and, in a magnetic field, according to their momentum. By careful design of the magnetic fields, ions with identical  $Q/M$  ratios leaving the ion source at various angles are focused at a point at the end of the spectrometer where a detector can be placed.

For technical reasons, it is very convenient to use the  $^{12}\text{C}$  nuclide as the reference mass. Carbon and its many compounds are always present in a spectrometer and are well suited for mass calibration. An atomic mass unit  $u$  was therefore defined as 1/12 of the atomic mass of the  $^{12}\text{C}$  nuclide. We have:

$$1u = \frac{1}{12} M_{^{12}\text{C}} = 931.494 \text{ MeV}/c^2 = 1.66054 \cdot 10^{-27} \text{ kg}.$$

Mass spectrometers are still widely used both in research and industry.

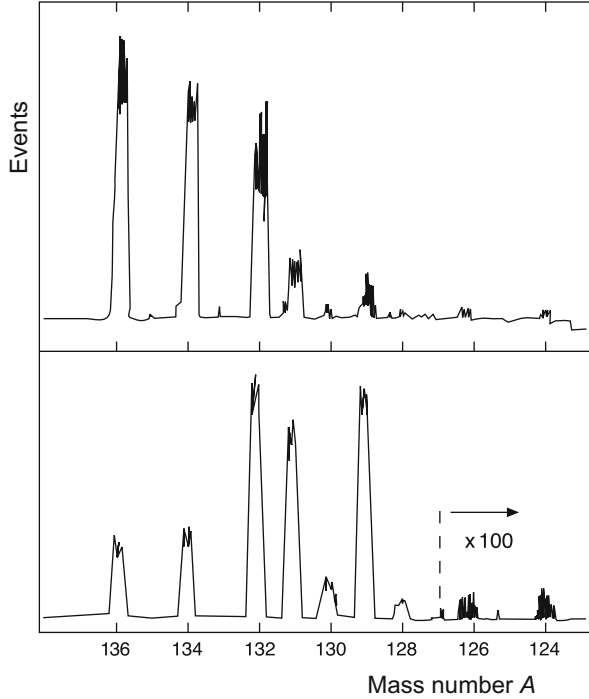
**Fig. 2.2** Abundance of the elements in the solar system as a function of their mass number  $A$ , normalised to the abundance of silicon ( $=10^6$ )



**Nuclear abundance** A current application of mass spectroscopy in fundamental research is the determination of isotope abundances in the solar system. The relative abundance of the various nuclides as a function of their mass number  $A$  is shown in Fig. 2.2. The relative abundances of isotopes in terrestrial, lunar, and meteoritic probes are, with few exceptions, identical and coincide with the nuclide abundances in cosmic rays from outside the solar system. According to current thinking, the synthesis of the presently existing deuterium and helium from hydrogen fusion mainly took place at the beginning of the universe (minutes after the big bang [2]). Nuclei up to  $^{56}\text{Fe}$ , the most stable nucleus, were produced by nuclear fusion in stars. Nuclei heavier than this last were created in the explosion of very heavy stars (supernovae) [6].

Deviations from the universal abundance of isotopes occur locally when nuclides are formed in radioactive decays. Figure 2.3 shows the abundances of various xenon isotopes in a drill core which was found at a depth of 10 km. The isotope distribution strongly deviates from that which is found in the Earth's atmosphere. This deviation is a result of the atmospheric xenon being, for the most part, already present when the Earth came into existence, while the xenon isotopes from the core come from radioactive decays (spontaneous fission of uranium isotopes).

**Fig. 2.3** Mass spectrum of xenon isotopes, found in a roughly  $2.7 \cdot 10^9$  year old gneiss sample from a drill core produced in the Kola peninsula (*top*) and, for comparison, the spectrum of Xe-isotopes as they occur in the atmosphere (*bottom*). The Xe-isotopes in the gneiss were produced by spontaneous fission of uranium (Picture courtesy of Klaus Schäfer, Max-Planck-Institut für Kernphysik)



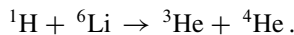
**Determining masses from nuclear reactions** Binding energies may also be determined from systematic studies of nuclear reactions. Consider, as an example, the capture of thermal neutrons ( $E_{\text{kin}} \approx 1/40$  eV) by hydrogen,



The energy of the emitted photon is directly related to the binding energy  $B$  of the deuterium nucleus  ${}^2\text{H}$ :

$$B = (M_n + M_{{}^1\text{H}} - M_{{}^2\text{H}}) \cdot c^2 = E_\gamma + \frac{E_\gamma^2}{2M_{{}^2\text{H}}c^2} = 2.225 \text{ MeV}, \quad (2.6)$$

where the last term takes into account the recoil energy of the deuteron. As a further example, we consider the reaction



The energy balance of this reaction is given by

$$E_{{}^1\text{H}} + E_{{}^6\text{Li}} = E_{{}^3\text{He}} + E_{{}^4\text{He}}, \quad (2.7)$$

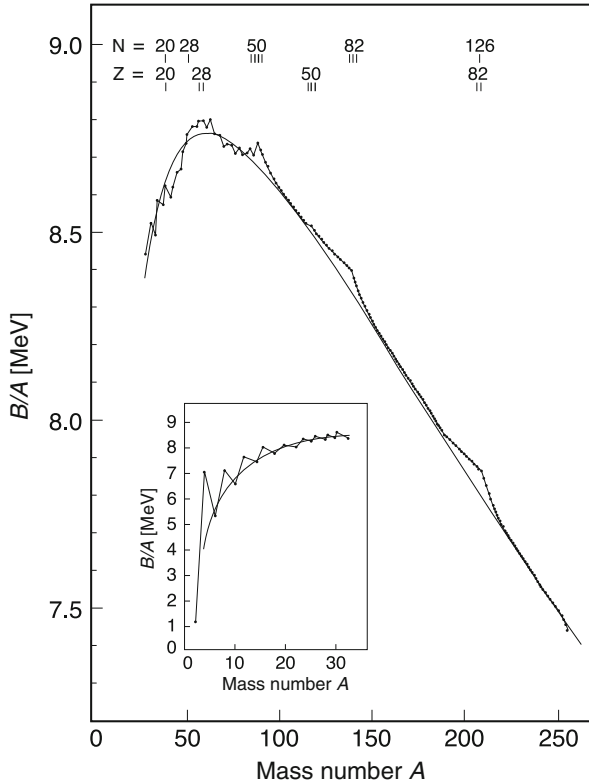


**Fig. 2.4** Binding energy per nucleon of nuclei with even mass number  $A$ . The *solid line* corresponds to the Weizsäcker mass formula (2.8). Nuclei with a small number of nucleons display relatively large deviations from the general trend, and should be considered on an individual basis. For heavy nuclei deviations in the form of a somewhat stronger binding per nucleon are also observed for certain proton and neutron numbers. These so-called “magic numbers” will be discussed in Sect. 18.3

where the energies  $E_X$  each represent the total energy of the nuclide  $X$ , i.e., the sum of its rest mass and kinetic energy. If three of these nuclide masses are known, and if all of the kinetic energies have been measured, then the binding energy of the fourth nuclide can be determined.

The measurement of binding energies from nuclear reactions was mainly accomplished using low-energy (van de Graaff, cyclotron, betatron) accelerators. Following two decades of measurements in the 1950s and 1960s, the systematic errors of both methods, mass spectrometry and the energy balance of nuclear reactions, have been considerably reduced and both now provide high precision results which are consistent with each other. Figure 2.4 shows schematically the results of the binding energies per nucleon measured for stable nuclei. Nuclear reactions even provide mass determinations for nuclei which are so short-lived that they cannot be studied by mass spectroscopy.

## 2.3 Parametrisation of Binding Energies

Apart from the lightest elements, the binding energy per nucleon for most nuclei is about 8–9 MeV. Depending only weakly on the mass number, it can be described with the help of just a few parameters. The parametrisation of nuclear masses as a function of  $A$  and  $Z$ , which is known as the *Weizsäcker formula* or the *semi-empirical mass formula*, was first introduced in 1935 [3, 7]. It allows the calculation of the binding energy according to (2.2). The mass of an atom with  $Z$  protons and  $N$  neutrons is given by the following phenomenological formula:

$$\begin{aligned}
 M(A, Z) &= NM_n + ZM_p + Zm_e - a_v A + a_s A^{2/3} \\
 &+ a_c \frac{Z^2}{A^{1/3}} + a_a \frac{(N - Z)^2}{4A} + \frac{\delta}{A^{1/2}} \quad (2.8) \\
 &\text{with } N = A - Z.
 \end{aligned}$$

The exact values of the parameters  $a_v$ ,  $a_s$ ,  $a_c$ ,  $a_a$  and  $\delta$  depend on the range of masses for which they are optimised. One possible set of parameters is given below:

$$\begin{aligned}
 a_v &= 15.67 \text{ MeV}/c^2 \\
 a_s &= 17.23 \text{ MeV}/c^2 \\
 a_c &= 0.714 \text{ MeV}/c^2 \\
 a_a &= 93.15 \text{ MeV}/c^2 \\
 \delta &= \begin{cases} -11.2 \text{ MeV}/c^2 & \text{for even } Z \text{ and } N \text{ (even-even nuclei)} \\ 0 \text{ MeV}/c^2 & \text{for odd } A \text{ (odd-even nuclei)} \\ +11.2 \text{ MeV}/c^2 & \text{for odd } Z \text{ and } N \text{ (odd-odd nuclei)} \end{cases}
 \end{aligned}$$

To a great extent the mass of an atom is given by the sum of the masses of its constituents (protons, neutrons and electrons). The nuclear binding responsible for the deviation from this sum is reflected in five additional terms. The physical meaning of these five terms can be understood by recalling that the nuclear radius  $R$  and mass number  $A$  are connected by the relation

$$R \propto A^{1/3}. \quad (2.9)$$

The experimental proof of this relation and a quantitative determination of the coefficient of proportionality will be discussed in Sect. 5.4. The individual terms can be interpreted as follows:

**Volume term** This term, which dominates the binding energy, is proportional to the number of nucleons. Each nucleon in the interior of a (large) nucleus contributes an energy of about 16 MeV. From this we deduce that the nuclear force has a short range, corresponding approximately to the distance between two nucleons. This

phenomenon is called saturation. If each nucleon would interact with each of the other nucleons in the nucleus, the total binding energy would be proportional to  $A(A - 1)$  or approximately to  $A^2$ . Due to saturation, the central density of nucleons is the same for all nuclei, with few exceptions. The central density is

$$\rho_0 \approx 0.17 \text{ nucleons/fm}^3 = 3 \cdot 10^{17} \text{ kg/m}^3. \quad (2.10)$$

The average nuclear density, which can be deduced from the mass and radius (see (5.56)), is smaller ( $0.13 \text{ nucleons/fm}^3$ ). The average inter-nucleon distance in the nucleus is about 1.8 fm.

**Surface term** For nucleons at the surface of the nucleus, which are surrounded by fewer nucleons, the above binding energy is reduced. This contribution is proportional to the surface area of the nucleus ( $R^2$  or  $A^{2/3}$ ).

**Coulomb term** The electrical repulsive force acting between the protons in the nucleus further reduces the binding energy. This term is calculated to be

$$E_{\text{Coulomb}} = \frac{3}{5} \frac{Z(Z - 1) \alpha \hbar c}{R}. \quad (2.11)$$

This is approximately proportional to  $Z^2/A^{1/3}$ .

**Asymmetry term** As long as mass numbers are small, nuclei tend to have the same number of protons and neutrons. Heavier nuclei accumulate more and more neutrons, to partly compensate for the increasing Coulomb repulsion by increasing the nuclear force. This creates an asymmetry in the number of neutrons and protons. For, e.g.,  $^{208}\text{Pb}$  it amounts to  $N - Z = 44$ . The dependence of the nuclear force on the surplus of neutrons is described by the asymmetry term  $(N - Z)^2/(4A)$ . This shows that the symmetry decreases as the nuclear mass increases. We will further discuss this point in Sect. 18.1. The dependence of the above terms on  $A$  is shown in Fig. 2.5.

**Pairing term** A systematic study of nuclear masses shows that nuclei are more stable when they have an even number of protons and/or neutrons. This observation is interpreted as a coupling of protons and neutrons in pairs. The pairing energy depends on the mass number, as the overlap of the wave functions of these nucleons is smaller in larger nuclei. Empirically this is described by the term  $\delta \cdot A^{-1/2}$  in (2.8).

All in all, the global properties of the nuclear force are rather well described by the mass formula (2.8). However, the details of nuclear structure which we will discuss later (mainly in Chap. 18) are not accounted for by this formula.

The Weizsäcker formula is often mentioned in connection with the *liquid drop model*. In fact, the formula is based on some properties known from liquid drops: constant density, short-range forces, saturation, deformability and surface tension. An essential difference, however, is found in the mean free path of the particles. For molecules in liquid drops, this is far smaller than the size of the drop; but for nucleons in the nucleus, it is large. Therefore, the nucleus has to be treated as a



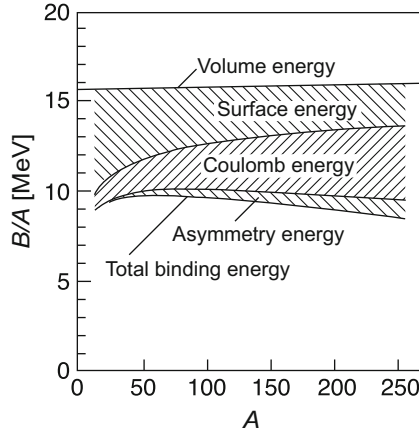


**Fig. 2.5** The different contributions to the binding energy per nucleon versus mass number  $A$ . The horizontal line at  $\approx 16$  MeV represents the contribution of the volume energy. This is reduced by the surface energy, the asymmetry energy and the Coulomb energy to the effective binding energy of  $\approx 8$  MeV (lower line). The contributions of the asymmetry and Coulomb terms increase rapidly with  $A$ , while the contribution of the surface term decreases

quantum liquid, and not as a classical one. At low excitation energies, the nucleus may be even more simply described as a Fermi gas; i.e., as a system of free particles only weakly interacting with each other. This model will be discussed in more detail in Sect. 18.1.

## 2.4 Charge Independence of the Nuclear Force and Isospin

Protons and neutrons not only have nearly equal masses, they also have similar nuclear interactions. This is particularly visible in the study of *mirror nuclei*. Mirror nuclei are pairs of isobars, in which the proton number of one of the nuclides equals the neutron number of the other and vice versa.

Figure 2.6 shows the lowest energy levels of the mirror nuclei  ${}^{14}_6\text{C}_8$  and  ${}^{14}_8\text{O}_6$ , together with those of  ${}^{14}_7\text{N}_7$ . The energy-level diagrams of  ${}^{14}_6\text{C}_8$  and  ${}^{14}_8\text{O}_6$  are very similar with respect to the quantum numbers  $J^P$  of the levels as well as with respect to the distances between them. The small differences and the global shift of the levels as a whole in  ${}^{14}_6\text{C}_8$ , as compared to  ${}^{14}_8\text{O}_6$  can be explained by differences in the Coulomb energy. Further examples of mirror nuclei will be discussed in Sect. 18.3 (Fig. 18.8). The energy levels of  ${}^{14}_6\text{C}_8$  and  ${}^{14}_8\text{O}_6$  are also found in the isobaric nucleus  ${}^{14}_7\text{N}_7$ . Other states in  ${}^{14}_7\text{N}_7$  have no analogy in the two neighbouring nuclei. We therefore can distinguish between triplet and singlet states.

These multiplets of states are reminiscent of the multiplets known from the coupling of angular momenta (spins). The symmetry between protons and neutrons

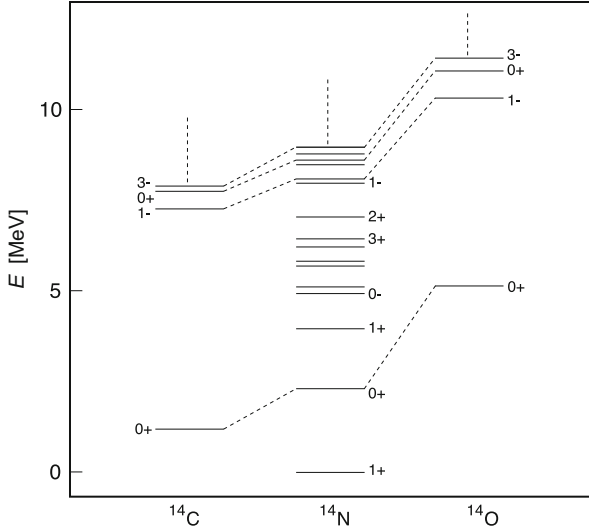


**Fig. 2.6** Low-lying energy levels of the three most stable  $A = 14$  isobars. Angular momentum  $J$  and parity  $P$  are shown for the most important levels. The analogous states of the three nuclei are joined by *dashed lines*. The zero of the energy scale is set to the ground state of  ${}^{14}_7\text{N}_7$

may therefore be described by a similar formalism, called *isospin*  $I$ . The proton and neutron are treated as two states of the nucleon which form a doublet ( $I = 1/2$ ).

$$\text{Nucleon : } I = 1/2 \quad \left\{ \begin{array}{l} \text{proton : } I_3 = +1/2 \\ \text{neutron : } I_3 = -1/2. \end{array} \right. \quad (2.12)$$

Formally, isospin is treated as a quantum mechanical angular momentum. For example, a proton-neutron pair can be in a state of total isospin 1 or 0. The third ( $z$ -) component of isospin is additive:

$$I_3^{\text{nucleus}} = \sum I_3^{\text{nucleon}} = \frac{Z-N}{2}. \quad (2.13)$$

This enables us to describe the appearance of similar states in Fig. 2.6:  ${}^{14}_6\text{C}_8$  and  ${}^{14}_8\text{O}_6$ , have respectively  $I_3 = -1$  and  $I_3 = +1$ . Therefore, their isospin cannot be less than  $I = 1$ . The states in these nuclei thus necessarily belong to a triplet of similar states in  ${}^{14}_6\text{C}_8$ ,  ${}^{14}_7\text{N}_7$  and  ${}^{14}_8\text{O}_6$ . The  $I_3$  component of the nuclide  ${}^{14}_7\text{N}_7$ , however, is 0. This nuclide can, therefore, have additional states with isospin  $I = 0$ .

Since  ${}^{14}_7\text{N}_7$  is the most stable  $A = 14$  isobar, its ground state is necessarily an isospin singlet since otherwise  ${}^{14}_6\text{C}_8$  would possess an analogous state, which, with less Coulomb repulsion, would be lower in energy and so more stable. States with  $I = 2$  are not shown in Fig. 2.6. Such states would have analogous states in  ${}^{14}_5\text{B}_9$  and in  ${}^{14}_9\text{F}_5$ . These nuclides, however, are very unstable (i.e., highly energetic), and

lie above the energy range of the diagram. The  $A = 14$  isobars are rather light nuclei in which the Coulomb energy is not strongly felt. In heavier nuclei, the influence of the Coulomb energy grows, which increasingly disturbs the isospin symmetry.

The concept of isospin is of great importance not only in nuclear physics, but also in particle physics. As we will see quarks, and particles composed of quarks, can be classified by isospin into isospin multiplets. In dynamical processes of the strong-interaction type, the isospin of the system is conserved.

## Problem

### 1. Isospin symmetry

One could naively imagine the three nucleons in the  ${}^3\text{H}$  and  ${}^3\text{He}$  nuclei as being rigid spheres. If one solely attributes the difference in the binding energies of these two nuclei to the electrostatic repulsion of the protons in  ${}^3\text{He}$ , how large must the separation of the protons be? (The maximal energy of the electron in the  $\beta^-$ -decay of  ${}^3\text{H}$  is 18.6 keV.)

## References

1. G. Audi et al., Nucl. Phys. **A729**, 3 (2003)
2. J.D. Barrow, J. Silk, Sci. Am. **242**, 98 (1980)
3. H.A. Bethe, Rev. Mod. Phys. **8**, 139 (1936)
4. G. Bressi et al., Phys. Rev. **A83**, 052101 (2011)
5. C. Brunnée, H. Voshage, *Massenspektroskopie* (Karl-Thiemig, Munich, 1964)
6. E.M. Burbidge et al., Rev. Mod. Phys. **29**, 547 (1957)
7. C.F. von Weizsäcker, Z. Phys **96**, 431 (1935)

# Chapter 3

## Nuclear Stability

Stable nuclei only occur in a very narrow band in the  $Z - N$  plane (Fig. 3.1). All other nuclei are unstable and decay spontaneously in various ways. Isobars with a large surplus of neutrons gain energy by converting a neutron into a proton. In the case of a surplus of protons, the inverse reaction may occur: i.e., the conversion of a proton into a neutron. These transformations are called  $\beta$ -decays and they are manifestations of the weak interaction. After dealing with the weak interaction in Chap. 10, we will discuss these decays in more detail in Sects. 16.6 and 18.6. In the present chapter, we will merely survey certain general properties, paying particular attention to the energy balance of  $\beta$ -decays.

Iron and nickel isotopes possess the maximum binding energy per nucleon and they are therefore the most stable nuclides. In heavier nuclei the binding energy is smaller because of the larger Coulomb repulsion. For still heavier masses nuclei become unstable to fission and decay spontaneously into two or more lighter nuclei should the mass of the original atom be larger than the sum of the masses of the daughter atoms. For a two-body decay, this condition has the form

$$M(A, Z) > M(A - A', Z - Z') + M(A', Z'). \quad (3.1)$$

This relation takes into account the conservation of the number of protons and neutrons. However, it does not give any information about the probability of such a decay. An isotope is said to be stable if its lifetime is considerably longer than the age of the solar system. We will not consider many-body decays any further since they are much rarer than two-body decays. It is very often the case that one of the daughter nuclei is a  ${}^4\text{He}$  nucleus, i.e.,  $A' = 4$ ,  $Z' = 2$ . This decay mode is called  $\alpha$ -decay, and the Helium nucleus is called an  $\alpha$ -particle. If a heavy nucleus decays into two similarly massive daughter nuclei we speak of *spontaneous fission*. The probability of spontaneous fission exceeds that of  $\alpha$ -decay only for nuclei with  $Z \gtrsim 110$  and is a fairly unimportant process for the naturally occurring heavy elements.

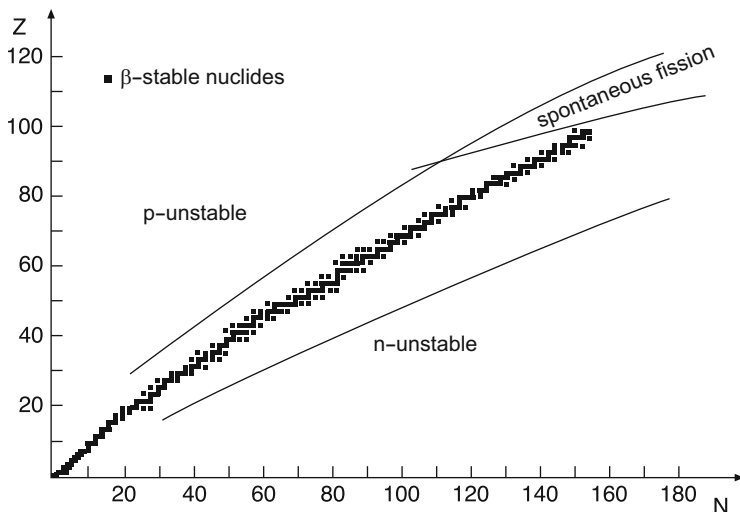


Fig. 3.1 Beta-stable nuclei in the  $Z - N$  plane (From [1])

**Decay constants** The probability per unit time for a radioactive nucleus to decay is known as the *decay constant*  $\lambda$ . It is related to the *lifetime*  $\tau$  and the *half-life*  $t_{1/2}$  by

$$\tau = \frac{1}{\lambda} \quad \text{and} \quad t_{1/2} = \frac{\ln 2}{\lambda}. \quad (3.2)$$

The measurement of the decay constants of radioactive nuclei is based upon finding the *activity* (the number of decays per unit time)

$$A = -\frac{dN}{dt} = \lambda N, \quad (3.3)$$

where  $N$  is the number of radioactive nuclei in the sample. The unit of activity is defined to be

$$1 \text{ Bq [Becquerel]} = 1 \text{ decay/s}. \quad (3.4)$$

For short-lived nuclides, the fall-off over time of the activity

$$A(t) = \lambda N(t) = \lambda N_0 e^{-\lambda t}, \quad \text{where } N_0 = N(t = 0), \quad (3.5)$$

may be measured using fast electronic counters. This method of measuring is not suitable for lifetimes larger than about a year. For longer-lived nuclei both the number of nuclei in the sample and the activity must be measured in order to obtain the decay constant from (3.3).

### 3.1 Beta Decay

Let us consider nuclei with equal mass number  $A$  (isobars). Equation (2.8) can be transformed into

$$M(A, Z) = \alpha \cdot A - \beta \cdot Z + \gamma \cdot Z^2 + \frac{\delta}{A^{1/2}}, \quad (3.6)$$

where

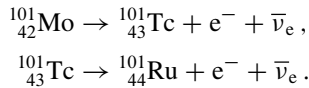
$$\begin{aligned} \alpha &= M_n - a_v + a_s A^{-1/3} + \frac{a_a}{4}, \\ \beta &= a_a + (M_n - M_p - m_e), \\ \gamma &= \frac{a_a}{A} + \frac{a_c}{A^{1/3}}, \\ \delta &= \text{as in (2.8)}. \end{aligned}$$

The nuclear mass is now a quadratic function of the charge number  $Z$ . A plot of such nuclear masses, for constant mass number  $A$ , as a function of  $Z$  yields a parabola for odd  $A$ . For even  $A$ , the masses of the even-even and the odd-odd nuclei are found to lie on two vertically shifted parabolas. The odd-odd parabola lies at twice the pairing energy ( $2\delta/\sqrt{A}$ ) above the even-even one. The minimum of the parabolas is found at  $Z = \beta/2\gamma$ . The nucleus with the smallest mass in an isobaric spectrum is stable with respect to  $\beta$ -decay.

**Beta decay in odd mass nuclei** In what follows we wish to discuss the different kinds of  $\beta$ -decay, using the example of the  $A = 101$  isobars. For this mass number, the parabola minimum is at the isobar  $^{101}\text{Ru}$  which has  $Z = 44$ . Isobars with more neutrons, such as  $^{101}_{42}\text{Mo}$  and  $^{101}_{43}\text{Tc}$ , decay through the conversion



The charge number of the daughter nucleus is one unit larger than that of the parent nucleus (Fig. 3.2). An electron and an electron-antineutrino are also produced:

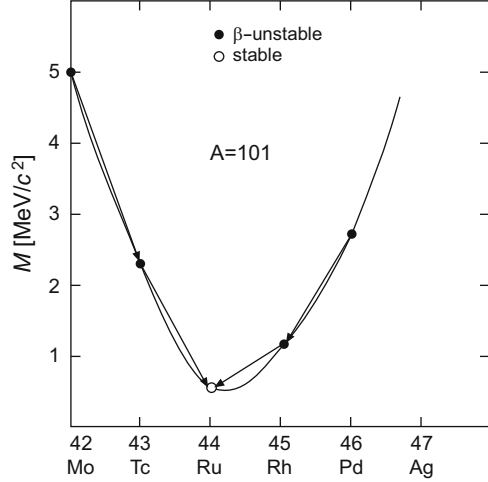


Historically such decays where a negative electron is emitted are called  $\beta^-$ -decays. Energetically,  $\beta^-$ -decay is possible whenever the mass of the daughter atom  $M(A, Z + 1)$  is smaller than the mass of its isobaric neighbour:

$$M(A, Z) > M(A, Z + 1). \quad (3.8)$$

We consider here the mass of the whole atom and not just that of the nucleus alone and so the rest mass of the electron created in the decay is automatically taken into

**Fig. 3.2** Mass parabola of the  $A = 101$  isobars (From [4]). Possible  $\beta$ -decays are shown by *arrows*. The abscissa co-ordinate is the atomic number,  $Z$ . The zero point of the mass scale was chosen arbitrarily

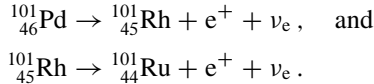


account. The tiny mass of the (anti-)neutrino ( $<2 \text{ eV}/c^2$ ) [3] is negligible in the mass balance.

Isobars with a proton excess, compared to  $^{101}_{44}\text{Ru}$ , decay through proton conversion



The stable isobar  $^{101}_{44}\text{Ru}$  is eventually produced via



Such decays are called  $\beta^+$ -decays. Since the mass of a free neutron is larger than the proton mass, the process (3.9) is only possible inside a nucleus. By contrast, neutrons outside nuclei can and do decay via (3.7). Energetically,  $\beta^+$ -decay is possible whenever the following relationship between the masses  $M(A, Z)$  and  $M(A, Z - 1)$  (of the parent and daughter atoms respectively) is satisfied:

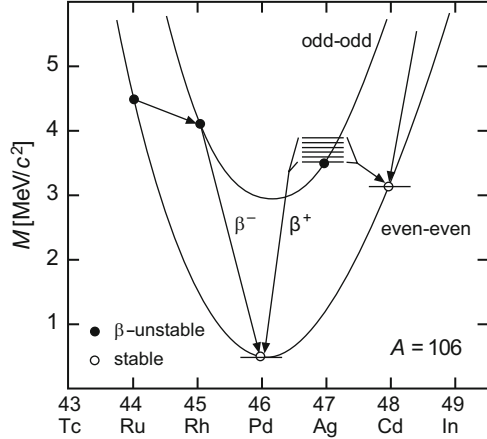
$$M(A, Z) > M(A, Z - 1) + 2m_e . \quad (3.10)$$

This relationship takes into account the creation of a positron and the existence of an excess electron in the parent atom.

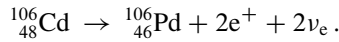
**Beta decay in even nuclei** Even mass-number isobars form, as we described above, two separate (one for even-even and one for odd-odd nuclei) parabolas which are split by an amount equal to twice the pairing energy.

Often there is more than one  $\beta$ -stable isobar, especially in the range  $A > 70$ . Let us consider the example of the nuclides with  $A = 106$  (Fig. 3.3). The even-even

**Fig. 3.3** Mass parabolas of the  $A = 106$ -isobars (From [4]). Possible  $\beta$ -decays are indicated by arrows. The abscissa coordinate is the charge number  $Z$ . The zero point of the mass scale was chosen arbitrarily



$^{106}_{46}\text{Pd}$  and  $^{106}_{48}\text{Cd}$  isobars are on the lower parabola, and  $^{106}_{46}\text{Pd}$  is the stablest.  $^{106}_{48}\text{Cd}$  is  $\beta$ -stable, since its two odd-odd neighbours both lie above it. The conversion of  $^{106}_{48}\text{Cd}$  is thus only possible through a double  $\beta$ -decay into  $^{106}_{46}\text{Pd}$ :



The probability for such a process is so small that  $^{106}_{48}\text{Cd}$  may be considered to be a stable nuclide. Details of double  $\beta$ -decay will be discussed in Sect. 18.7.

Odd-odd nuclei always have at least one more strongly bound even-even neighbour nucleus in the isobaric spectrum. They are therefore unstable. The only exceptions to this rule are the very light nuclei  $^2_1\text{H}$ ,  $^6_3\text{Li}$ ,  $^{10}_5\text{B}$  and  $^{14}_7\text{N}$ , which are stable to  $\beta$ -decay, since the increase in the asymmetry energy would exceed the decrease in pairing energy. Some odd-odd nuclei can undergo both  $\beta^-$ -decay and  $\beta^+$ -decay. Well-known examples of this are  $^{40}_{19}\text{K}$  (Fig. 3.4) and  $^{64}_{29}\text{Cu}$ .

**Electron capture** Another possible decay process is the capture of an electron from the cloud surrounding the atom. There is a finite probability of finding such an electron inside the nucleus. In such circumstances it can combine with a proton to form a neutron and a neutrino in the following way:



This reaction occurs mainly in heavy nuclei where the nuclear radii are larger and the electronic orbits are more compact. Usually the electrons that are captured are from the innermost (the “K”) shell since such K-electrons are closest to the nucleus and their radial wave function has a maximum at the centre of the nucleus. Since an electron is missing from the K-shell after such a *K-capture*, electrons from higher energy levels will successively cascade downwards and in so doing they emit characteristic X-rays.



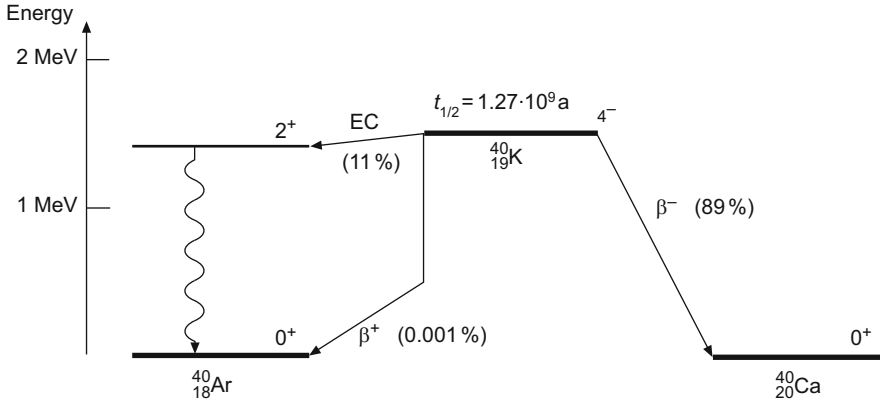


**Fig. 3.4** The  $\beta$ -decay of  $^{40}\text{K}$ . In this nuclear conversion,  $\beta^-$ - and  $\beta^+$ -decay as well as electron capture (EC) compete with each other. The relative frequency of these decays is given in parentheses. The bent arrow in  $\beta^+$ -decay indicates that the production of an  $e^+$  and the presence of the surplus electron in the  $^{40}\text{Ar}$  atom requires 1.022 MeV, and the remainder is carried off as kinetic energy by the positron and the neutrino. The excited state of  $^{40}\text{Ar}$  produced in the electron capture reaction decays by photon emission into its ground state

Electron-capture reactions compete with  $\beta^+$ -decay. The following condition is a consequence of energy conservation

$$M(A, Z) > M(A, Z - 1) + \varepsilon, \quad (3.12)$$

where  $\varepsilon$  is the excitation energy of the atomic shell of the daughter nucleus (electron capture always leads to a hole in the electron shell). This process has, compared to  $\beta^+$ -decay, more kinetic energy ( $2m_e c^2 - \varepsilon$  more) available to it and so there are some cases where the mass difference between the initial and final atoms is too small for conversion to proceed via  $\beta^+$ -decay and yet K-capture can take place.

**Lifetimes** The lifetimes  $\tau$  of  $\beta$ -unstable nuclei vary between a few ms and  $10^{16}$  years. They strongly depend upon both the energy  $E$  which is released ( $1/\tau \propto E^5$ ) and upon the nuclear properties of the mother and daughter nuclei. The decay of a free neutron into a proton, an electron and an antineutrino releases 0.78 MeV and this particle has a lifetime of  $\tau = 880.1 \pm 1.1$  s [3]. No two neighbouring isobars are known to be  $\beta$ -stable.<sup>1</sup>

A well-known example of a long-lived  $\beta$ -emitter is the nuclide  $^{40}\text{K}$ . It transforms into other isobars by both  $\beta^-$ - and  $\beta^+$ -decay. Electron capture in  $^{40}\text{K}$  also competes

<sup>1</sup>In some cases, however, one of two neighbouring isobars is stable and the other is extremely long-lived. The most common isotopes of indium ( $^{115}\text{In}$ , 96 %) and rhenium ( $^{187}\text{Re}$ , 63 %)  $\beta^-$ -decay into stable nuclei ( $^{115}\text{Sn}$  and  $^{187}\text{Os}$ ), but they are so long-lived ( $\tau = 3 \cdot 10^{14}$  years and  $\tau = 3 \cdot 10^{11}$  years respectively) that they may also be considered stable.

here with  $\beta^+$ -decay. The stable daughter nuclei are  $^{40}\text{Ar}$  and  $^{40}\text{Ca}$  respectively, which is a case of two stable nuclei having the same mass number  $A$  (Fig. 3.4).

The  $^{40}\text{K}$  nuclide was chosen here because it contributes considerably to the radiation exposure of human beings and other biological systems. Potassium is an essential element: for example, signal transmission in the nervous system functions by an exchange of potassium ions. The fraction of radioactive  $^{40}\text{K}$  in natural potassium is 0.01 %, and the decay of  $^{40}\text{K}$  in the human body contributes about 16 % of the total natural radiation which we are exposed to.

## 3.2 Alpha Decay

Protons and neutrons have binding energies, even in heavy nuclei, of about 8 MeV (Fig. 2.4) and cannot generally escape from the nucleus. In many cases, however, it is energetically possible for a bound system of a group of nucleons to be emitted, since the binding energy of this system increases the total energy available to the process. The probability for such a system to be formed in a nucleus decreases rapidly with the number of nucleons required. In practice the most significant decay process is the emission of a  $^4\text{He}$  nucleus; i.e., a system of 2 protons and 2 neutrons. Contrary to systems of 2 or 3 nucleons, this so-called  $\alpha$ -particle is extraordinarily strongly bound – 7 MeV/nucleon (cf. Fig. 2.4). Such decays are called  $\alpha$ -decays.

Figure 3.5 shows the potential energy of an  $\alpha$ -particle as a function of its separation from the centre of the nucleus. Beyond the nuclear force range, the  $\alpha$ -particle feels only the Coulomb potential  $V_C(r) = 2(Z-2)\alpha\hbar c/r$ , which increases closer to the nucleus. Within the nuclear force range a strongly attractive nuclear potential prevails. Its strength is characterised by the depth of the potential well. Since we are considering  $\alpha$ -particles which are energetically allowed to escape from the nuclear potential, the total energy of this  $\alpha$ -particle is positive. This energy is released in the decay.

The range of lifetimes for the  $\alpha$ -decay of heavy nuclei is extremely large. Experimentally, lifetimes have been measured between 10 ns and  $10^{17}$  years. These

**Fig. 3.5** Potential energy of an  $\alpha$ -particle as a function of its separation from the centre of the nucleus. The probability that it tunnels through the Coulomb barrier can be calculated as the superposition of tunnelling processes through thin potential walls of thickness  $\Delta r$  (cf. Fig. 3.6)

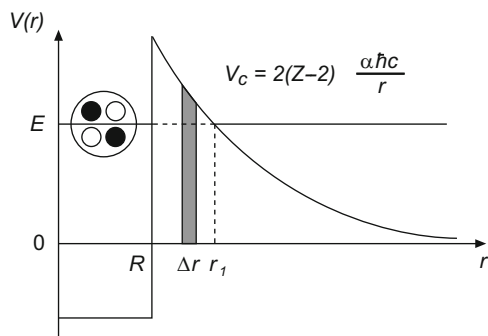
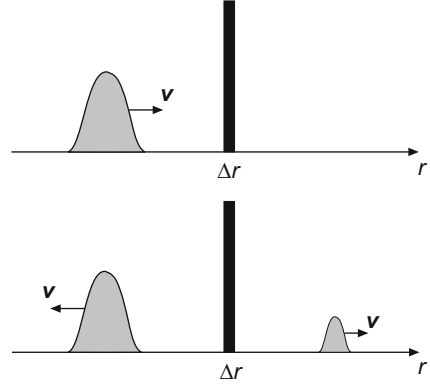


**Fig. 3.6** Illustration of the tunnelling probability of a wave packet with energy  $E$  and velocity  $v$  faced with a potential barrier of height  $V$  and thickness  $\Delta r$



lifetimes can be calculated in quantum mechanics by treating the  $\alpha$ -particle as a wave packet. The probability for the  $\alpha$ -particle to escape from the nucleus is given by the probability for its penetrating the *Coulomb barrier* (the tunnel effect). If we divide the Coulomb barrier into thin potential walls and look at the probability of the  $\alpha$ -particle tunnelling through one of these (Fig. 3.6), then the transmission  $T$  is given by

$$T \approx e^{-2\kappa\Delta r}, \quad \text{where } \kappa = \sqrt{2m|E - V|}/\hbar, \quad (3.13)$$

and  $\Delta r$  is the thickness of the barrier and  $V$  is its height.  $E$  is the energy of the  $\alpha$ -particle. A Coulomb barrier can be thought of as a barrier composed of a large number of thin potential walls of different heights. The transmission can be described accordingly by

$$T = e^{-2G}. \quad (3.14)$$

The *Gamow factor*  $G$  can be approximated by the integral [4]

$$G = \frac{1}{\hbar} \int_R^{r_1} \sqrt{2m|E - V|} dr \approx \frac{\pi \cdot 2 \cdot (Z - 2) \cdot \alpha}{\beta}, \quad (3.15)$$

where  $\beta = v/c$  is the velocity of the outgoing  $\alpha$ -particle and  $R$  is the nuclear radius.

The probability per unit time  $\lambda$  for an  $\alpha$ -particle to escape from the nucleus is therefore proportional to: the probability  $w(\alpha)$  of finding such an  $\alpha$ -particle in the nucleus, the number of collisions ( $\propto v_0/2R$ ) of the  $\alpha$ -particle with the barrier and the transmission probability:

$$\lambda = w(\alpha) \frac{v_0}{2R} e^{-2G}, \quad (3.16)$$

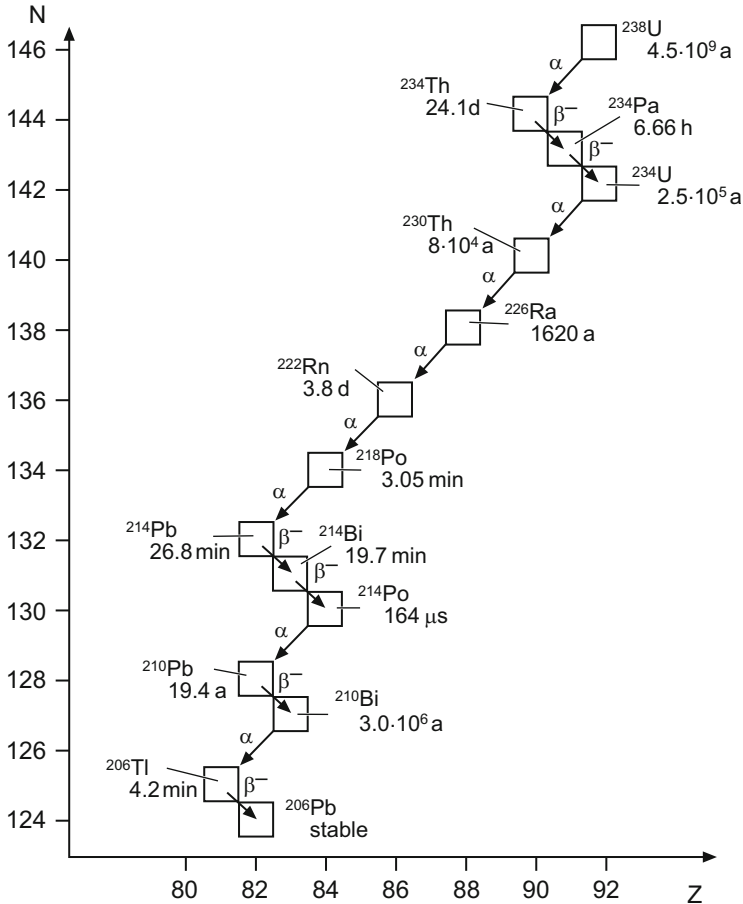


**Fig. 3.7** Illustration of the  $^{238}\text{U}$  decay chain in the  $N$ - $Z$  plane. The half-life of each of the nuclides is given together with its decay mode

where  $v_0$  is the velocity of the  $\alpha$ -particle in the nucleus ( $v_0 \approx 0.1c$ ). The large variation in the lifetimes is explained by the Gamow factor in the exponent: since  $G \propto Z/\beta \propto Z/\sqrt{E}$ , small differences in the energy of the  $\alpha$ -particle have a strong effect on the lifetime.

Most  $\alpha$ -emitting nuclei are heavier than lead. For lighter nuclei with  $A \lesssim 140$ ,  $\alpha$ -decay is energetically possible, but the energy released is extremely small. Therefore, their nuclear lifetimes are so long that decays are usually not observable.

An example of an  $\alpha$ -unstable nuclide with a long lifetime,  $^{238}\text{U}$ , is shown in Fig. 3.7. Since uranium compounds are common in granite, uranium and its radioactive daughters are a part of the stone walls of buildings. They therefore contribute to the environmental radiation background. This is particularly true of

the inert gas  $^{222}\text{Rn}$ , which escapes from the walls and is inhaled into the lungs. The  $\alpha$ -decay of  $^{222}\text{Rn}$  is responsible for about 40% of the average natural human radiation exposure.

### 3.3 Nuclear Fission

**Spontaneous fission** The largest binding energy per nucleon is found in those nuclei in the region of  $^{56}\text{Fe}$ . For heavier nuclei, it decreases as the nuclear mass increases (Fig. 2.4). A nucleus with  $Z > 40$  can thus, in principle, split into two lighter nuclei. The potential barrier which must be tunnelled through is, however, so large that such spontaneous fission reactions are generally speaking extremely unlikely.

The lightest nuclides where the probability of spontaneous fission is comparable to that of  $\alpha$ -decay are certain uranium isotopes. The shape of the fission barrier is shown in Fig. 3.8.

It is interesting to find the charge number  $Z$  above which nuclei become fission unstable, i.e., the point from which the mutual Coulombic repulsion of the protons outweighs the attractive nature of the nuclear force. An estimate can be obtained by considering the surface and the Coulomb energies during the fission deformation. As the nucleus is deformed the surface energy increases, while the Coulomb energy decreases. If the deformation leads to an energetically more favourable configuration, the nucleus is unstable. Quantitatively, this can be calculated as follows: keeping the volume of the nucleus constant, we deform its spherical shape into an ellipsoid with axes  $a = R(1 + \varepsilon)$  and  $b = R(1 + \varepsilon)^{-1/2} \approx R(1 - \varepsilon/2)$  (Fig. 3.9).

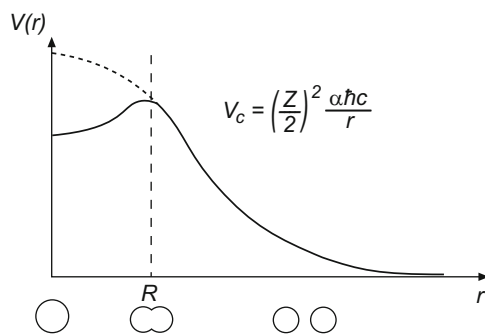


**Fig. 3.8** Potential energy during different stages of a fission reaction. A nucleus with charge  $Z$  decays spontaneously into two daughter nuclei. The *solid line* corresponds to the shape of the potential in the parent nucleus. The height of the barrier for fission determines the probability of spontaneous fission. The fission barrier disappears for nuclei with  $Z^2/A \gtrsim 48$  and the shape of the potential then corresponds to the *dashed line*

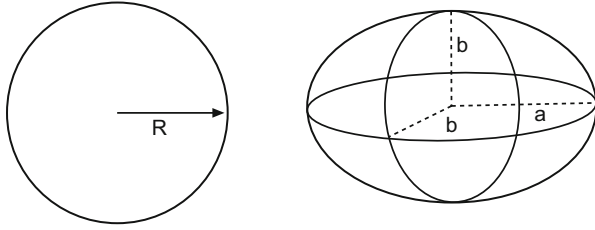


**Fig. 3.9** Deformation of a heavy nucleus. For a constant volume  $V$  ( $V = 4\pi R^3/3 = 4\pi ab^2/3$ ), the surface energy of the nucleus increases and its Coulomb energy decreases

The surface energy then has the form

$$E_s = a_s A^{2/3} \left( 1 + \frac{2}{5} \varepsilon^2 + \dots \right), \quad (3.17)$$

while the Coulomb energy is given by

$$E_c = a_c Z^2 A^{-1/3} \left( 1 - \frac{1}{5} \varepsilon^2 + \dots \right). \quad (3.18)$$

Hence a deformation  $\varepsilon$  changes the total energy by

$$\Delta E = \frac{\varepsilon^2}{5} (2a_s A^{2/3} - a_c Z^2 A^{-1/3}). \quad (3.19)$$

If  $\Delta E$  is negative, a deformation is energetically favoured. The fission barrier disappears for

$$\frac{Z^2}{A} \geq \frac{2a_s}{a_c} \approx 48. \quad (3.20)$$

This is the case for nuclei with  $Z > 114$  and  $A > 270$ .

**Induced fission** For very heavy nuclei ( $Z \approx 92$ ) the fission barrier is only about 6 MeV. This energy may be supplied if one uses a flow of low energy neutrons to induce neutron capture reactions. These push the nucleus into an excited state above the fission barrier and it splits up. This process is known as *induced nuclear fission*.

Neutron capture by nuclei with an odd neutron number releases not just some binding energy but also a pairing energy. This small extra contribution to the energy balance makes a decisive difference to nuclide fission properties: in neutron capture by  $^{238}\text{U}$ , for example, 4.9 MeV binding energy is released, which is below the threshold energy of 5.5 MeV for nuclear fission of  $^{239}\text{U}$ . Neutron capture by  $^{238}\text{U}$  can therefore only lead to immediate nuclear fission if the neutron possesses a kinetic

energy at least as large as this difference (“fast neutrons”). On top of this the reaction probability is proportional to  $v^{-1}$ , where  $v$  is the velocity of the neutron (4.21), and so it is very small. By contrast neutron capture in  $^{235}\text{U}$  releases 6.4 MeV and the fission barrier of  $^{236}\text{U}$  is just 5.5 MeV. Thus fission may be induced in  $^{235}\text{U}$  with the help of low-energy (thermal) neutrons. This is exploited in nuclear reactors and nuclear weapons. Similarly both  $^{233}\text{Th}$  and  $^{239}\text{Pu}$  are suitable fission materials.

### 3.4 Decay of Excited Nuclear States

Nuclei usually have many excited states. Most of the lowest-lying states are understood theoretically, at least in a qualitative way as will be discussed in more detail in Chaps. 18 and 19.

Figure 3.10 schematically shows the energy levels of an even-even nucleus with  $A \approx 100$ . Above the ground state, individual discrete levels with specific  $J^P$  quantum numbers can be seen. The excitation of even-even nuclei generally corresponds to the break-up of nucleon pairs, which requires about 1–2 MeV. Even-even nuclei with  $A \gtrsim 40$ , therefore, rarely possess excitations below 2 MeV.<sup>2</sup> In odd-even and odd-odd nuclei, the number of low-energy states (with excitation energies of a few 100 keV) is considerably larger.

**Electromagnetic decays** Low lying excited nuclear states usually decay by emitting electromagnetic radiation. This can be described in a series expansion as a superposition of different multiplicities each with its characteristic angular distribution. Electric dipole, quadrupole, octupole radiation etc. are denoted by E1, E2, E3, etc. Similarly, the corresponding magnetic multipoles are denoted by M1, M2, M3 etc. Conservation of angular momentum and parity determine which multiplicities are possible in a transition. A photon of multipolarity  $E\ell$  has angular momentum  $\ell$  and parity  $(-1)^\ell$ , a photon of multipolarity  $M\ell$  has angular momentum  $\ell$  and parity  $(-1)^{(\ell+1)}$  (Table 3.1). In a transition  $J_i \rightarrow J_f$ , conservation of angular momentum means that the triangle inequality  $|J_i - J_f| \leq \ell \leq J_i + J_f$  must be satisfied.

**Table 3.1** Selection rules for some electromagnetic transitions

Multi-polarity	Electric			Magnetic		
	$E\ell$	$ \Delta J $	$\Delta P$	$M\ell$	$ \Delta J $	$\Delta P$
Dipole	E1	1	–	M1	1	+
Quadrupole	E2	2	+	M2	2	–
Octupole	E3	3	–	M3	3	+

<sup>2</sup>Collective states in deformed nuclei are an exception to this: they cannot be understood as single particle excitations (Chap. 19).

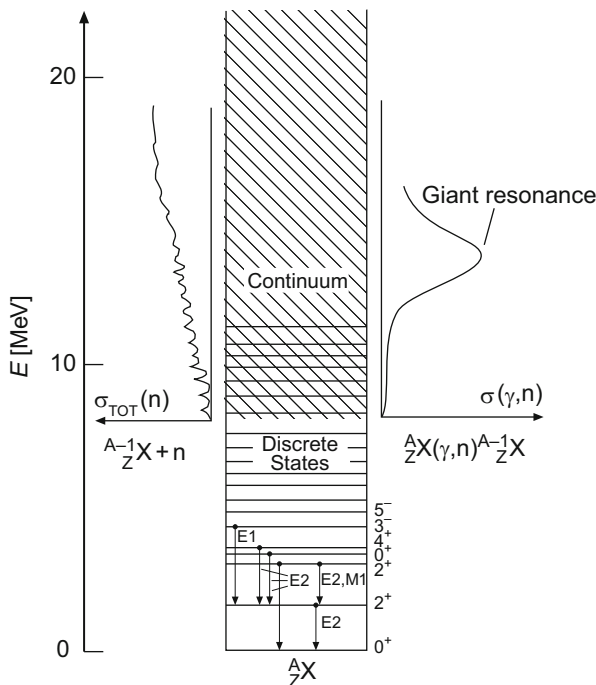


**Fig. 3.10** Sketch of typical nuclear energy levels. The example shows an even-even nucleus whose ground state has the quantum numbers  $0^+$ . To the left the total cross-section for the reaction of the nucleus  $A-1_Z X$  with neutrons (elastic scattering, inelastic scattering, capture) is shown; to the right the total cross-section for  $\gamma$ -induced neutron emission  $A_Z X + \gamma \rightarrow A-1_Z X + n$

The lifetime of a state strongly depends upon the multipolarity of the  $\gamma$ -transitions by which it can decay. The lower the multipolarity, the larger the transition probability. A magnetic transition  $M\ell$  has approximately the same probability as an electric  $E(\ell + 1)$  transition. A transition  $3^+ \rightarrow 1^+$ , for example, is in principle a mixture of E2, M3, and E4, but will be easily dominated by the E2 contribution. A  $3^+ \rightarrow 2^+$  transition will usually consist of an M1/E2 mixture, even though M3, E4, and M5 transitions are also possible. In a series of excited states  $0^+$ ,  $2^+$ ,  $4^+$ , the most probable decay is by a cascade of E2-transitions  $4^+ \rightarrow 2^+ \rightarrow 0^+$ , and not by a single  $4^+ \rightarrow 0^+$  E4-transition. The lifetime of a state and the angular distribution of the electromagnetic radiation which it emits are signatures for the multipolarity of the transitions, which in turn betray the spin and parity of the nuclear levels. The decay probability also strongly depends upon the energy. For radiation of multipolarity  $\ell$  it is proportional to  $E_\gamma^{2\ell+1}$  (cf. Sect. 19.1).

The excitation energy of a nucleus may also be transferred to an electron in the atomic shell. This process is called *internal conversion*. It is most important in transitions for which  $\gamma$ -emission is suppressed (high multipolarity, low energy) and the nucleus is heavy (high probability of the electron being inside the nucleus).



$0^+ \rightarrow 0^+$  transitions cannot proceed through photon emission. If a nucleus is in an excited  $0^+$ -state, and all its lower lying levels also have  $0^+$  quantum numbers (e.g. in  $^{16}\text{O}$  or  $^{40}\text{Ca}$ , cf. Fig. 19.6), then this state can only decay in a different way: by internal conversion, by emission of 2 photons or by the emission of an  $e^+e^-$ -pair, if this last is energetically possible. Parity conservation does not permit internal conversion transitions between two levels with  $J = 0$  and opposite parity.

The lifetime of excited nuclear states typically varies between  $10^{-9}$  and  $10^{-15}$  s, which corresponds to a state width of less than 1 eV. States which can only decay by low energy and high multipolarity transitions have considerably longer lifetimes. They are called *isomers* and are designated by an “m” superscript on the symbol of the element. An extreme example is the second excited state of  $^{110}\text{Ag}$ , whose quantum numbers are  $J^P = 6^+$  and excitation energy is 117.7 keV. It relaxes via an M4-transition into the first excited state (1.3 keV;  $2^-$ ) since a decay directly into the ground state ( $1^+$ ) is even more improbable. The half-life of  $^{110}\text{Ag}^m$  is extremely long ( $t_{1/2} = 235$  days) [2].

**Continuum states** Most nuclei have a binding energy per nucleon of about 8 MeV (Fig. 2.4). This is approximately the energy required to separate a single nucleon from the nucleus (*separation energy*). States with excitation energies above this value can therefore emit single nucleons. The emitted nucleons are primarily neutrons since they are not hindered by the Coulomb threshold. Such a strong interaction process is clearly preferred to  $\gamma$ -emission.

The excitation spectrum above the threshold for particle emission is called the *continuum*, just as in atomic physics. Within this continuum there are also discrete, quasi-bound states. States below this threshold decay only by (relatively slow)  $\gamma$ -emission and are, therefore, very narrow. But for excitation energies above the particle threshold, the lifetimes of the states decrease dramatically, and their widths increase. The density of states increases approximately exponentially with the excitation energy. At higher excitation energies, the states therefore start to overlap, and states with the same quantum numbers can begin to mix.

The continuum can be especially effectively investigated by measuring the cross-sections of neutron capture and neutron scattering. Even at high excitation energies, some narrow states can be identified. These are states with exotic quantum numbers (high spin) which therefore cannot mix with neighbouring states.

Figure 3.10 shows schematically the cross-sections for neutron capture and  $\gamma$ -induced neutron emission (*nuclear photoelectric effect*). A broad resonance is observed, the *giant dipole resonance*, which will be interpreted in Sect. 19.2.

## Problems

### 1. Alpha decay

The  $\alpha$ -decay of a  $^{238}\text{Pu}$  ( $\tau = 127$  years) nuclide into a long-lived  $^{234}\text{U}$  ( $\tau = 3.5 \cdot 10^5$  years) daughter nucleus releases 5.49 MeV kinetic energy. The heat so

produced can be converted into useful electricity by radio-thermal generators (RTG's). The *Voyager 2* space probe, which was launched on the 20.8.1977, flew past four planets, including Saturn which it reached on the 26.8.1981. Saturn's separation from the Sun is 9.5 AU; 1 AU = separation of the Earth from the Sun.

- (a) How much plutonium would an RTG on *Voyager 2* with 5.5 % efficiency have to carry so as to deliver at least 395 W electric power when the probe flies past Saturn?
- (b) How much electric power would then be available at Neptune (24.8.1989; 30.1 AU separation)?
- (c) To compare: the largest ever "solar paddles" used in space were those of the space laboratory *Skylab* which would have produced 10.5 kW from an area of 730 m<sup>2</sup> if they had not been damaged at launch. What area of solar cells would *Voyager 2* have needed?

## 2. Radioactivity

Naturally occurring uranium is a mixture of the <sup>238</sup>U (99.28 %) and <sup>235</sup>U (0.72 %) isotopes.

- (a) How old must the material of the solar system be if one assumes that at its creation both isotopes were present in equal quantities? How do you interpret this result? The lifetime of <sup>235</sup>U is  $\tau = 1.015 \cdot 10^9$  years. For the lifetime of <sup>238</sup>U use the data in Fig. 3.7.
- (b) How much of the <sup>238</sup>U has decayed since the formation of the Earth's crust 2.5·10<sup>9</sup> years ago?
- (c) How much energy per uranium nucleus is set free in the decay chain <sup>238</sup>U → <sup>206</sup>Pb? A small proportion of <sup>238</sup>U spontaneously splits into, e.g., <sup>142</sup>Xe and <sup>96</sup>Sr.

## 3. Radon activity

After a lecture theatre whose walls, floor and ceiling are made of concrete (10 × 10 × 4 m<sup>3</sup>) has not been aired for several days, a specific activity *A* from <sup>222</sup>Rn of 100 Bq/m<sup>3</sup> is measured.

- (a) Calculate the activity of <sup>222</sup>Rn as a function of the lifetimes of the parent and daughter nuclei.
- (b) How high is the concentration of <sup>238</sup>U in the concrete if the effective thickness from which the <sup>222</sup>Rn decay product can diffuse is 1.5 cm?

#### 4. Mass formula

Isaac Asimov in his novel *The Gods Themselves* describes a universe where the stablest nuclide with  $A = 186$  is not  ${}_{74}^{186}\text{W}$  but rather  ${}_{94}^{186}\text{Pu}$ . This is claimed to be a consequence of the ratio of the strengths of the strong and electromagnetic interactions being different to that in our universe. Assume that only the electromagnetic coupling constant  $\alpha$  differs and that both the strong interaction and the nucleon masses are unchanged. How large must  $\alpha$  be in order that  ${}_{82}^{186}\text{Pb}$ ,  ${}_{88}^{186}\text{Ra}$  and  ${}_{94}^{186}\text{Pu}$  are stable?

#### 5. Alpha decay

The binding energy of an  $\alpha$  particle is 28.3 MeV. Estimate, using the mass formula (2.8), from which mass number  $A$  onwards  $\alpha$ -decay is energetically allowed for all nuclei.

#### 6. Quantum numbers

An even-even nucleus in the ground state decays by  $\alpha$ -emission. Which  $J^P$  states are available to the daughter nucleus?

## References

1. A. Bohr, B.R. Mottelson, *Nuclear Structure* (Benjamin, New York, 1969)
2. C.M. Lederer, V.S. Shirley, *Table of Isotopes*, 7th edn. (Wiley, New York, 1978)
3. Particle Data Group, J. Beringer et al., *Review of particle properties*. Phys. Rev. D **86**, 010001 (2012)
4. E. Segrè, *Nuclei and Particles* (Benjamin, New York, 1977)

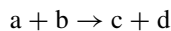
# Chapter 4

## Scattering

### 4.1 General Observations About Scattering Processes

Scattering experiments are an important tool of nuclear and particle physics. They are used both to study details of the interactions between different particles and to obtain information about the internal structure of atomic nuclei and their constituents. These experiments will therefore be discussed at length in the following.

In a typical scattering experiment, the object to be studied (the *target*) is bombarded with a beam of particles with (mostly) well-defined energy. Occasionally, a reaction of the form



between the projectile and the target occurs. Here,  $a$  and  $b$  denote the beam- and target particles, and  $c$  and  $d$  denote the products of the reaction. In inelastic reactions, the number of the reaction products may be larger than two. The rate, the energies and masses of the reaction products and their angles relative to the beam direction may be determined with suitable systems of detectors.

It is nowadays possible to produce beams of a broad variety of particles (electrons, protons, neutrons, heavy ions,...). The beam energies available vary between  $10^{-3}$  eV for “cold” neutrons up to several  $10^{12}$  eV for protons. It is even possible to produce beams of secondary particles which themselves have been produced in high energy reactions. Some such beams are very short-lived, such as muons,  $\pi$ - or K-mesons, or hyperons ( $\Sigma^{\pm}$ ,  $\Xi^{-}$ ,  $\Omega^{-}$ ).

Solid, liquid or gaseous targets may be used as scattering material or, in storage ring experiments, another beam of particles may serve as the target. Examples of this last are the electron-positron storage ring LEP (Large Electron Positron collider) at

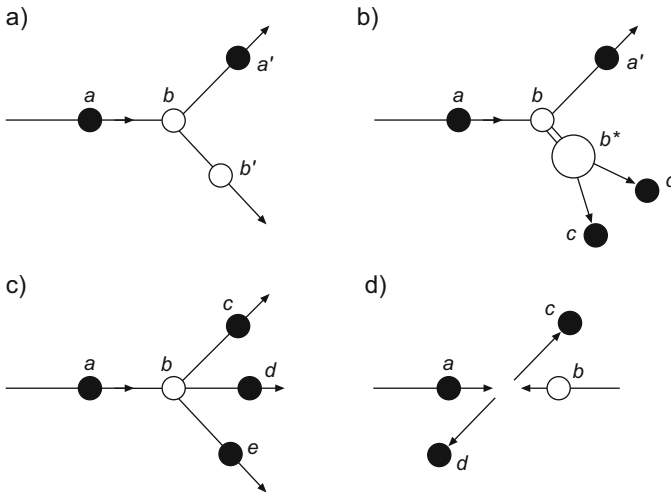
CERN<sup>1</sup> in Geneva (maximum beam energy  $E_{e^+e^-} = 104.6$  GeV), the “Tevatron” proton-antiproton storage ring at the FNAL<sup>2</sup> in the USA ( $E_{p,\bar{p}} = 980$  GeV) and HERA (Hadron-Elektron-Ringanlage), the electron-proton storage ring at DESY<sup>3</sup> in Hamburg ( $E_e = 27.6$  GeV,  $E_p = 920$  GeV), which last was operated from 1992 to 2007, or the proton-proton storage ring LHC (Large Hadron Collider) at CERN with a nominal expected beam energy of  $E_p = 7$  TeV.

Figure 4.1 shows some scattering processes. We distinguish between elastic and inelastic scattering reactions.

**Elastic scattering** In an elastic process

$$a + b \rightarrow a' + b',$$

the same particles are present both before and after the scattering (Fig. 4.1a). The target  $b$  remains in its ground state, absorbing merely the recoil momentum and hence changing its kinetic energy. The apostrophe indicates that the particles in the initial and in the final state are identical up to momenta and energy. The scattering angle and the energy of the  $a'$  particle and the production angle and energy of  $b'$  are unambiguously correlated. As in optics, conclusions about the spatial shape of the



**Fig. 4.1** Scattering processes: (a) elastic scattering; (b) inelastic scattering – production of an excited state which then decays into two particles; (c) inelastic production of new particles; (d) reaction of colliding beams

<sup>1</sup>Conseil Européen pour la Recherche Nucléaire.

<sup>2</sup>Fermi National Accelerator Laboratory.

<sup>3</sup>Deutsches Elektronen-Synchrotron.

scattering object can be drawn from the dependence of the scattering rate upon the beam energy and scattering angle.

It is easily seen that in order to resolve small target structures, larger beam energies are required. The reduced de Broglie wavelength  $\lambda = \lambda/2\pi$  of a particle with momentum  $p$  is given by

$$\lambda = \frac{\hbar}{p} = \frac{\hbar c}{\sqrt{2mc^2 E_{\text{kin}} + E_{\text{kin}}^2}} \approx \begin{cases} \hbar/\sqrt{2mE_{\text{kin}}} & \text{for } E_{\text{kin}} \ll mc^2 \\ \hbar c/E_{\text{kin}} \approx \hbar c/E & \text{for } E_{\text{kin}} \gg mc^2. \end{cases} \quad (4.1)$$

The largest wavelength that can resolve structures of linear extension  $\Delta x$ , is of the same order:  $\lambda \lesssim \Delta x$ .

From Heisenberg’s uncertainty principle the corresponding particle momentum is:

$$p \gtrsim \frac{\hbar}{\Delta x}, \quad pc \gtrsim \frac{\hbar c}{\Delta x} \approx \frac{200 \text{ MeV fm}}{\Delta x}. \quad (4.2)$$

Thus to study nuclei, whose radii are of a few fm, beam momenta of the order of 10–100 MeV/c are necessary. Individual nucleons have radii of about 0.8 fm; and may be resolved if the momenta are above  $\approx 100 \text{ MeV}/c$ . To resolve the constituents of a nucleon, the quarks, one has to penetrate deeply into the interior of the nucleon. For this purpose, beam momenta of many GeV/c are necessary (see Fig. 4.2).

**Inelastic scattering** In inelastic reactions

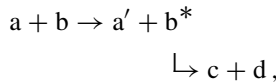
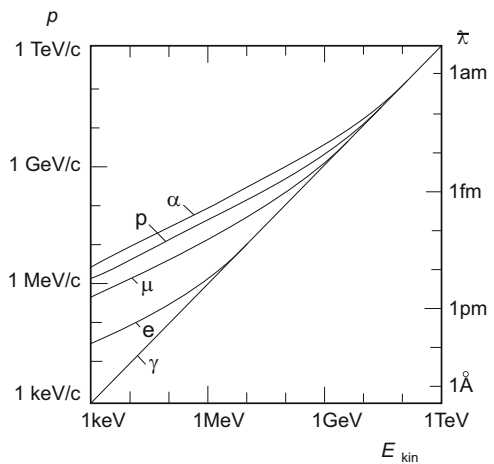


**Fig. 4.2** The connection between kinetic energy, momentum and reduced wavelength of photons ( $\gamma$ ), electrons ( $e$ ), muons ( $\mu$ ), protons ( $p$ ), and  $^4\text{He}$  nuclei ( $\alpha$ ). Atomic diameters are typically a few Å ( $10^{-10} \text{ m}$ ), nuclear diameters a few fm ( $10^{-15} \text{ m}$ )



part of the kinetic energy transferred from a to the target b excites it into a higher energy state  $b^*$  (Fig. 4.1b). The excited state will afterwards return to the ground state by emitting a light particle (e.g., a photon or a  $\pi$ -meson) or it may decay into two or more different particles.

A measurement of a reaction in which only the scattered particle  $a'$  is observed (and the other reaction products are not), is called an *inclusive* measurement. If all reaction products are detected, we speak of an *exclusive* measurement.

When allowed by the laws of conservation of lepton and baryon number (see Sects. 8.1 and 10.1), the beam particle may completely disappear in the reaction (Fig. 4.1c, d). Its total energy then goes into the excitation of the target or into the production of new particles. Such inelastic reactions represent the basis of nuclear and particle *spectroscopy*, which will be discussed in more detail in the second part of this book.

## 4.2 Cross-Sections

The reaction rates measured in scattering experiments, and the energy spectra and angular distributions of the reaction products yield, as we have already mentioned, information about the dynamics of the interaction between the projectile and the target, i.e., about the shape of the interaction potential and the coupling strength. The most important quantity for the description and interpretation of these reactions is the *cross-section*  $\sigma$ , which is a yardstick of the probability of a reaction between the two colliding particles.

**Geometric reaction cross-section** We consider an idealised experiment, in order to elucidate this concept. Imagine a thin scattering target of thickness  $d$  with  $N_b$  scattering centres b and with a particle density  $n_b$ . Each target particle has a cross-sectional area  $\sigma_b$ , to be determined by experiment. We bombard the target with a mono-energetic beam of point-like particles a. A reaction occurs whenever a beam particle hits a target particle, and we assume that the beam particle is then removed from the beam. We do not distinguish between the final target states, i.e., whether the reaction is elastic or inelastic. The total reaction rate  $\dot{N}$ , i.e., the total number of reactions per unit time, is given by the difference in the beam particle rate  $\dot{N}_a$  upstream and downstream of the target. This is a direct measure for the cross-sectional area  $\sigma_b$  (Fig. 4.3).

We further assume that the beam has cross-sectional area  $A$  and particle density  $n_a$ . The number of projectiles hitting the target per unit area and per unit time is called the *flux*  $\Phi_a$ . This is just the product of the particle density and the particle velocity  $v_a$ :

$$\Phi_a = \frac{\dot{N}_a}{A} = n_a \cdot v_a, \quad (4.3)$$

and has dimensions  $[(\text{area} \times \text{time})^{-1}]$ .

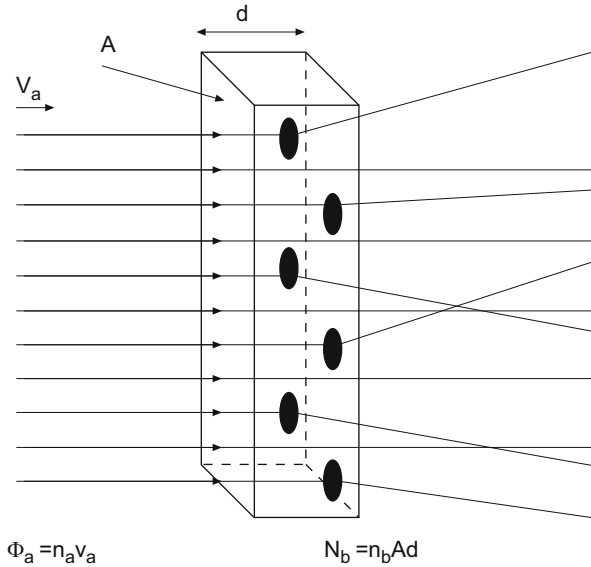


**Fig. 4.3** Measurement of the geometric reaction cross-section. The particle beam, a, coming from the left with velocity  $v_a$  and density  $n_a$ , corresponds to a particle flux  $\Phi_a = n_a v_a$ . It hits a (macroscopic) target of thickness  $d$  and cross-sectional area  $A$ . Some beam particles are scattered by the scattering centres of the target, i.e., they are deflected from their original trajectory. The frequency of this process is a measure of the cross-sectional area of the scattering particles

The total number of target particles within the beam area is  $N_b = n_b \cdot A \cdot d$ . Hence the reaction rate  $\dot{N}$  is given by the product of the incoming flux and the total cross-sectional area seen by the particles:

$$\dot{N} = \Phi_a \cdot N_b \cdot \sigma_b . \tag{4.4}$$

This formula is valid as long as the scattering centres do not overlap and particles are only scattered off individual scattering centres. The area presented by a single scattering centre to the incoming projectile a, will be called the *geometric reaction cross-section*: in what follows:

$$\begin{aligned} \sigma_b &= \frac{\dot{N}}{\Phi_a \cdot N_b} & (4.5) \\ &= \frac{\text{number of reactions per unit time}}{\text{beam particles per unit time per unit area} \times \text{scattering centres}} . \end{aligned}$$



This definition assumes a homogeneous, constant beam (e.g., neutrons from a reactor). In experiments with particle accelerators, the formula used is

$$\sigma_b = \frac{\text{number of reactions per unit time}}{\text{beam particles per unit time} \times \text{scattering centres per unit area}} ,$$

since the beam is then generally not homogeneous but the area density of the scattering centres is.

**Cross-sections** This naive description of the geometric reaction cross-section as the effective cross-sectional area of the target particles, (if necessary convoluted with the cross-sectional area of the beam particles) is in many cases a good approximation to the true reaction cross-section. An example is high-energy proton-proton scattering where the geometric extent of the particles is comparable to their interaction range.

The reaction probability for two particles is, however, generally very different to what these geometric considerations would imply. Furthermore a strong energy dependence is also observed. The reaction rate for the capture of thermal neutrons by uranium, for example, varies by several orders of magnitude within a small energy range. The reaction rate for scattering of (point-like) neutrinos, which only feel the weak interaction, is much smaller than that for the scattering of (also point-like) electrons which feel the electromagnetic interaction.

The shape, strength and range of the interaction potential, and not the geometric forms involved in the scattering process, primarily determine the effective cross-sectional area. The interaction can be determined from the reaction rate if the flux of the incoming beam particles, and the area density of the scattering centres are known, just as in the model above. The *total cross-section* is defined analogously to the geometric one:

$$\sigma_{\text{tot}} = \frac{\text{number of reactions per unit time}}{\text{beam particles per unit time} \times \text{scattering centres per unit area}} .$$

In analogy to the *total* cross-section, cross-sections for *elastic* reactions  $\sigma_{\text{el}}$  and for *inelastic* reactions  $\sigma_{\text{inel}}$  may also be defined. The inelastic part can be further divided into different reaction channels. The *total cross-section* is the sum of these parts:

$$\sigma_{\text{tot}} = \sigma_{\text{el}} + \sigma_{\text{inel}} . \quad (4.6)$$

The cross-section is a physical quantity with dimensions of [area], and is independent of the specific experimental design. A commonly used unit is the *barn*, which is defined as

$$\begin{aligned} 1 \text{ barn} &= 1 \text{ b} = 10^{-28} \text{ m}^2 \\ 1 \text{ millibarn} &= 1 \text{ mb} = 10^{-31} \text{ m}^2 \\ &\text{etc.} \end{aligned}$$

Typical total cross-sections at a beam energy of 10 GeV, for example, are

$$\sigma_{pp}(10 \text{ GeV}) \approx 40 \text{ mb} \quad (4.7)$$

for proton-proton scattering, and

$$\sigma_{\nu p}(10 \text{ GeV}) \approx 7 \cdot 10^{-14} \text{ b} = 70 \text{ fb} \quad (4.8)$$

for neutrino-proton scattering.

**Luminosity** The quantity

$$\mathcal{L} = \Phi_a \cdot N_b \quad (4.9)$$

is called the *luminosity*. Like the flux, it has dimensions of  $[(\text{area} \times \text{time})^{-1}]$ . From (4.3) and  $N_b = n_b \cdot d \cdot A$  we have

$$\mathcal{L} = \Phi_a \cdot N_b = \dot{N}_a \cdot n_b \cdot d = n_a \cdot v_a \cdot N_b . \quad (4.10)$$

Hence the luminosity is the product of the number of incoming beam particles per unit time  $\dot{N}_a$ , the target particle density in the scattering material  $n_b$ , and the target's thickness  $d$ ; or the beam particle density  $n_a$ , their velocity  $v_a$  and the number of target particles  $N_b$  exposed to the beam.

There is an analogous equation for the case of two particle beams colliding in a storage ring. Assume that  $j$  particle packets, each of  $N_a$  or  $N_b$  particles, have been injected into a ring of circumference  $U$ . The two particle types circulate with velocity  $v$  in opposite directions. Steered by magnetic fields, they collide at an interaction point  $j \cdot v/U$  times per unit time. The luminosity is then

$$\mathcal{L} = \frac{N_a \cdot N_b \cdot j \cdot v/U}{A}, \quad (4.11)$$

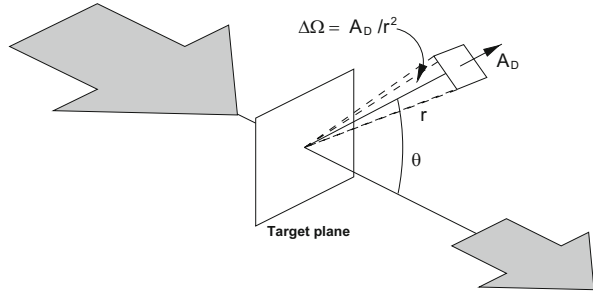
where  $A$  is the beam cross-section at the collision point. For a Gaussian distribution of the beam particles around the beam centre (with horizontal and vertical standard deviations  $\sigma_x$  and  $\sigma_y$  respectively),  $A$  is given by

$$A = 4\pi\sigma_x\sigma_y. \quad (4.12)$$

To achieve a high luminosity, the beams must be focused at the interaction point into the smallest possible cross-sectional area possible. Typical beam diameters are of the order of tenths of millimetres or less.

An often used quantity in storage ring experiments is the integrated luminosity  $\int \mathcal{L} dt$ . The number of reactions which can be observed in a given reaction time is just the product of the integrated luminosity and the cross-section. With a 1 nb

**Fig. 4.4** Description of the differential cross-section. Only particles scattered into the small solid angle  $\Delta\Omega$  are recorded by the detector of cross-sectional area  $A_D$



cross-section and a  $100 \text{ pb}^{-1}$  integrated luminosity, for example,  $10^5$  reactions would be expected.

**Differential cross-sections** In practice, only a fraction of all the reactions are measured. A detector of area  $A_D$  is placed at a distance  $r$  and at an angle  $\theta$  with respect to the beam direction, covering a solid angle  $\Delta\Omega = A_D / r^2$  (Fig. 4.4). The rate of reactions seen by this detector is then proportional to the *differential cross-section*  $d\sigma(E, \theta) / d\Omega$ :

$$\dot{N}(E, \theta, \Delta\Omega) = \mathcal{L} \cdot \frac{d\sigma(E, \theta)}{d\Omega} \Delta\Omega . \quad (4.13)$$

If the detector can determine the energy  $E'$  of the scattered particles then one can measure the *doubly differential* cross-section  $d^2\sigma(E, E', \theta) / d\Omega dE'$ . The total cross-section  $\sigma$  is then the integral over the total solid angle and over all scattering energies:

$$\sigma_{\text{tot}}(E) = \int_0^{E'_{\text{max}}} \int_{4\pi} \frac{d^2\sigma(E, E', \theta)}{d\Omega dE'} d\Omega dE' . \quad (4.14)$$

### 4.3 The “Golden Rule”

The cross-section can be experimentally determined from the reaction rate  $\dot{N}$ , as we saw above. We now outline how it may be found from theory.

First, the reaction rate is dependent upon the properties of the interaction potential described by the Hamilton operator  $\mathcal{H}_{\text{int}}$ . In a reaction, this potential transforms the initial-state wave function  $\psi_i$  into the final-state wave function  $\psi_f$ . The *transition matrix element* is given by

$$\mathcal{M}_{fi} = \langle \psi_f | \mathcal{H}_{\text{int}} | \psi_i \rangle = \int \psi_f^* \mathcal{H}_{\text{int}} \psi_i dV . \quad (4.15)$$

This matrix element is also called the *probability amplitude* for the transition.

Furthermore, the reaction rate will depend upon the number of final states available to the reaction. According to the uncertainty principle, each particle occupies a volume  $h^3 = (2\pi\hbar)^3$  in *phase space*, the six-dimensional space of momentum and position. Consider a particle scattered into a volume  $V$  and into a momentum interval between  $p'$  and  $p' + dp'$ . In momentum space, the interval corresponds to a spherical shell with inner radius  $p'$  and thickness  $dp'$  which has a volume  $4\pi p'^2 dp'$ . Excluding processes where the spin changes, the number of final states available is

$$dn(p') = \frac{V \cdot 4\pi p'^2}{(2\pi\hbar)^3} dp' . \quad (4.16)$$

The energy and momentum of a particle are connected by

$$dE' = v' dp' . \quad (4.17)$$

Hence the density of final states in the energy interval  $dE'$  is given by

$$\varrho(E') = \frac{dn(E')}{dE'} = \frac{V \cdot 4\pi p'^2}{v' \cdot (2\pi\hbar)^3} . \quad (4.18)$$

The connection between the reaction rate, the transition matrix element and the density of final states is expressed by Fermi’s *second golden rule*. Its derivation can be found in quantum mechanics textbooks (e.g. [2]). It expresses the reaction rate  $W$  per target particle and per beam particle in the form:

$$W = \frac{2\pi}{\hbar} |\mathcal{M}_{fi}|^2 \cdot \varrho(E') . \quad (4.19)$$

We also know, however, from (4.3) and (4.4) that

$$W = \frac{\dot{N}(E)}{N_b \cdot N_a} = \frac{\sigma \cdot v_a}{V} , \quad (4.20)$$

where  $V = N_a/n_a$  is the spatial volume occupied by the beam particles. Hence, the cross-section is

$$\sigma = \frac{2\pi}{\hbar \cdot v_a} |\mathcal{M}_{fi}|^2 \cdot \varrho(E') \cdot V . \quad (4.21)$$

If the interaction potential is known, the cross-section can be calculated from (4.21). Otherwise, the cross-section data and Eq.(4.21) can be used to determine the transition matrix element.

The golden rule applies to both scattering and spectroscopic processes. Examples of the latter are the decay of unstable particles, excitation of particle resonances and transitions between different atomic or nuclear energy states. In these cases we have

$$W = \frac{1}{\tau}, \quad (4.22)$$

and the transition probability per unit time can be either directly determined by measuring the lifetime  $\tau$  or indirectly read off from the energy width of the state  $\Delta E = \hbar/\tau$ .

## 4.4 Feynman Diagrams

In QED, as in other quantum field theories, we can use the little pictures invented by my colleague Richard Feynman, which are supposed to give the illusion of understanding what is going on in quantum field theory.

M. Gell-Mann [1]

Elementary processes such as the scattering of two particles off each other or the decay of a single particle are nowadays commonly depicted by *Feynman diagrams*. Originally, these diagrams were introduced by Feynman as a sort of shorthand for the individual terms in his calculations of transition matrix elements  $\mathcal{M}_{fi}$  in electromagnetic processes in the framework of *quantum electrodynamics* (QED). Each symbol in such a space-time diagram corresponds to a term in the matrix element. The meaning of the individual terms and the links between them are fixed by the *Feynman rules*. Similarly to the QED rules, corresponding prescriptions exist for the calculation of weak and strong processes as well, in *quantum chromodynamics* (QCD). We will not use such diagrams for quantitative calculations, since this requires knowledge of relativistic field theory. Instead, they will serve as pictorial illustrations of the processes that occur. We will therefore merely treat a few examples below and explain some of the definitions and rules.

Figure 4.5 shows some typical diagrams. We use the convention that the time axis runs upwards and the space axis from left to right. The straight lines in the graphs correspond to the wave functions of the initial and final fermions. Antiparticles (in our examples: the positron  $e^+$ , the positive muon  $\mu^+$  and the electron-antineutrino  $\bar{\nu}_e$ ) are symbolised by arrows pointing backwards in time; photons by wavy lines; heavy vector bosons by dashed lines; and gluons by corkscrew-like lines.

As we mentioned in Chap. 1, the electromagnetic interaction between charged particles proceeds via photon exchange. Figure 4.5a depicts schematically the elastic

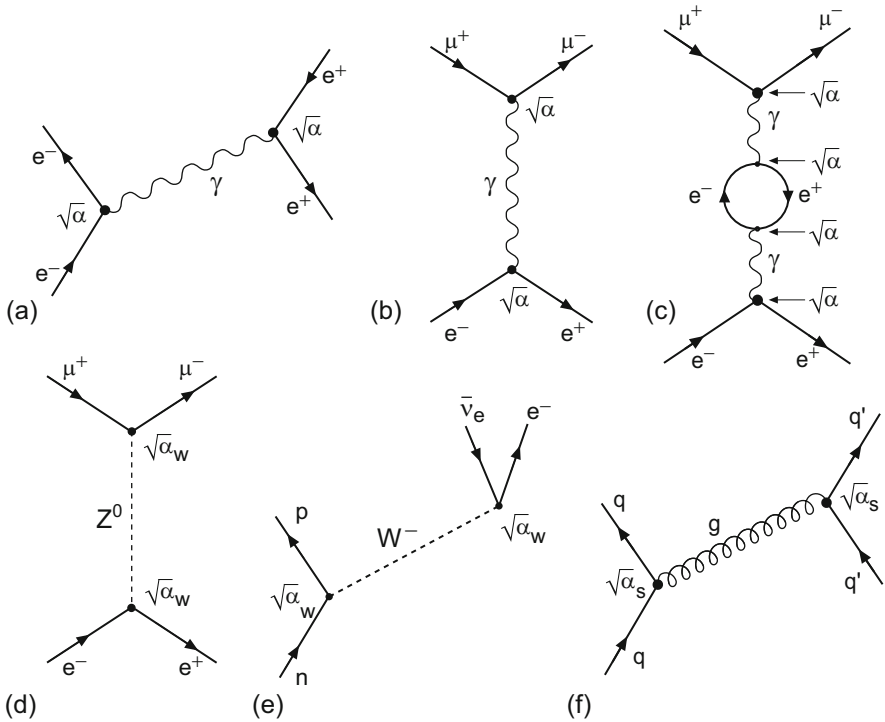


**Fig. 4.5** Feynman diagrams for the electromagnetic (a–c), weak (d, e) and strong interactions (f)

scattering of an electron off a positron. The interaction process corresponds to a photon being emitted by the electron and absorbed by the positron. Particles appearing neither in the initial nor in the final state, such as this exchanged photon, are called *virtual particles*. Because of the uncertainty principle, virtual particles do not have to satisfy the energy-momentum relation  $E^2 = \mathbf{p}^2c^2 + m^2c^4$ . This may be interpreted as meaning that the exchanged particle has a mass different from that of a free (real) particle, or that energy conservation is violated for a brief period of time.

Points at which three or more particles meet are called *vertices*. Each vertex corresponds to a term in the transition matrix element which includes the structure and strength of the interaction. In (a), the exchanged photon couples to the charge of the electron at the left vertex and to that of the positron at the right vertex. For each vertex the transition amplitude contains a factor which is proportional to  $e$ , i.e.,  $\sqrt{\alpha}$ .

Figure 4.5b represents the annihilation of an electron-positron pair. A photon is created as an intermediate state which then decays into a negatively charged  $\mu^-$  and its positively charged antiparticle, a  $\mu^+$ . Figure 4.5c shows a slightly more complicated version of the same process. Here, the photon, by vacuum polarisation, is briefly transformed into an intermediate state made up of an  $e^+e^-$  pair. This and

additional, more complicated, diagrams contributing to the same process are called *higher-order diagrams*.

The transition matrix element includes the superposition of amplitudes of all diagrams leading to the same final state. Because the number of vertices is greater in higher-order diagrams these graphs include higher powers of  $\alpha$ . The amplitude of diagram (b) is proportional to  $\alpha$ , while diagram (c)'s is proportional to  $\alpha^2$ . The cross-section for conversion of an electron-positron pair into a  $\mu^+\mu^-$  pair is therefore given to a good approximation by diagram (b). Diagram (c) and other diagrams of even higher order produce only small corrections to (b).

Figure 4.5d shows electron-positron annihilation followed by muon pair production in a weak interaction proceeding through exchange of the neutral, heavy vector boson  $Z^0$ . In Fig. 4.5e, we see a neutron transform into a proton via  $\beta$ -decay in which it emits a negatively charged heavy vector boson  $W^-$  which subsequently decays into an electron and antineutrino  $\bar{\nu}_e$ . Figure 4.5f depicts a strong interaction process between two quarks  $q$  and  $q'$  which exchange a gluon, the field quantum of the strong interaction.

In weak interactions, a heavy vector boson is exchanged which couples to the “weak charge”  $g$  and not to the electric charge  $e$ . Accordingly,  $\mathcal{M}_f \propto g^2 \propto \alpha_w$ . In strong interactions the gluons which are exchanged between the quarks couple to the “colour charge” of the quarks,  $\mathcal{M}_f \propto \sqrt{\alpha_s} \cdot \sqrt{\alpha_s} = \alpha_s$ .

The exchange particles contribute a *propagator* term to the transition matrix element. This contribution has the general form

$$\frac{1}{Q^2 + M^2c^2} \quad (4.23)$$

Here  $Q^2$  is the square of the four-momentum (cf. (5.3) and (6.3)) which is transferred in the interaction and  $M$  is the mass of the exchange particle. In the case of a virtual photon, this results in a factor  $1/Q^2$  in the amplitude and  $1/Q^4$  in the cross-section. In the weak interaction, the large mass of the exchanged vector boson causes the cross-section to be much smaller than that of the electromagnetic interaction – although at very high momentum transfers, of the order of the masses of the vector bosons, the two cross-sections become comparable in size, as it has been demonstrated at the electron-proton storage ring HERA (cf. Sect. 12.2).

## Problems

### 1. Cross-section

Deuterons with an energy  $E_{\text{kin}} = 5 \text{ MeV}$  are perpendicularly incident upon a tritium target, which has a mass occupation density  $\mu_t = 0.2 \text{ mg/cm}^2$ , so as to investigate the reaction  ${}^3\text{H}(d, n){}^4\text{He}$ .

- (a) How many neutrons per second pass through a detector with a reception area of  $A = 20 \text{ cm}^2$  which is at a distance  $R = 3 \text{ m}$  from the target and an angle  $\theta = 30^\circ$  to the deuteron beam direction, if the differential cross-section  $d\sigma/d\Omega$  at this angle is  $13 \text{ mb/sr}$  and the deuteron current applied to the target is  $I_d = 2 \mu\text{A}$ ?
- (b) How many neutrons per second does the detector receive if the target is tilted so that the same deuteron current now approaches it at  $80^\circ$  instead of  $90^\circ$ ?

## 2. Absorption length

A particle beam is incident upon a thick layer of an absorbing material (with  $n$  absorbing particles per unit volume). How large is the absorption length, i.e., the distance over which the intensity of the beam is reduced by a factor of  $1/e$  for the following examples?

- (a) Thermal neutrons ( $E \approx 25 \text{ meV}$ ) in cadmium ( $\rho = 8.6 \text{ g/cm}^3$ ,  $\sigma = 24\,506 \text{ barn}$ ).
- (b)  $E_\gamma = 2 \text{ MeV}$  photons in lead ( $\rho = 11.3 \text{ g/cm}^3$ ,  $\sigma = 15.7 \text{ barn/atom}$ ).
- (c) Antineutrinos from a reactor in earth ( $\rho = 5 \text{ g/cm}^3$ ,  $\sigma \approx 10^{-19} \text{ barn/electron}$ ; interactions with nuclei may be neglected;  $Z/A \approx 0.5$ ).

## References

1. M. Gell-Mann, in *The Nature of Matter*, ed. by J.H. Mulvey. Wolfson College Lectures (Clarendon Press, Oxford, 1980)
2. F. Schwabl, *Quantum Mechanics*, 4th edn. (Springer, Berlin/Heidelberg/New York, 2007)



# Chapter 5

## Geometric Shapes of Nuclei

In this chapter we shall study nuclear sizes and shapes. In principle, this information may be obtained from scattering experiments (e.g., scattering of protons or  $\alpha$ -particles) and when Rutherford discovered that nuclei have a radial extent of less than  $10^{-14}$  m, he employed  $\alpha$ -scattering. In practice, however, there are difficulties in extracting detailed information from such experiments. Firstly, these projectiles are themselves extended objects. Therefore, the cross-section reflects not only the structure of the target, but also that of the projectile. Secondly, the nuclear forces between the projectile and the target are complex and not well understood.

Electron scattering is particularly valuable for investigating small objects. As far as we know electrons are point-like objects without any internal structure. The interactions between an electron and a nucleus, nucleon or quark take place via the exchange of a virtual photon – this may be very accurately calculated within quantum electrodynamics (QED). These processes are in fact manifestations of the well known electromagnetic interaction, whose coupling constant  $\alpha \approx 1/137$  is much less than one. This means that higher order corrections play only a tiny role.

### 5.1 Kinematics of Electron Scattering

In electron scattering experiments one employs highly relativistic particles. Hence it is advisable to use four-vectors in kinematical calculations. The zero component of space-time four-vectors is time, the zero component of four-momentum vectors is energy:

$$\begin{aligned}x &= (x_0, x_1, x_2, x_3) = (ct, \mathbf{x}), \\p &= (p_0, p_1, p_2, p_3) = (E/c, \mathbf{p}).\end{aligned}\tag{5.1}$$

Three-vectors are designated by bold-faced type to distinguish them from four-vectors. The Lorentz-invariant scalar product of two four-vectors  $a$  and  $b$  is defined by

$$a \cdot b = a_0 b_0 - a_1 b_1 - a_2 b_2 - a_3 b_3 = a_0 b_0 - \mathbf{a} \cdot \mathbf{b} . \quad (5.2)$$

In particular, this applies to the four-momentum squared:

$$p^2 = \frac{E^2}{c^2} - \mathbf{p}^2 . \quad (5.3)$$

This squared product is equal to the square of the rest mass  $m$  (multiplied by  $c^2$ ). This is so since a reference frame in which the particle is at rest can always be found and there  $\mathbf{p} = 0$ , and  $E = mc^2$ . The quantity

$$m = \sqrt{p^2} / c \quad (5.4)$$

is called the *invariant mass*. From (5.3) and (5.4) we obtain the relativistic energy-momentum relation

$$E^2 - \mathbf{p}^2 c^2 = m^2 c^4 \quad (5.5)$$

and thus

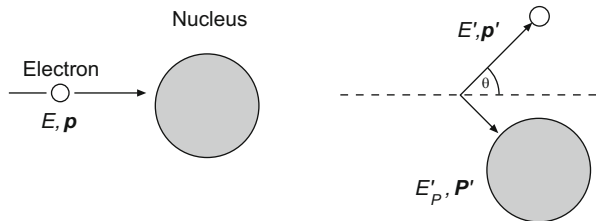
$$E \approx |\mathbf{p}| c \quad \text{if} \quad E \gg mc^2 . \quad (5.6)$$

For electrons, this approximation is already valid at energies of a few MeV.

■ Consider the scattering of an electron with four-momentum  $p$  off a particle with four-momentum  $P$  (Fig. 5.1). Energy and momentum conservation imply that the sums of the four-momenta before and after the reaction are identical:

$$p + P = p' + P' , \quad (5.7)$$

**Fig. 5.1** Kinematics of elastic electron-nucleus scattering



or squared:

$$p^2 + 2pP + P^2 = p'^2 + 2p'P' + P'^2. \quad (5.8)$$

In elastic scattering the invariant masses  $m_e$  and  $M$  of the colliding particles are unchanged. Hence from

$$p^2 = p'^2 = m_e^2 c^2 \quad \text{and} \quad P^2 = P'^2 = M^2 c^2 \quad (5.9)$$

it follows that

$$p \cdot P = p' \cdot P'. \quad (5.10)$$

Usually only the scattered electron is detected and not the recoiling particle. In this case the relation

$$p \cdot P = p' \cdot (p + P - p') = p'p + p'P - m_e^2 c^2 \quad (5.11)$$

is used. Consider the laboratory frame where the particle with four-momentum  $P$  is at rest before the collision. Then the four-momenta can be written as

$$p = (E/c, \mathbf{p}) \quad p' = (E'/c, \mathbf{p}') \quad P = (Mc, \mathbf{0}) \quad P' = (E_p'/c, \mathbf{P}'). \quad (5.12)$$

Hence (5.11) yields

$$E \cdot Mc^2 = E'E - \mathbf{p} \cdot \mathbf{p}' c^2 + E' Mc^2 - m_e^2 c^4. \quad (5.13)$$

At high energies,  $m_e^2 c^4$  may be neglected and  $E \approx |\mathbf{p}| \cdot c$  (Eq. (5.6)) can be safely used. One thus obtains a relation between the angle and the energy

$$E \cdot Mc^2 = E'E \cdot (1 - \cos \theta) + E' \cdot Mc^2. \quad (5.14)$$

In the laboratory system, the energy  $E'$  of the scattered electron is

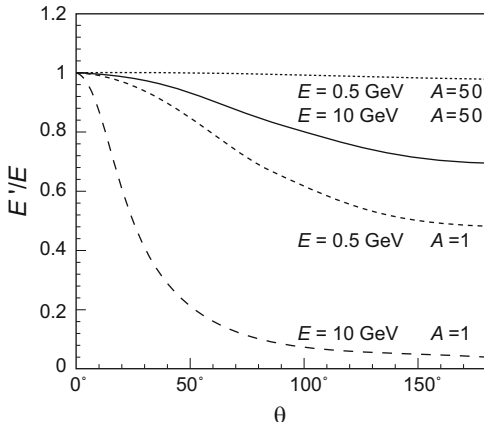
$$E' = \frac{E}{1 + E/Mc^2 \cdot (1 - \cos \theta)}. \quad (5.15)$$

The angle  $\theta$  through which the electron is deflected is called the *scattering angle*. The recoil which is transferred to the target is given by the difference  $E - E'$ . In elastic scattering, a one-to-one relationship (5.15) exists between the scattering angle  $\theta$  and the energy  $E'$  of the scattered electron; (5.15) does not hold for inelastic scattering.

The angular dependence of the scattering energy  $E'$  is described by the term  $(1 - \cos \theta)$  multiplied by  $E/Mc^2$ . Hence the recoil energy of the target increases with the ratio of the relativistic electron mass  $E/c^2$  to the target mass  $M$ . This is in accordance with the classical laws of collision.

In electron scattering at the relatively low energy of 0.5 GeV off a nucleus with mass number  $A = 50$  the scattering energy varies by only 2% between forward and backward scattering. The situation is very different for 10 GeV-electrons scattering

**Fig. 5.2** Angular dependence of the scattering energy of electrons normalised to beam energy,  $E'/E$ , in elastic electron-nucleus scattering. The curves show this dependence for two different beam energies (0.5 and 10 GeV) and for two nuclei with different masses ( $A = 1$  and  $A = 50$ )



off protons. The scattering energy  $E'$  then varies between 10 GeV ( $\theta \approx 0^\circ$ ) and 445 MeV ( $\theta = 180^\circ$ ) (cf. Fig. 5.2).

## 5.2 The Rutherford Cross-Section

We will now consider the cross-section for an electron with energy  $E$  scattering off an atomic nucleus with charge  $Ze$ . For the calculation of the reaction kinematics to be sufficiently precise, it must be both relativistic and quantum mechanical. We will approach this goal step by step. Firstly, we introduce the Rutherford scattering formula. By definition, this formula yields the cross-section up to spin effects. For heavy nuclei and low energy electrons, the recoil can, from (5.15), be neglected. In this case, the energy  $E$  and the modulus of the momentum  $p$  are the same before and after the scattering. The kinematics can be calculated in the same way as, for example, the hyperbolic trajectory of a comet which is deflected by the Sun as it traverses the solar system. As long as the radius of the scattering centre (nucleus, Sun) is smaller than the closest approach of the projectile (electron, comet) then the spatial extension of the scattering centre does not affect this purely classical calculation. This leads to the Rutherford formula for the scattering of a particle with charge  $ze$  and kinetical energy  $E_{\text{kin}}$  on a target nucleus with charge  $Ze$ :

$$\left(\frac{d\sigma}{d\Omega}\right)_{\text{Rutherford}} = \frac{(zZe^2)^2}{(4\pi\epsilon_0)^2 \cdot (4E_{\text{kin}})^2 \sin^4 \frac{\theta}{2}}. \quad (5.16)$$

Exactly the same equation is obtained by a calculation of this cross-section in non-relativistic quantum mechanics using Fermi's golden rule. This we will now demonstrate. To avoid unnecessary repetitions we will consider the case of a central charge with finite spatial distribution.

**Scattering off an extended charge distribution** Consider the case of a target so heavy that the recoil is negligible. We can then use three-momenta. If  $Ze$  is small, i.e., if

$$Z\alpha \ll 1, \quad (5.17)$$

the *Born approximation* can be applied, and the wave functions  $\psi_i$  and  $\psi_f$  of the incoming and of the outgoing electron can be described by plane waves

$$\psi_i = \frac{1}{\sqrt{V}} e^{i\mathbf{p}x/\hbar} \quad \psi_f = \frac{1}{\sqrt{V}} e^{i\mathbf{p}'x/\hbar}. \quad (5.18)$$

We can sidestep any difficulties related to the normalisation of the wave functions by considering only a finite volume  $V$ . We need this volume to be large compared to the scattering centre, and also large enough that the discrete energy states in this volume can be approximated by a continuum. The physical results have, of course, to be independent of  $V$ .

We consider an electron beam with a density of  $n_a$  particles per unit volume. With the volume of integration chosen to be sufficiently large, the normalisation condition is given by

$$\int_V |\psi_i|^2 dV = n_a \cdot V \quad \text{where} \quad V = \frac{N_a}{n_a}, \quad (5.19)$$

i.e.,  $V$  is the normalisation volume that must be chosen for a single beam particle.

According to (4.20), the reaction rate  $W$  is given by the product of the cross-section  $\sigma$  and the beam particle velocity  $v_a$  divided by the above volume. When applying the golden rule (4.19), we get

$$\frac{\sigma v_a}{V} = W = \frac{2\pi}{\hbar} |\langle \psi_f | \mathcal{H}_{\text{int}} | \psi_i \rangle|^2 \frac{dn}{dE_f}. \quad (5.20)$$

Here,  $E_f$  is the total energy (kinetic energy and rest mass) of the final state. Since we neglect the recoil and since the rest mass is a constant,  $dE_f = dE' = dE$ .

The density  $n$  of possible final states in phase space (cf. (4.16)) is

$$dn(|\mathbf{p}'|) = \frac{4\pi |\mathbf{p}'|^2 d|\mathbf{p}'| \cdot V}{(2\pi\hbar)^3}. \quad (5.21)$$

Therefore the cross-section for the scattering of an electron into a solid angle element  $d\Omega$  is

$$d\sigma \cdot v_a \cdot \frac{1}{V} = \frac{2\pi}{\hbar} |\langle \psi_f | \mathcal{H}_{\text{int}} | \psi_i \rangle|^2 \frac{V |\mathbf{p}'|^2 d|\mathbf{p}'|}{(2\pi\hbar)^3 dE_f} d\Omega. \quad (5.22)$$

The velocity  $v_a$  can be replaced, to a good approximation, by the velocity of light  $c$ . For large electron energies,  $|\mathbf{p}'| \approx E'/c$  applies, and we obtain

$$\frac{d\sigma}{d\Omega} = \frac{V^2 E'^2}{(2\pi)^2 (\hbar c)^4} |\langle \psi_f | \mathcal{H}_{\text{int}} | \psi_i \rangle|^2. \quad (5.23)$$

The interaction operator for a charge  $e$  in an electric potential  $\phi$  is  $\mathcal{H}_{\text{int}} = e\phi$ . Hence, the matrix element is

$$\langle \psi_f | \mathcal{H}_{\text{int}} | \psi_i \rangle = \frac{e}{V} \int e^{-i\mathbf{p}'\cdot\mathbf{x}/\hbar} \phi(\mathbf{x}) e^{i\mathbf{p}\cdot\mathbf{x}/\hbar} d^3x. \quad (5.24)$$

Defining the *momentum transfer*  $\mathbf{q}$  by

$$\mathbf{q} = \mathbf{p} - \mathbf{p}', \quad (5.25)$$

we may re-write the matrix element as

$$\langle \psi_f | \mathcal{H}_{\text{int}} | \psi_i \rangle = \frac{e}{V} \int \phi(\mathbf{x}) e^{i\mathbf{q}\cdot\mathbf{x}/\hbar} d^3x. \quad (5.26)$$

■ Green's theorem permits us to use a clever trick here: for two arbitrarily chosen scalar fields  $u$  and  $v$ , which fall off fast enough at large distances, the following equation holds for a sufficiently large integration volume:

$$\int (u\Delta v - v\Delta u) d^3x = 0, \quad \text{with } \Delta = \nabla^2. \quad (5.27)$$

Inserting

$$e^{i\mathbf{q}\cdot\mathbf{x}/\hbar} = \frac{-\hbar^2}{|\mathbf{q}|^2} \cdot \Delta e^{i\mathbf{q}\cdot\mathbf{x}/\hbar} \quad (5.28)$$

into (5.26), we may rewrite the matrix element as

$$\langle \psi_f | \mathcal{H}_{\text{int}} | \psi_i \rangle = \frac{-e\hbar^2}{V|\mathbf{q}|^2} \int \Delta\phi(\mathbf{x}) e^{i\mathbf{q}\cdot\mathbf{x}/\hbar} d^3x. \quad (5.29)$$

The potential  $\phi(\mathbf{x})$  and the charge density  $\varrho(\mathbf{x})$  are related by Poisson's equation

$$\Delta\phi(\mathbf{x}) = \frac{-\varrho(\mathbf{x})}{\varepsilon_0}. \quad (5.30)$$

In the following, we will assume the charge density  $\varrho(\mathbf{x})$  to be static, i.e. independent of time.

We now define a charge distribution function  $f$  by  $\varrho(\mathbf{x}) = Zef(\mathbf{x})$  which satisfies the normalisation condition  $\int f(\mathbf{x}) d^3x = 1$ , and re-write the matrix element as

$$\begin{aligned} \langle \psi_f | \mathcal{H}_{\text{int}} | \psi_i \rangle &= \frac{e\hbar^2}{\varepsilon_0 \cdot V |\mathbf{q}|^2} \int \varrho(\mathbf{x}) e^{i\mathbf{q}\mathbf{x}/\hbar} d^3x \\ &= \frac{Z \cdot 4\pi\alpha\hbar^3 c}{|\mathbf{q}|^2 \cdot V} \int f(\mathbf{x}) e^{i\mathbf{q}\mathbf{x}/\hbar} d^3x . \end{aligned} \quad (5.31)$$

The integral

$$F(\mathbf{q}) = \int e^{i\mathbf{q}\mathbf{x}/\hbar} f(\mathbf{x}) d^3x \quad (5.32)$$

is the Fourier transform of the charge function  $f(\mathbf{x})$ , normalised to the total charge. It is called the *form factor* of the charge distribution. The form factor contains all the information about the spatial distribution of the charge of the object being studied. We will discuss form factors and their meaning in the following chapters in some detail.

To calculate the Rutherford cross-section we, by definition, neglect the spatial extension – i.e., we replace the charge distribution by a  $\delta$ -function. Hence, the form factor is fixed to unity. By inserting the matrix element into (5.23) we obtain

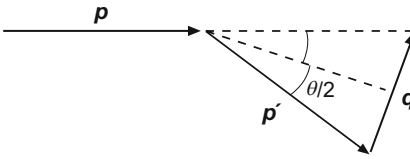
$$\left( \frac{d\sigma}{d\Omega} \right)_{\text{Rutherford}} = \frac{4Z^2\alpha^2(\hbar c)^2 E'^2}{|\mathbf{q}c|^4} . \quad (5.33)$$

The  $1/q^4$ -dependence of the electromagnetic cross-section implies very low event rates for electron scattering with large momentum transfers. The event rates drop off so sharply that small measurement errors in  $\mathbf{q}$  can significantly falsify the results.

■ Since recoil is neglected in Rutherford scattering, the electron energy and the magnitude of its momentum do not change in the interaction:

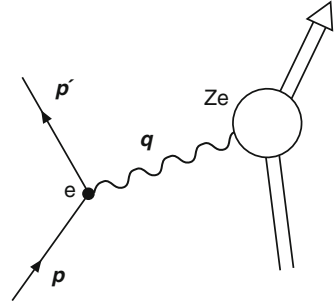
$$E = E' , \quad |\mathbf{p}| = |\mathbf{p}'| . \quad (5.34)$$

The magnitude of the momentum transfer  $\mathbf{q}$  is therefore



$$|\mathbf{q}| = 2 \cdot |\mathbf{p}| \sin \frac{\theta}{2} . \quad (5.35)$$

**Fig. 5.3** Sketch of elastic electron scattering off a nucleus with charge  $Z \cdot e$



If we recall that  $E = |\mathbf{p}| \cdot c$  is a good approximation we obtain the relativistic Rutherford scattering formula

$$\left( \frac{d\sigma}{d\Omega} \right)_{\text{Rutherford}} = \frac{Z^2 \alpha^2 (\hbar c)^2}{4E^2 \sin^4 \frac{\theta}{2}}. \quad (5.36)$$

The classical Rutherford formula (5.16) may be obtained from (5.33) by applying non-relativistic kinematics:  $\mathbf{p} = m\mathbf{v}$ ,  $E_{\text{kin}} = mv^2/2$  and  $E' \approx mc^2$ .

**Field-theoretical considerations** Figure 5.3 is a pictorial representation of a scattering process. In the language of field theory, the electromagnetic interaction of an electron with the charge distribution is mediated by the exchange of a photon, the field quantum of this interaction. The photon which does not itself carry any charge, couples to the charges of the two interacting particles. In the transition matrix element, this yields a factor  $Ze \cdot e$  and in the cross-section we have a term  $(Ze^2)^2$ . The three-momentum transfer  $\mathbf{q}$  defined in (5.25) is the momentum transferred by the exchanged photon. Hence the reduced de Broglie wavelength of the photon is

$$\lambda = \frac{\hbar}{|\mathbf{q}|} = \frac{\hbar}{|\mathbf{p}|} \cdot \frac{1}{2 \sin \frac{\theta}{2}}. \quad (5.37)$$

If  $\lambda$  is considerably larger than the spatial extent of the target particle, internal structures cannot be resolved, and the target particle may be considered to be point-like. The Rutherford cross-section from (5.33) was obtained for this case.

In the form (5.33), the dependence of the cross-section on the momentum transfer is clearly expressed. To lowest order the interaction is mediated by the exchange of a single photon. Since the photon is massless, the propagator (4.23) in the matrix element is  $1/Q^2$ , or  $1/|\mathbf{q}|^2$  in a non-relativistic approximation. The propagator enters the cross-section squared which leads to the characteristic fast  $1/|\mathbf{q}|^4$  fall-off of the cross-section.

If the Born approximation condition (5.17) no longer holds, then our simple picture must be modified. Higher order corrections (exchange of several photons) must be included and more complicated calculations (phase shift analyses) are necessary.



### 5.3 The Mott Cross-Section

Up to now we have neglected the spins of the electron and of the target. At relativistic energies, however, the Rutherford cross-section is modified by spin effects. The *Mott cross-section*, which describes electron scattering and includes effects due to the electron spin, may be written as

$$\left(\frac{d\sigma}{d\Omega}\right)_{\text{Mott}}^* = \left(\frac{d\sigma}{d\Omega}\right)_{\text{Rutherford}} \cdot \left(1 - \beta^2 \sin^2 \frac{\theta}{2}\right), \quad \text{with } \beta = \frac{v}{c}. \quad (5.38)$$

The asterisk indicates that the recoil of the nucleus has been neglected in deriving this equation. The expression shows that, at relativistic energies, the Mott cross-section drops off more rapidly at large scattering angles than does the Rutherford cross-section. In the limiting case of  $\beta \rightarrow 1$ , and using  $\sin^2 x + \cos^2 x = 1$ , the Mott cross-section can be written in a simpler form:

$$\left(\frac{d\sigma}{d\Omega}\right)_{\text{Mott}}^* = \left(\frac{d\sigma}{d\Omega}\right)_{\text{Rutherford}} \cdot \cos^2 \frac{\theta}{2} = \frac{4Z^2\alpha^2(\hbar c)^2 E'^2}{|qc|^4} \cos^2 \frac{\theta}{2}. \quad (5.39)$$

The additional factor in (5.38) can be understood by considering the extreme case of scattering through  $180^\circ$ . For relativistic particles in the limit  $\beta \rightarrow 1$ , the projection of their spin  $s$  on the direction of their motion  $\mathbf{p}/|\mathbf{p}|$  is a conserved quantity. This conservation law follows from the solution of the Dirac equation in relativistic quantum mechanics [3]. It is usually called conservation of *helicity* rather than conservation of the projection of the spin. Helicity is defined by

$$h = \frac{\mathbf{s} \cdot \mathbf{p}}{|\mathbf{s}| \cdot |\mathbf{p}|}. \quad (5.40)$$

Particles with spin pointing in the direction of their motion have helicity  $+1$ , particles with spin pointing in the opposite direction have helicity  $-1$ .

Figure 5.4 shows the kinematics of scattering through  $180^\circ$ . We here choose the momentum direction of the incoming electron as the axis of quantisation  $z$ . Because of conservation of helicity, the projection of the spin on the  $z$ -axis would have to turn over (spin-flip). This, however, is impossible with a spinless target, because of conservation of total angular momentum. The orbital angular momentum  $\mathbf{L}$  is perpendicular to the direction of motion  $z$ . It therefore cannot cause any change in the  $z$ -component of the angular momentum. Hence in the limiting case  $\beta \rightarrow 1$ , scattering through  $180^\circ$  must be completely suppressed.

If the target has spin, the spin projection of the electron can be changed, as conservation of angular momentum can be compensated by a change in the spin direction of the target. In this case, the above reasoning is not valid, and scattering through  $180^\circ$  is possible.

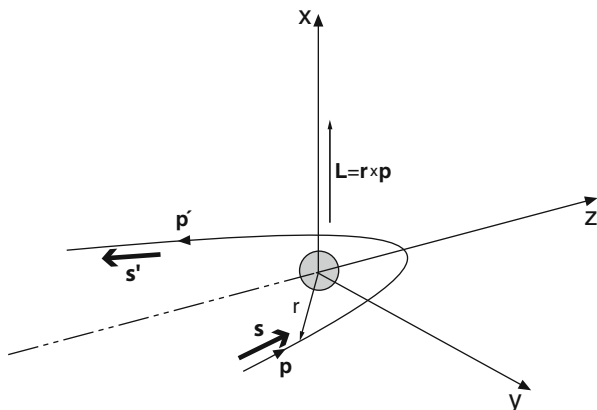


**Fig. 5.4** Helicity,  $h = \mathbf{s} \cdot \mathbf{p} / (|\mathbf{s}| \cdot |\mathbf{p}|)$ , is conserved in the  $\beta \rightarrow 1$  limit. This means that the spin projection on the  $z$ -axis would have to change its sign in scattering through  $180^\circ$ . This is impossible if the target is spinless, because of conservation of angular momentum

## 5.4 Nuclear Form Factors

In actual scattering experiments with nuclei or nucleons, we see that the Mott cross-sections agree with the experimental cross-sections only in the limit  $|\mathbf{q}| \rightarrow 0$ . At larger values of  $|\mathbf{q}|$ , the experimental cross-sections are systematically smaller. The reason for this lies in the spatial extension of nuclei and nucleons. At larger values of  $|\mathbf{q}|$ , the reduced wavelength of the virtual photon decreases (5.37), and the resolution increases. The scattered electron no longer sees the total charge, but only parts of it. Therefore, the cross-section decreases.

As we have seen, the spatial extension of a nucleus is described by a form factor (5.32). In the following, we will restrict the discussion to the form factors of spherically symmetric systems which have no preferred orientation in space. In this case, the form factor only depends on the momentum transfer  $\mathbf{q}$ . We symbolise this fact by writing the form factor as  $F(q^2)$ .

Experimentally, the magnitude of the form factor is determined by the ratio of the measured cross-section to the Mott cross-section

$$\left( \frac{d\sigma}{d\Omega} \right)_{\text{exp.}} = \left( \frac{d\sigma}{d\Omega} \right)_{\text{Mott}}^* \cdot |F(q^2)|^2 . \quad (5.41)$$

One therefore measures the cross-section for a fixed beam energy at various angles (and thus different values of  $|\mathbf{q}|$ ) and divides by the calculated Mott cross-section.

In Fig. 5.5, a typical experimental set-up for the measurement of form factors is depicted. The electron beam is provided by a linear accelerator and is directed at a thin target. The scattered electrons are measured in a magnetic spectrometer. In an

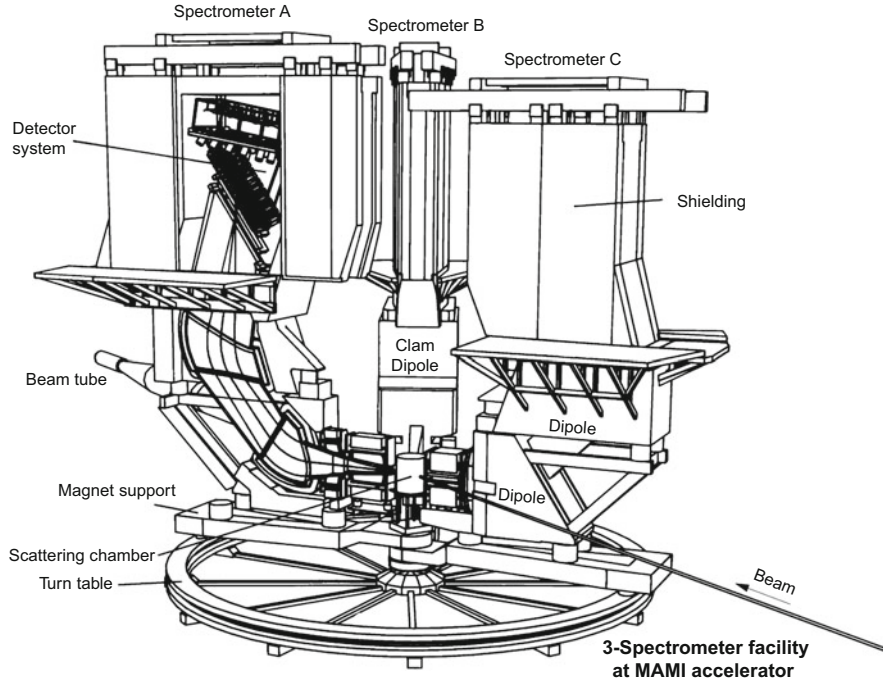


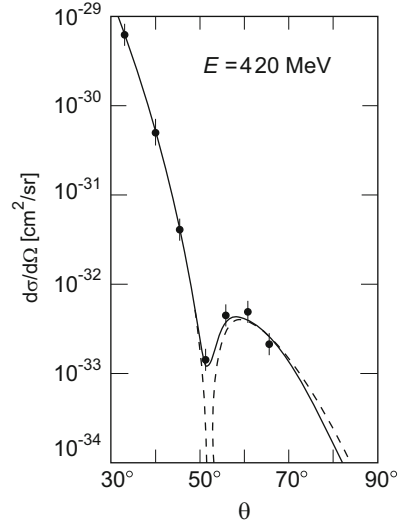
**Fig. 5.5** Experimental set-up for the measurement of electron scattering off protons and nuclei at the electron accelerator MAMI-B (Mainzer Microtron). The maximum energy available is 820 MeV. The figure shows three magnetic spectrometers. They can be used individually to detect elastic scattering or in coincidence for a detailed study of inelastic channels. Spectrometer A is shown in cutaway view. The scattered electrons are analysed according to their momentum by two dipole magnets supplemented by a system of detectors made up of wire chambers and scintillation counters. The diameter of the rotating ring is approximately 12 m (Courtesy of Arnd P. Liesenfeld (Mainz), who produced this picture)

analysing magnet the electrons are deflected according to their momentum, and are then detected in wire chambers. The spectrometer can be rotated around the target in order to allow measurements at different angles  $\theta$ .

**Examples of form factors** The first measurements of nuclear form factors were carried out in the early 1950s at a linear accelerator at Stanford University, California. Cross-sections were measured for a large variety of nuclei at electron energies of about 500 MeV.

An example of one of the first measurements of form factors can be seen in Fig. 5.6. It shows the  $^{12}\text{C}$  cross-section measured as a function of the scattering angle  $\theta$ . The fast fall-off of the cross-section at large angles corresponds to the  $1/|q|^4$ -dependence. Superimposed is a typical diffraction pattern associated with the form factor. It has a minimum at  $\theta \approx 51^\circ$  or  $|q|/\hbar \approx 1.8 \text{ fm}^{-1}$ . We want to now

**Fig. 5.6** Measurement of the form factor of  $^{12}\text{C}$  by electron scattering (From [4]). The figure shows the differential cross-section measured at a fixed beam energy of 420 MeV, at 7 different scattering angles. The *dashed line* corresponds to scattering of a plane wave off an homogeneous sphere with a diffuse surface (Born approximation). The *solid line* corresponds to an exact phase shift analysis which was fitted to the experimental data



discuss this figure and describe what information about the nucleus can be extracted from it.

As we have seen, the form factor  $F(\mathbf{q}^2)$  is under certain conditions (negligible recoil, Born approximation) the Fourier transform of the charge distribution  $f(\mathbf{x})$

$$F(\mathbf{q}^2) = \int e^{i\mathbf{q}\mathbf{x}/\hbar} f(\mathbf{x}) d^3x. \quad (5.42)$$

For spherically symmetric cases  $f$  only depends upon the radius  $r = |\mathbf{x}|$ . Integration over the total solid angle then yields

$$F(\mathbf{q}^2) = 4\pi \int f(r) \frac{\sin |\mathbf{q}|r/\hbar}{|\mathbf{q}|r/\hbar} r^2 dr, \quad (5.43)$$

with the normalisation

$$1 = \int f(\mathbf{x}) d^3x = \int_0^\infty \int_{-1}^+1 \int_0^{2\pi} f(r) r^2 d\phi d \cos \vartheta dr = 4\pi \int_0^\infty f(r) r^2 dr. \quad (5.44)$$

**Table 5.1** Connection between charge distributions and form factors for some spherically symmetric charge distributions in Born approximation

Charge distribution $f(r)$		Form factor $F(q^2)$	
Point	$\delta(r)/4\pi$	1	Constant
Exponential	$(a^3/8\pi) \cdot \exp(-ar)$	$(1 + q^2/a^2\hbar^2)^{-2}$	Dipole
Gaussian	$(a^2/2\pi)^{3/2} \cdot \exp(-a^2r^2/2)$	$\exp(-q^2/2a^2\hbar^2)$	Gaussian
Homogeneous sphere	$\begin{cases} 3/4\pi R^3 & \text{for } r \leq R \\ 0 & \text{for } r > R \end{cases}$	$3\alpha^{-3}(\sin\alpha - \alpha\cos\alpha)$ with $\alpha =  q R/\hbar$	Oscillating

In principle, the radial charge distribution could be determined from the inverse Fourier transform, using the  $q^2$ -dependence of the experimental form factor

$$f(r) = \frac{1}{(2\pi)^3} \int F(q^2) e^{-iqx/\hbar} d^3q. \quad (5.45)$$

In practice, however, the form factor can be measured only over a limited range of momentum transfer  $|q|$ . The limitation is due to the finite beam energy available and the sharp drop in the cross-section for large momentum transfer. One therefore chooses various parametrisations of  $f(r)$ , determines the theoretical prediction for  $F(q^2)$  and varies the parameters to obtain a best fit between theory and the measured value of  $F(q^2)$ .

The form factor can be calculated analytically for certain charge distributions described by some simple radial functions  $f(r)$ . The form factors for some special cases of  $f(r)$  are listed in Table 5.1, and are depicted in Fig. 5.7. A charge distribution which drops off gently corresponds to a smooth form factor. The more extended the charge distribution, the stronger the fall-off of the form factor with  $q^2$ . On the other hand if the object is small, the form factor falls off slowly. In the limit of a point-like target, the form factor approaches unity.

Scattering off an object with a sharp surface generally results in well-defined diffraction maxima and minima. For a homogeneous sphere with radius  $R$ , for example, a minimum is found at

$$\frac{|q| \cdot R}{\hbar} \approx 4.5. \quad (5.46)$$

The location of the minima thus tells us the size of the scattering nucleus.

In Fig. 5.6 we saw that the minimum in the cross-section of electron scattering off  $^{12}\text{C}$  (and thus the minimum in the form factor) is found at  $|q|/\hbar \approx 1.8 \text{ fm}^{-1}$ . One concludes that the carbon nucleus has a radius  $R = 4.5 \hbar/|q| \approx 2.5 \text{ fm}$ .

Figure 5.8 shows the result of an experiment comparing the two isotopes  $^{40}\text{Ca}$  and  $^{48}\text{Ca}$ . This picture is interesting in several respects:

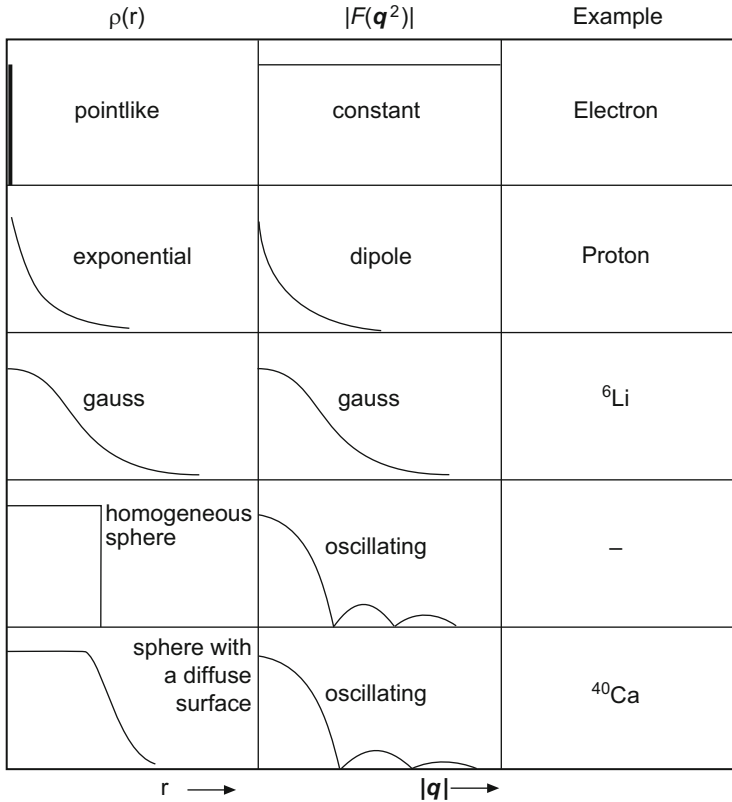


**Fig. 5.7** Relation between the radial charge distribution  $\rho(r)$  and the corresponding form factor in Born approximation. A constant form factor corresponds to a point-like charge (e.g., an electron); a dipole form factor to a charge distribution which falls off exponentially (e.g., a proton); a Gaussian form factor to a Gaussian charge distribution (e.g.,  ${}^6\text{Li}$  nucleus); and an oscillating form factor corresponds to a homogeneous sphere with a more or less sharp edge. All nuclei except for the lightest ones, display an oscillating form factor

- The cross-section was measured over a large range of  $|\mathbf{q}|$ . Within this range, it changes by seven orders of magnitude.<sup>1</sup>
- Not *one* but three minima are visible in the diffraction pattern. This behaviour of the cross-section means that  $F(\mathbf{q}^2)$  and the charge distribution  $\rho(r)$  can be determined very accurately.
- The minima of  ${}^{48}\text{Ca}$  are shifted to slightly lower values of  $|\mathbf{q}|$  than those of  ${}^{40}\text{Ca}$ . This shows that  ${}^{48}\text{Ca}$  is larger.

Information about the nuclear radius can be obtained not only from the location of the minima of the form factor, but also from its behaviour for

<sup>1</sup> Even measurements over 12 (!) orders of magnitude have been carried out (cf., e.g., [5]).

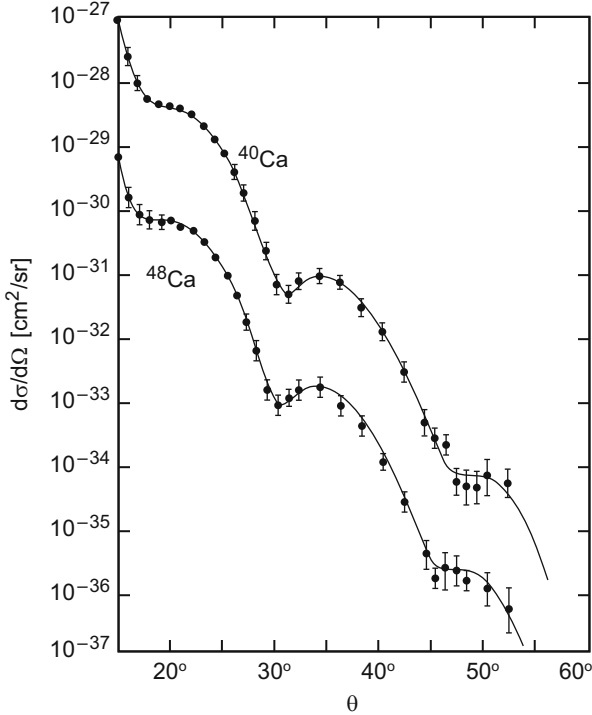


**Fig. 5.8** Differential cross-sections for electron scattering off the calcium isotopes  $^{40}\text{Ca}$  and  $^{48}\text{Ca}$  [1]. For clarity, the cross-sections of  $^{40}\text{Ca}$  and  $^{48}\text{Ca}$  have been multiplied by factors of 10 and  $10^{-1}$ , respectively. The *solid lines* are the charge distributions obtained from a fit to the data. The location of the minima shows that the radius of  $^{48}\text{Ca}$  is larger than that of  $^{40}\text{Ca}$

$q^2 \rightarrow 0$ . If the wavelength is considerably larger than the nuclear radius  $R$ , then

$$\frac{|q| \cdot R}{\hbar} \ll 1, \tag{5.47}$$

and  $F(q^2)$  can from (5.42) be expanded in powers of  $|q|$ :

$$\begin{aligned} F(q^2) &= \int f(\mathbf{x}) \sum_{n=0}^{\infty} \frac{1}{n!} \left( \frac{i|q||x| \cos \vartheta}{\hbar} \right)^n d^3x && \text{with } \vartheta = \sphericalangle(\mathbf{x}, \mathbf{q}) \\ &= \int_0^{\infty} \int_{-1}^{+1} \int_0^{2\pi} f(r) \left[ 1 - \frac{1}{2} \left( \frac{|q|r}{\hbar} \right)^2 \cos^2 \vartheta + \dots \right] d\phi \, d \cos \vartheta \, r^2 dr \\ &= 4\pi \int_0^{\infty} f(r) r^2 dr - \frac{1}{6} \frac{q^2}{\hbar^2} 4\pi \int_0^{\infty} f(r) r^4 dr + \dots \end{aligned} \tag{5.48}$$

Defining the *mean square charge radius* according to the normalisation condition (5.44) by

$$\langle r^2 \rangle = 4\pi \int_0^\infty r^2 \cdot f(r) r^2 dr, \quad (5.49)$$

then

$$F(\mathbf{q}^2) = 1 - \frac{1}{6} \frac{\mathbf{q}^2 \langle r^2 \rangle}{\hbar^2} + \dots \quad (5.50)$$

Hence it is necessary to measure the form factor  $F(\mathbf{q}^2)$  down to very small values of  $\mathbf{q}^2$  in order to determine  $\langle r^2 \rangle$ . The following equation holds:

$$\langle r^2 \rangle = -6 \hbar^2 \left. \frac{dF(\mathbf{q}^2)}{d\mathbf{q}^2} \right|_{\mathbf{q}^2=0}. \quad (5.51)$$

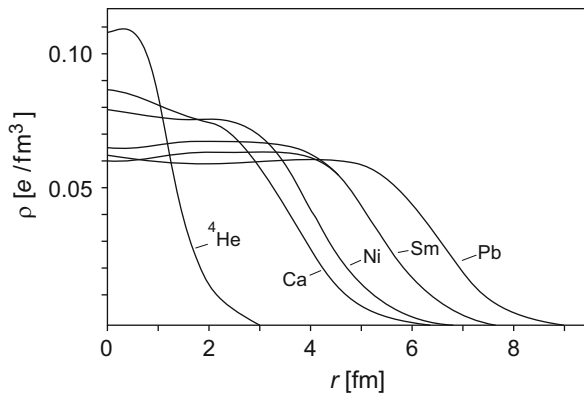
**Charge distributions of nuclei** Many high-precision measurements of this kind have been carried out at different accelerators since the middle of the 1950s. Radial charge distributions  $\varrho(r)$  have been determined from the results. The following has been understood:

- Nuclei are not spheres with a sharply defined surface. In their interior, the charge density is nearly constant. At the surface the charge density falls off over a relatively large range. The radial charge distribution can be described to good approximation by a Fermi function with two parameters

$$\varrho(r) = \frac{\varrho(0)}{1 + e^{(r-c)/a}}. \quad (5.52)$$

This is shown in Fig. 5.9 for different nuclei.

**Fig. 5.9** Radial charge distributions of various nuclei. These charge distributions can be approximately described by the Fermi distribution (5.52), i.e., as spheres with diffuse surfaces





- The constant  $c$  is the radius at which  $\rho(r)$  has decreased by half. Empirically, for larger nuclei,  $c$  and  $a$  are measured to be

$$c = 1.07 \text{ fm} \cdot A^{1/3}, \quad a = 0.54 \text{ fm}. \tag{5.53}$$

- From this charge density, the mean square radius can be calculated. Approximately, for medium and heavy nuclei

$$\langle r^2 \rangle^{1/2} = r_0 \cdot A^{1/3}, \quad \text{where } r_0 = 0.94 \text{ fm}. \tag{5.54}$$

The nucleus is often approximated by a homogeneously charged sphere. The radius  $R$  of this sphere is then quoted as the nuclear radius. The following connection exists between this radius and the mean square radius:

$$R^2 = \frac{5}{3} \langle r^2 \rangle. \tag{5.55}$$

Quantitatively we have

$$R = 1.21 \cdot A^{1/3} \text{ fm}. \tag{5.56}$$

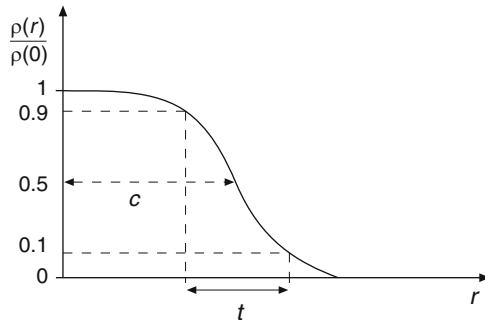
This definition of the radius is used in the mass formula (2.8).

- The surface thickness  $t$  is defined as the thickness of the layer over which the charge density drops from 90 % to 10 % of its maximal value

$$t = r_{(\rho/\rho_0=0.1)} - r_{(\rho/\rho_0=0.9)}. \tag{5.57}$$

Its value is roughly the same for all heavy nuclei, namely

$$t = 2a \cdot \ln 9 \approx 2.40 \text{ fm}. \tag{5.58}$$



- The charge density  $\varrho(0)$  at the centre of the nucleus decreases slightly with increasing mass number. If one takes the presence of the neutrons into account by multiplying by  $A/Z$  one finds an almost identical nuclear density in the nuclear interior for nearly all nuclei. For “infinitely large” nuclear matter, it would amount to<sup>2</sup>

$$\varrho_n \approx 0.17 \text{ nucleons/fm}^3. \quad (5.59)$$

This corresponds to a value of  $c = 1.12 \text{ fm} \cdot A^{1/3}$  in (5.53).

- Some nuclei deviate from a spherical shape and possess ellipsoidal deformations. In particular, this is found in the lanthanides (the “rare earth” elements). Their exact shape cannot be determined by elastic electron scattering. Only a rather diffuse surface can be observed.
- Light nuclei such as  ${}^6\text{Li}$ ,  ${}^9\text{Be}$ , and in particular  ${}^4\text{He}$ , are special cases. Here, no constant density plateau is formed in the nuclear interior, and the charge density is approximately Gaussian.

This summary describes only the global shape of nuclear charge distributions. Many details specific to individual nuclei are known, but will not be treated further here [2].

## 5.5 Inelastic Nuclear Excitations

Above, we have mainly discussed elastic scattering off nuclei. In this case the initial and final state particles are identical. The only energy transferred is recoil energy and the target is not excited to a higher energy level. For fixed scattering angles, the incoming and scattering energies are then uniquely connected by (5.15).

The measured energy spectrum of the scattered electrons, at a fixed scattering angle  $\theta$ , contains events where the energy transfer is larger than we would expect from recoil. These events correspond to inelastic reactions.

Figure 5.10 shows a high-resolution spectrum of electrons with an initial energy of 495 MeV, scattered off  ${}^{12}\text{C}$  and detected at a scattering angle of  $65.4^\circ$ . The sharp peak at  $E' \approx 482 \text{ MeV}$  is due to elastic scattering off the  ${}^{12}\text{C}$  nucleus. Below this energy, excitations of individual nuclear energy levels are clearly seen. The prominent maximum at  $E' \approx 463 \text{ MeV}$  is caused by the giant dipole resonance (Sect. 19.2). At even lower scattering energies a broad distribution from quasi-elastic scattering off the nucleons bound in the nucleus (Sect. 6.2) is seen.

---

<sup>2</sup>This quantity is usually denoted by  $\varrho_0$  in the literature. To avoid any confusion with the charge density we have used the symbol  $\varrho_n$  here.

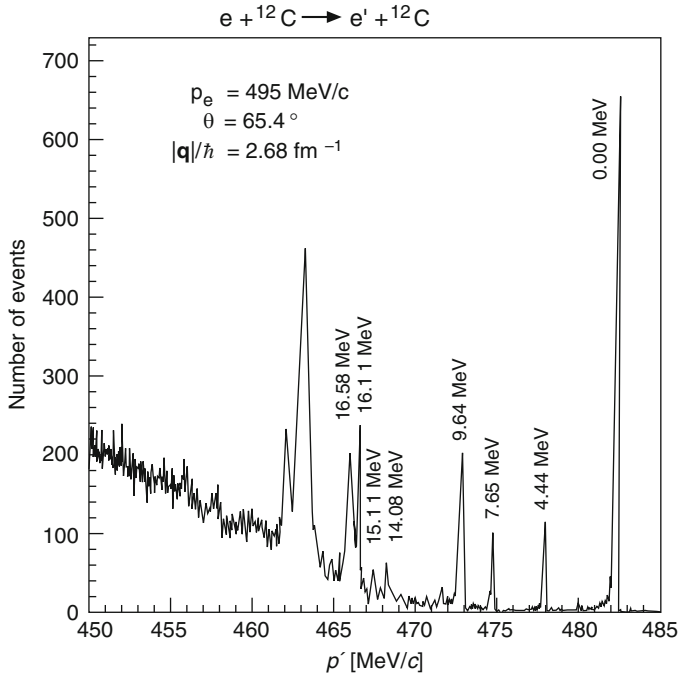


**Fig. 5.10** Spectrum of electron scattering off  ${}^{12}\text{C}$ . The sharp peaks correspond to elastic scattering and to the excitation of discrete energy levels in the  ${}^{12}\text{C}$  nucleus by inelastic scattering. The excitation energy of the nucleus is given for each peak. The 495 MeV electrons were accelerated with the linear accelerator MAMI-B in Mainz and were detected using a high-resolution magnetic spectrometer (cf. Fig. 5.5) at a scattering angle of  $65.4^\circ$  (Courtesy of Th. Walcher and G. Rosner, Mainz)

## Problems

### 1. Kinematics of electromagnetic scattering

An electron beam with energy  $E$  is elastically scattered off a heavy nucleus.

- (a) Calculate the maximal momentum transfer.
- (b) Calculate the momentum and energy of the backwardly scattered nucleus in this case.
- (c) Obtain the same quantities for the elastic scattering of photons with the same energy (nuclear Compton effect).

### 2. Wavelength

Fraunhofer diffraction upon a circular disc with diameter  $D$  produces a ring shaped diffraction pattern. The first minimum appears at  $\theta = 1.22 \lambda/D$ .

Calculate the angular separation of the diffraction minima of  $\alpha$  particles with energy  $E_{\text{kin}} = 100 \text{ MeV}$  scattered off a  $^{56}\text{Fe}$  nucleus. The nucleus should be considered as an impenetrable disc.

### 3. Rutherford scattering

Alpha particles with  $E_{\text{kin}} = 6 \text{ MeV}$  from a radioactive source are scattered off  $^{197}\text{Au}$  nuclei. At which scattering angle are deviations from the cross-section (5.16) to be expected?

### 4. Form factor

Instead of  $\alpha$ -particles with  $E_{\text{kin}} = 6 \text{ MeV}$  we now consider the scattering of electrons with the same de Broglie wavelength off gold. How large must the kinetic energy of the electrons be? How many maxima and minima will be visible in the angular distribution (cf. Fig. 5.8)?

Since the recoil is small in this case, we may assume that the kinematical quantities are the same in both the centre-of-mass and laboratory frames.

### 5. Elastic scattering of X-rays

X-rays are scattered off liquid helium. Which charge carriers in the helium atom are responsible for the scattering? Which of the form factors of Fig. 5.7 corresponds to this scattering off helium?

### 6. Compton scattering

Compton scattering off bound electrons can be understood in analogy to quasi-elastic and deep-inelastic scattering. Gamma rays from positronium annihilation are scattered off helium atoms (binding energy of the “first” electron: 24 eV). Calculate the angular spread of the Compton electrons that are measured in coincidence with photons that are scattered by  $\theta_\gamma = 30^\circ$ .

## References

1. J.B. Bellicard et al., Phys. Rev. Lett. **19**, 527 (1967)
2. J. Friedrich, N. Vögler, Nucl. Phys. **A373**, 192 (1982)
3. K. Gottfried, V.F. Weisskopf, *Concepts of Particle Physics*, vol. 2 (Clarendon Press, Oxford, 1986)
4. R. Hofstadter, Ann. Rev. Nucl. Sci. **7**, 231 (1957)
5. I. Sick et al., Phys. Lett. **B88**, 245 (1979)

# Chapter 6

## Elastic Scattering Off Nucleons

### 6.1 Form Factors of the Nucleons

Elastic electron scattering off the lightest nuclei, hydrogen and deuterium, yields information about the nuclear building blocks, the proton and the neutron. Certain subtleties have, however, to be taken into account in any discussion of these experiments.

**Recoil** As we will soon see, nucleons have a radius of about 0.8 fm. Their study therefore requires energies from some hundred MeV up to several GeV. Comparing these energies with the mass of the nucleon,  $M \approx 938 \text{ MeV}/c^2$ , we see that they are of the same order of magnitude. Hence the target recoil can no longer be neglected. In the derivation of the cross-sections (5.33) and (5.39) we “prepared” for this by using  $E'$  rather than  $E$ . On top of this, however, the phase-space density  $dn/dE_f$  in (5.20) must be modified. We so eventually find an additional factor of  $E'/E$  in the Mott cross-section [13]:

$$\left(\frac{d\sigma}{d\Omega}\right)_{\text{Mott}} = \left(\frac{d\sigma}{d\Omega}\right)_{\text{Mott}}^* \cdot \frac{E'}{E}. \quad (6.1)$$

Since the energy loss of the electron due to the recoil is now significant, it is no longer possible to describe the scattering in terms of a three-momentum transfer. Instead, the Lorentz-invariant squared four-momentum transfer,

$$\begin{aligned} q^2 &= (p - p')^2 = 2m_e^2c^2 - 2(EE'/c^2 - |\mathbf{p}||\mathbf{p}'| \cos \theta) \\ &\approx \frac{-4EE'}{c^2} \sin^2 \frac{\theta}{2}, \end{aligned} \quad (6.2)$$

must be used. In order to only work with positive quantities we define:

$$Q^2 = -q^2. \quad (6.3)$$

In the Mott cross-section,  $q^2$  must be replaced by  $q^2$  or  $Q^2$ .

**Magnetic moment** We must now not only take the interaction of the electron with the nuclear charge into account, but also we have to consider the interaction between the current of the electron and the nucleon's magnetic moment.

The magnetic moment of a spin-1/2 particle is given by

$$\mu = g \cdot \frac{e}{2M} \cdot \frac{\hbar}{2}, \quad (6.4)$$

where  $M$  is the mass of the particle. For a charged, point-like particle which does not possess any internal structure, the factor  $g$  is equal to 2 as a result of relativistic quantum mechanics (the Dirac equation). The magnetic interaction is associated with a flip of the spin of the nucleon. Scattering through  $0^\circ$  is not consistent with conservation of both angular momentum and helicity and scattering through  $180^\circ$  is preferred. The magnetic interaction is taken into account by an additional term in the cross-section that contains a factor of  $\sin^2 \frac{\theta}{2}$ . With  $\sin^2 \frac{\theta}{2} = \cos^2 \frac{\theta}{2} \cdot \tan^2 \frac{\theta}{2}$  the cross-section for elastic electron scattering on a charged Dirac particle reads:

$$\left( \frac{d\sigma}{d\Omega} \right)_{\text{spin } 1/2}^{\text{point}} = \left( \frac{d\sigma}{d\Omega} \right)_{\text{Mott}} \cdot \left[ 1 + 2\tau \tan^2 \frac{\theta}{2} \right], \quad (6.5)$$

where

$$\tau = \frac{Q^2}{4M^2 c^2}. \quad (6.6)$$

The factor  $2\tau$  can be fairly easily understood: the matrix element of the interaction is proportional to the magnetic moment of the nucleon (and thus to  $1/M$ ) and to the magnetic field which is produced at the target in the scattering process. Integrated over time, this is proportional to the deflection of the electron (i.e., to the momentum transfer  $Q$ ). These quantities then enter the cross-section quadratically.

The magnetic term in (6.5) is large at large values of the four-momentum transfer  $Q$  and at large scattering angles  $\theta$ . Because of this additional term, the cross-section decreases less steeply with the scattering angle than for the electric interaction alone and the distribution is more isotropic.

**Anomalous magnetic moment** For charged Dirac particles without internal structure the  $g$ -factor in (6.4) should be exactly 2, while for neutral such particles the magnetic moment should vanish. Indeed, measurements of the magnetic moments of electrons and muons yield the value  $g = 2$  up to small deviations that are caused

by (theoretically well understood) quantum electrodynamical processes of higher order.

Nucleons, however, are not point-like particles since they are made up of quarks. Therefore their  $g$ -factors are determined by their sub-structure. The values measured for protons and neutrons are

$$\mu_p = \frac{g_p}{2} \mu_N = +2.793 \cdot \mu_N , \quad (6.7)$$

$$\mu_n = \frac{g_n}{2} \mu_N = -1.913 \cdot \mu_N , \quad (6.8)$$

where the nuclear magneton  $\mu_N$  is:

$$\mu_N = \frac{e\hbar}{2M_p} = 3.1525 \cdot 10^{-14} \text{ MeV T}^{-1} . \quad (6.9)$$

**Form factors** Charge and current distributions can be described by form factors, just as in the case of nuclei. For nucleons, two form factors are necessary to characterise both the electric and magnetic distributions. The cross-section for the scattering of an electron off a nucleon is described by the *Rosenbluth formula* [16]:

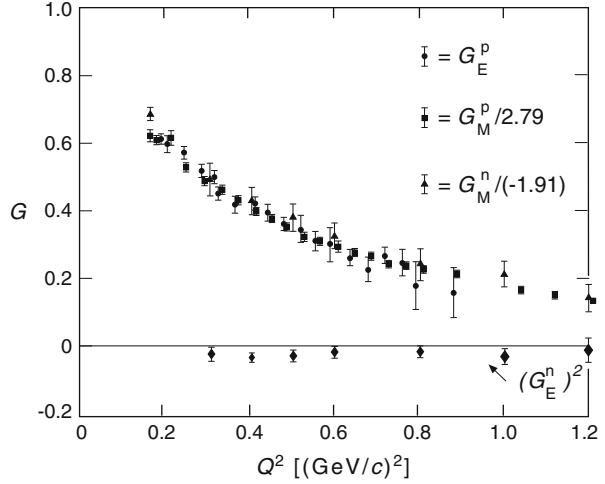
$$\left( \frac{d\sigma}{d\Omega} \right) = \left( \frac{d\sigma}{d\Omega} \right)_{\text{Mott}} \cdot \left[ \frac{G_E^2(Q^2) + \tau G_M^2(Q^2)}{1 + \tau} + 2\tau G_M^2(Q^2) \tan^2 \frac{\theta}{2} \right] . \quad (6.10)$$

Here  $G_E(Q^2)$  and  $G_M(Q^2)$  are the *electric and magnetic form factors* which depend on  $Q^2$ . The measured  $Q^2$  dependence of the form factors gives us information about the radial distributions of charge and magnetisation. The limiting case  $Q^2 \rightarrow 0$  is particularly important. In this case  $G_E$  coincides with the electric charge of the target, normalised to the elementary charge  $e$ ; and  $G_M$  is equal to the magnetic moment  $\mu$  of the target, normalised to the nuclear magneton. The limiting values are:

$$\begin{aligned} G_E^p(Q^2 = 0) &= 1 & G_E^n(Q^2 = 0) &= 0 \\ G_M^p(Q^2 = 0) &= 2.793 & G_M^n(Q^2 = 0) &= -1.913 . \end{aligned} \quad (6.11)$$

In order to independently determine  $G_E(Q^2)$  and  $G_M(Q^2)$  the cross-sections must be measured at fixed values of  $Q^2$  for various scattering angles  $\theta$  (i.e., at different beam energies  $E$ ). The measured cross-sections are then divided by the Mott cross-sections. If we display the results as a function of  $\tan^2 \frac{\theta}{2}$  then the measured points form a straight line, in accordance with the Rosenbluth formula.  $G_M(Q^2)$  is determined by the slope of the line, and the intercept  $(G_E^2 + \tau G_M^2)/(1 + \tau)$  at  $\theta = 0$  yields  $G_E(Q^2)$ . If we perform this analysis for various values of  $Q^2$ , we can obtain the  $Q^2$  dependence of the form factors.

**Fig. 6.1** Proton and neutron electric and magnetic form factors as functions of  $Q^2$ . The data points are scaled by the factors noted in the diagram so that they coincide and thus more clearly display the global dipole-like behaviour [9]



Measurements of the electromagnetic form factors were carried out mainly in the 1960s and 1970s at various electron accelerators in the United States and in Europe. Figure 6.1 shows the results of a pioneering experiment at Stanford where, by elastic electron scattering off protons and deuterons, the  $Q^2$  dependence of the two form factors for both proton and neutron were determined up to  $Q^2$  values of  $1.2 \text{ (GeV/c)}^2$  [9].

It turned out that the proton electric form factor and the magnetic form factors of both the proton and the neutron fall off similarly with  $Q^2$ . They can be described to a good approximation by a so-called *dipole form factor*

$$G_E^p(Q^2) \approx \frac{\mu_N G_M^p(Q^2)}{\mu_p} \approx \frac{\mu_N G_M^n(Q^2)}{\mu_n} \approx G^{\text{dipole}}(Q^2),$$

$$\text{where } G^{\text{dipole}}(Q^2) = \left(1 + \frac{Q^2}{0.71 \text{ (GeV/c)}^2}\right)^{-2}. \quad (6.12)$$

The neutron, being electrically neutral, has a very small electric form factor.

We may obtain distributions of charge and magnetisation inside the nucleon from the  $Q^2$  dependence of the form factors, just as we saw could be done for nuclei. The interpretation of the form factors as the Fourier transform of the static charge distribution is, however, only correct for small values of  $Q^2$ , since only then the three- and four-momentum transfers are approximately equal. The observed dipole form factor (6.12) corresponds to a charge distribution which falls off exponentially (cf. Fig. 5.7):

$$\varrho(r) = \varrho(0) e^{-ar} \quad \text{with } a = 4.27 \text{ fm}^{-1}. \quad (6.13)$$



Nucleons are, we see, neither point-like particles nor homogeneously charged spheres, but rather quite diffuse systems.

The mean square radii of the charge distribution in the proton and of the distributions of magnetisation in the proton and the neutron are similarly large. They may be found from the slope of  $G_{E,M}(Q^2)$  at  $Q^2 = 0$ . The dipole form factor yields:

$$\langle r^2 \rangle_{\text{dipole}} = -6\hbar^2 \left. \frac{dG^{\text{dipole}}(Q^2)}{dQ^2} \right|_{Q^2=0} = \frac{12}{a^2} = 0.66 \text{ fm}^2 ,$$

$$\sqrt{\langle r^2 \rangle_{\text{dipole}}} = 0.81 \text{ fm} . \quad (6.14)$$

Precise measurements of the form factors at small values of  $Q^2$  show slight deviations from the dipole parametrisation. The slope at  $Q^2 \rightarrow 0$  determined from these data yields the present best value [5] of the charge radius of the proton:

$$\sqrt{\langle r^2 \rangle_p} = 0.879 \text{ fm} . \quad (6.15)$$

In subsequent measurements at the linear accelerator SLAC at Stanford, the  $Q^2$  range has been extended beyond 30  $(\text{GeV}/c)^2$  [6]. Small deviations from the relation  $\mu_N G_M^p(Q^2)/\mu_p G^{\text{dipole}}(Q^2) = 1$  have been observed. Figure 6.2 shows the results of a global analysis of all presently available data [4]. Below  $Q^2 \approx 10$   $(\text{GeV}/c)^2$  the deviations amount to a few percent only. At larger  $Q^2$  values  $G_M^p$  decreases faster with  $Q^2$  than the dipole form factor. At  $Q^2 \approx 30$   $(\text{GeV}/c)^2$   $\mu_N G_M^p/\mu_p$  is about 30 % smaller than  $G^{\text{dipole}}$ .

Of special interest are more recent experiments that have been performed at the beginning of this century at the Thomas Jefferson Accelerator Facility (JLab) in the

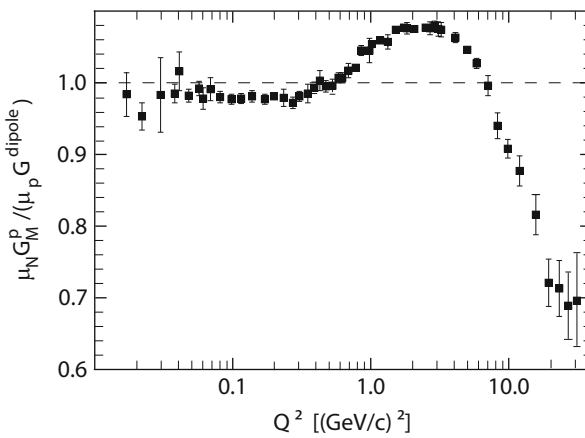
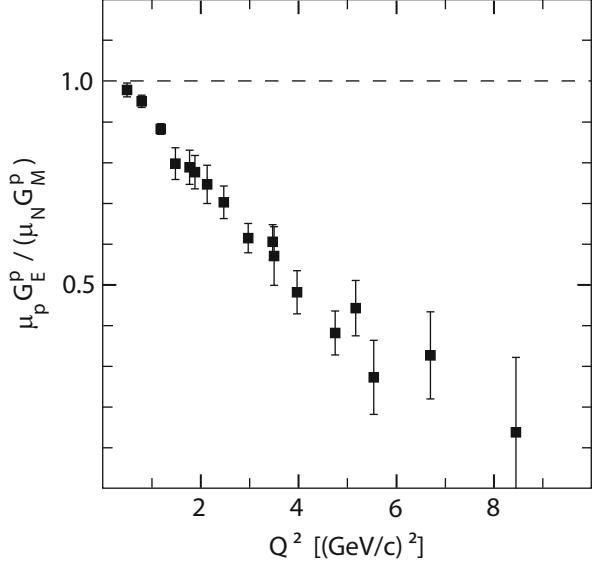


**Fig. 6.2** Ratio of the normalised magnetic form factor  $\mu_N G_M^p/\mu_p$  of the proton and the dipole form factor  $G^{\text{dipole}}$  as a function of  $Q^2$  (After [4])

**Fig. 6.3** Ratio of the electric form factor  $G_E^p$  and the normalised magnetic form factor  $\mu_N G_M^p / \mu_p$  of the proton as a function of  $Q^2$  from double-polarisation measurements [7, 14, 15]



USA. In these measurements  $G_E^p$  and  $G_M^p$  have not been determined by means of the Rosenbluth separation. Instead, longitudinally polarised electrons whose spin is oriented preferentially parallel to the beam direction or opposite to it are scattered off unpolarised protons. Thereby the recoil proton gets polarised:  $\vec{e} + p \rightarrow e' + \vec{p}$ . It acquires two polarisation components,  $P_t$ , perpendicular to the proton momentum in the scattering plane and  $P_\ell$ , parallel to it. Their ratio directly yields [3]

$$\frac{G_E}{G_M} = -\frac{P_t}{P_\ell} \cdot \frac{E + E'}{2Mc^2} \tan \frac{\theta}{2}. \quad (6.16)$$

Figure 6.3 shows results of such measurements. The experimentally determined ratio  $\mu_p G_E^p(Q^2) / (\mu_N G_M^p(Q^2))$  decreases nearly linearly with  $Q^2$  in the range  $0.5 \text{ (GeV/c)}^2 < Q^2 < 8.5 \text{ (GeV/c)}^2$  down to approximately 0.2 at the highest  $Q^2$  value [7, 10, 14, 15]. Therefore, the spatial distributions of the electric charge and the magnetisation in the proton are substantially different: the charge distribution extends to larger radii than the distribution of the magnetisation.

The discrepancy of the results obtained by the two methods is astounding. At present, a favoured explanation is a possible contribution of two-photon exchange in the scattering process. This might give rise to large corrections for the Rosenbluth separation while it hardly affects the double-polarisation measurement.

**The electric form factor of the neutron** In the absence of a free neutron target, the measurement of the two elastic form factors for the neutron is less straightforward than for the proton. Most of the information about  $G_M^n(Q^2)$  and  $G_E^n(Q^2)$  has been obtained from elastic electron scattering from deuterium. In this case it is necessary to correct the measured data for the effects of the nuclear force between the

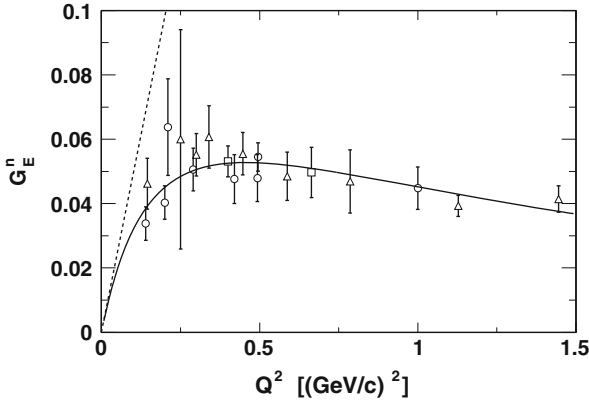


**Fig. 6.4** World data on the electric form factor of the neutron from double-polarisation experiments (After [8]). The symbols characterise the measurement method: *circles* – polarised deuterium, *squares* – polarised  $^3\text{He}$ , *triangles* – measurement of the polarisation of the recoil neutron. The *solid line* is a parametrisation of the data, the *dashed straight line* shows the slope of  $G_E^n(Q^2)$  at  $Q^2 = 0$   $(\text{GeV}/c)^2$  that is proportional to the (negative) mean square radius of the neutron

proton and the neutron. Incomplete corrections of this kind are responsible for the negative values of  $(G_E^n)^2$  seen in Fig. 6.1. Initially the authors of these measurements speculated that  $G_E^n$  might be imaginary, but subsequently it was shown that  $G_E^n$  is positive, leading, seemingly, to a contradiction.

To explain this contradiction, precise results have been obtained from double-polarisation experiments with longitudinally polarised electron beams and either polarised targets or the measurement of the polarisation of the recoil neutron. Usually either deuterium or  $^3\text{He}$  are used as polarised neutron targets. The deuteron nucleus has spin-1, caused by the parallel spins of the proton and the neutron and in addition a small D-state admixture to the deuteron wave function (cf. Sect. 17.2). Polarised  $^3\text{He}$  is regarded as an effective polarised neutron target, as the spins of the two protons largely cancel. The world's data on  $G_E^n$  from double-polarisation experiments [8] are displayed in Fig. 6.4 as a function of  $Q^2$ . The form factor rises from zero at  $Q^2 = 0$   $(\text{GeV}/c)^2$  up to a value of approximately 0.06 at  $Q^2 \approx 0.3$   $(\text{GeV}/c)^2$  and then decreases slowly with increasing  $Q^2$ . The slope at  $Q^2 \rightarrow 0$  is positive. Consequently the mean square radius of the neutron must be negative.

An elegant approach has been developed to determine the charge radius of the free neutron. Low-energy neutrons from a nuclear reactor are scattered off electrons in an atomic shell of a heavy nucleus and the resulting ejected electrons are then measured. This reaction corresponds to electron-neutron scattering at small  $Q^2$ . The result of these measurements is [11]:

$$-6\hbar^2 \left. \frac{dG_E^n(Q^2)}{dQ^2} \right|_{Q^2=0} = -0.115 \pm 0.004 \text{ fm}^2. \quad (6.17)$$

The dashed straight line in Fig. 6.4 corresponds to these measurements. The neutron only appears electrically neutral from the outside; its interior contains electrically charged constituents which also possess magnetic moments. Since both the charges and their magnetic moments contribute to the electric form factor, we cannot separate their contributions in a Lorentz-invariant fashion. An interpretation as a Fourier transform of the static charge distribution has to be taken with caution, as already stated above. When (despite these restrictions) a Fourier transformation of the parametrisation shown in Fig. 6.4 is performed, one obtains a radial charge density  $\varrho^n(r)$  that is positive for  $r$  below approximately 0.5–0.6 fm and negative for larger values of  $r$ , and which extends to radii of approximately 2.5 fm. Calculations within the framework of various models yield a similar radial dependence of the charge density of the neutron [17].

## 6.2 Quasi-elastic Scattering

In Sect. 6.1 we considered the elastic scattering of electrons off free protons (neutrons) at rest. For a given beam energy  $E$  and at a fixed scattering angle  $\theta$ , scattered electrons from this reaction always have a definite scattering energy  $E'$  which is given by (5.15)

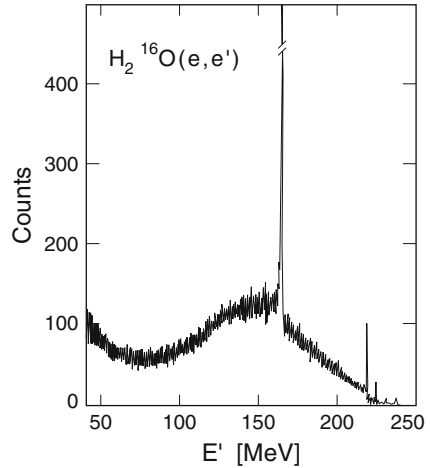
$$E' = \frac{E}{1 + \frac{E}{Mc^2}(1 - \cos \theta)}. \quad (6.18)$$

Repeating the scattering experiment at the same beam energy and at the same detector angle, but now off a nucleus containing several nucleons, a more complicated energy spectrum is observed. Figure 6.5 shows a spectrum of electrons which were scattered off a thin  $\text{H}_2\text{O}$  target, i.e., some were scattered off free protons, some off oxygen nuclei.

The narrow peak observed at  $E' \approx 160 \text{ MeV}$  stems from elastic scattering off the free protons in hydrogen. Superimposed is a broad distribution with a maximum shifted a few MeV towards smaller scattering energies. This part of the spectrum may be identified with the scattering of electrons off individual nucleons within the  $^{16}\text{O}$  nucleus. This process is called *quasi-elastic scattering*. The sharp peaks at high energies are caused by scattering off the  $^{16}\text{O}$  nucleus as a whole (cf. Fig. 5.10). At the left side of the picture, the tail of the  $\Delta$ -resonance can be recognised; this will be discussed in Sect. 7.1.

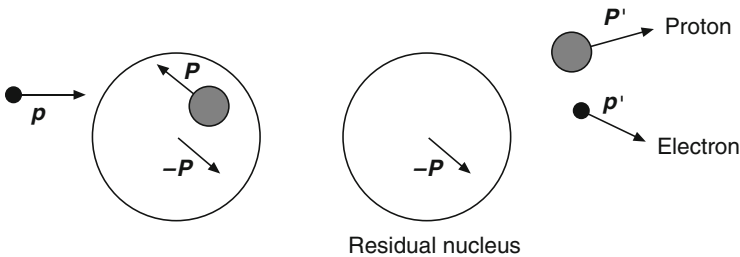
Both the shift and the broadening of the quasi-elastic spectrum contain information about the internal structure of atomic nuclei. In the *impulse approximation* we assume that the electron interacts with a single nucleon. The nucleon is knocked out of the nuclear system by the scattering process without any further interactions with the remaining nucleons in the nucleus. The shift of the maximum in the energy distribution of the scattered electrons towards lower energies compared to the free-proton case is due to the energy needed to remove the nucleon from the nucleus.

**Fig. 6.5** Energy spectrum of electrons scattered off a thin H<sub>2</sub>O target. The data were taken at the linear accelerator MAMI-A at Mainz with a beam energy of 246 MeV and at a scattering angle of 148.5° (Courtesy of J. Friedrich, Mainz)



From the broadening of the maximum compared to elastic scattering off free protons in the hydrogen atom, we conclude that the nucleus is not a static object with locally fixed nucleons. The nucleons rather move around “quasi-freely” within the nucleus. This motion causes a change in the kinematics compared to scattering off a nucleon at rest.

Let us consider a bound nucleon moving with momentum  $\mathbf{P}$  in an effective average nuclear potential of strength  $S$ . This nucleon’s binding energy is then  $S - \mathbf{P}^2/2M$ . We neglect residual interactions with other nucleons, and the kinetic energy of the remaining nucleus and consider the scattering of an electron off this nucleon.



In this case, the following kinematic connections apply:

$$\begin{aligned}
 \mathbf{p} + \mathbf{P} &= \mathbf{p}' + \mathbf{P}' && \text{momentum conservation in the e-p system} \\
 \mathbf{P}' &= \mathbf{q} + \mathbf{P} && \text{momentum conservation in the } \gamma\text{-p system} \\
 E + E_p &= E' + E'_p && \text{energy conservation in the e-p system}
 \end{aligned}$$

The energy transfer  $\nu$  from the electron to the proton for  $E, E' \gg m_e c^2$  and  $|\mathbf{P}|, |\mathbf{P}'| \ll Mc$  is given by

$$\begin{aligned} \nu &= E - E' = E'_p - E_p = \left( Mc^2 + \frac{\mathbf{P}^2}{2M} \right) - \left( Mc^2 + \frac{\mathbf{P}^2}{2M} - S \right) \\ &= \frac{(\mathbf{P} + \mathbf{q})^2}{2M} - \frac{\mathbf{P}^2}{2M} + S = \frac{\mathbf{q}^2}{2M} + S + \frac{2|\mathbf{q}||\mathbf{P}|\cos\alpha}{2M}, \end{aligned} \quad (6.19)$$

where  $\alpha$  is the angle between  $\mathbf{q}$  and  $\mathbf{P}$ . We now assume that the motion of the nucleons within the nucleus is isotropic (i.e., a spherically symmetric distribution). This leads to a symmetric distribution for  $\nu$  around an average value

$$\nu_0 = \frac{\mathbf{q}^2}{2M} + S \quad (6.20)$$

with a width of

$$\sigma_\nu = \sqrt{\langle (\nu - \nu_0)^2 \rangle} = \frac{|\mathbf{q}|}{M} \sqrt{\langle \mathbf{P}^2 \cos^2 \alpha \rangle} = \frac{|\mathbf{q}|}{M} \sqrt{\frac{1}{3} \langle \mathbf{P}^2 \rangle}. \quad (6.21)$$

**Fermi momentum** As we will discuss in Sect. 18.1, the nucleus can be described as a *Fermi gas* in which the nucleons move around like quasi-free particles. The *Fermi momentum*  $P_F$  is related to the mean square momentum by (cf. (18.9)):

$$P_F^2 = \frac{5}{3} \langle \mathbf{P}^2 \rangle. \quad (6.22)$$

An analysis of quasi-elastic scattering off different nuclei can thus determine the effective average potential  $S$  and the Fermi momentum  $P_F$  of the nucleons.

Studies of the  $A$ -dependence of  $S$  and  $P_F$  were first carried out in the early seventies. The results of the first systematic analysis are shown in Table 6.1 and can be summarised as follows:

- The effective average nuclear potential  $S$  increases continuously with the mass number  $A$ , varying between 17 MeV in Li to 44 MeV in Pb.

**Table 6.1** Fermi momentum  $P_F$  and effective average potential  $S$  for various nuclei. These values were obtained from an analysis of quasi-elastic electron scattering at beam energies between 320 and 500 MeV and at a fixed scattering angle of  $60^\circ$  [12, 18]. The errors are approximately 5 MeV/ $c$  ( $P_F$ ) and 3 MeV ( $S$ )

Nucleus	${}^6\text{Li}$	${}^{12}\text{C}$	${}^{24}\text{Mg}$	${}^{40}\text{Ca}$	${}^{59}\text{Ni}$	${}^{89}\text{Y}$	${}^{119}\text{Sn}$	${}^{181}\text{Ta}$	${}^{208}\text{Pb}$
$P_F$ (MeV/ $c$ )	169	221	235	249	260	254	260	265	265
$S$ (MeV)	17	25	32	33	36	39	42	42	44

- Apart from in the lightest nuclei, the Fermi momentum is nearly independent of  $A$  and is:

$$P_F \approx 250 \text{ MeV}/c . \quad (6.23)$$

This behaviour is consistent with the Fermi gas model. The density of nuclear matter is independent of the mass number except for in the lightest nuclei.

### 6.3 Charge Radii of Pions and Kaons

The charge radii of various other particles can also be measured by the same method that was used for the neutron. For example those of the  $\pi$ -meson [1] and the K-meson [2], particles which we will introduce in Sect. 8.1. High-energy mesons are scattered off electrons in the hydrogen atom. The form factor is then determined by analysing the angular distribution of the ejected electrons. Since the pion and the kaon are spin-0 particles, they have an electric but not a magnetic form factor.

The  $Q^2$ -dependence of these form factors is shown in Fig. 6.6. Both can be described by a *monopole form factor*:

$$F(Q^2) = G_E(Q^2) = (1 + Q^2/a^2\hbar^2)^{-1} \quad \text{with} \quad a^2 = \frac{6}{\langle r^2 \rangle} . \quad (6.24)$$

The slopes near the origin yield the mean square charge radii:

$$\begin{aligned} \langle r^2 \rangle_\pi &= 0.44 \pm 0.02 \text{ fm}^2 ; \quad \sqrt{\langle r^2 \rangle}_\pi = 0.67 \pm 0.02 \text{ fm} \\ \langle r^2 \rangle_K &= 0.34 \pm 0.05 \text{ fm}^2 ; \quad \sqrt{\langle r^2 \rangle}_K = 0.58 \pm 0.04 \text{ fm} . \end{aligned}$$

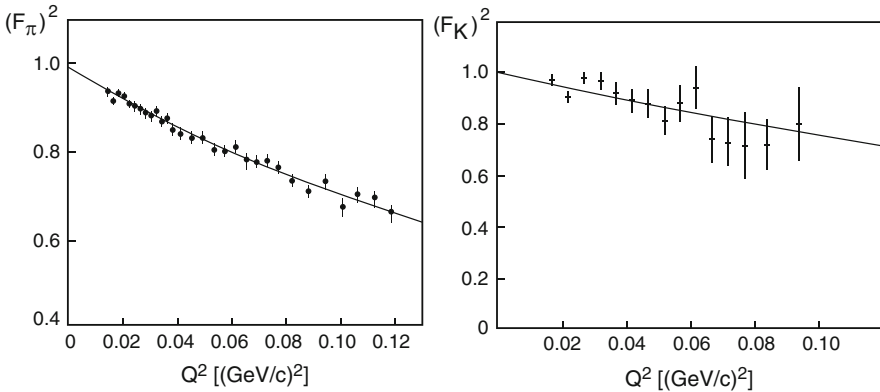


**Fig. 6.6** Pion and kaon form factors as functions of  $Q^2$  (From [1] and [2]). The *solid lines* correspond to a monopole form factor,  $(1 + Q^2/a^2\hbar^2)^{-1}$

We see that the pion and the kaon have a different charge distribution than the proton; in particular it is less spread out. This may be understood as a result of the different internal structures of these particles. We will see in Chap. 8 that the proton is composed of three quarks, while the pion and kaon are both composed of a quark and an antiquark.

The kaon has a smaller radius than that of the pion. This can be traced back to the fact that the kaon, in contrast to the pion, contains a heavy quark (an s-quark). In Sect. 14.5 we will demonstrate in a heavy quark-antiquark system that the radius of a system of quarks decreases if the mass of its constituents increases.

## Problems

### 1. Electron radius

Suppose one wants to obtain an upper bound for the electron's radius by looking for a deviation from the Mott cross-section in electron-electron scattering. What centre-of-mass energy would be necessary to set an upper limit on the radius of  $10^{-3}$  fm?

### 2. Electron-pion scattering

State the differential cross-section,  $d\sigma/d\Omega$ , for elastic electron-pion scattering. Write out explicitly the  $Q^2$  dependence of the form factor part of the cross-section in the limit  $Q^2 \rightarrow 0$  assuming that  $\langle r^2 \rangle_\pi = 0.44 \text{ fm}^2$ .

## References

1. S.R. Amendolia et al., Phys. Lett. **B146**, 116 (1984)
2. S.R. Amendolia et al., Phys. Lett. **B178**, 435 (1986)
3. R.G. Arnold et al., Phys. Rev. **C23**, 363 (1981)
4. J. Arrington et al., Phys. Rev. **C76**, 035205 (2007)
5. J.C. Bernauer et al., Phys. Rev. Lett. **105**, 242001 (2010)
6. P.E. Bosted et al., Phys. Rev. **C42**, 38 (1990)
7. O. Gayou et al., Phys. Rev. Lett. **88**, 092301 (2002)
8. D.K. Hasell et al., Annu. Rev. Nucl. Part. Sci. **61**, 409 (2011)
9. E.B. Hughes et al., Phys. Rev. **B139**, 458 (1965)
10. Ch.E. Hyde-Wright, K. de Jager, Annu. Rev. Nucl. Part. Sci. **54**, 217 (2004)
11. S. Kopecky et al., Phys. Rev. **C56**, 2229 (1997)
12. E.J. Moniz et al., Phys. Rev. Lett. **26**, 445 (1971)
13. D.H. Perkins, *Introduction to High Energy Physics*, 4th edn. (Addison-Wesley, Wokingham, 2000)
14. A.J.R. Puckett et al., Phys. Rev. Lett. **104**, 242301 (2010)
15. V. Punjabi et al., Phys. Rev. **C71**, 055202 (2005)
16. M.N. Rosenbluth, Phys. Rev. **79**, 615 (1950)
17. A.W. Thomas, W. Weise, *The Structure of the Nucleon* (Wiley-VCH, Berlin, 2001)
18. R.R. Whitney et al., Phys. Rev. **C9**, 2230 (1974)



# Chapter 7

## Deep-Inelastic Scattering

*Verlockend ist der äußere Schein der Weise dringet tiefer ein.*

Wilhelm Busch  
Der Geburtstag

In the present chapter we will discuss deep-inelastic scattering of charged leptons off nucleons and demonstrate that these nucleons are not fundamental particles but that they have a substructure of quarks and gluons. To resolve the nucleon's constituents experimentally, the wavelength of the exchanged virtual photon has to be small compared to the nucleon's radius,  $\lambda \ll R$ , and consequently high beam energies are required. The first generation of such experiments was carried out in the late 1960s and in the 1970s at SLAC using a linear electron accelerator with a maximum energy of 25 GeV. The second generation was performed in the 1980s and 1990s at CERN and FNAL using beams of muons instead of electrons. Like electrons, muons are point-like charged particles; the scattering processes are completely analogous and the cross-sections are the same. Muon beams have the advantage that they can be produced at much higher energies than electron beams. In order to make those muon beams, protons with energies of several hundred GeV impinge on a target producing a large number of pions. On a several hundred metre long decay line, a fraction of these pions decays in flight into muons (cf. Sect. 10.1) which are then momentum-selected and focused by a series of magnetic lenses to form a beam. At CERN (FNAL) average beam energies of up to 280 GeV (490 GeV) and  $Q^2$ -values of several hundred  $(\text{GeV}/c)^2$  have been achieved. The last generation of such experiments has been performed in the years 1992–2007 at the electron-proton collider HERA located at DESY. Here electrons or positrons with 27.6 GeV and protons with a maximum beam energy of 920 GeV circulated in two separate storage rings in opposite directions and were brought to collision at two crossing points. The resulting kinematic region extended to  $Q^2$ -values of several  $10^4 (\text{GeV}/c)^2$ .

The basic properties of the quark and gluon structure of the hadrons were established by the experiments at SLAC, which will be discussed and interpreted in this chapter. The second and the third generations of experiments served for detailed studies of this structure and tests of Quantum Chromodynamics (QCD), the theory of the strong interaction, which we will discuss in the subsequent chapter.

## 7.1 Excited States of the Nucleons

In Fig. 5.10 of Sect. 5.5 we presented the spectrum observed in electron scattering off the  $^{12}\text{C}$  nucleus where, in addition to the sharp peak due to elastic scattering off the whole nucleus, further peaks appeared associated with nuclear excitations. Similar spectra are observed for electron-nucleon scattering.

Figure 7.1 shows a spectrum from electron-proton scattering. It was obtained at an electron energy  $E = 4.9\text{ GeV}$  and at a scattering angle of  $\theta = 10^\circ$  by varying the accepted scattering energy of a magnetic spectrometer in small steps. Besides the sharp elastic scattering peak (scaled down by a factor of 15 for clarity), peaks at lower scattering energies are observed associated with inelastic excitations of the proton. These peaks correspond to excited states of the nucleon which we call *nucleon resonances*. The existence of these excited states of the proton already indicates that the proton is a composite system. In Chap. 16 we will explain the structure of these resonances in the framework of the quark model.

The invariant mass of these states is denoted by  $W$ . It is calculated from the four-momenta of the exchanged photon ( $q$ ) and of the incoming proton ( $P$ ) according to

$$W^2 c^2 = P'^2 = (P + q)^2 = M^2 c^2 + 2Pq + q^2 = M^2 c^2 + 2M\nu - Q^2. \quad (7.1)$$

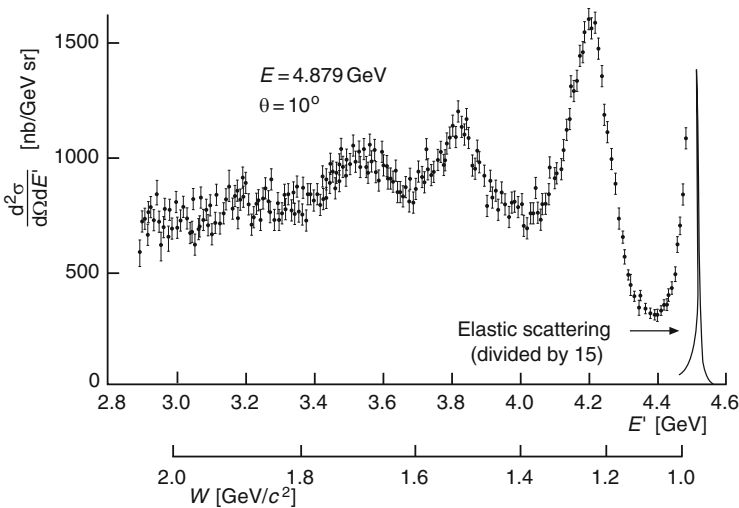


**Fig. 7.1** Spectrum of scattered electrons from electron-proton scattering at an electron energy of  $E = 4.9\text{ GeV}$  and a scattering angle of  $\theta = 10^\circ$  (From [4])

Here the Lorentz-invariant quantity  $\nu$  is defined as

$$\nu = \frac{Pq}{M} . \quad (7.2)$$

The target proton is at rest in the laboratory system. This corresponds to  $P = (Mc, \mathbf{0})$  and  $q = ((E - E')/c, \mathbf{q})$ . Therefore the energy transferred by the virtual photon from the electron to the proton in the laboratory frame is:

$$\nu = E - E' . \quad (7.3)$$

For the following discussion it is useful to introduce two additional dimensionless Lorentz-invariant quantities. These are the variable

$$y := \frac{Pq}{Pp} \stackrel{\text{Lab.}}{=} 1 - \frac{E'}{E} \quad (7.4)$$

and the *Bjorken scaling variable*

$$x := \frac{Q^2}{2Pq} = \frac{Q^2}{2M\nu} . \quad (7.5)$$

We will interpret the latter quantity in more detail further down in Sect. 7.3. It is a measure for the inelasticity of the process. For elastic scattering the invariant mass  $W$  is equal to the nucleon mass  $M$  and therefore we get with (7.1)

$$2M\nu - Q^2 = 0 \implies x = 1 , \quad (7.6)$$

while for inelastic processes  $W$  is larger than  $M$  and we get

$$2M\nu - Q^2 > 0 \implies 0 < x < 1 . \quad (7.7)$$

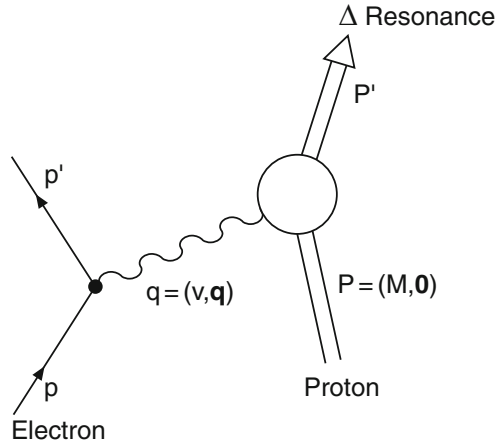
**The  $\Delta(1232)$  resonance** The nucleon resonance  $\Delta(1232)$ , which appears in Fig. 7.1 at about  $E' = 4.2$  GeV, has a mass  $W = 1,232$  MeV/ $c^2$ . As we will see in Chap. 16, this resonance exists in four different charge states:  $\Delta^{++}$ ,  $\Delta^+$ ,  $\Delta^0$ , and  $\Delta^-$ . In Fig. 7.1, the  $\Delta^+$  excitation is observed since charge is not transferred in the reaction (Fig. 7.2).

The width observed for the elastic peak is a result of the finite resolution of the spectrometer, but resonances have a real width<sup>1</sup> of typically  $\Gamma \approx 100$  MeV. The uncertainty principle then implies that such resonances have very short lifetimes. The  $\Delta(1232)$  resonance has a width of approximately 120 MeV and thus a lifetime of

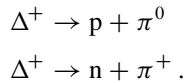
$$\tau = \frac{\hbar}{\Gamma} = \frac{6.6 \cdot 10^{-22} \text{ MeV s}}{120 \text{ MeV}} = 5.5 \cdot 10^{-24} \text{ s} .$$

<sup>1</sup>The exact meaning of “width” will be discussed in Sect. 9.2.

**Fig. 7.2** Inelastic electron-nucleon scattering with the excitation of the nucleon to a  $\Delta^+$  resonance



This is the typical time scale for strong interaction processes. The  $\Delta^+$  resonance decays by:



A light particle, the  $\pi$ -meson (or pion) is produced in such decays in addition to the nucleon.

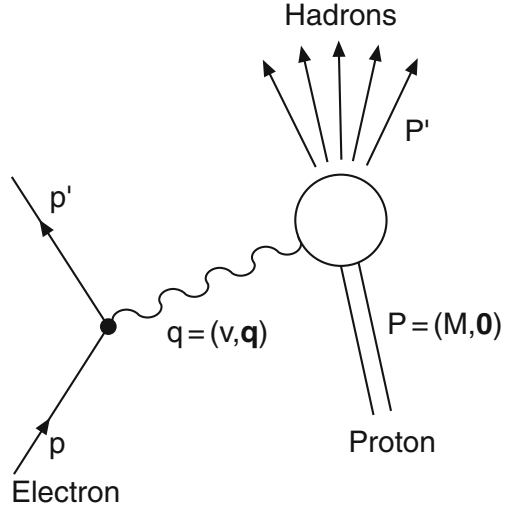
## 7.2 Structure Functions

Individual resonances cannot be distinguished in the excitation spectrum for invariant masses  $W \gtrsim 2.5 \text{ GeV}/c^2$ . Instead, one observes that many further strongly interacting particles (hadrons) are produced (Fig. 7.3).

Electron scattering in the kinematic region where  $W$ ,  $\sqrt{Q^2}/c$  and  $\nu/c^2$  are much larger than the nucleon mass  $M$ , we denote as *deep-inelastic scattering*. The dynamics of such production processes may be, similar to the case of elastic scattering, described in terms of form factors. In the inelastic case they are usually termed *structure functions*  $W_1$  and  $W_2$ , or  $F_1$  and  $F_2$ , respectively.

In *elastic* scattering, at a given beam energy  $E$ , only *one* of the kinematical parameters may vary freely. For example, if the scattering angle  $\theta$  is fixed, kinematics requires that the squared four-momentum transfer  $Q^2$ , the energy transfer  $\nu$ , the energy of the scattered electron  $E'$  etc. are also fixed. In *inelastic* scattering, however, the excitation energy of the proton adds a further degree of freedom. Hence these structure functions and cross-sections are functions of *two* independent, free parameters, e.g.,  $(E', \theta)$ ,  $(Q^2, \nu)$  or  $(Q^2, x)$ .

**Fig. 7.3** Inelastic electron-nucleon scattering leading to several hadrons in the final state



The Rosenbluth formula (6.10) is now replaced by the cross-section:

$$\frac{d^2\sigma}{d\Omega dE'} = \left(\frac{d\sigma}{d\Omega}\right)_{\text{Mott}}^* \left[ W_2(Q^2, \nu) + 2W_1(Q^2, \nu) \tan^2 \frac{\theta}{2} \right]. \quad (7.8)$$

The second term again stems from the magnetic interaction.

This notation of the cross-section is mainly used for didactic and historical purposes. Instead of the two structure functions  $W_1(Q^2, \nu)$  and  $W_2(Q^2, \nu)$  usually the two dimensionless structure functions

$$\begin{aligned} F_1(x, Q^2) &= Mc^2 W_1(Q^2, \nu), \\ F_2(x, Q^2) &= \nu W_2(Q^2, \nu) \end{aligned} \quad (7.9)$$

are used and the differential cross-section is expressed in terms of the two variables  $x$  and  $Q^2$ :

$$\frac{d^2\sigma}{dQ^2 dx} = \frac{4\pi\alpha^2\hbar^2}{Q^4} \left[ \left( \frac{1-y}{x} - \frac{My}{2E} \right) F_2(x, Q^2) + y^2 F_1(x, Q^2) \right]. \quad (7.10)$$

Measurements of the deep-inelastic cross-section at fixed values of  $x$  and  $Q^2$  but several values of  $y$ , i.e., several beam energies  $E$ , are required for the determination of both structure functions  $F_1(x, Q^2)$  and  $F_2(x, Q^2)$ .

The first deep-inelastic scattering experiments were carried out in the late 1960s at SLAC [5, 6]. Figure 7.4 shows one of the results of these experiments that came as a surprise. Displayed is the structure function  $F_2(x, Q^2)$  as a function of  $x$ , for

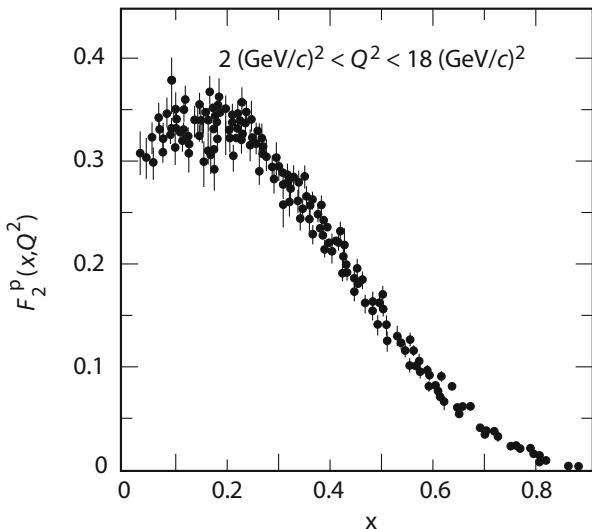


**Fig. 7.4** The structure function  $F_2$  of the proton as a function of  $x$ , for  $Q^2$  between  $2 (\text{GeV}/c)^2$  and  $18 (\text{GeV}/c)^2$  [3].

data covering a range of  $Q^2$  between  $2 (\text{GeV}/c)^2$  and  $18 (\text{GeV}/c)^2$ . At fixed values of  $x$  the structure function depends only weakly, if at all, on  $Q^2$ .

The fact that the structure functions are independent of  $Q^2$  means, according to our previous discussion, that the electrons are scattered off a point charge (cf. Fig. 5.7). Since nucleons are extended objects, it follows from the above result that:

*Nucleons have a sub-structure made up of point-like constituents.*

The  $F_1$  structure function results from the magnetic interaction. It vanishes for scattering off spin-zero particles. For spin-1/2 Dirac particles (6.5) and (7.8) imply the so called *Callan-Gross relation* [7] (see the exercises)

$$2xF_1(x) = F_2(x). \quad (7.11)$$

The ratio  $2xF_1/F_2$  is shown in Fig. 7.5 as a function of  $x$ . It can be seen that the ratio is consistent with unity within experimental uncertainties. Hence we can further conclude that:

*The point-like constituents of the nucleon have spin 1/2.*

### 7.3 The Parton Model

The interpretation of deep-inelastic scattering off protons may be considerably simplified if the reference frame is chosen judiciously. The physics of the process is, of course, independent of this choice. If one looks at the proton in a fast moving

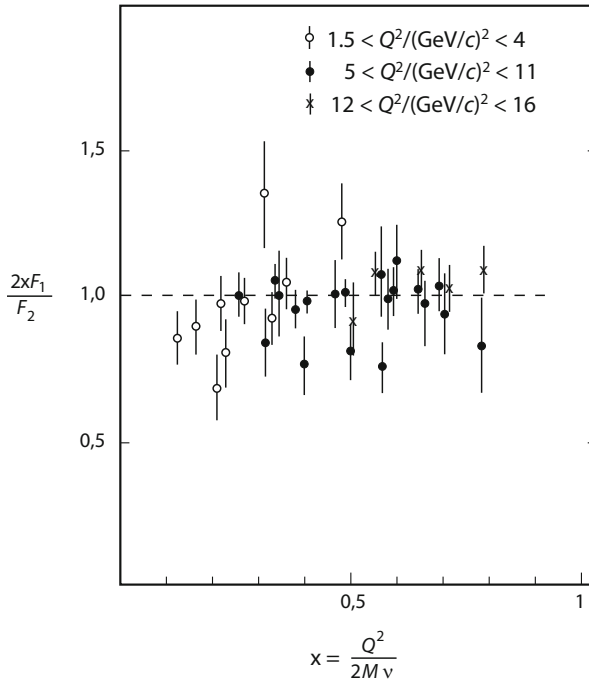


**Fig. 7.5** Ratio of the structure functions  $2xF_1(x)$  and  $F_2(x)$ . The data are from experiments at SLAC (From [9])

system, then the transverse momenta and the rest masses of the proton constituents can be neglected. The structure of the proton is then given to a first approximation by the longitudinal momenta of its constituents. This is the basis of the *parton model* of Feynman and Bjorken. In this model the constituents of the proton are called *partons*. Today the charged partons are identified with the quarks and the electrically neutral ones with the gluons – the field quanta of the strong interaction.

Decomposing the proton into independently moving partons, the interaction of the electron with the proton can be viewed as the incoherent sum of its interactions with the individual partons. These interactions in turn can be regarded as elastic scattering. This approximation is valid as long as the duration of the photon-parton interaction is so short that the interaction between the partons themselves can be safely neglected (Fig. 7.6). This is the *impulse approximation* which we have already met in quasi-elastic scattering (p. 82). In deep-inelastic scattering this approximation is valid because the interaction between partons at short distances is weak, as we will see in Sect. 8.2.

If we make this approximation and assume both that the parton masses can be safely neglected and that  $Q^2 \gg M^2c^2$ , we obtain a direct interpretation of the Bjorken scaling variable  $x = Q^2/2Mv$  which we defined in (7.5). It is that fraction of the four-momentum of the proton which is carried by the struck parton. A photon

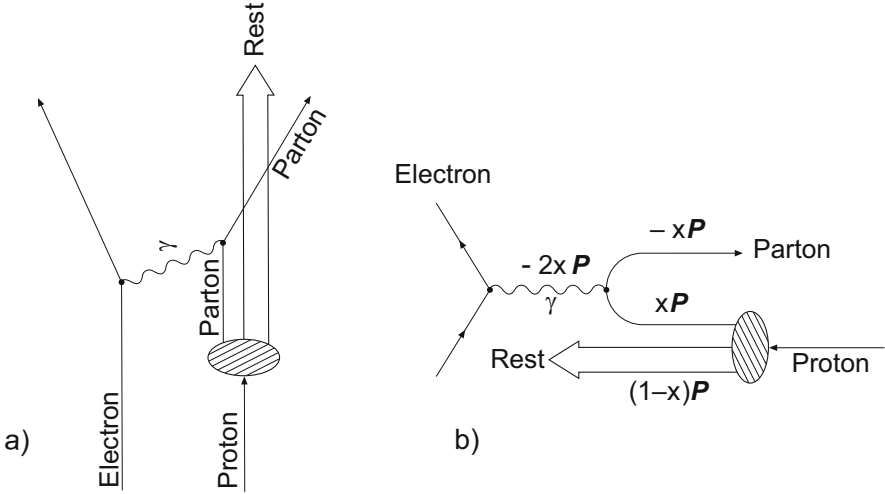


**Fig. 7.6** Schematic representation of deep-inelastic electron-proton scattering according to the parton model, in the laboratory system (a) and in a fast moving system (b). This diagram shows the process in two spatial dimensions. The *arrows* indicate the directions of the momenta. Diagram (b) depicts the scattering process in the Breit frame in which the energy transferred by the virtual photon is zero. Hence the momentum of the struck parton is turned around but its magnitude is unchanged

which, in the laboratory system, has four-momentum  $q = (v/c, \mathbf{q})$  interacts with a parton carrying the four-momentum  $xP$ . We emphasise that this interpretation of  $x$  is only valid in the impulse approximation, and then only if we neglect transverse momenta and the rest mass of the parton; i.e. in a very fast moving system.

A popular reference frame satisfying these conditions is the *Breit frame* (Fig. 7.6b), where the photon does not transfer any energy ( $q_0 = 0$ ). In this system  $x$  is the three-momentum fraction of the parton.

The spatial resolution of deep-inelastic scattering is given by the reduced wavelength  $\lambda$  of the virtual photon. This quantity is not Lorentz-invariant but depends upon the reference frame. In the laboratory system ( $q_0 = v/c$ ) it is:

$$\lambda = \frac{\hbar}{|q|} = \frac{\hbar c}{\sqrt{v^2 + Q^2 c^2}} \approx \frac{\hbar c}{v} = \frac{2Mx\hbar c}{Q^2}. \tag{7.12}$$

For example, if  $x = 0.1$  and  $Q^2 = 4 \text{ (GeV/c)}^2$  one finds  $\lambda \simeq 10^{-17} \text{ m}$  in the laboratory system. In the Breit frame, the equation simplifies to

$$\lambda = \frac{\hbar}{|q|} = \frac{\hbar}{\sqrt{Q^2}}. \tag{7.13}$$



The quantity  $Q^2$ , therefore, has an obvious interpretation in the Breit frame: it is a measure for the spatial resolution with which structures can be studied.

## 7.4 The Quark Structure of Nucleons

**Quarks** The quark model was conceived in the mid-1960s of the last century in order to systematise the great diversity of strongly interacting particles (hadrons) which had been discovered up to then. By means of deep-inelastic scattering, we found that nucleons consist of electrically charged, point-like particles. We now identify them with the *quarks*. It should be possible to reconstruct and to explain the properties of the nucleons (charge, mass, magnetic moment, isospin, etc.) from the quantum numbers of these constituents. For this purpose, we need at least two different types of quarks, which are designated by u (*up*) and d (*down*). The quarks have spin  $1/2$  and, in the naive quark model, their spins must combine to give the total spin  $1/2$  of the nucleon. Hence nucleons are built up out of at least 3 quarks. The proton has two u-quarks and one d-quark, while the neutron has two d-quarks and one u-quark.

		u	d	p (uud)	n (udd)
Charge number	$z_q$	$+2/3$	$-1/3$	1	0
Isospin	$I$		$1/2$		$1/2$
	$I_3$	$+1/2$	$-1/2$	$+1/2$	$-1/2$
Spin	$s$	$1/2$	$1/2$	$1/2$	$1/2$

Formally, the proton and the neutron maybe transformed to each other by interchanging the u- and d-quarks. They form an isospin doublet with  $I = 1/2$  (cf. (2.12)). This is attributed to the fact that u- and d-quarks form an isospin doublet as well. The charges of proton and neutron are obtained by assigning charges to the quarks that are multiples of  $e/3$ , the charge of the u-quark being  $e_u = z_u \cdot e = 2e/3$  and the charge of the d-quark being  $e_d = z_d \cdot e = -1e/3$ . These charges of the quarks are not unequivocally fixed by the charges of the proton and the neutron. This assignment is rather related to other clues; such as the fact that the maximum positive charge found in hadrons is two (e.g.,  $\Delta^{++}$ ), and the maximum negative charge is one (e.g.,  $\Delta^-$ ). Hence the charges of these hadrons are attributed to 3 u-quarks (charge:  $3 \cdot (2e/3) = 2e$ ) and 3 d-quarks (charge:  $3 \cdot (-1e/3) = -1e$ ) respectively.

**Valence quarks and sea quarks** The three quarks that determine the quantum numbers of the nucleons are called *valence quarks*. As well as these there also exist quark-antiquark pairs in the nucleon. They are produced and annihilated as virtual particles in the field of the strong interaction (cf. Sect. 8.2). This process is

analogous to the production of virtual electron-positron pairs in the Coulomb field. These quark-antiquark pairs are called *sea quarks*. Their effective quantum numbers average out to zero and do not alter those of the nucleon. Because of their electrical charge, they are “visible” in deep-inelastic scattering, too. However, they carry only very small fractions  $x$  of the nucleon’s momentum.

As well as u- and d-quarks, further types of quark-antiquark pairs are found in the “sea”; they will be discussed in more detail in Chap. 9. The different types of quarks are called “flavours”. The additional quarks were named s (*strange*), c (*charm*), b (*bottom*) and t (*top*). As we will see later, the six quark types can be arranged in doublets (called *families* or *generations*), according to their increasing mass:

$$\begin{pmatrix} \text{u} \\ \text{d} \end{pmatrix} \quad \begin{pmatrix} \text{c} \\ \text{s} \end{pmatrix} \quad \begin{pmatrix} \text{t} \\ \text{b} \end{pmatrix}.$$

The quarks of the top row have charge number  $z_q = +2/3$ , those of the bottom row  $z_q = -1/3$ . The c-, b- and t- quarks are so heavy that they play a very minor role at  $Q^2$ -values attainable in experiments with stationary targets. We will therefore neglect them in what follows.

## 7.5 Interpretation of Structure Functions in the Parton Model

Structure functions describe the internal composition of the nucleon. We now assume the nucleon to be built from different types of quarks  $q$  carrying an electrical charge  $z_q \cdot e$ . The cross-section for electromagnetic scattering from a quark is proportional to the square of its charge, and hence to  $z_q^2$ .

We denote the distribution function of the quark momenta by  $q(x)$ , i.e.,  $q(x)dx$  is the expectation value of the number of quarks of type  $q = u, d, s$  in the nucleon whose momentum fraction lies within the interval  $[x, x + dx]$ . The momentum distribution of the valence quarks we denote by  $q_v(x)$  and correspondingly the distribution of the antiquarks in the “sea” by  $\bar{q}_s(x)$ . The proton consists of two valence u-quarks and one valence d-quark. Therefore we have

$$\int_0^1 u_v(x) dx = 2, \quad \int_0^1 d_v(x) dx = 1. \quad (7.14)$$

The structure function  $F_2$  is the sum of the momentum distributions weighted by  $x$  and  $z_q^2$ . Here the sum is over all types of quarks and antiquarks:

$$F_2(x) = x \cdot \sum_{q=u,d,s} z_q^2 [q(x) + \bar{q}_s(x)], \quad (7.15)$$

with  $q(x) = q_u(x) + q_d(x)$  for u- and d-quarks and  $q(x) = q_s(x)$  for s-quarks.

**Structure functions of proton and neutron** Much detailed information about the distribution functions of quarks can be obtained by the study of combinations of the structure functions  $F_2^p$  and  $F_2^n$  of proton and neutron. In the absence of free neutron targets, information about  $F_2^n$  must be obtained from deep-inelastic scattering of deuterons. By convention in scattering off nuclei, the structure function is always given per nucleon. Except for small corrections due to the Fermi motion of the nucleons, the structure function of the deuteron  $F_2^D$  is equal to the proton-neutron average structure function  $F_2^N$

$$F_2^D \approx \frac{F_2^p + F_2^n}{2} =: F_2^N, \quad (7.16)$$

and hence we have  $F_2^n \approx 2F_2^D - F_2^p$ .

According to (7.15), the structure functions  $F_2$  of the proton and the neutron are given by

$$\begin{aligned} F_2^p(x) &= x \cdot \left[ \frac{4}{9} (u_v^p + u_s^p + \bar{u}_s^p) + \frac{1}{9} (d_v^p + d_s^p + \bar{d}_s^p) + \frac{1}{9} (s_s^p + \bar{s}_s^p) \right] \\ F_2^n(x) &= x \cdot \left[ \frac{4}{9} (u_v^n + u_s^n + \bar{u}_s^n) + \frac{1}{9} (d_v^n + d_s^n + \bar{d}_s^n) + \frac{1}{9} (s_s^n + \bar{s}_s^n) \right], \end{aligned} \quad (7.17)$$

where  $u_v^{p,n}(x)$  denotes the distribution of valence u-quarks in the proton and the neutron, respectively, and  $u_s(x)^{p,n}$  the distribution of the sea u-quarks etc.

From *isospin symmetry* we obtain for the quark distributions

$$\begin{aligned} u_{v,s}^p(x) &= d_{v,s}^n(x) =: u_{v,s}(x), \\ d_{v,s}^p(x) &= u_{v,s}^n(x) =: d_{v,s}(x). \end{aligned} \quad (7.18)$$

**Ratio of the neutron and proton structure functions** The effective quantum numbers of the sea quarks average out to zero and we therefore have  $q_s(x) = \bar{q}_s(x)$ . We assume that the distributions of s-quarks in the proton and the neutron are identical ( $\bar{s}_s^p(x) = \bar{s}_s^n(x)$ ), and also that the contributions of the two light u- and d-quarks to the ‘‘sea’’ are equal ( $\bar{u}_s(x) = \bar{d}_s(x)$ ). (Below we will see that this relation is only approximately true.) Because of the larger mass of s-quarks, fluctuations into quark-antiquark pairs of this flavour have a smaller probability and we have  $\bar{u}_s(x) > \bar{s}_s(x)$ .

Summing up the  $z_q^2$ -weighted contributions of all sea quarks we can define

$$S(x) = 10 \bar{u}_s(x) + 2 \bar{s}_s(x). \quad (7.19)$$

Then we obtain for the ratio of the neutron and proton structure functions:

$$\frac{F_2^n(x)}{F_2^p(x)} = \frac{[u_v(x) + 4d_v(x) + S(x)]}{[4u_v(x) + d_v(x) + S(x)]}. \quad (7.20)$$

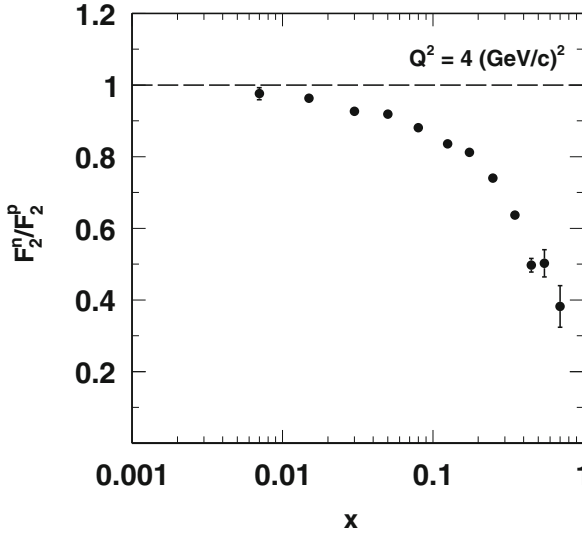


**Fig. 7.7** The structure function ratio  $F_2^n/F_2^p$  as a function of  $x$  [2]. The data were obtained from muon scattering with beam energies of 90 and 280 GeV. Shown are results at  $Q^2 = 4 \text{ (GeV/c)}^2$

Figure 7.7 shows the ratio  $F_2^n/F_2^p$  as a function of  $x$ . Plotted are data of one of the second-generation muon experiments [1, 2]. This experiment has a beam energy that is more than an order of magnitude higher than the experiments done at SLAC, and therefore the data cover much smaller values of  $x$ . Since the proton is composed of two valence u-quarks and one valence d-quark we could assume that their distributions are related by  $u_v(x) = 2d_v(x)$ . For a vanishing contribution of the sea quarks ( $S(x) = 0$ ),  $F_2^n/F_2^p$  would obtain the value  $2/3$  independent of  $x$ . In reality, however, the ratio approaches unity for  $x \rightarrow 0$  and decreases with  $x$  down to a value of approximately  $1/4$  for  $x \rightarrow 1$ . We can interpret this behaviour as follows: for small values of  $x$  the distribution of sea quarks  $S(x)$  is much larger than the two valence quark distributions, the ratio is mainly determined by the last term in the numerator and denominator of (7.20). As  $x \rightarrow 1$ , the situation is reversed: the sea quarks no longer play a role and we obtain the value  $1/4$  for the ratio by neglecting in (7.20) both  $S(x)$  and  $d_v(x)$  compared to  $u_v(x)$ . The distribution of d-quarks drops much faster with  $x$  than the u-quark distribution. This implies that large momentum fractions in the proton (neutron) are carried by u-quarks (d-quarks).

**Difference of the proton and neutron structure functions** The difference of the proton and neutron structure functions is given by

$$F_2^p(x) - F_2^n(x) = x \cdot \left[ \frac{1}{3}(u_v(x) - d_v(x)) + \frac{2}{3}(\bar{u}_s(x) - \bar{d}_s(x)) \right]. \quad (7.21)$$

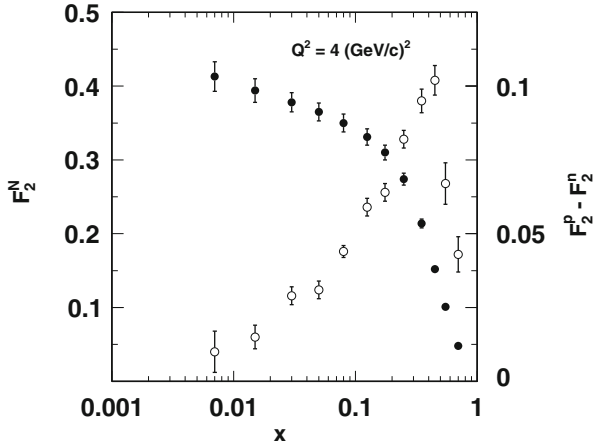


**Fig. 7.8** The structure function  $F_2^N$  for an “average” nucleon (closed symbols, left scale) and the difference of the proton and neutron structure functions  $F_2^p - F_2^n$  (open symbols, right scale) as function of  $x$  [2]. The data were obtained from muon scattering with beam energies of 90 and 280 GeV. Shown are results at  $Q^2 = 4 \text{ (GeV/c)}^2$

Thus if and only if the “sea” is symmetric in the two light-quark flavours, i.e.,  $\bar{u}_s(x) = \bar{d}_s(x)$ , then the contributions from sea quarks drop out and the difference (7.21) is a pure valence quark distribution. In Fig. 7.8 data from the same muon experiment are shown for  $F_2^p - F_2^n$  (open symbols, right scale) as a function of  $x$ . The distribution has a maximum near  $x \approx 1/3$  and drops down to zero for  $x \rightarrow 0$  and  $x \rightarrow 1$ . This supports our assumption, made above, that at low values of  $x$  mainly sea quarks contribute to the structure function. Also at large values of  $x$  the distribution becomes very small. Thus it is very unlikely that *one* quark alone carries the major part of the momentum of the nucleon.

The observed behaviour has often been interpreted as resulting from three valence quarks, each of them carrying on average one third of the nucleon’s momentum and the sharply defined momentum at  $x = 1/3$  is then washed out by the Fermi motion of the quarks inside the nucleon. This interpretation is incorrect. As we will see below, quarks carry only about half of the nucleon’s momentum. The distributions  $u_v(x)$  and  $d_v(x)$  both have a maximum near  $x \approx 0.17$  and the maximum of  $F_2^p - F_2^n$  near  $x = 1/3$  accidentally arises from the different  $x$  dependencies of these two distributions.

When we divide (7.21) by  $x$  and integrate over  $x$ , we obtain

$$S_G = \int_0^1 \frac{1}{x} [F_2^p(x) - F_2^n(x)] dx = \frac{1}{3}(2 - 1) + \frac{2}{3} \int_0^1 (\bar{u}_s(x) - \bar{d}_s(x)) dx . \quad (7.22)$$

For  $\bar{u}_s(x) = \bar{d}_s(x)$  the last term drops out and we get  $S_G = \frac{1}{3}$ . This is the *Gottfried Sum Rule* [8]. Experimentally, however, the integral amounts to [2]

$$S_G = 0.235 \pm 0.026 . \quad (7.23)$$

This leads to the conclusion that  $\bar{d}_s(x) > \bar{u}_s(x)$  and that consequently the quark-antiquark “sea” is not symmetric in the two light-quark flavours. We will come back to this finding in Sect. 8.4.

**Quark charges** All of the quantitative statements made in the present chapter confirm the assignment of the fractional quark charges  $e_u = 2e/3$  and  $e_d = -1e/3$ . In addition, a convincing confirmation comes from the comparison of the nucleon structure functions measured in deep-inelastic scattering of electrons or muons and of neutrinos that we will discuss in Sect. 10.6. Thus we can conclude:

*Quarks carry fractional charges of  $2e/3$  and  $-1e/3$ .*

**Structure function for an “average” nucleon** Finally, after having discussed the ratio and the difference of the proton and neutron structure functions, we can get another important information about the structure of the nucleon by looking at their average. The structure function for an “average” nucleon (7.16) reads:

$$\begin{aligned} F_2^N(x) &= \frac{5}{18} x \cdot \sum_{q=d,u} [q(x) + \bar{q}_s(x)] + \frac{1}{9} x \cdot [s_s(x) + \bar{s}_s(x)] \\ &= \frac{5}{18} x \cdot \sum_{q=d,u,s} [q(x) + \bar{q}_s(x)] - \frac{1}{3} x \cdot \bar{s}_s(x) . \end{aligned} \quad (7.24)$$

The last term in the equation is small, since s-quarks occur only as sea quarks. To a good approximation,  $F_2^N$  is therefore given by the product of the average squared charges  $5/18$  of u- and d-quarks (in units of  $e^2$ ) and the sum over all quark distributions.

The integral of  $F_2^N(x)$  is taken over all quark momenta weighted by their distribution functions and the average squared quark charges. Therefore, the integral should yield the value  $5/18$ , provided that the whole nucleon momentum is carried by its charged constituents, the quarks.

However, integration of the data shown in Fig. 7.8 only yields the value

$$\int_0^1 F_2^N(x) dx \approx 0.55 \cdot \frac{5}{18} . \quad (7.25)$$

Thus we have to conclude:

*Quarks carry only about half of the nucleon’s momentum.*

The other half must be carried by uncharged particles interacting neither electromagnetically nor weakly. This finding was the starting point for the development of

QCD, the field theory of the strong interaction. The electrically neutral constituents have been identified with the field quanta of this interaction, the *gluons*.

## Problems

### 1. Deep-inelastic scattering

Derive the Callan-Gross relation (7.11). Which value for the mass of the target must be used?

### 2. Parton momentum fractions and $x$

Show that in the parton model of deep-inelastic scattering, if we do **not** neglect the masses of the nucleon  $M$  and of the parton  $m$ , the momentum fraction  $\xi$  of the scattered parton in a nucleon with momentum  $P$  is given by

$$\xi = x \left[ 1 + \frac{m^2 c^2 - M^2 c^2 x^2}{Q^2} \right].$$

In the deep-inelastic domain  $\frac{x^2 M^2 c^2}{Q^2} \ll 1$  and  $\frac{m^2 c^2}{Q^2} \ll 1$ . (Hint: for small  $\varepsilon, \varepsilon'$  we can approximate  $\sqrt{1 + \varepsilon(1 + \varepsilon')} \approx 1 + \frac{\varepsilon}{2}(1 + \varepsilon' - \frac{\varepsilon}{4})$ .)

## References

1. P. Amaudruz et al., Nucl. Phys. **B371**, 3 (1992)
2. M. Arneodo et al., Phys. Rev. **D50**, 1 (1994)
3. W.B. Atwood, *Lectures on Lepton Nucleon Scattering and Quantum Chromodynamics*. Progress in Physics, vol. 4 (Birkhäuser, Boston/Basel/Stuttgart, 1982)
4. W. Bartel et al., Phys. Lett. **B28**, 148 (1968)
5. E.D. Bloom et al., Phys. Rev. Lett. **23**, 930 (1969)
6. M. Breidenbach et al., Phys. Rev. Lett. **23**, 935 (1969)
7. C.G. Callan Jr., D.J. Gross, Phys. Rev. Lett. **22**, 156 (1969)
8. K. Gottfried, Phys. Rev. Lett. **18**, 1174 (1967)
9. D.H. Perkins, *Introduction to High Energy Physics*, 4th edn. (Addison-Wesley, Wokingham, 2000)

# Chapter 8

## Quarks, Gluons, and the Strong Interaction

*Quark* [aus dem Slaw.], aus Milch durch Säuerung oder Labfällung und Abtrennen der Molke gewonnenes Frischkäseprodukt, das vor allem aus geronnenem, weiß ausgeflocktem (noch stark wasserhaltigem).

Kasein besteht  
Brockhaus-Encyclopaedia, 19th edition

In the previous chapter we learnt how deep-inelastic scattering may be used as a tool to study the structure and composition of the nucleons. Complementary information about the structure of the nucleons and of other strongly interacting objects (the hadrons) can be obtained from the spectroscopy of these particles. This gives us information about the strong interaction and its field quanta which describe the internal dynamics of the hadrons and the forces acting between them.

### 8.1 Quarks in Hadrons

A multitude of unstable hadrons are known in addition to the nucleons. Through the study of these hadrons the diverse properties of the strong interaction are revealed. Hadrons can be classified in two groups: the *baryons*, fermions with half-integral spin, and the *mesons*, bosons with integral spin. The hadronic spectrum was uncovered step by step: initially from analyses of photographic plates which had been exposed to cosmic radiation and later in experiments at particle accelerators. Many short-lived particles were thus detected, including excited states of the nucleon. This led to the conclusion that nucleons themselves are composed of smaller structures. This conclusion was then extended to all known hadrons.

**Baryons** The lowest mass baryons are the proton and the neutron. They are the “ground states” of a rich excitation spectrum of well-defined energy (or mass) states. This will be discussed further in Chap. 16. In this respect, baryon spectra have many parallels to atomic and molecular spectra. Yet, there is an important difference. The energy (or mass) gaps between individual states are of the same order of magnitude as the nucleon mass. These gaps are then relatively much larger than those of atomic



or molecular physics. Consequently these states are also classified as individual particles with corresponding lifetimes.

Like the proton and neutron, other baryons are also composed of three quarks. Since quarks have spin  $1/2$ , baryons have half-integral spin.

When baryons are produced in particle reactions the same number of antibaryons are simultaneously created. To describe this phenomenon a new additive quantum number is introduced: *baryon number*  $B$ . We assign  $B = 1$  to baryons and  $B = -1$  to antibaryons. Accordingly, baryon number  $+1/3$  is attributed to quarks, and baryon number  $-1/3$  to antiquarks. All other particles have baryon number  $B = 0$ . Experiments indicate that baryon number is conserved in all particle reactions and decays. Thus, the quark minus antiquark number is conserved. This would be violated by, e.g., the hypothetical decay of the proton:

$$p \rightarrow \pi^0 + e^+ .$$

Without conservation of baryon number this decay mode would be energetically favoured. Yet, it has not been observed. The experimental limit of the partial lifetime is given by  $\tau(p \rightarrow \pi^0 + e^+) > 8.2 \cdot 10^{33}$  years [18, 20].

**Mesons** The lightest hadrons are the pions. Their mass, about  $140 \text{ MeV}/c^2$ , is much less than that of the nucleon. They are found in three different charge states:  $\pi^-$ ,  $\pi^0$  and  $\pi^+$ . Pions have spin 0. It is, therefore, natural to assume that they are composed of two quarks, or, more exactly, of a quark and an antiquark: this is the only way to build the three charge states out of quarks. Pions have the following quark structure:

$$|\pi^+\rangle = |u\bar{d}\rangle \quad |\pi^-\rangle = |\bar{u}d\rangle \quad |\pi^0\rangle = \frac{1}{\sqrt{2}} \{ |u\bar{u}\rangle - |d\bar{d}\rangle \} .$$

The  $|\pi^0\rangle$  is a mixed state of  $|u\bar{u}\rangle$  and  $|d\bar{d}\rangle$ . The above expression includes the correct symmetry and normalisation.

Hadrons composed of quark-antiquark pairs are called *mesons*. Mesons have integer spin: their total spin results from a vector sum of the quark and antiquark spins, including a possible integer orbital angular momentum contribution. Mesons eventually decay into electrons, neutrinos and/or photons; there is no “meson number conservation”, in contrast to baryon number conservation. This is understood in the quark model: mesons are quark-antiquark combinations  $|q\bar{q}\rangle$  and so the number of quarks minus the number of antiquarks is zero. Hence any number of mesons may be produced or annihilated. It is just a matter of convention which mesons are called particles and which antiparticles.

## 8.2 The Quark-Gluon Interaction

**Colour** Quarks have another important property called *colour* which we have previously neglected. This is needed to ensure that quarks in hadrons obey the Pauli principle. Consider the  $\Delta^{++}$ -resonance which consists of three u-quarks. The  $\Delta^{++}$

has spin  $J = 3/2$  and positive parity; it is the lightest baryon with  $J^P = 3/2^+$ . We therefore can assume that its orbital angular momentum is  $\ell = 0$ ; so it has a symmetric spatial wave function. In order to yield total angular momentum  $3/2$ , the spins of all three quarks have to be parallel:

$$|\Delta^{++}\rangle = |u^\uparrow u^\uparrow u^\uparrow\rangle.$$

Thus, the spin wave function is also symmetric. The wave function of this system is furthermore symmetric under the interchange of any two quarks, as only quarks of the same flavour are present. Therefore the total wave function appears to be symmetric, in violation of the Pauli principle.

Including the *colour* property, a kind of quark charge, the Pauli principle may be salvaged. The quantum number colour can assume three values, which may be called *red*, *blue* and *green*. Accordingly, antiquarks carry the anticolours *anti-red*, *anti-blue*, and *anti-green*. Now the three u-quarks may be distinguished by their colour. Thus, a colour wave function antisymmetric under particle interchange can be constructed, and we so have antisymmetry for the total wave function. The quantum number colour was introduced for theoretical reasons, yet experimental clues indicate that this hypothesis is correct. This will be discussed in Sect. 9.3.

**Gluons** The interaction binding quarks into hadrons is called the *strong interaction*. Such a fundamental interaction is, in our current understanding, always connected with a particle exchange. For the strong interaction, *gluons* are the exchange particles that couple to the colour charge. This is analogous to the electromagnetic interaction in which photons are exchanged between electrically charged particles.

The experimental findings of Sect. 7.4 led to the development of a field theory called *quantum chromodynamics* (QCD). As its name implies, QCD is modelled upon quantum electrodynamics (QED). In both, the interaction is mediated by exchange of a massless field particle with  $J^P = 1^-$  (a vector boson).

The gluons carry simultaneously colour and anticolour. According to group theory, the  $3 \times 3$  colour combinations form two multiplets of states: a singlet and an octet. The octet states form a basis from which all other colour states may be constructed. They correspond to an octet of gluons. The way in which these eight states are constructed from colours and anticolours is a matter of convention. One possible choice is

$$r\bar{g}, \quad r\bar{b}, \quad g\bar{b}, \quad g\bar{r}, \quad b\bar{r}, \quad b\bar{g}, \quad \sqrt{1/2} (r\bar{r} - g\bar{g}), \quad \sqrt{1/6} (r\bar{r} + g\bar{g} - 2b\bar{b}).$$

The colour singlet

$$\sqrt{1/3} (r\bar{r} + g\bar{g} + b\bar{b}),$$

which is symmetrically constructed from the three colours and the three anticolours is invariant with respect to a re-definition of the colour names (rotation in colour space). It, therefore, has no effect in colour space and cannot be exchanged between colour charges.

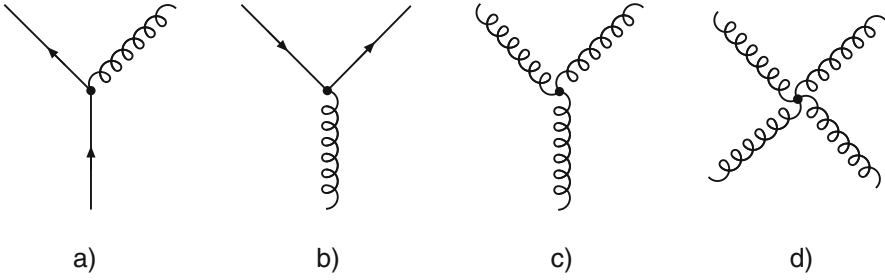


**Fig. 8.1** The fundamental interaction diagrams of the strong interaction: emission of a gluon by a quark (a), splitting of a gluon into a quark-antiquark pair (b) and “self-coupling” of gluons (c, d)

By their exchange the eight gluons mediate the interaction between particles carrying colour charge, i.e., not only the quarks but also the gluons themselves. This is an important difference to the electromagnetic interaction, where the photon field quanta have no charge, and therefore cannot couple with each other.

In analogy to the elementary processes of QED (emission and absorption of photons, pair production and annihilation), emission and absorption of gluons (Fig. 8.1a) take place in QCD, as do production and annihilation of quark-antiquark pairs (Fig. 8.1b). In addition, however, three or four gluons can couple to each other in QCD (Fig. 8.1c, d).

**Hadrons as colour-neutral objects** With colour, quarks gain an additional degree of freedom. One might, therefore, expect each hadron to exist in a multitude of versions which, depending upon the colours of the constituent quarks involved, would have different total (net) colours but would be equal in all other respects. In practice only one type of each hadron is observed (one  $\pi^-$ , p,  $\Delta^0$  etc.). This implies the existence of an additional condition: only colourless particles, i.e., with no net colour, can exist as free particles.

This condition explains why quarks are not observed as free particles. A single quark can be detached from a hadron only by producing at least two free objects carrying colour: the quark, and the remainder of the hadron. This phenomenon is, therefore, called *confinement*. Accordingly, the potential acting on a quark limitlessly increases (cf. Sect. 14.3) with increasing separation – in sharp contrast to the Coulomb potential. This phenomenon is due to the inter-gluonic interactions.

The combination of a colour with the corresponding anticolour results in a colourless (“white”) state. Putting the three different colours together results in a colourless (“white”) state as well. This can be graphically depicted by three vectors in a plane symbolising the three colours, rotated with respect to each other by  $120^\circ$  (Fig. 8.2).

Hence, e.g., the  $\pi^+$  meson has three possible colour combinations:

$$|\pi^+\rangle = \begin{cases} |u_r \bar{d}_r\rangle \\ |u_b \bar{d}_b\rangle \\ |u_g \bar{d}_g\rangle \end{cases},$$

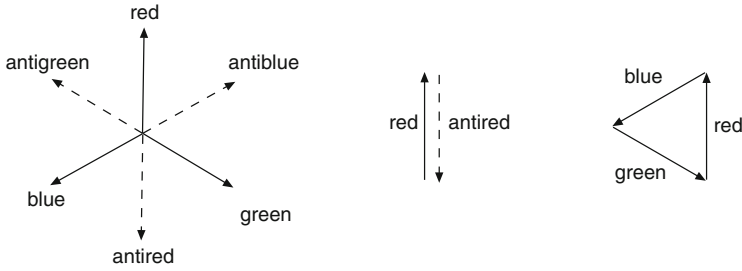


**Fig. 8.2** Graphical presentation of the colour vectors in colour space (left); colour and anticoulour in a meson combine to ‘white’ (middle) as do the three colours in a baryon (right)

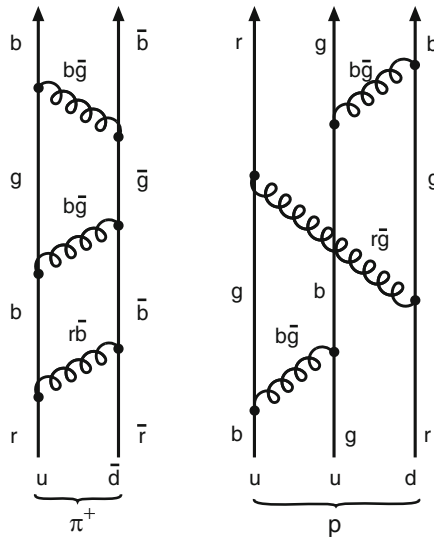


**Fig. 8.3** By the exchange of coloured gluons quark and antiquark in a meson (left) and the three quarks in a baryon (right) continuously change their colour, preserving always the net colour ‘white’

where the index designates the colour or anticoulour. The physical pion is a mixture of these states. By exchange of gluons, which by themselves simultaneously transfer colour and anticoulour, the colour combination continuously changes; yet the net-colour “white” is preserved (Fig. 8.3).

In baryons, the colours of the three quarks also combine to yield “white”. Hence, to obtain a colour-neutral baryon, each quark must have a different colour. The proton is a mixture of such states:

$$|p\rangle = \begin{cases} |u_b u_r d_g\rangle \\ |u_r u_g d_b\rangle \\ \vdots \end{cases} .$$

From this argument, it also becomes clear why no hadrons exist which are  $|qq\rangle$ , or  $|qq\bar{q}\rangle$  combinations, or the like. These states would not be colour neutral, no matter what combination of colours were chosen.

**Constituent and current quarks** In (7.25) we saw that only about half of the momentum of a nucleon is carried by valence and sea quarks. In dealing with the spectroscopic properties of nucleons, sea quarks and gluons need not be explicitly dealt with. We can combine them with the valence quarks. One then acts as though there were only three valence quarks, with enlarged masses but unchanged quantum numbers. We will return to this point in Chaps. 14–16. These “effective valence quarks” are called *constituent quarks*.

In interpreting deep-inelastic scattering, we neglected the rest masses of the bare u- and d-quarks. This is justified since they are small [20]:  $m_u = 1.8\text{--}3\text{ MeV}/c^2$ ,  $m_d = 4.5\text{--}5.5\text{ MeV}/c^2$ . These masses are commonly called *current quark* masses. However, these are not the masses obtained from hadron spectroscopy; e.g., from calculations of magnetic moments and hadron excitation energies that we will discuss in detail in Chaps. 15 and 16. The *constituent-quark* masses are much larger with values of about  $300\text{ MeV}/c^2$ . They are mainly due to the cloud of gluons and sea quarks. Their values for all the quark flavours are compiled in Table 9.1.

The bare d-quark is heavier than the bare u-quark, which can be easily understood as follows. The proton (uud) and the neutron (ddu) are isospin symmetric as stated above; i.e., they transform into each other under interchange of the u- and d-quarks. Since the strong interaction is independent of quark flavour, the neutron-proton mass difference can only be due to the intrinsic quark masses and to the electromagnetic interaction between them. If we assume that the spatial distribution of the u- and d-quarks in the proton corresponds to the distribution of d- and u-quarks in the neutron, then it is easily seen that the Coulomb energy must be higher in the proton. Despite this, the neutron is heavier than the proton which implies that the mass of the d-quark is larger.

**The strong coupling constant  $\alpha_s$**  In quantum field theory, the coupling “constant” describing the interaction between two particles is an effective constant which in fact depends on  $Q^2$ . In the electromagnetic interaction this dependence is very weak; in the strong interaction, however, it is rather strong. The reason for this is that gluons, the field quanta of the strong interaction, carry colour themselves, and therefore can also couple to other gluons. In Fig. 8.4 the different  $Q^2$  behaviours of the electromagnetic and the strong coupling constants are presented. The contribution of the fluctuation of the photon into an electron-positron pair as well as of the gluon into a quark-antiquark pair results in the screening of the electric and strong charge. The higher  $Q^2$  is, the smaller are the distances between the interacting particles, and thus the effective charge of the interacting particles increases and the coupling constant increases. Gluons couple to other gluons and can fluctuate into gluons. This fluctuation causes antiscreening. The closer the interacting particles are, the smaller the charge they see. The coupling constant decreases with increasing  $Q^2$ . In the case of gluons the antiscreening is far stronger than the screening.

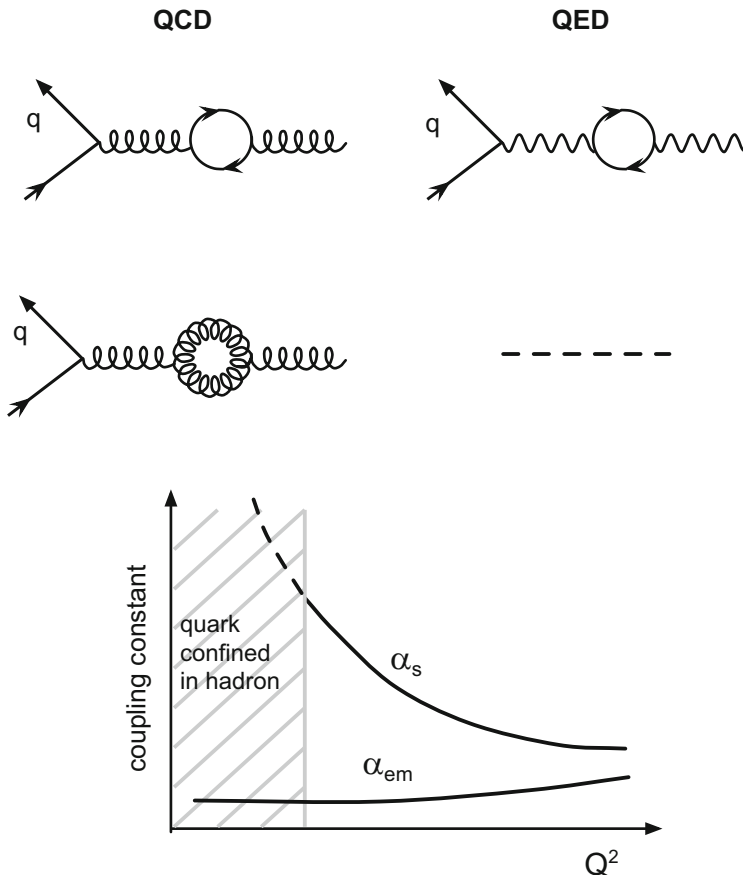


**Fig. 8.4** The  $Q^2$  dependence of the strong  $\alpha_s$  and the electromagnetic  $\alpha_{em}$  coupling constants is shown. The fluctuation of the photon into an electron-positron pair leads to the screening of the electric charge. Analogously, the fluctuation of the gluon into a quark-antiquark pair leads to the screening of the strong charge. The self coupling of the gluons results in the antiscreening

A first-order perturbation calculation in QCD yields:

$$\alpha_s(Q^2) = \frac{12\pi}{(33 - 2n_f) \cdot \ln(Q^2/\Lambda^2)}. \tag{8.1}$$

Here,  $n_f$  denotes the number of quark types involved. Since a heavy virtual quark-antiquark pair has a very short lifetime and range, it can be resolved only at very high  $Q^2$ . Hence,  $n_f$  depends on  $Q^2$ , with  $n_f \approx 3-6$ . The parameter  $\Lambda$  is the only free parameter of QCD. It was found to be  $\Lambda \approx 250 \text{ MeV}/c$  by comparing the prediction with the experimental data. The application of perturbative expansion procedures in QCD is valid only if  $\alpha_s \ll 1$ . This is satisfied for  $Q^2 \gg \Lambda^2 \approx 0.06 \text{ (GeV}/c)^2$ .

From (7.13) we can see that the  $Q^2$ -dependence of the coupling strength corresponds to a dependence on separation. For very small distances and correspondingly high values of  $Q^2$ , the interquark coupling decreases, vanishing asymptotically. In the limit  $Q^2 \rightarrow \infty$ , quarks can be considered “free”, this is called *asymptotic freedom*. By contrast, at large distances, the interquark coupling increases so strongly that it is impossible to detach individual quarks from hadrons (confinement).

### 8.3 Scaling Violations of the Structure Functions

In Sect. 7.2 we showed that the structure function  $F_2$  depends solely on the scaling variable  $x$ . We thereby concluded that the nucleon is composed of point-like, charged constituents. Yet, high precision measurements show that to a small degree,  $F_2$  does also depend on  $Q^2$ . Figure 8.5 shows the experimental measurements of the deuteron structure function  $F_2^D$  as a function of  $Q^2$  at several fixed values of  $x$ . The data cover a large kinematic range in  $x$  and  $Q^2$ . We see that the structure function increases with  $Q^2$  at small values of  $x$  and decreases with increasing  $Q^2$  at large values of  $x$ . This behaviour is called *scaling violation*. With increasing values of  $Q^2$  there are fewer quarks with large momentum fractions in the nucleon while more quarks with small momentum fractions are found.

A particularly large range in  $x$  and  $Q^2$  is covered by the two experiments H1 [1] and ZEUS [14] at the HERA storage ring, which took data during the years 1992–2007 [10]. As already explained in the previous chapter, electrons or positrons of 27.6 GeV and protons with energies up to 920 GeV were stored in two separate storage rings. For short periods also proton energies of 460, 575 and 820 GeV were used. These latter measurements enabled also the measurement of the second structure function  $F_1^p(x, Q^2)$  that we will, however, not discuss further. The two beams circulated in opposite directions and were brought to head-on collision at two interaction points that were hermetically surrounded by the two magnetic spectrometers H1 and ZEUS. These  $4\pi$  detectors allowed a complete reconstruction of deep-inelastic scattering events.

One of the textbook deep-inelastic scattering events in the H1 detector is shown in Fig. 8.6. Because of the confinement, discussed above, neither the scattered quark nor the proton remnant can be observed directly. They hadronise into colour-neutral hadrons. In the detector one observes the scattered electron and two bundles of charged-particle tracks, mostly hadrons, that stem either from the struck quark or from the target remnant. In most cases they can be nicely separated from each other. The trajectories of all charged particles are determined in the inner part of the apparatus by position sensitive detectors. The energy of the scattered electrons is measured in an electromagnetic calorimeter, that of the hadrons in a hadron calorimeter.

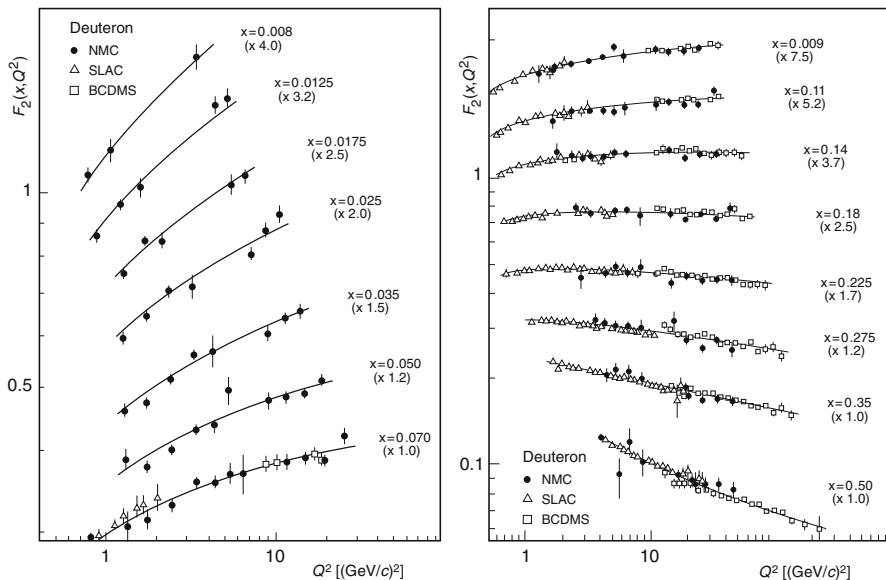


**Fig. 8.5** Structure function  $F_2$  of the deuteron as a function of  $Q^2$  at different values of  $x$  on a logarithmic scale. The results shown are from muon scattering at CERN (NMC and BCDMS collaboration) [5, 9] and from electron scattering at SLAC [21]. For clarity, the data at the various values of  $x$  are multiplied by constant factors. The solid line is a QCD fit, taking into account the theoretically predicted scaling violation. The gluon distribution and the strong coupling constant are free parameters here

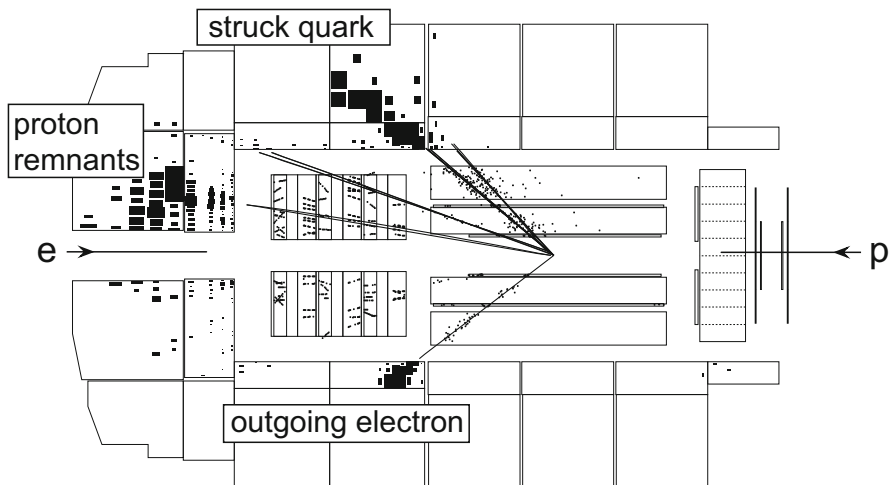


**Fig. 8.6** A deep-inelastic scattering event in the H1 detector. The proton beam enters from the right, the electron beam from the left



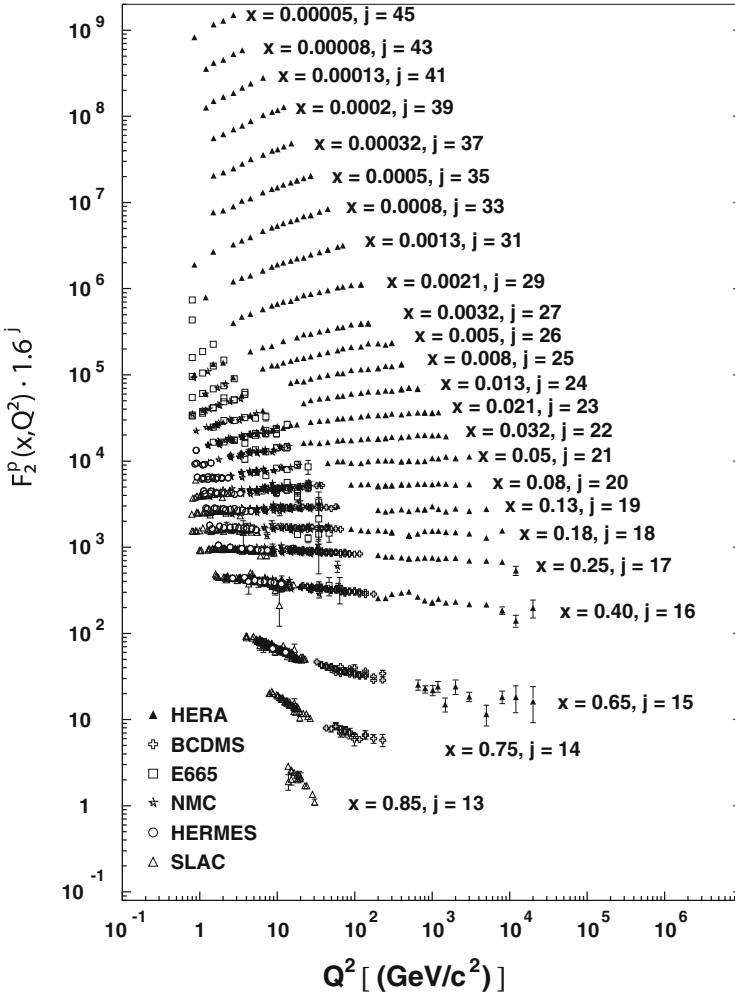


**Fig. 8.7** The proton structure function  $F_2^p$  as a function of  $Q^2$  in intervals of  $x$ . Shown is a combined data set of the two HERA experiments H1 and ZEUS together with data from deep-inelastic scattering experiments of the first and second generation with a stationary proton target

In Fig. 8.7 a combined data set of both experiments is presented for the structure function  $F_2^p(x, Q^2)$  measured in deep-inelastic positron-proton scattering at a centre-of-mass energy  $\sqrt{s} = 319 \text{ GeV}$ . Also shown are data from deep-inelastic scattering experiments with electrons, positrons or muons using stationary proton targets. Only data in the  $Q^2$  region above  $Q_{\min}^2 = 0.8 (\text{GeV}/c)^2$  are shown, where the structure function  $F_2$  can be interpreted in the framework of the quark-parton model. For better visibility the data at each  $x$  value have been multiplied by constant factors and a few  $x$  intervals have been omitted.

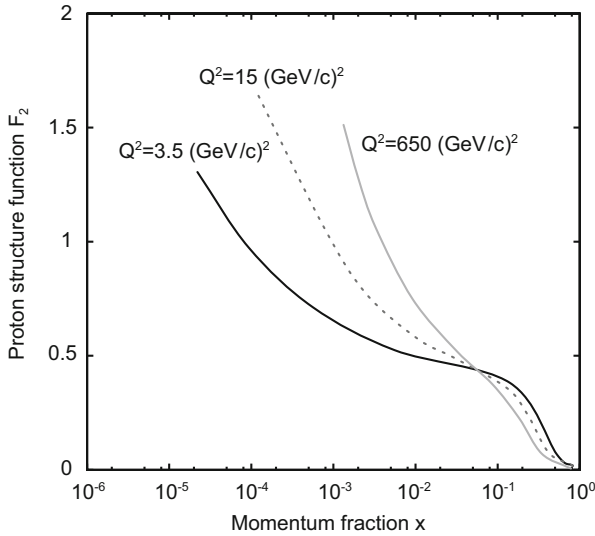


**Fig. 8.8** Schematic presentation of the proton structure function  $F_2$  as function of  $x$  at three values of  $Q^2$

The HERA data cover the impressive large kinematic range  $10^{-6} < x < 0.7$  and  $0.04 (\text{GeV}/c)^2 < Q^2 < 10^5 (\text{GeV}/c)^2$ . This is many times larger than for the experiments of the first and second generation using a stationary proton target. Also here we see at low values of  $x$  a considerable increase of  $F_2$  with  $Q^2$ ; the smaller  $x$ , the steeper the increase. At large values of  $x$  a somewhat weaker decrease of the structure function with  $Q^2$  is observed.

The variation of the  $x$  dependence of the proton structure function with  $Q^2$  is schematically shown in Fig. 8.8 for three values of  $Q^2$ . The lines are a fit to the experimental data of all the experiments of the three generations taking into account the scaling violation predicted by QCD. The experimental points were omitted as to clearly show the decrease of the structure function with increasing  $Q^2$  at large values of  $x$ .

**The DGLAP equations** This violation of scaling is not caused by a finite size of the quarks. In the framework of QCD, it can be traced back to fundamental processes in which the constituents of the nucleon continuously interact with each other (Fig. 8.1). Quarks can emit or absorb gluons, gluons may split into  $q\bar{q}$  pairs, or emit gluons themselves. Thus, the momentum distribution between the constituents of the nucleon is continually changing.

Figure 8.9 is an attempt to illustrate how this alters the measurements of structure functions at different values of  $Q^2$ . A virtual photon can resolve dimensions of the order of  $\hbar/\sqrt{Q^2}$ . At small  $Q^2 = Q_0^2$ , quarks and any possibly emitted gluons cannot be distinguished and a quark distribution  $q(x, Q_0^2)$  is measured. At larger  $Q^2$  and higher space-time resolution, emission and splitting processes must be considered.

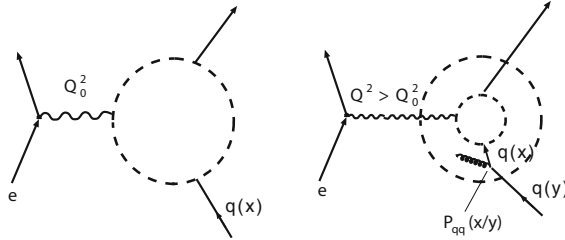


**Fig. 8.9** With increasing  $Q^2$  the space-time resolution of the virtual photon increases, allowing to resolve more partons

A quark with the momentum fraction  $x$  can originate from a parent quark with a larger momentum fraction  $y$  that has radiated a gluon (cf. Fig. 8.1a). The probability that this happens is proportional to  $\alpha_s(Q^2)P_{qq}(x/y)$ , where  $P_{qq}(x/y)$  is a so-called *splitting function*.

But a quark with momentum fraction  $x$  can also originate from a gluon with higher momentum fraction  $y$  (cf. Fig. 8.1b). The probability for this process is proportional to another splitting function  $P_{gq}(x/y)$ . Similarly the gluon distribution  $g(x, Q^2)$  is modified by radiation of gluons from a quark ( $\sim P_{gq}(x/y)$ ) or from another gluon ( $\sim P_{gg}(x/y)$ ), respectively (cf. Fig. 8.1c, d). The splitting functions can be calculated in QCD. Thus, with increasing  $Q^2$  the number of *resolved* partons sharing the nucleon's momentum increases. The quark distribution  $q(x, Q^2)$  at small momentum fractions  $x$ , therefore, is larger than  $q(x, Q_0^2)$ , whereas the effect is reversed for large  $x$ . This is the origin of the increase of the structure function with  $Q^2$  at small values of  $x$  and its decrease at large  $x$ .

The change in the quark distribution and in the gluon distribution with  $Q^2$  at fixed values of  $x$  is proportional to the strong coupling constant  $\alpha_s(Q^2)$  and depends upon the size of the quark and gluon distributions at all larger values of  $x$ . The mutual dependence of the quark and gluon distributions can be described by a system of coupled integral-differential equations [3, 12, 16], named after their authors as DGLAP equations:

$$\frac{dq(x, Q^2)}{d \ln Q^2} = \frac{\alpha_s(Q^2)}{2\pi} \int_x^1 \frac{dy}{y} [P_{qq}(x/y) \cdot q(y, Q^2) + P_{gq}(x/y) \cdot g(y, Q^2)], \quad (8.2)$$

$$\frac{dg(x, Q^2)}{d \ln Q^2} = \frac{\alpha_s(Q^2)}{2\pi} \int_x^1 \frac{dy}{y} \left[ \sum_q P_{gq}(x/y) \cdot q(y, Q^2) + P_{gg}(x/y) \cdot g(y, Q^2) \right]. \quad (8.3)$$

In higher orders of  $\alpha_s(Q^2)$  one obtains similar expressions with more and different splitting functions which take into account more complicated processes, as for example those sketched in Fig. 8.10, where the gluon or an antiquark that

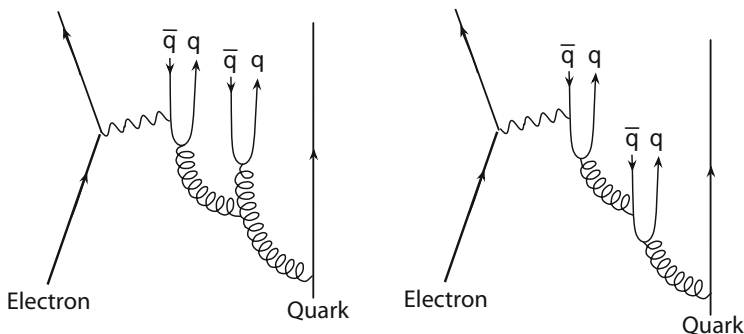


**Fig. 8.10** Examples of higher-order contributions to deep-inelastic scattering

already originates from gluon splitting radiate another gluon that then produces another generation of sea quarks.

If  $\alpha_s(Q^2)$  and the shape of  $q(x, Q_0^2)$  and  $g(x, Q_0^2)$  are known at a given value  $Q_0^2$ , then  $q(x, Q^2)$  and  $g(x, Q^2)$  can be predicted via the DGLAP equations for all other values of  $Q^2$ . Alternatively, the coupling  $\alpha_s(Q^2)$  and the gluon distribution  $g(x, Q^2)$ , which cannot be directly measured, can be determined from the observed scaling violation of the structure function  $F_2(x, Q^2)$ .

The solid lines in Fig. 8.5 show a fit to the scaling violation of the measured structure functions from a QCD calculation [6]. The fit value of  $\Lambda \approx 250 \text{ MeV}/c$  corresponds to a coupling constant:

$$\alpha_s(Q^2 = 100 \text{ (GeV}/c)^2) \approx 0.16. \tag{8.4}$$

Also the data shown in Fig. 8.7 can be excellently described by QCD. They allow a determination of  $\alpha_s$  at a much larger  $Q^2$  than was possible from the experiments with a stationary target. In a so-called double-logarithmic perturbative calculation one obtains for the strong coupling constant

$$\alpha_s(Q^2 = 10^4 \text{ (GeV}/c)^2) \approx 0.12. \tag{8.5}$$

As predicted by theory,  $\alpha_s$  decreases with increasing  $Q^2$ .

**Conclusion** Scaling violation in the structure functions is a highly interesting phenomenon. It is not unusual that particles which appear point-like turn out to be composite when studied more closely (e.g., atomic nuclei in Rutherford scattering with low-energy  $\alpha$  particles or in elastic high-energy electron scattering). In deep-inelastic scattering, however, a new phenomenon is observed. With increasing resolution, quarks and gluons turn out to be composed of quarks and gluons; which themselves, at even higher resolutions, turn out to be composite as well. The quantum numbers (spin, flavour, colour, . . .) of these particles remain the same; only

the mass, size, and the effective coupling  $\alpha_s$  change. Hence, there appears to be in some sense a self similarity in the internal structure of strongly interacting particles.

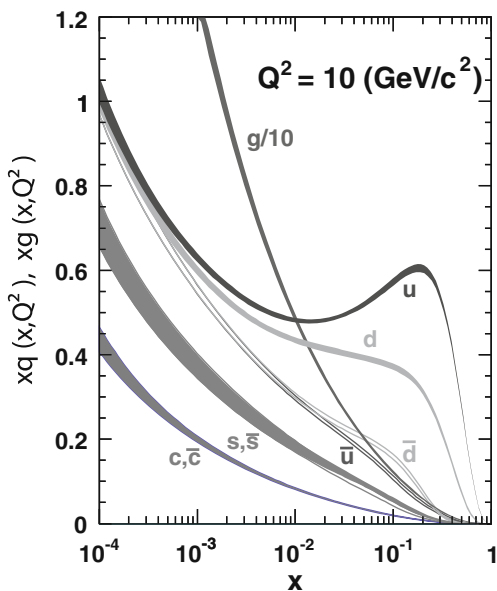
## 8.4 Flavour-separated Parton Distributions

It has to be pointed out that theoretically only the *change* in the structure function with  $Q^2$  can be calculated but not the  $x$  dependence of the structure functions themselves or of the parton distributions which are non-perturbative objects. Thus at least at one  $Q^2 = Q_0^2$  the  $x$ -dependence of the  $F_2(x, Q^2)$  has to be well determined experimentally.

In Fig. 8.11 the quark distributions  $xq(x)$  and the gluon distribution  $xg(x)$  are shown at a scale  $Q^2 = 10 (\text{GeV}/c)^2$ . These distributions stem from a common analysis of all the data presented so far and of many other data, amongst others from deep-inelastic neutrino-nucleon scattering experiments and proton-proton scattering at high energies. It can be seen that the distributions of gluons and of sea quarks strongly increase with decreasing  $x$ ; valence quarks dominate only for  $x$  values above approximately  $x \approx 0.1$ .

In Sect. 7.5 we have shown that the distribution of the light  $u$ - and  $d$ -antiquarks is not flavour symmetric:  $\bar{d}_s > \bar{u}_s$ . This conclusion resulted from the violation of the *Gottfried sum rule* for the integral over  $[F_2^p(x) - F_2^n(x)]/x$ . This finding was confirmed by dedicated experiments [2, 13]. The most precise results have been obtained by the Drell-Yan process [11] in proton-nucleon scattering:  $pN \rightarrow$

**Fig. 8.11** Schematic presentation of the parton distributions at  $Q^2 = 10 (\text{GeV}/c)^2$  for quarks and gluons as function of the scaling variable  $x$  (After [17])



$(\ell^+\ell^-)X$ . In the Drell-Yan process a quark (antiquark) with the four-momentum fraction  $x_1$  from the beam proton and an antiquark (quark) of the target nucleon with  $x_2$  annihilate electromagnetically into a virtual photon, which immediately decays into a  $\mu^+\mu^-$  or  $e^+e^-$  pair:  $q(x_1)\bar{q}(x_2) \rightarrow \gamma^* \rightarrow \ell^+\ell^-$ .

The longitudinal momentum of the  $\ell^+\ell^-$  pair in the proton-nucleon centre-of-mass system is given by  $p_L^{\ell^+\ell^-} \approx (x_1 - x_2)\sqrt{s}/2$  and its invariant mass by  $(M_{\ell^+\ell^-} c^2)^2 = x_1 x_2 s$ . Here,  $s$  is the centre-of-mass energy (cf. (9.1)). By a suitable choice of the kinematics of the  $\ell^+\ell^-$  pair the quark and antiquark distributions in the target can be determined separately and from a comparison of the count rates for hydrogen and deuterium targets one obtains the ratio  $\bar{d}_s(x)/\bar{u}_s(x)$ .

In the quark-parton model, a suppression of  $u\bar{u}$  pairs compared to  $d\bar{d}$  pairs can be explained by the Pauli principle: the proton already contains two valence u-quarks of different colour and one valence d-quark. It is therefore possible to add one more u-quark but two more d-quarks before the colour quantum numbers are saturated. In another model this asymmetry originates from the pion cloud of the nucleon. Here one assumes that the nucleon fluctuates for a short period into a baryon and a pion:  $p \leftrightarrow B + \pi$ . Thereby the fluctuation into a positive pion  $p \leftrightarrow n + \pi^+$ , i.e.,  $|uud\rangle \leftrightarrow |udd\rangle + |u\bar{d}\rangle$ , has a higher probability than the fluctuation into a  $\pi^-$ , as in the latter the proton has to be excited to a  $\Delta^{++}$  resonance,  $p \leftrightarrow \Delta^{++} + \pi^-$ , i.e.,  $|uud\rangle \leftrightarrow |uuu\rangle + |\bar{u}d\rangle$ . In this hybrid model naturally an excess of  $\bar{d}_s$  compared to  $\bar{u}_s$  is obtained.

## 8.5 Nuclear Effects in Deep-Inelastic Scattering

Typical energies in nuclear physics (e.g., binding energies) are of the order of several MeV and typical momenta (e.g., Fermi momenta) are of the order of  $250 \text{ MeV}/c$ . These are many orders of magnitude less than the momentum transfers  $Q$  of scattering experiments used to determine the structure functions. Therefore one would expect the structure functions to be the same for scattering off free nucleons or scattering off nucleons bound in nuclei, except, of course, for kinematic effects due to the Fermi motion of the nucleons in the nucleus. In practice, however, a definite influence of the surrounding nuclear medium on the momentum distribution of the quarks is observed [19]. This phenomenon is called *EMC Effect* after the collaboration that first detected it in 1983 [8].

For illustration, Fig. 8.12 shows data of the NMC muon experiment at CERN and of an experiment at SLAC for the ratio of the structure functions per nucleon of  $^4\text{He}$ , carbon and calcium to deuterium. The deuteron is only weakly bound and proton and neutron can be roughly considered to be free nucleons.  $^4\text{He}$  and deuterium are isoscalar nuclides, i.e. nuclides with the same number of protons and neutrons. Approximately this is also true for carbon and calcium. In natural abundance, carbon consists to 99% of the isotope  $^{12}\text{C}$  and calcium to 97% of the isotope  $^{40}\text{Ca}$ , the heaviest stable isoscalar nuclide. The advantage of comparing isoscalar nuclides,

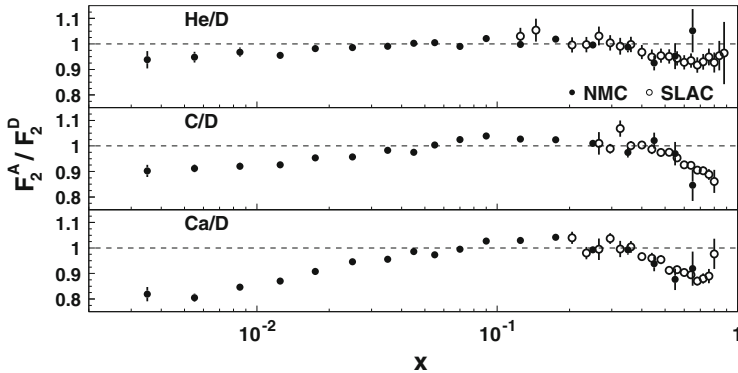


**Fig. 8.12** Ratio of the structure functions  $F_2$  of  ${}^4\text{He}$ , carbon, and calcium over deuterium as a function of  $x$  [4, 7]

i.e., nuclides with the same number of protons and neutrons is that we can study the influence of nuclear binding on the structure function  $F_2$ , without having to worry about the differences between  $F_2^p$  and  $F_2^n$ .

A distinct deviation of the ratio from unity is visible throughout the entire  $x$ -range. For  $x \lesssim 0.06$ , where the structure functions are dominated by the sea quarks, the ratio is smaller than unity, and decreases with decreasing values of  $x$ . The effect increases with increasing nuclear mass  $A$ . For  $0.06 \lesssim x \lesssim 0.3$ , the ratio is slightly larger than unity. In the range of  $0.3 \lesssim x \lesssim 0.8$  where the valence quarks prevail, the ratio is again smaller than unity, with a minimum at  $x \approx 0.65$ . This effect demonstrates that the momentum distributions of the quarks are shifted towards smaller  $x$  when nucleons are bound in the nucleus. Also in the valence-quark region the effect increases with increasing nuclear mass, although somewhat weaker than at small values of  $x$ . For  $x \rightarrow 1$  the ratio  $F_2^A/F_2^D$  increases rapidly with  $x$ . The rapid change of the ratio in this region disguises the fact that the absolute changes in  $F_2$  are very small since the structure functions themselves are tiny.

Notwithstanding the small size of the observed effects, they have generated great theoretical interest. There is a plethora of models attempting to explain this phenomenon [19]. So far, none of the models is able to convincingly describe the observed behaviour over the entire range of  $x$ . This suggests that the effect is probably due to several factors. Some possible explanations for the EMC effect are: interactions between quarks in different nucleons over the nucleon's boundaries; the "swelling" of the radius of the nucleon within the nucleus; short-range correlation between nucleons leading in the extreme case to a coalescence of nucleons to form "multi-quark clusters" of 6, 9, ... valence quarks; kinematical effects caused by the reduction in the effective nucleon mass due to nuclear binding; Fermi motion – and many other reasons.

As an example we want to briefly present two rather different models to describe the decline of the nuclear structure function at  $x < 0.1$ . In the first approach the effect is attributed to a modification of the quark and gluon distributions in

the nucleus. The interaction of the virtual photon with the nucleus is viewed in a fast moving system like the *Breit frame*. In its rest system the nucleon has the diameter  $D$ . In the *Breit frame* it has the energy  $E_N$  and is Lorentz contracted to a disc of thickness

$$D' = D/\gamma = D \cdot \frac{Mc^2}{E_N} \approx D \cdot \frac{Mc^2}{|\mathbf{P}|c}. \quad (8.6)$$

Here  $\gamma = [1 - (v/c)^2]^{-1/2}$  is the Lorentz factor. The longitudinal position of its constituents, however, has an uncertainty of

$$\Delta z = \frac{\hbar c}{x|\mathbf{P}|c}. \quad (8.7)$$

At small values of  $x$  this uncertainty  $\Delta z$  can be much larger than  $D'$ . Now we consider a nucleus with mass number  $A$  with several nucleons along the direction of the virtual photon. In the rest system of the nucleus its diameter is  $D_A$  and the mean nucleon distance is  $d \approx 2$  fm. When

$$\Delta z > d' = d \cdot \frac{Mc^2}{|\mathbf{P}|c}, \quad (8.8)$$

or equivalently

$$x < \frac{1}{d} \cdot \frac{\hbar c}{|\mathbf{P}|c} \cdot \frac{|\mathbf{P}|c}{Mc^2} = \frac{1}{d} \cdot \frac{\hbar}{Mc}, \quad (8.9)$$

then there will be a spatial overlap of sea quarks and gluons of different nucleons. The quantity  $\hbar/Mc$  is the reduced Compton wavelength of the nucleon with a value of  $\approx 0.2$  fm. At  $x \approx 0.1$  the uncertainty in the longitudinal position of the constituents becomes comparable with the average distance of the nucleons in the nucleus. The smaller  $x$ , the larger is the number of nucleons sharing their contents of sea quarks and gluons. The effect increases with increasing mass number  $A$  and saturates for  $x \approx 1/D_A \cdot \hbar/Mc$ . Thus, the density of gluons and sea quarks at the position of a nucleon in a nucleus can be much larger than for a free nucleon. Due to this “overcrowding”, the probability for an interaction between sea quarks and gluons is increased and by pair annihilation their density is reduced again.

Consequently, fewer gluons and sea quarks are found at low values of  $x$  in a nucleus compared to a free nucleon resulting in the observed reduction of the nuclear structure function. Momentum conservation requires that this reduction of the number of partons at low values of  $x$  is compensated by an enhancement at larger  $x$ . This naturally explains the enhancement of  $F_2^A/F_2^D$  in the range  $0.06 \lesssim x \lesssim 0.3$ .

In the second approach, the parton distributions in a nucleus remain unchanged compared to those in the free nucleon. The nuclear effect is attributed to a modification of the interaction of the virtual photon with the atomic nucleus [15].



We view the interaction in the rest system of the nucleus and take into account that the virtual photon can fluctuate into a quark-antiquark pair. This pair then interacts with the nucleus via the *strong* interaction. Since the strength of the strong interaction is much larger than of the electromagnetic one, the interaction does no longer happen incoherently with all the nucleons in the nucleus but preferentially with those at the front surface. The nucleons in the “shadow” of the nucleons at the front surface then do not contribute, or contribute much less, to the cross-section. This effect is called *nuclear shadowing*.

When the virtual photon fluctuates into a quark-antiquark pair, its three-momentum is conserved, but not its energy. For simplicity we treat the quark-antiquark pair as one particle with the mass  $2m_q$ . Its energy is then with (7.12) given by

$$v' = \sqrt{(\mathbf{q}c)^2 + (2m_q c^2)^2} = \sqrt{v^2 + (Qc)^2 + (2m_q c^2)^2}. \quad (8.10)$$

At small values of  $x$ , where we observe the shadowing effect, the energy of the virtual photon  $v$  is large and  $v \gg m_q c^2$ . Then we have

$$v' \approx v \left( 1 + \frac{Q^2 c^2}{2v^2} \right), \quad (8.11)$$

and the non-conservation of energy during the fluctuation has the magnitude

$$\Delta v = v' - v = \frac{(Qc)^2}{2v} = \frac{M(Qc)^2}{2Mv} = Mc^2 x. \quad (8.12)$$

The fluctuation extends over the distance

$$\Delta l = \Delta tc = \frac{\hbar c}{\Delta v} = \frac{\hbar}{Mcx}. \quad (8.13)$$

For  $x \approx 0.1$  the fluctuation length of the quark-antiquark pair becomes comparable to the distance between the nucleons in the nucleus and nuclear shadowing becomes influential. The “thicker” the nucleus is, the more pronounced is the effect.

Although the two approaches on the first sight seem to be very different, they lead to the same conclusions for the reduction of the nuclear structure functions at low values of  $x$ . This is not really surprising, since only observables are Lorentz invariant but not our pictures about the dynamics of the interaction. In a fast moving system we have fusion of partons from different nucleons that leads to an overall reduction of parton densities seen by the virtual photon. In the rest system of the nucleus the same process looks like a fluctuation of the virtual photon into a colourless quark-antiquark pair that interacts strongly with one of the nucleons thereby reducing the photon flux in its shadow. In both cases it is the same phenomenon, but viewed in a different reference frame.

## Problems

### 1. Partons

Consider deep-inelastic scattering of muons with energy 600 GeV off protons at rest. The data analysis is to be carried out at  $Q^2 = 4 \text{ GeV}^2/c^2$ .

- What is the smallest value of  $x$  which can be attained under these circumstances? You may assume that the minimal scattering energy is  $E' = 0$ .
- How many partons may be resolved with  $x > 0.3$ ,  $x > 0.03$  and in the full measurable range of  $x$  if we parametrise the parton distribution as follows:

$$\begin{aligned} q_v(x) &= A(1-x)^3/\sqrt{x} \quad \text{for the valence quarks,} \\ q_s(x) &= 0.4(1-x)^8/x \quad \text{for the sea quarks and} \\ g(x) &= 4(1-x)^6/x \quad \text{for the gluons.} \end{aligned}$$

The role of the normalisation constant,  $A$ , is to take into account that there are three valence quarks.

### 2. Deep-inelastic scattering

Deep-inelastic electron-proton scattering is studied at the HERA collider. Electrons with 27.6 GeV are collided head on with 920 GeV protons.

- Calculate the centre-of-mass energy of this reaction. What energy does an electron beam which hits a stationary proton target have to have to reproduce this centre-of-mass energy?
- The relevant kinematical quantities in deep-inelastic scattering are the square of the four momentum transfer  $Q^2$  and the Bjorken scaling variable  $x$ .  $Q^2$  may, e.g., be found from (6.2). Only the electron's kinematical variables (the beam energy  $E$ , the energy of the scattered electron  $E'$  and the scattering angle  $\theta$ ) appear here. In certain kinematical regions it is better to extract  $Q^2$  from other variables since their experimental values give  $Q^2$  with smaller errors. Find a formula for  $Q^2$  where the scattering angles of the electron  $\theta$  and of the scattered quark  $\gamma$  appear. The latter may be determined experimentally from measurements of the final state hadron energies and momenta. How?
- What is the largest possible four momentum transfer  $Q^2$  at HERA? What  $Q^2$  values are attainable in experiments with stationary targets and 300 GeV beam energies? What spatial resolution of the proton does this value correspond to?
- Find the kinematical region in  $Q^2$  and  $x$  that can be reached with the ZEUS calorimeter which covers the angular region  $7^\circ$ – $178^\circ$ . The scattered electron needs to have at least 5 GeV energy to be resolved.
- The electron-quark interaction can occur through neutral currents ( $\gamma$ ,  $Z^0$ ) or through charged ones ( $W^\pm$ ). Estimate at which value of  $Q^2$  the electromagnetic and weak interaction cross-sections are of the same size.

## References

1. I. Abt et al., Nucl. Instr. Methods **A386**, 310 (1997)
2. K. Ackerstaff et al., Phys. Rev. Lett. **81**, 5519 (1998)
3. G. Altarelli, G. Parisi, Nucl. Phys. **B126**, 298 (1977)
4. P. Amaudruz et al., Z. Phys. **C51**, 387 (1991);  
corrected data: P. Amaudruz et al., Nucl. Phys. **B441**, 3 (1995)
5. P. Amaudruz et al., Phys. Lett. **B295**, 159 (1992)
6. M. Arneodo et al., Phys. Lett. **B309**, 222 (1993)
7. R.G. Arnold et al., Phys. Rev. Lett. **52**, 727 (1984);  
corrected data: J. Gomez et al., Phys. Rev. **D49**, 4348 (1994)
8. J.J. Aubert et al., Phys. Lett. **B123**, 275 (1983)
9. A.C. Benvenuti et al., Phys. Lett. **B237**, 592 (1990)
10. C. Diaconu et al., Annu. Rev. Nucl. Part. Sci. **60**, 101 (2010)
11. S.D. Drell, T.M. Yan, Ann. Phys. (NY) **66**, 578 (1971)
12. V.N. Gribov, L.N. Lipatov, Sov. J. Nucl. Phys. **15**, 438 (1972)
13. E.A. Hawker et al., Phys. Rev. Lett. **80**, 3715 (1998)
14. U. Holm et al., *ZEUS Status Report* (1993), <http://www-zeus.desy.de/bluebook/bluebook.html>
15. B.Z. Kopeliovich, J. Morfin, I. Schmidt, Prog. Part. Nucl. Phys. **68**, 314 (2013)
16. L.N. Lipatov, Sov. J. Nucl. Phys. **20**, 94 (1975)
17. A. Martin et al., Eur. Phys. J. **C63**, 189 (2009)
18. H. Nishino et al., Phys. Rev. Lett. **102**, 141801 (2009)
19. P.R. Norton, Rep. Prog. Phys. **66**, 1253 (2003)
20. Particle Data Group, J. Beringer et al., *Review of particle properties*. Phys. Rev. D **86**, 010001 (2012)
21. L. Whitlow et al., Phys. Lett. **B282**, 475 (1992)

# Chapter 9

## Particle Production in $e^+e^-$ Collisions

So far, we have mainly discussed the light quarks,  $u$  and  $d$ , and those hadrons composed of these two quarks. The easiest way to produce hadrons with heavier quarks is in  $e^+e^-$  collisions. Free electrons and positrons may be produced rather easily. They can be accelerated, stored and made to collide in accelerators. In an electron-positron collision process, all particles which interact electromagnetically and weakly can be produced, as long as the energy of the beam particles is sufficiently high. In an electron-positron electromagnetic annihilation, a virtual photon is produced, which immediately decays into a pair of charged elementary particles Fig. 9.1 (left). In a weak interaction, the exchanged particle is the heavy vector boson  $Z^0$  (cf. Fig. 9.1 (right) and see Chap. 12). The symbol  $f$  denotes an elementary fermion (quark or lepton) and  $\bar{f}$  its antiparticle. The  $f\bar{f}$  system must have the quantum numbers of the photon or the  $Z^0$ , respectively. In these reactions all fundamental, charged particle-antiparticle pairs can be produced; lepton-antilepton and quark-antiquark pairs. Neutrinos are electrically neutral; hence, neutrino-antineutrino pairs can only be produced by  $Z^0$  exchange.

**Colliding beams** Which particle-antiparticle pairs can be produced only depends upon the energy of the electrons and positrons (Fig. 9.2). In a storage ring, electrons and positrons with beam energies  $E_1$  and  $E_2$  orbit in opposite directions and collide head-on. It is conventional to use the Lorentz-invariant energy variable  $s$ , the square of the centre-of-mass energy:

$$\begin{aligned} s &= (p_1c + p_2c)^2 \\ &= m_1^2c^4 + m_2^2c^4 + 2E_1E_2 - 2\mathbf{p}_1\mathbf{p}_2c^2. \end{aligned} \tag{9.1}$$

In a storage ring with colliding particles of the same energy  $E$ ,

$$s = 4E^2. \tag{9.2}$$

**Fig. 9.1** Fermion-antifermion production in electron-positron collisions via the exchange of a virtual photon (left) and a  $Z^0$ -boson (right)

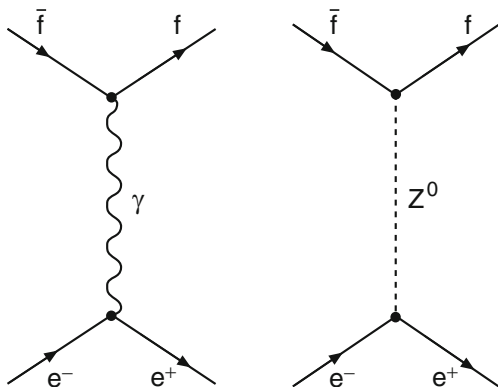
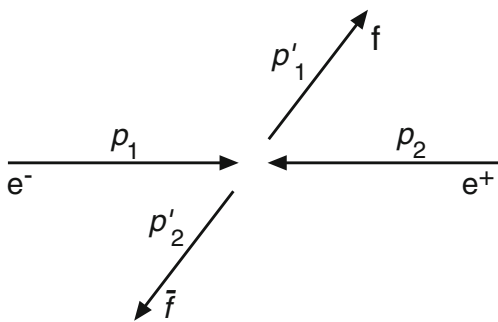


**Fig. 9.2** For colliding particles of the same energy the fermion and anti fermion are produced back-to-back



Hence, particle-antiparticle pairs with masses of up to  $2m = \sqrt{s}/c^2$  can be produced. To discover new particles, the storage ring energy must be raised. One then looks for an increase in the reaction rate, or for resonances in the cross-section.

The great advantage of colliding beam experiments is that the total beam energy is available in the centre-of-mass system. In a fixed target experiment, with  $m$  satisfying  $mc^2 \ll E$ ,  $s$  is related to  $E$  by:

$$s \approx 2mc^2 \cdot E. \quad (9.3)$$

Here, the centre-of-mass energy only increases proportionally to the square root of the beam energy.

**Particle detection** To detect the particles produced back-to-back in  $e^+e^-$  annihilation (Fig. 9.2) one requires a detector set up around the collision point which covers as much as possible of the total  $4\pi$  solid angle. The detector should permit us to trace the tracks back to the interaction point and to identify the particles themselves. The basic form of such a detector is sketched in Fig. 9.3.

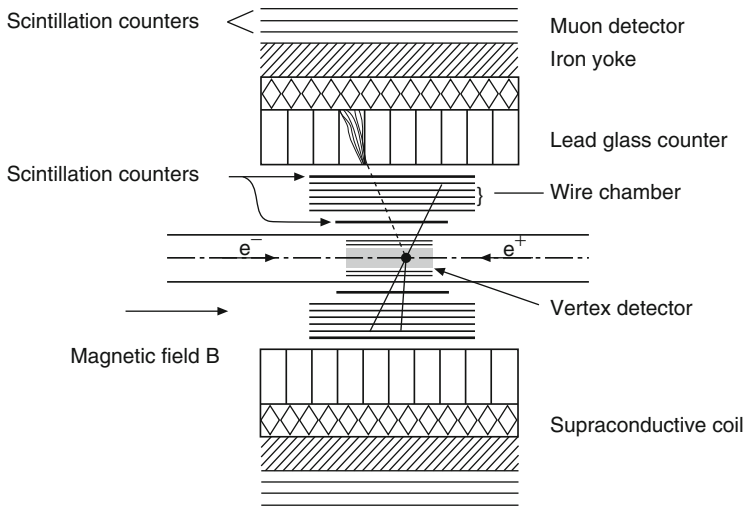


**Fig. 9.3** Sketch of a  $4\pi$ -detector, as used in  $e^+e^-$  collision experiments. The detector is inside the coil of a solenoid, which typically produces a magnetic field of around 1 T along the beam direction. Charged particles are detected in a vertex detector, mostly composed of silicon microstrip counters, and in wire chambers. The vertex detector is used to locate the interaction point. The curvature of the tracks in the magnetic field tell us the momenta. Photons and electrons are detected as shower formations in electromagnetic calorimeters (of, e.g., lead glass). Muons pass through the iron yoke with little energy loss. They are then seen in the exterior scintillation counters

## 9.1 Lepton Pair Production

Before we turn to the creation of heavy quarks, we want to initially consider the leptons. *Leptons* are elementary spin-1/2 particles which feel the weak and, if they are charged, the electromagnetic interaction – but not, however, the strong interaction.

**Muons** The lightest particles which can be produced in electron-positron collisions are muon pairs:

$$e^+ + e^- \rightarrow \mu^+ + \mu^- .$$

The muon  $\mu^-$  and its antiparticle<sup>1</sup> the  $\mu^+$  both have a mass of only  $105.7 \text{ MeV}/c^2$  and they are produced in all usual  $e^+e^-$  storage ring experiments. They penetrate matter very easily,<sup>2</sup> whereas electrons because of their small mass and hadrons because of the strong interaction have much smaller ranges. After that of the

<sup>1</sup>Antiparticles are generally symbolised by a bar (e.g.,  $\bar{\nu}_e$ ). This symbol is generally skipped over for charged leptons since knowledge of the charge alone tells us whether we have a particle or an antiparticle. We thus write  $e^+$ ,  $\mu^+$ ,  $\tau^+$ .

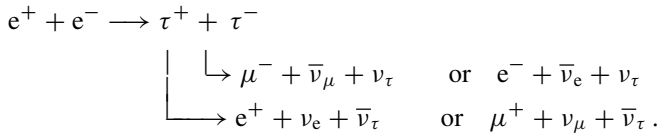
<sup>2</sup>Muons from cosmic radiation can still be detected in underground mines!

neutron, theirs is the longest lifetime ( $2\ \mu\text{s}$ ) of any unstable particle. This means that experimentally they may easily be identified. Therefore the process of muon pair production is often used as a reference point for other  $e^+e^-$  reactions.

**Tau leptons** If the centre-of-mass energy in an  $e^+e^-$  reaction suffices, a further lepton pair, the  $\tau^-$  and  $\tau^+$ , may be produced. Their lifetime,  $3 \cdot 10^{-13}\ \text{s}$ , is much shorter. They may weakly decay into muons or electrons as will be discussed in Sect. 10.1f.

The tau was discovered at the SPEAR  $e^+e^-$  storage ring at SLAC when oppositely charged electron-muon pairs were observed whose energy was much smaller than the available centre-of-mass energy [16].

These events were interpreted as the creation and subsequent decay of a heavy lepton-antilepton pair:



The neutrinos which are created are not detected.

The threshold for  $\tau^+\tau^-$ -pair production, and hence the mass of the  $\tau$ -lepton, may be read off from the increase of the cross-section of the  $e^+e^-$  reaction with the centre-of-mass energy. One should use as many leptonic and hadronic decay channels as possible to provide a good signature for  $\tau$ -production (Fig. 9.4). The experimental threshold at  $\sqrt{s} = 2m_\tau c^2$  implies that the tau mass is  $1.777\ \text{GeV}/c^2$ .

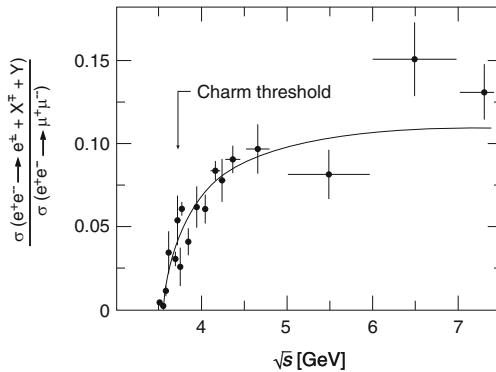


**Fig. 9.4** Ratio of the cross-sections for the production of two particles with opposite charges in the reaction  $e^+ + e^- \rightarrow e^\pm + X^\mp + Y$ , to the cross-sections for the production of  $\mu^+\mu^-$  pairs [5, 6]. Here  $X^\mp$  denotes a charged lepton or meson and  $Y$  symbolises the unobserved, neutral particles. The sharp increase at  $\sqrt{s} \approx 3.55\ \text{GeV}$  is a result of  $\tau$ -pair production, which here becomes energetically possible. The threshold for the creation of mesons containing a charmed quark (arrow) is only a little above that for  $\tau$ -lepton production. Both particles have similar decay modes which makes it more difficult to detect  $\tau$ -leptons

**Cross-section** The creation of charged lepton pairs may, to a good approximation, be viewed as a purely electromagnetic process ( $\gamma$  exchange). The exchange of  $Z^0$  bosons, and interference between photon and  $Z^0$  exchange, may be neglected if the energy is small compared to the mass of the  $Z^0$ . The cross-section may then be found relatively easily. The most complicated case is the elastic process  $e^+e^- \rightarrow e^+e^-$ , *Bhabha scattering*. Here two processes must be taken into account: the annihilation of the electron and positron into a virtual photon with subsequent  $e^+e^-$ -pair creation (Fig. 9.5 (left)) and secondly the scattering of the electron and positron off each other (Fig. 9.5 (right)). These processes lead to the same final state and so their amplitudes must be added in order to obtain the cross-section.

Muon pair creation is more easily calculated. Other  $e^+e^-$  reactions are therefore usually normalised with respect to it. The differential cross-section for this reaction is:

$$\frac{d\sigma}{d\Omega} = \frac{\alpha^2}{4s} (\hbar c)^2 \cdot (1 + \cos^2 \theta) . \tag{9.4}$$

Integrating over the solid angle  $\Omega$  yields the total cross-section:

$$\sigma = \frac{4\pi\alpha^2}{3s} (\hbar c)^2 , \tag{9.5}$$

and one finds

$$\sigma(e^+e^- \rightarrow \mu^+\mu^-) = 21.7 \frac{\text{nbarn}}{(E^2/\text{GeV}^2)} . \tag{9.6}$$

The formal derivation of (9.4) may be found in many standard text books [10, 14, 15], we will merely try to make it plausible: The photon couples to two elementary charges. Hence the matrix element contains two powers of  $e$  and the cross-section, which is proportional to the square of the matrix element, is proportional to  $e^4$  or  $\alpha^2$ .

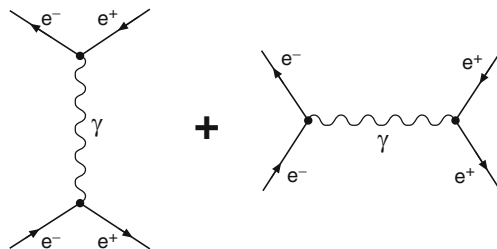


**Fig. 9.5** The two processes contributing to Bhabha scattering



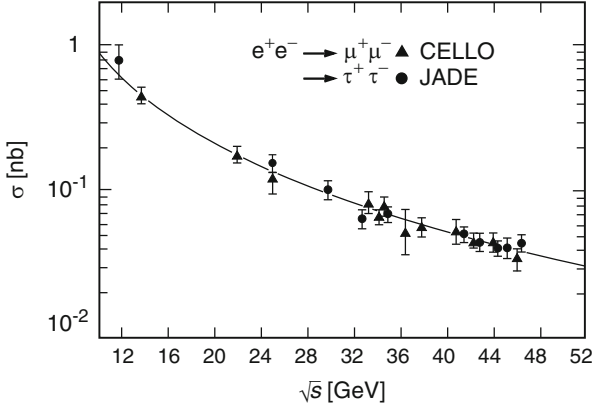


**Fig. 9.6** Cross-sections of the reactions  $e^+e^- \rightarrow \mu^+\mu^-$  and  $e^+e^- \rightarrow \tau^+\tau^-$  as functions of the centre-of-mass energy  $\sqrt{s}$  (From [7] and [8]). The *solid line* shows the cross-section (9.6) predicted by quantum electrodynamics

The length scale is proportional to  $\hbar c$ , which enters twice over since cross-sections have the dimension of area. We must further divide by a quantity with dimensions of [energy<sup>2</sup>]. Since the masses of the electron and the muon are very small compared to  $s$ , this last is the only reasonable choice. The cross-section then falls off with the square of the storage ring's energy. The  $(1 + \cos^2 \theta)$  angular dependence is typical for the production of two spin-1/2 particles such as muons. Note that (9.4) is, up to this angular dependence, completely analogous to the equation for Mott scattering (5.39) once we recognise that  $Q^2 c^2 = s = 4E^2 = 4E'^2$  holds here.

Figure 9.6 shows the cross-section for  $e^+e^- \rightarrow \mu^+\mu^-$  and the prediction of quantum electrodynamics. One sees an excellent agreement between theory and experiment. The cross-section for  $e^+e^- \rightarrow \tau^+\tau^-$  is also shown in the figure. If the centre-of-mass energy  $\sqrt{s}$  is large enough that the difference in the  $\mu$  and  $\tau$  rest masses can be neglected, then the cross-sections for  $\mu^+\mu^-$  and  $\tau^+\tau^-$  production are identical. One speaks of *lepton universality*, which means that the electron, the muon and the tau behave, apart from their masses and associated effects, identically in all reactions. The muon and the tau may to a certain extent be viewed as being heavier copies of the electron.

Since (9.6) describes the experimental cross-section so well, the form factors of the  $\mu$  and  $\tau$  are unity – which according to Table 5.1 means they are point-like particles. No spatial extension of the leptons has yet been seen. The upper limit for the electron is  $10^{-18}$  m. Since the hunt for excited leptons so far has also been unsuccessful, it is currently believed that leptons are indeed elementary, point-like particles.

## 9.2 Resonances

If the cross-sections for the production of muon pairs and hadrons in  $e^+e^-$  scattering are plotted as a function of the centre-of-mass energy  $\sqrt{s}$ , one finds in both cases the  $1/s$ -dependence of (9.5). In the hadronic final state channels this trend is broken by various strong peaks which are sketched in Fig. 9.7. These so-called *resonances* are short lived states which have a fixed mass and well-defined quantum numbers such as angular momentum. It is therefore reasonable to call them particles.

**Breit-Wigner formula** The energy dependence of the cross-section of a reaction between two particles a and b close to a resonance energy  $E_0$  is generally described by the *Breit-Wigner formula* (see, e.g., [15]). In the case of elastic scattering, it is approximately given by:

$$\sigma(E) = \frac{\pi \lambda^2 (2J + 1)}{(2s_a + 1)(2s_b + 1)} \cdot \frac{\Gamma^2}{(E - E_0)^2 + \Gamma^2/4}. \tag{9.7}$$

Here  $\lambda$  is the reduced wavelength in the centre-of-mass system,  $s_a$  and  $s_b$  are the spins of the reacting particles and  $\Gamma$  is the *width* (half width) of the resonance. The lifetime of such a resonance is  $\tau = \hbar/\Gamma$ . This formula is similar to that for the resonance of a forced oscillator with large damping. The energy  $E$  corresponds to the excitation frequency  $\omega$ ,  $E_0$  to the resonance frequency  $\omega_0$  and the width  $\Gamma$  to the damping.

For an inelastic reaction like the case at hand, the cross-section depends upon the *partial widths*  $\Gamma_i$  and  $\Gamma_f$  in the initial and final channels and on the total width  $\Gamma_{\text{tot}}$ . The latter is the sum of the partial widths of all possible final channels. The result

**Fig. 9.7** Cross-section of the reaction  $e^+e^- \rightarrow \text{hadrons}$  as a function of the centre-of-mass energy  $\sqrt{s}$  (sketch) [11]. The cross-section for direct muon pair production (9.5) is denoted by a *dashed curve*

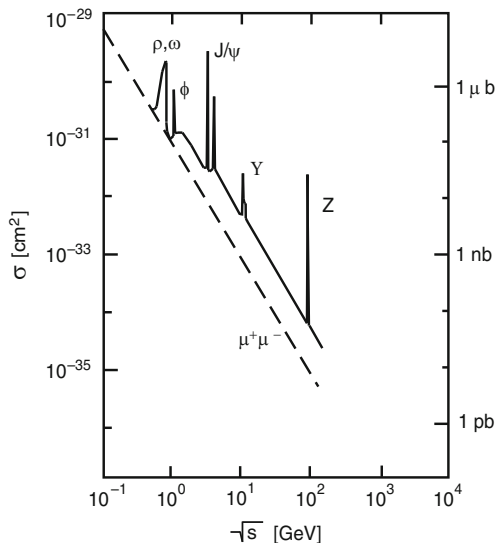
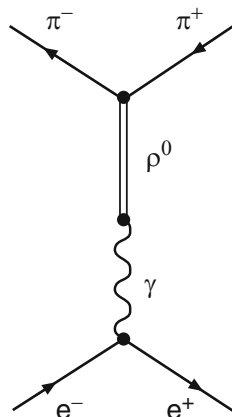


**Fig. 9.8** Production of a  $\rho^0$  vector meson in  $e^+e^-$  annihilation with its subsequent decay into a charged pion pair



for an individual decay channel  $f$  is

$$\sigma_f(E) = \frac{3\pi\lambda^2}{4} \cdot \frac{\Gamma_i\Gamma_f}{(E - E_0)^2 + \Gamma_{\text{tot}}^2/4}, \quad (9.8)$$

where we have replaced  $s_a$  and  $s_b$  by the spins of the electrons (1/2) and  $J$  by the spin of the photon (1).

**The resonances  $\rho$ ,  $\omega$ , and  $\phi$**  First, we discuss resonances at low energies. The width  $\Gamma$  of these states varies between 4 and 150 MeV, corresponding to lifetimes from about  $10^{-22}$  to  $10^{-24}$  s. These values are typical of the strong interaction. These resonances are therefore interpreted as quark-antiquark bound states whose masses are just equal to the total centre-of-mass energy of the reaction. The quark-antiquark states must have the same quantum numbers as the virtual photon; in particular, they must have total angular momentum  $J = 1$  and negative parity. Such quark-antiquark states are called *vector mesons*; they decay into lighter mesons. Figure 9.8 depicts schematically the production and the decay of the  $\rho^0$  resonance.

The analysis of the peak at 770–780 MeV reveals that it is caused by the interference of two resonances, the  $\rho^0$ –meson ( $m_{\rho^0} = 776 \text{ MeV}/c^2$ ) and the  $\omega$ –meson ( $m_\omega = 782 \text{ MeV}/c^2$ ). These resonances are produced via the creation of  $u\bar{u}$  and  $d\bar{d}$  pairs. Since u-quarks and d-quarks have nearly identical masses, the  $u\bar{u}$ - and  $d\bar{d}$ -states are approximately degenerate. The  $\rho^0$  and  $\omega$  are mixed states of  $u\bar{u}$  and  $d\bar{d}$ .

These two mesons undergo different decays and may be experimentally identified by them (cf. Sect. 15.3):

$$\begin{aligned} \rho^0 &\rightarrow \pi^+\pi^-, \\ \omega &\rightarrow \pi^+\pi^0\pi^-. \end{aligned}$$

At an energy of 1,019 MeV, the  $\phi$ -resonance is produced. It has a width of only  $\Gamma = 4.3$  MeV, and hence a relatively long lifetime compared to other hadrons. The main decay modes ( $\approx 85\%$ ) of the  $\phi$  are into two kaons, which have masses of  $494 \text{ MeV}/c^2$  ( $K^\pm$ ) and  $498 \text{ MeV}/c^2$  ( $K^0$ ):

$$\begin{aligned} \phi &\rightarrow K^+ + K^- , \\ \phi &\rightarrow K^0 + \bar{K}^0 . \end{aligned}$$

Kaons are examples of the so-called *strange particles*. This name reflects the unusual fact that they are produced by the strong interaction, but only decay by the weak interaction; this despite the fact that their decay products include hadrons, i.e., strongly interacting particles.

This behaviour is explained by the fact that kaons are quark-antiquark combinations containing an s or “strange” quark:

$$\begin{aligned} |K^+\rangle &= |u\bar{s}\rangle & |K^0\rangle &= |d\bar{s}\rangle \\ |K^-\rangle &= |\bar{u}s\rangle & |\bar{K}^0\rangle &= |\bar{d}s\rangle . \end{aligned}$$

The constituent mass attributed to the s-quark is  $450 \text{ MeV}/c^2$ . In a kaon decay, the s-quark must turn into a light quark which can only happen in weak interaction processes. Kaons and other “strange particles” can be produced in the strong interaction, as long as equal numbers of s-quarks and  $\bar{s}$ -antiquarks are produced. At least two “strange particles” must therefore be produced simultaneously. We introduce the quantum number  $S$  (the *strangeness*), to indicate the number of  $\bar{s}$ -antiquarks minus the number of s-quarks. This quantum number is conserved in the strong and electromagnetic interactions, but it can be changed in weak interactions.

The  $\phi$  meson decays mainly into two kaons because it is an  $s\bar{s}$  system. When it decays a  $u\bar{u}$  pair or a  $d\bar{d}$  pair are produced in the colour field of the strong interaction. The kaons are produced by combining these with the  $s\bar{s}$  quarks, as shown in Fig. 9.9.

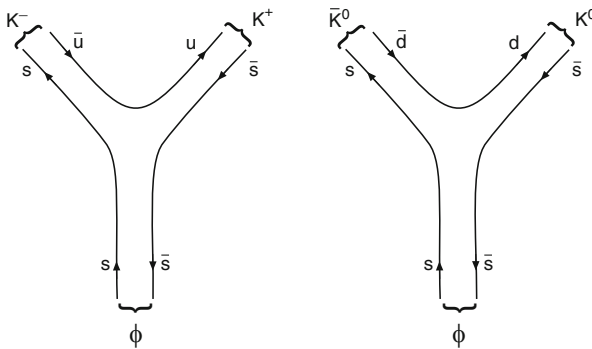
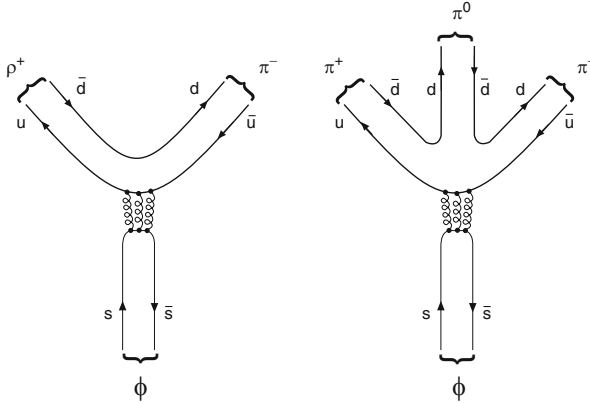


Fig. 9.9 The decay of the  $\phi$  meson into two Kaons with continuous s- and  $\bar{s}$ -quark lines



**Fig. 9.10** The decay of the  $\phi$  meson into light mesons requires the annihilation of the  $s\bar{s}$  pair and a virtual state with three gluons

Because of the small mass difference  $m_\phi - 2m_K$ , the phase space available to this decay is very small. This accounts for the narrow width of the  $\phi$  resonance.

One could ask: why does the  $\phi$  not decay mainly into light mesons? The decay into pions is very rare (2.5%), although the phase space available is much larger. Such a decay is only possible if the  $s$  and  $\bar{s}$  first annihilate, producing two or three quark-antiquark pairs (Fig. 9.10). According to QCD, this proceeds through a virtual intermediate state with at least three gluons. Hence, this process is suppressed with respect to the decay into two kaons which can proceed through the exchange of one gluon. The enhancement of processes with continuous quark lines is called the *Zweig rule*.

**The resonances  $J/\psi$  and  $\Upsilon$**  Although the  $s$ -quarks were known from hadron spectroscopy, it was a surprise when in 1974 an extremely narrow resonance whose width was only 93 keV was discovered at a centre-of-mass energy of 3,097 MeV. It was named  $J/\psi$ .<sup>3</sup> The resonance was attributed to the production of a new heavy quark. There were already theoretical suggestions that such a  $c$ -quark (“charmed” quark) exists. The long lifetime of the  $J/\psi$  is explained by its  $c\bar{c}$  structure. The decay into two mesons each containing a  $c$ - (or  $\bar{c}$ )-quark plus a light quark (in analogy to the decay  $\phi \rightarrow K + \bar{K}$ ) would be favoured by the Zweig rule, but is impossible due to energy conservation. This is because the mass of any pair of  $D$  mesons ( $c\bar{u}$ ,  $c\bar{d}$  etc.), which were observed in later experiments, is larger than the mass of the  $J/\psi$ . More resonances were found at centre-of-mass energies some 100 MeV higher. They were called  $\psi'$ ,  $\psi''$  etc., and were interpreted as excited states of the  $c\bar{c}$  system. The  $J/\psi$  is the lowest  $c\bar{c}$  state with the quantum numbers of the photon  $J^P = 1^-$ .

<sup>3</sup>This particle was discovered nearly simultaneously in two differently conceived experiments (pp collision and  $e^+e^-$  annihilation). One collaboration called it  $J$  [3], the other  $\psi$  [4].

**Table 9.1** Charges and masses of the quarks

Quark	Colour	Electr. charge	Mass (MeV/c <sup>2</sup> )	
			Bare quark	Const. quark
Down	b, g, r	-1/3	4.5–5.5	≈300
Up	b, g, r	+2/3	1.8–3.0	≈300
Strange	b, g, r	-1/3	90–100	≈450
Charm	b, g, r	+2/3	1,250–1,300	
Bottom	b, g, r	-1/3	4,150–4,210	
Top	b, g, r	+2/3	172.5 · 10 <sup>3</sup> –174.5 · 10 <sup>3</sup>	

A  $c\bar{c}$  state, the  $\eta_c$ , exists at a somewhat lower energy, it has quantum numbers  $0^-$  (cf. Sect. 14.2 ff) and cannot be produced directly in  $e^+e^-$  annihilation.

A similar behaviour in the cross-section was found at about 10 GeV. Here the series of Upsilon ( $\Upsilon$ ) resonances was discovered [12, 13]. These  $b\bar{b}$  states are due to the even heavier b-quark (“bottom” quark). The lowest-lying state at 9.46 GeV also has an extremely narrow width (only 54 keV) and hence a long lifetime.

The t-quark (“top” quark) was found in 1995 by the two experiments D0 and CDF at the Tevatron (FNAL) in  $p\bar{p}$  collisions [1, 2]. From these experiments and more recently also from the LHC experiments a t-quark mass of  $173.5 \pm 1.0$  GeV/c<sup>2</sup> [17] has been derived. The  $e^+e^-$ -storage ring LEP could only attain centre-of-mass energies of up to 209.2 GeV, which is not enough for  $t\bar{t}$  pair production. An actual review of the experimental results and the properties of the t-quark can be found, e.g., in [18].

Table 9.1 shows a compilation of the colour charges, the electric charges and the masses of the quarks;  $b, g, r$  denote the colours blue, green and red. Listed are the masses of “bare” quarks (current quarks) which would be measured in the limit  $Q^2 \rightarrow \infty$  [17] as well as the masses of constituent quarks, i.e., the effective masses of quarks bound in hadrons. The masses of the quarks, in particular those of the current quarks, are strongly model dependent. For heavy quarks, the relative difference between the two masses is small.

**The  $Z^0$  resonance** At  $\sqrt{s} = 91.2$  GeV, an additional resonance is observed with a width of 2,495 MeV. It decays into lepton and quark pairs. The properties of this resonance are such that it is thought to be a real  $Z^0$ , the vector boson of the weak interaction. In Sect. 12.2, we will describe what we can learn from this resonance.

### 9.3 Non-resonant Hadron Production

Up to now we have solely considered resonances in the cross-sections of electron-positron annihilation. Quark-antiquark pairs can, naturally, also be produced among the resonances. Further quark-antiquark pairs are then produced and form hadrons, around the primarily produced quark (or antiquark). This process is called *hadro-*

*nisation*. Of course only those quarks can be produced whose masses are less than half the centre-of-mass energy available.

In hadron production, a quark-antiquark pair is initially produced. Hence the cross-section is given by the sum of the individual cross-sections of quark-antiquark pair production. The production of the primary quark-antiquark pair by an electromagnetic interaction can be calculated analogously to muon pair production. Unlike muons, quarks do not carry a full elementary charge of  $1 \cdot e$ ; but rather a charge  $z_f \cdot e$  which is  $-1/3 e$  or  $+2/3 e$ , depending on the quark flavour  $f$ . Hence the transition matrix element is proportional to  $z_f e^2$ , and the cross-section is proportional to  $z_f^2 \alpha^2$ . Since quarks (antiquarks) carry colour (anticolour), a quark-antiquark pair can be produced in three different colour states. Therefore there is an additional factor of 3 in the cross-section formula. The cross-section is given by:

$$\sigma(e^+e^- \rightarrow q_f\bar{q}_f) = 3 \cdot z_f^2 \cdot \sigma(e^+e^- \rightarrow \mu^+\mu^-), \quad (9.9)$$

and the ratio of the cross-sections by

$$R := \frac{\sigma(e^+e^- \rightarrow \text{hadrons})}{\sigma(e^+e^- \rightarrow \mu^+\mu^-)} = \frac{\sum_f \sigma(e^+e^- \rightarrow q_f\bar{q}_f)}{\sigma(e^+e^- \rightarrow \mu^+\mu^-)} = 3 \cdot \sum_f z_f^2. \quad (9.10)$$

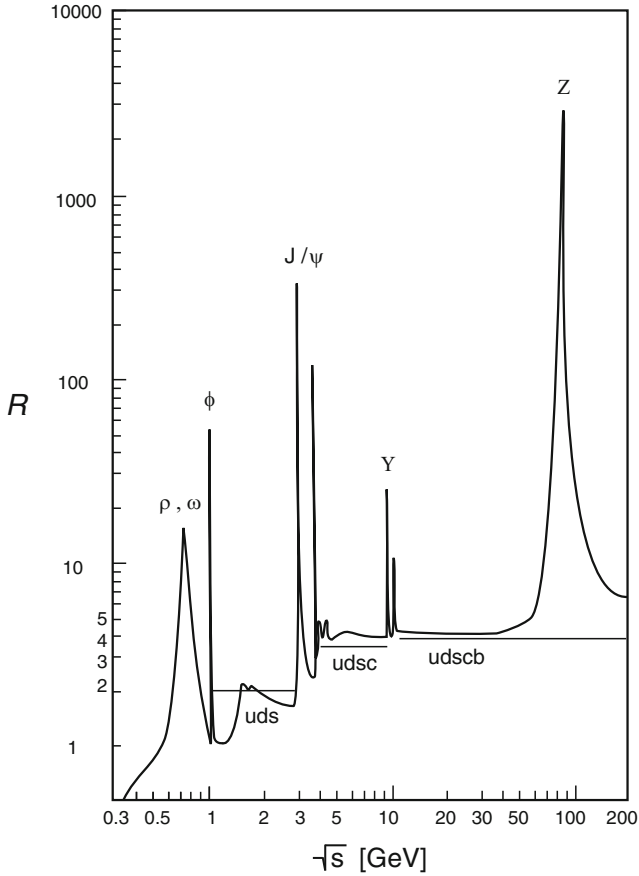
Here only those quark types  $f$  which can be produced at the centre-of-mass energy of the reaction contribute to the sum over the quarks.

Figure 9.11 shows schematically the ratio  $R$  as a function of the centre-of-mass energy  $\sqrt{s}$ . Many experiments had to be carried out at different particle accelerators, each covering a specific region of energy, to obtain such a picture. In the non-resonant regions  $R$  increases step by step with increasing energy  $\sqrt{s}$ . This becomes plausible if we consider the contributions of the individual quark flavours. Below the threshold for  $J/\psi$  production, only  $u\bar{u}$ ,  $d\bar{d}$ , and  $s\bar{s}$  pairs can be produced. Above it,  $c\bar{c}$  pairs can also be produced; and at even higher energies,  $b\bar{b}$  pairs are produced. The sum in (9.10) thus contains at higher energies ever more terms. As a corollary, the increase in  $R$  tells us about the charges of the quarks involved. Depending on the energy region, i.e., depending upon the number of quark flavours involved, one expects:

$$R = 3 \cdot \sum_f z_f^2 = 3 \cdot \left\{ \underbrace{\left( \frac{2}{3} \right)^2 + \left( -\frac{1}{3} \right)^2 + \left( -\frac{1}{3} \right)^2}_{3 \cdot 6/9} + \underbrace{\left( \frac{2}{3} \right)^2 + \left( -\frac{1}{3} \right)^2}_{3 \cdot 10/9} \right\}. \quad (9.11)$$

$\underbrace{\hspace{15em}}_{3 \cdot 11/9}$

These predictions are in good agreement with the experimental results. The measurement of  $R$  represents an additional way to determine the quark charges



**Fig. 9.11** Cross-section of the reaction  $e^+e^- \rightarrow \text{hadrons}$ , normalised to  $e^+e^- \rightarrow \mu^+\mu^-$ , as a function of the centre of mass energy  $\sqrt{s}$  (sketch). The horizontal lines correspond to  $R = 6/3$ ,  $R = 10/3$  and  $R = 11/3$ , the values we expect from (9.10), depending upon the number of quarks involved. The value  $R = 15/3$  which is expected if the t-quark participates lies outside the plotted energy range (Courtesy of G. Myatt, Oxford)

and is simultaneously an impressive confirmation of the existence of exactly three colours.

### 9.4 Gluon Emission

Using  $e^+e^-$  scattering it has proven possible to experimentally establish the existence of gluons and to measure the value of  $\alpha_s$ , the strong coupling constant.

The first indications for the existence of gluons were provided by deep-inelastic scattering of leptons off the “average nucleon”. The integral of the structure function



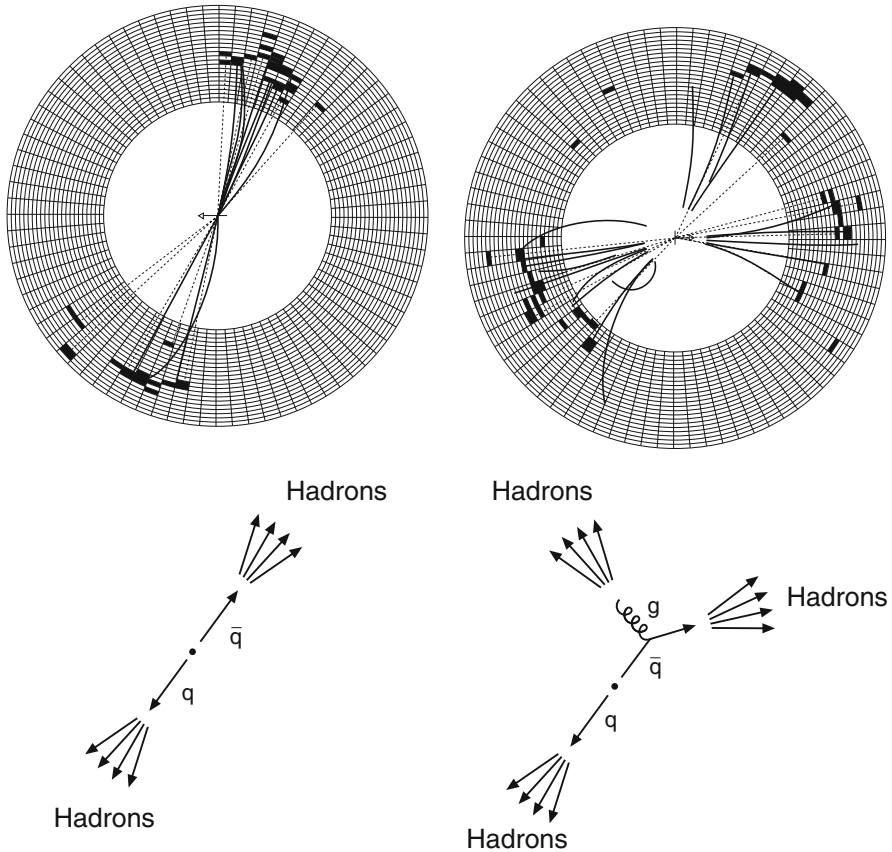


**Fig. 9.12** Typical 2-jet and 3-jet events, measured with the JADE detector at the PETRA  $e^+e^-$  storage ring. The figures show a projection perpendicular to the beam axis, which is at the centre of the cylindrical detector. The tracks of charged particles (*solid lines*) and of neutral particles (*dotted lines*) are shown. They were reconstructed from the signals in the central wire chamber and in the lead glass calorimeter surrounding the wire chamber. In this projection, the concentration of the produced hadrons in two or three particle jets is clearly visible (Courtesy of DESY)

$F_2$  was only half the expected value (cf. Sect. 7.5). The missing half of the nucleon momentum was apparently carried by electrically neutral particles which were also not involved in weak interactions. They were identified with the gluons. The coupling constant  $\alpha_s$  was determined from the scaling violation of the structure function  $F_2$  (Sect. 8.3).

A direct measurement of these quantities is possible by analysing “jets”. At high energies, hadrons are typically produced in two jets, emitted in opposite directions. These jets are produced in the hadronisation of the primary quarks and antiquarks (left side of Fig. 9.12).

In addition to simple  $q\bar{q}$  production, higher-order processes can occur. For example, a high-energy (“hard”) gluon can be emitted, which can then manifest itself as a third jet of hadrons. This corresponds to the emission of a photon in electromagnetic bremsstrahlung. Emission of a hard photon, however, is a relatively rare process, as the electromagnetic coupling constant  $\alpha$  is rather small. By contrast, the probability of gluon bremsstrahlung is given by the coupling constant  $\alpha_s$ . Such 3-jet events are indeed detected. Figure 9.12 (right) shows a particularly nice example. The coupling constant  $\alpha_s$  may be deduced directly from a comparison of the 3- and 2-jet event rates. Measurements at different centre-of-mass energies also demonstrate that  $\alpha_s$  decreases with increasing  $Q^2 = s/c^2$  as (8.1) predicts. The experimental determination of the  $Q^2$  dependence of the strong coupling constant  $\alpha_s$  has been reviewed in detail, e.g., in Ref. [9].

## Problems

### 1. Electron-positron collisions

- (a) Electrons and positrons each with a beam energy  $E$  of 4 GeV collide head on in a storage ring. What production rate of  $\mu^+\mu^-$ -pairs would you expect at a luminosity of  $10^{32} \text{ cm}^{-2} \text{ s}^{-1}$ ? What production rate for events with hadronic final states would you expect?
- (b) It is planned to construct two linear accelerators aimed at each other (a linear collider) from whose ends electrons and positrons will collide head on with a centre-of-mass energy of 500 GeV. How big must the luminosity be if one wants to measure the hadronic cross-section within two hours with a 10% statistical error?

### 2. $\Upsilon$ resonance

Detailed measurements of the  $\Upsilon(1S)$  resonance, whose mass is roughly 9,460 MeV, are performed at the CESR electron-positron storage ring.

- (a) Calculate the uncertainty in the beam energy  $E$  and the centre-of-mass energy  $W$  if the radius of curvature of the storage ring is  $R = 100 \text{ m}$ . We have:

$$\delta E = \left( \frac{55}{32\sqrt{3}} \frac{\hbar c m_e c^2}{2R} \gamma^4 \right)^{1/2}$$

What does this uncertainty in the energy tell us about the experimental measurement of the  $\Upsilon$  (Use the information given in Part b)?

- (b) Integrate the Breit-Wigner formula across the region of energy where the  $\Upsilon(1S)$  resonance is found. The experimentally observed value of this integral for hadronic final states is  $\int \sigma(e^+e^- \rightarrow \Upsilon \rightarrow \text{hadrons}) dW \approx 300 \text{ nb MeV}$ .

The decay probabilities for  $\Upsilon \rightarrow \ell^+\ell^-$  ( $\ell = e, \mu, \tau$ ) are each around 2.5%. How large is the total natural decay width of the  $\Upsilon$ ? What cross-section would one expect at the resonance peak if there was no uncertainty in the beam energy (and the resonance was not broadened by radiative corrections)?

## References

1. S. Abachi et al., Phys. Rev. Lett. **74**, 2632 (1995)
2. F. Abe et al., Phys. Rev. Lett. **74**, 2626 (1995);  
Phys. Rev. Lett. **73**, 225 (1994)
3. J.J. Aubert et al., Phys. Rev. Lett. **33**, 1404 (1974)
4. J.-E. Augustin et al., Phys. Rev. Lett. **33**, 1406 (1974)
5. W. Bacino et al., Phys. Rev. Lett. **41**, 13 (1978)
6. B.C. Barish, R. Stroynowski, Phys. Rep. **157**, 1 (1988)
7. J.W. Bartel et al., Phys. Lett. **B161**, 188 (1985)
8. H.-J. Behrend et al., Phys. Lett. **B191**, 209 (1987)
9. S. Bethke, Eur. Phys. J. **C64**, 689 (2009)
10. K. Gottfried, V.F. Weisskopf, *Concepts of Particle Physics*, vol. 2 (Clarendon Press, Oxford/New York, 1986)
11. P. Große-Wiesmann, Cern Cour. **31**, 15 (1991)
12. S.W. Herb et al., Phys. Rev. Lett. **39**, 252 (1977)
13. W.R. Innes et al., Phys. Rev. Lett. **39**, 1240 (1977)
14. O. Nachtmann, *Elementary Particle Physics: Concepts and Phenomena* (Springer, Berlin/Heidelberg/New York, 1990)
15. D.H. Perkins, *Introduction to High Energy Physics*, 4th edn. (Addison-Wesley, Wokingham, 2000)
16. M.L. Perl et al., Phys. Rev. Lett. **35**, 1489 (1975)
17. Particle Data Group, J. Beringer et al., *Review of particle properties*. Phys. Rev. D **86**, 010001 (2012)
18. D. Wicke, Eur. Phys. J. **C71**, 1627 (2011)

# Chapter 10

## Phenomenology of the Weak Interaction

The discovery and the first theories of the weak interaction were based on the phenomenology of  $\beta$ -decay. Bound states formed by the weak interaction are not known, in contrast to those of the electromagnetic, strong and gravitational interactions. The weak interaction is in this sense somewhat foreign. We cannot, for example, base its description on any analogous phenomena in atomic physics. The weak interaction is, however, responsible for the decay of quarks and leptons.

In scattering experiments weak interaction effects are difficult to observe. Reactions of particles which are solely subject to the weak interaction (neutrinos) have extremely tiny cross-sections. In scattering experiments involving charged leptons and hadrons the effects of the weak interaction are clouded by those of the strong and electromagnetic interactions. Thus, most of our knowledge of the weak interaction has been obtained from particle decays.

The first theoretical description of  $\beta$ -decay, due to Fermi [12], was constructed analogously to that of the electromagnetic interaction. With some modifications, it is still applicable to low-energy processes. Further milestones in the investigation of the weak interaction were the discovery of parity violation [21], of different neutrino families [11] and of CP violation in the  $K^0$  system [8].

Quarks and leptons are equally affected by the weak interaction. In the previous chapter we discussed the quarks at length. We now want to treat the leptons in more detail before we turn to face the phenomena of the weak interaction.

### 10.1 Properties of Leptons

**Charged leptons** In our treatment of  $e^+e^-$  scattering we encountered the charged leptons: the electron ( $e$ ), the muon ( $\mu$ ) and the tau ( $\tau$ ) as well as their antiparticles (the  $e^+$ ,  $\mu^+$  and  $\tau^+$ ) which have the same masses as their partners but are oppositely charged.

The electron and the muon are the lightest electrically charged particles. Charge conservation thus ensures that the electron is stable and that an electron is produced when a muon decays. Muon decay proceeds via

$$\mu^- \rightarrow e^- + \bar{\nu}_e + \nu_\mu.$$

In a very few cases an additional photon or  $e^+e^-$  pair is produced. The energetically allowed process

$$\mu^- \not\rightarrow e^- + \gamma,$$

is, on the other hand, never observed. The muon is therefore not just an excited state of the electron.

The  $\tau$ -lepton is much heavier than the muon and, indeed, more so than many hadrons. Thus it does not have to decay solely into lighter leptons

$$\tau^- \rightarrow e^- + \bar{\nu}_e + \nu_\tau \quad \tau^- \rightarrow \mu^- + \bar{\nu}_\mu + \nu_\tau,$$

but can also turn into hadrons, e.g., into a pion and a neutrino

$$\tau^- \rightarrow \pi^- + \nu_\tau.$$

In fact more than half of all  $\tau$  decays follow the hadronic route [4].

**Neutrinos** We have already seen several processes in which neutrinos are produced: nuclear  $\beta$ -decay and the decays of charged leptons. Neutrinos are electrically neutral leptons and, as such, do not feel the electromagnetic or strong forces. Since neutrinos interact only weakly, they can as a rule only be detected indirectly in processes where charged particles are produced. Typically the energy, momentum and spin carried away or brought in by the neutrino is determined by measuring the other particles involved in the reaction and applying conservation laws. For example, the sums of the energies and angular momenta of the observed particles in  $\beta$ -decays indicate that another particle as well as the electron must also have been emitted. Experiment has made it completely clear that neutrinos and antineutrinos are distinct particles. The antineutrinos produced in a  $\beta$ -decay

$$n \rightarrow p + e^- + \bar{\nu}_e$$

for example, only induce further reactions in which positrons are produced and do not lead to electrons being created:

$$\begin{aligned} \bar{\nu}_e + p &\rightarrow n + e^+ \\ \bar{\nu}_e + n &\not\rightarrow p + e^- . \end{aligned}$$

Neutrinos and antineutrinos produced in charged pion decays

$$\begin{aligned}\pi^- &\rightarrow \mu^- + \bar{\nu}_\mu \\ \pi^+ &\rightarrow \mu^+ + \nu_\mu\end{aligned}$$

also behave differently. They are distinct particles: neutrinos from  $\pi^+$  decays only generate negatively charged muons, while antineutrinos from  $\pi^-$  decays only produce positive muons. Furthermore, they induce reactions in which  $\mu^-$  or  $\mu^+$  are created but never produce electrons or positrons [11]. This implies that the electron neutrino  $\nu_e$  and the muon neutrino  $\nu_\mu$  are different sorts of neutrinos: an electron neutrino, which is associated with the creation and annihilation of electrons, and a muon neutrino, which we similarly associate with the muon. Accordingly we can assign a tau neutrino  $\nu_\tau$  to the tau lepton.

Thus, we may conclude that there are three sorts of neutrinos: the electron neutrino  $\nu_e$  associated with the creation or annihilation of electrons, the muon neutrino  $\nu_\mu$  allocated to the muon, and the tau neutrino  $\nu_\tau$ , assigned to the tau lepton.

**The lepton families** We now know a total of six different leptons. Three of them ( $e^-$ ,  $\mu^-$ ,  $\tau^-$ ) are electrically charged, the other three, the neutrinos ( $\nu_e$ ,  $\nu_\mu$ ,  $\nu_\tau$ ), are neutral. To each of them there exists an antiparticle. We denote the various types of leptons as *leptonic flavour* in analogy to the classification of the six types of quarks by their flavour u, d, c, s, t and b (cf. Sect. 7.4). All leptons have spin- $\frac{1}{2}$  and are therefore fermions. We have seen that the three charged leptons and their neutrinos are intimately connected and, therefore, denote them in three families, each of which is made up of two particles whose charges differ by one unit:

$$\begin{pmatrix} \nu_e \\ e^- \end{pmatrix} \quad \begin{pmatrix} \nu_\mu \\ \mu^- \end{pmatrix} \quad \begin{pmatrix} \nu_\tau \\ \tau^- \end{pmatrix}.$$

The neutrinos in the upper row are electrically neutral, the leptons in the lower row have charge  $-1e$ . The charged leptons have, like the quarks, very different masses: ( $m_\mu/m_e \approx 207$ ,  $m_\tau/m_\mu \approx 17$ ). To each of these families there exists the corresponding family of antiparticles.

There is one important difference between neutrinos and charged leptons in addition to their charge: the otherwise very successful standard model of particle physics (cf. Chap. 13) predicts neutrinos to be massless. From neutrino oscillations, that we will discuss in the subsequent chapter, we learn, however, that neutrinos must possess a mass. As a consequence, a neutrino from one family, e.g., an electron neutrino  $\nu_e$ , can transmute into a neutrino of another family, e.g., a tau neutrino  $\nu_\tau$ . The masses of the neutrinos are still unknown, we only know the differences of their masses squared. Details will be discussed in Sects. 11.2 and 11.3.

Despite intensive searches at ever higher energies, no further leptons have yet been found. The lower bound for the mass of any further charged lepton is currently approximately  $100 \text{ GeV}/c^2$  and of any further neutral lepton approximately  $40 \text{ GeV}/c^2$ . In Sect. 12.2 we will see that there cannot be more than three light

neutrinos ( $m_\nu \ll 10 \text{ GeV}/c^2$ ). We still do not have a generally accepted reason for why the fundamental fermions come in three families and we do not understand their masses.

**Lepton number conservation** In all the reactions we have mentioned above, the creation or annihilation of a lepton was always associated with the creation or annihilation of an antilepton of the same flavour family. To our present knowledge this is true for all reactions. As with the baryons, we therefore have a conservation law: in all reactions the number of leptons of a particular family minus the number of the corresponding antileptons is conserved. We write

$$L_\ell = N(\ell) - N(\bar{\ell}) + N(\nu_\ell) - N(\bar{\nu}_\ell) = \text{const.}, \quad \text{where } \ell = e, \mu, \tau. \quad (10.1)$$

The  $L_\ell$ 's are individually referred to as *lepton family numbers* and the sum  $L = L_e + L_\mu + L_\tau$  is called *lepton number*.

In consequence the following production reactions are allowed or forbidden:

	Allowed		Forbidden
$p + \mu^-$	$\rightarrow \nu_\mu + n$		$p + \mu^- \not\rightarrow \pi^0 + n$
$e^+ + e^-$	$\rightarrow \nu_\mu + \bar{\nu}_\mu$		$e^+ + e^- \not\rightarrow \nu_e + \nu_\mu$
$\pi^-$	$\rightarrow \mu^- + \bar{\nu}_\mu$		$\pi^- \not\rightarrow e^- + \nu_e$
$\mu^-$	$\rightarrow e^- + \bar{\nu}_e + \nu_\mu$		$\mu^- \not\rightarrow e^- + \bar{\nu}_\mu + \nu_e$
$\tau^-$	$\rightarrow \pi^- + \nu_\tau$		$\tau^- \not\rightarrow \pi^- + \nu_e$

Experimentally the upper limits for any violation of the lepton family number  $L_\ell$  or the lepton number  $L$  in electromagnetic and weak decays are very small. Examples are [19]

$$\frac{\Gamma(\mu^\pm \rightarrow e^\pm \gamma)}{\Gamma(\mu^\pm \rightarrow \text{all channels})} < 2.4 \cdot 10^{-12} \quad (L_\ell)$$

$$\frac{\Gamma(\tau^- \rightarrow e^+ \pi^- \pi^-)}{\Gamma(\tau^- \rightarrow \text{all channels})} < 8.8 \cdot 10^{-8} \quad (L). \quad (10.2)$$

Note though that this conservation rule only really refers to production processes. Neutrino oscillations lead to a change of lepton family numbers and so only lepton number as a whole is truly conserved. Many theorists believe that neutrinos are so-called Majorana-particles. This would lead to a small violation of the lepton number, cf. Sect. 11.4. The only realistic hope for the observation of this effect is the neutrinoless double  $\beta$ -decay, which we will treat in some detail in Sect. 18.7.

All the allowed reactions that we have listed above proceed exclusively through the weak interaction, since in all these cases neutrinos are involved and these particles are only subject to the weak interaction. The opposite conclusion is,

however, incorrect. We will see in the following section that there are indeed weak processes which involve neither neutrinos nor any other leptons.

## 10.2 The Types of Weak Interactions

Recall that the weak interaction can transform a charged lepton into its family's neutrino and that it can produce a charged lepton (antilepton) and its antineutrino (neutrino). In just the same manner quarks of one flavour can be transformed into quarks with another flavour in weak interactions: a typical example of this is the transformation of a d-quark into a u-quark – this takes place in the  $\beta$ -decay of a neutron. In all such reactions the identity of the quarks and leptons involved changes and, simultaneously, the charge changes by  $+1e$  or  $-1e$ . The term *charged current* was coined to describe such reactions. They are mediated by charged particles, the  $W^+$  and  $W^-$ .

For a long time only this type of weak interaction was known. Nowadays we know that weak interactions may also proceed via the exchange of an additional, electrically neutral particle, the  $Z^0$ . In these reactions the quarks and leptons are not changed. One refers to them as *neutral currents*.

The  $W^\pm$  and the  $Z^0$  are vector bosons, i.e., they have spin-1. Their masses are large:  $80 \text{ GeV}/c^2$  ( $W^\pm$ ) and  $91 \text{ GeV}/c^2$  ( $Z^0$ ). We will return to their experimental detection in Sect. 12.1. In this chapter we will, following the historical development, initially concern ourselves with the *charged currents*. These may be straightforwardly divided up into three categories (Fig. 10.1): *leptonic processes*, *semileptonic processes* and *non-leptonic processes*.

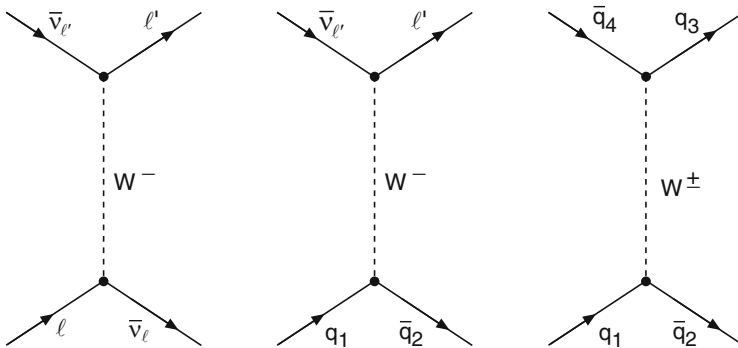
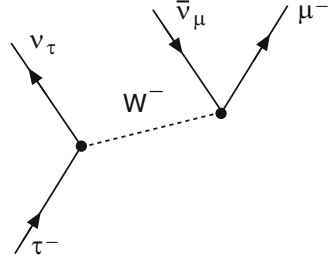


**Fig. 10.1** The three sorts of charged current reactions: a leptonic process (*left*), a semileptonic process (*middle*) and a non-leptonic process (*right*)



**Fig. 10.2** Leptonic decay of the  $\tau$ -lepton



**Leptonic processes** If the  $W$  boson only couples to leptons, one speaks of a leptonic process. The underlying reaction is

$$\ell + \bar{\nu}_\ell \longleftrightarrow \ell' + \bar{\nu}_{\ell'}$$

Examples of this reaction are the leptonic decay of the  $\tau$ -lepton (Fig. 10.2):

$$\tau^- \rightarrow \mu^- + \bar{\nu}_\mu + \nu_\tau$$

$$\tau^- \rightarrow e^- + \bar{\nu}_e + \nu_\tau$$

and the scattering process

$$\nu_\mu + e^- \rightarrow \mu^- + \nu_e$$

**Semileptonic processes** *Semileptonic processes* are those where the exchanged  $W$  boson couples to both leptons and quarks. The fundamental process here is

$$q_1 + \bar{q}_2 \longleftrightarrow \ell + \bar{\nu}_\ell$$

A prominent example is the  $\beta$ -decay of a neutron (Fig. 10.3) which may be reduced to the decay of a  $d$ -quark in which the two other quarks are not involved. The latter are called *spectator quarks*. Inverse reactions are processes such as the inverse  $\beta$ -decay  $\bar{\nu}_e + p \rightarrow n + e^+$  or  $\nu_e + n \rightarrow p + e^-$  and electron capture  $p + e^- \rightarrow n + \nu_e$ . (Anti-)Neutrinos were directly detected for the first time in the first of these reactions [10] – antineutrinos from the  $\beta^-$ -decay of neutron-rich fission products were seen to react with hydrogen. The second reaction may be used to detect solar and stellar neutrinos emanating from  $\beta^+$ -decays of proton-rich nuclei produced in fusion reactions.

Further examples of semileptonic processes are charged pion or kaon decay:

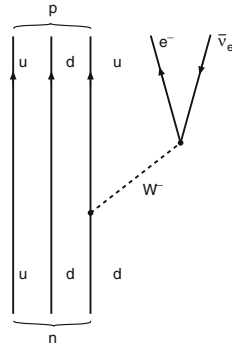


**Fig. 10.3** Semileptonic decay of the neutron

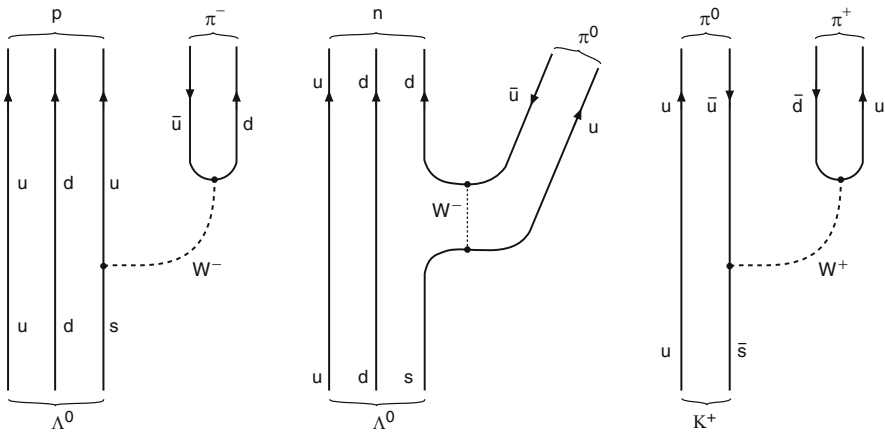


**Fig. 10.4** Non-leptonic decays of the  $\Lambda^0$  hyperon (*left, middle*) and of the  $K^+$  meson (*right*)

Hadron description	Quark description
$\pi^- \rightarrow \mu^- + \bar{\nu}_\mu$	$d + \bar{u} \rightarrow \mu^- + \bar{\nu}_\mu$
$K^- \rightarrow \mu^- + \bar{\nu}_\mu$	$s + \bar{u} \rightarrow \mu^- + \bar{\nu}_\mu$ ,

or deep-inelastic neutrino-nucleon scattering, which we will treat in more detail in Sect. 10.6.

**Non-leptonic processes** Finally non-leptonic processes do not involve leptons at all. The basic reaction is

$$q_1 + \bar{q}_2 \longleftrightarrow q_3 + \bar{q}_4.$$

Charge conservation requires that the only allowed quark combinations have a total charge  $\pm 1e$ . Examples are the hadronic decays of baryons and mesons with strangeness, such as the decay of the  $\Lambda^0$  hyperon into a nucleon and a pion, or that of  $K^+$  ( $u\bar{s}$ ) into two pions (Fig. 10.4).

### 10.3 Coupling Strength of the Weak Interaction

We now want to deal with charged currents in a more quantitative manner. We will treat leptonic processes in what follows since leptons, in contrast to quarks, exist as free particles which simplifies matters.

As with Mott scattering or  $e^+e^-$  annihilation, the transition matrix element for such processes is proportional to the square of the *weak charge*  $g$  to which the W Boson couples and to the propagator (4.23) of a massive spin-1 particle:

$$\mathcal{M}_{fi} \propto g \cdot \frac{1}{Q^2 c^2 + M_W^2 c^4} \cdot g \xrightarrow{Q^2 \rightarrow 0} \frac{g^2}{M_W^2 c^4}. \quad (10.3)$$

The difference to an electromagnetic interaction is seen in the finite mass of the exchange particle. Instead of the photon propagator  $(Qc)^{-2}$ , we see a propagator which is almost a constant for small enough momenta  $Q^2 \ll M_W^2 c^2$ . We will see in Sect. 12.2 that the weak charge  $g$  and the electric charge  $e$  are of a similar size. In fact,  $g$  is slightly larger than  $e$ . The very large mass of the exchange boson means that at small  $Q^2$  the weak interaction appears to be much weaker than the electromagnetic interaction. It also means that its range  $\hbar/M_W c \approx 2.5 \cdot 10^{-3}$  fm is very limited.

In the approximation of small four-momentum transfers one may then describe this interaction as a point-like interaction of the four particles involved (Fig. 10.5). This was in fact the original description of the weak interaction before the idea of the W and Z bosons was brought in. The coupling strength of this interaction is described by the *Fermi constant*  $G_F$ , which is proportional to the square of the weak charge  $g$ , very much as the electromagnetic coupling constant  $\alpha = e^2/(4\pi\epsilon_0\hbar c)$  is

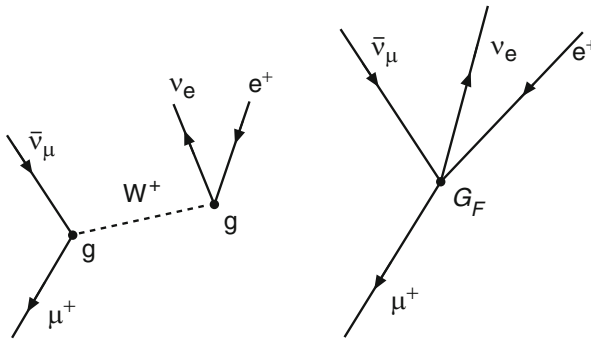


**Fig. 10.5** Sketch of the leptonic muon decay with the exchange of a  $W^+$  boson (*left*) and as point-like interaction (*right*)

proportional to the square of the electric charge  $e$ . It is so defined that  $G_F/(\hbar c)^3$  has dimensions of  $[1/\text{energy}^2]$  and is related to  $g$  by

$$\frac{G_F}{\sqrt{2}} = \frac{\pi\alpha}{2} \cdot \frac{g^2}{e^2} \cdot \frac{(\hbar c)^3}{M_W^2 c^4}. \quad (10.4)$$

**The decay of the muon** The most exact value for the Fermi constant is obtained from muon decay. The muon decays, as explained in Sect. 10.1, by

$$\mu^- \rightarrow e^- + \bar{\nu}_e + \nu_\mu, \quad \mu^+ \rightarrow e^+ + \nu_e + \bar{\nu}_\mu.$$

Since the muon mass is tiny compared to that of the W boson, it is reasonable to treat this interaction as point-like and to describe the coupling via the Fermi constant.

In this approximation the lifetime of the muon may be calculated with the help of the golden rule, if we use the Dirac equation and take into account the amount of phase space available to the three outgoing leptons. One finds that the decay width is:

$$\Gamma_\mu = \frac{\hbar}{\tau_\mu} = \frac{G_F^2}{192\pi^3(\hbar c)^6} \cdot (m_\mu c^2)^5 \cdot (1 + \varepsilon). \quad (10.5)$$

The correction term  $\varepsilon$ , which reflects higher order (radiative) corrections and phase-space effects resulting from the finite electron mass, is small (see Eq. 5 in [16]). It should be noted that the transition rate is proportional to the fifth power of the energy and hence the mass of the decaying muon. In Sect. 16.6 we will show in detail how the phase space may be calculated and how the  $E^5$ -dependence can be derived (in the example of the  $\beta$ -decay of the neutron).

The muon mass and lifetime have been measured to a high precision:

$$\begin{aligned} m_\mu &= (105.6583715 \pm 0.0000035) \text{ MeV}/c^2, \\ \tau_\mu &= (2.1969811 \pm 0.0000022) \cdot 10^{-6} \text{ s}. \end{aligned} \quad (10.6)$$

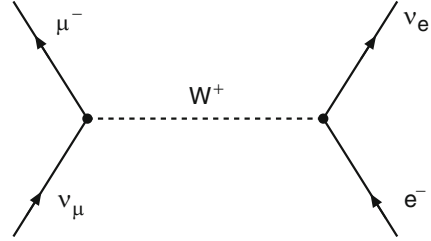
This yields a value for the Fermi constant

$$\frac{G_F}{(\hbar c)^3} = (1.1663787 \pm 0.0000006) \cdot 10^{-5} \text{ GeV}^{-2} \approx \frac{1.03 \cdot 10^{-5}}{(M_p c^2)^2}. \quad (10.7)$$

**Neutrino-electron scattering** Neutrino-electron scattering is a reaction between free, elementary particles. It proceeds exclusively through the weak interaction. We can discuss the effects of the effective coupling strength  $G_F$  on the cross-section of this reaction and show why the weak interaction is called “weak”.

In Fig. 10.6 the scattering of muon neutrinos off electrons in which the  $\nu_\mu$  is changed into a  $\mu^-$  is shown.

**Fig. 10.6** Sketch of the charged-current reaction  $\nu_\mu e^- \rightarrow \mu^- \nu_e$



We have chosen this process as our example since it can only take place via W-exchange.

For small four-momenta the total cross-section for neutrino-electron scattering is proportional to the square of the effective coupling constant  $G_F$ . Similarly to our discussion of the total cross-section in  $e^+e^-$  annihilation in Sect. 9.1, the characteristic length and energy scales of the reaction (the constants  $\hbar c$  and the centre-of-mass energy  $\sqrt{s}$ ) must enter the cross-section in such a way as to yield the correct dimensions (area):

$$\sigma = \frac{G_F^2}{\pi(\hbar c)^4} \cdot s, \quad (10.8)$$

where  $s$  may be found in the laboratory frame from (9.3) to be  $s = 2m_e c^2 E_\nu$ . From (10.7) one finds that the cross-section in the laboratory frame is

$$\sigma_{\text{lab}} = 1.7 \cdot 10^{-41} \text{ cm}^2 \cdot E_\nu / \text{GeV}. \quad (10.9)$$

This is an extremely tiny cross-section. To illustrate this point we now estimate the distance  $L$  which a neutrino must traverse in iron until it may weakly interact with an electron. The electron density in iron is

$$n_e = \frac{Z}{A} \rho N_A \approx 22 \cdot 10^{23} \text{ cm}^{-3}. \quad (10.10)$$

For neutrinos with an energy of 1 MeV the mean free path is therefore  $L = (n_e \cdot \sigma)^{-1} = 2.6 \cdot 10^{17} \text{ m}$ , which is about 30 light years!<sup>1</sup>

At very high energies the simple formula (10.9) is no longer valid, since the cross-section would limitlessly grow with the neutrino energy. This of course will not happen in practice: at large four-momentum transfers  $Q^2 \gg M_W^2 c^2$  the propagator term primarily determines the energy dependence of the cross-section. The approximation of a point-like interaction no longer holds. At a fixed centre-of-mass

<sup>1</sup>The absorption of neutrinos by the atomic nuclei is neglected here. This is a reasonable approximation for neutrino energies less than 1 MeV, but would need to be modified for higher energies.

energy  $\sqrt{s}$  the cross-section falls off, as in electromagnetic scattering, as  $1/Q^4$ . The total cross-section is on the other hand [9]:

$$\sigma = \frac{G_F^2}{\pi(\hbar c)^4} \cdot \frac{M_W^2 c^4}{s + M_W^2 c^4} \cdot s. \quad (10.11)$$

It does not increase linearly with  $s$ , as the point-like approximation implies, rather it asymptotically approaches a constant value.

**Neutral currents** Up to now we have only considered neutrino-electron scattering via  $W^+$  exchange, i.e., through charged currents. Neutrinos and electrons can, however, interact via  $Z^0$  exchange, i.e., neutral-current interactions are possible. The  $Z^0$  changes neither the mass nor the charge of the involved particles.

Elastic muon-neutrino scattering off electrons,  $\nu_\mu e^- \rightarrow \nu_\mu e^-$  (Fig. 10.7), is particularly suitable for investigating the weak interaction via  $Z^0$  exchange. This is because conservation of lepton family number precludes  $W$  exchange. Reactions of this kind were first seen in 1973 at CERN [14]. This was the first experimental signal for weak neutral currents.

We can estimate the total cross-section for the reaction  $\nu_\mu e^- \rightarrow \nu_\mu e^-$  for small four-momenta by repeating the calculation we did for the scattering via charged currents but modifying the coupling  $G_F$ . The only difference between the two interactions is in the mass of the two exchange bosons. The mass of the exchange boson squared appears in the propagator, so that the  $G_F$  should be multiplied by  $M_W^2/M_{Z^0}^2 \approx 0.78$ . The total cross-section at low energies reads then

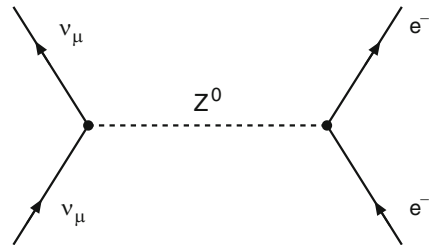
$$\sigma = \frac{M_W^4}{M_{Z^0}^4} \cdot \frac{G_F^2}{\pi(\hbar c)^4} \cdot s, \quad (10.12)$$

or

$$\sigma(\nu_\mu e^- \rightarrow \nu_\mu e^-) \approx 0.6 \cdot \sigma(\nu_\mu e \rightarrow \mu^- \nu_e). \quad (10.13)$$

Calculating  $\nu_e e^-$  scattering is more complicated since both  $Z$  and  $W$  exchange lead to the same final state and thus interfere with each other.

**Fig. 10.7** Sketch of the neutral-current reaction  $\nu_\mu e^- \rightarrow \nu_\mu e^-$



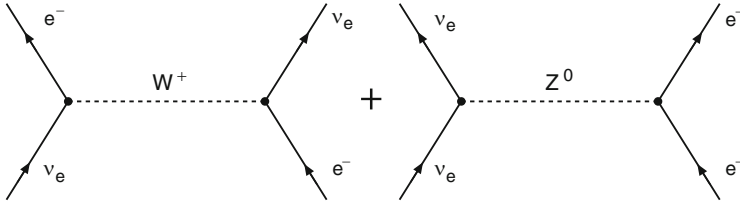


**Fig. 10.8** Superposition of the charged-current reaction (*left*) and the neutral-current reaction (*right*) in the process  $\nu_e e^- \rightarrow \nu_e e^-$

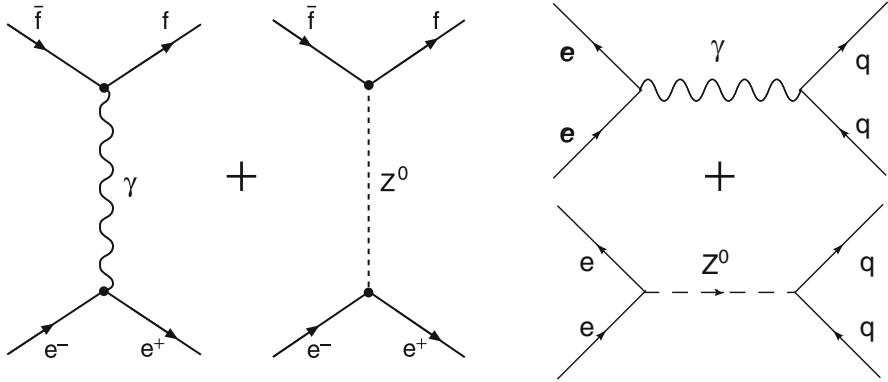


**Fig. 10.9** Superposition of the electromagnetic and weak interaction in  $e^+ e^-$  annihilation (*left*) and for electron-quark scattering (*right*)

Normally weak interactions via neutral currents will be hardly observed, since they will be superposed by the much stronger electromagnetic interaction and in case of the quarks by the strong interaction. In electron-positron annihilation (Fig. 10.9(left)) or for electron-quark scattering (Fig. 10.9(right)) a superposition of the weak and the electromagnetic interactions occurs.

Only when the centre-of-mass energy is comparable to the mass of the  $Z^0$  the two interactions become comparably large (cf. Sect. 12.2). The interference between the weak and the electromagnetic neutral currents has been observed very clearly in experiments at the electron-positron collider LEP and in deep-inelastic scattering at very high  $Q^2$  at HERA (cf. Sect. 12.2).

**Universality of the weak interaction** If we assume that the weak charge  $g$  is the same for all quarks and leptons, then (10.5) must hold for all possible charged decays of the fundamental fermions into lighter leptons or quarks. All the decay channels then contribute equally to the total decay width, up to a phase-space correction coming from the different masses.

We choose to consider the example of the decay of the  $\tau$ -lepton. This particle has essentially three routes open to it

$$\begin{aligned}\tau^- &\rightarrow \nu_\tau + \bar{\nu}_e + e^- \\ \tau^- &\rightarrow \nu_\tau + \bar{\nu}_\mu + \mu^- \\ \tau^- &\rightarrow \nu_\tau + \bar{u} + d,\end{aligned}\tag{10.14}$$

whose widths are  $\Gamma_{\tau e} \approx \Gamma_{\tau\mu}$  and  $\Gamma_{\tau d\bar{u}} \approx 3\Gamma_{\tau\mu}$ .<sup>2</sup> The factor of three follows from the  $\bar{u}d$ -pair having the possibility of appearing in three different colour combinations ( $\bar{r}r$ ,  $\bar{b}b$ ,  $\bar{g}g$ ).

From the mass term in (10.5) we have:

$$\Gamma_{\tau e} = (m_\tau/m_\mu)^5 \cdot \Gamma_{\mu e},\tag{10.15}$$

and the lifetime is thus predicted to be:

$$\tau_\tau = \frac{\hbar}{\Gamma_{\tau e} + \Gamma_{\tau\mu} + \Gamma_{\tau d\bar{u}}} \approx \frac{\tau_\mu}{5 \cdot (m_\tau/m_\mu)^5} \approx 3.1 \cdot 10^{-13} \text{ s}.\tag{10.16}$$

Experimentally we find [19]

$$\tau_\tau^{\text{exp}} = (2.906 \pm 0.010) \cdot 10^{-13} \text{ s}.\tag{10.17}$$

This good agreement confirms that quarks occur in three different colours and is strongly supportive of the quark and lepton weak charges being identical.

## 10.4 The Quark Families

We have claimed that the weak charge is universal, and that all the weak reactions which proceed through W exchange can therefore be calculated using the one coupling constant  $g$  or  $G_F$ . The lifetime of the  $\tau$ -lepton seemed to illustrate this point: our expectations, based on the assumption that the W boson couples with the same strength to both quarks and leptons were fulfilled. However, the lifetime does not contain the decay widths for leptonic and hadronic processes separately, but only their sum. Furthermore it is very sensitive to the mass of the  $\tau$ -lepton. Hence, this is not a particularly precise test of weak charge universality.

The coupling to quarks can be better determined from semileptonic hadron decays. This yields a smaller value for the coupling than that obtained from the leptonic muon decay. If a d-quark is transformed into a u-quark, as in the  $\beta$ -decay

---

<sup>2</sup>The appearance of further hadronic decay channels will be treated in the next section.



of the neutron, the coupling constant appears to be about 4 % smaller. In processes in which an s-quark is transformed into a u-quark, as in  $\Lambda^0$  decay, it even appears to be 20 times smaller.

**The Cabibbo angle** An explanation of these findings was proposed by Cabibbo as early as 1963 [7], at a time at which quarks had not been introduced. We will re-express Cabibbo’s hypothesis in modern terms. We may group the quarks into families, according to their charges and masses, as we did for the leptons:

$$\begin{pmatrix} u \\ d \end{pmatrix} \quad \begin{pmatrix} c \\ s \end{pmatrix} \quad \begin{pmatrix} t \\ b \end{pmatrix}.$$

Quark transitions in the weak decays indeed are observed predominantly within a family but also, to a lesser degree, from one family to another. For charged currents, the “partner” of the flavour eigenstate  $|u\rangle$  is therefore not the flavour eigenstate  $|d\rangle$ , but a linear combination of  $|d\rangle$  and  $|s\rangle$ . We call this linear combination  $|d'\rangle$ . Similarly the partner of the c-quark is a linear combination of  $|s\rangle$  and  $|d\rangle$ , orthogonal to  $|d'\rangle$ , which we call  $|s'\rangle$ .

The coefficients of these linear combinations can be written as the cosine and sine of an angle called the *Cabibbo angle*  $\theta_C$ . The quark eigenstates  $|d'\rangle$  and  $|s'\rangle$  of W exchange are related to the eigenstates  $|d\rangle$  and  $|s\rangle$  of the strong interaction, by a rotation through  $\theta_C$ :

$$\begin{aligned} |d'\rangle &= \cos \theta_C |d\rangle + \sin \theta_C |s\rangle \\ |s'\rangle &= \cos \theta_C |s\rangle - \sin \theta_C |d\rangle, \end{aligned} \quad (10.18)$$

which may be written as a matrix:

$$\begin{pmatrix} |d'\rangle \\ |s'\rangle \end{pmatrix} = \begin{pmatrix} \cos \theta_C & \sin \theta_C \\ -\sin \theta_C & \cos \theta_C \end{pmatrix} \cdot \begin{pmatrix} |d\rangle \\ |s\rangle \end{pmatrix}. \quad (10.19)$$

Whether the state vectors  $|d\rangle$  and  $|s\rangle$  or the state vectors  $|u\rangle$  and  $|c\rangle$  are rotated, or indeed both pairs simultaneously, is a matter of convention alone. Only the difference in the rotation angles is of physical importance. Usually the vectors of the charge  $-e/3$  quarks are rotated while those of the charge  $+2e/3$  quarks are left untouched. In view of neutrino oscillations that we will discuss in the next chapter we emphasise here that only the eigenstates  $|d\rangle$  and  $|s\rangle$  of the strong interaction have a well defined mass, but not the states  $|d'\rangle$  and  $|s'\rangle$ .

Experimentally,  $\theta_C$  is determined by comparing the lifetimes and branching ratios of the semileptonic and hadronic decays of various particles as shown in Fig. 10.10. This yields:

$$\sin \theta_C \approx 0.22, \quad \text{and} \quad \cos \theta_C \approx 0.98. \quad (10.20)$$

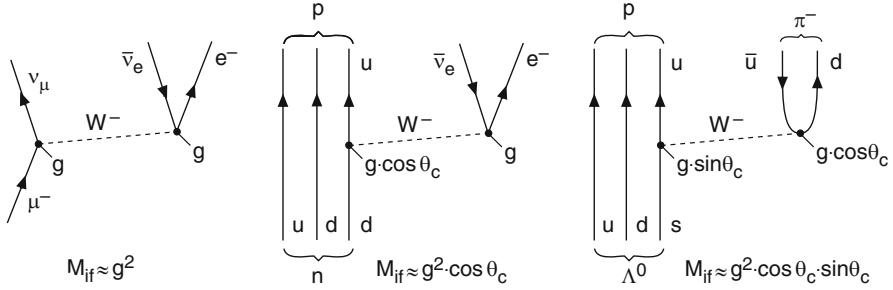


**Fig. 10.10** Leptonic decay of the muon (*left*) and the Cabibbo-suppressed semileptonic decays of the neutron (*middle*) and the  $\Lambda^0$  hyperon (*right*)

The transitions  $c \leftrightarrow d$  and  $s \leftrightarrow u$ , as compared to  $c \leftrightarrow s$  and  $d \leftrightarrow u$ , are therefore suppressed by a factor of

$$\sin^2 \theta_C : \cos^2 \theta_C \approx 1 : 20. \tag{10.21}$$

We can now make our treatment of  $\tau$  decay more precise. In (10.14), we stated that  $\tau \rightarrow \nu_\tau + \bar{u} + d$  is “essentially” the only hadronic decay of the  $\tau$ . But  $\tau \rightarrow \nu_\tau + \bar{u} + s$  is also energetically possible. Whereas the former decay is only slightly suppressed by a factor of  $\cos^2 \theta_C$ , the latter is faced with a factor of  $\sin^2 \theta_C$ . However, since  $\cos^2 \theta_C$  and  $\sin^2 \theta_C$  add to one our conclusion concerning the lifetime of the  $\tau$ -lepton is not affected, as long as we ignore the difference in the quark masses.

**The Cabibbo-Kobayashi-Maskawa matrix** Adding the third generation of quarks, the  $2 \times 2$  matrix of (10.19) is replaced by a  $3 \times 3$  matrix [15]. This is called the *Cabibbo-Kobayashi-Maskawa matrix* (CKM matrix):

$$\begin{pmatrix} |d'\rangle \\ |s'\rangle \\ |b'\rangle \end{pmatrix} = \begin{pmatrix} V_{ud} & V_{us} & V_{ub} \\ V_{cd} & V_{cs} & V_{cb} \\ V_{td} & V_{ts} & V_{tb} \end{pmatrix} \cdot \begin{pmatrix} |d\rangle \\ |s\rangle \\ |b\rangle \end{pmatrix}. \tag{10.22}$$

The probability for a transition from a quark  $q_i$  to a quark  $q_j$  is proportional to  $|V_{q_i q_j}|^2$ , the square of the magnitude of the matrix element.

The matrix elements are correlated since the matrix is unitary. The total number of independent parameters is four: three real angles and an imaginary phase. The phase affects weak processes of higher order via the interference terms. *CP violation* (cf. Sect. 15.5) is attributed to the existence of this imaginary phase [17].

The matrix elements have been determined from a large number of decays and meanwhile are known very well [19]. Their magnitudes are approximately:

$$\left( |V_{ij}| \right) = \begin{pmatrix} 0.974 & 0.225 & 0.003 \\ 0.225 & 0.973 & 0.041 \\ 0.008 & 0.040 & 0.999 \end{pmatrix}. \tag{10.23}$$

The diagonal elements of this matrix describe transitions within a family; they deviate from unity by only a few percent. The values of the matrix elements  $V_{cb}$  and  $V_{ts}$  are nearly one order of magnitude smaller than those of  $V_{us}$  and  $V_{cd}$ . Accordingly, transitions from the third to the second generation ( $t \rightarrow s$ ,  $b \rightarrow c$ ) are suppressed by nearly two orders of magnitude compared to transitions from the second to the first generation. This applies to an even higher degree for transitions from the third to the first generation. The direct transition  $b \rightarrow u$  was detected in the semileptonic decay of B mesons into non-charmed mesons [2, 3, 13]. Many decays of this kind have been observed during the last decade by the experiments Babar, Belle and CLEO [19].

Weak quark decays only proceed through W exchange. Neutral currents which change the quark flavour (e.g.,  $c \rightarrow u$ ) are only possible in higher-order processes and are therefore strongly suppressed in the standard model. The decay  $K^+ \rightarrow \pi^+ \nu \bar{\nu}$ , for example, has been observed, corresponding to a transition  $\bar{s} \rightarrow \bar{d}$ . The branching ratio of this decay is  $1.5 \cdot 10^{-10}$  [19].

## 10.5 Parity Violation

A property unique to the weak interaction is parity violation. This means that weak interaction reactions are not invariant under space inversion.

An example of a quantity which changes sign under a spatial inversion is *helicity*

$$h = \frac{\mathbf{s} \cdot \mathbf{p}}{|\mathbf{s}| \cdot |\mathbf{p}|}, \quad (10.24)$$

which we introduced in Sect. 5.3. The numerator is a scalar product of an axial vector (spin) and a vector (momentum). Whereas spin preserves its orientation under mirror reflection, the direction of the momentum is reversed. Thus helicity is a pseudoscalar, changing sign when the parity operator is applied to it. An interaction which depends upon helicity is therefore not invariant under spatial reflections. Helicity is only Lorentz-invariant for massless particles. For particles with a non-vanishing rest mass it is always possible to find a reference frame in which the particle is “overtaken”, i.e., in which its direction of motion and thus its helicity are reversed.

Strictly speaking, helicity has to be distinguished from *chirality*, i.e., handedness. A fermion can be left-handed or right-handed. Helicity and chirality are not to be distinguishable from each other when the fermion mass  $mc^2$  is negligible compared to its energy  $E$ . For relativistic fermions, a state with negative helicity is dominantly left-handed, but it also has a small right-handed component. This is suppressed by  $mc^2/E$  or  $\sqrt{1 - \beta^2}$ , where  $\beta = v/c$ . Right-handed and left-handed states, therefore, have a small admixture of the opposite helicity which is the larger the smaller  $\beta$ .

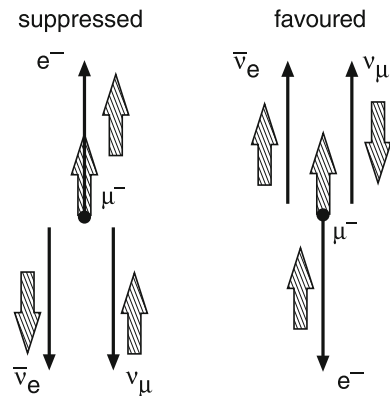
In weak-interaction experiments the participating particles are mostly relativistic and the difference between helicity and chirality is normally irrelevant.

In general, the operator of an interaction described by the exchange of a spin-1 particle can have a vector or an axial vector nature. In order for an interaction to conserve parity, and therefore to couple identically to both right- and left-handed particles, it must be either purely vectorial or purely axial-vectorial. In electromagnetic interactions, for example, it is experimentally observed that only a vector part is present. But in parity-violating interactions, the matrix element has a vector part as well as an axial vector part. Their strengths are described by two coefficients,  $c_V$  and  $c_A$ . The closer the size of the two parts the stronger is the parity violation. *Maximum parity violation* occurs if both contributions are equal in magnitude. A  $(V+A)$  interaction, i.e., a sum of vector and axial interactions of equal strength ( $c_V = c_A$ ), couples exclusively to right-handed fermions and left-handed antifermions. A  $(V-A)$  interaction ( $c_V = -c_A$ ) only couples to left-handed fermions and right-handed antifermions.

As we will show, the angular distribution of electrons produced in the decay of polarised muons exhibits parity violation. This decay can be used to measure the ratio  $c_V/c_A$ . Such experiments yield  $c_V = -c_A = 1$  for the coupling strength of W bosons to leptons. One therefore speaks of a *V-minus-A theory* of charged currents. Parity violation is maximal. If a neutrino or an antineutrino is produced by W exchange, the neutrino helicity is negative, while the antineutrino helicity is positive. Indeed all experiments are consistent with *neutrinos being always left-handed and antineutrinos right-handed*. We will describe such an experiment in Sect. 18.6.

**Parity violation in muon decay** An instructive example of parity violation is the muon decay  $\mu^- \rightarrow e^- + \nu_\mu + \bar{\nu}_e$ . In the rest frame of the muon, the momentum of the electron is maximised if the momenta of the neutrinos are parallel to each other, and antiparallel to the momentum of the electron. From Fig. 10.11 it is apparent that the spin of the emitted electron must be in the same direction as that of the muon since the spins of the  $(\nu_e, \bar{\nu}_\mu)$  pair cancel.

**Fig. 10.11** Parity-violating decay of a polarised muon,  $\mu^- \rightarrow e^- + \nu_\mu + \bar{\nu}_e$ . Electrons are emitted preferentially with their spin opposite to their momentum (*right*)



Experimentally it is observed that electrons from polarised muon decays are preferentially emitted with their spin opposite to their momentum; i.e., they are left-handed. This left-right asymmetry is a manifestation of parity violation. The ratio of the vector to axial vector strengths can be determined from the angular distribution [6].

**Helicity suppressed pion decay** Our second example is the decay of the charged pion. The lightest hadron with electric charge, the  $\pi^-$ , can only decay in a semileptonic weak process, i.e., through a charged current, according to

$$\begin{aligned}\pi^- &\rightarrow \mu^- + \bar{\nu}_\mu, \\ \pi^- &\rightarrow e^- + \bar{\nu}_e.\end{aligned}$$

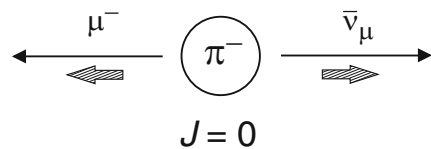
The muon mass is only slightly smaller than the pion mass, therefore in pion decay the muon is non-relativistic and we have to distinguish between helicity and chirality. The second process is suppressed, compared to the first one, by a factor of 1:8,000 [5] (cf. Table 15.3). From the amount of phase space available, however, one would expect the pion to decay about 3.5 times more often into an electron than into a muon. This behaviour may be explained from helicity considerations.

The particles created in such two-particle pion decays are emitted, in the centre-of-mass system, in opposite directions. Since the pion has spin zero, the spins of the two leptons must be opposite to each other. Thus, the projections on the direction of motion are either  $+1/2$  for both, or  $-1/2$  for both. The latter case is impossible as the helicity of antineutrinos is fixed. Therefore, the spin projection of the muon (electron) is  $+1/2$  (Fig. 10.12).

If electrons and muons were massless, two-body pion decays would be forbidden. A massless electron, or muon, would have to be 100% right-handed, but W bosons only couple to left-handed leptons. Because of their finite mass, electrons and muons with their spins pointing in their directions of motion actually also have a left-handed component. This leads to a factor  $(1 - \beta)$  in the decay width (Fig. 10.12). The W boson couples to this component. Since the electron mass is so small,  $1 - \beta_e = 2.6 \cdot 10^{-5}$  is very small in pion decay, compared to  $1 - \beta_\mu = 0.72$ . Hence, the left-handed component of the electron is far smaller than that of the muon, and the electron decay is accordingly strongly suppressed.

**CP conservation** It may be easily seen that if the helicity of the neutrinos is fixed, then *C-parity* (“charge conjugation”) is simultaneously violated. Application of the C-parity operator replaces all particles by their antiparticles. Thus, left-handed

**Fig. 10.12** Allowed spin projections of  $\mu^-$  and  $\bar{\nu}_\mu$  in  $\pi^-$  decay



neutrinos would be transformed into left-handed antineutrinos, which do not appear in the standard model. Therefore, physical processes which involve neutrinos, and in general all weak processes, a priori violate C-parity. The combined application of space inversion (P) and of charge conjugation (C), however, yields a process which is physically possible. Here, left-handed fermions are transformed into right-handed antifermions, which interact with equal strength. This is called the *CP conservation* property of the weak interaction. Cases in which CP symmetry is not conserved (CP violation) will be discussed in Sects. 15.4 and 15.5.

## 10.6 Deep-Inelastic Scattering with Charged Currents

**Deep-inelastic scattering of neutrinos** Deep-inelastic scattering of neutrinos and antineutrinos off nucleons gives us information about the quark distributions in the nucleon which cannot be obtained from electron or muon scattering alone. In contrast to photon exchange, the exchange of W bosons (charged currents) in neutrino scattering distinguishes between the helicity and charged states of the fermions involved. This is then exploited to separately determine the quark and antiquark distributions in the nucleon.

In deep-inelastic neutrino scattering experiments, muon (anti)neutrinos are generally used, which, as discussed in Sect. 10.5, stem from weak pion and kaon decays. These latter particles can be produced in large numbers by bombarding a solid block of material with a beam of high-energy protons. After a several hundred metre long decay line the decay muons are ranged out by a long shield of iron and soil. What remains is a beam of neutrinos impinging on a target. Since (anti)neutrinos have very small cross-sections the targets that are used (e.g., iron) are generally many metres long. The deep-inelastic scattering takes place off both the protons and the neutrons in the target.

When left-handed neutrinos scatter off nucleons, the exchanged  $W^+$  can only interact with the negatively charged, left-handed quarks ( $d_L, s_L$ ) and negatively charged, right-handed antiquarks ( $\bar{u}_R, \bar{c}_R$ ) which are thereby transformed into the corresponding (anti)quarks of the same family (Fig. 10.13 (left)). In analogy to

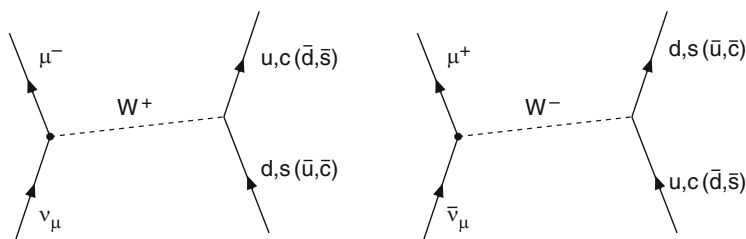


**Fig. 10.13** Charged-current interactions of neutrinos (*left*) and antineutrinos (*right*) with the possible selected quark and antiquark flavours

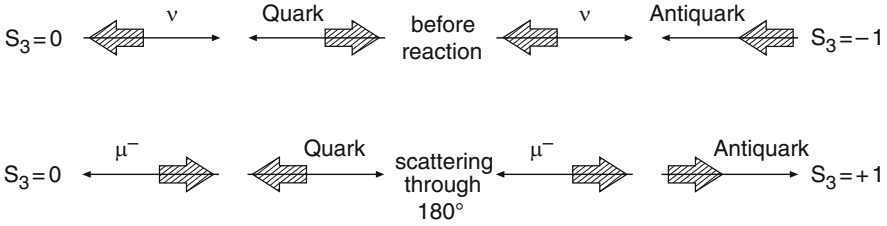


**Fig. 10.14** Charged-current  $\nu q$  scattering (left) and  $\nu \bar{q}$  scattering (right) before the reaction (top) and after scattering through  $180^\circ$  in the neutrino-quark centre-of-mass system

our description of  $\tau$  decay, we can neglect complications due to Cabibbo mixing if the energies are large enough that we can ignore the differences in the quark masses. Equivalently for the scattering of right-handed antineutrinos, the  $W^-$  which is exchanged can only interact with the positively charged, left-handed quarks ( $u_L, c_L$ ) and positively charged, right-handed antiquarks ( $\bar{d}_R, \bar{s}_R$ ) (Fig. 10.13 (right)).

**Separation of quark and antiquark distributions** The scattering off the quarks and antiquarks is characterised by different angle and energy distributions for the outgoing leptons. This becomes plausible if one (analogously to our considerations in the case of Mott scattering in Sect. 5.3) considers the extreme case of scattering through  $\theta_{c.m.} = 180^\circ$  in the centre-of-mass frame for the neutrino and the quark (Fig. 10.14). We choose the quantisation axis  $\hat{z}$  to be the momentum direction of the incoming neutrino. Since the  $W$  boson only couples to left-handed fermions, both the neutrino and the quark have in the high-energy limit negative helicities and the projection of the total spin on the  $\hat{z}$  axis is, both before and after scattering through  $180^\circ$   $S_3 = 0$ .

This also holds for all other scattering angles, i.e., the scattering is isotropic.

On the other hand if a left-handed neutrino interacts with a right-handed antiquark, the spin projection before the scattering is  $S_3 = -1$  but after being scattered through  $180^\circ$  it is  $S_3 = +1$ . Hence scattering through  $180^\circ$  is forbidden by conservation of angular momentum. An angular dependence, proportional to  $(1 + \cos \theta_{c.m.})^2$ , is found in the differential cross-section. In the laboratory frame this corresponds to an energy dependence proportional to  $(1 - y)^2$  where

$$y = \frac{E_{\nu, \bar{\nu}} - E'_\mu}{E_{\nu, \bar{\nu}}} \tag{10.25}$$

is that fraction of the neutrino energy which is transferred to the quark. Completely analogous considerations hold for antineutrino scattering.

The cross-section for neutrino-nucleon scattering may be written analogously to the cross-section for neutrino-electron scattering (10.9) if we take into account the fact that the interacting quark only carries a fraction  $x$  of the momentum of the

nucleon and that the centre-of-mass energy in the neutrino-quark centre-of-mass system is  $x$  times smaller than in the neutrino-nucleon system. For an isoscalar target the double differential cross-section per (proton-neutron average) nucleon then reads:

$$\frac{d^2\sigma^{\nu,\bar{\nu}-N}}{dx dy} = \sigma_0^{\nu,\bar{\nu}-N} \cdot K^{\nu,\bar{\nu}-N}(x, y), \quad (10.26)$$

where

$$\sigma_0^{\nu,\bar{\nu}-N} = \frac{G_F^2}{\pi(\hbar c)^4} \cdot \left( \frac{M_W^2 c^4}{Q^2 c^2 + M_W^2 c^4} \right)^2 \cdot M_p c^2 E^{\nu,\bar{\nu}} \quad (10.27)$$

and

$$K^{\nu-N}(x, y) = x[u(x) + d(x) + 2s_s(x) + (\bar{u}_s(x) + \bar{d}_s(x) + 2\bar{c}_s(x))(1-y)^2], \quad (10.28)$$

$$K^{\bar{\nu}-N}(x, y) = x[\bar{u}_s(x) + \bar{d}_s(x) + 2\bar{s}_s(x) + (u(x) + d(x) + 2c_s(x))(1-y)^2]. \quad (10.29)$$

The latter equations hold in the quark-parton model assuming isospin symmetry for the quark distributions and with  $u(x) = u_v(x) + u_s(x)$  and  $d(x) = d_v(x) + d_s(x)$ .

Figure 10.15 shows the dependence of the differential cross-section  $d\sigma/dy$  as a function of  $y$  upon integration over  $x$ . For neutrino scattering we have two contributions: a large constant contribution from scattering off the quarks, and a small contribution from scattering off the antiquarks which falls off as  $(1-y)^2$ . In antineutrino scattering one observes a strong  $(1-y)^2$  dependence from the

**Fig. 10.15** Differential cross-sections  $d\sigma/dy$  for neutrino and antineutrino scattering off nucleons as a function of  $y$  (in arbitrary units)

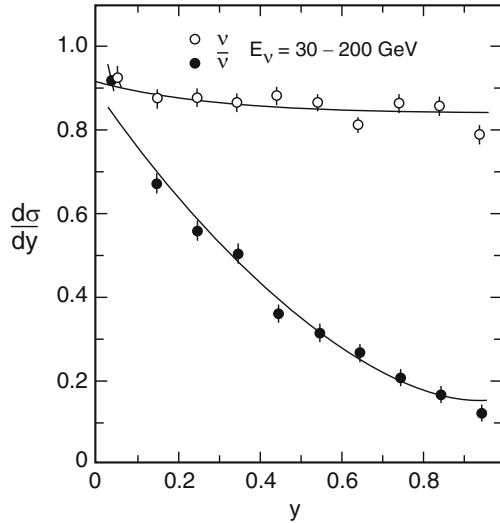
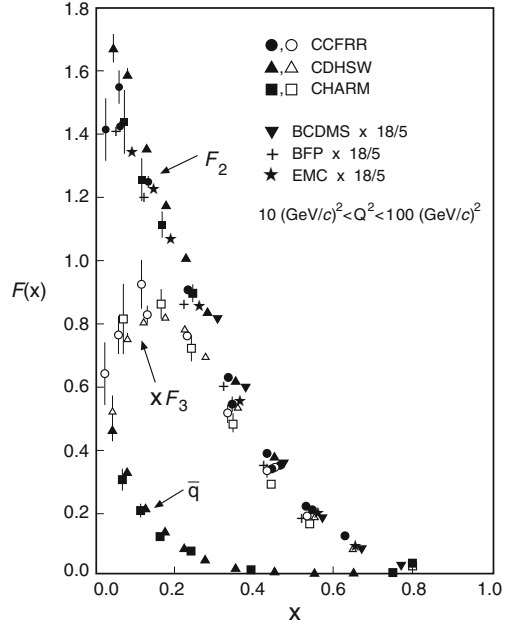




**Fig. 10.16** Comparison of the structure function  $F_2(x)$  per proton-neutron averaged nucleon, measured in deep-inelastic scattering of muons and neutrinos [18]. Also shown is the structure function  $x F_3(x)$  which describes the distribution of valence quarks, and the distribution of antiquarks  $\bar{q}(x)$  which yields the sea quark distribution



interaction with the quarks and a small energy independent part from the antiquarks. Suitable combinations of the data from neutrino and antineutrino scattering off protons and neutrons can be used to separate the distributions of valence and sea quarks shown in Fig. 10.16.

**Structure functions in deep-inelastic neutrino scattering** In Chap. 7 we have expressed the cross-section for deep-inelastic scattering of charged leptons off nucleons (7.10) in terms of the *two* structure functions  $F_1(x, Q^2)$  and  $F_2(x, Q^2)$ . Similarly also the cross-section for deep-inelastic neutrino-nucleon scattering can be written in terms of *three* structure functions  $F_i(x, Q^2)$  ( $i = 1, 2, 3$ ), three each for  $\nu p$ ,  $\bar{\nu} p$ ,  $\nu n$ , and  $\bar{\nu} n$  scattering:

$$\frac{d^2\sigma^{\nu,\bar{\nu}}}{dx dy} = \sigma_0^{\nu,\bar{\nu}} \cdot \left[ \left( 1 - y - xy \frac{Mc^2}{2E^{\nu,\bar{\nu}}} \right) F_2^{\nu,\bar{\nu}} + \frac{y^2}{2} 2xF_1^{\nu,\bar{\nu}} \pm y \left( 1 - \frac{y}{2} \right) xF_3^{\nu,\bar{\nu}} \right]. \quad (10.30)$$

Here the  $x$  and  $Q^2$  dependence of the structure functions has been omitted for brevity. The structure function  $x F_3^{\nu,\bar{\nu}}$  appears here for the first time. It is a consequence of the parity violating ( $V-A$ ) structure of the weak charged current. The term with  $x F_3^{\nu,\bar{\nu}}$  has positive sign for neutrino scattering and negative sign for antineutrino scattering. Equation (10.30) is also valid in the kinematic region of small values of  $Q^2$ , where the quark-parton model can no longer be used for the

interpretation of the data. Assuming  $2xF_1^{v,\bar{v}} = F_2^{v,\bar{v}}$ , we obtain in the region of sufficiently high values of  $Q^2$  from Eqs. (10.26) to (10.30) the following relations between the structure functions for the proton-neutron averaged nucleon and the quark distributions:

$$xF_3^N(x) = \frac{1}{2}[xF_3^{v-N}(x) + xF_3^{\bar{v}-N}(x)] = x[u_v(x) + d_v(x)], \quad (10.31)$$

$$F_2^{v-N}(x) = F_2^{\bar{v}-N}(x) = x \sum_{q=d,u,s,c} [q(x) + \bar{q}_s(x)], \quad (10.32)$$

$$\bar{q}^{\bar{v}-N}(x) = x [\bar{u}_s(x) + \bar{d}_s(x) + 2\bar{s}_s(x)], \quad (10.33)$$

with  $q(x) = q_v(x) + q_s(x)$  for u- and d-quarks and  $q(x) = q_s(x)$  for s- and c-quarks.

Thus, comparing (10.32) and (7.24) we see that apart from small corrections for the contributions of the heavier s- and c-quarks the structure functions  $F_2$  per proton-neutron averaged nucleon in electron and neutrino scattering are related by

$$F_2^{v-N}(x) \simeq \frac{18}{5} F_2^{e-N}(x). \quad (10.34)$$

In Fig. 10.16 data from deep-inelastic scattering experiments of the second generation with muon beams (BCDMS, BFP, EMC) and neutrino beams (CCFR, CDHSW, CHARM) are presented as a function of  $x$  in the  $Q^2$  range 10–100 (GeV/c)<sup>2</sup>.

The structure functions  $F_2(x)$  per proton-neutron averaged nucleon are essentially equal, apart from the factor 18/5. This is again a confirmation for the proper assignment of the fractional quark charges  $+2e/3$  for u- and c-quarks and  $-1e/3$  for d- and s-quarks. We also see from this figure that the sea-quark distribution  $\bar{q}(x)$  falls off steeply with  $x$  and is negligible for  $x > 0.35 - 0.4$ . At larger values of  $x$  only valence quarks contribute to  $F_2$ ; their distribution has a maximum near  $x \approx 0.17$ .

**Polarised deep-inelastic scattering at high  $Q^2$**  The two experiments H1 and ZEUS at HERA mainly investigated deep-inelastic events of the type  $e^\pm + p \rightarrow e'^\pm + X$ , where the interaction between lepton and nucleon is mediated by the exchange of a virtual photon or a  $Z^0$  boson. Occasionally also events of the type  $e^\pm + p \rightarrow X$  occurred where no scattered electron or positron was observed in the detector. These were attributed to the reactions  $e^- + p \rightarrow \nu_e + X$  or  $e^+ + p \rightarrow \bar{\nu}_e + X$ , respectively (Fig. 10.17).

In these reactions the interaction is mediated by the exchange of  $W^\pm$  bosons, i.e., by charged currents. Due to the hermetic  $4\pi$ -detectors, the kinematics of these events could be fully reconstructed from the tracks and energies of the quark fragments and the remnants of the struck proton (cf. Fig. 8.6).

The lepton beam in the HERA storage ring could be longitudinally polarised. This happened as follows: based on an asymmetry in the spin-flip probability

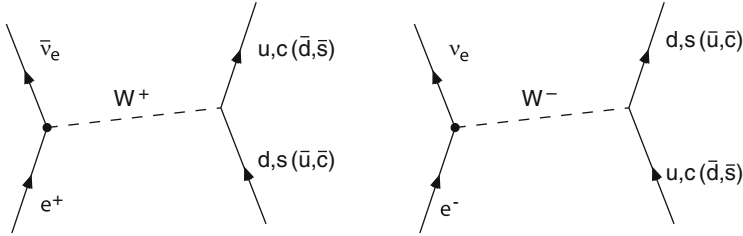


**Fig. 10.17** Charged-current reactions in deep-inelastic positron (*left*) and electron (*right*) scattering off nucleons

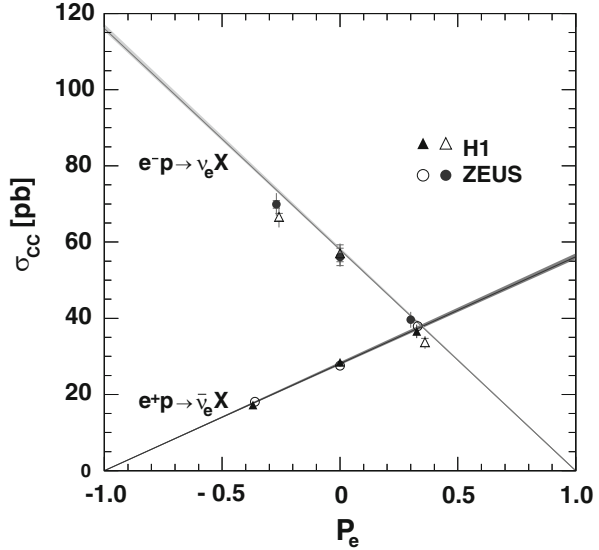
for the emission of synchrotron radiation, the spins of the circulating electrons gradually became oriented antiparallel to the direction of the magnetic fields in the arcs (Sokolov-Ternov-Effect [20], cf. Problem 10.6). A system of magnets, so-called spin rotators, on both sides of the experiments changed this transverse polarisation of the beam into a longitudinal one and back again to transverse behind the experiments. The degree of longitudinal polarisation  $P_e$  is given by  $P_e = (N^\rightarrow - N^\leftarrow) / (N^\rightarrow + N^\leftarrow)$ . Here  $N^\rightarrow$  ( $N^\leftarrow$ ) is the number of electrons with spin orientation parallel (antiparallel) to the beam momentum. Neutrinos are always left-handed. But here we can choose the handedness: electrons or positrons with positive polarisation are predominantly right-handed, those with negative polarisation are predominantly left-handed.

The cross-section for charged-current reactions depends linearly on the lepton-beam polarisation:

$$\sigma_{CC}^{e^\pm p}(P_e) = (1 \pm P_e) \sigma_{CC}^{e^\pm p}(P_e = 0), \quad (10.35)$$

where the minus sign holds for electrons. For  $P_e = +1$  the cross-section for the reaction  $e^- + p \rightarrow \nu_e + X$  should vanish, since by helicity conservation a right-handed electron cannot be transformed into a left-handed neutrino, while the cross-section is maximal for  $P_e = -1$ . For positrons the situation is just reversed. The experimental data of H1 and ZEUS excellently confirm these considerations. In Fig. 10.18 the charged-current cross-sections  $\sigma_{CC}$  for electrons and positrons are shown as a function of the degree of longitudinal polarisation  $P_e$  [1]. The data fulfil the requirements  $Q^2 > 400$  (GeV/c) $^2$  and  $y > 0.9$ . As expected, they lie on a straight line. The extrapolation to either  $P_e = +1$  or  $P_e = -1$  provides information about the possible existence of right-handed charged currents which are excluded in the standard model of particle physics (cf. Chap. 13). No deviations from this expectation are observed. In addition, the data show another interesting feature: the maximal cross-sections for electrons and positrons are of different magnitude. This observation can be easily traced back to the circumstance that the  $W^-$  boson

**Fig. 10.18** The cross-section  $\sigma_{CC}$  of deep-inelastic scattering of electrons and positrons with charged currents as a function of the beam polarisation  $P_e$



exchanged in electron scattering couples preferentially to the u-quark, while in positron scattering the exchanged  $W^+$  boson couples preferentially to the d-quark, and that the quark distribution  $u(x)$  is nearly a factor of two larger than the quark distribution  $d(x)$ .

## Problems

### 1. Particle reactions

Show whether the following particle reactions and decays are possible or not. State which interaction is concerned and sketch the quark composition of the hadrons involved.

$$\begin{aligned}
 p + \bar{p} &\rightarrow \pi^+ + \pi^- + \pi^0 + \pi^+ + \pi^- \\
 p + K^- &\rightarrow \Sigma^+ + \pi^- + \pi^+ + \pi^- + \pi^0 \\
 p + \pi^- &\rightarrow \Lambda^0 + \bar{\Sigma}^0 \\
 \bar{\nu}_\mu + p &\rightarrow \mu^+ + n \\
 \nu_e + p &\rightarrow e^+ + \Lambda^0 + K^0 \\
 \Sigma^0 &\rightarrow \Lambda^0 + \gamma
 \end{aligned}$$

### 2. Parity and C-parity

(a) Which of the following particle states are eigenstates of the charge conjugation operator  $\mathcal{C}$  and what are their respective eigenvalues?

$$|\gamma\rangle; |\pi^0\rangle; |\pi^+\rangle; |\pi^-\rangle; |\pi^+\rangle - |\pi^-\rangle; |\nu_e\rangle; |\Sigma^0\rangle.$$

- (b) How do the following quantities behave under the parity operation? (Supply a brief explanation.)

Position vector $\mathbf{r}$	Momentum $\mathbf{p}$
Angular momentum $\mathbf{L}$	Spin $\boldsymbol{\sigma}$
Electric field $\mathbf{E}$	Magnetic field $\mathbf{B}$
Electric dipole moment $\boldsymbol{\sigma} \cdot \mathbf{E}$	Magnetic dipole moment $\boldsymbol{\sigma} \cdot \mathbf{B}$
Helicity $\boldsymbol{\sigma} \cdot \mathbf{p}$	Transversal polarisation $\boldsymbol{\sigma} \cdot (\mathbf{p}_1 \times \mathbf{p}_2)$

3. **Parity and C-parity of the  $f_2$ -mesons** The  $f_2(1270)$ -meson has spin 2 and decays, amongst other routes, into  $\pi^+\pi^-$ .

- (a) Use this decay to find the parity and C-parity of the  $f_2$ .  
 (b) Investigate whether the decays  $f_2 \rightarrow \pi^0\pi^0$  and  $f_2 \rightarrow \gamma\gamma$  are allowed.

#### 4. Pion decay and the Golden Rule

Calculate the ratio of the partial decay widths

$$\frac{\Gamma(\pi^+ \rightarrow e^+\nu)}{\Gamma(\pi^+ \rightarrow \mu^+\nu)}$$

and so verify the relevant claims in the text. From the Golden Rule it holds that  $\Gamma(\pi \rightarrow \ell\nu) \propto |\mathcal{M}_{\pi\ell}|^2 \varrho(E_0)$ , where  $|\mathcal{M}_{\pi\ell}|$  is the transition matrix element and  $\varrho(E_0) = dn/dE_0$  is the density of states ( $\ell$  denotes the charged lepton). The calculation may be approached as follows:

- (a) Derive formulae for the momenta and energies of the charged leptons  $\ell^+$  as functions of  $m_\ell$  and  $m_\pi$  and so find numerical values for  $1 - v/c$ .  
 (b) We have  $|\mathcal{M}_{\pi\ell}|^2 \propto 1 - v/c$ . Use this to express the ratio of the squares of the matrix elements as a function of the particle masses involved and find its numerical value.  
 (c) Calculate the ratio of the densities of states  $\varrho_e(E_0)/\varrho_\mu(E_0)$  as a function of the masses of the particles involved. Exploit the fact that the density of states in momentum space is  $dn/d|\mathbf{p}| \propto |\mathbf{p}|^2$  ( $|\mathbf{p}| = |\mathbf{p}_{\ell^+}| = |\mathbf{p}_\nu|$ ) and that  $E_0 = E_{\ell^+} + E_\nu$ . For which of the two decays is the “phase space” bigger?  
 (d) Combine the results from (b) and (c) to obtain the ratio of the partial decay widths as a function of the masses of the particles involved. Find its numerical value and compare it with its experimental value of  $(1.230 \pm 0.004) \cdot 10^{-4}$ .
5. **Spin polarisation of muon beams**

Muons are used to carry out deep inelastic scattering experiments at high beam energies. First a static target is bombarded with a proton beam. This produces charged pions which decay in flight into muons and neutrinos.

- (a) What is the energy range of the muons in the laboratory frame if magnetic fields are used to select a 350 GeV pion beam?
- (b) Why are the spins of such a monoenergetic muon beam polarised? How does the polarisation vary as a function of the muon energy?

### 6. Compton scattering

At the HERA collider ring the spins of the electrons going around the ring align themselves over time antiparallel to the magnetic guide fields (Sokolov-Ternov effect [20]). This spin polarisation may be measured with the help of the spin dependence of Compton scattering. We solely consider the kinematics below.

- (a) Circularly polarised photons from an argon laser (514 nm) hit the electrons (26.67 GeV, straight flight path) head on. What energy does the incoming photon have in the rest frame of the electron?
- (b) Consider photon scattering through  $90^\circ$  and  $180^\circ$  in the electron rest frame. What energy does the scattered photon possess in each case? How large are the energies and scattering angles in the lab frame?
- (c) How good does the spatial resolution of a calorimeter have to be if it is 64 m away from the interaction vertex and should spatially distinguish between these photons?

## References

1. F.D. Aaron et al., JHEP **1209**, 061 (2012)
2. H. Albrecht et al., Phys. Lett. **B234**, 409 (1990)
3. H. Albrecht et al., Phys. Lett. **B255**, 297 (1991)
4. B.C. Barish, R. Stroynowski, Phys. Rep. **157**, 1 (1988)
5. D.I. Britton et al., Phys. Rev. Lett. **68**, 3000 (1992)
6. H. Burkard et al., Phys. Lett. **B160**, 343 (1985)
7. N. Cabibbo, Phys. Rev. Lett. **10**, 531 (1963)
8. J.H. Christenson, J.W. Cronin, V.L. Fitch, R. Turlay, Phys. Rev. Lett. **13**, 138 (1964)
9. E.D. Commins, *Weak Interactions* (McGraw-Hill, New York, 1973)
10. C.L. Cowan Jr., F. Reines et al., Science **124**, 103 (1956)
11. G. Danby et al., Phys. Rev. Lett. **9**, 36 (1962)
12. E. Fermi, Z. Phys. **88**, 161 (1934)
13. R. Fulton et al., Phys. Rev. Lett. **64**, 16 (1990)
14. F.J. Hasert et al., Phys. Lett. **B46**, 138 (1973)
15. M. Kobayashi, T. Maskawa, Prog. Theor. Phys. **49**, 652 (1973)
16. W.J. Marciano, Annu. Rev. Nucl. Part. Sci. **41**, 469 (1991)
17. E.A. Paschos, U. Türke, Phys. Rep. **178**, 145 (1989)
18. Particle Data Group, L. Montanet et al., *Review of Particle Properties*. Phys. Rev. **D50**, 1173 (1994)
19. Particle Data Group, J. Beringer et al., *Review of Particle Properties*. Phys. Rev. D **86**, 010001 (2012)
20. A.A. Sokolov, J.M. Ternov, Sov. Phys. Dokl. **8**, 1203 (1964)
21. C.S. Wu et al., Phys. Rev. **105**, 1413 (1957)

# Chapter 11

## Neutrino Oscillations and Neutrino Mass

*Today I have done something which you never should do in theoretical physics. I have explained something which is not understood by something which can never be observed!*

Wolfgang Pauli

The existence of neutrinos was proposed by Wolfgang Pauli in 1930, in order to explain the puzzling continuous energy spectrum of electrons in  $\beta$ -decay. If the neutron would decay only into a proton and an electron, the energy of the latter would be constant. In case of a 3-body decay, however, the third particle would carry away a certain amount of energy, and thereby generate a continuous energy spectrum for the electron. As we have seen in the last chapter, the interaction of neutrinos with other elementary particles is extremely weak, see (10.9). Therefore it was thought for a long time that the direct experimental verification of the existence of neutrinos was impossible. Only in 1956 Cowan and Reines finally succeeded in detecting electron antineutrinos originating from a nuclear reactor [8].

In the otherwise enormously successful standard model of particle physics (see Chap. 13), neutrinos are massless. However, in 1998 it was shown beyond doubt that neutrinos possess a non-vanishing rest mass. Till this date, this represents the only directly testable and in laboratories accessible physics beyond the standard model. This fact alone renders neutrinos highly interesting. In addition, neutrinos show some remarkable properties. For instance, they can transform from one flavour into another one, with a transition probability that changes periodically. These neutrino oscillations are a quantum mechanical interference effect on macroscopic distances, whose basic features and important experiments we will discuss in what follows. The precise value of the neutrino mass is a currently unresolved problem, we will discuss the most important approaches to answer this important question. Finally, neutrinos are the only known electrically neutral fermions and, therefore, have the option to be identical with their antiparticles. This would lead to processes that violate the conservation of total lepton number.

## 11.1 Lepton Families

**The leptonic mixing matrix** We have outlined in Sect. 10.1 that leptons can be written in terms of three family doublets:

$$\begin{pmatrix} \nu_e \\ e^- \end{pmatrix} \quad \begin{pmatrix} \nu_\mu \\ \mu^- \end{pmatrix} \quad \begin{pmatrix} \nu_\tau \\ \tau^- \end{pmatrix}.$$

The flavour states  $|\nu_e\rangle$ ,  $|\nu_\mu\rangle$  and  $|\nu_\tau\rangle$  are not identical to the states  $|\nu_1\rangle$ ,  $|\nu_2\rangle$  and  $|\nu_3\rangle$ , which possess a well-defined mass. However, in analogy to the quarks, we can write the flavour states as orthogonal linear combinations of the mass states:

$$\begin{pmatrix} |\nu_e\rangle \\ |\nu_\mu\rangle \\ |\nu_\tau\rangle \end{pmatrix} = \begin{pmatrix} U_{e1} & U_{e2} & U_{e3} \\ U_{\mu1} & U_{\mu2} & U_{\mu3} \\ U_{\tau1} & U_{\tau2} & U_{\tau3} \end{pmatrix} \cdot \begin{pmatrix} |\nu_1\rangle \\ |\nu_2\rangle \\ |\nu_3\rangle \end{pmatrix}. \quad (11.1)$$

The  $3 \times 3$  matrix  $U$  is analogous to the CKM matrix  $V$ , which has been introduced in Sect. 10.4. In particular, it is unitary and contains three mixing angles and one phase (see also Sect. 15.4). The possibility of neutrino mixing was investigated theoretically very early. Pontecorvo [15] was the first to consider neutrino-antineutrino oscillations. Maki, Nakagawa and Sakata [14] have discussed flavour mixing of two neutrinos (interestingly already before the Cabibbo angle for quark mixing was introduced). Therefore  $U$  is called the PMNS matrix. Recall that mass states are not constants of motion. The relative phases of these states change with time. If neutrinos were massless, this would not be the case. It would make no sense to distinguish between flavour and mass states and the PMNS matrix would not exist. The indirect proof that neutrinos possess a mass, in contrast to the prediction of the standard model, was possible by observing *neutrino oscillations*.

## 11.2 Neutrino Oscillations

To understand how the elements of  $U$  can be determined, consider two generations of neutrinos,  $|\nu_e\rangle$  and  $|\nu_\mu\rangle$ , which in analogy to (10.19) are written as

$$\begin{pmatrix} |\nu_e\rangle \\ |\nu_\mu\rangle \end{pmatrix} = \begin{pmatrix} \cos \theta & \sin \theta \\ -\sin \theta & \cos \theta \end{pmatrix} \cdot \begin{pmatrix} |\nu_1\rangle \\ |\nu_2\rangle \end{pmatrix}. \quad (11.2)$$

Neutrinos are produced as flavour states by the weak interaction, e.g. a  $|\nu_e\rangle = \cos \theta |\nu_1\rangle + \sin \theta |\nu_2\rangle$  by a charged current electron-quark interaction. The time



evolution of the mass states leads after a time  $t$  to the following wave function of the electron neutrino:

$$|\nu_e(t)\rangle = \cos\theta e^{-iE_{\nu_1}t/\hbar} |\nu_1\rangle + \sin\theta e^{-iE_{\nu_2}t/\hbar} |\nu_2\rangle. \quad (11.3)$$

Neutrinos are ultra-relativistic, hence their energy is:

$$E_{\nu_i} = \sqrt{p^2c^2 + m_{\nu_i}^2c^4} \approx pc \left(1 + \frac{1}{2} \frac{m_{\nu_i}^2c^4}{p^2c^2}\right). \quad (11.4)$$

The probability to find an electron neutrino after the time  $t$  is therefore

$$\begin{aligned} P_{\nu_e \rightarrow \nu_e} &= |\langle \nu_e(t) | \nu_e \rangle|^2 = \cos^4\theta + \sin^4\theta + 2\cos^2\theta \sin^2\theta \cos\left(\frac{1}{2} \frac{\Delta m_{21}^2 c^4}{\hbar c} \frac{L}{pc}\right) \\ &= 1 - \sin^2 2\theta \sin^2\left(\frac{1}{4} \frac{\Delta m_{21}^2 c^4}{\hbar c} \frac{L}{pc}\right). \end{aligned} \quad (11.5)$$

Here

$$\Delta m_{21}^2 = m_{\nu_2}^2 - m_{\nu_1}^2 \quad (11.6)$$

is the difference of the squares of the masses of the states  $\nu_1$  and  $\nu_2$ , and  $L = ct$  is the distance between production and detection travelled by the neutrino in the time  $t$ . We see that the survival probability  $P_{\nu_e \rightarrow \nu_e}$  oscillates as a function of the ratio of  $L$  and  $p$ . This is a known interference effect in quantum mechanics, and we will cover it once more later in this book, when we discuss oscillations of  $K^0$  and  $\bar{K}^0$  mesons in Sect. 15.4.

It follows that by measuring the survival probability one can determine the amplitude  $\sin^2 2\theta$  (hence the elements of the mixing matrix) and the mass-squared difference  $\Delta m_{21}^2$ , which is proportional to the oscillation frequency. The transition probability, i.e., the probability that the electron neutrino becomes a muon neutrino follows from

$$P_{\nu_e \rightarrow \nu_\mu} = 1 - P_{\nu_e \rightarrow \nu_e} = \sin^2 2\theta \sin^2\left(\frac{1}{4} \frac{\Delta m_{21}^2 c^4}{\hbar c} \frac{L}{pc}\right). \quad (11.7)$$

There is no oscillation in case neutrinos were massless, or when neutrinos had identical mass; the transition and survival probabilities would simply be  $P_{\nu_e \rightarrow \nu_\mu} = 0$

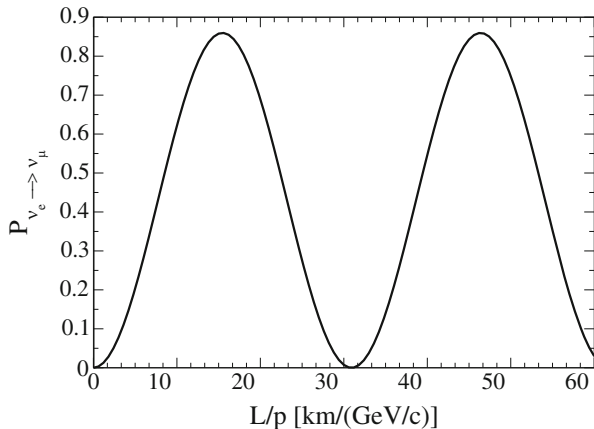


**Fig. 11.1** Typical oscillation curve for the transition probability of electron neutrinos in muon neutrinos, see (11.7). The chosen parameters are  $\theta = 34^\circ$  and  $m_{\nu_2}^2 - m_{\nu_1}^2 = 8 \cdot 10^{-5} \text{ eV}^2/c^4$ . Hence the transition probability is zero for  $L/p \approx 31 \text{ km}/(\text{MeV}/c)$  and maximal ( $\sin^2 2\theta = 0.86$ ) for half this value. The oscillation length for a momentum of  $3 \text{ MeV}/c$  is  $L_{\text{osc}} \approx 93 \text{ km}$

and  $P_{\nu_e \rightarrow \nu_e} = 1$ . At the end we provide a very useful numerical form of the argument of the sine in the oscillation formula:

$$\frac{1}{4} \frac{\Delta m_{21}^2 c^4}{\hbar c} \frac{L}{pc} = 1.27 \left( \frac{\Delta m_{21}^2}{\text{eV}^2/c^4} \right) \left( \frac{\text{MeV}}{pc} \right) \left( \frac{L}{m} \right). \quad (11.8)$$

A simple example curve is shown in Fig. 11.1. The characteristic scale of oscillations is the distance between two minima or maxima, which is denoted as oscillation length:

$$L_{\text{osc}} = 4\pi \frac{\hbar pc^2}{\Delta m_{21}^2 c^4}. \quad (11.9)$$

An experiment is especially well suited to test oscillations when the argument (11.8) is of order 1. This rule of thumb allows to estimate the sensitivity on the mass-squared difference of an experiment. For instance, experiments that detect neutrinos at a distance of 1 km from nuclear power plants, which have an average momentum of  $3 \text{ MeV}/c$ , are sensitive to  $\Delta m_{21}^2 \approx 10^{-3} \text{ eV}^2/c^4$ . Such considerations are confirmed in actual experiments. One should note from this example that we are talking about quantum mechanical interference effects on macroscopic distances.

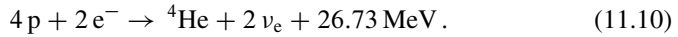
Two extreme cases of the oscillation formula are of particular interest: if the argument of the sine is very small (small distances when compared to the oscillation length), then the oscillations have not yet taken place. If the argument is very large (large distances when compared to the oscillation length), then the oscillations take place on scales which are too small to be resolved by a detector.

## 11.3 Neutrino Oscillation Experiments

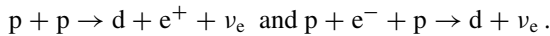
The existence of neutrino oscillations has been confirmed by various experiments. We will discuss in this section the basic physics behind this important area of modern particle physics. With three generations of neutrinos the expressions for the oscillation probabilities are lengthy and complicated (they can be found, e.g., in [12]). To a good approximation, however, one can describe all experiments with the 2-generation formulae (11.5) and (11.7), respectively, because the 3-generation probabilities simplify when the actual experimental parameters  $pc$  and  $L$  are inserted. The amplitude and mass-squared difference depends on the kind of experiment considered. Before we go into detail, let us stress again that only the mass-squared difference and not the masses themselves can be determined. Approaches to measure the neutrino mass will be discussed later. Oscillation experiments are often classified as “*appearance*” and “*disappearance*” experiments, depending on whether one looks for neutrino flavours that are not produced in the source, or whether one measures the expected flux of neutrinos.

**Solar neutrinos** Historically the first measurements that pointed towards oscillations were performed with solar neutrinos. The experimentally determined flux of solar  $\nu_e$  was, depending on energy, about one third to half the value predicted in solar models. The interpretation is of course that the  $\nu_e$  oscillate into  $\nu_\mu$  and  $\nu_\tau$ .

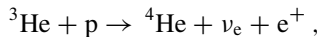
Solar models describe in detail the Sun’s energy production through a number of nuclear reactions. Effectively, the following fusion reaction takes place: (see Sect. 20.5):



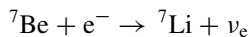
It is realised by a complicated network of reactions. Of interest are here only the ones that generate neutrinos. The first step is the production of the deuteron:



The first reaction leads to a continuous energy spectrum with a maximal energy of  $E_\nu^{\text{max}} = 0.42 \text{ MeV}$ , while for the second a fixed energy of  $E_\nu = 1.44 \text{ MeV}$  is predicted. The deuteron fuses with a proton to  ${}^3\text{He}$ . This isotope can either fuse with another  ${}^3\text{He}$  nucleus to  ${}^4\text{He}$  and two protons, or generate neutrinos via



which have  $E_\nu^{\text{max}} = 18.77 \text{ MeV}$ . Now we fuse  ${}^4\text{He}$  and  ${}^3\text{He}$  to  ${}^7\text{Be}$ , which reacts via



and again generates neutrinos. Because this reaction can end in the ground state (in about 90% of the cases) or the excited state of  ${}^7\text{Li}$ , the neutrino energy is

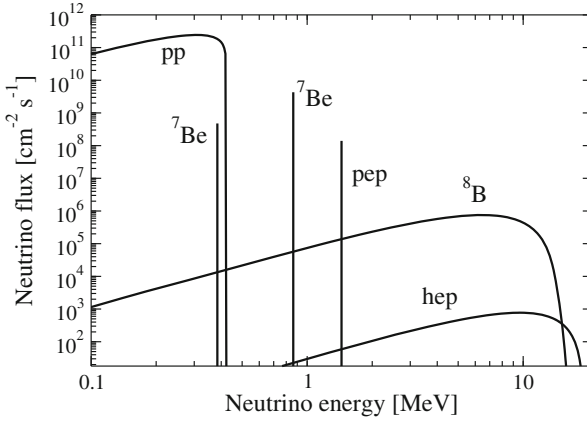
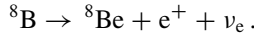


**Fig. 11.2** The solar neutrino spectrum from [7]. Plotted are the individual spectra of the five different neutrino sources

either  $E_\nu = 0.862 \text{ MeV}$  or  $E_\nu = 0.384 \text{ MeV}$ .<sup>1</sup> Through proton capture  ${}^7\text{Be}$  is transformed into  ${}^8\text{B}$ , which is another source of neutrinos ( $E_\nu^{\text{max}} = 14.06 \text{ MeV}$ ) since it undergoes  $\beta$ -decay:



All in all there are five different neutrino sources with different spectra and calculable percentage of the total flux [7]. Their sum should give the total solar neutrino spectrum, see Fig. 11.2. We can estimate this flux once we know the so-called solar constant  $\Phi$ , which denotes the Sun's electromagnetic power reaching the Earth per area and time unit. Ignoring seasonal variations due to the Earth's elliptic orbit, it is given by  $\Phi \approx 8.5 \cdot 10^{11} \text{ MeV cm}^{-2} \text{ s}^{-1}$ . With two produced neutrinos per reaction in (11.10), one finds

$$\Phi(\nu_e) \approx 2 \frac{\Phi}{27 \text{ MeV}} \approx 6 \cdot 10^{10} \text{ cm}^{-2} \text{ s}^{-1},$$

almost  $10^{11}$  neutrinos per square centimetre and second. Their energy is at most  $18.77 \text{ MeV}$ , its average value however only  $0.3 \text{ MeV}$ . Therefore the energy of solar neutrinos is too low to produce  $\mu$  or  $\tau$  leptons in charged-current reactions after the  $\nu_e$  oscillate into  $\nu_\mu$  or  $\nu_\tau$ .

Early experiments [16] were only sensitive on  $\nu_e$ , for instance via the reaction  $\nu_e + {}^{37}\text{Cl} \rightarrow {}^{37}\text{Ar} + e^-$  that is mediated by charged currents. The radioactive Argon can be detected since it decays with a half-life of about 35 days:

<sup>1</sup>The direct detection of this small and low-energy flux was possible only in 2007 by the Borexino experiment [6].

$^{37}\text{Ar} \rightarrow ^{37}\text{Cl} + e^- + \bar{\nu}_e$ . To generate  $^{37}\text{Ar}$  one requires a threshold energy of 0.81 MeV, and therefore only part of the solar spectrum can be tested. Measurements with lower energy values were possible by constructing a similar experiment taking advantage of neutrino capture on  $^{71}\text{Ga}$  (threshold energy 0.23 MeV) and detection of the generated  $^{71}\text{Ge}$ , which is radioactive (see Exercise 11.1).

Another possibility to measure solar neutrinos is through elastic scattering on electrons,  $\nu_e + e^- \rightarrow \nu_e + e^-$ . In this reaction interference between charged and neutral currents occurs. In contrast to this, the reaction  $\nu_{\mu,\tau} + e^- \rightarrow \nu_{\mu,\tau} + e^-$  can only be mediated by neutral currents of the  $\nu_\mu$  and  $\nu_\tau$ , see Sect. 10.3. The result is

$$\sigma(\nu_e e^- \rightarrow \nu_e e^-) \approx 6.14 \cdot \sigma(\nu_{\mu,\tau} e^- \rightarrow \nu_{\mu,\tau} e^-). \quad (11.11)$$

Consequently one has some sensitivity on the  $\nu_{\mu,\tau}$ . This reaction was examined mainly in the SuperKamiokande experiment [11], a Cherenkov detector filled with 50,000 tons of water and located 1,000 m below the surface of the Earth. The reaction is detected by the Cherenkov light of the scattered electrons. This radiation in the form of photons is generated when the electrons move within a medium (for SuperKamiokande this is water) with a velocity that is larger than the speed of light in that medium (see Sect. A.2). A light cone is produced whose opening angle is  $\theta = \arccos \frac{1}{\beta_e n}$ , where  $n = 1.33$  is the index of refraction of water. Since electrons lose energy through bremsstrahlung, they move faster than light only for a short amount of time, and a so-called Cherenkov ring is formed. By determining the position of the original reaction and the opening angle of the Cherenkov cone one can measure the energy of the electron. At high energies, the scattering occurs mainly in forward direction.

The last doubts whether the solar models were really correct were removed by the SNO Experiment (Sudbury Neutrino Observatory) [2, 3]. This experiment determines the total neutrino flux by measuring also reactions which are mediated by neutral currents only. To those reactions the  $\nu_\mu$  and  $\nu_\tau$  are contributing as well, which implies that the total flux should come out in case the  $\nu_e$  oscillate into  $\nu_\mu$  and  $\nu_\tau$ . The Cherenkov detector is located in a depth of 2,000 m in a mine in Canada, and was filled with 1,000 tons of heavy water. Here the oxygen atom is bound to two deuterium atoms. The following reactions can now be measured:

$$\text{CC: } \nu_e + d \rightarrow p + p + e^- \quad (11.12)$$

$$\text{NC: } \nu_{e,\mu,\tau} + d \rightarrow p + n + \nu_{e,\mu,\tau} \quad (11.13)$$

$$\text{ES: } \nu_{e,\mu,\tau} + e^- \rightarrow \nu_{e,\mu,\tau} + e^-. \quad (11.14)$$

The first one is only mediated by charged currents, and is measured by the Cherenkov light of the electrons.<sup>2</sup> It determines the incoming flux of electron

<sup>2</sup>The refractive index of heavy water is essentially identical to the one of normal water.

neutrinos,  $\phi_{CC} = \phi_e$ . The second reaction is mediated by neutral currents. It is independent of flavour and determines the total flux,  $\phi_{NC} = \phi_e + \phi_{\mu\tau}$ . The elastic scattering reaction (11.14) is sensitive on all three flavours, though slightly more on the  $\nu_e$ , namely  $\phi_{ES} \approx \phi_e + 0.16 \phi_{\mu\tau}$ , see (11.11). It can however also serve to measure the total flux.

All three reactions can experimentally be distinguished. Electrons from elastic scattering point, as mentioned above, in the same direction as the incoming neutrinos. Since in the charged current reaction the proton is much heavier than the electron, there is basically no direction dependence for the produced electron. The free neutron in the neutral current reaction is captured by a deuterium nucleus, whose de-excitation generates within typically 10 ms photons with a total energy of 6 MeV. Compton scattering of those photons with electrons results in Cherenkov light. The detector was furthermore spiced with NaCl, because  $^{35}\text{Cl}$  has a high capture rate for neutrons. In addition, special counters equipped with  $^3\text{He}$  were added to the experiment.

The result was that the total neutrino flux is about 3 times as large as the flux of the  $\nu_e$ , and more importantly, consistent with the prediction of the solar models, see Fig. 11.3. The theoretical analysis of the solar models is complicated by so-called matter effects, which influence the oscillations of neutrinos in a medium such as the interior of the Sun, see Exercise 11.2.<sup>3</sup> The extracted survival probability  $P_{\nu_e \rightarrow \nu_e}$

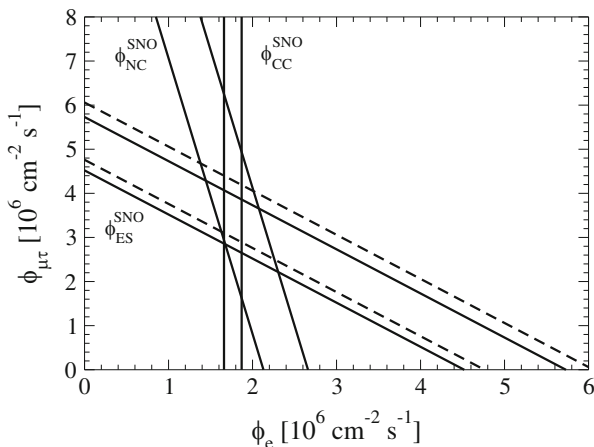


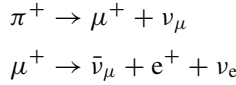
**Fig. 11.3** Results of the SNO experiment, see [3]. Plotted are the determined neutrino fluxes (including measuring errors) from elastic scattering  $\phi_{ES}$ , charged current  $\phi_{CC}$  and neutral current  $\phi_{NC}$ , see (11.12)–(11.14). The prediction of the solar standard model (shown here with theoretical uncertainty) lies within the *dashed lines*. Calculation and measurement agree excellently

<sup>3</sup>The reason lies in the fact that in a medium consisting of electrons, protons and neutrons, electron neutrinos can react through neutral and charged currents, whereas the other flavours only feel neutral currents.

gives for the mixing angle and the mass-squared difference that are relevant for solar neutrinos:

$$\theta_{12} \approx 34^\circ \text{ and } \Delta m_{21}^2 = m_{\nu_2}^2 - m_{\nu_1}^2 \approx 8.0 \cdot 10^{-5} \text{ eV}^2/c^4 .$$

**Atmospheric neutrinos** Oscillations were also observed in the flux of atmospheric neutrinos. The atmosphere is constantly bombarded with protons and heavy nuclei from cosmic rays, and the reactions generate a large number of pions. Their decays produce the so-called atmospheric neutrinos



and the appropriate antiparticles. The ratio of the two neutrino flavours is  $[n(\nu_\mu) + n(\bar{\nu}_\mu)]/[n(\nu_e) + n(\bar{\nu}_e)] = 2$ , if effects coming from the finite lifetime of the muon are neglected. The energies of the neutrinos are determined again by the Cherenkov radiation of the scattered charged leptons. The most important measurement of atmospheric neutrinos was performed by the SuperKamiokande experiment in Kamioka, Japan. The electrons and muons, and therefore the incoming  $\nu_e$  and  $\nu_\mu$ , are identified by their Cherenkov light. The Cherenkov ring of the electrons is smeared with respect to the one of the muons, since the lighter electrons scatter much more frequently in the water tank than the heavier muons. The neutrino energies that are of interest in our discussion are a few 100 MeV and more. It follows that the produced charged leptons point in the same direction as the neutrinos. This allows to determine if the neutrinos crossed only the atmosphere above the detector, or if they originate from the other side of the Earth. The important observable is the zenith angle  $\theta$  of the charged leptons. For down-going particles this angle is  $\theta = 0$ , or  $\cos \theta = 1$ . The original neutrinos therefore were generated above the detector and have travelled about 20 km. Up-going neutrinos are characterised by  $\theta = 180^\circ$ , or  $\cos \theta = -1$ . They stem from the other side of the Earth, and have therefore travelled about  $10^4$  km.

A flux too low by a factor of 2 was measured [10] for neutrinos with energies above 1 GeV and travelled distances of  $10^4$  km, see Fig. 11.4. Since the Earth is transparent to such neutrinos, there should be no attenuation of the flux. In contrast to muon neutrinos, electron neutrinos did not show any deviation from the expected flux; on length scales comparably to the radius of the Earth they do not develop appreciable oscillations. The decreased flux of the  $\nu_\mu$  is therefore attributed to the oscillation of  $\nu_\mu$  into  $\nu_\tau$ , which cannot be identified in the detector. Analysing the data with the transition probability  $P_{\nu_\mu \rightarrow \nu_\tau}$  gives the parameters

$$\theta_{23} \approx 45^\circ \text{ and } |\Delta m_{31}^2| = |m_{\nu_3}^2 - m_{\nu_1}^2| \approx |m_{\nu_3}^2 - m_{\nu_2}^2| \approx 2.4 \cdot 10^{-3} \text{ eV}^2/c^4 .$$

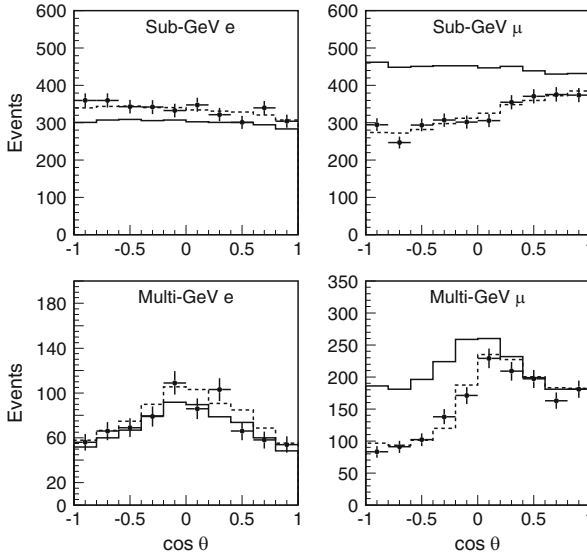


**Fig. 11.4** Measured fluxes of atmospheric neutrinos, see [10]. Shown are the event numbers including measurement errors for low (*upper plots*) and high (*lower plots*) energy neutrinos as function of the cosine of the zenith angle  $\theta$ . The *left plots* are events that have been identified as electrons, the *right plots* are muons. The *solid line* is the expectation in absence of neutrino oscillations, the *dashed line* is a fit to the data assuming oscillation of  $\nu_\mu$  into  $\nu_\tau$

The value of the mass-squared difference can be easily understood (using  $L \approx 10^4$  km and  $E \approx 1$  GeV) by our rule of thumb, which states that the argument of the sine in the oscillation formula should be one. Currently the sign of the larger mass-squared difference  $\Delta m_{31}^2$  is not known. This is called the problem of the neutrino mass ordering, and can be solved by future neutrino oscillation experiments.

**Reactor neutrinos** Additional information comes from observing oscillations of antineutrinos produced in nuclear reactors. Here, we need the 3-generation oscillation formulae. For the survival probability we have an expression containing three different terms, which are proportional to  $\Delta m_{21}^2$ ,  $\Delta m_{32}^2$  and  $\Delta m_{31}^2$ , respectively. The results considered so far imply that  $|\Delta m_{32}^2| \gg \Delta m_{21}^2$ , which leads to  $|\Delta m_{31}^2| \approx |\Delta m_{32}^2|$ , since the relation  $\Delta m_{21}^2 + \Delta m_{32}^2 - \Delta m_{31}^2 = 0$  must hold. It follows

$$\begin{aligned}
 P_{\nu_e \rightarrow \nu_e} = & 1 - 4 c_{12}^2 s_{12}^2 c_{13}^4 \sin^2 \left( \frac{1}{4} \frac{\Delta m_{21}^2 c^4}{\hbar c} \frac{L}{pc} \right) \\
 & - 4 c_{13}^2 s_{13}^2 \sin^2 \left( \frac{1}{4} \frac{\Delta m_{32}^2 c^4}{\hbar c} \frac{L}{pc} \right). \quad (11.15)
 \end{aligned}$$



We have abbreviated here  $c_{12}^2 = \cos^2 \theta_{12}$ ,  $s_{12}^2 = \sin^2 \theta_{12}$  etc.<sup>4</sup> The smaller one of the two oscillation lengths is proportional to  $1/|\Delta m_{32}^2|$ . If the distance of a detector is small when compared to this oscillation length, then we have  $P_{\nu_e \rightarrow \nu_e} \approx 1$ . If we increase the distance, the sine including  $\Delta m_{32}^2$  becomes of order one, while the term including  $\Delta m_{21}^2$  is negligible. This occurs at about  $L \approx 1,000$  m. One is in this case sensitive to  $\theta_{13}$ . Increasing the distance further to  $L \approx 100$  km, one sees that the sine including  $\Delta m_{21}^2$  becomes of order one, while the fast oscillations of the other terms can no longer be resolved, and are negligible in the limit of small  $\theta_{13}$ . One expects to test in this case the parameters of solar neutrinos. Figure 11.5 plots (11.15) together with the results of experiments that were performed over many years at different distances.

In Kamioka (Japan) the KamLAND detector is located, which contains 1,000 tons of a liquid scintillator to detect charged particles. Nuclear reactors in Japan and South Korea generate  $\bar{\nu}_e$ , and have a typical distance of 200 km from the detector. As estimated above, KamLAND is sensitive to the same mass-squared difference as solar experiments. Indeed, the same neutrino parameters as with solar neutrino experiments could be measured [9].

The third mixing angle  $\theta_{13}$  is determined, as estimated above, also in experiments with nuclear reactors, but with detectors which are located rather close (about 1 km) to the reactor core, e.g. Daya Bay [4] in China or Double Chooz [1] in France. The

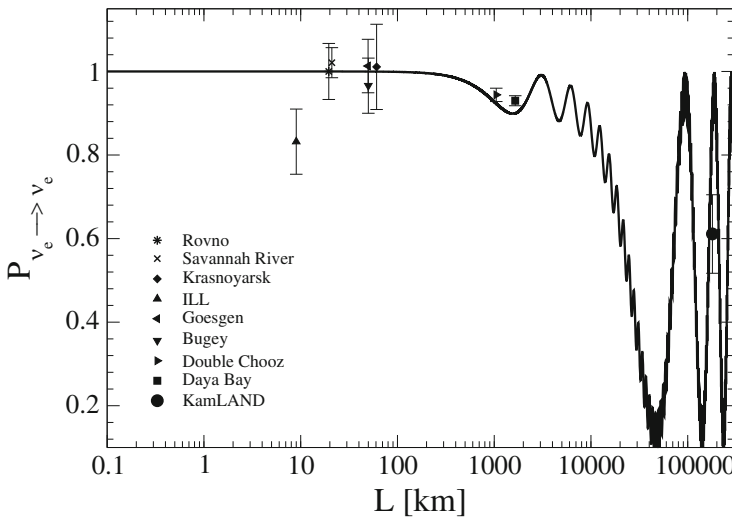


**Fig. 11.5** Oscillation curve  $P_{\nu_e \rightarrow \nu_e}$  in the 3-generation case with a neutrino momentum  $3 \text{ MeV}/c$ . Plotted are the averaged results of several neutrino oscillation experiments at nuclear reactors

<sup>4</sup>One can show that  $P_{\nu_e \rightarrow \nu_e} = P_{\bar{\nu}_e \rightarrow \bar{\nu}_e}$ , and analogously for the survival probabilities of muon and tau neutrinos, see Exercise 11.3.

method to detect the  $\bar{\nu}_e$  is inverse  $\beta$ -decay,

$$\bar{\nu}_e + p \rightarrow n + e^+ .$$

The produced positron annihilates with electrons. To determine the neutron, one adds Gadolinium to the detector, which has a very high capture rate for neutrons, and de-excites to its ground state after emitting photons with a total energy of about 8 MeV.

Comparing expected and measured flux gives  $P_{\nu_e \rightarrow \bar{\nu}_e}$ , and one finds an angle  $\theta_{13}$  of about  $9^\circ$ ; the mass-squared difference is  $\Delta m_{31}^2$ , the same as for atmospheric neutrinos.

**Mixing matrix of neutrinos** The absolute values of the lepton mixing matrix elements are obtained from the results of all oscillation experiments. Their central values are

$$(|U_{\alpha i}|) \approx \begin{pmatrix} 0.826 & 0.544 & 0.151 \\ 0.427 & 0.642 & 0.635 \\ 0.368 & 0.540 & 0.757 \end{pmatrix} . \quad (11.16)$$

The precision is not as high as for the CKM matrix (10.23). Possible effects of the CP phase in  $U$  are not yet seen.

Let us finally summarise the main features of lepton mixing. First one notes that all elements of the mixing matrix are about the same size. It is therefore much different from the CKM matrix, see (10.23), for which the diagonal elements dominate. Such a drastically different mixing of quarks and leptons can be an important hint for the understanding of physics beyond the standard model (Sect. 20.4). In analogy to the electroweak unification (Sect. 12.2) one suspects a grander unification (Sect. 12.6) which unites also quarks and leptons.

**Neutrino mass** A second peculiarity of neutrinos is the smallness of their masses. Upper limits on  $m_{\nu_i}$  are about  $2 \text{ eV}/c^2$ , and neutrinos are therefore much lighter than all other fermions. The explanation which theorists consider the most plausible one is treated in Sect. 11.4.

Let us discuss here shortly the current information on neutrino masses. As mentioned above, oscillation experiments can only probe the differences of the squared masses. The sign of the larger mass-squared difference,  $\Delta m_{31}^2 = m_3^2 - m_1^2$ , is unknown. The two possibilities are called normal and inverted ordering, Fig. 11.6 shows both cases. Per definition the largest mass in the normal ordering is  $m_3$ , whereas it is  $m_2$  in the inverted ordering. Accordingly the smallest mass is  $m_1$  or  $m_3$ , respectively. The smallest mass can be zero, for the normal ordering this case is called normal hierarchy:

$$m_2 = \sqrt{\Delta m_{21}^2} \approx 0.009 \text{ eV}/c^2, \quad m_3 = \sqrt{\Delta m_{31}^2} \approx 0.05 \text{ eV}/c^2 . \quad (11.17)$$

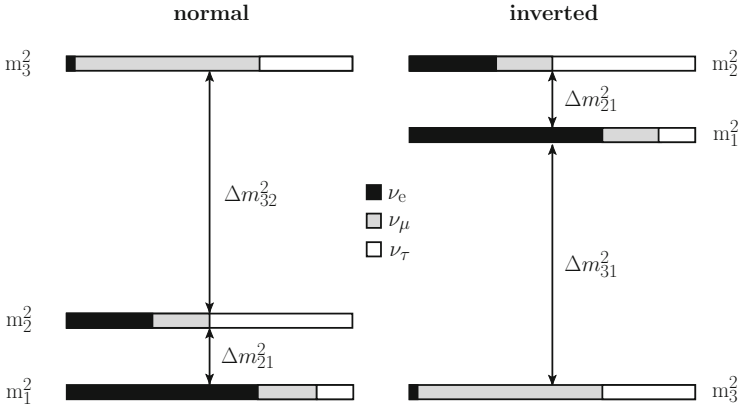


**Fig. 11.6** Possible ordering of neutrino masses. Shown are the normal (*left*) and the inverted (*right*) ordering. The size of the shaded areas of neutrino  $\nu_i$  with mass  $m_i$  corresponds to the size of  $|U_{\alpha i}|^2$ , i.e. the amount of the flavour state  $\nu_\alpha$

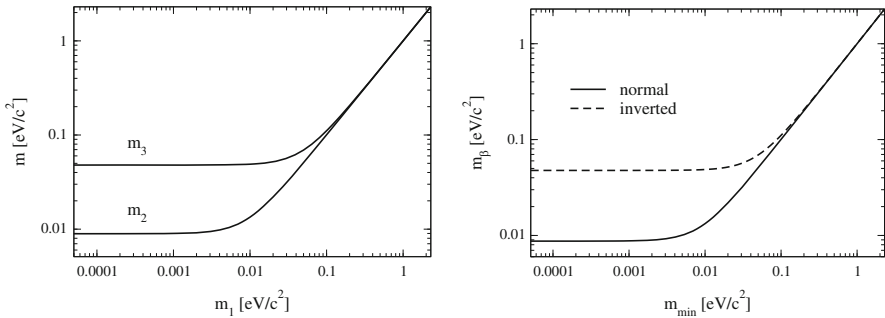


**Fig. 11.7** In the left plot the neutrino masses  $m_2$  and  $m_3$  are shown as functions of the smallest mass  $m_1$  in the normal ordering. In the inverted ordering the according plot would be  $m_2$  and  $m_1$  as functions of  $m_3$ . Both curves would be indistinguishable. The right plot shows the quantity  $m_\beta = \sqrt{\sum |U_{ei}|^2 m_i^2}$ , which is measurable in  $\beta$ -decays, as function of the smallest neutrino mass for both mass orderings

If in the inverted ordering the smallest mass is zero we talk about the inverted hierarchy:

$$m_2 \approx m_1 = \sqrt{|\Delta m_{31}^2|} \approx 0.05 \text{ eV}/c^2. \tag{11.18}$$

The difference between  $m_2$  and  $m_1$  in the inverted hierarchy is  $\sqrt{\Delta m_{21}^2}$ . One notes that the ratio of neutrino masses is less extreme than for quarks or charged leptons, compare for instance  $m_3/m_2$  with  $m_t/m_c$  or  $m_\tau/m_\mu$ . In case the smallest mass is non-zero, the ratios of neutrino masses are even larger, see Fig. 11.7. If the smallest

mass exceeds about  $0.1 \text{ eV}/c^2$ , the differences in masses are negligible and one speaks of quasi-degenerate neutrinos. The largest possible neutrino mass value can be obtained from experiments on the energy spectrum of  $\beta$ -decays, which we will discuss in more detail in Sect. 18.6. Effectively one can measure or constrain the quantity  $\sqrt{\sum |U_{ei}|^2 m_i^2}$ , for which a current upper limit of  $2.3 \text{ eV}/c^2$  is quoted [13]. One can easily show that this is the largest possible value of  $m_1$ ,  $m_2$  and  $m_3$ . New experiments, one example is KATRIN, will be able to improve this number by a factor of 10 in the near future.

Another approach to determine neutrino mass is neutrinoless double beta decay, which we will discuss in Sect. 18.7. Here the observable is  $|\sum U_{ei}^2 m_i|$ . This method is however quite model-dependent, because one has to assume that neutrinos are Majorana particles (see the next section).

Yet another possibility to measure neutrino mass exists in cosmology, where observations of galaxy distributions can probe the influence of neutrinos in the hot early universe. This method is also very model-dependent.

## 11.4 Majorana Neutrinos?

Charged leptons and quarks are obviously different from their respective antiparticles, since those have opposite electric charge. Fermions which are different from their antiparticles are called *Dirac particles*. They can formally be described by four degrees of freedom, namely particle and antiparticle, each with positive and negative helicity. If an electron neutrino was a Dirac particle, we would write those four degrees of freedom as

$$\text{Dirac particle: } (\nu_{e\uparrow}, \nu_{e\downarrow}, \bar{\nu}_{e\uparrow}, \bar{\nu}_{e\downarrow}).$$

The arrow  $\uparrow$  denotes here positive helicity,  $\downarrow$  accordingly negative helicity. However, since neutrinos are electrically neutral, they can be their own antiparticles. Such particles are called *Majorana particles*. They possess two degrees of freedom, namely particle = antiparticle with positive or negative helicity:

$$\text{Majorana particle: } (\nu_{e\uparrow}, \nu_{e\downarrow}).$$

The distinction we have made so far, namely that in charged current reactions neutrinos generate electrons, and antineutrinos generate positrons, has to be discussed in a more subtle manner: As we have seen in Sect. 10.5, weak interactions couple only to left-handed electrons and right-handed positrons. Chirality is identical to helicity up to corrections of order mass divided by energy. The particle that is produced by a  $W^-$  together with a left-handed electron is now a right-handed Majorana fermion, which in case its mass is non-zero possesses mainly positive helicity, but also a small contribution of negative helicity:  $\nu_{e\uparrow} + \epsilon \nu_{e\downarrow}$ . Here  $\epsilon$  is of the order  $m_\nu c^2/E_\nu$ .

This very tiny contribution can now interact with a second  $W^-$  and generate in a charged current reaction a left-handed electron. All in all we have transformed two  $W^-$  in two electrons:

$$\begin{aligned} W^- &\rightarrow e^- + (\nu_{e\uparrow} + \epsilon \nu_{e\downarrow}) \\ \nu_{e\downarrow} + W^- &\rightarrow e^- . \end{aligned} \quad (11.19)$$

The total reaction chain violates lepton number conservation by two units. It is only possible if neutrinos are Majorana particles. If neutrinos were Dirac particles, then the particle that is produced in the first step would be  $\bar{\nu}_{e\uparrow} + \epsilon \bar{\nu}_{e\downarrow}$ , and the small contribution with negative helicity  $\bar{\nu}_{e\downarrow}$  would not interact with a  $W^-$ . The reaction chain in (11.19) would not take place.

In case of massive Majorana neutrinos the conservation of lepton number, as discussed at the end of Sect. 10.1 should not be obeyed exactly. However, the rates of lepton-number violating processes are strongly suppressed with the ratio of neutrino mass and their energy. As a numerical example, consider neutrinos from nuclear reactors, whose energy is  $E_\nu \approx \text{MeV}$ . Assuming they have their largest allowed mass of  $m_\nu \approx 1 \text{ eV}/c^2$ , one finds that they have a small fraction  $\epsilon$  of “wrong helicity” of about  $m_\nu c^2/E_\nu \approx 10^{-6}$ . The probability to absorb this part is then proportional to this small number squared. The dependence on neutrino mass implies that massless Majorana neutrinos cannot be distinguished from massless Dirac neutrinos.

The search for neutrinoless double beta decay, discussed in Sect. 18.7, is the most realistic possibility to prove the Majorana character of neutrinos. The factor that compensates the strong suppression  $(m_\nu c^2/E_\nu)^2$  is the sheer number of atoms if one searches with several kg of the decaying isotope. In case neutrinos are Majorana particles the PMNS matrix contains two additional phases which however do not influence neutrino oscillation, and only become important in processes that violate lepton number.

**Seesaw mechanism** The idea of neutrinos being Majorana particles is appealing to most theorists, since it is realised in most theories that extend the standard model. In these models there are for each neutrino  $\nu_1$ ,  $\nu_2$  and  $\nu_3$  (linear combinations of which form  $\nu_e$ ,  $\nu_\mu$  and  $\nu_\tau$ ) additional neutrinos  $N_1$ ,  $N_2$  and  $N_3$ . The latter are Majorana particles with extremely large masses, whose magnitude is expected to correspond to the characteristic energy scale of the theory that extends the standard model. The different neutrinos interact with each other and thereby change their masses. For the sake of simplicity one can consider the case of one family, i.e. one neutrino  $\nu$  and a heavy neutrino  $N$ . The initial mass  $m_{\text{SM}}$  of  $\nu$  is similar to the masses of the quarks and charged leptons, since one assumes that it is generated by the same mechanism that gives them masses. The interaction between  $N$  and  $\nu$  leads now to a suppression of the mass of the neutrinos, in the form of

$$m_\nu \approx \frac{m_{\text{SM}}^2}{M_N} = m_{\text{SM}} \frac{m_{\text{SM}}}{M_N} . \quad (11.20)$$

The mass is therefore much lighter than the one of the other fermions of the standard model, suppressed with a factor  $m_{\text{SM}}/M_{\text{N}}$ .<sup>5</sup> In addition the light neutrinos are, thanks to their interaction with their heavy partners, now Majorana fermions, too. As one can see from (11.20),  $m_\nu$  becomes smaller when  $M_{\text{N}}$  becomes larger. Therefore this mechanism is called *seesaw mechanism*. Estimating  $m_{\text{SM}} \approx m_t$  and  $m_\nu \approx \sqrt{|m_{\nu_3}^2 - m_{\nu_2}^2|}$  as largest standard model and neutrino mass, respectively, gives  $M_{\text{N}} \approx 10^{15} \text{ GeV}/c^2$ . The corresponding energy scale of  $10^{15} \text{ GeV}$  is highly interesting for theorists, since it is the scale at which all three interactions are unified in Grand Unified Theories (Sect. 12.6). The fact that the same energy scale arises from considerations of Grand Unified Theories as well as from the neutrino masses makes the seesaw mechanism so plausible. As an additional bonus, the violation of lepton number and the possible CP violation in the decays of the heavy Majorana neutrinos help in understanding the generation of the matter-antimatter asymmetry in the early universe, see Sect. 20.4.

The distinction between Dirac and Majorana neutrino is for most practical purposes irrelevant, and we therefore return to the notation of neutrino and antineutrino.

## Problems

### 1. Solar neutrinos

The GALLEX experiment measures solar neutrinos by the reaction  ${}_{31}^{71}\text{Ga} + \nu_e \rightarrow {}_{32}^{71}\text{Ge}$ . The cross-section of this reaction at typical neutrino energies is about  $2.5 \cdot 10^{-45} \text{ cm}^2$ . One looks for radioactive  ${}_{32}^{71}\text{Ge}$  atoms (lifetime  $\tau = 16$  days), which are produced in a tank containing 30 t Gallium (40 %  ${}_{31}^{71}\text{Ga}$ , 60 %  ${}_{31}^{69}\text{Ga}$ ) as dissolved chloride [5]. About 50 % of all neutrinos have energies above the reaction threshold. All Germanium atoms are extracted from the tank. Estimate how many  ${}_{32}^{71}\text{Ge}$  atoms are generated per day. How many should be in the tank after 3 weeks? How many if one waits for an infinite amount of time?

### 2. Matter effects

Convince yourself that the matrix

$$H = \frac{c^4 \Delta m^2}{4E} \begin{pmatrix} -\cos 2\theta & \sin 2\theta \\ \sin 2\theta & \cos 2\theta \end{pmatrix}$$

is diagonalised by the matrix

$$U = \begin{pmatrix} \cos \theta & \sin \theta \\ -\sin \theta & \cos \theta \end{pmatrix}$$

---

<sup>5</sup>A useful analogy exists with the effective 4-fermion description of weak interactions at low energies with the Fermi constant. The presence of the W bosons is indirect, and only apparent at high energies. In the same way the presence of the heavy Majorana neutrinos is felt only indirectly at low energies, namely by the smallness of neutrino masses.

i.e.  $U^T H U = c^4 \text{diag}(-\Delta m^2/4E, \Delta m^2/4E)$ . The effect of neutrino oscillations in matter can now be described by adding a term to the upper left entry of  $H$ :

$$H_M = \frac{c^4 \Delta m^2}{4E} \begin{pmatrix} -\cos 2\theta + \frac{4\sqrt{2} G_F N_e E}{c^4 \Delta m^2} \sin 2\theta & \\ \sin 2\theta & \cos 2\theta \end{pmatrix}.$$

Here  $N_e$  is the number density of electrons (assumed constant) in the medium through which the neutrinos travel. Diagonalising this matrix with  $U_M^T H_M U_M$  yields the mixing angle in matter  $\theta_M$ . Show with

$$U_M = \begin{pmatrix} \cos \theta_M & \sin \theta_M \\ -\sin \theta_M & \cos \theta_M \end{pmatrix}$$

that it is given as

$$\sin^2 2\theta_M = \frac{\left(\frac{c^4 \Delta m^2}{2E}\right)^2 \sin^2 2\theta}{\left(\frac{c^4 \Delta m^2}{2E} \cos 2\theta - \sqrt{2} G_F N_e\right)^2 + \left(\frac{c^4 \Delta m^2}{2E}\right)^2 \sin^2 2\theta}.$$

When is this angle maximal ( $\theta_M = 45^\circ$ )?

### 3. CP and T violation in neutrino oscillations

Starting from the oscillation probability  $P_{\nu_\alpha \rightarrow \nu_\beta}$  for arbitrary flavours  $\alpha = e, \mu, \tau$ , find the CP- and T-transformed channels. When the combination CPT is conserved, what does this imply for the survival probabilities  $P_{\nu_\alpha \rightarrow \nu_\alpha}$ ?

### 4. The effective mass in neutrinoless double beta decay

The so-called effective mass, to which squared value the lifetime of neutrinoless double beta decay is proportional, can be written as:

$$m_{\beta\beta} = \left| \cos^2 \theta_{12} \cos^2 \theta_{13} m_1 + \sin^2 \theta_{12} \cos^2 \theta_{13} m_2 e^{i\gamma} + \sin^2 \theta_{13} m_3 e^{i\delta} \right|.$$

Here  $\gamma$  and  $\delta$  are additional phases in the PMNS matrix which show up only for Majorana neutrinos. Show with the neutrino parameters given in the book that in case of an inverted mass ordering there is a lower limit on the effective mass. Argue how the Majorana character of the neutrinos can be ruled out.

## References

1. Y. Abe et al., Phys. Rev. Lett. **108**, 131801 (2012)
2. Q.R. Ahmad et al., Phys. Rev. Lett. **87**, 071301 (2001)
3. Q.R. Ahmad et al., Phys. Rev. Lett. **89**, 011301 (2002)
4. F.P. An et al., Phys. Rev. Lett. **108**, 171803 (2012)
5. P. Anselmann et al., Phys. Lett. **B285**, 376 (1992); Phys. Lett. **B314**, 445 (1993); Phys. Lett. **B327**, 377 (1994)
6. C. Arpesella et al., Phys. Lett. **B658**, 101 (2008)

7. J.N. Bahcall, *Neutrino Astrophysics* (Cambridge University Press, Cambridge, 1989)
8. C.L. Cowan Jr., F. Reines et al., *Science* **124**, 103 (1956)
9. K. Eguchi et al., *Phys. Rev. Lett.* **90**, 021802 (2003)
10. Y. Fukuda et al., *Phys. Lett.* **B436**, 33 (1998); *Phys. Rev. Lett.* **81**, 1562 (1998)
11. S. Fukuda et al., *Phys. Lett.* **86**, 5651 (2001); *Phys. Rev. Lett.* **81**, 1562 (1998)
12. C. Giunti, C.W. Kim, *Fundamentals of Neutrino Physics and Astrophysics* (Oxford University Press, Oxford, 2007)
13. C. Kraus et al., *Eur. Phys. J.* **C40**, 447 (2005)
14. Z. Maki, M. Nagakawa, S. Sakata, *Prog. Part. Nucl. Phys.* **28**, 870 (1962)
15. B. Pontecorvo, *Zh. Eksp. Teor. Fiz.* **33**, 549 (1957); **34**, 247 (1958)
16. K. Zuber, *Neutrino Physics* (Taylor & Francis, Boca Raton, 2011)



# Chapter 12

## Exchange Bosons of the Weak Interaction and the Higgs Boson

The idea that the weak interaction is mediated by very heavy exchange bosons was generally accepted long before they were discovered. The structure of the Fermi theory of  $\beta$ -decay implies that the interaction is point-like, which in turn implies that the exchange bosons have to be very heavy particles. Quantitatively, however, this was confirmed only when the W and the Z bosons were detected experimentally [6, 8] and their properties could be measured. The  $Z^0$  boson's properties imply a mixing of the electromagnetic and weak interactions. The electroweak unification theory due to Glashow, Salam and Weinberg from the early seventies was thus confirmed. Today it is the basis of the standard model of elementary particle physics. Necessary for a consistent description of electromagnetic and weak interactions is a concept called symmetry breaking, related to a new scalar particle. The discovery of this Higgs particle was a spectacular confirmation of the ideas and concepts behind the standard model.

### 12.1 Real W and Z Bosons

The production of a real W or Z boson requires that a lepton and antilepton or a quark and antiquark interact. The centre-of-mass energy necessary for this is  $\sqrt{s} = M_{W,Z} c^2$ . This energy is most easily reached using colliding particle beams.

In  $e^+e^-$  colliders, a centre-of-mass energy of  $\sqrt{s} = 2E_e = M_Z c^2$  is necessary for the production of  $Z^0$  particles via

$$e^+ + e^- \rightarrow Z^0.$$

This became technically possible in 1989, when the SLC (Stanford Linear Collider) and the LEP became operational; now large numbers of  $Z^0$  bosons can be produced.

W bosons can also be produced in  $e^+e^-$  reactions, but only in pairs:

$$e^+ + e^- \rightarrow W^+ + W^-.$$

Hence, significantly higher energies are necessary for their production:  $\sqrt{s} > 2M_W c^2$ .

In 1996 the beam energy at LEP was upgraded from 50 to 86 GeV and later even to 104.6 GeV. This made a precise measurement of the W-mass and of the decay products of the  $W^+W^-$  pairs possible.

For many years the production of  $W^\pm$  or  $Z^0$  bosons was only possible with the help of quarks and antiquarks in the proton via the reactions

$$\begin{aligned} u + \bar{u} &\rightarrow Z^0, & d + \bar{u} &\rightarrow W^-, \\ d + \bar{d} &\rightarrow Z^0, & u + \bar{d} &\rightarrow W^+. \end{aligned}$$

For these reactions, however, it is insufficient to collide two proton beams each with half the rest energy of the vector bosons. Rather, the quarks which participate have to carry enough centre-of-mass energy  $\sqrt{\hat{s}}$  to produce the bosons. In a fast moving system, quarks carry only a fraction  $xP_p$  of the proton momentum  $P_p$  (cf. Sect. 7.3). About half the total momentum is carried by gluons; the rest is distributed among several quarks, with the mean  $x$  for valence quarks and sea quarks given by

$$\langle x_v \rangle \approx 0.12 \quad \langle x_s \rangle \approx 0.04. \quad (12.1)$$

One can produce a  $Z^0$  boson in a head-on collision of two protons according to

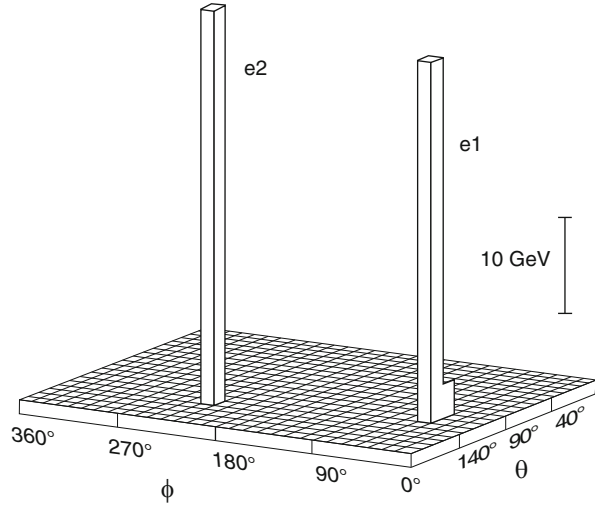
$$u + \bar{u} \rightarrow Z^0.$$

But the proton beam energy  $E_p$  must be close to  $E_p \approx 600$  GeV in order to satisfy

$$M_Z c^2 = \sqrt{\hat{s}} \approx \sqrt{\langle x_u \rangle \langle x_{\bar{u}} \rangle \cdot s} = 2 \cdot \sqrt{0.12 \cdot 0.04} \cdot E_p. \quad (12.2)$$

Proton-antiproton collisions are more favourable, since the momentum distributions of the  $\bar{u}$ - and  $\bar{d}$ -valence quarks in antiprotons are equal to those of the u- and d-valence quarks in protons. Consequently, only about half the energy is necessary. Since a p and a  $\bar{p}$  have opposite charges, it is also not necessary to build two separate accelerator rings; both beams can in fact be injected in opposite directions into the same ring. At the SPS (Super Proton Synchrotron) at CERN, which was renamed Sp $\bar{p}$ S (Super Proton Antiproton Storage ring) for this, protons and antiprotons of up to 318 GeV were stored; at the Tevatron (FNAL), 980 GeV beam energies were attained.

**Fig. 12.1** “Lego diagram” of one of the first events of the reaction  $q\bar{q} \rightarrow Z^0 \rightarrow e^+e^-$ , in which the  $Z^0$  boson was detected at CERN. The transverse energies of the electron and positron detected in the calorimeter elements are plotted as a function of the polar and azimuthal angles [7]



The bosons were detected for the first time in 1983 at CERN at the UA1 [6] and UA2 [5, 8] experiments in the decays

$$\begin{aligned} Z^0 & e^+ + e^-, & W^+ & e^+ + \nu_e, \\ Z^0 & \mu^+ + \mu^-, & W^+ & \mu^+ + \nu_\mu. \end{aligned}$$

The  $Z^0$  boson has a very simple experimental signature. One observes a high-energy  $e^+e^-$  or  $\mu^+\mu^-$  pair with the lepton and antilepton flying off in opposite directions. Figure 12.1 shows a so-called “lego diagram” of one of the first events. The figure shows the transverse energy measured in the calorimeter cells plotted against the polar and azimuthal angles of the leptons relative to the incoming proton beam. The height of the “lego bars” measures the energy of the leptons. The total energy of both leptons corresponds to the mass of the  $Z^0$ .

The detection of the charged vector bosons is somewhat more complicated, since only the charged lepton leaves a trail in the detector and the neutrino is not seen. The presence of the neutrino may be inferred from the momentum balance. When the transverse momenta (the momentum components perpendicular to the beam direction) of all the detected particles are added together the sum is found to be different from zero. This *missing* (transverse) *momentum* is ascribed to the neutrino.

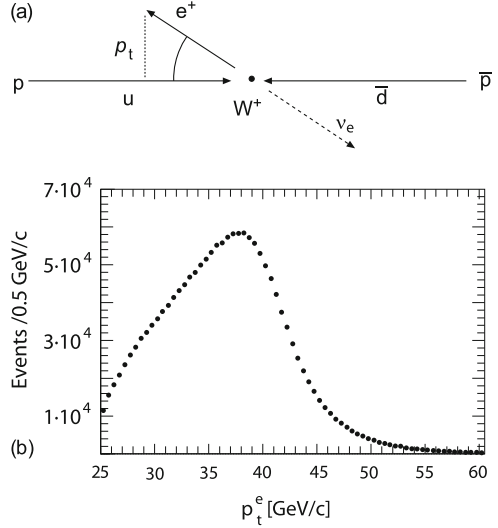
**Mass and width of the W boson** The distribution of the transverse momenta of the charged leptons may also be used to find the mass of the  $W^\pm$ . Consider a  $W^+$  produced at rest and then decaying into an  $e^+$  and a  $\nu_e$ , as shown in Fig. 12.2a. The transverse momentum of the positron is roughly given by

$$p_t^{e^+} \approx \frac{M_W \cdot c}{2} \sin \theta, \tag{12.3}$$

**Fig. 12.2 (a)** Kinematics of the decay  $W^+ \rightarrow e^+ + \nu_e$ .

The maximum possible transverse momentum  $p_t$  of the  $e^+$  is  $M_W c/2$ .

**(b)** Distribution of the transverse momentum  $p_t$  of  $e^+$  and  $e^-$  in the reaction  $q_1 + \bar{q}_2 \rightarrow e^\pm + \text{“nothing”}$ , from the D0 experiment at the Tevatron (After [3])



where  $\theta$  is the angle at which the positron is emitted with respect to the beam axis. We now consider the dependence of the cross-section on  $p_t$  or on  $\cos \theta$ . We have

$$\frac{d\sigma}{dp_t} = \frac{d\sigma}{d\cos\theta} \cdot \frac{d\cos\theta}{dp_t}, \quad (12.4)$$

from which follows

$$\frac{d\sigma}{dp_t} = \frac{d\sigma}{d\cos\theta} \cdot \frac{2p_t}{M_W c} \cdot \frac{1}{\sqrt{(M_W c/2)^2 - p_t^2}}. \quad (12.5)$$

The cross-section should have a maximum at  $p_t = M_W c/2$  (because of the transformation of variables, also called a *Jacobian peak*) and should then drop off rapidly. Since the  $W$  is not produced at rest and has a finite decay width the distribution is smeared out. In Fig. 12.2b a recent high statistics measurement of the  $p_t$  distribution by the D0 experiment at the Tevatron/FNAL [3] is shown.<sup>1</sup> The data have been obtained in  $p\text{-}\bar{p}$  collisions at a centre-of-mass energy of 1.96 TeV. The most precise figures to date for the width and mass of the  $W$  are [19]

$$\begin{aligned} M_W &= 80.385 \pm 0.015 \text{ GeV}/c^2, \\ \Gamma_W &= 2.085 \pm 0.042 \text{ GeV}. \end{aligned} \quad (12.6)$$

<sup>1</sup>Instead of the transverse momentum, one nowadays rather uses the transverse mass  $m_t^2 = 2 \frac{p_t^{e^+}}{c} \frac{p_t^{\nu_e}}{c} (1 - \cos \Delta\phi(e^+, \nu_e))$ , where  $\Delta\phi$  is the opening angle between the electron momentum and the reconstructed neutrino momentum [15].

**Mass and width of the Z boson** Since the cross-section for creating Z-bosons in  $e^+e^-$  collisions is much larger than the cross-section for creating W bosons, in either  $e^+e^-$  or  $p\bar{p}$  collisions, the mass and width of the  $Z^0$  boson have been much more precisely determined than their W boson counterparts. Furthermore, the energies of the  $e^+$  and  $e^-$  beams are known to an accuracy of a few MeV, which means that the measurements are very precise. The experimental values of the  $Z^0$  parameters and width are [19]

$$\begin{aligned} M_Z &= 91.1876 \pm 0.0021 \text{ GeV}/c^2, \\ \Gamma_Z &= 2.4952 \pm 0.0023 \text{ GeV}. \end{aligned} \quad (12.7)$$

**Decays of the W boson** When we dealt with the charged-current decays of hadrons and leptons we saw that the W boson only couples to left-handed fermions (maximum parity violation) and that the coupling is always the same (universality). Only the Cabibbo rotation causes a small correction in the coupling to the quarks.

If this universality of the weak interaction holds, then all types of fermion-antifermion pairs should be equally likely to be produced in the decay of real W bosons. The colour charges mean that an extra factor of 3 is expected for quark-antiquark production. The production of a t-quark is impossible because of its larger mass. Thus, if we neglect the differences between the fermion masses, a ratio of 1 : 1 : 1 : 3 : 3 is expected for the production of the pairs  $e^+ \nu_e$ ,  $\mu^+ \nu_\mu$ ,  $\tau^+ \nu_\tau$ ,  $u\bar{d}'$ , and  $c\bar{s}'$ , in the decay of the  $W^+$  boson. Here, the states  $\bar{d}'$  and  $\bar{s}'$  are the Cabibbo-rotated eigenstates of the weak interaction.

Because of the process of hadronisation, it is not always possible in an experiment to unequivocally determine the type of quark-antiquark pair into which a W boson decays. Leptonic decay channels can be identified much more easily. According to the above estimate, a decay fraction of 1/9 is expected for each lepton pair. The experimental results are [19]

$$\begin{aligned} W^\pm &\rightarrow e^\pm + \bar{\nu}_e^{(-)} & 10.75 \pm 0.13 \% \\ &\mu^\pm + \bar{\nu}_\mu^{(-)} & 10.57 \pm 0.15 \% \\ &\tau^\pm + \bar{\nu}_\tau^{(-)} & 11.25 \pm 0.20 \% , \end{aligned} \quad (12.8)$$

in very good agreement with our prediction.

**Decays of the Z boson** If the Z boson mediates the weak interaction in the same way as the W boson does, it should also couple with the same strength to all lepton-antilepton pairs and to all quark-antiquark pairs. One therefore should expect a ratio of 1 : 1 : 1 : 1 : 1 : 1 : 3 : 3 : 3 : 3 : 3 for the six leptonic channels and the five hadronic channels which are energetically accessible; i.e., 1/21 for each lepton-antilepton pair, and 1/7 for each quark-antiquark pair.

To determine the branching ratios, the various pairs of charged leptons and hadronic decays must be distinguished with appropriate detectors. The different quark-antiquark channels cannot always be separated. Decays into neutrino-antineutrino pairs cannot be directly detected. In order to measure their contribution, the cross-sections for all other decays are measured, and compared to the total width of the  $Z^0$  boson. Treating the spin dependencies correctly [18], we rewrite the Breit-Wigner formula (9.8) in the form

$$\sigma_{i \rightarrow f}(s) = 12\pi(\hbar c)^2 \cdot \frac{\Gamma_i \cdot \Gamma_f}{(s - M_Z^2 c^4)^2 + M_Z^2 c^4 \Gamma_{\text{tot}}^2}. \quad (12.9)$$

Here,  $\Gamma_i$  is the partial width of the initial channel (the partial width for the decay  $Z^0 \rightarrow e^+e^-$ ) and  $\Gamma_f$  is the partial width of the final channel. The total width of the  $Z^0$  is the sum of the partial widths of all the possible decays into fermion-antifermion pairs:

$$\Gamma_{\text{tot}}(Z^0) = \sum_{\text{all fermions } f} \Gamma(Z^0 \rightarrow f\bar{f}). \quad (12.10)$$

Each final channel thus yields a resonance curve with a maximum at  $\sqrt{s} = M_Z c^2$ , and a total width of  $\Gamma_{\text{tot}}$ . Its height is proportional to the partial width  $\Gamma_f$ . The partial width  $\Gamma_f$  can experimentally be determined from the ratio of the events of the corresponding channel to the total number of all  $Z^0$  events.

Analyses of the experiments at LEP and SLC yield the following branching ratios [19]:

$Z^0 \rightarrow e^+ + e^-$	3.363 ± 0.004 %	
$\mu^+ + \mu^-$	3.366 ± 0.007 %	
$\tau^+ + \tau^-$	3.370 ± 0.008 %	
$\nu_{e,\mu,\tau} + \bar{\nu}_{e,\mu,\tau}$	20.00 ± 0.06 %	
hadrons	69.91 ± 0.06 %	(12.11)

Thus, the probability for a decay into charged leptons is significantly different from the decay probability into neutrinos. The coupling of the  $Z^0$  boson apparently depends on the electric charge. Hence the  $Z^0$  cannot simply be a “neutral W boson” coupling with the same strength to all fermions; rather it mediates a more complicated interaction.

## 12.2 Electroweak Unification

The properties of the  $Z^0$  boson are attractively described in the theory of the *electroweak interaction*. In this framework, developed by Salam and Weinberg, the electromagnetic and weak interactions are understood as two aspects of the same interaction.

**Weak isospin** The electroweak interaction theory can be elegantly described by introducing a new quantum number, the *weak isospin*  $T$ , in analogy to the isospin of the strong interaction. Each family of left-handed quarks and leptons forms a doublet of fermions which can transform into each other by emitting (or absorbing) a  $W$  boson. The electric charges  $z_f \cdot e$  of the two fermions in a doublet always differ by one unit. The weak isospin ascribed to them is  $T = 1/2$ , and the third component is  $T_3 = \pm 1/2$ . For right-handed antifermions, the signs of  $T_3$  and  $z_f$  are inverted. By contrast, right-handed fermions (and left-handed antifermions) do not couple to  $W$  bosons. They are described as singlets ( $T = T_3 = 0$ ). Hence, the left-handed leptons and the (Cabibbo-rotated) left-handed quarks of each family form two doublets and there are additionally three right-handed fermion singlets (Table. 12.1).

**The Weinberg angle** We now continue our description of the weak isospin formalism. One requires conservation of  $T_3$  in reactions with charged currents. The  $W^-$  boson must then be assigned the quantum number  $T_3(W^-) = -1$  and the  $W^+$  boson  $T_3(W^+) = +1$ . A third state should therefore exist with  $T = 1$ ,  $T_3 = 0$ , coupling with the same strength  $g$  as the  $W^\pm$  to the fermion doublets. This state is denoted by  $W^0$ ; and together with the  $W^+$  and the  $W^-$  it forms a weak isospin triplet.

**Table 12.1** Multiplets of the electroweak interaction. The quarks  $d'$ ,  $s'$  and  $b'$  emerge from the mass eigenstates through a generalised Cabibbo rotation (CKM matrix). Weak isospin  $T$  doublets are joined in parentheses. The electric charges of the two states of each doublet always differ by one unit. The sign of the third component  $T_3$  is defined so that the difference  $z_f - T_3$  is constant within each doublet

	Fermion multiplets			$T$	$T_3$	$z_f$
Leptons	$\begin{pmatrix} \nu_e \\ e \end{pmatrix}_L$	$\begin{pmatrix} \nu_\mu \\ \mu \end{pmatrix}_L$	$\begin{pmatrix} \nu_\tau \\ \tau \end{pmatrix}_L$	1/2	+1/2	0
					-1/2	-1
	$e_R$	$\mu_R$	$\tau_R$	0	0	-1
Quarks	$\begin{pmatrix} u \\ d' \end{pmatrix}_L$	$\begin{pmatrix} c \\ s' \end{pmatrix}_L$	$\begin{pmatrix} t \\ b' \end{pmatrix}_L$	1/2	+1/2	+2/3
					-1/2	-1/3
	$u_R$	$c_R$	$t_R$	0	0	+2/3
	$d_R$	$s_R$	$b_R$	0	0	-1/3

The  $W^0$  cannot be identical to the  $Z^0$ , since we saw that the coupling of the latter also depends on the electric charge. One now postulates the existence of an additional state  $B^0$ , a singlet of the weak isospin ( $T = 0, T_3 = 0$ ). Its coupling strength does not have to be equal to that of the triplet ( $W^\pm, W^0$ ). The corresponding weak charge is denoted by  $g'$ . The  $B^0$  and  $W^0$  couple to fermions without changing their weak isospin and hence without changing their type.

Experimentally two neutral vector bosons, the photon and the  $Z^0$ , are indeed known. The basic idea of the electroweak unification is to describe the photon and the  $Z^0$  as mutually orthogonal, linear combinations of the  $B^0$  and the  $W^0$ . This mixing is, analogously to the description of quark mixing in terms of the Cabibbo angle (10.18), expressed as a rotation through the so-called *electroweak mixing angle*  $\theta_W$  (also called the *Weinberg angle*)

$$\begin{aligned} |\gamma\rangle &= \cos\theta_W|B^0\rangle + \sin\theta_W|W^0\rangle \\ |Z^0\rangle &= -\sin\theta_W|B^0\rangle + \cos\theta_W|W^0\rangle. \end{aligned} \quad (12.12)$$

The connection between the Weinberg angle  $\theta_W$ , the weak charges  $g$  and  $g'$  and the electric charge  $e$  is given by demanding that the photon couples to the charges of the left- and right-handed fermions but not to the neutrinos. One so obtains [18]

$$\tan\theta_W = \frac{g'}{g}, \quad \sin\theta_W = \frac{g'}{\sqrt{g^2 + g'^2}}, \quad \cos\theta_W = \frac{g}{\sqrt{g^2 + g'^2}}. \quad (12.13)$$

The electromagnetic charge is given by

$$e = g \cdot \sin\theta_W. \quad (12.14)$$

The Weinberg angle can be determined, for example, from  $\nu$ - $e$  scattering, from electroweak interference in  $e^+e^-$  scattering, from the width of the  $Z^0$ , or from the ratio of the masses of the  $W^\pm$  and the  $Z^0$  [4, 10]. A combined analysis of such experiments gives the result [19]

$$\sin^2\theta_W = 0.23116 \pm 0.00012. \quad (12.15)$$

Hence, the weak coupling constant ( $\alpha_w \propto g \cdot g$ ) is about four times stronger than the electromagnetic one ( $\alpha \propto e \cdot e$ ). It is the propagator term in the matrix element (10.3), which is responsible for the tiny effective strength of the weak interaction at low energies.

This Weinberg mixing somewhat complicates the interaction. The  $W$  boson couples with equal strength to all the quarks and leptons (universality) but always to only left-handed particles and right-handed antiparticles (maximum parity violation). In the coupling of the  $Z$  boson, however, the electric charges of the fundamental fermions play a part as well. The coupling strength of the  $Z^0$  to a



fermion  $f$  is

$$g_Z(f) = \frac{g}{\cos \theta_W} \cdot \hat{g}(f) \quad \text{where} \quad \hat{g}(f) = T_3 - z_f \sin^2 \theta_W, \quad (12.16)$$

and  $z_f$  is the electric charge of the fermion in units of the elementary charge  $e$ .

**The ratio of the masses of the W and Z bosons** The electroweak unification theory could be used to predict the absolute masses of the W and the Z fairly well before their actual discovery. According to (10.4) and (12.14), the electromagnetic coupling constant  $\alpha$ , the Fermi constant  $G_F$  and the mass of the W boson are related by

$$M_W^2 c^4 = \frac{4\pi\alpha}{8 \sin^2 \theta_W} \cdot \frac{\sqrt{2} (\hbar c)^3}{G_F}. \quad (12.17)$$

It is important to realise that in quantum field theory the “constants”  $\alpha$  and  $\sin^2 \theta_W$  are in fact weakly dependent upon the energy range (renormalisation) [11, 13]. For the mass region of (12.17), we have  $\alpha \approx 1/128$  and  $\sin^2 \theta_W \approx 0.231$ . The mass of the Z boson is fixed by the relation

$$\frac{M_W}{M_Z} = \cos \theta_W \approx 0.88. \quad (12.18)$$

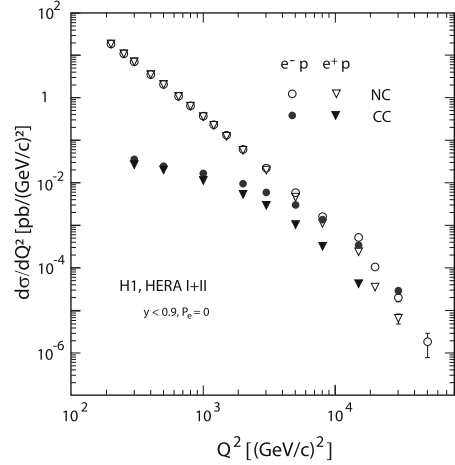
This is in good agreement with the ratio calculated from the experimentally measured masses (12.6) and (12.7):

$$\frac{M_W}{M_Z} = 0.8818 \pm 0.0011. \quad (12.19)$$

The resulting value of  $\sin^2 \theta_W$  is in very good agreement with the results of other experiments. The value given in (12.15) is from the combined analysis of all experiments.

**Neutral and charged currents at large  $Q^2$**  The aspects discussed so far can be illustrated nicely with the  $Q^2$  dependence of cross-sections for neutral currents ( $\sigma_{NC}$ ) and charged currents ( $\sigma_{CC}$ ) in deep-inelastic scattering of electrons and positrons. In Fig. 12.3 we show results of the H1 experiment [2] for those cross-sections as a function of  $Q^2$  in the regime of 200 to  $5 \cdot 10^4$  (GeV/c) $^2$ . For small values of  $Q^2$  the neutral current cross-section is almost a factor 1,000 larger than  $\sigma_{CC}$ . Here the cross-section is dominated by exchange of a virtual photon. This contribution decreases quickly with  $1/Q^4$  and is for electrons and positrons of the same size. The  $Z^0$  exchange becomes significant only for values of  $Q^2$  larger than 3,000 (GeV/c) $^2$ . For larger values of  $Q^2$  electrons have a larger  $\sigma_{NC}$  than positrons. This is caused by the interference of  $Z^0$  and  $\gamma$  exchange, discussed already in Sect. 10.3.

**Fig. 12.3** Differential cross-section  $d\sigma/dQ^2$  for reactions with neutral and charged currents in deep-inelastic  $e^\pm p$  scattering as function of  $Q^2$ , measured by the H1 experiment (see [2])



The cross-section for charged currents  $\sigma_{CC}$  decreases much weaker with  $Q^2$  than  $\sigma_{NC}$ , since the mass term in the propagator  $(Q^2 c^2 + M_W^2 c^4)^{-1}$  dominates over  $Q^2 c^2$ . At  $Q^2 \approx 10^4 (\text{GeV}/c)^2$  the differences between electromagnetic and weak propagator become small and  $\sigma_{NC}$  becomes almost identical to  $\sigma_{CC}$ . As already mentioned in Sect. 10.6,  $\sigma_{CC}^- > \sigma_{CC}^+$ , because  $u(x)$  is larger than  $d(x)$ .

### 12.3 Width of the $Z^0$ and the Number of Neutrinos

A detailed study of the production of  $Z^0$  bosons in electron-positron annihilation delivers a very precise check of the predictions of the standard model of electroweak unification.

The coupling of a  $Z^0$  to a fermion  $f$  is proportional to the quantity  $\hat{g}(f)$  defined in (12.16). The partial width  $\Gamma$  for a decay  $Z^0 \rightarrow f\bar{f}$  is a superposition of two parts, one for each helicity state:

$$\Gamma_f = \Gamma_0 \cdot [\hat{g}_L^2(f) + \hat{g}_R^2(f)], \quad (12.20)$$

where

$$\Gamma_0 = \frac{G_F}{3\pi\sqrt{2}(\hbar c)^3} \cdot M_Z^3 c^6 \approx 663 \text{ MeV}. \quad (12.21)$$

For left-handed neutrinos,  $T_3 = 1/2$ ,  $z_f = 0$ ; hence,

$$\hat{g}_L(\nu) = \frac{1}{2}. \quad (12.22)$$

Right-handed neutrinos would have  $T_3 = z_f = \hat{g}_R = 0$  and would not be subject to the interactions of the standard model. The contribution of each  $\nu\bar{\nu}$  pair to the total width is therefore

$$\Gamma_\nu \approx 165.8 \text{ MeV} . \quad (12.23)$$

The d-, s- and b-quarks have  $T_3 = -1/2$  (left-handed) or  $T_3 = 0$  (right-handed) and  $z_f = -1/3$ . This yields

$$\hat{g}_L(d) = -\frac{1}{2} + \frac{1}{3} \sin^2 \theta_W, \quad \hat{g}_R(d) = \frac{1}{3} \sin^2 \theta_W. \quad (12.24)$$

Recalling that quark-antiquark pairs can be produced in three colour combinations ( $r\bar{r}$ ,  $g\bar{g}$ ,  $b\bar{b}$ ), the total contribution of these quarks is

$$\Gamma_d = \Gamma_s = \Gamma_b = 3 \cdot 122.4 \text{ MeV} . \quad (12.25)$$

Similarly the contribution of the u- and c-quarks is

$$\Gamma_u = \Gamma_c = 3 \cdot 94.9 \text{ MeV} , \quad (12.26)$$

and the contribution of the charged leptons is

$$\Gamma_e = \Gamma_\mu = \Gamma_\tau = 83.3 \text{ MeV} . \quad (12.27)$$

Decays into  $\nu\bar{\nu}$  pairs cannot be directly detected in an experiment, but they manifest themselves in their contributions to the total width. Taking account of the finite masses of the quarks and charged leptons only produces small corrections, as these masses are small compared to the mass of the Z boson.

Including all known quarks and leptons in the calculations, one finds that the total width is 2,418 MeV. After incorporating quantum field theoretical corrections due to higher-order processes (radiative corrections) the width predicted is [17]

$$\Gamma_{\text{tot}}^{\text{theor.}} = (2,497 \pm 6) \text{ MeV} . \quad (12.28)$$

This is in very good agreement with the experimental value (12.7) of

$$\Gamma_{\text{tot}}^{\text{exp.}} = (2,490 \pm 7) \text{ MeV} . \quad (12.29)$$

The proportion of the total number of decays into pairs of charged leptons is equal to the ratio of the widths (12.27) and (12.28)

$$\frac{\Gamma_{e,\mu,\tau}}{\Gamma_{\text{tot}}} = 3.37 \% . \quad (12.30)$$

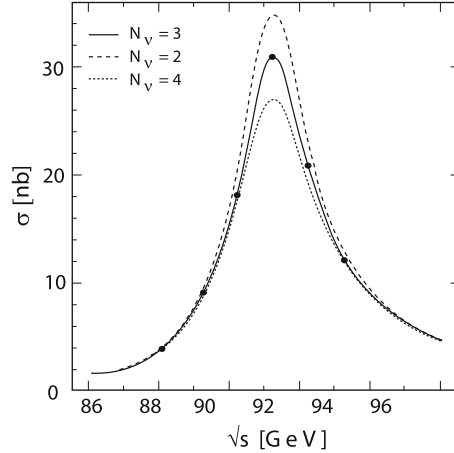


**Fig. 12.4** Cross-section of the reaction  $e^+e^- \rightarrow \text{hadrons}$  close to the  $Z^0$  resonance. The data shown are the results of the OPAL experiment at CERN [9]. According to (12.9) the measured width of the resonance yields the total cross-section. The more types of light leptons exist, the smaller the fraction of the total cross-section that remains for the production of hadrons. The lines show the theoretical predictions, based on the measured width of the resonance, assuming that 2, 3, or 4 massless neutrinos exist

The experimental branching ratios (12.11) are in excellent agreement with this theoretical value.

If a fourth type of light neutrino were to couple to the  $Z^0$  in the same way, then the total width would be larger by 166 MeV. We thus can deduce from the experimental result that exactly three types of *light* neutrinos exist (Fig. 12.4). This may be interpreted as implying that the total number of generations of quarks and leptons is three (and three only).

## 12.4 Symmetry Breaking

Notwithstanding the successes of electroweak unification, the theory is aesthetically flawed: the mixture of states described by the Weinberg rotation (12.12) should only occur for states with similar energies (masses). Yet, the photon is massless and the W and Z bosons have very large masses. Furthermore, in the naive mathematical description of electroweak unification the masses of W and Z bosons turn out to be forbidden. How the W and Z bosons obtain masses and the photon stays massless is a central question in particle physics.

A possible answer is associated with *spontaneous symmetry breaking*, a concept known from the physics of phase transitions. This assumes an asymmetric vacuum ground state. The best-known examples of this idea are the magnetic properties of iron, and the Meissner effect (or Meissner-Ochsenfeld effect) in superconductivity.

In a theoretical model, proposed independently by Englert and Brout [12] and by Higgs [16], the masses of the  $Z^0$  and of the  $W^\pm$  bosons are explained in analogy to the Meissner effect. In this model, so-called Higgs fields are postulated, which – compared to our example – correspond to the ground state of correlated Cooper pairs in superconductivity. At sufficiently high temperatures (or energies) the  $Z^0$  and  $W^\pm$  bosons are massless like the photon. Below the energy of the phase transition, the boson masses are produced by the Higgs fields, just as the “photon mass” is in the Meissner effect.

The masses of the  $Z^0$  and the  $W^\pm$  bosons must be independent of their location and orientation in the universe. Hence, the Higgs fields must be scalars. In the theory of electroweak unification, there are thus four Higgs fields, one for each boson. During the cooling of the system, three *Higgs bosons*, the quanta of the Higgs field, are absorbed by the  $Z^0$  and by the  $W^\pm$ . This generates their masses. Since the photon remains massless there must still be a free Higgs boson.

**Higgs potential and spontaneous symmetry breaking** To illustrate what spontaneous symmetry breaking means in case of the Higgs boson, consider the simple one-dimensional and real case (in the standard model one deals with the two-dimensional complex generalisation). We write the Higgs field as  $\varphi$  and assign it the following potential<sup>2</sup>:

$$V(\varphi) = \mu^2 \varphi^2 + \lambda \varphi^4. \quad (12.31)$$

The quadratic term corresponds in quantum field theory to a mass term  $\frac{1}{2} m_\varphi^2 \varphi^2$ . Like any physical system, the Higgs field attempts to reach the energetically lowest state. In case of positive  $\mu^2$  and  $\lambda$  this is at  $\varphi = 0$ , see Fig. 12.5. The interesting case occurs when  $\lambda > 0$  and  $\mu^2 < 0$ . The quadratic term would now correspond

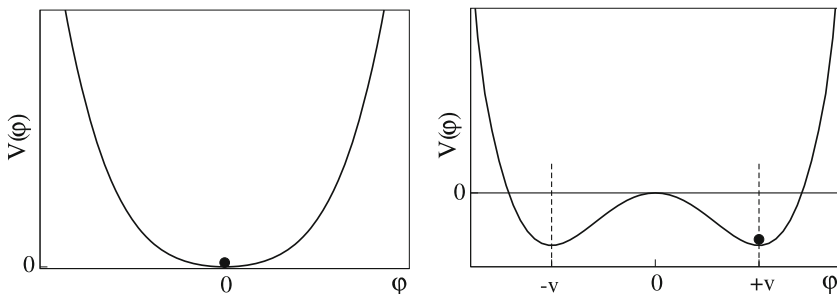


**Fig. 12.5** The potential (12.31) of the Higgs field. The case  $\mu^2 > 0$  and  $\lambda > 0$  (left) implies a minimum for  $\varphi$  at the origin; the corresponding position of  $\varphi$  is indicated by the *black point*. The case  $\mu^2 < 0$  and  $\lambda > 0$  (right) implies a shifted minimum at  $v = \sqrt{-\mu^2/(2\lambda)}$

<sup>2</sup>For the rest of this section we will for simplicity ignore factors of  $c$  and  $\hbar$ , as common in modern literature of high energy physics.

to a negative squared mass which lacks a meaningful physical interpretation. This problem gets resolved when we consider the minimum of the potential, which is given by

$$\varphi_0 \equiv v = \pm \sqrt{\frac{-\mu^2}{2\lambda}}. \quad (12.32)$$

Without loss of generality we can choose the positive sign.<sup>3</sup> The quantity  $v$  is denoted *vacuum expectation value* of the Higgs field. The original potential possesses reflection symmetry, replacing  $\varphi \rightarrow -\varphi$  has no effect. The “ground state” of the system (12.32) does no longer possess this symmetry, the reflection symmetry is “spontaneously broken”. Since in quantum field theory we do not know any exact solutions, we need to do perturbation theory around the minimum. We write therefore

$$\varphi = v + H,$$

with the constant minimum  $v$  and the physical Higgs boson  $H$ . Inserting this expression in the original potential (12.31) yields that terms which are linear in  $H$  disappear, while the quadratic term is given by  $4\lambda v^2 H^2$ . This term is now a positive squared mass  $m_H^2 = 8\lambda v^2$  for the Higgs boson  $H$ .

In case of a complex field  $\phi$  we would replace  $\varphi^2$  in the potential by  $\phi^*\phi$ . The symmetry that is broken when the field enters the minimum  $v$  is now a phase transformation  $\phi \rightarrow e^{i\alpha} \phi$ . Again we develop around the minimum:

$$\phi = v + H + iK.$$

The field  $H$  is again a physical Higgs boson, while  $K$  turns out to be massless: there is no quadratic term when we insert the above term in the original potential. Such a massless scalar particle always appears when a continuous symmetry, such as the one corresponding to a phase transformation, is spontaneously broken. They are called *Goldstone bosons*, sometimes also Nambu Goldstone bosons. Such particles have never been observed in experiments, and seem to pose a problem. However, in theories in which massless gauge bosons are present, the degree of freedom corresponding to the Goldstone boson  $K$  can be absorbed by that massless boson, in case it has the same quantum numbers as the Higgs boson [18]. The number of degrees of freedom of the exchange bosons (i.e., its polarisations) has increased from 2 to 3, which corresponds to a massive boson. Recall that a massless spin-1 boson possesses two transversal polarisation degrees of freedom, while a

---

<sup>3</sup>An analogy is here a knitting needle which we compress with a force along its axis. For sufficiently high pressure the needle will buckle in a bent position. The arbitrary direction in which it bends can be chosen as coordinate axis.

massive spin-1 particle possesses in addition a third, longitudinal one. Therefore, the exchange boson has obtained a mass.

In the standard model one deals with a complex Higgs doublet, containing 4 degrees of freedom. Those correspond to a physical, massive Higgs boson and three massless ones, which get absorbed by the  $W^+$ ,  $W^-$  and  $Z^0$ , thereby providing them with masses.

■ To further illustrate how symmetry breaking can generate a mass, we now consider the analogy of ferromagnetism. Above the Curie temperature, iron is paramagnetic and the spins of the valence electrons are isotropically distributed. No force is required to alter spin orientations. The fields that carry the magnetic interaction may, as far as spatial rotations are concerned, be considered massless. When the temperature drops below the Curie point, a phase transition takes place and iron becomes ferromagnetic. The spins, or the magnetic moments of the valence electrons turn spontaneously to point in a common direction which is not fixed a priori. The space within the ferromagnet is no longer isotropic, rather it has a definite preferred direction. Force must be used to turn the spins away from the preferred direction. Thus the carriers of the magnetic interaction now have a mass as far as rotations are concerned.

The Meissner effect, the absence of external magnetic fields in superconductors, provides an even better analogy to particle production by symmetry breaking. Above the transition temperature of the superconductor, magnetic fields propagate freely within the conductor. With the transition to the superconducting phase, however, they are expelled from the superconductor. They can only penetrate the superconductor at its surface and drop off exponentially inside. An observer within the superconductor could explain this effect by a finite range of the magnetic field in the superconductor. In analogy to the discussion of the Yukawa force (Sect. 17.3) he therefore would ascribe a finite mass to the photon.

Where is the spontaneous symmetry breaking in this process? This is what actually happens in superconductivity: below the critical temperature, Cooper pairs are formed out of the conduction electrons which organise themselves into a correlated state of definite energy: the energy of the superconducting ground state. For an observer within the superconductor, the ground state of the superconductor is the ground state of the vacuum. As the temperature decreases, a current is induced in the superconductor which compensates the external magnetic field and expels it from the superconductor. The correlated Cooper pairs are responsible for this current. Just as in the case of the ferromagnet where the spins are no longer free to choose their orientation, the phase of a Cooper pair is here fixed by the phase of the other Cooper pairs. This effect corresponds to a symmetry breaking of the ground state.

The existence of these Higgs fields is fundamental to the modern interpretation of elementary particle physics. The search for a non-absorbed Higgs boson was the main motivation for the construction of a new accelerator and storage ring at CERN, the *Large Hadron Collider* (LHC). The experimental proof of its existence would be a complete confirmation of the Glashow-Salam-Weinberg theory of electroweak unification. The non-existence of the Higgs bosons, however, would require completely new theoretical concepts. One could compare this situation with that at the end of the nineteenth century, when the existence of the aether had a similar importance for the interpretation of physics. However, the discovery of the Higgs boson in 2012 made the standard model conclusively a consistent theory. Details regarding the search for the Higgs boson are discussed in the next section.

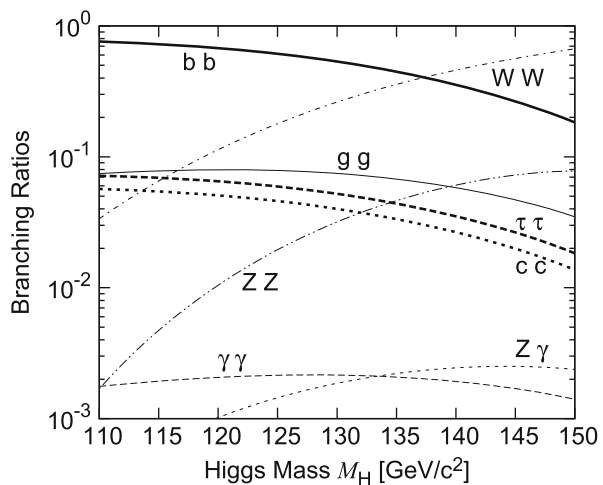
## 12.5 The Higgs Boson

As mentioned above, a consistent interpretation of the masses of the  $W, Z^0$  particles and a massless photon requires the existence of a scalar particle: the Higgs boson  $H$ . It would be the only fundamental scalar particle. Other known spin-0 particles, such as the  $\pi^0$ , are composite objects, made out of fermionic quarks. Furthermore, one can show that the masses of the charged leptons and quarks can be generated by the coupling with the Higgs field to which the Higgs boson is associated [18].  $H$  couples, since it is electrically neutral, to a fermion-antifermion pair, a  $W^+W^-$  pair, or to two  $Z^0$ . For all particles  $x$  with mass  $m_x$  holds that the coupling to the Higgs boson is proportional to  $m_x$ . Therefore electrons and the light up and down quarks couple only very weakly to  $H$ , which makes its production at collider experiments rather difficult. For many years the Higgs boson was the last missing piece of the standard model.

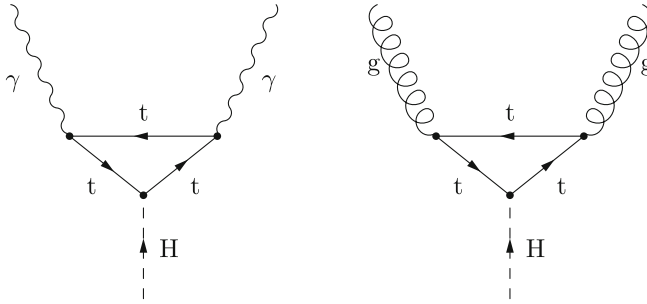
For the case that the Higgs boson  $H$  exists, one knew indirect theoretical upper and lower limits of about  $10^3$  and  $10^2 \text{ GeV}/c^2$  on its mass. These limits depend in a complicated way on other parameters such as the masses of the  $W$  or the top quark, and are strong tests for the consistency of the standard model. However, except for its mass all properties and couplings of the Higgs boson are predicted by the theory, and one can calculate its total width and its branching ratios in standard model particles. The total width of  $H$  in its interesting mass regime is of the order of a few MeV, corresponding to lifetimes of order  $10^{-23}$  s. Experimental searches for the Higgs boson are thus very difficult.

Figure 12.6 shows the branching ratios as a function of the Higgs boson mass  $M_H$ . One should note that the decay  $H \rightarrow \gamma\gamma$  is given, even though the photon should not couple to the Higgs boson because it is massless. The decay into two photons can however occur indirectly via a pair of top quark and antiquark, see

**Fig. 12.6** Branching ratios in fermions and vector bosons of the Higgs boson  $H$  as function of its mass







**Fig. 12.7** Decays of the Higgs boson H in two photons and gluons, respectively. By inverting the direction of the right process we obtain gluon fusion as a possible production mechanism of the Higgs boson in hadron accelerators

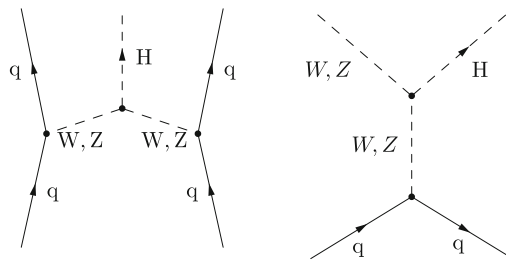


**Fig. 12.8** Important Feynman diagrams for the production of Higgs bosons at accelerators: Vector boson fusion (*left*) and with W or Z associated production or Higgs-strahlung (*right*). We can translate the diagrams also to electron-positron accelerators, if we replace the incoming quarks as  $e^-$  or  $e^+$ , and the outgoing quarks as  $e^\pm$  or neutrinos

Fig. 12.7. Such processes of higher order are usually strongly suppressed. In this case the suppression is compensated by the large coupling of the Higgs-boson with the top quark. The decay channel  $H \rightarrow \gamma\gamma$  is, as we will later see, very important. A similar looking decay channel,  $H \rightarrow gg$  exists as well. Here the photons in the diagram are replaced by gluons. By inverting the direction of this decay we end up with a possible production channel for the Higgs boson:  $gg \rightarrow H$ . Here two gluons from two colliding protons or a proton and an antiproton fuse to a Higgs boson (*Gluon fusion*).

**Higgs production in electron-positron annihilation** Direct searches were first performed at LEP. The reaction  $e^+ e^- \rightarrow H$  is not realistic because of the tiny coupling of electrons with the Higgs-boson. Therefore one searched for the reaction

$$e^+ e^- \rightarrow Z \rightarrow ZH \tag{12.33}$$

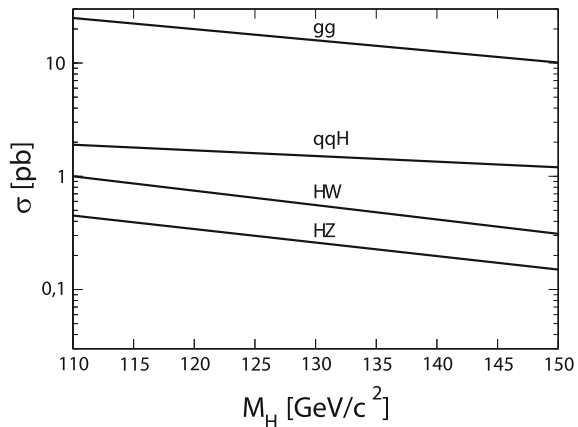
(with the *Z associated production*), see Fig. 12.8. The analogy to bremsstrahlung has led to the name *Higgs-Strahlung* for this process. The known decays of the

(depending on centre-of-mass energy and Higgs mass) real or virtual  $Z$  and the postulated decays of the Higgs boson as a function of its mass allow this search. One mainly investigated the channels  $H \rightarrow b\bar{b}$  and  $H \rightarrow \tau^+\tau^-$ , in which the  $Z^0$  additionally decays into two quarks or leptons. Since those decays were not observed, a lower limit of  $M_H > 114.4 \text{ GeV}/c^2$  at 95 % confidence level was set.

**Higgs production in proton-antiproton reactions** At the Tevatron the most important production processes are the already mentioned gluon fusion, the associated  $W$  or  $Z$  production and *vector boson fusion*, which is also displayed in Fig. 12.8. An important channel was, e.g. the detection of a  $b\bar{b}$  pair from  $H \rightarrow b\bar{b}$  in connection to associated production with identification of the  $W$  or  $Z$ . The decay  $H \rightarrow WW$  after gluon fusion and associated production is also of interest. Gluon fusion followed by  $H \rightarrow b\bar{b}$  is overwhelmed with background from  $b\bar{b}$  pair production in the  $p\bar{p}$  collisions. A Higgs boson with a mass between 147 and 180  $\text{GeV}/c^2$  could be ruled out in this way.

**Higgs production in proton-proton reactions at LHC** The start of the Large Hadron Collider brought the long awaited breakthrough. The LHC is a proton-proton storage ring with a final centre-of-mass energy of  $\sqrt{s} = 14 \text{ TeV}$  and a planned luminosity of  $10^{34} \text{ cm}^{-2} \text{ s}^{-1}$ . Initial technical difficulties lead in the years 2010–2012 to a reduced centre-of-mass energy of  $\sqrt{s} = 7 \text{ TeV}$ , later followed by  $\sqrt{s} = 8 \text{ TeV}$ . Two large experiments are here important [14], *ATLAS* (A Toroidal LHC Apparatus) and *CMS* (Compact Muon Solenoid). Since two protons instead of proton and antiproton collide, and since the available centre-of-mass energy is higher than at the Tevatron, the relative contributions of the production processes changes. Gluon fusion has now the largest cross-section, followed by vector boson fusion and associated production, see Fig. 12.9. The decay  $H \rightarrow b\bar{b}$  is for all production channels covered by  $b\bar{b}$  pair production. Interesting decay channels are now  $H \rightarrow WW$ ,  $H \rightarrow ZZ$  and  $H \rightarrow \gamma\gamma$ . The branching ratio into two photons is only about 0.002, however, the detectors are very sensitive to such a signal.

**Fig. 12.9** Production of a Higgs boson  $H$  in  $pp$  collisions at a centre-of-mass energy of  $\sqrt{s} = 8 \text{ TeV}$  as function of its mass: Shown are (from top to bottom) gluon fusion, vector boson fusion, and with  $W$  or  $Z$  associated production



The invariant mass of both photons is a clear evidence for a resonantly produced particle. In all studied channels events were found which can be explained by a Higgs particle. The results of the analyses in summer 2012 are

$$M_H = (126.0 \pm 0.4 \text{ (stat.)} \pm 0.4 \text{ (sys.)}) \text{ GeV}/c^2 \text{ (ATLAS [20])}$$

$$M_H = (125.3 \pm 0.4 \text{ (stat.)} \pm 0.5 \text{ (sys.)}) \text{ GeV}/c^2 \text{ (CMS [21])} ,$$

where we have given statistical and systematical uncertainty. Figure 12.10 shows the result of a follow-up analysis focusing on some channels, including the decay into two photons. The width of the resonance corresponds to the resolution of the detector, and not to the actual width of the Higgs particle. There are hints that the new particle also decays into  $\tau^+\tau^-$  and  $b\bar{b}$  pairs. The complete reconstruction of all decay channels, and thus the absolutely certain confirmation that the new particle is the Higgs boson of the standard model, will be difficult because its couplings are proportional to the masses of the standard model particles. A Higgs mass of  $M_H = 126 \text{ GeV}/c^2$  corresponds to a decay width of  $4.2 \text{ MeV}$ , or a lifetime of  $1.6 \times 10^{-23} \text{ s}$ . The total cross-section for Higgs production at  $\sqrt{s} = 8 \text{ TeV}$  is about  $22 \text{ pb}$ , i.e., nine orders of magnitude below the total  $pp \rightarrow X$  cross-section at this energy!

Both measured values for  $M_H$  agree within the uncertainties. In addition, when the mass is determined for the individual decay channels the results agree as well.

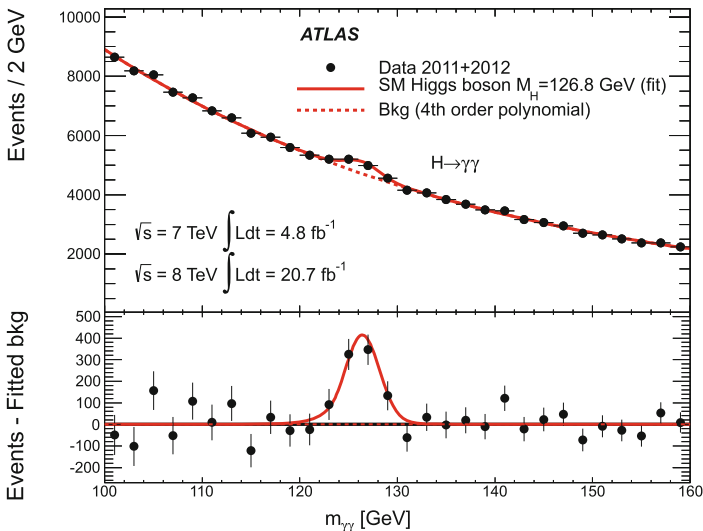


**Fig. 12.10** Invariant-mass spectrum of diphoton candidates after combining data at centre-of-mass energies of 7 and 8 TeV. The expected background (fitted as a fourth order polynomial) is given as a *dashed line*, the observation as a *solid line*. The *lower plot* shows the observed events minus the expected background. The peak corresponds to the Higgs boson decaying into 2 photons. The result of this analysis is  $M_H = 126.8 \text{ GeV}/c^2$  (From [1], ATLAS Experiment © 2013 CERN)

The identification of this new elementary particle, which behaves so far as the postulated Higgs boson, is a grand triumph of particle physics, and is a spectacular confirmation of the theoretical ideas.

## 12.6 Grand Unification

One can extend further the idea of unification and try to combine also the strong interaction with the weak and electromagnetic ones. The *Grand Unification Theory* (GUT) unifies in the spirit of the electroweak interaction the three interactions (strong, weak, electromagnetic) as well as quarks and leptons. The grand unification occurs at very high energies ( $10^{16}$  GeV). This means that at such an energy no differences between fermions, quarks and leptons exist, and that all interactions are of equal strength.

**Cosmology** Modern cosmological models use the ideas of unification and symmetry breaking. They assume that at some stage also gravity can be unified with the other interactions. Today's picture is that the universe – consisting of a very dense initial state of primordial particles with some primordial interaction – cooled down after the big bang and underwent a number of phase transitions. At each phase transition the primordial elementary particles and their interactions differentiated, ending finally with the interactions of the standard model.

## Problem

### 1. Number of neutrino generations

At the LEP storage ring at CERN  $Z^0$ -bosons are produced in electron-positron annihilations at a centre-of-mass energy of about 91 GeV before decaying into fermions:  $e^+e^- \rightarrow Z^0 \rightarrow f\bar{f}$ . Use the following measurements from the OPAL experiment to verify the statement that there are exactly three sorts of light neutrinos (with  $m_\nu < m_{Z^0}/2$ ). The measurement of the resonance curve (12.9) yielded:  $\sigma_{\text{had}}^{\text{max}} = 41.45 \pm 0.31$  nb,  $\Gamma_{\text{had}} = 1,738 \pm 12$  MeV,  $\Gamma_\ell = 83.27 \pm 0.50$  MeV,  $M_Z = 91.182 \pm 0.009$  GeV/ $c^2$ . All quark final states are here combined into a single width  $\Gamma_{\text{had}}$  and  $\Gamma_\ell$  is the decay width of the  $Z^0$  into (single) charged leptons. Derive a formula for the number of neutrino species  $N_\nu$  and use the ratio  $\Gamma_\ell/\Gamma_\nu$  from the text to calculate  $N_\nu$ . Estimate the error in  $N_\nu$  from the experimental errors.

## References

1. G. Aad et al., Phys. Lett. **B726**, 88 (2013)
2. F.D. Aaron et al., JHEP **1209**, 061 (2012)
3. V.M. Abazov et al., Phys. Rev. Lett. **108**, 151804 (2012)
4. U. Amaldi et al., Phys. Rev. **D36**, 1385 (1987)
5. R. Ansari et al., Phys. Lett. **B186**, 440 (1987)
6. G. Arnison et al., Phys. Lett. **B122**, 103 (1983); Phys. Lett. **B126**, 398 (1983); Phys. Lett. **B166**, 484 (1986)
7. P. Bagnaia et al., Phys. Lett. **B129**, 130 (1983)
8. M. Banner et al., Phys. Lett. **B122**, 476 (1983)
9. H. Burkhardt, J. Steinberger, Annu. Rev. Nucl. Part. Sci. **41**, 55 (1991)
10. G. Costa et al., Nucl. Phys. **B297**, 244 (1988)
11. J. Ellis et al., Annu. Rev. Nucl. Part. Sci. **32**, 443 (1982)
12. F. Englert, R. Brout, Phys. Rev. Lett. **13**, 321 (1964)
13. S. Fanchiotti, A. Sirlin, Phys. Rev. **D41**, (1990) 319
14. D. Froidevaux, P. Sphicas, Annu. Rev. Nucl. Part. Sci. **56**, 375 (2006)
15. P.D. Granis, M.J. Shochet, Annu. Rev. Nucl. Part. Sci. **63**, 467 (2013)
16. P.W. Higgs, Phys. Rev. Lett. **13**, 508 (1964)
17. P. Langacker, in *Precision Tests of the Standard Electroweak Model*, ed. by P. Langacker (World Scientific, Singapur, 1995)
18. O. Nachtmann, *Elementary Particle Physics: Concepts and Phenomena* (Springer, Berlin/Heidelberg/New York, 1990)
19. Particle Data Group, J. Beringer et al., *Review of Particle Properties*. Phys. Rev. D **86**, 010001 (2012)
20. The ATLAS collaboration, Phys. Lett. **B716**, 1 (2012)
21. The CMS collaboration, Phys. Lett. **B716**, 30 (2012)

# Chapter 13

## The Standard Model

*Se non è vero, è ben trovato.*

Giordano Bruno  
Gli eroici furori

*Die Wissenschaft hat ewig Grenzen,  
aber keine ewigen Grenzen.*

P. du Bois-Reymond  
Über die Grenzen  
des Naturerkennens

The *standard model* of elementary particle physics comprises the unified theory of the electroweak interaction and quantum chromodynamics. In the following, we will once more summarise what we have learnt in previous chapters about the different particles and interactions.

- As well as gravitation, we know of three elementary interactions which have very similar structures. Each of them is mediated by the exchange of vector bosons.

Interaction	Couples to	Exchange particle(s)	Mass (GeV/c <sup>2</sup> )	J <sup>P</sup>
Strong	Colour charge	8 gluons (g)	0	1 <sup>−</sup>
Electromagnetic	Electric charge	Photon (γ)	0	1 <sup>−</sup>
Weak	Weak charge	W <sup>±</sup> , Z <sup>0</sup>	≈10 <sup>2</sup>	1

Gluons carry colour and therefore interact with each other. The bosons of the weak interaction themselves carry weak charge and couple with each other as well.

- As well as the exchange bosons, the known fundamental particles are the quarks and the leptons. They are fermions with spin-1/2. They are grouped, according to their masses, into three “families”, or “generations”.

Fermions	Family			Electr. charge	Colour	Weak Isospin		Spin
	1	2	3			Left-hd.	Right-hd.	
Leptons	$\nu_e$	$\nu_\mu$	$\nu_\tau$	0	—	1/2	—	1/2
	e	$\mu$	$\tau$	−1		0		
Quarks	u	c	t	+2/3	r, b, g	1/2	0	1/2
	d	s	b	−1/3			0	

Each fermion has an associated antifermion. It has the same mass as the fermion, but opposite electric charge, colour and third component of weak isospin.

From the measured width of the  $Z^0$  resonance, one can deduce that no further (fourth) light neutrino exists. Thus, the existence of a fourth generation of fermions (at least one with a light neutrino) can be excluded.

- In the standard model neutrinos are predicted as massless. The observation of neutrino oscillations, however, showed that they have to possess a mass (see Chap. 11). The resulting lepton mixing can be described in analogy to the mixing in the quark sector without having to give up the standard model.
- Quarks can change their flavour. They prefer transitions within one family, transitions from the first to the second family are suppressed by one order of magnitude, from the first to the third by two. Transitions of leptons do not display such a hierarchy, but are almost generation independent.
- The consistency of the standard model necessitates the existence of a neutral spin-0 particle, which couples to the other elementary particles with strength proportional to their masses. This *Higgs particle* seems to have been detected, having a mass of  $126 \text{ GeV}/c^2$ .
- The range of the electromagnetic interaction is infinite since photons are massless. Because of the large mass of the exchange bosons of the weak interaction, its range is limited to  $10^{-3} \text{ fm}$ . Gluons have zero rest mass. Yet, the effective range of the strong interaction is limited by the mutual interaction of the gluons. The energy of the colour field increases with increasing distance. At distances  $\gtrsim 1 \text{ fm}$ , it is sufficiently large to produce real quark-antiquark pairs. “Free” particles always have to be colour neutral.
- The electromagnetic interaction and the weak interaction can be interpreted as two aspects of a single interaction: the electroweak interaction. The corresponding charges are related by the Weinberg angle, cf. (12.14).
- Different conservation laws apply to the different interactions:
  - In all three interactions, energy ( $E$ ), momentum ( $\mathbf{p}$ ), angular momentum ( $\mathbf{L}$ ), charge ( $Q$ ), colour, baryon number ( $B$ ) and the lepton number  $L$  are conserved.
  - The  $P$  and  $C$  parities are conserved in the strong and in the electromagnetic interaction; but not in the weak interaction. For the charged current of the weak interaction, parity violation is maximal. The charged current only couples to left-handed fermions and right-handed antifermions. The neutral weak current is partly parity violating. It couples to left-handed and right-handed fermions

and antifermions, but with different strengths. The combined CP parity is not conserved in weak interactions.

- Only the charged current of the weak interaction transforms one type of quark into another type (quarks of a different flavour) and one type of lepton into another. Thus, the quantum numbers determining the quark flavour (third component of isospin ( $I_3$ ), strangeness ( $S$ ), charm ( $C$ ) etc.) are conserved in all other interactions.
- The magnitude of the isospin ( $I$ ) is conserved in strong interactions.

The allowed transitions within lepton families are shown in Fig. 13.1. The transitions are shown between the leptonic weak interaction eigenstates and also between leptonic mass operator eigenstates. The corresponding quark family transitions are shown in Fig. 13.2. Here the transitions between the quark eigenstates of the weak interaction are shown, as are those between quark flavours. These pictures are

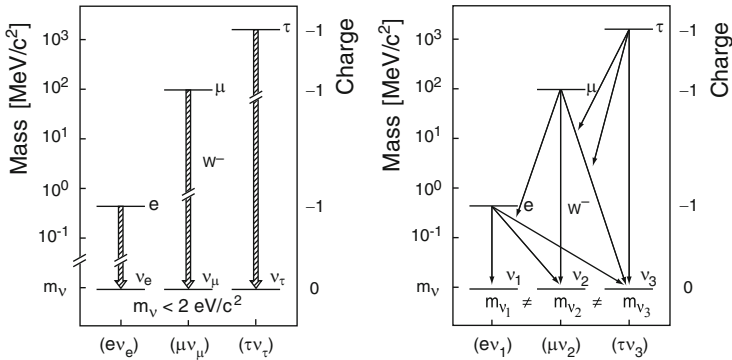


**Fig. 13.1** Transitions between lepton states via charged currents. On the *left* for leptonic weak interaction eigenstates, on the *right* for mass operator eigenstates

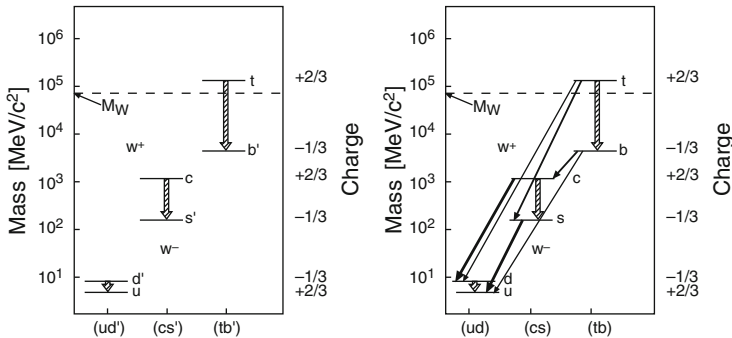


**Fig. 13.2** Transitions between quark states via charged currents. On the *left* quark weak interaction eigenstates, on the *right*, mass operator eigenstates. The strength of the coupling is reflected in the width of the *arrows*. The mass of the t-quark is so large, that it decays by emission of a *real*  $W^+$  boson



perhaps the forerunner of a new type of spectroscopy, more elementary than the atomic, nuclear or hadronic spectroscopies.

In summary, experiments are in astoundingly good quantitative agreement with the assumptions of the standard model. These include the grouping of the fermions into left-handed doublets and right-handed singlets of weak isospin, the strength of the coupling of the  $Z^0$  to left-handed and right-handed fermions, the three-fold nature of the quark families because of colour and the ratio of the masses of the  $W^\pm$  and  $Z^0$ . We thus possess a self-contained picture of the fundamental building blocks of matter and of their interactions.

And yet today's standard model is unsatisfactory in many respects. A large number of free parameters remain: 3 coupling constants for the interactions, 6 quark masses, 3 masses of charged leptons, 4 parameters in the CKM mixing matrix and 2 parameters that describe the properties of the Higgs boson. If one includes neutrino masses, 3 neutrino masses and 4 (or 6) parameters in the PMNS matrix are added. Those parameters do not follow from the standard model, but have to be determined experimentally. In addition, effects and observations which cannot be explained in the standard model at all are present: for instance, dark energy or dark matter, both of which dominate the evolution and the structure of the universe.

Many questions are still completely open. Why do exactly three families of fermions exist? Is it a coincidence that within every family the fermions which carry more charge (strong, electromagnetic, weak) have larger masses? Are baryon number and lepton number strictly conserved? What is the origin of CP violation? What is the origin of the mixture of lepton families, described by the Pontecorvo-Maki-Nakagawa-Sakata matrix? What is the origin of the mixture of quark families, described by the Cabibbo-Kobayashi-Maskawa matrix? What is the origin of small neutrino masses? Why are there just four interactions? What determines the magnitudes of the coupling constants of the different interactions? Is it possible to unify the strong and electroweak interactions, as one has unified the electromagnetic and weak interactions? Will it be possible to include gravitation in a complete unification?

Such questions reflect the experience physicists have gained in analysing the building blocks of matter. On their journey from solid bodies to quarks via molecules, atoms, nuclei, and hadrons, they have constantly found new, fundamental particles. The question "Why?" implicitly assumes that more fundamental reasons exist for observed phenomena – new experiments are the only way to check this assumption.

*Nature has always looked like a horrible mess, but as we go along we see patterns and put theories together; a certain clarity comes and things get simpler.*

Richard P. Feynman [1]

**Reference**

1. R.P. Feynman, *QED – The Strange Theory of Light and Matter* (Princeton University Press, Princeton, 1985)

# **Part II**

## **Synthesis:**

### **Composite Systems**

*Naturam expelles furca, tamen usque recurret.*

Horace, epist. I,XX

# Chapter 14

## Quarkonia

*Analogy is perhaps the physicist's most powerful conceptual tool for understanding new phenomena or opening new areas of investigation. Early in this century, for example, Ernest Rutherford and Niels Bohr conceived the atom as a miniature solar system in which electrons circle the nucleus as planets circle the Sun.*

V. L. Telegdi [9]

In the second part of this book we are going to consider hadronic bound-states. We will at first discuss the properties of mesons and baryons and subsequently details of the structure of atomic nuclei. The simplest example are heavy quark-antiquark ( $c\bar{c}$  and  $b\bar{b}$ ) pairs, which are known as *quarkonia*. Due to the large quark masses they may be approximately treated in a non-relativistic manner. The *hydrogen atom* and *positronium* will serve as electromagnetic analogues.

### 14.1 The Hydrogen Atom and Positronium Analogues

The simplest atomic bound-state is the hydrogen atom, which is composed of a proton and an electron. To a first approximation the bound-states and energy levels may be calculated from the non-relativistic Schrödinger equation. The static Coulomb potential  $V_C \propto 1/r$  is then incorporated into the Hamiltonian

$$\left( -\frac{\hbar^2}{2m} \Delta - \frac{\alpha \hbar c}{r} \right) \psi(\mathbf{r}) = E \psi(\mathbf{r}). \quad (14.1)$$

The eigenstates are characterised by the number of nodes  $N$  in the radial wave functions and the orbital angular momentum  $\ell$ . For the particular case of the Coulomb potential, states with identical  $n = N + \ell + 1$  are degenerate and  $n$  is therefore called the *principal quantum number*. The allowed energy levels  $E_n$  are found to be

$$E_n = -\frac{\alpha^2 m c^2}{2n^2}, \quad (14.2)$$

where  $\alpha$  is the electromagnetic coupling constant and  $m$  is the reduced mass of the system:

$$m = \frac{M_p m_e}{M_p + m_e} \approx m_e = 0.511 \text{ MeV}/c^2. \tag{14.3}$$

The binding energy of the hydrogen ground state ( $n = 1$ ) is  $E_1 = -13.6 \text{ eV}$ . The Bohr radius  $r_b$  is given by

$$r_b = \frac{\hbar \cdot c}{\alpha \cdot m c^2} \approx \frac{197 \text{ MeV} \cdot \text{fm}}{137^{-1} \cdot 0.511 \text{ MeV}} = 0.53 \cdot 10^5 \text{ fm}. \tag{14.4}$$

The spin-orbit interaction (“fine structure”) and the spin-spin-interaction (“hyperfine structure”) split the degeneracy of the principal energy levels as is shown in Fig. 14.1. These corrections to the general  $1/n^2$  behaviour of the energy levels are, however, very small. The fine structure correction is of order  $\alpha^2$  while that of the hyperfine structure is of order  $\alpha^2 \cdot \mu_p/\mu_e$ . The ratio of the hyperfine splitting of the  $1s_{1/2}$  level to the gap between the  $n = 1$  and  $n = 2$  principal energy levels is therefore merely  $E_{\text{HFS}}/E_n \approx 5 \cdot 10^{-7}$ . Here we employ the notation  $n\ell_j$  for states when fine structure effects are taken into account. The orbital angular momenta quantum numbers  $\ell = 0, 1, 2, 3$  are then denoted by the letters s, p, d, f. The quantum number  $j$  is the total angular momentum of the electron,  $\mathbf{j} = \mathbf{\ell} + \mathbf{s}$ . A fourth quantum number  $f$  is used to describe the hyperfine effects (see Fig. 14.1 left). This describes the total angular momentum of the atom,  $\mathbf{f} = \mathbf{j} + \mathbf{i}$ , with the proton’s spin  $\mathbf{i}$  included.

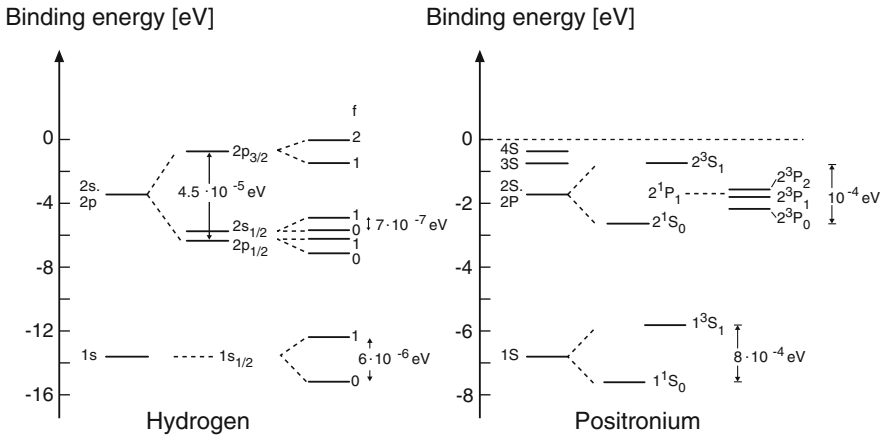


**Fig. 14.1** The energy levels of the hydrogen atom and of positronium. The ground states ( $n = 1$ ) and the first excited states ( $n = 2$ ) are shown together with their fine and hyperfine splitting. The shown splitting is not to scale

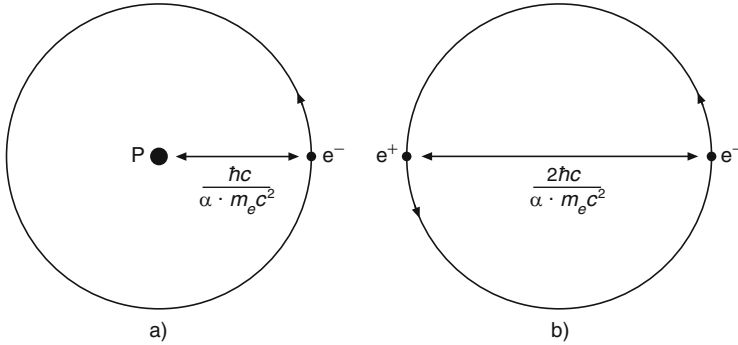


**Fig. 14.2** The first Bohr orbits of the hydrogen atom (a) and positronium (b) (From [6]). The Bohr radius describes the average separation of the two bound particles

The energy states of positronium, the bound  $e^+e^-$  system, can be found in an analogous way to the above. The main differences are that the reduced mass ( $m = m_e/2$ ) is only half the value of the hydrogen case and the spin-spin coupling is much larger than before, since the electron magnetic moment is roughly 650 times larger than that of the proton. The smaller reduced mass means that the binding energies of the bound states are only half the size of those of the hydrogen atom while the Bohr radius is twice its previous value (Fig. 14.2). The stronger spin-spin coupling now means that the positronium spectrum does not display the clear hierarchy of fine and hyperfine structure effects that we know from the hydrogen atom. The spin-orbit and spin-spin forces are of a similar size (Fig. 14.1).

Thus for positronium the total spin  $S$  and the total angular momentum  $J$  as well as the principal quantum number  $n$  and the orbital angular momentum  $L$  are the useful quantum numbers.  $S$  can take on the values 0 (singlet) and 1 (triplet), and  $J$  obeys the triangle inequality,  $|L - S| \leq J \leq L + S$ . The notation  $n^{2S+1}L_J$  is commonly employed, where the orbital angular momentum  $L$  is represented by the capital letters (S, P, D, F). Thus  $2^3P_1$  signifies a positronium state with  $n = 2$  and  $S = L = J = 1$ .

Since electrons and positrons annihilate, positronium has a finite lifetime. It primarily decays into two or three photons, depending upon whether the total spin is 0 or 1. The decay width for the two-photon decay of the  $1^1S_0$  state is found to be [6]

$$\Gamma(1^1S_0 \rightarrow 2\gamma) = \frac{4\pi\alpha^2\hbar^3}{m_e^2c} |\psi(0)|^2. \quad (14.5)$$

Note that  $|\psi(0)|^2$  is the square of the wave function at the origin, i.e. the probability that  $e^+$  and  $e^-$  meet at a point. Equation (14.5) yields a lifetime of  $\approx 10^{-10}$  s.

The potential and the coupling constant of the electromagnetic interaction are very well known, and electromagnetic transitions in positronium as well as its lifetime can be calculated to high precision and excellent agreement with experiment is found. Quarkonia, i.e., systems built up of strongly interacting heavy quark-antiquark pairs, can be investigated in an analogous manner. The effective potential and the coupling strength of the strong interaction can thus be determined from the experimental spectrum and transition strengths between the various states.

## 14.2 Charmonium

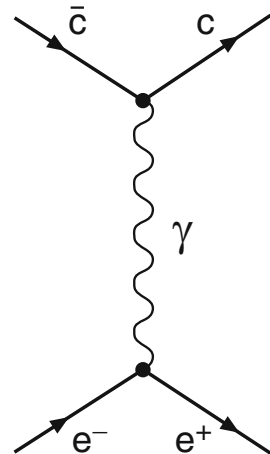
Bound states of  $c$ - and  $\bar{c}$ -quarks are, in analogy to positronium, called *charmonium*. For historical reasons a somewhat different nomenclature is employed for charmonium states than is used for positronium. The first number is  $n_{q\bar{q}} = N + 1$ , where  $N$  is the number of nodes in the radial wave function, while for positronium the atomic convention, according to which the principal quantum number is defined as  $n_{\text{atom}} = N + \ell + 1$ , is used.

$c\bar{c}$  pairs are most easily produced in the decay of virtual photons generated in  $e^+e^-$  collisions (Fig. 14.3) with a centre-of-mass energy of around 3–4.5 GeV

$$e^+ + e^- \rightarrow \gamma \rightarrow c\bar{c}.$$

Various resonances may be detected by varying the beam energy and looking for peaks in the cross-section. These are then ascribed to the various charmonium states (Fig. 14.4). Because of the intermediate virtual photon, only  $c\bar{c}$  states with the quantum numbers of a photon, ( $J^P = 1^-$ ), can be created in this way. The lowest state with such quantum numbers is the  $1^3S_1$ , which is called the  $J/\psi$  (see p. 132)

**Fig. 14.3** Production of  $c\bar{c}$  pairs in  $e^+e^-$  collisions



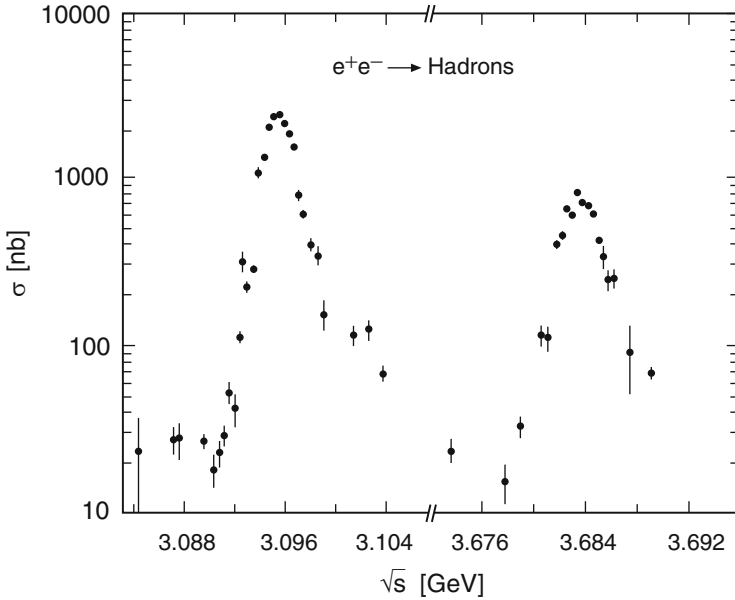


**Fig. 14.4** The cross-section of the reaction  $e^+e^- \rightarrow \text{hadrons}$ , plotted against the centre-of-mass energy in two different intervals each of 25 MeV. The two peaks which are both 100 times larger than the continuum represent the lowest charmonium states with  $J^P = 1^-$  (the  $J/\psi$  ( $1^3S_1$ ) and the  $\psi$  ( $2^3S_1$ )). That the experimental width of these resonances is a few MeV is a consequence of the detector's resolution: widths of 87 and 286 keV respectively may be extracted from the lifetimes of the resonances. The results shown are early data from the  $e^+e^-$  ring SPEAR at Stanford [1]

and has a mass of  $3.097 \text{ GeV}/c^2$ . Higher resonances with masses up to  $4.4 \text{ GeV}/c^2$  have been detected.

Charmonium states only have a finite lifetime. They predominantly decay via the strong interaction into hadrons. Excited states can, however, by the emission of a photon, decay into lower energy states, just as in atomic physics or for positronium. The emitted photons may be measured with a detector that covers the entire solid angle around the  $e^+e^-$  interaction zone ( $4\pi$  detectors). *Crystal balls*, which are composed of spherically arranged scintillators (NaI crystals) are particularly well suited to this task (Fig. 14.5).

If one generates, say, the excited charmonium  $\psi$  ( $2^3S_1$ ) state one then may measure the photon spectrum shown in Fig. 14.6, in which various sharp lines are clearly visible. The photon energy is between 100 and 700 MeV. The stronger lines are electric dipole transitions which obey the selection rules,  $\Delta L = 1$  and  $\Delta S = 0$ . Intermediate states with total angular momentum 0, 1 or 2 and positive parity must therefore be created in such decays. The parity of the spatial wave function is just  $(-1)^L$ , where  $L$  is the orbital angular momentum. Furthermore from the Dirac theory fermions and antifermions have opposite intrinsic parity. Thus the parity of  $q\bar{q}$  states is generally  $(-1)^{L+1}$ . Armed with this information we can reconstruct the diagram



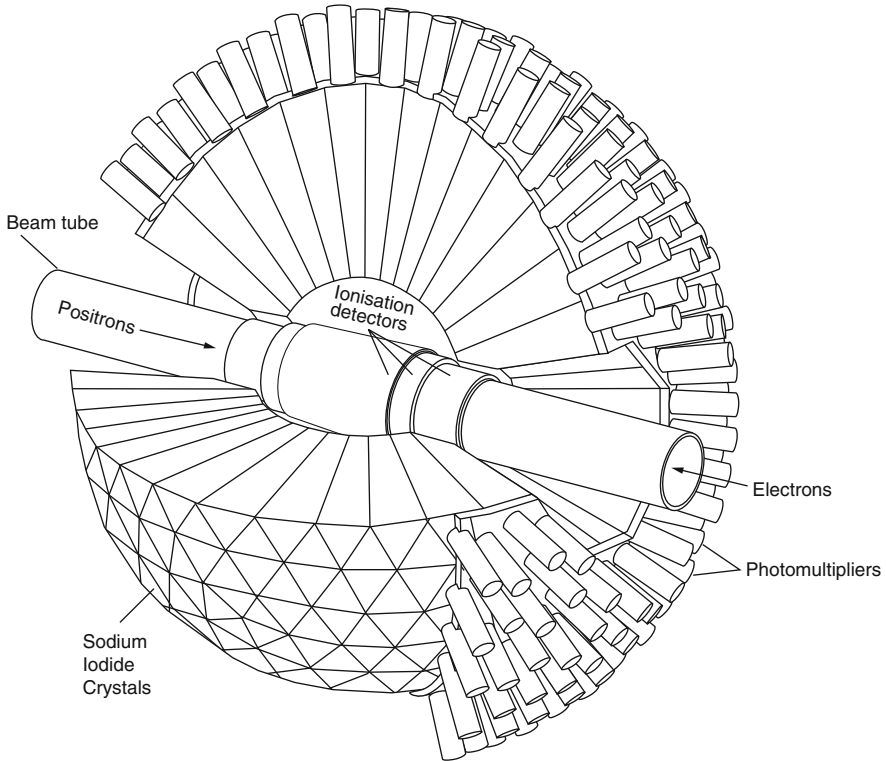


**Fig. 14.5** A (crystal ball) detector built out of spherically arranged NaI crystals. High energy photons from electromagnetic  $c\bar{c}$  transitions are absorbed by the crystals. This creates a shower of electron-positron pairs which generate many low energy, visible photons. These are then detected by photomultipliers attached to the rear of the crystals. The current measured from the photomultipliers is proportional to the energy of the initial photon (From [3])

in Fig. 14.6. We see that after the  $\psi$  ( $2^3S_1$ ) state is generated it primarily decays into the  $1^3P_J$  charmonium triplet system which is known as  $\chi_c$ . These  $\chi_c$  states then decay into  $J/\psi$ 's. The spin-0 charmonium states ( $n^1S_0$ ), which are called  $\eta_c$ , and cannot be produced in  $e^+e^-$  collisions, are only produced in magnetic dipole transitions from  $J/\psi$  or  $\psi$  ( $2^3S_1$ ). These obey the selection rules  $\Delta L = 0$  and  $\Delta S = 1$  and thus connect states with the same parity. They correspond to a spin flip of one of the  $c$ -quarks. Magnetic dipole transitions are weaker than electric dipole transitions. They are, however, observed in charmonium, since the spin-spin interaction for  $c\bar{c}$  states is significantly stronger than in atomic systems. This is due to the much smaller separation between the partners compared to atomic systems.

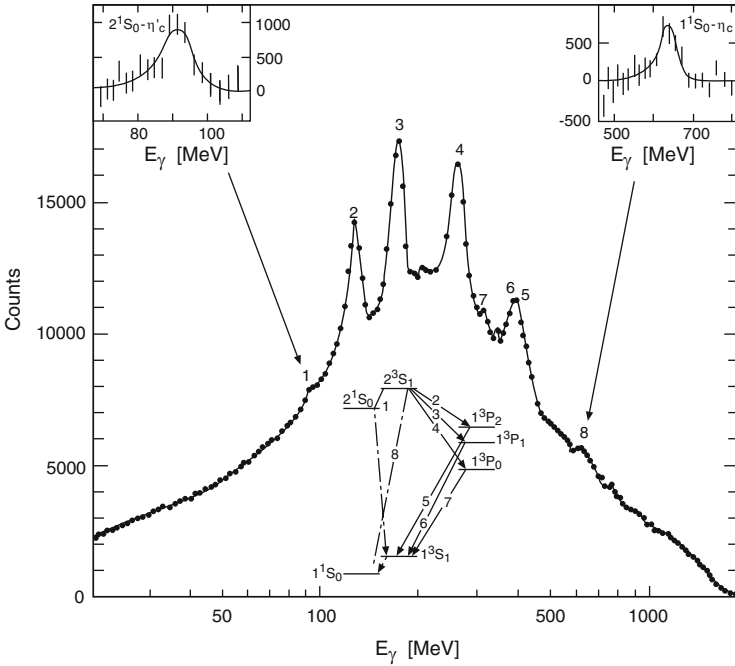


**Fig. 14.6** The photon spectrum in the decay of  $\psi$  ( $2^3S_1$ ), as measured in a crystal ball, and a sketch of the so extracted charmonium energy levels. The strong peaks in the photon spectrum represent the so numbered transitions in the sketch. The *continuous lines* in the sketch represent parity changing electric dipole transitions and the *dashed lines* denote magnetic dipole transitions which do not change parity [3]

### 14.3 Quark-Antiquark Potential

If we compare the spectra of charmonium and positronium, we find that the states with  $n = 1$  and  $n = 2$  are very similarly arranged once an overall increase in the positronium scale of about  $10^8$  is taken into account (Fig. 14.7). The higher charmonium states do not, on the other hand, display the  $1/n^2$  behaviour we see in positronium.

What can we learn from this about the potential and the coupling constant of the strong interaction? Since the potential determines the relative positions of the energy levels, it is clear that the potential of the strong interaction must, similarly to the electromagnetic one, be of a Coulomb type (at least at very short distances, i.e., for  $n = 1, 2$ ). This observation is supported by quantum chromodynamics which describes the force between the quarks via gluon exchange and predicts a  $r^{-1}$  potential at short distances. The absence, in comparison to positronium, of any degeneracy between the  $2^3S$  and  $1^3P$  states suggests that the potential is not of a pure Coulomb form even at fairly small quark-antiquark separations. Since free quarks have not been experimentally observed, it is plausible to postulate a potential which

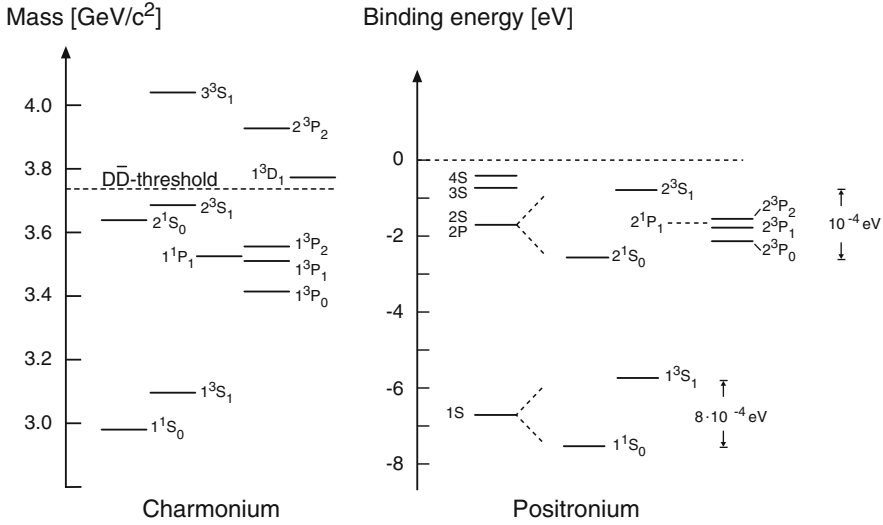


**Fig. 14.7** Comparison of the energy levels of positronium and charmonium. The energy scales were chosen such that the 1S and 2S states of the two systems coincide horizontally. As a result of the differences in nomenclature for the first quantum number, the 2P states in positronium actually correspond to the 1P levels in charmonium. The splitting of the positronium states has been magnified. Dashed states have been calculated but not yet experimentally detected. Note that the  $n = 1$  and  $n = 2$  level patterns are very similar, while the 2S-3S separations are distinctly different. The *dashed, horizontal line* marks the threshold where positronium breaks up and charmonium decays into two D mesons (see Sect. 14.6)

is of a Coulomb type at short distances and grows linearly at greater separations, thus leading to the confinement of quarks in hadrons.

An ansatz for the potential is therefore

$$V = -\frac{4}{3} \frac{\alpha_s(r)\hbar c}{r} + k \cdot r, \tag{14.6}$$

which displays the asymptotic behaviour  $V(r \rightarrow 0) \propto 1/r$  and  $V(r \rightarrow \infty) \rightarrow \infty$ . The factor of 4/3 is a theoretical consequence of quarks coming in three different colours. The strong coupling constant  $\alpha_s$  is actually not a constant at all, but depends upon the separation  $r$  of the quarks (8.1), becoming smaller as the separation increases. This is a direct consequence of QCD and results in the so-called *asymptotic freedom* property of the strong force. This behaviour allows us to view quarks as quasi-free particles at short distances as we have already discussed for deep-inelastic scattering.

While a Coulomb potential corresponds to a dipole field, where the field lines are spread out in space (Fig. 14.8a), the  $kr$  term leads to a so-called flux tube. The lines of force between the quarks are “stretched” (Fig. 14.8b) and the field energy increases linearly with the separation of the quarks. The constant  $k$  in the second

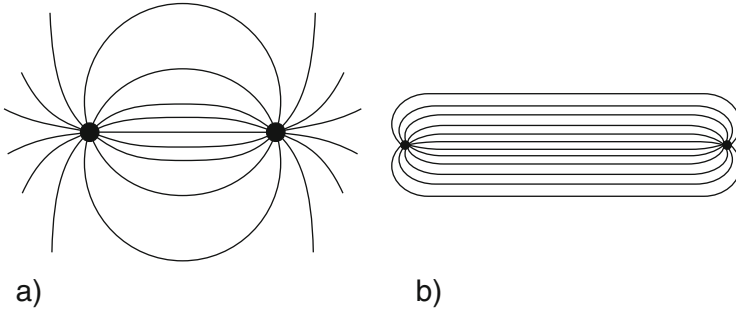


**Fig. 14.8** Field lines for (a) a dipole field ( $V \propto 1/r$ ) between two electric charges, (b) a potential  $V \propto r$  between two widely separated quarks

term of the potential determines the field energy per unit length and is called the “string tension”.

The charmonium energy levels depend not only upon the potential but also upon the kinetic terms in the Hamiltonian, which contain the a priori unknown c-quark mass  $m_c$ . The three unknown quantities  $\alpha_s$ ,  $k$  and  $m_c$  may be roughly determined by fitting the principal energy levels of the  $c\bar{c}$  states from the non-relativistic Schrödinger equation with the potential (14.6). Typical results are:  $\alpha_s \approx 0.15\text{--}0.25$ ,  $k \approx 1 \text{ GeV/fm}$  and  $m_c \approx 1.5 \text{ GeV}/c^2$ . Note that  $m_c$  is the constituent mass of the c-quark. The strong coupling constant in the charmonium system is about 20–30 times larger than the electromagnetic coupling,  $\alpha = 1/137$ . Figure 14.9 shows a potential, based upon (14.6), where the calculated radii of the charmonium states are given. The  $J/\psi$  ( $1^3S_1$ ) has, for example, a radius<sup>1</sup> of approximately  $r \approx 0.4 \text{ fm}$ , which is five orders of magnitude smaller than that of positronium.

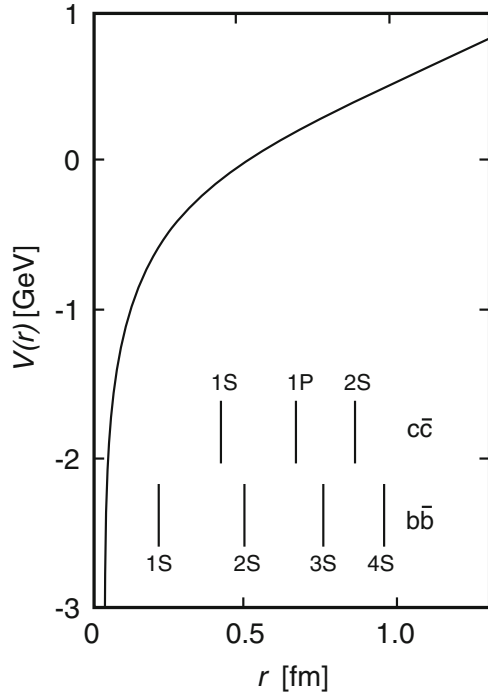
To fully describe the energy levels of Fig. 14.7 one must incorporate further terms into the potential. Similarly to the case of atomic physics, one can describe the splitting of the P states very well through a spin-orbit interaction. The splitting of the S states of charmonium and the related spin-spin interaction will be treated in the next section.

The Coulomb potential describes forces that decrease with distance. The integral of this force is the ionisation energy. The strong interaction potential, (14.6), on the other hand, describes a force between quarks which remains constant at large separations. To remove a coloured particle such as a quark from a hadron would require an infinitely high energy. Thus, since the isolation of coloured objects is impossible, we find only colourless objects in nature. This does not, however, mean that quarks cannot be detached from one another.

Quarks are not liberated in such circumstances, rather fresh hadrons are produced if the energy in the flux tube crosses a specific threshold. The now detached quarks become constituents of these new hadrons. If, for example, a quark is knocked out

<sup>1</sup>By this we mean the average separation between the quark and the antiquark (see Fig. 14.2).

**Fig. 14.9** Strong interaction potential versus the separation  $r$  of two quarks. This potential is roughly described by (14.6). The vertical lines mark the radii of the  $c\bar{c}$  and  $b\bar{b}$  states as calculated from such a potential (From [2])



of a hadron in deep-inelastic scattering, the flux tube between this quark and the remainder of the original hadron breaks when the tube reaches a length of about 1–2 fm. The field energy is converted into a quark and an antiquark. These then separately attach themselves to the two ends of the flux tube and thus produce two colour neutral hadrons. This is the previously mentioned *hadronisation* process.

## 14.4 The Chromomagnetic Interaction

The similarity between the potential of the strong force and that of the electromagnetic interaction is due to the short distance  $r^{-1}$  Coulombic term. This part corresponds to 1-gluon (1-photon) exchange. Charmonium displays a strong splitting of the S states, as does positronium, and this is due to a spin-spin interaction. This force is only large at small distances and thus 1-gluon exchange should essentially account for it in quarkonium. The spin-spin interaction splitting, and hence the force itself, is, however, roughly 1,000 times larger for charmonium than in positronium.

The spin-spin interaction for positronium takes the form

$$V_{ss}(e^+e^-) = \frac{-2\mu_0}{3} \boldsymbol{\mu}_1 \cdot \boldsymbol{\mu}_2 \delta(x), \quad (14.7)$$

where  $\mu_0$  is the vacuum permeability. This equation describes the point interaction of the magnetic moments  $\boldsymbol{\mu}_{1,2}$  of  $e^+$  and  $e^-$ . The magnetic moment of the electron (positron) is just

$$\boldsymbol{\mu}_i = \frac{z_i e \hbar}{2m_i} \boldsymbol{\sigma}_i, \quad \text{where } z_i = Q_i/e = \pm 1, \quad (14.8)$$

and the components of the vector  $\boldsymbol{\sigma}$  are the Pauli matrices;  $\sigma_x^2 = \sigma_y^2 = \sigma_z^2 = \mathbb{1}$ . The potential  $V_{ss}(e^+e^-)$  may then be expressed as

$$V_{ss}(e^+e^-) = \frac{-\hbar^2 \mu_0 z_1 z_2 e^2}{6 m_1 m_2} \boldsymbol{\sigma}_1 \cdot \boldsymbol{\sigma}_2 \delta(\mathbf{x}) = \frac{2\pi \hbar^3}{3c} \alpha \frac{\boldsymbol{\sigma}_1 \cdot \boldsymbol{\sigma}_2}{m_e^2} \delta(\mathbf{x}). \quad (14.9)$$

The quark colour charges lead to a spin-spin interaction called the *chromomagnetic* or *colour magnetic interaction*. To generalise the electromagnetic spin-spin force to describe the chromomagnetic spin-spin interaction we have to replace the electromagnetic coupling constant  $\alpha$  by  $\alpha_s$  and alter the factor to take the three colour charges into account. We thus obtain for the quark-antiquark spin-spin interaction

$$V_{ss}(q\bar{q}) = \frac{8\pi \hbar^3}{9c} \alpha_s \frac{\boldsymbol{\sigma}_q \cdot \boldsymbol{\sigma}_{\bar{q}}}{m_q m_{\bar{q}}} \delta(\mathbf{x}). \quad (14.10)$$

The chromomagnetic energy thus depends upon the relative spin orientations of the quark and the antiquark. The expectation value of  $\boldsymbol{\sigma}_q \cdot \boldsymbol{\sigma}_{\bar{q}}$  is found to be

$$\begin{aligned} \boldsymbol{\sigma}_q \cdot \boldsymbol{\sigma}_{\bar{q}} &= 4s_q \cdot s_{\bar{q}}/\hbar^2 = 2 \cdot [S(S+1) - s_q(s_q+1) - s_{\bar{q}}(s_{\bar{q}}+1)] \\ &= \begin{cases} -3 & \text{for } S = 0, \\ +1 & \text{for } S = 1, \end{cases} \end{aligned} \quad (14.11)$$

where  $S$  is the total spin of the charmonium state and we have used the identity  $S^2 = (s_q + s_{\bar{q}})^2$ . One thus obtains an energy splitting from this chromomagnetic interaction of the form

$$\Delta E_{ss} = \langle \psi | V_{ss} | \psi \rangle = 4 \cdot \frac{8\pi \hbar^3}{9c} \frac{\alpha_s}{m_q m_{\bar{q}}} |\psi(0)|^2. \quad (14.12)$$

This splitting is only important for S states, since only then the wave function at the origin  $\psi(0)$  is non-vanishing.

The observed charmonium transition from the state  $1^3S_1$  to  $1^1S_0$  (i.e.,  $J/\psi \rightarrow \eta_c$ ) is a magnetic transition, which corresponds to one of the quarks flipping its spin. The measured photon energy, and hence the gap between the states, is approximately

120 MeV. The colour magnetic force (14.12) should account for this splitting. Although an exact calculation of the wave function is not possible, we can use the values of  $\alpha_s$  and  $m_c$  from the last section to see that our ansatz for the chromomagnetic interaction is consistent with the observed splitting of the states. We will see in Chap. 15 that the spin-spin force also plays a role for light mesons and indeed describes their mass spectrum very well.

**The c-quark’s mass** The c-quark mass which we obtained from our study of the charmonium spectrum is its constituent-quark mass, i.e., the effective quark mass in the bound state. This constituent mass has two parts: the intrinsic (or “bare”) quark mass and a “dynamical” part which comes from the cloud of sea quarks and gluons that surrounds the quark. The fact that charmed hadrons are 4–10 times heavier than light hadrons implies that the constituent mass of the c-quark is predominantly intrinsic since the dynamical masses themselves should be more or less similar for all hadrons. We should not forget that even if the dynamical masses are small compared to the heavy quark constituent mass, the potential we have used is a phenomenological one which merely describes the interaction between *constituent* quarks.

## 14.5 Bottonium and Toponium

A further group of narrow resonances are found in  $e^+e^-$  scattering at centre-of-mass energies of around 10 GeV. These are understood as  $b\bar{b}$  bound states and are called *bottomium*. The lowest  $b\bar{b}$  state which can be obtained from  $e^+e^-$  annihilation is called the  $\Upsilon$  and has a mass of 9.46 GeV/ $c^2$ . Higher  $b\bar{b}$  excitations have been found with masses up to 11 GeV/ $c^2$ .

Various electromagnetic transitions between the various bottomium states are also observed. As well as a  $1^3P_J$  state, a  $2^3P_J$  state has been observed. The spectrum of these states closely parallels that of charmonium (Fig. 14.10). This indicates that the quark-antiquark potential is independent of quark flavour. The b-quark mass is about 3 times as large as that of the c-quark. The radius of the quarkonium ground state is from (14.4) inversely proportional both to the quark mass and to the strong coupling constant  $\alpha_s$ . The 1S  $b\bar{b}$  state thus has a radius of roughly 0.2 fm (cf. Fig. 14.9), i.e., about half that of the equivalent  $c\bar{c}$  state. Furthermore the non-relativistic treatment of bottomium is better justified than was the case for charmonium. The approximately equal mass difference between the 1S and 2S states in both systems is, however, astounding. A purely Coulombic potential would cause the levels to be proportional to the reduced mass of the system, (14.2). It is thus clear that the long distance part of the potential  $kr$  cancels the mass dependence of the energy levels at the c- and b-quark mass scales.

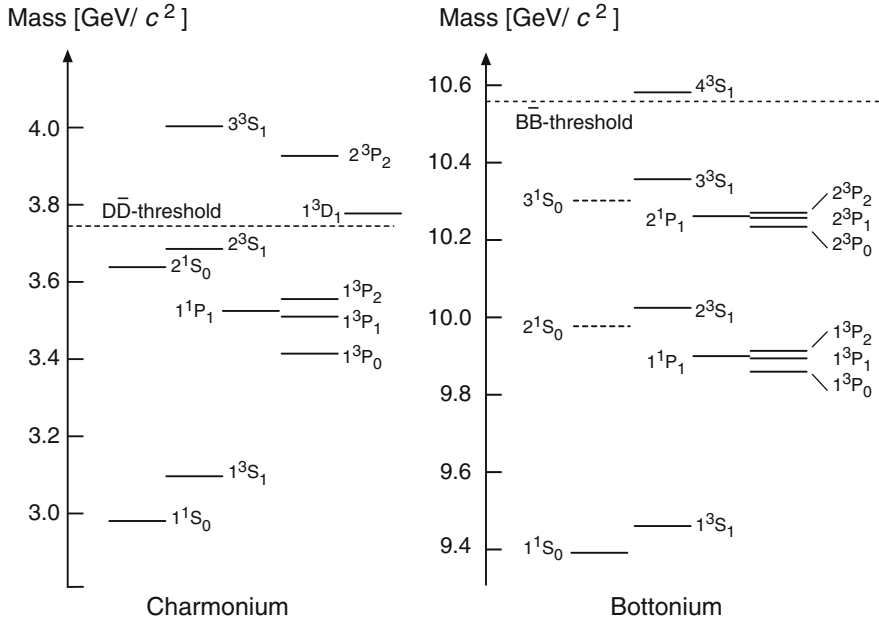


**Fig. 14.10** Energy levels of charmonium and bottomonium. Dashed levels are theoretically predicted, but not yet experimentally observed. The spectra display a very similar structure. The *dashed line* shows the threshold beyond which charmonium (bottomonium) decays into hadrons containing the initial quarks, i.e., D (B) mesons. Below the threshold electromagnetic transitions from <sup>3</sup>S states into <sup>3</sup>P and <sup>1</sup>S states are observed. For bottomonium the first and second excitations ( $n = 2, 3$ ) lie below this threshold, for charmonium only the first does

The t-quark has, due to its large mass, only a fleeting lifetime. Thus no pronounced  $t\bar{t}$  states (*toponium*) are expected.

## 14.6 The Decay Channels of Heavy Quarkonia

Up to now we have essentially dealt with the electromagnetic transitions between various levels of quarkonia. But actually it is astonishing that electromagnetic decays occur at all at an observable rate. One would naively expect a strongly interacting object to decay “strongly”. The decays of heavy quarkonia have been in fact investigated very thoroughly [4] so as to obtain the most accurate possible picture of the quark-antiquark interaction. There are in principle four different ways in which quarkonia can change its state or decay. They are:

- (a) A change of excitation level via photon emission (electromagnetic), e.g.,

$$\chi_{c1} (1^3P_1) \rightarrow J/\psi (1^3S_1) + \gamma .$$



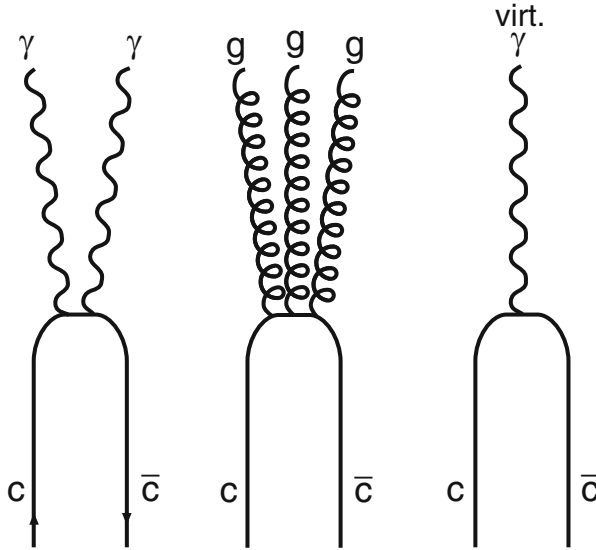


**Fig. 14.11** Various channels of  $c\bar{c}$  annihilation

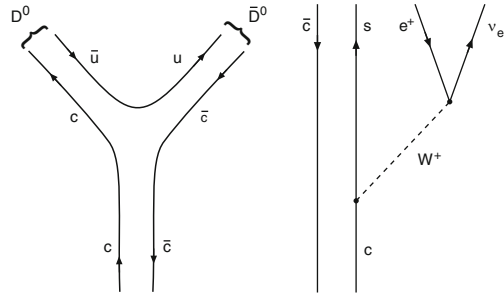
- (b) Quark-antiquark annihilation (Fig. 14.11) into real or virtual photons or gluons (electromagnetic or strong), e.g.,

$$\begin{aligned} \eta_c (1^1S_0) &\rightarrow 2\gamma \\ J/\psi (1^3S_1) &\rightarrow ggg \rightarrow \text{hadrons} \\ J/\psi (1^3S_1) &\rightarrow \text{virt. } \gamma \rightarrow \text{hadrons} \\ J/\psi (1^3S_1) &\rightarrow \text{virt. } \gamma \rightarrow \text{leptons.} \end{aligned}$$

The  $J/\psi$  decays about 30% of the time electromagnetically into hadrons or charged leptons and about 70% of the time strongly. The electromagnetic route can, despite the smallness of  $\alpha$ , compete with the strong one, since in the strong case three gluons must be exchanged to conserve colour and parity. A factor of  $\alpha_s^3$  thus lowers this decay probability (compared to  $\alpha^2$  in the electromagnetic case). States such as  $\eta_c$ , which have  $J = 0$ , can decay into two gluons or two real photons. The decay of the  $J/\psi$  ( $J = 1$ ) is mediated by three gluons or a single virtual photon.

- (c) Creation of one or more light  $q\bar{q}$  pairs from the vacuum to form light mesons via the strong interaction (Fig. 14.12 (left)).  
 (d) Weak decay of one or both heavy quarks (Fig. 14.12 (right)).

**Fig. 14.12** Strong decay  
 $\psi(3778) \rightarrow D^0 + \bar{D}^0$  (left);  
 weak decay  
 $J/\psi \rightarrow D_s^- + e^+ + \nu_e$   
 (right)



In practice the weak decay (d) is unimportant since the strong and electromagnetic decays proceed much more quickly. The strong decay (c) is, in principle, the most likely, but this can only take place above a certain threshold since the light  $q\bar{q}$  pairs need to be created from the quarkonia binding energy. Hence only options (a) and (b) are available to quarkonia below this threshold.

Electromagnetic processes like deexcitation via photon emission are relatively slow. Furthermore, although hadronisation via the annihilation (b) into gluons is a strong process such decays are, according to the *Zweig rule* (cf. Sect. 9.2) suppressed relative to those decays (c) where the initial quarks still exist in the final state. For these reasons the width of those quarkonium levels below the mesonic threshold is very small (e.g.,  $\Gamma = 93$  keV for the  $J/\psi$ ).

The first charmonium state beyond this threshold is the  $\psi(1^3D_1)$  which has a mass of  $3,778 \text{ MeV}/c^2$ . It has, compared to the  $J/\psi$ , rather a large width,  $\Gamma \approx 27 \text{ MeV}$ . For the more strongly bound  $b\bar{b}$  system the decay channel into mesons with b-quarks is first open to the third excitation, the  $\Upsilon(4^3S_1)$  ( $10,579 \text{ MeV}/c^2$ ) (cf. Fig. 14.10).

The lightest quarks are the u- and d-quarks and their pair production opens the mesonic decay channels (cf. Fig. 14.12 (left)). Charmonium, say, decays into

$$c\bar{c} \rightarrow c\bar{u} + \bar{c}u,$$

$$c\bar{c} \rightarrow c\bar{d} + \bar{c}d,$$

where  $c\bar{u}$  is called the  $D^0$  meson,  $\bar{c}u$  the  $\bar{D}^0$ ,  $c\bar{d}$  the  $D^+$  and  $\bar{c}d$  the  $D^-$ . The masses of these mesons are  $1,864.9 \text{ MeV}/c^2$  ( $D^0$ ) and  $1,869.6 \text{ MeV}/c^2$  ( $D^\pm$ ). The preferred decays of bottomonium are analogously

$$b\bar{b} \rightarrow b\bar{u} + \bar{b}u,$$

$$b\bar{b} \rightarrow b\bar{d} + \bar{b}d.$$

These mesons are called<sup>2</sup>  $B^-$  and  $B^+$  ( $m = 5,279.3 \text{ MeV}/c^2$ ), as well as  $\bar{B}^0$  and  $B^0$  ( $m = 5,279.6 \text{ MeV}/c^2$ ). For higher excitations decays into mesons with s-quarks are also possible:

$$\begin{aligned} c\bar{c} &\rightarrow c\bar{s} + \bar{c}s && (D_s^+ \text{ and } D_s^-), \\ b\bar{b} &\rightarrow b\bar{s} + \bar{b}s && (\bar{B}_s^0 \text{ and } B_s^0). \end{aligned}$$

Such mesons are accordingly heavier. The mass of  $D_s^\pm$  meson is, for example,  $1,968.5 \text{ MeV}/c^2$ . All of these mesons eventually decay weakly into lighter mesons such as pions.

## 14.7 Decay Widths as a Test of QCD

The decays and decay rates of quarkonia can provide us with information about the strong coupling constant  $\alpha_s$ . Let us consider the  $1^1S_0$  charmonium state ( $\eta_c$ ) which can decay into either two photons or two gluons. (In the latter case we will experimentally only observe the end products of hadronisation.) Measurements of the ratio of these two decay widths can determine  $\alpha_s$ , in principle, in a very elegant way.

The formula for the decay width into two *real* photons is essentially just the same as for positronium (14.5), one needs only to recall that the c-quarks have fractional electric charge  $z_c = 2/3$  and come in three flavours.

$$\Gamma(1^1S_0 \rightarrow 2\gamma) = \frac{3 \cdot 4\pi z_c^4 \alpha^2 \hbar^3}{m_c^2 c} |\psi(0)|^2 (1 + \varepsilon'). \quad (14.13)$$

The  $\varepsilon'$  term signifies higher order QCD corrections which can be approximately calculated.

To consider the two gluon decay, one must replace  $\alpha$  by  $\alpha_s$ . In contrast to photons, gluons do not exist as real particles but rather have to hadronise. For this process we set the strong coupling constant to one. The different colour-anticolour combinations also mean we must use a different overall colour factor which takes the various gluon combinations into account:

$$\Gamma(1^1S_0 \rightarrow 2g \rightarrow \text{hadrons}) = \frac{8\pi}{3} \frac{\alpha_s^2 \hbar^3}{m_c^2 c} |\psi(0)|^2 (1 + \varepsilon''), \quad (14.14)$$

<sup>2</sup>The standard nomenclature for mesons containing heavy quarks is such that the neutral meson with a b-quark is called a  $\bar{B}^0$  and the meson with a  $\bar{b}$  is known as a  $B^0$ . An electrically neutral  $q\bar{q}'$  state is marked with a bar, if the heavier quark/antiquark is negatively charged [8].

where  $\varepsilon''$  signifies QCD corrections once again. The ratio of these decay widths is

$$\frac{\Gamma(2\gamma)}{\Gamma(2g)} = \frac{8}{9} \frac{\alpha^2}{\alpha_s^2} (1 + \varepsilon). \quad (14.15)$$

The correction factor  $\varepsilon$  itself depends upon  $\alpha_s$  and is about  $\varepsilon \approx -0.5$ . From the experimentally determined ratio  $\Gamma(2\gamma)/\Gamma(2g) \approx (3.0 \pm 1.2) \cdot 10^{-4}$  [8] one finds the value  $\alpha_s(m_{J/\psi}^2/c^2) \approx 0.25 \pm 0.05$ . This is consistent with the value from the charmonium spectrum. From (8.1) we see that  $\alpha_s$  always depends upon a distance or, equivalently, energy or mass scale. In this case the scale is fixed by the constituent mass of the c-quark or by the  $J/\psi$  mass.

The above result, despite the simplicity of the original idea, suffers from both experimental and theoretical uncertainties. As well as QCD corrections, there are further corrections from the relativistic motion of the quarks. For a better determination of  $\alpha_s$  from charmonium physics one can investigate other decay channels. The comparison, for instance, of the decay rates

$$\frac{\Gamma(J/\psi \rightarrow 3g \rightarrow \text{hadrons})}{\Gamma(J/\psi \rightarrow \gamma \rightarrow 2 \text{ leptons})} \propto \frac{\alpha_s^3}{\alpha^2}, \quad (14.16)$$

is simpler from an experimental viewpoint. Both here and in studies of other channels one finds  $\alpha_s(m_{J/\psi}^2/c^2) \approx 0.2 \dots 0.3$  [5].

The comparison of various bottomium decays yields the coupling strength  $\alpha_s$  in a more accurate way since both QCD corrections and relativistic effects are smaller. From QCD one expects  $\alpha_s$  to be smaller, the coupling is supposed to decrease with the separation. This is indeed the case. One finds from the ratio

$$\frac{\Gamma(\Upsilon \rightarrow \gamma g g \rightarrow \gamma + \text{hadrons})}{\Gamma(\Upsilon \rightarrow g g g \rightarrow \text{hadrons})} \propto \frac{\alpha}{\alpha_s}, \quad (14.17)$$

which is  $(2.75 \pm 0.04)\%$ , that  $\alpha_s(m_\Upsilon^2/c^2) = 0.163 \pm 0.016$  [7]. The error is dominated by uncertainties in the theoretical corrections.

These examples demonstrate that the annihilation of a  $q\bar{q}$  pair in both the electromagnetic and strong interactions may formally be described in the same manner. The only essential difference is the coupling constant. This comparison can be understood as a test of the applicability of QCD at short distances, which, after all, is where the  $q\bar{q}$  annihilation takes place. In this region QCD and QED possess the same structure since both interactions are well described by the exchange of a single vector boson (a gluon or a photon).

## Problems

### 1. Weak charge

Bound states are known to exist for the strong interaction (hadrons, nuclei), electromagnetism (atoms, solids) and gravity (the solar system, stars) but we do not have such states for the weak force. Estimate, in analogy to positronium, how heavy two particles would have to be if the Bohr radius of their bound state would be roughly equal to the range of the weak interaction.

### 2. Muonic and hadronic atoms

Negatively charged particles that live long enough ( $\mu^-$ ,  $\pi^-$ ,  $K^-$ ,  $\bar{p}$ ,  $\Sigma^-$ ,  $\Xi^-$ ,  $\Omega^-$ ), can be captured by the field of an atomic nucleus. Calculate the energy of atomic ( $2p \rightarrow 1s$ ) transitions in hydrogen-type “atoms” where the electron is replaced by the above particles. Use the formulae of Chap. 14. The lifetime of the  $2p$  state in the H atom is  $\tau_H = 1.76 \cdot 10^9$  s. What is the lifetime, as determined from electromagnetic transitions, of the  $2p$  state in a  $p\bar{p}$  system (protonium)? Remember to take the scaling of the matrix element and of phase space into account.

### 3. Hyperfine structure

In a two-fermion system the hyperfine structure splitting between the levels  $1^3S_1$  and  $1^1S_0$  is proportional to the product of the magnetic moments of the fermions,  $\Delta E \propto |\psi(0)|^2 \mu_1 \mu_2$ , where  $\mu_i = g_i \frac{e_i}{2m_i}$ . The  $g$ -factor of the proton is  $g_p = 5.5858$  and those of the electron and the muon are  $g_e \approx g_\mu \approx 2.0023$ . In positronium an additional factor of  $7/4$  arises in the formula for  $\Delta E$ , which takes the level shifts of the triplet state by pair annihilation graphs into account.

In the hydrogen atom, the level splitting corresponds to a transition frequency  $f_H = 1,420$  MHz. Estimate the values for positronium and muonium ( $\mu^+e^-$ ). (Hint:  $\psi(0) \propto r_b^{-3/2}$ ; use the reduced mass in the expression for  $|\psi(0)|^2$ .) Compare your result with the measured values of the transition frequencies, 203.4 GHz for positronium and 4.463 GHz for muonium. How can the (tiny) difference be explained?

## References

1. G.J. Feldman, M.L. Perl, Phys. Rep. **19**, 233 (1975)
2. K. Gottfried, V.F. Weisskopf, *Concepts of Particle Physics*, vol. 1 (Clarendon Press, Oxford/New York, 1984)
3. K. Königsmann, Phys. Rep. **139**, 243 (1986)
4. L. Köpke, N. Wermes, Phys. Rep. **174**, 67 (1989)
5. W. Kwong, J.L. Rosner, C. Quigg, Annu. Rev. Part. Nucl. Sci. **37**, 325 (1987)
6. O. Nachtmann, *Elementary Particle Physics: Concepts and Phenomena* (Springer, Berlin/Heidelberg/New York, 1990)
7. B. Nemati et al., Phys. Rev. **D55**, 5273 (1997)
8. Particle Data Group, J. Beringer et al., *Review of Particle Properties*. Phys. Rev. D **86**, 010001 (2012)
9. V.A. Telegdi, Sci. Am. **206**, 50 (1962)

# Chapter 15

## Mesons

We have seen that the mesons containing the heavy  $c$ - and  $b$ -quarks may be relatively simply described. In particular since charmonium and bottomonium have very different masses they cannot be confused with each other. Furthermore the  $D$  and  $B$  mesons may be straightforwardly identified with specific quark-antiquark flavour and charge combinations.

Turning now to those mesons that are solely built out of the light flavours (i.e.,  $u$ ,  $d$  and  $s$ ) we encounter a more complicated situation. The constituent masses of these quarks, especially those of the  $u$ - and  $d$ -quarks, are so similar that we cannot expect to straightforwardly distinguish the mesons according to their quark content but must expect to encounter mixed states of all three light flavours. We shall therefore now consider all of the mesons that are made up of  $u$ -,  $d$ - and  $s$ -quarks.

Another consequence of the light-quark masses is that we cannot expect to treat these mesons in a non-relativistic manner. However, our investigation of the light-meson spectrum will lead us to the surprising conclusion that these particles can be at least semi-quantitatively described in a non-relativistic model. The constituent quark concept is founded upon this finding.

Of special interest are neutral quark-antiquark states containing a light quark and a heavier  $s$ -,  $c$ - or  $b$ -quark, like the  $|K^0\rangle = |d\bar{s}\rangle$  or the  $|B^0\rangle = |d\bar{b}\rangle$  and their antiparticles. These mesons have very peculiar properties: particle and antiparticle can oscillate into each other and their weak decays violate conservation of  $CP$  symmetry. We will discuss these exciting aspects in some detail at the end of this chapter.

### 15.1 Meson Multiplets

**Meson quantum numbers** We assume that the quarks and antiquarks of the lowest lying mesons do not have any relative orbital angular momentum ( $L = 0$ ). We will only treat such states in what follows. Recall first that quarks and antiquarks have

opposite intrinsic parities and so these mesons all have parity,  $(-1)^{L+1} = -1$ . The quark spins now determine the mesonic total angular momentum. They can add up to either  $S = 1$  or  $S = 0$ . The  $J^P = 0^-$  states are called *pseudoscalar mesons* while the  $J^P = 1^-$  are the *vector mesons*. One naturally expects nine different meson combinations from the three quarks and three antiquarks.

**Isospin and strangeness** Let us initially consider just the two lightest quarks. Since the u- and d-quark constituent masses are both around  $300 \text{ MeV}/c^2$  (see Table 9.1) there is a natural mixing of degenerate states with the same quantum numbers. To describe  $u\bar{u}$ - and  $d\bar{d}$ -quarkonia it is helpful to introduce the idea of *isospin*. The u- and d-quarks form an isospin doublet ( $I = 1/2$ ) with  $I_3 = +1/2$  for the u-quark and  $I_3 = -1/2$  for the d-quark. This strong isospin is conserved by the strong interaction which does not distinguish between directions in strong isospin space. Quantum mechanically, isospin is treated in analogy to angular momentum, which reflects itself in isospin addition and the use of ladder operators. The spins of two electrons may combine to form a (spin-)triplet or a singlet, and one can similarly form an (isospin-)triplet or singlet from the  $2 \times 2$  combinations of a u- or a d-quark with a  $\bar{u}$ - or a  $\bar{d}$ -quark.

These ideas must be extended to include the s-quark. Its flavour is associated with a further additive quantum number, *strangeness*. The s-quark has  $S = -1$  and the antiquark  $S = +1$ . Mesons containing one s-(anti)quark are eigenstates of the strong interaction, since strangeness can only be changed in weak processes. Zero strangeness  $s\bar{s}$  states, on the other hand, can mix with  $u\bar{u}$  and  $d\bar{d}$  states since these possess the same quantum numbers. Note that the somewhat larger s-quark constituent mass of about  $450 \text{ MeV}/c^2$  implies that this mixing is smaller than that of  $u\bar{u}$  and  $d\bar{d}$  states.

Group theory now tells us that the  $3 \times 3$  combinations of three quarks and three antiquarks form an octet and a singlet. Recall that the  $3 \times 3$  combinations of colours and anticolours also form an octet and a singlet for the case of the gluons (Sect. 8.2). The underlying symmetry is known as SU(3) in group theory.

We will see below that the larger s-quark mass leads to this symmetry being less evident in the spectrum. Thus, while the mesons inside an isospin triplet have almost identical masses, those of an octet vary noticeably. Were we now to include the c-quark in these considerations we would find that the resulting symmetry was much less evident in the mesonic spectrum.

**Vector mesons** Light vector mesons are produced in  $e^+e^-$  collisions, just as heavy quarkonia can be. As we saw in Sect. 9.2 (Fig. 9.7), there are three resonances at a centre-of-mass energy of around 1 GeV. The highest one is at 1,019 MeV and is called the  $\phi$  meson. Since the  $\phi$  mostly decays into strange mesons, it is interpreted as the following  $s\bar{s}$  state:

$$|\phi\rangle = |s^\uparrow \bar{s}^\uparrow\rangle,$$

**Table 15.1** The quantum numbers of the light quarks and antiquarks:  $B$  = baryon number,  $J$  = spin,  $I$  = isospin,  $I_3$  = 3-component of the isospin,  $S$  = strangeness,  $Q/e$  = charge

	$B$	$J$	$I$	$I_3$	$S$	$Q/e$
u	+1/3	1/2	1/2	+1/2	0	+2/3
d	+1/3	1/2	1/2	-1/2	0	-1/3
s	+1/3	1/2	0	0	-1	-1/3
$\bar{u}$	-1/3	1/2	1/2	-1/2	0	-2/3
$\bar{d}$	-1/3	1/2	1/2	+1/2	0	+1/3
$\bar{s}$	-1/3	1/2	0	0	+1	+1/3

where the arrows signify the 3-component of the quark spins. The pair of light resonances with nearly equal masses, the  $\rho$  and  $\omega$  mesons, are interpreted as mixed states of u- and d-quarks.

The broad first resonance at 775 MeV is called the  $\rho^0$  meson. It has two charged partners with almost the same mass. These arise in other reactions. Together they form the isospin triplet:  $\rho^+$ ,  $\rho^0$ ,  $\rho^-$ . These  $\rho$  mesons are states with isospin 1 built out of the u-,  $\bar{u}$ -, d- and  $\bar{d}$ -quarks. They may be easily constructed if we recall the quark quantum numbers given in Table 15.1. The charged  $\rho$  mesons are then the states

$$|\rho^+\rangle = |u^\uparrow \bar{d}^\uparrow\rangle \quad |\rho^-\rangle = |\bar{u}^\uparrow d^\uparrow\rangle,$$

with  $I = 1$  and  $I_3 = \pm 1$ . We may now construct their uncharged partner (for example by applying the ladder operators  $I^\pm$ ). We find

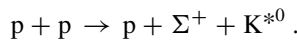
$$|\rho^0\rangle = \frac{1}{\sqrt{2}} \{ |u^\uparrow \bar{u}^\uparrow\rangle - |d^\uparrow \bar{d}^\uparrow\rangle \}.$$

The orthogonal wave function with zero isospin is then just the  $\omega$ -meson:

$$|\omega\rangle = \frac{1}{\sqrt{2}} \{ |u^\uparrow \bar{u}^\uparrow\rangle + |d^\uparrow \bar{d}^\uparrow\rangle \}.$$

In contradistinction to coupling the angular momentum of two spin-1/2 particles, there is here a minus sign in the triplet state and a plus in the singlet. The real reason for this is that we have here particle-antiparticle combinations (see, e.g., [15]).

Vector mesons with strangeness  $S \neq 0$  are called  $K^*$  mesons and may be produced by colliding high energy protons against a target:



The final state in such experiments must contain an equal number of s-quarks and  $\bar{s}$ -antiquarks bound inside hadrons. In this example the  $K^{*0}$  contains the  $\bar{s}$ -antiquark and the  $\Sigma^+$ -baryon contains the s-quark. Strangeness is a conserved quantum number in the strong interaction.



There are four combinations of light quarks which each have just one  $s$ - or  $\bar{s}$ -quark:

$$\begin{aligned}
 |K^{*-}\rangle &= |s^\uparrow \bar{u}^\uparrow\rangle & |\bar{K}^{*0}\rangle &= |s^\uparrow \bar{d}^\uparrow\rangle \\
 |K^{*+}\rangle &= |u^\uparrow \bar{s}^\uparrow\rangle & |K^{*0}\rangle &= |d^\uparrow \bar{s}^\uparrow\rangle.
 \end{aligned}$$

The two pairs  $K^{*-}, \bar{K}^{*0}$  and  $K^{*0}, K^{*+}$  are both strong isospin doublets.

The  $\rho, \omega, \phi$  and  $K^*$  are all of the possible  $3 \times 3 = 9$  combinations. They have all been seen in experiments – which is clear evidence of the correctness of the quark model.<sup>1</sup> This classification is made clear in Fig. 15.1. The vector mesons are ordered according to their strangeness  $S$  and the third component of the isospin  $I_3$ . The threefold symmetry of this scheme is due to the three fundamental quark flavours from which the mesons are made. Mesons and antimesons are diagonally opposite to each other and the three mesons at the centre are each their own antiparticles.

**Pseudoscalar mesons** The quark and antiquark pair in pseudoscalar mesons have opposite spins and their angular momentum and parity are  $J^P = 0^-$ . The name “pseudoscalar” arises as follows: spin-0 particles are usually called scalars, while spin-1 particles are known as vectors, but scalar quantities should be invariant under parity transformations. The prefix “pseudo” reflects that these particles possess an unnatural, odd (negative) parity.

The quark structure of the pseudoscalar mesons mirrors that of the vector mesons (Fig. 15.1). The  $\pi$  meson isospin triplet corresponds to the  $\rho$  mesons. The pseudoscalars with the quark content of the  $K^*$  vector mesons are known as  $K$

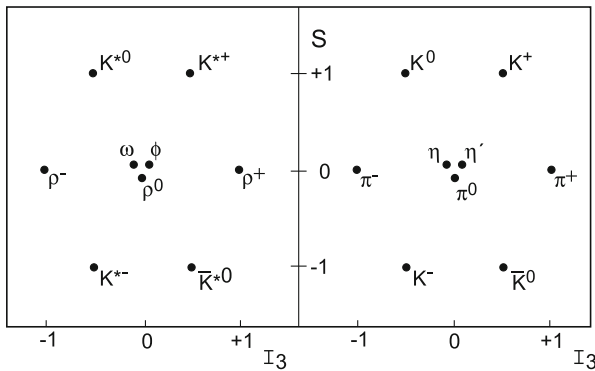


**Fig. 15.1** The lightest vector ( $J^P = 1^-$ ) (left) and pseudoscalar mesons ( $J^P = 0^-$ ) (right), classified according to their isospin  $I_3$  and strangeness  $S$

<sup>1</sup>Historically it was the other way around. The quark model was developed so as to order the various mesons into multiplets and hence explain the mesons.

mesons. Finally, the  $\eta'$  and  $\eta$  correspond to the  $\phi$  and the  $\omega$ . There are, however, differences in the quark mixings in the isospin singlets. As shown in Fig. 15.1 there are three mesonic states with the quantum numbers  $S = I_3 = 0$ . These are a symmetric flavour singlet and two octet states. One of these last two has isospin 1 and is therefore a mixture of  $u\bar{u}$  and  $d\bar{d}$ . The  $\pi^0$  and  $\rho^0$  occupy this slot in their respective multiplets. The remaining octet state and the singlet can mix with each other since the SU(3) flavour symmetry is broken ( $m_s \neq m_{u,d}$ ). This mixing is rather small for the pseudoscalar case and  $\eta$  and  $\eta'$  are fairly pure octet and singlet states:

$$|\eta\rangle \approx |\eta_8\rangle = \frac{1}{\sqrt{6}} \left\{ |u\uparrow\bar{u}\downarrow\rangle + |d\uparrow\bar{d}\downarrow\rangle - 2|s\uparrow\bar{s}\downarrow\rangle \right\},$$

$$|\eta'\rangle \approx |\eta_1\rangle = \frac{1}{\sqrt{3}} \left\{ |u\uparrow\bar{u}\downarrow\rangle + |d\uparrow\bar{d}\downarrow\rangle + |s\uparrow\bar{s}\downarrow\rangle \right\}.$$

The vector meson octet and singlet states are, on the other hand, more strongly mixed. It so happens that the mixing angle is roughly  $\arctan 1/\sqrt{2}$ , which means that the  $\phi$  meson is an almost pure  $s\bar{s}$  state and that the  $\omega$  is a mix of  $u\bar{u}$  and  $d\bar{d}$  whose strange content can safely be neglected [20].

## 15.2 Meson Masses

The masses of the light mesons can be read off from Fig. 15.2. It is striking that the  $J = 1$  states have much larger masses than their  $J = 0$  partners. The gap between the  $\pi$  and  $\rho$  masses is, for example, about  $600 \text{ MeV}/c^2$ . This should be contrasted with the splitting of the  $1^1S_0$  and  $1^3S_1$  states of charmonium and bottomonium, which is only around  $100 \text{ MeV}/c^2$ .

Just as for the states of heavy quarkonia with total spins  $S = 0$  and  $S = 1$ , the mass difference between the light pseudoscalars and vectors can be traced back to a spin-spin interaction. From (14.10) and (14.11) we find a mass difference of

$$\Delta M_{ss} = \begin{cases} -3 \cdot \frac{8\hbar^3}{9c^3} \frac{\pi\alpha_s}{m_q m_{\bar{q}}} |\psi(0)|^2 & \text{for pseudoscalar mesons,} \\ +1 \cdot \frac{8\hbar^3}{9c^3} \frac{\pi\alpha_s}{m_q m_{\bar{q}}} |\psi(0)|^2 & \text{for vector mesons.} \end{cases} \quad (15.1)$$

Note the dependence of the mass gap on the constituent-quark masses. The increase of the gap as the constituent mass decreases is the dominant effect, despite an opposing tendency from the  $|\psi(0)|^2$  term (this is proportional to  $1/r_b^3$  and thus grows with the quark mass). Hence this mass gap is larger for the light systems.

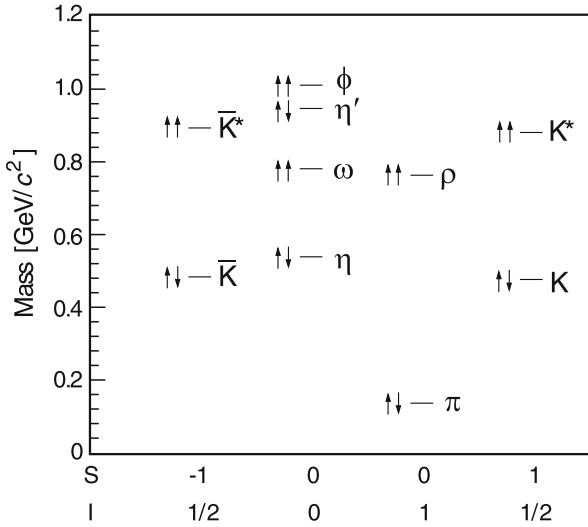


**Fig. 15.2** The spectrum of the light pseudoscalar and vector mesons. The multiplets are ordered according to their strangeness  $S$  and isospin  $I$ . The angular momenta of the various mesons are indicated by arrows. Note that the vector mesons are significantly heavier than their pseudoscalar equivalents

The absolute masses of all the light mesons can be described by a phenomenological formula

$$M_{q\bar{q}} = m_q + m_{\bar{q}} + \Delta M_{ss}, \tag{15.2}$$

where  $m_{q,\bar{q}}$  once again refers to the constituent-quark mass. The unknowns in this equation are the constituent masses of the three light quarks. We assume that the  $u$  and  $d$  masses are the same, and that the product  $\alpha_s \cdot |\psi(0)|^2$  is to a rough approximation the same for all of the mesons under consideration here. We may now, with the help of (15.2), extract the quark masses from the experimental results for the meson masses. We thus obtain the following constituent-quark masses:  $m_{u,d} \approx 310 \text{ MeV}/c^2$ ,  $m_s \approx 483 \text{ MeV}/c^2$  [14]. The use of these values yields mesonic masses which only deviate from their true values at the level of a few percent (Table 15.2). These light-quark constituent masses are predominantly generated by the cloud of gluons and virtual quark-antiquark pairs that surround the quark. The bare masses are only around 5–10  $\text{MeV}/c^2$  for the  $u$ - and  $d$ -quarks and about 150  $\text{MeV}/c^2$  for the  $s$ . This simple calculation of the mesonic masses demonstrates that the constituent-quark concept is valid, even for those quarks with only a tiny bare mass.

It is actually highly surprising that (15.2) describes the mesonic spectrum so very well. After all, the equation takes no account of possible mass terms which could depend upon the quark kinetic energy or upon the strong potential (14.6). It appears

**Table 15.2** Light meson masses both from experiment [20] and from (15.2) [14]. The calculations are fitted to the average mass of an isospin multiplet and do not cover those, albeit minor, mass differences arising from electromagnetic effects

Meson	$J^P$	$I$	Mass (MeV/c <sup>2</sup> )	
			Calculated	Experiment
$\pi$	$0^-$	1	140	$\left\{ \begin{array}{l} 135.0 \pi^0 \\ 139.6 \pi^\pm \end{array} \right.$
K	$0^-$	1/2	485	$\left\{ \begin{array}{l} 497.6 K^0 \\ 493.7 K^\pm \end{array} \right.$
$\eta$	$0^-$	0	559	547.9
$\eta'$	$0^-$	0	–	957.8
$\varrho$	$1^-$	1	780	775.5
$K^*$	$1^-$	1/2	896	$\left\{ \begin{array}{l} 896.0 K^{*0} \\ 891.7 K^{*\pm} \end{array} \right.$
$\omega$	$1^-$	0	780	782.7
$\phi$	$1^-$	0	1,032	1,019.5

to be a peculiarity of the potential of the strong interaction that its make up from a Coulombic and a linearly increasing term effectively cancels these mass terms to a very good approximation.

### 15.3 Decay Channels

The masses and quantum numbers of the various mesons may also be used to make sense of how these particles decay. The most important decay channels of the pseudoscalar and vector mesons treated here are listed in Table 15.3.

We start with the lightest mesons, the pions. The  $\pi^0$  is the lightest of all the hadrons and so, although it can decay electromagnetically, it cannot decay strongly. The  $\pi^\pm$  can, on the other hand, only decay semileptonically, i.e., through the weak interaction. This is because conservation of charge and of lepton number require that the final state must comprise of a charged lepton and a neutrino. This means that these mesons have long lifetimes. The decay  $\pi^- \rightarrow e^- + \bar{\nu}_e$  is strongly suppressed compared to  $\pi^- \rightarrow \mu^- + \bar{\nu}_\mu$  because of helicity conservation (see p. 156).

The next heavier mesons are the K mesons (kaons). Since these are the lightest mesons containing an s-quark, their decay into a lighter particle requires the s-quark to change its flavour, which is only possible in weak processes. Kaons are thus also relatively long lived. They decay both non-leptonically (into pions) and semileptonically. The decay of the  $K^0$  is a case for itself and will be treated in Sect. 15.4 in some depth.

As pions and kaons are both long lived and easy to produce it is possible to produce beams of them with a definite momentum. These beams may then be used in scattering experiments. High energy pions and kaons can furthermore be used to produce secondary particle beams of muons or neutrinos if they are allowed to decay in flight (cf. Sect. 10.6).

**Table 15.3** The most important decay channels of the lightest pseudoscalar and vector mesons. The resonance's width is often given, instead of the lifetime, for those mesons which can decay in strong processes. The two quantities are related by  $\Gamma = \hbar/\tau$  (where  $\hbar = 6.6 \cdot 10^{-22}$  MeV s)

	Meson	Lifetime (s)	Most common decay channels		Comments
Pseudoscalar mesons	$\pi^\pm$	$2.6 \cdot 10^{-8}$	$\mu^\pm \nu_\mu^{(-)}$	$\approx 100\%$	(see Sect. 10.5)
			$e^\pm \nu_e^{(-)}$	$1.2 \cdot 10^{-4}$	
	$\pi^0$	$8.5 \cdot 10^{-17}$	$2\gamma$	99%	Electromagnetic
	$K^\pm$	$1.2 \cdot 10^{-8}$	$\mu^\pm \nu_\mu^{(-)}$	64%	
			$\pi^\pm \pi^0$	21%	
			$3\pi$	7%	
	$K_S^0$	$8.9 \cdot 10^{-11}$	$2\pi$	$\approx 100\%$	(K <sup>0</sup> decay: see Sect. 15.4)
	$K_L^0$	$5.1 \cdot 10^{-8}$	$3\pi$	32%	
			$\pi\mu\nu$	27%	
			$\pi e\nu$	41%	
$2\pi$			$3 \cdot 10^{-3}$	CP violating	
$\eta$	$5.5 \cdot 10^{-19}$	$3\pi$	55%	Electromagnetic	
		$2\gamma$	39%	Electromagnetic	
$\eta'$	$3.3 \cdot 10^{-21}$	$\pi\pi\eta$	65%	Electromagnetic	
		$\varrho^0\gamma$	29%		
Vector mesons	$\varrho$	$4.3 \cdot 10^{-24}$	$2\pi$	$\approx 100\%$	
	$K^{*-}$	$1.3 \cdot 10^{-23}$	$K\pi$	$\approx 100\%$	
	$\omega$	$7.8 \cdot 10^{-23}$	$3\pi$	89%	
	$\phi$	$1.5 \cdot 10^{-22}$	$2K$	83%	Zweig-suppressed
			$\varrho\pi$	15%	

The strong decays of vector mesons are normally into their lighter pseudoscalar counterparts with some extra pions as a common byproduct. The decays of the  $\varrho$  and the  $K^*$  are typical here. Their lifetimes are roughly  $10^{-23}$  s.

The  $\omega$  meson, in contrast to the  $\varrho$ , is not allowed to strongly decay into two pions for reasons of isospin and angular momentum conservation. More precisely, this is a consequence of *G-parity* conservation in the strong interaction. *G-parity* is a combination of *C-parity* and isospin symmetry [13] and will not be treated here.

How the  $\phi$  decays has already been mentioned in Sect. 9.2 (p. 131). According to the Zweig rule it prefers to decay into one meson with an s-quark and one with an  $\bar{s}$ , or, in other words, into a pair of kaons. Since their combined mass is almost as large as that of the original  $\phi$ , the phase space available is small and the  $\phi$  meson consequently has a relatively long lifetime.

The  $\eta$  and  $\eta'$  decay in a somewhat unusual manner. It is easily seen that the  $\eta$  is not allowed to strongly decay into two pions. Note first that the two pion state must have relative angular momentum  $\ell = 0$ . This follows from angular momentum conservation: both the  $\eta$  and  $\pi$  have spin 0, the pion has odd intrinsic parity and the final two pion state must have total parity  $P_{\pi\pi} = (-1)^2 \cdot (-1)^{\ell=0} = +1$ .

The  $\eta$  has, however, negative parity and so this final state can only be reached by a weak process. A decay into three pions can conserve parity but not isospin since pions, for reasons of symmetry, cannot couple to zero isospin. The upshot is that the  $\eta$  predominantly decays electromagnetically, as isospin need not then be conserved, and its lifetime is orders of magnitudes greater than those of strongly decaying particles.

The  $\eta'$  prefers to decay into  $\pi\pi\eta$  but this rate is still broadly comparable to that of its electromagnetic decay into  $\rho\gamma$ . This shows that the strong process must also be suppressed and the  $\eta'$  must have a fairly long lifetime. The story underlying this is a complicated one [19] and will not be recounted here.

### 15.4 Neutral-Kaon Decay

The decays of the  $K^0$  and the  $\bar{K}^0$  are of great importance for our understanding of the P- and C-parities (spatial reflection and particle-antiparticle conjugation).

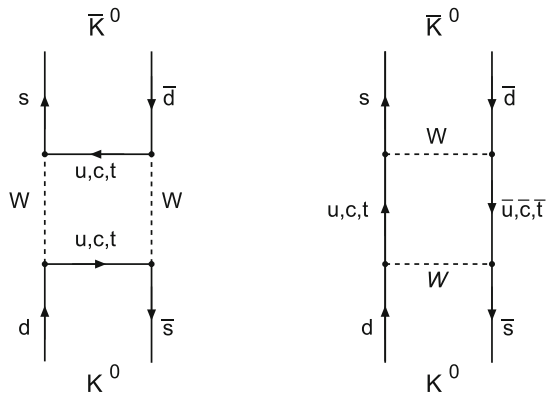
Neutral kaons can decay to either two or three pions. The two-pion final state must have positive parity, recall our discussion of the decay of the  $\eta$ , while the three-pion system has negative parity. The fact that both decays are possible is a classic example of parity violation.

**$K^0$  and  $\bar{K}^0$  mixing** The  $K^0$  and  $\bar{K}^0$  are distinct eigenstates of the strong interaction with definite strangeness. They can mix, however, via the weak interaction. Since they can decay to the same final states, they can also transform into each other via an intermediate state of virtual pions:

$$K^0 \longleftrightarrow \left\{ \begin{matrix} 2\pi \\ 3\pi \end{matrix} \right\} \longleftrightarrow \bar{K}^0 .$$

In terms of quarks this oscillation corresponds to the box diagrams in Fig. 15.3:

**Fig. 15.3** Box diagrams for  $K^0 - \bar{K}^0$  oscillation



**CP conservation** This possible mixing of particles and antiparticles leads to highly interesting effects. In Sect. 10.5 we discussed that the weak interaction violates parity maximally. This was particularly clear for the neutrino, which only occurs as a left-handed particle  $|\nu_L\rangle$  and a right-handed antiparticle  $|\bar{\nu}_R\rangle$ . In  $K^0$  decay parity violation shows itself via decays to two and three pions. For the neutrinos we further saw that the combined application of spatial reflection and charge conjugation ( $\mathcal{P}$  and  $\mathcal{C}$ ) lead to a physically allowed state:  $\mathcal{C}\mathcal{P}|\nu_L\rangle \rightarrow |\bar{\nu}_R\rangle$ . The V-minus-A theory of the weak interaction may be formulated in such a way that the combined CP quantum number is conserved.

Let us now apply this knowledge to the  $K^0$ - $\bar{K}^0$  system. The two-pion and three-pion final states are both eigenstates of the combined  $\mathcal{C}\mathcal{P}$  operator and have distinct eigenvalues

$$\begin{aligned} \mathcal{C}\mathcal{P}|\pi^0\pi^0\rangle &= +1 \cdot |\pi^0\pi^0\rangle & \mathcal{C}\mathcal{P}|\pi^0\pi^0\pi^0\rangle &= -1 \cdot |\pi^0\pi^0\pi^0\rangle \\ \mathcal{C}\mathcal{P}|\pi^+\pi^-\rangle &= +1 \cdot |\pi^-\pi^+\rangle & \mathcal{C}\mathcal{P}|\pi^+\pi^-\pi^0\rangle &= -1 \cdot |\pi^-\pi^+\pi^0\rangle, \end{aligned}$$

but neither  $K^0$  nor  $\bar{K}^0$  have well-defined CP parity:

$$\mathcal{C}\mathcal{P}|K^0\rangle = -1 \cdot |\bar{K}^0\rangle \quad \mathcal{C}\mathcal{P}|\bar{K}^0\rangle = -1 \cdot |K^0\rangle.$$

The relative phase between the  $K^0$  and the  $\bar{K}^0$  can be chosen arbitrarily. We have picked the convention  $\mathcal{C}|\bar{K}^0\rangle = +|K^0\rangle$  and this together with the kaon's odd parity leads to the minus sign under the  $\mathcal{C}\mathcal{P}$  transformation.

If we suppose that the weak interaction violates both the P- and C-parities but is invariant under  $\mathcal{C}\mathcal{P}$  then the initial kaon state has to have well-defined CP parity before its decay. Such CP eigenstates can be constructed from linear combinations in the following way:

$$\begin{aligned} |K_1^0\rangle &= \frac{1}{\sqrt{2}} \{|K^0\rangle - |\bar{K}^0\rangle\} & \text{where } \mathcal{C}\mathcal{P}|K_1^0\rangle &= +1 \cdot |K_1^0\rangle \\ |K_2^0\rangle &= \frac{1}{\sqrt{2}} \{|K^0\rangle + |\bar{K}^0\rangle\} & \text{where } \mathcal{C}\mathcal{P}|K_2^0\rangle &= -1 \cdot |K_2^0\rangle. \end{aligned}$$

This assumption of CP conservation means that we have to understand the hadronic decay of a neutral kaon as the decay of either a  $K_1^0$  into two pions or of a  $K_2^0$  into three pions. The two decay probabilities must differ sharply from one another. The phase space available to the three-pion decay is significantly smaller than for the two-pion case (this follows from the rest mass of three pions being nearly that of the neutral kaon) and so the  $K_2^0$  state ought to be much longer lived than its  $K_1^0$  sibling.

Kaons may be produced in large numbers by colliding high energy protons onto a target. An example is the reaction  $p + n \rightarrow p + \Lambda^0 + K^0$ . The strong interaction conserves strangeness  $S$  and so the neutral kaons are in an eigenstate of the strong interaction. In the case at hand it is  $|K^0\rangle$  which has strangeness  $S = +1$ . This state

may be understood in quantum mechanics as a linear combination of the two CP eigenstates  $|K_1^0\rangle$  and  $|K_2^0\rangle$ . In practice, both in reactions where  $K^0$  and in those where  $\bar{K}^0$  mesons are produced, an equal mixture of short- and long-lived particles are observed. These are called  $K_S^0$  and  $K_L^0$  (for *short* and *long*), respectively (Table 15.3). The short-lived kaons decay to two pions and the long-lived ones to three.

**Strangeness oscillations** This degree of mixing of initially 50 %  $K_S^0$  and 50 %  $K_L^0$  will not be constant with time. The time dependence of  $K^0$  and  $\bar{K}^0$  exhibits the typical oscillating behaviour of a quantum mechanical two-state system with the two base states having slightly different energies [12]. We have already discussed such a behaviour for the case of neutrino oscillations in Chap. 11. Suppose that at  $t = 0$ , a beam consists of pure  $K^0$ . Then we get in its rest system for the time dependence of the  $K^0$  and  $\bar{K}^0$  intensities:

$$\mathcal{I}_{K^0, \bar{K}^0}(t) = \frac{1}{4} \mathcal{I}_{K^0}(0) \left[ e^{-t/\tau_1} + e^{-t/\tau_2} \pm 2 \cos(|\Delta m_{12} c^2| t / \hbar) e^{-t/[2(\tau_1 + \tau_2)]} \right], \quad (15.3)$$

where  $\Delta m_{12} c^2 = m_1 c^2 - m_2 c^2$ . Here  $m_1, m_2$  are the masses of the states  $K_1^0$  and  $K_2^0$ . The + sign in front of the interference term holds for  $K^0$ , the – sign for  $\bar{K}^0$ . Besides the exponential decrease of the intensities due to the lifetimes  $\tau_1$  and  $\tau_2$ , the number of  $K^0$  and  $\bar{K}^0$  oscillates with the frequency  $\Delta m_{12} c^2 / \hbar$ . The measurement of this frequency permits a very precise determination of the mass difference of the two CP eigenstates. The number of  $\bar{K}^0$  in the initially pure  $K^0$  beam can be determined from, e.g., the yield of produced hyperons as a function of position from the source of the beam. We will show in the next chapter that the cross-section for  $\bar{K}^0$  interactions with matter is much larger than for  $K^0$ , since hyperons like  $\Lambda^0 = |uds\rangle$  or  $\Sigma^+ = |uus\rangle$  can be produced in strong interactions by  $\bar{K}^0 = |\bar{d}s\rangle$  according to  $\bar{K}^0 p \rightarrow \Lambda^0 \pi^+$  or  $\bar{K}^0 p \rightarrow \Sigma^+ \pi^0$ , but not by  $K^0 = |\bar{s}d\rangle$ . Another possibility to detect the appearance of  $\bar{K}^0$  is the observation of negatively charged leptons in semileptonic  $\bar{K}^0$  decays:  $\bar{K}^0 \rightarrow \mu^- \bar{\nu}_\mu \pi^+$  or  $\bar{K}^0 \rightarrow e^- \bar{\nu}_e \pi^+$ . In contrast, positively charged leptons are produced in  $K^0$  decays.

Precision measurements of strangeness oscillations yield the tiny mass difference

$$|\Delta m_{12} c^2| = 0.53 \cdot 10^{10} \cdot \hbar s^{-1} = 3.48 \cdot 10^{-12} \text{ MeV}. \quad (15.4)$$

**$K_S^0$  regeneration** Consider a pure  $K^0$  beam produced by the reaction  $p + n \rightarrow p + \Lambda^0 + K^0$ . Initially we will observe the rapid decays to two pions. After a flight time of many  $K_S^0$  mean-lives, essentially all of the short-lived  $K_S^0$  component has decayed. At a sufficiently large distance from the source we will now observe a pure  $K_L^0$  beam, i.e., it will only decay to three pions. We can regenerate  $K_S^0$  mesons by inserting a slice of material into the  $K_L^0$  beam. This happens as follows:  $K_L^0$  consists of 50 %  $\bar{K}^0$  and 50 %  $K^0$ . When traversing the material, the  $\bar{K}^0$  component will undergo more strong interactions than the  $K^0$  component. As a result, behind the material the beam



will contain a larger portion of  $K^0$  than of  $\bar{K}^0$  and thereby again a  $K_S^0$  component manifesting itself by decays into two pions.

**CP violation** In 1964 Christenson, Cronin, Fitch and Turlay demonstrated for the first time that also the long-lived  $K_L^0$  decays with a small probability to two pions [11]. This is mainly explained by the supposition that the mass eigenstate  $K_L^0$  is not identical to the CP eigenstate  $K_2^0$  but contains a small admixture  $\epsilon$  of the CP eigenstate  $K_1^0$  (and accordingly for  $K_S^0$ ):

$$\begin{aligned} |K_L^0\rangle &= \frac{1}{\sqrt{1+|\epsilon|^2}}(\epsilon|K_1^0\rangle + |K_2^0\rangle), \\ |K_S^0\rangle &= \frac{1}{\sqrt{1+|\epsilon|^2}}(|K_1^0\rangle + \epsilon|K_2^0\rangle). \end{aligned} \quad (15.5)$$

This CP violation due to an asymmetry in the mixing of the states  $K_1^0$  and  $K_2^0$ , where only  $K_1^0$  decays to two pions but not  $K_2^0$ , is called *indirect* CP violation. The mixing parameter  $\epsilon$  is a complex number. We can determine its magnitude by a measurement of the relative decay widths for the decays into two charged pions:

$$|\epsilon| = \sqrt{\frac{\Gamma_L(\pi^+\pi^-)}{\Gamma_S(\pi^+\pi^-)}}. \quad (15.6)$$

The present average value from several such measurements is  $|\epsilon| = (2.220 \pm 0.011) \cdot 10^{-3}$  [20].

Studies of semileptonic  $K_L^0$  decays

$$K_L^0 \rightarrow \pi^\pm + \mu^\mp + \bar{\nu}_\mu \quad K_L^0 \rightarrow \pi^\pm + e^\mp + \bar{\nu}_e$$

reveal an asymmetry  $\delta_C = (\Gamma^+ - \Gamma^-)/(\Gamma^+ + \Gamma^-) = 2\text{Re}(\epsilon)$  between the creation of particles and antiparticles: there is a slight preponderance of decays with positively charged leptons in the final state (the ratio is 1.00664 : 1). This is a further, albeit very tiny, case of CP violation.

In addition to this *indirect* CP violation in the mixing of the states  $K_1^0$  and  $K_2^0$ , also *direct* CP violation in the decay can occur when various processes with different weak and strong phases contribute to the decay and interfere. In Fig. 15.4, two different processes are shown for the decay of  $\bar{K}^0$  into neutral and charged pions. The diagrams in which the  $W^-$  decays directly into a  $\bar{u}d$  are called tree diagrams, the other two with the loop of a virtual  $W^-$  and an u-, c-, t-quark, are named penguin diagrams since in a special version they are supposed to resemble a penguin. The latter diagrams involve gluon exchange and thus strong interactions.

The complex parameter for *direct* CP violation is called  $\epsilon'$ . The parameters  $\epsilon$  and  $\epsilon'$  are related to the ratio of amplitudes  $\mathcal{A}$  for the CP-violating and the CP-

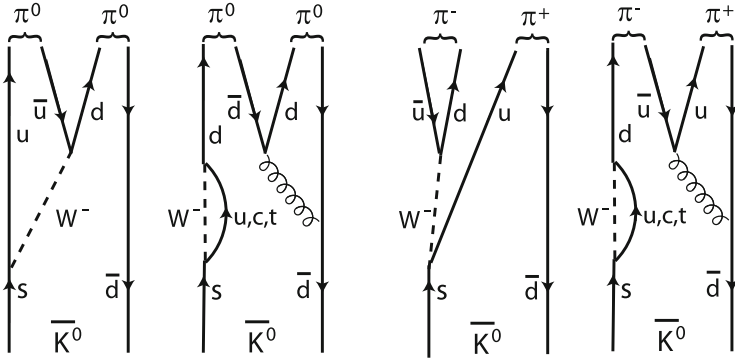


**Fig. 15.4** Diagrams for the decay of  $\bar{K}^0$  into pairs of neutral and charged pions

conserving decays to two neutral or two charged pions:

$$\frac{\mathcal{A}(K_L^0 \rightarrow \pi^+ \pi^-)}{\mathcal{A}(K_S^0 \rightarrow \pi^+ \pi^-)} \approx \epsilon + \epsilon',$$

$$\frac{\mathcal{A}(K_L^0 \rightarrow \pi^0 \pi^0)}{\mathcal{A}(K_S^0 \rightarrow \pi^0 \pi^0)} \approx \epsilon - 2\epsilon'. \quad (15.7)$$

The measurement of  $\epsilon'$  requires large experimental efforts. At both CERN and FNAL two parallel  $K_L^0$  beams were produced [2, 9]. After a long distance from the source a movable regenerator was inserted in one of the two beams to regenerate  $K_S^0$ . This method allows a comparison of  $K_L^0$  and  $K_S^0$  decays occurring at the same distance from the detector and thus with the same geometrical acceptance. In the double ratio

$$\frac{\Gamma(K_L^0 \rightarrow \pi^+ \pi^-) / \Gamma(K_S^0 \rightarrow \pi^+ \pi^-)}{\Gamma(K_L^0 \rightarrow \pi^0 \pi^0) / \Gamma(K_S^0 \rightarrow \pi^0 \pi^0)} \approx 1 + 6 \operatorname{Re}(\epsilon' / \epsilon) \quad (15.8)$$

many systematic uncertainties are minimised.

The current average value of  $\operatorname{Re}(\epsilon' / \epsilon)$  is  $(1.66 \pm 0.23) \cdot 10^{-3}$  [20]. Thus, in  $K^0$  decays the *direct* CP violation is about a thousand times smaller than the *indirect* CP violation in the mixing of the CP eigenstates that is common to all decay channels.

For quite some time CP violation had only been experimentally observed in the  $K^0 \leftrightarrow \bar{K}^0$  system. Other electrically neutral meson-antimeson systems were expected, however, to display a similar behaviour. In 1987  $B^0 \leftrightarrow \bar{B}^0$  mixing was indeed observed at DESY [3–5]. The mixing of  $D^0$  and  $\bar{D}^0$  was observed for the first time in 2007 by the experiments *BaBar* and *Belle* [7, 22]. In the following section we will discuss CP violation in the  $B^0$  system.

## 15.5 CP Violation and the CKM Matrix

In Sect. 10.4 we introduced the CKM matrix (10.22). For weak interactions with charged currents this matrix quantifies the relative strengths for transitions of quarks within a family or from one family to another one (cf. Fig. 13.2). Kobayashi and Maskawa had already introduced this matrix, by which they wanted to explain CP violation, before the second quark family had been established by the discovery of the  $c$ -quark. As we subsequently will show, CP violation requires the existence of a complex unitary ( $n \times n$ ) matrix with  $n \geq 3$ . This matrix has to be complex, since only then the mixing of quarks is different from the mixing of antiquarks that is described by the corresponding conjugate matrix.

A complex unitary ( $3 \times 3$ ) matrix  $V$  has 18 independent parameters. These can be reduced to nine parameters by the unitarity requirement  $V_{\alpha\beta}V_{\beta\gamma}^* = \delta_{\alpha\gamma}$ . We can absorb an arbitrary phase in every left-handed quark field. This removes an arbitrary phase from each row and each column. But we still have to consider a common phase, since  $V$  is unaffected by a common phase transformation of all six quark fields. Consequently,  $V$  can be described by  $18 - 9 - 5 = 4$  independent physical parameters. In general, the mixing matrix for  $n$  generations contains  $(n-1)^2$  independent parameters. For two families only one parameter is needed, the Cabibbo angle  $\theta_C$ . A complex phase, which is responsible for CP violation, only appears for  $n \geq 3$ .

For three families we thus have four parameters: the mixing angles  $\theta_{12}$ ,  $\theta_{13}$  and  $\theta_{23}$  between the three quark families and the complex phase  $\delta$ . The elements of the CKM matrix are linear combinations of products of  $\cos \theta_{ij}$  and  $\sin \theta_{ij}$  ( $i, j = 1, 2, 3$ ;  $i \neq j$ ), with some elements containing the phase term  $e^{-i\delta}$ .

**Wolfenstein presentation of the CKM matrix** The CKM matrix can be parametrised to good approximation very vividly [23], when one bears in mind that with increasing family number the off-diagonal elements become successively smaller. We define

$$\begin{aligned} s_{12} &= \sin \theta_{12} = \sin \theta_C = \lambda, \\ s_{13} &= \sin \theta_{13} = A \cdot \lambda^2, \\ s_{23} e^{-i\delta} &= A \cdot \lambda^3 (\varrho - i\eta). \end{aligned} \quad (15.9)$$

Considering only terms up to the order  $\mathcal{O}(\lambda^3)$ , we obtain:

$$V_{\text{CKM}} = \begin{pmatrix} 1 - \lambda^2/2 & \lambda & A\lambda^3(\varrho - i\eta) \\ -\lambda & 1 - \lambda^2/2 & A\lambda^2 \\ A\lambda^3(1 - \varrho - i\eta) & -A\lambda^2 & 1 \end{pmatrix}. \quad (15.10)$$

In this approximation we have two elements with an imaginary part. The phase factor appears for transitions between the first and the third family, i.e., in the elements  $V_{ub}$  and  $V_{td}$ .

**CP violation in the  $B^0$  sector and the unitarity triangle** The effects of CP violation can be nicely illustrated with help of the so-called unitarity triangle. For products of different columns and rows of  $V$  and  $V^*$  we have:

$$V_{ki}V_{kj}^* = V_{il}V_{jl}^* = 0; \quad i \neq j; \quad k = u, c, t; \quad l = s, d, b. \quad (15.11)$$

From the product of the first row of  $V$  and the third row of  $V^*$  we obtain, for example, information about the CP violation in the  $B^0$  sector:

$$V_{ud}V_{ub}^* + V_{cd}V_{cb}^* + V_{td}V_{tb}^* = 0. \quad (15.12)$$

This is the equation for a triangle in the complex plane with the lengths of all three sides being of order  $A\lambda^3$ . In Fig. 15.5 the rescaled unitarity triangle is shown, where the sides are normalised to  $V_{cd}V_{cb}^*$ . The corners of this triangle have the coordinates  $(0,0)$ ,  $(1,0)$  and  $(\rho, \eta)$ . CP violation requires the imaginary parts  $A\lambda^3\eta$  of  $V_{ub}^*$  and of  $V_{td}$  to be different from zero. Hence, a measurement of CP violation is equivalent to a determination of at least one of the three angles  $\alpha$ ,  $\beta$  and  $\gamma$ .

For the CP violation in the  $K^0$  sector we consider the unitarity relation

$$V_{ud}V_{us}^* + V_{cd}V_{cs}^* + V_{td}V_{ts}^* = 0. \quad (15.13)$$

Here, the term with the complex part,  $V_{td}V_{ts}^*$ , is proportional to  $A^2\lambda^5$ . This is the reason that the parameter  $\epsilon'$  is so small in  $K^0$  decays. CP violation in the  $B^0$  sector should, therefore, be substantially larger than in the  $K^0$  sector.

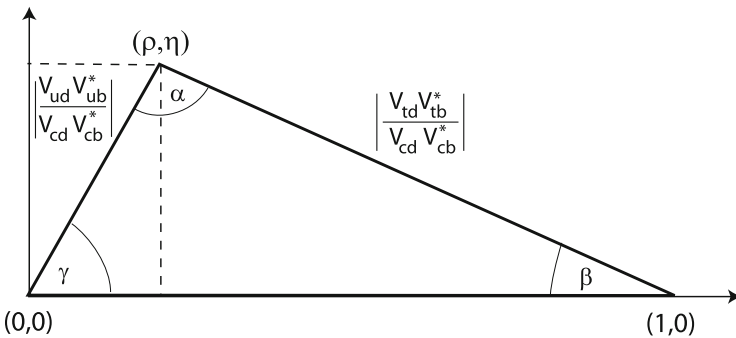


Fig. 15.5 The rescaled unitarity triangle in the  $B^0$  sector

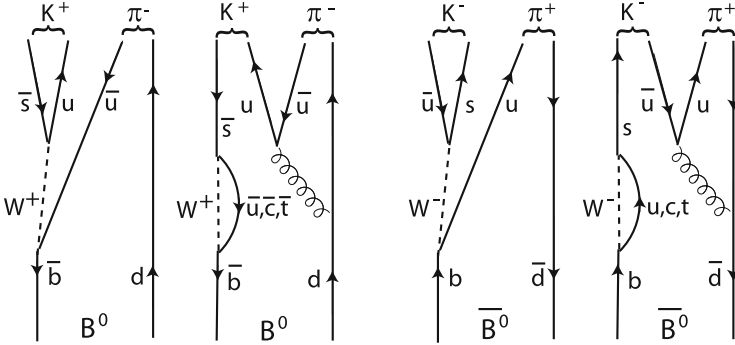


Fig. 15.6 Diagrams for the decays  $B^0 \rightarrow K^+ \pi^-$  (left) and  $\bar{B}^0 \rightarrow K^- \pi^+$  (right)

**Experimental determination of CP violation in the B sector** At the end of the 1990s two high-luminosity electron-positron storage rings were constructed to detect the relatively large CP violation predicted by the standard model in the B sector and to study it in detail: KEK-B in Japan with the detector *Belle* [1] and PEP-II at SLAC with the detector *BaBar* [6]. These were predominantly operated at the centre-of-mass energy of the  $\Upsilon$  ( $4^3S_1$ ) which is slightly above the threshold for  $B\bar{B}$  production (cf. Sect. 14.6). The  $\Upsilon$  ( $4^3S_1$ ) decays with a branching ratio of more than 96 % to  $B\bar{B}$  pairs. In order to increase the decay length in the laboratory system (cf. Problem 15.4) and to thereby allow the measurement of time-dependent CP asymmetries, the  $e^+$ - and  $e^-$  beams had different energies; at KEK-B they were 3.5 and 8 GeV, whereas at PEP-II they were 3.1 and 9 GeV. These experiments investigated a plethora of B-meson decays and their decay products that allowed, amongst other things, the determination of many of the elements of the CKM matrix with high precision. A detailed discussion of the measurements and the results can be found, e.g., in [10, 16].

Here we will only present two measurements and their results. One example for *direct* CP violation is the decay  $B^0 \rightarrow K^+ \pi^-$  and  $\bar{B}^0 \rightarrow K^- \pi^+$ , to which tree and penguin diagrams with different weak and strong phases contribute. We have already discussed this in Sect. 15.4 about CP violation in the  $K^0$  sector. The diagrams for the B sector are shown in Fig. 15.6.

Experimentally one obtains an asymmetry in the decay width [8, 18, 20]

$$\frac{\Gamma(\bar{B}^0 \rightarrow K^- \pi^+) - \Gamma(B^0 \rightarrow K^+ \pi^-)}{\Gamma(\bar{B}^0 \rightarrow K^- \pi^+) + \Gamma(B^0 \rightarrow K^+ \pi^-)} = -0.098 \pm 0.013, \quad (15.14)$$

which is many times larger than the corresponding asymmetry in the  $K^0$  sector.

Of great interest is also the decay of  $B^0$  and  $\bar{B}^0$  to the common final state  $f = J/\psi K_S^0 \rightarrow \ell^+ \ell^- \pi^+ \pi^-$ . Because of its clear signature, this is often called the “golden channel”. The decay to two pions selects from the originally-generated  $K^0$  (in the case of  $B^0$ ) or  $\bar{K}^0$  (in the case of  $\bar{B}^0$ ) the CP eigenstate with the CP eigenvalue  $\eta_K = +1$ . The final state has a CP eigenvalue  $\eta_f = -1$ , since the  $K_S^0$  (spin-0) and

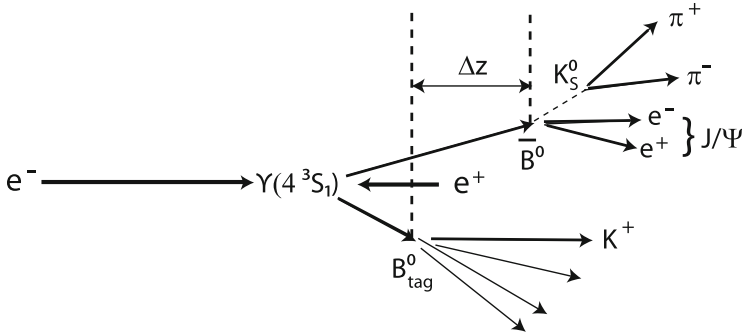


**Fig. 15.7** The method of ‘tagging’ in the decay  $\Upsilon(4^3S_1) \rightarrow B^0\bar{B}^0$

the  $J/\psi$  (spin-1) from the decay of the  $B^0$  (spin-0) must have the relative orbital angular momentum  $\ell = 1$ . Here, CP violation is caused by the interference of decays with and without mixing of the neutral mesons. The time dependence of the asymmetry of the rates for  $B^0 \rightarrow f$  and  $\bar{B}^0 \rightarrow f$  has been investigated. This presupposes knowledge of whether the decay stems from a  $B^0$  or from a  $\bar{B}^0$ . For this purpose the method of “tagging” was used as shown in Fig. 15.7 and described below.

In the decay of the  $\Upsilon(4^3S_1)$ , the two B-mesons are produced in a coherent state. Suppose that one observes the decay of one of the mesons, for instance to the final state  $\ell^+ \nu_\ell X$  or  $K^+ X$ . Then it is clear that the decaying particle is a  $B^0$  and its partner has to be a  $\bar{B}^0$ . Correspondingly decays to  $\ell^- \nu_\ell X$  or  $K^- X$  tag a  $\bar{B}^0$  and the partner is a  $B^0$ . The distance between the two decay vertices  $\Delta z$  then corresponds to the relative decay time  $\Delta t = \Delta z / (c\beta\gamma)$ . For the asymmetry of the decay rates to the final states  $f = J/\psi K_S^0$ , we obtain (a detailed derivation can be found, e.g., in [17, 21]):

$$\frac{\Gamma(\bar{B}^0 \rightarrow f)(\Delta t) - \Gamma(B^0 \rightarrow f)(\Delta t)}{\Gamma(\bar{B}^0 \rightarrow f)(\Delta t) + \Gamma(B^0 \rightarrow f)(\Delta t)} = \eta_f \sin 2\beta \sin(\Delta M_{12} c^2 / \hbar \cdot \Delta t). \quad (15.15)$$

Here,  $\beta$  is the angle in the rescaled unitarity triangle at the corner (1,0) and  $\Delta M_{12}$  is the mass difference of the two CP eigenstates  $B_1^0$  and  $B_2^0$ . (There are very many decay channels for the two CP eigenstates. Consequently, only their masses are different but not their lifetimes.) The asymmetry oscillates with the frequency  $\Delta M_{12} c^2 / \hbar$  and the amplitude  $\sin 2\beta$ . The present average values from various measurements are [20]:  $\sin 2\beta = 0.679 \pm 0.020$  and  $\Delta M_{12} c^2 = 0.5 \cdot 10^{12} \hbar s^{-1} = 3.3 \cdot 10^{-10} \text{ MeV}$ .

These are only two examples from a large number of measurements by which CP violation in the B sector has been investigated and the elements of the CKM matrix have been determined [16]. Other examples are the measurement of the asymmetry  $B^0/\bar{B}^0 \rightarrow \pi^- \pi^+$ , from which the angle  $\alpha$  can be determined, or the asymmetry  $B_s^0/\bar{B}_s^0 \rightarrow D_s^\mp K^\pm$ , that fixes the angle  $\gamma$ .

Many more precise results (amongst others on the CP violation in D-meson decay) are expected from the LHCb experiment at the LHC, where the production rates of B-mesons will be larger than those at B factories by more than three orders of magnitude. These measurements possibly will also allow a glimpse into physics beyond the standard model.

## Problems

### 1. $\rho^0$ -decay

The  $\rho^0$  ( $J^P = 1^-, I = 1$ ) almost 100 % decays into  $\pi^+ + \pi^-$ . Why does it not also decay into  $2\pi^0$ ?

### 2. $D^+$ -decay

$D^+$  ( $c\bar{d}$ ) decays into many channels. What value would you expect for the ratio:

$$R = \frac{\Gamma(D^+ \rightarrow K^- + \pi^+ + \pi^+)}{\Gamma(D^+ \rightarrow \pi^- + \pi^+ + \pi^+)}.$$

### 3. Pion and kaon decay

High energy neutrino beams can be generated using the decay of high energy, charged pions and kaons:

$$\begin{aligned}\pi^\pm &\rightarrow \mu^\pm + \overset{(-)}{\nu}_\mu \\ K^\pm &\rightarrow \mu^\pm + \overset{(-)}{\nu}_\mu.\end{aligned}$$

- What fraction  $F$  of the pions and kaons in a 200 GeV beam decays inside a distance  $d = 100$  m? (Use the particle masses and lifetimes given in Tables 15.2 and 15.3)
- How large are the minimal and maximal neutrino energies in both cases?

### 4. B-meson factory

$\Upsilon$ -mesons with masses  $10.58 \text{ GeV}/c^2$  were produced in the reaction  $e^+e^- \rightarrow \Upsilon(4S)$  at the DORIS and CESR storage rings. The  $\Upsilon(4S)$ -mesons were produced at rest in the laboratory frame and decayed immediately to a pair of B-mesons:  $\Upsilon \rightarrow B^+B^-$ . The mass  $m_B$  of the B-mesons is  $5.28 \text{ GeV}/c^2$  and its lifetime  $\tau$  is 1.5 ps.

- How large is the average decay length of the B-mesons in the laboratory frame?
- To increase the decay length, the  $\Upsilon(4S)$ -mesons need to be given momentum in the laboratory frame. This idea was employed at the asymmetric ‘‘B-factories’’ PEP-II at SLAC and KEK-B in Japan, where electrons and

- positrons with different energies collide. What momentum do the B-mesons need to have, if their average decay length is to be 0.2 mm?
- (c) What energy do the  $\Upsilon(4S)$ -mesons, in whose decay the B-mesons are produced, need to have for this?
- (d) What energy do the electron and positron beams need to have to produce these  $\Upsilon(4S)$ -mesons? To simplify the last three questions, without altering the result, assume that the B-mesons have a mass of  $5.29 \text{ GeV}/c^2$  (instead of the correct  $5.28 \text{ GeV}/c^2$ ).

## References

1. K. Abe et al., Nucl. Instr. Methods **A479**, 117 (2002)
2. E. Abouzaid et al., Phys. Rev. D **83**, 092001 (2011)
3. C. Albajar et al., Phys. Lett. **B186**, 247 (1987)
4. H. Albrecht et al., Phys. Lett. **B192**, 245 (1987)
5. H. Albrecht et al., Z. Phys **C55**, 357 (1992)
6. B. Aubert et al., Nucl. Instr. Methods **A479**, 1 (1997)
7. B. Aubert et al., Phys. Rev. Lett. **98**, 211802 (2007)
8. B. Aubert et al., Phys. Rev. Lett. **99**, 021603 (2007)
9. J.R. Batley et al., Phys. Lett. **B595**, 75 (2002)
10. T.E. Browder, R. Faccini, Annu. Rev. Nucl. Part. Sci. **53**, 353 (2003)
11. J.H. Christenson, J.W. Cronin, V.L. Fitch, R. Turlay, Phys. Rev. Lett. **13**, 138 (1964)
12. R.P. Feynman, *Feynman Lectures on Physics. The New Millenium Editon*, vol. III, Chap. 8 (Perseus-Basic Books, New York, 2011)
13. S. Gasiorowicz, *Elementary Particle Physics* (Wiley, New York, 1966)
14. S. Gasiorowicz, J.L. Rosner, Am. J. Phys. **49**, 954 (1981)
15. K. Gottfried, V.F. Weisskopf, *Concepts of Particle Physics*, vol. 1 (Clarendon Press, Oxford/New York, 1984)
16. A. Höcker, Z. Ligeti, Annu. Rev. Nucl. Part. Sci. **56**, 501 (2006)
17. K. Kleinknecht, *Uncovering CP Violation*. Springer Tracts in Modern Physics, vol. 195 (Springer, Berlin/Heidelberg, 2003)
18. S.-W. Lin et al., Nature **452**, 332 (2008)
19. B.M.K. Nefkens, *Proceedings of the Workshop on Meson Production, Interaction and Decay*, Kraków/Poland (World Scientific, Singapore, 1991)
20. Particle Data Group, J. Beringer et al., *Review of Particle Properties*. Phys. Rev. D **86**, 010001 (2012)
21. A. Seiden, *Particle Physics, A Comprehensive Introduction* (Addison Wesley, San Francisco, 2005)
22. M. Staric et al., Phys. Rev. Lett. **98**, 211803 (2007)
23. L. Wolfenstein, Phys. Rev. Lett. **51**, 1945 (1983)



# Chapter 16

## Baryons

The best known baryons are the proton and the neutron. These are collectively referred to as the nucleons. Our study of deep-inelastic scattering has taught us that they are composed of three valence quarks, gluons and a “sea” of quark-antiquark pairs. The following treatment of the baryon spectrum will, analogously to our description of the mesons, be centred around the concept of the constituent quark.

**Nomenclature** This chapter will be solely concerned with those baryons which are made up of u-, d- and s-quarks. The baryons whose valence quarks are just u- and d-quarks are the nucleons (isospin  $I = 1/2$ ) and the  $\Delta$  particles ( $I = 3/2$ ). Baryons containing s-quarks are collectively known as *hyperons*. These particles, the  $\Lambda$ ,  $\Sigma$ ,  $\Xi$  and  $\Omega$ , are distinguished from each other by their isospin and the number of s-quarks they contain.

Name		N	$\Delta$	$\Lambda$	$\Sigma$	$\Xi$	$\Omega$
Isospin	$I$	1/2	3/2	0	1	1/2	0
Strangeness	$S$	0		-1		-2	-3
Number of s-quarks		0		1		2	3

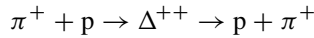
The antihyperons have strangeness +1, +2 or +3, respectively.

The discovery of baryons containing c- and b-quarks has caused this scheme to be extended. The presence of quarks heavier than the s-quark is signified by an subscript attached to the relevant hyperon symbol: thus the  $\Lambda_c^+$  corresponds to a ( $udc$ ) state and the  $\Xi_{cc}^{++}$  has the valence structure ( $ucc$ ). Such heavy baryons will not, however, be discussed in what follows.

## 16.1 The Production and Detection of Baryons

**Formation experiments** Baryons can be produced in many different ways at accelerators. In Sect. 7.1 we have already described how nucleon resonances may be produced in inelastic electron scattering. These excited nucleon states are also created when pions are scattered off protons.

One can then study, for example, the energy (mass) and width (lifetime) of the  $\Delta^{++}$  resonance in the reaction



by varying the energy of the incoming pion beam and measuring the total cross-section. The largest and lowest energy peak in the cross-section is found at 1,232 MeV. This is known as the  $\Delta^{++}(1232)$ . Figure 16.1 shows its creation and decay in terms of quark lines. In simple terms we may say that the energy which is released in the quark-antiquark annihilation is converted into the excitation energy of the resonance and that this process is reversed in the decay of the resonance to form a new quark-antiquark pair. This short-lived state decays about  $0.5 \cdot 10^{-23}$  s after it is formed and it is thus only possible to detect the decay products, i.e., the proton and the  $\pi^+$ . Their angular distribution, however, may be used to determine the resonances' spin and parity. The result is found to be  $J^P = 3/2^+$ . The extremely short lifetime attests to the decay taking place through the strong interaction. At higher centre-of-mass energies in this reaction further resonances may be seen in the cross-section. These correspond to excited  $\Delta^{++}$  states where the quarks occupy higher energy levels. Strangeness may be brought into the game by replacing the pion beam by a kaon

**Fig. 16.1** Quark-line diagram for the formation and the decay of the  $\Delta^{++}$  resonance in the reaction  $\pi^+ + p \rightarrow \Delta^{++} p + \pi^+$

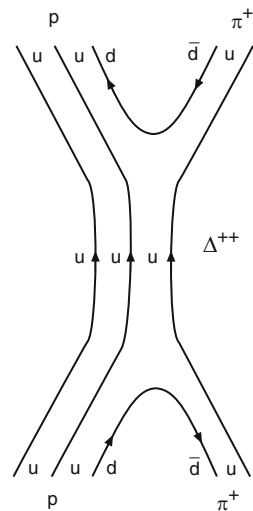
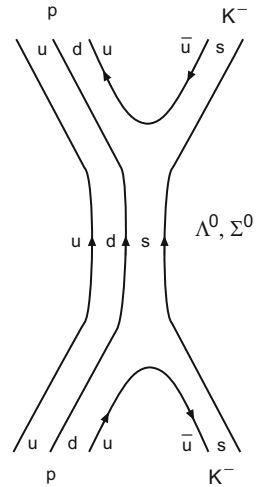
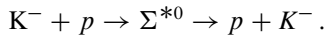


**Fig. 16.2** Quark-line diagram for the formation and decay of  $\Lambda^0$  and  $\Sigma^0$  hyperons in the reaction  $K^- p \rightarrow (\Lambda^0, \Sigma^0) \rightarrow p K^-$



beam and one may thus generate hyperons as sketched in Fig. 16.2. A possible reaction is



The intermediate resonance state, an excited state of the  $\Sigma^0$ , is, like the  $\Delta^{++}$ , extremely short-lived and “immediately” decays, primarily back into a proton and a negatively charged kaon. The quark line diagram offers a general description of all those resonances whose quark composition is such that they may be produced in this process. Thus excited  $\Lambda^0$ 's may also be created in the above reaction. The cross-sections of the above reactions are displayed in Fig. 16.3 as functions of the centre-of-mass energy. The resonance structures may be easily recognised. The individual peaks, which give us the masses of the excited baryon states, are generally difficult to separate from each other. This is because their widths are typically of the order of 100 MeV and the various peaks hence overlap. Such large widths are characteristic for particles which decay via strong processes.

In *formation experiments*, like those discussed above, the baryon that is formed is detected as a resonance in a cross-section. Due to the limited number of particle beams available to us this method may only be used to generate nucleons and their excited states or those hyperons with strangeness  $S = -1$ .

**Production experiments** A more general way of generating baryons is in *production experiments*. In these one fires a beam of protons, pions or kaons with as high an energy as possible at a target. The limit on the energy available for the production of new particles is the centre-of-mass energy of the scattering process. As can be seen from Fig. 16.3, for centre-of-mass energies greater than 3 GeV no further resonances can be recognised and the elastic cross-section is thereafter only a minor part of the total cross-section. This energy range is dominated by inelastic particle production.

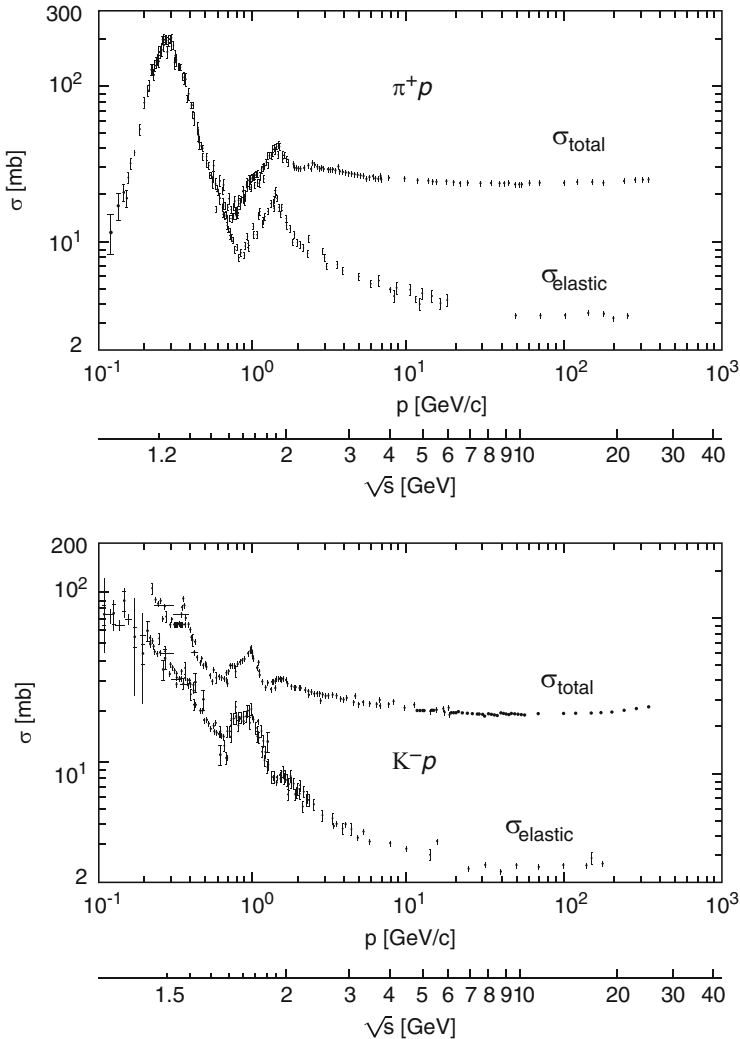


**Fig. 16.3** The total and elastic cross-sections for the scattering of  $\pi^+$  mesons off protons (*top*) and of  $K^-$  mesons off protons (*bottom*) as a function of the meson beam momentum (or centre-of-mass energy) [15]. The peaks are associated with short-lived states, and since the total initial charge in  $\pi^+ p$  scattering is  $+2e$  the relevant peaks must correspond to the  $\Delta^{++}$  particle. The strongest peak, at a beam momentum of around 300 MeV/c is due to the ground state of the  $\Delta^{++}$  which has a mass of 1,232 MeV/c<sup>2</sup>. The resonances that show up as peaks in the  $K^- p$  cross-section are excited, neutral  $\Sigma$  and  $\Lambda$  baryons. The most prominent peaks are the excited  $\Sigma^0(1775)$  and  $\Lambda^0(1820)$  states which overlap significantly

In such production experiments one does not look for resonances in the cross-section but rather studies the particles which are created, generally in generous quantities, in the reactions. If these particles are short-lived, then it is only possible

to actually detect their decay products. The short-lived states can, however, often be reconstructed by the invariant-mass method. If the momenta  $\mathbf{p}_i$  and energies  $E_i$  of the various products can be measured, then we may use the fact that the mass  $M_X$  of the decayed particle X is given by

$$M_X^2 c^4 = p_X^2 c^2 = \left( \sum_i p_i c \right)^2 = \left( \sum_i E_i \right)^2 - \left( \sum_i \mathbf{p}_i c \right)^2. \quad (16.1)$$

In practice one studies a great number of scattering events and calculates the invariant mass of some particular combination of the particles which have been detected. Short-lived resonances which have decayed into these particles reveal themselves as peaks in the invariant-mass spectrum. We may identify short-lived resonances that we already knew about in this way and we can also see if new, previously unknown particles are being formed.

As an example, Fig. 16.4 shows the invariant-mass spectrum of the  $\Lambda^0 + \pi^+$  final particles from an early measurement of the reaction

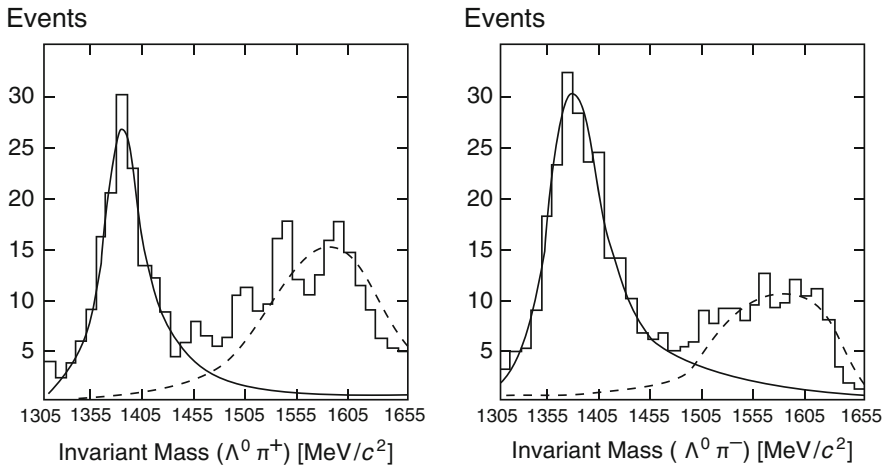
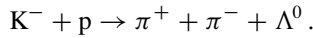
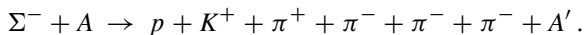


**Fig. 16.4** Invariant-mass spectrum of the particle combinations  $\Lambda^0 + \pi^+$  (left) and  $\Lambda^0 + \pi^-$  (right) in the reaction  $K^- + p \rightarrow \pi^+ + \pi^- + \Lambda^0$ . The momentum of the initial kaon was 1.11 GeV/c. The events were recorded in a bubble chamber. Both spectra display a peak around 1,385 MeV/c<sup>2</sup> that corresponds to  $\Sigma^{*+}$  and  $\Sigma^{*-}$  accordingly. A Breit-Wigner distribution (continuous line) has been fitted to the peak. The mass and width of the resonance may be found in this way. The energy of the pion which is not involved in the decay is kinematically fixed for any particular beam energy. Its combination together with the  $\Lambda^0$  yields a “false” peak at higher energies which does not correspond to a resonance (From [9])

This displays a clear peak at  $1,385 \text{ MeV}/c^2$  which corresponds to an excited  $\Sigma^+$ . The  $\Sigma^{*+}$  baryon is therefore identified from its decay  $\Sigma^{*+} \rightarrow \pi^+ + \Lambda^0$ . Since this is a strong decay all quantum numbers, e.g., strangeness and isospin, are conserved. In the above reaction it is just as likely to be the case that a  $\Sigma^{*-}$  state is produced. This would then decay to  $\Lambda^0 + \pi^-$ . Study of the invariant masses yields almost identical masses for these two baryons.<sup>1</sup> This may also be read off from Fig. 16.4. The somewhat flatter peak at higher energies visible in both spectra is a consequence of the possibility to create either of these two charged  $\Sigma$  resonances: the momentum and energy of the pion which is not created in the decay is fixed and so creates a “fictitious” peak in the invariant-mass spectrum. This ambiguity can be resolved by carrying out the experiment at various beam energies. There is a further small background in the invariant-mass spectrum which is not correlated with the above, i.e., it does not come from  $\Sigma^{*\pm}$  decay. We note that the excited  $\Sigma$  state was first found in 1960 using the invariant-mass method [5].

If the baryon state that we wish to investigate is already known, then the resonance may be investigated in individual events as well. This is, for example, important for the above identification of the  $\Sigma^{*+}$ , since the  $\Lambda^0$  itself decays via  $\Lambda^0 \rightarrow p + \pi^-$  and must first be reconstructed by the invariant-mass method. The detection of the  $\Lambda^0$  is rendered easier by its long lifetime of  $2.6 \cdot 10^{-10} \text{ s}$  (due to its weak decay). On average the  $\Lambda^0$  transverses a distance from several centimetres to a few metres, depending upon its energy, before it decays. From the tracks of its decay products, the position of the  $\Lambda^0$ 's decay may be localised and distinguished from that of the primary reaction.

A nice example of such a step-by-step reconstruction of the initially created, primary particles from a  $\Sigma^-$ +nucleus reaction is shown in Fig. 16.5. The method of invariant masses could be used to show a three-step process of baryon decays. The measured reaction is



The initial reaction takes place at one of the protons of a nucleus A. All of the particles in the final state were identified (except for the final nucleus A') and their momenta were measured. The tracks of a proton and a  $\pi^-$  could be measured in drift and proportional chambers and followed back to the point (3), where a  $\Lambda^0$  decayed (as a calculation of the invariant mass of the proton and the  $\pi^-$  shows). Since we thus have the momentum of the  $\Lambda^0$  we can extrapolate its path back to (2) where it meets the path of a  $\pi^-$ . The invariant mass of the  $\Lambda^0$  and of this  $\pi^-$  is roughly  $1,320 \text{ MeV}/c^2$  which is the mass of the  $\Xi^-$  baryon. This baryon can in turn be traced to the target at (1). The analysis then shows that the  $\Xi^-$  was in fact the decay product of a primary  $\Xi^{*0}$  state which “instantaneously” decayed via the strong interaction

---

<sup>1</sup>The mass difference between the  $\Sigma^{*-}$  and the  $\Sigma^{*+}$  is roughly  $4 \text{ MeV}/c^2$  (see Table 16.1 on p. 265).

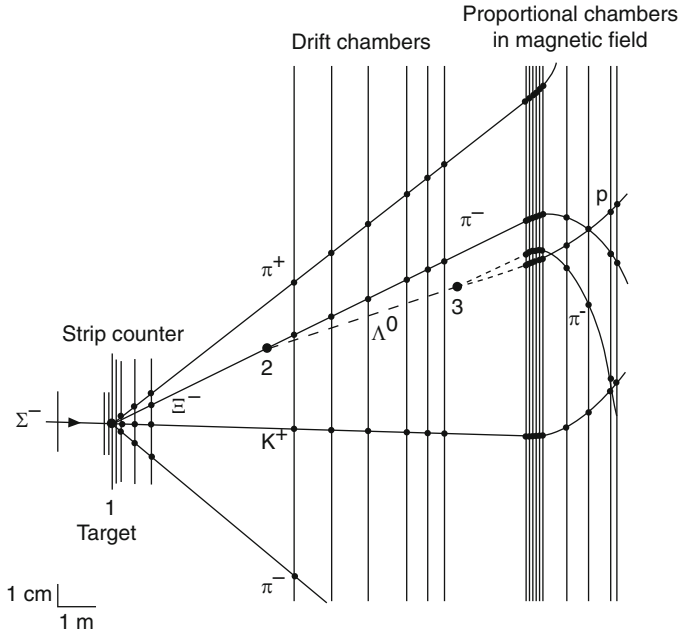
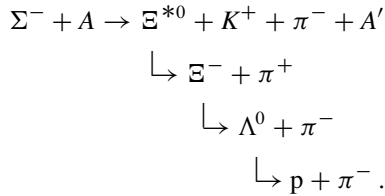


**Fig. 16.5** Detection of a baryon decay cascade at the WA89 detector at the CERN hyperon beam (based upon [16]). In this event a  $\Sigma^-$  hyperon with 370 GeV kinetic energy hits a thin carbon target. The paths of the charged particles thus produced are detected near the target by silicon strip detectors and further away by drift and proportional chambers. Their momenta are determined by measuring the deflection of the tracks in a strong magnetic field. The tracks marked in the figure are based upon the signals from the various detectors. The baryonic decay chain is described in the text

to a  $\Xi^-$  and a  $\pi^+$ . The complete reaction in all its glory was therefore the following



This reaction also exemplifies the associated production of strange particles: the  $\Sigma^-$  from the beam had strangeness  $-1$  and yet produces in the collision with the target a  $\Xi^{*0}$  with strangeness  $-2$ . Since the strange quantum number is conserved in strong interactions an additional  $K^+$  with strangeness  $+1$  was also created.

## 16.2 Baryon Multiplets

We now want to describe in somewhat more detail which baryons may be built up from the u-, d- and s-quarks. We will though limit ourselves to the lightest states, i.e., those for which the quarks have relative orbital angular momentum  $\ell = 0$  and are not radially excited.

The three valence quarks in the baryon must, by virtue of their fermionic character, satisfy the Pauli principle. In other words, the total baryonic wave function

$$\psi_{\text{total}} = \xi_{\text{spatial}} \cdot \zeta_{\text{flavour}} \cdot \chi_{\text{spin}} \cdot \phi_{\text{colour}}$$

must be antisymmetric under the exchange of any two of the quarks. The total baryonic spin  $S$  results from adding the three individual quark spins ( $s = 1/2$ ) and must be either  $S = 1/2$  or  $S = 3/2$ . Since we demand that  $\ell = 0$ , the total angular momentum  $J$  of the baryon is just the total spin of the three quarks.

**The baryon decuplet** Let us first investigate the  $J^P = 3/2^+$  baryons. Here the three quarks have parallel spins and the spin wave function is therefore symmetric under an interchange of two of the quarks. For  $\ell = 0$  states this is also true of the spatial wave function. Taking, for example, the  $uuu$  state it is obvious that the flavour wave function has to be symmetric and this then implies that the colour wave function must be totally antisymmetric in order to yield an antisymmetric total wave function and so fulfil the Pauli principle. Because baryons are colourless objects the totally antisymmetric colour wave function can be constructed as follows:

$$\phi_{\text{colour}} = \frac{1}{\sqrt{6}} \sum_{\alpha=r,g,b} \sum_{\beta=r,g,b} \sum_{\gamma=r,g,b} \varepsilon_{\alpha\beta\gamma} |q_{\alpha}q_{\beta}q_{\gamma}\rangle, \quad (16.2)$$

where we sum over the three colours, here denoted by *red*, *green* and *blue*, and  $\varepsilon_{\alpha\beta\gamma}$  is the totally antisymmetric tensor.

If we do not concern ourselves with radial excitations, we are left with ten different systems that can be built out of three quarks, are  $J^P = 3/2^+$  and have totally antisymmetric wave functions. These are

$$|\Delta^{++}\rangle = |u\uparrow u\uparrow u\uparrow\rangle \quad |\Delta^{+}\rangle = |u\uparrow u\uparrow d\uparrow\rangle \quad |\Delta^0\rangle = |u\uparrow d\uparrow d\uparrow\rangle \quad |\Delta^{-}\rangle = |d\uparrow d\uparrow d\uparrow\rangle$$

$$|\Sigma^{*+}\rangle = |u\uparrow u\uparrow s\uparrow\rangle \quad |\Sigma^{*0}\rangle = |u\uparrow d\uparrow s\uparrow\rangle \quad |\Sigma^{*-}\rangle = |d\uparrow d\uparrow s\uparrow\rangle$$

$$|\Xi^{*0}\rangle = |u\uparrow s\uparrow s\uparrow\rangle \quad |\Xi^{*-}\rangle = |d\uparrow s\uparrow s\uparrow\rangle$$

$$|\Omega^{-}\rangle = |s\uparrow s\uparrow s\uparrow\rangle.$$



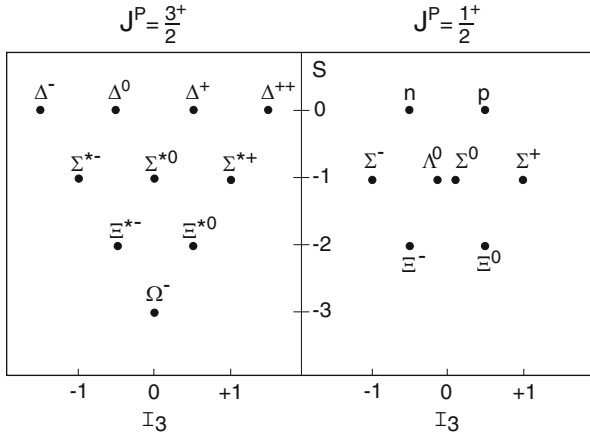


**Fig. 16.6** The baryon  $J^P = 3/2^+$  decuplet (*left*) and the  $J^P = 1/2^+$  octet (*right*) in  $I_3$  vs.  $S$  plots. In contradistinction to the mesonic case the baryon multiplets are solely composed of quarks. Antibaryons are purely composed of antiquarks and so form their own, equivalent antibaryon multiplets

Note that we have only given the spin-flavour part of the total baryonic wave function here, and that in an abbreviated fashion. It must be symmetric under quark exchange. In the above notation this is evident for the pure  $uuu$ ,  $ddd$  and  $sss$  systems. For baryons built out of more than one quark flavour the symmetrised version contains several terms. The symmetrised part of the wave function of, for example, the  $\Delta^+$  reads more fully:

$$|\Delta^+\rangle = \frac{1}{\sqrt{3}} \left\{ |u^\uparrow u^\uparrow d^\uparrow\rangle + |u^\uparrow d^\uparrow u^\uparrow\rangle + |d^\uparrow u^\uparrow u^\uparrow\rangle \right\}.$$

In what follows we will mostly employ the abbreviated notation for the baryonic quark wave function and quietly assume that the total wave function has in fact been correctly antisymmetrised.

If we display the states of this baryon decuplet on an  $I_3$  vs.  $S$  plot, we obtain (Fig. 16.6) an isosceles triangle. This reflects the threefold symmetry of these three-quark systems.

**The baryon octet** We are now faced with the question of bringing the nucleons into our model of the baryons. If three quarks, each with spin  $1/2$ , are to yield a spin- $1/2$  baryon, then the spin of one of the quarks must be antiparallel to the other two, i.e., we must have  $\uparrow\uparrow\downarrow$ . This spin state is then neither symmetric nor antisymmetric under spin swaps, but rather has a mixed symmetry. This must then also be the case for the flavour wave function, so that their product, the total spin-flavour wave function, is purely symmetric. This is not possible for the  $uuu$ ,  $ddd$  and  $sss$  quark combinations and indeed we do not find any ground state baryons of

this form with  $J = 1/2$ . There are then only two different possible combinations of u- and d-quarks which can fulfil the necessary symmetry conditions on the wave function of a spin-1/2 baryon, and these are just the proton and the neutron.

This simplified treatment of the derivation of the possible baryonic states and their multiplets can be put on a firmer quantitative footing with the help of SU(6) quark symmetry, we refer here to the literature (see, e.g., [7]).

The proton and neutron wave functions may be schematically written as

$$|p^\uparrow\rangle = |u^\uparrow u^\uparrow d^\downarrow\rangle \quad |n^\uparrow\rangle = |u^\downarrow d^\uparrow d^\uparrow\rangle.$$

We now want to construct the symmetrised wave function. For a proton with, e.g., the  $z$  spin component  $m_J = +1/2$ , we may write the spin wave function as a product of the spin wave function of one quark and that of the remaining pair:

$$\chi_p(J = \frac{1}{2}, m_J = \frac{1}{2}) = \sqrt{2/3} \chi_{uu}(1, 1) \chi_d(\frac{1}{2}, -\frac{1}{2}) - \sqrt{1/3} \chi_{uu}(1, 0) \chi_d(\frac{1}{2}, \frac{1}{2}). \quad (16.3)$$

Here we have chosen to single out the d-quark and coupled the u-quark pair. (If we initially single out one of the u-quarks we obtain the same result, but the notation becomes much more complicated.) The factors in this equation are the Clebsch-Gordan coefficients for the coupling of spin 1 and spin 1/2. Replacing  $\chi(1, 0)$  by the correct spin triplet wave function  $(\uparrow\downarrow + \downarrow\uparrow)/\sqrt{2}$  then yields in our spin-flavour notation

$$|p^\uparrow\rangle = \sqrt{2/3} |u^\uparrow u^\uparrow d^\downarrow\rangle - \sqrt{1/6} |u^\uparrow u^\downarrow d^\uparrow\rangle - \sqrt{1/6} |u^\downarrow u^\uparrow d^\uparrow\rangle. \quad (16.4)$$

This expression is still only symmetric in terms of the exchange of the first and second quarks, and not for two arbitrary quarks as we need. It can, however, be straightforwardly totally symmetrised by swapping the first and third as well as the second and third quarks in each term of this last equation and adding these new terms. With the correct normalisation factor the totally symmetric proton wave function is then

$$|p^\uparrow\rangle = \frac{1}{\sqrt{18}} \left\{ 2 |u^\uparrow u^\uparrow d^\downarrow\rangle + 2 |u^\uparrow d^\downarrow u^\uparrow\rangle + 2 |d^\downarrow u^\uparrow u^\uparrow\rangle - |u^\uparrow u^\downarrow d^\uparrow\rangle \right. \\ \left. - |u^\downarrow d^\uparrow u^\uparrow\rangle - |d^\uparrow u^\uparrow u^\downarrow\rangle - |u^\downarrow u^\uparrow d^\uparrow\rangle - |u^\downarrow d^\uparrow u^\uparrow\rangle - |d^\uparrow u^\downarrow u^\uparrow\rangle \right\}. \quad (16.5)$$

The neutron wave function is trivially found by exchanging the u- and d-quarks:

$$|n^\uparrow\rangle = \frac{1}{\sqrt{18}} \left\{ 2 |d^\uparrow d^\uparrow u^\downarrow\rangle + 2 |d^\uparrow u^\downarrow d^\uparrow\rangle + 2 |u^\downarrow d^\uparrow d^\uparrow\rangle - |d^\uparrow d^\downarrow u^\uparrow\rangle \right. \\ \left. - |d^\uparrow u^\downarrow d^\uparrow\rangle - |u^\uparrow d^\uparrow d^\downarrow\rangle - |d^\downarrow d^\uparrow u^\uparrow\rangle - |d^\downarrow u^\uparrow d^\uparrow\rangle - |u^\uparrow d^\downarrow d^\uparrow\rangle \right\}. \quad (16.6)$$

The nucleons have isospin 1/2 and so form an isospin doublet. A further doublet may be produced by combining two s-quarks with a light quark. This is schematically given by

$$|\Xi^{0\uparrow}\rangle = |u^\downarrow s^\uparrow s^\uparrow\rangle \quad |\Xi^{-\uparrow}\rangle = |d^\downarrow s^\uparrow s^\uparrow\rangle. \quad (16.7)$$

The remaining quark combinations are an isospin triplet and a singlet:

$$\begin{aligned} |\Sigma^{+\uparrow}\rangle &= |u^\uparrow u^\uparrow s^\downarrow\rangle \\ |\Sigma^{0\uparrow}\rangle &= |u^\uparrow d^\uparrow s^\downarrow\rangle \quad |\Lambda^{0\uparrow}\rangle = |u^\uparrow d^\downarrow s^\uparrow\rangle \\ |\Sigma^{-\uparrow}\rangle &= |d^\uparrow d^\uparrow s^\downarrow\rangle. \end{aligned} \quad (16.8)$$

Note that the uds quark combination appears twice here and depending upon the relative quark spins and isospins can correspond to two different particles. If the u and d spins and isospins couple to 1, as they do for the charged  $\Sigma$  baryons, then the above quark combination is a  $\Sigma^0$ . If they couple to zero we are dealing with a  $\Lambda^0$ . These two hyperons have a mass difference of about  $80 \text{ MeV}/c^2$ . This is evidence that a spin-spin interaction must also play an important role in the physics of the baryon spectrum. The eight  $J^P = 1/2^+$  baryons are displayed in an  $I_3$  vs.  $S$  plot in Fig. 16.6. Note again the threefold symmetry of the states.

## 16.3 Baryon Masses

The mass spectrum of the baryons is plotted in Fig. 16.7 against strangeness and isospin. The lowest energy levels are the  $J^P = 1/2^+$  and  $J^P = 3/2^+$  multiplets, as can be clearly seen. It is also evident that the baryon masses increase with the number of strange quarks, which we can put down to the larger mass of the s-quark. Furthermore we can see that the  $J^P = 3/2^+$  baryons are about  $300 \text{ MeV}/c^2$  heavier than their  $J^P = 1/2^+$  equivalents. As was the case with the mesons, this effect can be traced back to a spin-spin interaction

$$V_{ss}(q_i q_j) = \frac{4\pi \hbar^3}{9 c} \alpha_s \frac{\boldsymbol{\sigma}_i \cdot \boldsymbol{\sigma}_j}{m_i m_j} \delta(\mathbf{x}), \quad (16.9)$$

which is only important at short distances. The observant reader may notice that the  $4/9$  factor is only half that which we found for the quark-antiquark potential in the mesons (14.10); this is a result of QCD considerations. Equation (16.9), it should be noted, describes only the interaction of two quarks with each other and so to describe the baryon mass splitting we need to sum the spin-spin interactions over all quark pairs. The easiest cases are those where the constituent masses of all three quarks are the same, i.e., the nucleons, the  $\Delta$ 's and the  $\Omega$ . Then we just have to

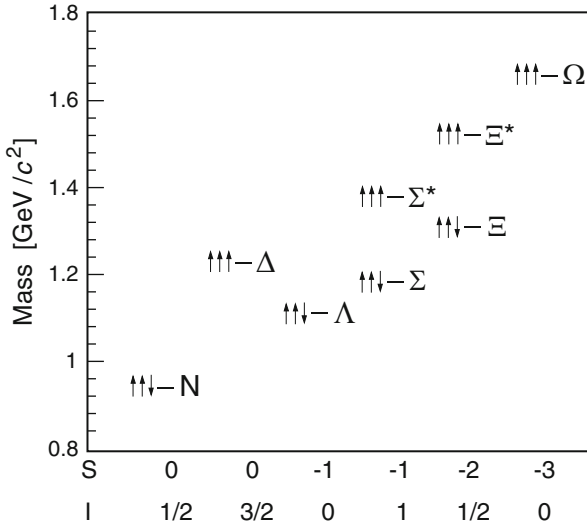


**Fig. 16.7** The masses of the decuplet and octet baryons plotted against their strangeness  $S$  and isospin  $I$ . The angular momenta  $J$  of the various baryons are shown through *arrows*. The  $J^P = 3/2^+$  decuplet baryons lie significantly above their  $J^P = 1/2^+$  octet partners

calculate the expectation values for the sums over  $\sigma_i \cdot \sigma_j$ . Denoting the total baryon spin by  $S$  and using the identity  $S^2 = (s_1 + s_2 + s_3)^2$  we find in a similar way to (14.11):

$$\sum_{\substack{i,j=1 \\ i < j}}^3 \sigma_i \cdot \sigma_j = \frac{4}{\hbar^2} \sum_{\substack{i,j=1 \\ i < j}}^3 s_i \cdot s_j = \begin{cases} -3 & \text{for } S = 1/2, \\ +3 & \text{for } S = 3/2. \end{cases} \quad (16.10)$$

The spin-spin energy (mass) splitting for these baryons is then just

$$\Delta M_{ss} = \begin{cases} -3 \cdot \frac{4 \hbar^3 \pi \alpha_s}{9 c^3 m_{u,d}^2} |\psi(0)|^2 & \text{for the nucleons,} \\ +3 \cdot \frac{4 \hbar^3 \pi \alpha_s}{9 c^3 m_{u,d}^2} |\psi(0)|^2 & \text{for the } \Delta \text{ states,} \\ +3 \cdot \frac{4 \hbar^3 \pi \alpha_s}{9 c^3 m_s^2} |\psi(0)|^2 & \text{for the } \Omega \text{ baryon.} \end{cases} \quad (16.11)$$

Here  $|\psi(0)|^2$  is the probability that two quarks are at the same place. Somewhat more complicated expressions may be obtained for those baryons made up of a mixture of heavier  $s$ - and lighter  $u$ - or  $d$ -quarks (see the exercises).

With the help of this mass-splitting formula a general expression for the masses of all the  $\ell = 0$  baryons may be written:

$$M = \sum_i m_i + \Delta M_{ss}. \tag{16.12}$$

The three unknowns here, i.e.,  $m_{u,d}$ ,  $m_s$  and  $\alpha_s |\psi(0)|^2$ , may be obtained by fitting to the experimental masses. As with the mesons we assume that  $\alpha_s |\psi(0)|^2$  is roughly the same for all of the baryons. We so obtain the following constituent-quark masses:  $m_{u,d} \approx 363 \text{ MeV}/c^2$ ,  $m_s \approx 538 \text{ MeV}/c^2$  [10]. The fitted baryon masses are within 1 % of their true values (Table 16.1). The constituent-quark masses obtained from such studies of baryons are a little larger than their mesonic counterparts. This is not necessarily a contradiction since constituent-quark masses are generated by the dynamics of the quark-gluon interaction and the effective interactions of a three-quark system will not be identical to those of a quark-antiquark one.

**Table 16.1** The masses of the lightest baryons both from experiment and as fitted from (16.12). The fits were to the average values of the various multiplets and are in good agreement with the measured masses. Also included in this table are the lifetimes and most important decay channels of these baryons [15]. The four charged  $\Delta$  resonances are not individually listed

	S	I	Baryon	Mass (MeV/c <sup>2</sup> )		$\tau$ (s)	Primary decay channels		Decay type
				Theor.	Exp.				
Octet ( $J^P = 1/2^+$ )	0	1/2	p	939	938.3	Stable?	-		-
			n		939.6		880.0	$p\bar{e}^- \bar{\nu}_e$	
	-1	0	$\Lambda$	1,114	1,115.7	$2.63 \cdot 10^{-10}$	$p\pi^-$	63.9 %	Weak
							$n\pi^0$	35.8 %	Weak
			1				$\Sigma^+$	1,179	1,189.4
			$\Sigma^0$		1,192.6	$7.4 \cdot 10^{-20}$	$\Lambda\gamma$	$\approx 100$ %	Elmgn.
			$\Sigma^-$		1,197.4	$1.48 \cdot 10^{-10}$	$n\pi^-$	99.8 %	Weak
	-2	1/2	$\Xi^0$	1,327	1,315	$2.90 \cdot 10^{-10}$	$\Lambda\pi^0$	$\approx 100$ %	Weak
$\Xi^-$			1,322		$1.64 \cdot 10^{-10}$		$\Lambda\pi^-$	$\approx 100$ %	Weak
Decuplet ( $J^P = 3/2^+$ )	0	3/2	$\Delta$	1,239	1,232	$0.55 \cdot 10^{-23}$	$N\pi$	99.4 %	Strong
	-1	1	$\Sigma^{*+}$	1,381	1,383	$1.7 \cdot 10^{-23}$	$\Lambda\pi$	87 %	Strong
			$\Sigma^{*0}$		1,384		$\Sigma\pi$	12 %	Strong
			$\Sigma^{*-}$		1,387				
	-2	1/2	$\Xi^{*0}$	1,529	1,532	$7 \cdot 10^{-23}$	$\Xi\pi$	$\approx 100$ %	Strong
			$\Xi^{*-}$		1,535				
	-3	0	$\Omega^-$	1,682	1,672.5	$0.82 \cdot 10^{-10}$	$\Lambda K^-$	68 %	Weak
							$\Xi^0\pi^-$	24 %	Weak
			$\Xi^-\pi^0$				9 %	Weak	

## 16.4 Magnetic Moments

The constituent-quark model is satisfyingly successful when its predictions for baryonic magnetic moments are compared with the results of experiment. In Dirac theory the magnetic moment  $\mu$  of a point particle with mass  $M$  and spin  $1/2$  is

$$\mu_{\text{Dirac}} = \frac{e\hbar}{2M}. \quad (16.13)$$

This relationship has been experimentally confirmed for both the electron and the muon. If the proton were an elementary particle without any substructure, then its magnetic moment should be one nuclear magneton:

$$\mu_{\text{N}} = \frac{e\hbar}{2M_{\text{p}}}. \quad (16.14)$$

Experimentally, however, the magnetic moment of the proton is measured to be  $\mu_{\text{p}} = 2.79 \mu_{\text{N}}$ .

**Magnetic moments in the quark model** The proton magnetic moment in the ground state, with  $\ell = 0$ , is a simple vectorial sum of the magnetic moments of the three quarks:

$$\boldsymbol{\mu}_{\text{p}} = \boldsymbol{\mu}_{\text{u}} + \boldsymbol{\mu}_{\text{u}} + \boldsymbol{\mu}_{\text{d}}. \quad (16.15)$$

The proton magnetic moment  $\mu_{\text{p}}$  then has the expectation value

$$\mu_{\text{p}} = \langle \boldsymbol{\mu}_{\text{p}} \rangle = \langle \psi_{\text{p}} | \boldsymbol{\mu}_{\text{p}} | \psi_{\text{p}} \rangle, \quad (16.16)$$

where  $\psi_{\text{p}}$  is the totally antisymmetric quark wave function of the proton. To obtain  $\mu_{\text{p}}$  we merely require the spin part of the wave function,  $\chi_{\text{p}}$ . From (16.3) we thus deduce

$$\mu_{\text{p}} = \frac{2}{3}(\mu_{\text{u}} + \mu_{\text{u}} - \mu_{\text{d}}) + \frac{1}{3}\mu_{\text{d}} = \frac{4}{3}\mu_{\text{u}} - \frac{1}{3}\mu_{\text{d}}, \quad (16.17)$$

where  $\mu_{\text{u,d}}$  are the quark magnetons:

$$\mu_{\text{u,d}} = \frac{z_{\text{u,d}} e\hbar}{2m_{\text{u,d}}}. \quad (16.18)$$

The other  $J^P = 1/2^+$  baryons with two identical quarks may be described by (16.17) with a suitable change of quark flavours. The neutron, for example, has a magnetic

moment

$$\mu_n = \frac{4}{3}\mu_d - \frac{1}{3}\mu_u \quad (16.19)$$

and analogously for the  $\Sigma^+$  we have

$$\mu_{\Sigma^+} = \frac{4}{3}\mu_u - \frac{1}{3}\mu_s. \quad (16.20)$$

The situation is a little different for the  $\Lambda^0$ . As we know this hyperon contains a u- and a d-quark whose spins are coupled to 0 and so contribute neither to the spin nor to the magnetic moment of the baryon (Sect. 16.2). Hence both the spin and the magnetic moment of the  $\Lambda^0$  are determined solely by the s-quark:

$$\mu_\Lambda = \mu_s. \quad (16.21)$$

To the extent that the u and d constituent-quark masses can be set equal to each other we have  $\mu_u = -2\mu_d$  and may then write the proton and neutron magnetic moments as follows

$$\mu_p = \frac{3}{2}\mu_u, \quad \mu_n = -\mu_u. \quad (16.22)$$

We thus obtain the following prediction for their ratio

$$\frac{\mu_n}{\mu_p} = -\frac{2}{3}, \quad (16.23)$$

which is in excellent agreement with the experimental result of  $-0.685$ .

The absolute magnetic moments can only be calculated if we can specify the quark masses. Let us first, however, look at this problem the other way round and use the measured value of  $\mu_p$  to determine the quark masses. From

$$\mu_p = 2.79 \mu_N = 2.79 \frac{e\hbar}{2M_p} \quad (16.24)$$

and

$$\mu_p = \frac{3}{2}\mu_u = \frac{e\hbar}{2m_u} \quad (16.25)$$

**Table 16.2** Experimental and theoretical values of the baryon magnetic moments [15]. The measured values of the p, n and  $\Lambda^0$  moments are used to predict those of the other baryons. The  $\Sigma^0$  hyperon has a very short lifetime ( $7.4 \cdot 10^{-20}$  s) and decays electromagnetically via  $\Sigma^0 \rightarrow \Lambda^0 + \gamma$ . For this particle the transition matrix element  $\langle \Lambda^0 | \mu | \Sigma^0 \rangle$  is given in place of its magnetic moment

Baryon	$\mu/\mu_N$ (experiment)	Quark model	$\mu/\mu_N$
p	+2.792847356 $\pm$ 0.000000023	$(4\mu_u - \mu_d)/3$	–
n	–1.9130427 $\pm$ 0.0000005	$(4\mu_d - \mu_u)/3$	–
$\Lambda^0$	–0.613 $\pm$ 0.004	$\mu_s$	–
$\Sigma^+$	+2.458 $\pm$ 0.010	$(4\mu_u - \mu_s)/3$	+2.67
$\Sigma^0$		$(2\mu_u + 2\mu_d - \mu_s)/3$	+0.79
$\Sigma^0 \rightarrow \Lambda^0$	–1.61 $\pm$ 0.08	$(\mu_d - \mu_u)/\sqrt{3}$	–1.63
$\Sigma^-$	–1.160 $\pm$ 0.025	$(4\mu_d - \mu_s)/3$	–1.09
$\Xi^0$	–1.250 $\pm$ 0.014	$(4\mu_s - \mu_u)/3$	–1.43
$\Xi^-$	–0.6507 $\pm$ 0.0025	$(4\mu_s - \mu_d)/3$	–0.49
$\Omega^-$	–2.02 $\pm$ 0.05	$3\mu_s$	–1.84

we obtain

$$m_u = \frac{M_p}{2.79} = 336 \text{ MeV}/c^2, \quad (16.26)$$

which is very close indeed to the mass we found in Sect. 16.3 from the study of the baryon spectrum.

**Measuring the magnetic moments** The agreement between the experimental values of the hyperon magnetic moments with the predictions of the quark model is impressive (Table 16.2). Our ability to measure the magnetic moments of many of the short-lived hyperons ( $\tau \approx 10^{-10}$  s) is due to a combination of two circumstances: hyperons produced in nucleon-nucleon interactions are polarised and the weak interaction violates parity maximally. In consequence the angular distributions of their decay products are strongly dependent upon the direction of the hyperons' spins (i.e., their polarisations).

Let us clarify these remarks by studying how the magnetic moment of the  $\Lambda^0$  is experimentally measured. Note that this is the most easily determined of the hyperon magnetic moments. The decay

$$\Lambda^0 \rightarrow p + \pi^-$$

is rather simple to identify and has the largest branching ratio (64%). If the  $\Lambda^0$  spin is, say, in the positive  $\hat{z}$  direction, then the proton will most likely be emitted in the positive  $\hat{z}$  direction, in accord with the angular distribution

$$W(\theta) \propto 1 + \alpha \cos \theta \quad \text{where} \quad \alpha \approx 0.64. \quad (16.27)$$



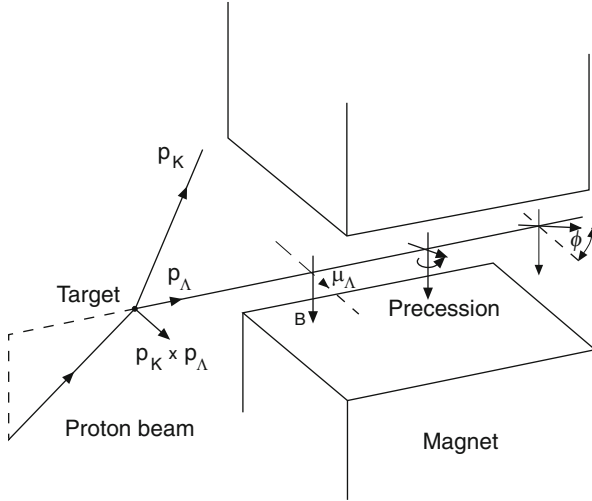
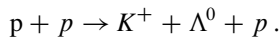


**Fig. 16.8** Sketch of the measurement of the magnetic moment of the  $\Lambda^0$ . The hyperon is generated by the interaction of a proton coming in from the left with a proton in the target. The spin of the  $\Lambda^0$  is, for reasons of parity conservation, perpendicular to the production plane. The  $\Lambda^0$  then passes through a magnetic field which is orthogonal to the particle's spin. After traversing a distance  $d$  in the magnetic field the spin has precessed through an angle  $\phi$

The angle  $\theta$  is the angle between the spin of the  $\Lambda^0$  and the momentum of the proton in the rest system of the  $\Lambda^0$ . The parameter  $\alpha$  depends upon the strength of the interference of those terms with orbital angular momentum  $\ell = 0$  and  $\ell = 1$  in the  $p-\pi^-$  system and its size must be determined by experiment.

The asymmetry in the angular distribution of the emitted protons then fixes the  $\Lambda^0$  polarisation. Highly polarised  $\Lambda^0$  particles may be obtained from the reaction



As shown in Fig. 16.8, the spin of the  $\Lambda^0$  is perpendicular to the production plane defined by the path of the incident proton and that of the  $\Lambda^0$  itself. This is because only this polarisation direction is allowed for unpolarised beams and targets by parity conservation in the strong interaction.

If the  $\Lambda^0$  baryon traverses a distance  $d$  in a magnetic field  $\mathbf{B}$ , where the field is perpendicular to the hyperon's spin, then its spin precesses with the Larmor frequency

$$\omega_L = \frac{\mu_\Lambda B}{\hbar} \tag{16.28}$$

through the angle

$$\phi = \omega_L \Delta t = \omega_L \frac{d}{v}, \quad (16.29)$$

where  $v$  is the speed of the  $\Lambda^0$  (this may be reconstructed by measuring the momenta of its decay products, i.e., a proton and a pion). The most accurate results may be obtained by reversing the magnetic field and measuring the angle  $2 \cdot \phi$  which is given by the difference between the directions of the  $\Lambda^0$  spins (after crossing the various magnetic fields). This trick neatly eliminates most of the systematic errors. The magnetic moment is thus found to be [15]

$$\mu_\Lambda = (-0.613 \pm 0.004) \mu_N. \quad (16.30)$$

If we suppose that the constituent s-quark is a point-like particle and that its magnetic moment obeys (16.18), then we see that this result for  $\mu_\Lambda$  is consistent with an s-quark mass of  $510 \text{ MeV}/c^2$ .

The magnetic moments of many of the hyperons have been measured in a similar fashion to the above. There is an additional complication for the charged hyperons in that their deflection by the magnetic field must be taken into account if one wants to study spin precession effects. The best results have been obtained at Fermilab and are listed in Table 16.2. These results are compared with quark-model predictions. The results for the proton, the neutron and the  $\Lambda^0$  were used to fix all the unknown parameters and so predict the other magnetic moments. The results of the experiments agree with the model predictions to within a few percent.

These results support our constituent-quark picture in two ways: firstly the constituent-quark masses from our mass formula and those obtained from the above analysis of the magnetic moments agree well with each other, and secondly the magnetic moments themselves are consistent with the quark model.

It should be noted, however, that the deviations of the experimental values from the predictions of the model show that the constituent-quark magnetic moments alone do not suffice to describe the magnetic moments of the hyperons exactly. Further effects, such as relativistic ones and those due to the quark orbital angular momenta, must be taken into account.

## 16.5 Spin Structure of the Nucleon

The statements made in the previous chapter can be illustrated especially well by the spin structure of the nucleon. We have shown in Sect. 16.2 that, in the constituent-quark model, the spin of the baryons is equal to the vector sum of the spins of the three constituent quarks and that the magnetic moments and the masses calculated with this assumption excellently agree with the experimental results. The situation is very different when the spin contribution of the current-quarks to

the spin of the nucleon is experimentally determined in deep-inelastic scattering of longitudinally-polarised electrons or muons on longitudinally-polarised targets. Pioneering experiments of this kind revealed the surprising result [6] that the fraction of the nucleon's spin which can be attributed to the spins of the current-quarks may be compatible with zero, but not compatible with one. This result caused enormous activity in both experiment and theory. Subsequently we will briefly explain the principle and some details of such measurements.

**Quark helicity distributions** We denote the relative alignment of the longitudinal spins of the leptons with respect to the lepton-beam direction by ( $\rightarrow$ ) and ( $\leftarrow$ ), and the corresponding ones of the target by ( $\Rightarrow$ ) and ( $\Leftarrow$ ). The quantisation axis is selected as the momentum direction of the longitudinally-polarised virtual photon. The projection of the total spin before and after the absorption of the virtual photon (spin-1) by a quark (spin- $\frac{1}{2}$ ) can only have the values  $S_z = +\frac{1}{2}$  or  $S_z = -\frac{1}{2}$ . Consequently the virtual photon can only be absorbed by a quark having opposite spin orientation. For equal polarisation direction of beam and target ( $\Rightarrow$ ), the spin of the struck quark must be oriented anti-parallel to the spin of the parent nucleon and vice versa. The corresponding quark-momentum distributions weighted with the quark helicity are denoted as  $q_-(x, Q^2)$  and  $q_+(x, Q^2)$ , respectively, and their difference

$$\Delta q(x, Q^2) = q_+(x, Q^2) - q_-(x, Q^2) \quad (16.31)$$

is known as the quark helicity distribution. The unpolarised quark distribution  $q(x, Q^2)$  is equal to the sum of  $q_-(x, Q^2)$  and  $q_+(x, Q^2)$ .

**Spin structure functions** The cross-sections for the two relative spin orientations of beam and target are generally of different magnitude and their difference is

$$\sigma_{LL} = \frac{1}{2} (\sigma_{\Rightarrow} - \sigma_{\Leftarrow}). \quad (16.32)$$

This difference of cross-sections is proportional to two additional structure functions, the spin structure functions  $g_1(x, Q^2)$  and  $g_2(x, Q^2)$ . In analogy to (7.10) we obtain

$$\frac{d^2\sigma_{LL}}{dQ^2 dx} = \frac{8\pi\alpha^2\hbar^2 y}{Q^4} \left[ \left( 1 - \frac{y}{2} - \frac{yxMc^2}{2E} \right) g_1(x, Q^2) - \frac{xMc^2}{E} g_2(x, Q^2) \right]. \quad (16.33)$$

The structure functions  $g_1$  and  $g_2$  depend only very weakly on  $Q^2$ , therefore we will omit the  $Q^2$  dependence in the subsequent discussion. The spin structure function  $g_1(x)$  is in analogy to (7.15) given by the sum of the helicity distributions

weighted by  $z_q^2$

$$g_1^{p,n}(x) = \frac{1}{2} \sum_q z_q^2 [\Delta q^{p,n}(x) + \Delta \bar{q}^{p,n}(x)], \quad (16.34)$$

where  $z_q$  is the quark charge normalised to the elementary charge. For the proton-neutron averaged nucleon we obtain (cf. (7.24))

$$g_1^N(x) = \frac{5}{36} \sum_{q=d,u,s} [\Delta q(x) + \Delta \bar{q}(x)] - \frac{3}{5} [\Delta s(x) + \Delta \bar{s}(x)]. \quad (16.35)$$

The second spin structure function  $g_2$  does not have any probabilistic interpretation. It is small and in the quark-parton model it even disappears. Therefore the second term in (16.33), which is anyway kinematically suppressed, can be neglected compared to the first term. As an example, data from the HERMES experiment for  $xg_1^p(x)$ ,  $xg_1^D(x)$  and  $xg_1^n(x)$  [4] are presented in Fig. 16.9. This experiment used gas targets of polarised atomic hydrogen and deuterium internal to the HERA storage ring. This technology has the advantage that essentially all of the target atoms are polarisable in contrast to polarised solid-state targets like  $\text{NH}_3$  or  $\text{ND}_3$ , where the fraction of polarisable nucleons is only 3/17 or 6/20, respectively, and hence the signal from the spin structure functions is substantially diluted. The data shown in

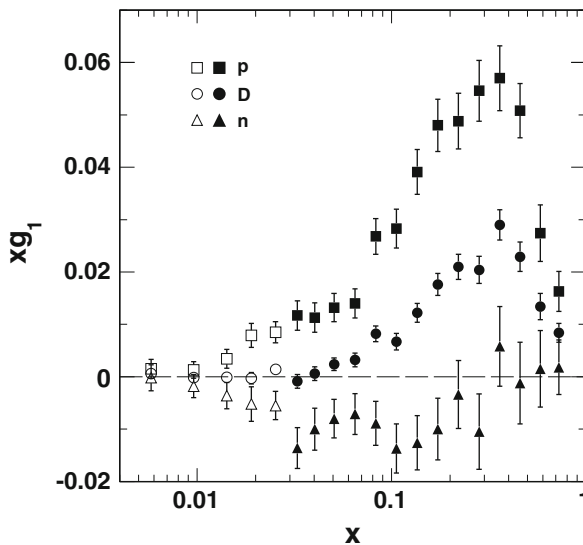


**Fig. 16.9** Experimental results for the structure functions  $xg_1(x)$  of the proton, deuteron and neutron as a function of  $x$  obtained by the HERMES experiment [4]. The average value of  $Q^2$  is different for each of the data points and increases with  $x$ . *Open symbols* represent data points with  $Q^2 < 1$  ( $\text{GeV}/c$ )<sup>2</sup>

Fig. 16.9 are in excellent agreement with the results of other experiments. From the comparison with Figs. 7.4 and 7.8 we see that the spin structure functions  $xg_1^p(x)$  and  $xg_1^d(x)$  are much smaller than the structure functions  $F_2^p(x)$  and  $F_2^d(x)$  in the unpolarised case. In the region of small  $x$  they approach zero. Obviously the contribution of sea-quark spins to the nucleon's spin is very small. The spin structure function  $xg_1^d(x)$  is small and negative and we can therefore conclude that also the helicity distribution of d-quarks is negative. Consequently the spin of current d-quarks is preferentially oriented opposite to the spin of the parent proton as it is in the case of the constituent-quark model.

**Integrated helicity distributions** The integral of the helicity distributions

$$\Delta q = \int_0^1 \Delta q(x) dx \quad (16.36)$$

is of special interest. This quantity corresponds to the fraction of quarks of type  $q$  with positive helicity in a nucleon with positive helicity. The sum over all quarks and antiquarks

$$\Delta \Sigma = \sum_{q=d,u,s} (\Delta q + \Delta \bar{q}) \quad (16.37)$$

then represents (for a nucleon moving with infinite momentum in  $z$ -direction) the fraction of the nucleon's spin which can be attributed to the spin of the quarks.

In analogy to the discussion in Sect. 7.5 we examine the integral of the structure function  $g_1^D(x)$ , which in good approximation is equal to the proton-neutron averaged structure function  $g_1^N(x)$ . We sum over all quark species and integrate over all distribution functions. When we neglect a possible small contribution of the s-quarks in the quark-antiquark sea, then this integral should have the value  $5/36$ , provided that the nucleon's spin can be attributed totally to the spins of the quarks. Integration of the data in Fig. 16.9 yields

$$\int_0^1 g_1^D(x) dx \approx 0.044 \approx 0.32 \cdot \frac{5}{36}. \quad (16.38)$$

Similar to the earlier observation that only half of the nucleon's momentum is carried by quarks we also here observe a deficit:

*Only about one third of the nucleon's spin can be attributed to the spins of the quarks.*

Although this result is only a simple approximation it agrees very well with a very detailed and refined analysis that also takes into account the d-wave contributions to the deuteron wave function (cf. Sect. 17.2), the contribution of s-quarks and higher-order QCD corrections. Hence, there must exist additional contributions to the nucleon's spin. One possible contribution, denoted by  $\Delta G$ , stems from the spin of the gluons. Furthermore there could be contributions from orbital angular momenta

$L_z$  of quarks and gluons. With all these contributions the expectation value of the nucleon's spin reads

$$S_z = \frac{1}{2} = \frac{1}{2} \Delta\Sigma + \Delta G + L_z. \quad (16.39)$$

The investigation of the nucleon's spin structure is a very active ongoing field of research. Experiments show that the contribution of gluon spins is very likely rather small, such that a substantial contribution may stem from orbital angular momenta of quarks and/or gluons. But no experimental observable has been found so far that can be related quantitatively to parton orbital angular momenta. A detailed up to date summary of the experimental results and relevant publications can be found in Ref. [3].

## 16.6 Semileptonic Baryon Decays

The weak decays of the baryons all follow the same pattern. A quark emits a virtual  $W^\pm$  boson and so changes its weak isospin and turns into a lighter quark. The  $W^\pm$  decays to a lepton-antilepton pair or, if its energy suffices, a quark-antiquark pair. In the decays to a quark-antiquark pair we actually measure one or more mesons in the final state. These decays cannot be exactly calculated because of the strong interaction's complications. Matters are simpler for semileptonic decays. The rich data available to us from semileptonic baryon decays have made a decisive contribution to our current understanding of the weak interaction as formulated in the generalised Cabibbo theory.

We now want to attempt to describe the weak decays of the baryons using our knowledge of the weak interaction from Chap. 10. The weak decays take place essentially at the quark level, but free quarks do not exist and experiments always see hadrons. We must therefore try to interpret hadronic observables within the framework of the fundamental theory of the weak interaction. We will start by considering the  $\beta$ -decay of the neutron, since this has been thoroughly investigated in various experiments. It will then be only a minor matter to extend the formalism to the semileptonic decays of the hyperons and to nuclear  $\beta$ -decays.

We have seen from leptonic decays such as  $\mu^- \rightarrow e^- + \bar{\nu}_e + \nu_\mu$  that the weak interaction violates parity conservation maximally, which must mean that the coupling constants for the vector and axial vector terms are of same size. Since neutrinos are left-handed and antineutrinos are right-handed the coupling constants must have opposite signs (V-A theory). The weak decay of a hadron actually means that a confined quark has decayed. It is therefore essential to take the quark wave function of the hadron into account. Furthermore strong-interaction effects of virtual particles cannot be neglected: although the effective electromagnetic coupling constant is (for reasons of charge conservation) not altered by the cloud of sea quarks and gluons, the weak coupling is indeed so changed. In what follows

we will initially take the internal structure of the hadrons into account and then discuss the coupling constants.

**Beta decay of the neutron** The  $\beta$ -decay of a free neutron

$$n \rightarrow p + e^- + \bar{\nu}_e \quad (16.40)$$

(maximum electron energy  $E_0 = 782$  keV, lifetime ca. 15 min) is a rich source of precise data about the low-energy behaviour of the weak interaction.

To find the form of the  $\beta$ -spectrum and the coupling constants of neutron  $\beta$ -decay we consider the decay probability. This may be calculated from the golden rule in the usual fashion. If the electron has energy  $E_e$ , then the decay rate is

$$dW(E_e) = \frac{2\pi}{\hbar} |\mathcal{M}_{fi}|^2 \frac{dQ_f(E_0, E_e)}{dE_e} dE_e, \quad (16.41)$$

where  $dQ_f(E_0, E_e)/dE_e$  is the density of antineutrino-electron final states with total energy  $E_0$  and the electron having energy  $E_e$  and  $\mathcal{M}_{fi}$  is the matrix element for the  $\beta$ -decay.

**Vector transitions** A  $\beta$ -decay which takes place through a vector coupling is called a *Fermi transition*. The direction of the quark's spin is unaltered in these decays. The change of a d- into a u-quark is described by the ladder operator of weak isospin  $T_+$  which changes a state with  $T = -1/2$  into one with  $T = +1/2$ .

The matrix element for neutron  $\beta$ -decay has a leptonic and a quark part. Conservation of angular momentum prevents any interference between vector and axial vector transitions, i.e., a quark vector transition necessarily implies a leptonic vector transition. Since we already have  $c_V = -c_A = 1$  for leptons, we do not need to worry further about their part of the matrix element.

The matrix element for Fermi decays may then be written as

$$|\mathcal{M}_{fi}|_F = \frac{G_F}{V} c_V |\langle uud | \sum_{i=1}^3 T_{i,+} | udd \rangle|, \quad (16.42)$$

where the sum is over the three quarks. According to the definition (10.4) the Fermi constant  $G_F$  includes the propagator term and the coupling to the leptons. The initial neutron state has the wave function  $|udd\rangle$  and the final state is described by the quark combination  $|uud\rangle$ . The wave functions of the electron and the antineutrino can each be replaced by  $1/\sqrt{V}$ , since we have  $pR/\hbar \ll 1$ .

The u- and d-quarks in the proton and neutron wave functions are eigenstates of strong isospin. In  $\beta$ -decay we need to consider the eigenstates of the weak interaction. We therefore recall that, while the ladder operators  $I_{\pm}$  of the strong force map  $|u\rangle$  and  $|d\rangle$  onto each other, the  $T_{\pm}$  operators connect the  $|u\rangle$  and  $|d'\rangle$

quark states. The overlap between  $|d\rangle$  and  $|d'\rangle$  is, according to (10.18), fixed by the cosine of the Cabibbo angle. Hence

$$\langle u|T_+|d\rangle = \langle u|I_+|d\rangle \cdot \cos \theta_C, \quad \text{where } \cos \theta_C \approx 0.98. \quad (16.43)$$

The vector component of the matrix element is then

$$\mathcal{M}_{fi} = \frac{G_F}{V} \cos \theta_C \cdot c_V \langle uud | \sum_{i=1}^3 I_{i,+} | udd \rangle = \frac{G_F}{V} \cos \theta_C \cdot c_V \cdot 1. \quad (16.44)$$

Here we have employed the fact that the sum  $\langle uud | \sum_i I_{i,+} | udd \rangle$  must be unity since the operator  $\sum_i I_{i,+}$  applied to the quark wave function of the neutron just gives the quark wave function of the proton. This follows from isospin conservation in the strong interaction and may be straightforwardly verified with the help of (16.5) and (16.6). We thus see that the Fermi matrix element is independent of the internal structure of the nucleon.

**Axial transitions** Those  $\beta$ -decays that take place as a result of an axial vector coupling are called *Gamow-Teller transitions*. In such cases the direction of the fermion spin flips over. The matrix element depends upon the overlap of the spin densities of the particles carrying the weak charge in the initial and final states. The transition operator is then  $c_A T_+ \sigma$ .

The universality of the weak interaction implies that this result should also hold for free point-like quarks. Since quarks are always trapped inside hadrons, we need to consider the internal structure of the nucleon if we want to calculate such matrix elements. From the constituent-quark model we have

$$|\mathcal{M}_{fi}|_{\text{GT}} = \frac{G_F}{V} c_A |\langle uud | \sum_{i=1}^3 T_{i,+} \sigma | udd \rangle|. \quad (16.45)$$

Since the squares of the expectation values of the components of  $\sigma$  are equal to each other,  $\langle \sum_i \sigma_{i,x} \rangle^2 = \langle \sum_i \sigma_{i,y} \rangle^2 = \langle \sum_i \sigma_{i,z} \rangle^2$ , it is sufficient to calculate the expectation value of  $\sigma_z = \langle uud | \sum_i I_{i,+} \sigma_{i,z} | udd \rangle$ . One finds from (16.5), (16.6) and some tedious arithmetic that

$$\langle uud | \sum_i I_{i,+} \sigma_{i,z} | udd \rangle = \frac{5}{3}. \quad (16.46)$$

**The total matrix element** In experiments we measure the properties of the nucleon, such as its spin, and not those of the quarks. To compare theory with experiment we must therefore reformulate the matrix element so that all operators act upon the *nucleon* wave function. The square of the neutron decay matrix element



may be written as

$$|\mathcal{M}_{fi}|^2 = \frac{g_V^2}{V^2} |\langle p | I_+ | n \rangle|^2 + \frac{g_A^2}{V^2} |\langle p | I_+ \sigma | n \rangle|^2 . \quad (16.47)$$

We stress that  $I_+$  and  $\sigma$  now act upon the wave function of the nucleon. The quantities  $g_V$  and  $g_A$  are those which are measured in neutron  $\beta$ -decay and describe the absolute strengths of the vector and axial vector contributions. They contain the product of the weak charges at the leptonic and hadronic vertices.

Since the proton and the neutron form an isospin doublet, (16.47) may be written as

$$|\mathcal{M}_{fi}|^2 = (g_V^2 + 3g_A^2)/V^2 . \quad (16.48)$$

We note that the factor of 3 in the axial vector part is due to the expectation value of the spin operator  $\sigma^2 = \sigma_x^2 + \sigma_y^2 + \sigma_z^2$ .

In the constituent-quark model  $g_V$  and  $g_A$  are related to the quark-dependent coupling constants  $c_V$  and  $c_A$  as follows:

$$g_V = G_F \cos \theta_C c_V , \quad (16.49)$$

$$g_A \approx G_F \cos \theta_C \frac{5}{3} c_A . \quad (16.50)$$

The Fermi matrix element (16.44) is independent of the internal structure of the neutron and (16.49) is as exact as the isospin symmetry of the proton and the neutron. The axial vector coupling, on the other hand, does depend upon the structure of the nucleon. In the constituent-quark model it is given by (16.50). It is important to understand that the factor of 5/3 is merely an estimate, since the constituent-quark model only gives us an approximation of the nucleon wave function.

**The neutron lifetime** The lifetime is given by the inverse of the total decay probability per unit time:

$$\frac{1}{\tau} = \int_{m_e c^2}^{E_0} \frac{dW}{dE_e} dE_e = \int_{m_e c^2}^{E_0} \frac{2\pi}{\hbar} |\mathcal{M}_{fi}|^2 \frac{dQ_f(E_0, E_e)}{dE_e} dE_e . \quad (16.51)$$

Assuming that the matrix element is independent of the energy, we can pull it outside the integral. The state density  $\rho_f(E_0, E_e)$  may, in analogy to (4.18) and (5.21), be written as

$$dQ_f(E_0, E_e) = \frac{(4\pi)^2}{(2\pi\hbar)^6} p_e^2 \frac{dp_e}{dE_e} p_\nu^2 \frac{dp_\nu}{dE_0} V^2 dE_e , \quad (16.52)$$

where we have taken into account that we here have an electron and a neutrino and hence a 2-particle state density and  $V$  is the volume in which the wave functions of the electron and of the neutrino are normalised. Since this normalisation enters the matrix element (16.48) via a  $1/V^2$  factor, the decay probability is independent of  $V$ .

In (16.51) we only integrate over the electron spectrum and so we need the density of states for a total energy  $E_0$  with a fixed electron energy  $E_e$ . Neglecting recoil effects, we have  $E_0 = E_e + E_\nu$  and hence  $dE_0 = dE_\nu$ . Using the relativistic energy-momentum relation  $E^2 = p^2c^2 + m^2c^4$  we thus find

$$p_e^2 dp_e = \frac{1}{c^2} p_e E_e dE_e = \frac{1}{c^3} E_e \sqrt{E_e^2 - m_e^2 c^4} dE_e \quad (16.53)$$

and an analogous relation for the neutrino. Assuming that the neutrino is massless we obtain

$$dQ_f(E_0, E_e) = (4\pi)^2 V^2 \frac{E_e \sqrt{E_e^2 - m_e^2 c^4} \cdot (E_0 - E_e)^2}{(2\pi \hbar c)^6} dE_e. \quad (16.54)$$

To find the lifetime  $\tau$  we now need to carry out the integral (16.51). It is usual to normalise the energies in terms of the electron rest mass and so define

$$f(E_0) = \int_1^{E_0} \mathcal{E}_e \sqrt{\mathcal{E}_e^2 - 1} \cdot (\mathcal{E}_0 - \mathcal{E}_e)^2 d\mathcal{E}_e, \quad \text{where } \mathcal{E} = E/m_e c^2. \quad (16.55)$$

Together with (16.48) this leads to

$$\frac{1}{\tau} = \frac{m_e^5 c^4}{2\pi^3 \hbar^7} \cdot (g_V^2 + 3g_A^2) \cdot f(E_0). \quad (16.56)$$

For ( $E_0 \gg m_e c^2$ ) we have

$$f(E_0) \approx \frac{\mathcal{E}_0^5}{30} \quad (16.57)$$

and so

$$\frac{1}{\tau} \approx \frac{1}{\hbar^7 c^6} \cdot (g_V^2 + 3g_A^2) \cdot \frac{E_0^5}{60\pi^3}. \quad (16.58)$$

This decrease of the lifetime as the fifth power of  $E_0$  is called *Sargent's rule*.

In neutron decays  $E_0$  is roughly comparable to  $m_e c^2$  and the approximation (16.57) is not applicable. The decay probability is roughly half the size of (16.58):

$$\frac{1}{\tau_n} \approx \frac{1}{\hbar^7 c^6} \cdot (g_V^2 + 3g_A^2) \cdot \frac{E_0^5}{60\pi^3} \cdot 0.47. \quad (16.59)$$

**Experimental results** The neutron lifetime has been measured very precisely in recent years. The storage of ultra cold neutrons has been a valuable tool in these experiments [11, 14]. Extremely slow neutrons can be stored between solid walls which represent a potential barrier. The neutrons are totally reflected since the refraction index in solid matter is smaller than that in air [12]. With such storage cells the lifetime of the neutron may be determined by measuring the number of neutrons in the cell as a function of time. To do this one opens the storage cell for a specific time to a cold neutron beam of a known, constant intensity. The cell is then closed and left undisturbed until after a certain time it is opened again and the remaining neutrons are counted with a neutron detector. The experiment is repeated for various storage times. The exponential decay in the number of neutrons in the cell (together with knowledge of the leakage rate from the cell) gives us the neutron lifetime. The average of the most recent measurements of the neutron lifetime is [15]

$$\tau_n = 880.0 \pm 0.9 \text{ s} . \quad (16.60)$$

To individually determine  $g_A$  and  $g_V$  we need to measure a second quantity [1, 8]. The decay asymmetry of polarised neutrons is a good candidate here. This comes from the parity violating properties of the weak interaction: the axial vector part emits electrons anisotropically while the vector contribution is spherically symmetric.<sup>2</sup> The number of electrons that are emitted in the direction of the neutron spin  $N^{\uparrow\uparrow}$  is smaller than the number  $N^{\uparrow\downarrow}$  emitted in the opposite direction. The asymmetry  $A$  is defined by

$$\frac{N^{\uparrow\uparrow} - N^{\uparrow\downarrow}}{N^{\uparrow\uparrow} + N^{\uparrow\downarrow}} = \beta \cdot A, \quad \text{where } \beta = \frac{v}{c} . \quad (16.61)$$

This asymmetry is connected to

$$\lambda = \frac{g_A}{g_V} \quad (16.62)$$

by

$$A = -2 \frac{\lambda(\lambda + 1)}{1 + 3\lambda^2} . \quad (16.63)$$

The asymmetry experiments are also best performed with ultra low energy neutrons. An electron spectrometer with an extremely high spatial resolution is needed [2, 13]. Such measurements yield [15]

$$A = -0.1176 \pm 0.0011 . \quad (16.64)$$

---

<sup>2</sup>The discovery of parity violation in the weak interaction was through the anisotropic emission of electrons in the  $\beta$ -decay of atomic nuclei [17].

Combining this information we have

$$\begin{aligned}\lambda &= -1.2701 \pm 0.0025, \\ g_V/(\hbar c)^3 &= +1.153 \cdot 10^{-5} \text{ GeV}^{-2}, \\ g_A/(\hbar c)^3 &= -1.454 \cdot 10^{-5} \text{ GeV}^{-2}.\end{aligned}\tag{16.65}$$

A comparison with (16.49) yields very exactly  $c_V = 1$ , which is the value we would expect for a point-like quark or lepton. The vector part of the interaction is conserved in weak baryon decays. This is known as *conservation of vector current* (CVC) and it is believed that this conservation is exact. It is considered to be as important as the conservation of electric charge in electromagnetism.

The axial vector term is on the other hand not that of a point-like Dirac particle. Rather than  $\lambda = -5/3$  experiment yields  $\lambda \approx -1.27$ . The strong force alters the spin dependent part of the weak decay and the axial vector current is only partially conserved (PCAC = *partially conserved axial vector current*).

**Semileptonic hyperon decays** The semileptonic decays of the hyperons can be calculated in a similar way to that of the neutron. Since the decay energies  $E_0$  are typically two orders of magnitude larger than in the neutron decay, Sargent's rule (16.58) predicts that the hyperon lifetimes should be at least a factor of  $10^{10}$  shorter. At the quark level these decays are all due to the decay  $s \rightarrow u + e^- + \bar{\nu}_e$ .

The two independent measurements to determine the semileptonic decay probabilities of the hyperons are their lifetimes  $\tau$  and the branching ratio  $V_{\text{semil.}}$  of the semileptonic channels. From

$$\frac{1}{\tau} \propto |\mathcal{M}_{fi}|^2 \quad \text{and} \quad V_{\text{semil.}} \equiv \frac{|\mathcal{M}_{fi}|^2_{\text{semil.}}}{|\mathcal{M}_{fi}|^2}$$

we have the relationship

$$\frac{V_{\text{semil.}}}{\tau} \propto |\mathcal{M}_{fi}|^2_{\text{semil.}}.\tag{16.66}$$

The lifetime may most easily be measured in production experiments. High energy proton or hyperon (e.g.,  $\Sigma^-$ ) beams with an energy of a few hundred GeV are fired at a fixed target and one detects the hyperons which are produced. One then calculates the average decay length of the secondary hyperons, i.e., the average distance between where they are produced (the target) and where they decay. This is done by measuring the tracks of the decay products with detectors which have a good spatial resolution and reconstructing the position where the hyperon decayed. The number of hyperons decreases exponentially with time and this is reflected in an exponential decrease in the number  $N$  of decay positions a distance  $l$  away from the target:

$$N = N_0 e^{-l/\tau} = N_0 e^{-l/L}.\tag{16.67}$$

The method of invariant masses must, of course, be used to identify which sort of hyperon has decayed. The average decay length  $L$  is then related to the lifetime  $\tau$  as follows

$$L = \gamma v \tau , \quad (16.68)$$

where  $v$  is the velocity of the hyperon. With high beam energies the secondary hyperons can have time dilation factors  $\gamma = E/mc^2$  of the order of 100. Since the hyperons typically have a lifetime of around  $10^{-10}$  s the decay length will typically be a few metres – which may be measured to a good accuracy.

The measurement of the branching ratios is much more complicated. This is because the vast majority of decays are into hadrons (which may therefore be used to measure the decay length). The semileptonic decays are only about one thousandth of the total. This means that those few leptons must be detected with a very high efficiency and that background effects must be rigorously analysed.

The experiments are in fact sufficiently precise to put the Cabibbo theory to the test. The method is similar to that which we used in the case of the  $\beta$ -decay of the neutron. Using the relevant matrix element and phase space factors one calculates the decay probability of the decay under consideration. The calculation, which still contains  $c_V$  and  $c_A$ , is then compared with experiment.

Consider the strangeness-changing decay  $\Xi^- \rightarrow \Lambda^0 + e^- + \bar{\nu}_e$ . The matrix element for the Fermi decay is

$$|\mathcal{M}_{fi}|_F = \frac{G_F}{V} |\langle uds | \sum_{i=1}^3 T_{i,+} | dss \rangle| , \quad (16.69)$$

where we have assumed that the coupling constant  $c_V = 1$  is unchanged. Applying the operator  $T_+$  to the flavour eigenstate  $|s\rangle$  yields a linear combination of  $|u\rangle$  and  $|c\rangle$ . Just as was the case for the  $\beta$ -decay of the neutron the matrix element thus contains a Cabibbo factor, here  $\sin \theta_C$ . The Gamow-Teller matrix element is obtained from

$$|\mathcal{M}_{fi}|_{GT} = \frac{g_A}{g_V} \frac{G_F}{V} |\langle uds | \sum_{i=1}^3 T_{i,+} \sigma_i | dss \rangle| . \quad (16.70)$$

Of course the evaluation of the  $\sigma$  operator depends upon the wave functions of the baryons involved in the decay.

The analysis of the data confirms the assumption that the ratio  $\lambda = g_A/g_V$  has the same value in both hyperon and neutron decays. The axial current is hence modified in the same way for all three light-quark flavours.

## 16.7 How Good Is the Constituent-Quark Concept?

We introduced the concept of constituent quarks so as to describe the meson and baryon mass spectrum as simply as possible. We thus viewed constituent quarks as the effective building blocks from which the hadrons can be constructed. This means, however, that we should be able to derive all the hadronic quantum numbers from these effective constituents. Furthermore we have tacitly assumed that we are entitled to treat constituent quarks as elementary particles whose magnetic moments, just like the electrons', obey a Dirac relation (16.13). That these ideas work has been seen in the chapters treating the meson and baryon masses and the magnetic moments. Various approaches led us to constituent-quark masses which were in good agreement with each other and furthermore the magnetic moments of the model were generally in very good agreement with experiment. Constituent quarks are not, however, fundamental elementary particles as we understand the term. This role is reserved for the "naked" valence quarks which are surrounded by a cloud of virtual gluons and quark-antiquark pairs. It is not at all obvious why constituent quarks may be treated as though they were elementary.

We can view the constituent-quark model as an extension of the model for the heavy quarkonia to mesons and baryons composed of light quarks. As we have seen, the excited states of the quarkonia allow us to construct the potential between the quarks and antiquarks using non-relativistic quantum mechanics. The potential has two components, the short-distance part with the  $1/r$  dependence and the confinement part at distances greater than approximately 0.2 fm. The simplicity of the quarkonia states is the consequence of the large masses of the charm and bottom quarks. The quark and antiquark move predominantly in the short-distance potential and their velocities are well non-relativistic. The bare masses of the charm and bottom quarks are determined from production experiments; only slightly higher constituent-quark masses are obtained from the best fits to the quarkonia spectra.

The situation in the light-quark domain is dramatically different. The three bare quarks defining the baryon properties have all together a mass of less than  $20 \text{ MeV}/c^2$ , while the nucleon mass is  $938 \text{ MeV}/c^2$ . Thus, approximately 98 % of the nucleon mass is coming from something else. From deep-inelastic scattering experiments we learned that this mass is due to gluons and quark-antiquark pairs. We denote the quantum mechanical state of these gluons and quark-antiquark pairs confined in the nucleon as a condensate in analogy to different degenerated states of bosons in solid state physics. What these condensates exactly are is one of the outstanding problems of non-perturbative QCD.

In constituent-quark models one ascribes the nucleon mass equally distributed to the constituent quarks without any theoretical justification. Constituent quarks with masses of  $330 \text{ MeV}/c^2$  move predominantly in the confinement potential and cannot be treated non-relativistically. As we do not know the effective masses of the constituent quarks we cannot separate their fitted masses into a mass and a kinetic energy term. From deep-inelastic scattering and other experiments we obtained two additional informations: the distribution of the light u- and d-antiquarks in the quark

sea of the nucleon is not flavour symmetric, i.e., in the proton there is an excess of  $\bar{d}$  compared to  $\bar{u}$ ; furthermore, only about one third of the nucleon's spin can be attributed to the spins of the quarks. The excess of the d-antiquarks can be interpreted by finding a  $\pi^+$ -meson with a certain probability ( $\sim 15\%$ ) in the proton. By isospin symmetry, we have the same probability of finding a  $\pi^-$ -meson in the neutron that also can be related to the neutron's negative charge density at large radii that we have derived from its electric form factor. This large probability of finding a pion in the nucleon can explain the dominance of the pion exchange in low-energy nucleon-nucleon interactions. The missing quark angular momentum to the nucleon's spin is an additional hint that the structure of the nucleon is more complicated than assumed by being composed of three constituent quarks.

## Problems

### 1. Particle production and identification

A liquid hydrogen target is bombarded with a  $|p| = 12 \text{ GeV}/c$  proton beam. The momenta of the reaction products are measured in wire chambers inside a magnetic field. In one event six charged particle tracks are seen. Two of them go back to the interaction vertex. They belong to positively charged particles. The other tracks come from two pairs of oppositely charged particles. Each of these pairs appears "out of thin air" a few centimetres away from the interaction point. Evidently two electrically neutral, and hence unobservable, particles were created which later both decayed into a pair of charged particles.

- (a) Make a rough sketch of the reaction (the tracks).
- (b) Use Tables 15.2, 15.3 and 16.1 as well as [15] to discuss which mesons and baryons have lifetimes such that they could be responsible for the two observed decays. How many decay channels into two charged particles are there?
- (c) The measured momenta of the decay pairs were:
  - (1)  $|p_+| = 0.68 \text{ GeV}/c$ ,  $|p_-| = 0.27 \text{ GeV}/c$ ,  $\angle(p_+, p_-) = 11^\circ$ ;
  - (2)  $|p_+| = 0.25 \text{ GeV}/c$ ,  $|p_-| = 2.16 \text{ GeV}/c$ ,  $\angle(p_+, p_-) = 16^\circ$ .

The relative errors of these measurements are about 5%. Use the method of invariant masses (16.1) to see which of your hypotheses from (b) are compatible with these numbers.

- (d) Using these results and considering all applicable conservation laws produce a scheme for all the particles produced in the reaction. Is there a unique solution?

## 2. Baryon masses

Calculate expressions analogous to (16.11) for the mass shifts of the  $\Sigma$  and  $\Sigma^*$  baryons due to the spin-spin interaction. What value do you obtain for  $\alpha_s |\psi(0)|^2$  if you use the constituent-quark masses from Sect. 16.3?

## 3. Isospin coupling

The  $\Lambda$  hyperon decays almost solely into  $\Lambda^0 \rightarrow p + \pi^-$  and  $\Lambda^0 \rightarrow n + \pi^0$ . Apply the rules for coupling angular momenta to isospin to estimate the ratio of the two decay probabilities.

## 4. Muon capture in nuclei

Negative muons are slowed down in a carbon target and then trapped in atomic  $1s$  states. Their lifetime is then  $2.02 \mu\text{s}$  which is less than that of the free muon ( $2.097 \mu\text{s}$ ). Show that the difference in the lifetimes is due to the capture reaction  $^{12}\text{C} + \mu^- \rightarrow ^{12}\text{B} + \nu_\mu$ . The mass difference between the  $^{12}\text{B}$  and  $^{12}\text{C}$  atoms is  $13.37 \text{ MeV}/c^2$  and the lifetime of  $^{12}\text{B}$  is  $20.2 \text{ ms}$ .  $^{12}\text{B}$  has, in the ground state, the quantum numbers  $J^P = 1^+$  and  $\tau = 20.2 \text{ ms}$ . The rest mass of the electron and the nuclear charge may be neglected in the calculation of the matrix element.

## 5. Quark mixing

The branching ratios for the semileptonic decays  $\Sigma^- \rightarrow n + e^- + \bar{\nu}_e$  and  $\Sigma^- \rightarrow \Lambda^0 + e^- + \bar{\nu}_e$  are  $1.02 \cdot 10^{-3}$  and  $5.7 \cdot 10^{-5}$  respectively – a difference of more than an order of magnitude. Why is this? The decay  $\Sigma^+ \rightarrow n + e^+ + \nu_e$  has not yet been observed (upper bound:  $5 \cdot 10^{-6}$ ). How would you explain this?

## 6. Parity

- The intrinsic parity of a baryon cannot be determined in an experiment; it is only possible to compare the parity of one baryon with that of another. Why is this?
- It is conventional to ascribe a positive parity to the nucleon. What does this say about the deuteron's parity (see Sect. 17.2) and the intrinsic parities of the  $u$ - and  $d$ -quarks?
- If one bombards liquid deuterium with negative pions, the latter are slowed down and may be captured into atomic orbits. How can one show that they cascade down into the  $1s$  shell (K shell)?
- A pionic deuterium atom in the ground state decays through the strong interaction via  $d + \pi^- \rightarrow n + n$ . In which  $^{2S+1}L_J$  state may the two neutron system be? Note that the two neutrons are identical fermions and that angular momentum is conserved.
- What parity follows from this for the pion? What parity would one expect from the quark model (see Chap. 15)?
- Would it be inconsistent to assign a positive parity to the proton and a negative one to the neutron? What would then be the parities of the quarks and of the pion? Which convention is preferable? What are the parities of the  $\Lambda$  and the  $\Lambda_c$  according to the quark model?



## References

1. H. Abele, Prog. Part. Nucl. Phys. **60**, 1 (2008)
2. H. Abele et al., Phys. Rev. Lett. **88**, 211801 (2002)
3. A. Aidala et al., Rev. Mod. Phys. **85**, 655 (2013)
4. A. Airapetian et al., Phys. Rev. **D75**, 012007 (2007)
5. M. Alston et al., Phys. Rev. Lett. **5**, 520 (1960)
6. J. Ashman et al., Phys. Lett. **B206**, 364 (1988)
7. F. Close, *An Introduction to Quarks and Partons* (Academic, London/New York/San Francisco, 1979)
8. D. Dubbers, Prog. Part. Nucl. Phys. **26**, 173 (1991)
9. R.P. Ely et al., Phys. Rev. Lett. **7**, 461 (1961)
10. S. Gasiorowicz, J.L. Rosner, Am. J. Phys. **49**, 954 (1981)
11. R. Golub, K. Lamoreaux, Phys. Rep. **237**, 1 (1994)
12. R. Golub et al., Sci. Am. **240**, 106 (1979)
13. J. Liu et al., Phys. Rev. Lett. **105**, 219903 (2010)
14. W. Mampe et al., Phys. Rev. Lett. **63**, 593 (1989)
15. Particle Data Group, J. Beringer et al., *Review of Particle Properties*. Phys. Rev. D **86**, 010001 (2012)
16. A. Trombini, Dissertation, University of Heidelberg (1992)
17. C.S. Wu et al., Phys. Rev. **105**, 1413 (1957)

## Chapter 17

# The Nuclear Force

*Unfortunately, nuclear physics has not profited as much from analogy as has atomic physics. The reason seems to be that the nucleus is the domain of new and unfamiliar forces, for which men have not yet developed an intuitive feeling.*

V. L. Telegdi [15]

The enormous richness of complex structures that we see all around us (molecules, crystals, amorphous materials) is due to chemical interactions. The short-distance forces through which electrically neutral atoms interact can and do produce large scale structures.

The interatomic potential can generally be determined from spectroscopic data about molecular excited states and from measuring the binding energies with which atoms are tied together in chemical substances. These potentials can be quantitatively explained in non-relativistic quantum mechanics. We thus nowadays have a consistent picture of chemical binding based upon atomic structure.

The nuclear force is responsible for holding the nucleus together. This is an interaction between colourless nucleons and its range is of the same order of magnitude as the nucleon diameter. The obvious analogy to the atomic force is, however, limited. In contrast to the situation in atomic physics, it is not possible to obtain detailed information about the nuclear force by studying the structure of the nucleus. The nucleons in the nucleus are in a state that may be described as a degenerate Fermi gas. To a first approximation the nucleus may be viewed as a collection of nucleons in a potential well. The behaviour of the individual nucleons is thus more or less independent of the exact character of the nucleon-nucleon force. It is therefore not possible to extract the nucleon-nucleon potential directly from the properties of the nucleus. The potential must rather be obtained by analysing two-body systems such as nucleon-nucleon scattering and the proton-neutron bound state, i.e., the deuteron.

There are also considerably greater theoretical difficulties in elucidating the connection between the nuclear forces and the structure of the nucleon than for the atomic case. This is primarily a consequence of the strong coupling constant  $\alpha_s$  being two orders of magnitude larger than  $\alpha$ , its electromagnetic equivalent. We will therefore content ourselves with an essentially qualitative explanation of the nuclear force.

## 17.1 Nucleon-Nucleon Scattering

Nucleon-nucleon scattering at low energies, below the pion production threshold, is purely elastic. At such energies the scattering may be described by non-relativistic quantum mechanics. The nucleons are then understood as point-like structureless objects that nonetheless possess spin and isospin. The physics of the interaction can then be understood in terms of a potential. It is found that the nuclear force depends upon the total spin and isospin of the two nucleons. A thorough understanding therefore requires experiments with polarised beams and targets, so that the spins of the particles involved in the reaction can be specified, and both protons and neutrons must be employed.

If we consider nucleon-nucleon scattering and perform measurements for both parallel and antiparallel spins perpendicular to the scattering plane, then we can single out the spin triplet and singlet parts of the interaction. If the nucleon spins are parallel, then the total spin must be 1, while for opposite spins there are equally large (total) spin 0 and 1 components.

The algebra of angular momentum can also be applied to isospin. In proton-proton scattering we always have a state with isospin 1 (an isospin triplet) since the proton has  $I_3 = +1/2$ . In proton-neutron scattering there are both isospin singlet and triplet contributions.

**Scattering phases** Consider a nucleon coming in “from infinity” with kinetic energy  $E$  and momentum  $\mathbf{p}$  which scatters off the potential of another nucleon. The incoming nucleon may be described by a plane wave and the outgoing nucleon as a spherical wave. The cross-section depends upon the phase shift between these two waves.

For states with well defined spin and isospin the cross-section of nucleon-nucleon scattering into a solid angle element  $d\Omega$  is given by the scattering amplitude  $f(\theta)$  of the reaction

$$\frac{d\sigma}{d\Omega} = |f(\theta)|^2. \quad (17.1)$$

For scattering off a short ranged potential a *partial wave decomposition* is used to describe the scattering amplitude. The scattered waves are expanded in terms with fixed angular momentum  $\ell$ . In the case of elastic scattering the following relation holds at large distances  $r$  from the centre of the scattering:

$$f(\theta) = \frac{1}{k} \sum_{\ell=0}^{\infty} (2\ell + 1) e^{i\delta_\ell} \sin \delta_\ell P_\ell(\cos \theta), \quad (17.2)$$

where

$$k = \frac{1}{\lambda} = \frac{|\mathbf{p}|}{\hbar} = \frac{\sqrt{2ME}}{\hbar} \quad (17.3)$$

is the wave number of the scattered nucleon,  $\delta_\ell$  a phase shift angle and  $P_\ell$ , the angular momentum eigenfunction, an  $\ell$ -th order Legendre polynomial. The phase shifts  $\delta_\ell$  describe the phase difference between the scattered and unscattered waves. They contain the information about the shape and strength of the potential and the energy dependence of the cross-section. The fact that  $\delta_\ell$  appears not only as a phase factor but also in the amplitude ( $\sin \delta_\ell$ ) follows from the conservation of the particle current in elastic scattering. This is also known as *unitarity*. The partial wave decomposition is especially convenient at low energies since only a few terms enter the expansion. This is because for a potential with range  $a$  we have

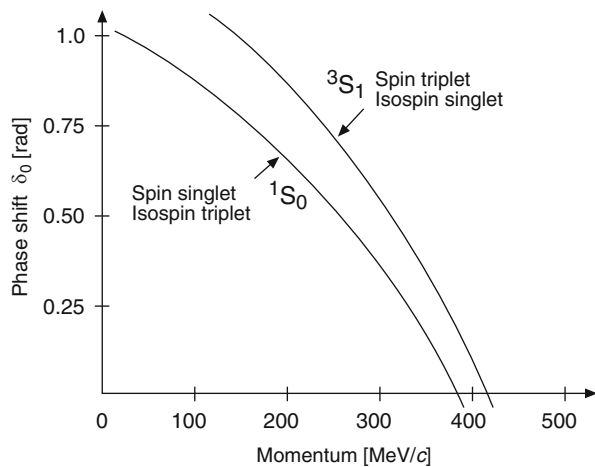
$$\ell \leq \frac{|\mathbf{p}| \cdot a}{\hbar}. \quad (17.4)$$

The phase shift  $\delta_0$  of the partial waves with  $\ell = 0$  (i.e., s waves) is decisive for nuclear binding. From (17.4) we see that the s waves dominate proton-proton scattering (potential range 2 fm) for relative momenta less than 100 MeV/c. The Legendre polynomial  $P_0$  is just 1, i.e., independent of  $\theta$ . The phase shifts  $\delta_0$  as measured in nucleon-nucleon scattering are separately plotted for spin triplet and singlet states against the momentum in the centre-of-mass frame in Fig. 17.1. For momenta larger than 400 MeV/c  $\delta_0$  is negative, below this it is positive. We learn from this that the nuclear force has a repulsive character at short distances and an attractive nature at larger separations. This may be simply seen as follows.

Consider a, by definition, spherically symmetric s wave  $\psi(\mathbf{x})$ . We may define a new radial function  $u(r)$  by  $u(r) = \psi(r) \cdot r$  which obeys the Schrödinger equation

$$\frac{d^2 u(r)}{dr^2} + \frac{2m(E - V)}{\hbar^2} u(r) = 0. \quad (17.5)$$

**Fig. 17.1** The phase shift  $\delta_0$  as determined from experiment both for the spin triplet-isospin singlet  ${}^3S_1$  and for the spin singlet-isospin triplet  ${}^1S_0$  systems plotted against the relative momenta of the nucleons. The rapid variation of the phases at small momenta is not plotted since the scale of the diagram is too small



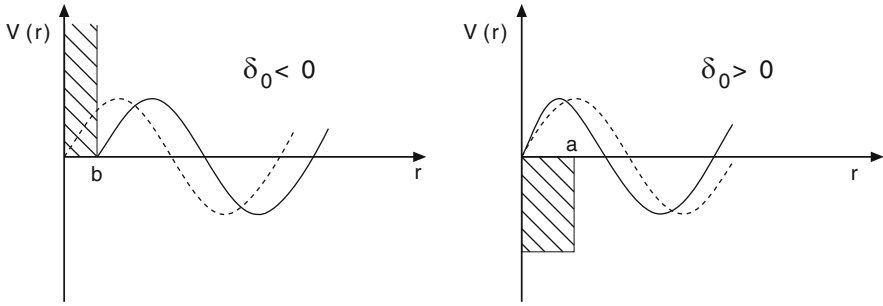


**Fig. 17.2** Sketch of the scattering phase for a repulsive (*left*) and an attractive (*right*) potential. The *dashed curves* denote unscattered waves, the continuous ones the scattered waves

If we now solve this equation for a repulsive rectangular potential  $V$  with radius  $b$  and  $V \rightarrow \infty$  (Fig. 17.2 (left)), we find

$$\delta_0 = -kb. \quad (17.6)$$

The scattering phase is negative and proportional to the range of the potential. A negative scattering phase means that the scattered wave lags behind the unscattered one.

For an attractive potential the scattered wave runs ahead of the unscattered one and  $\delta_0$  is positive (Fig. 17.2 (right)). The size of the phase shift is the difference between the phase of the wave scattered off the edge of the potential  $a$  and that of the unscattered wave:

$$\delta_0 = \arctan \left( \sqrt{\frac{E}{E + |V|}} \tan \frac{\sqrt{2mc^2(E + |V|)} \cdot a}{\hbar c} \right) - \frac{\sqrt{2mc^2 E} \cdot a}{\hbar c}. \quad (17.7)$$

The phase shift  $\delta_0$  is then positive and decreases at higher momenta. If we superimpose the phase shifts associated with a short ranged repulsive potential and a longer ranged attractive one we obtain Fig. 17.3, where the effective phase shift changes sign just as the observed one does.

The relationship between the scattering phase  $\delta_0$  and the scattering potential  $V$  is contained, in principle, in (17.6) and (17.7) since the wave number  $k$  in the region of the potential depends both upon the latter's size and shape and upon the initial energy  $E$  of the projectile. A complete scattering phase analysis leads to the nuclear potential shown in Fig. 17.4 which has – as remarked above – a short ranged repulsive and a longer ranged attractive nature. Since the repulsive part of the potential increases rapidly at small  $r$  it is known as the *hard core*.

**The nucleon-nucleon potential** We may obtain a general form of the nucleon-nucleon potential from a consideration of the relevant dynamical quantities. We will, however, neglect the internal structure of the nucleons, which means that

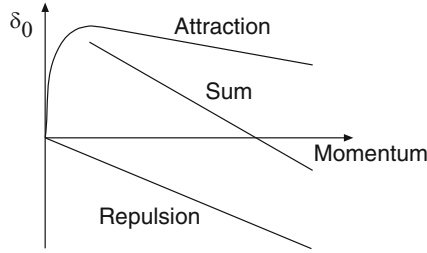


**Fig. 17.3** Superposition of negative and positive scattering phases  $\delta_0$  plotted against the relative momenta of the scattered particles. The resulting effective  $\delta_0$  is generated by a short distance repulsive and a longer range attractive nucleon-nucleon potential

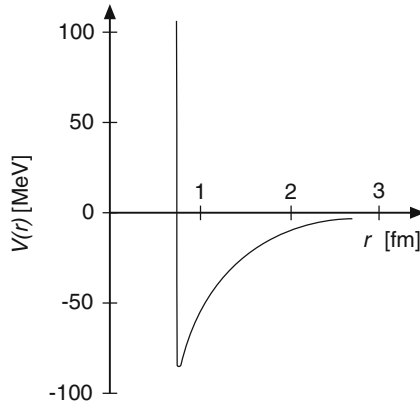


**Fig. 17.4** Sketch of the radial dependence of the nucleon-nucleon potential for  $\ell = 0$ . Note that the spin and isospin dependence of the potential is not shown

this potential will only be valid for nucleon-nucleon bound states and low energy nucleon-nucleon scattering.

The quantities which determine the interaction are the separation of the nucleons  $\mathbf{x}$ , their relative momenta  $\mathbf{p}$ , the total orbital angular momentum  $\mathbf{L}$  and the relative orientations of the spins of the two nucleons,  $s_1$  and  $s_2$ . The potential is a scalar and must at the very least be invariant under translations and rotations. Furthermore it should be symmetric under exchange of the two nucleons. These preconditions necessarily follow from various properties, such as parity conservation, of the underlying theory of the strong force and they limit the scalars which may appear in the potential. At the end of the day the potential, for fixed isospin, has the form [10]:

$$\begin{aligned}
 V(r) = & V_0(r) \\
 & + V_{ss}(r) \mathbf{s}_1 \cdot \mathbf{s}_2 / \hbar^2 \\
 & + V_T(r) (3(\mathbf{s}_1 \cdot \mathbf{x})(\mathbf{s}_2 \cdot \mathbf{x})/r^2 - \mathbf{s}_1 \mathbf{s}_2) / \hbar^2
 \end{aligned}$$

$$\begin{aligned}
& + V_{\text{LS}}(r) (\mathbf{s}_1 + \mathbf{s}_2) \cdot \mathbf{L} / \hbar^2 \\
& + V_{\text{LS}}(r) (\mathbf{s}_1 \cdot \mathbf{L})(\mathbf{s}_2 \cdot \mathbf{L}) / \hbar^4 \\
& + V_{\text{ps}}(r) (\mathbf{s}_2 \cdot \mathbf{p})(\mathbf{s}_1 \cdot \mathbf{p}) / (\hbar^2 m^2 c^2) .
\end{aligned} \tag{17.8}$$

$V_0$  is a standard central potential. The second term describes a pure spin-spin interaction, while the third term is called the *tensor potential* and describes a non-central force. These two terms have the same spin dependence as the interaction between two magnetic dipoles in electromagnetism. The tensor term is particularly interesting, since it alone can mix orbital angular momentum states. The fourth term originates from a spin-orbit force, which is generated by the strong interaction (the analogous force in atomic physics is of magnetic origin). The final two terms in (17.8) are included on formal grounds, since symmetry arguments do not exclude them. They are, however, both quadratic in momentum and thus mostly negligible in comparison to the LS-term.

The significance of this ansatz for the potential is not that the various terms can be merely formally written down, but rather that, as we will see in Sect. 17.3, the spin and isospin dependence of the nuclear force can be explained in meson exchange models. Attempts to fit the potential terms to the experimental data have not fixed it exactly, but a general agreement exists for the first four terms. It should be also noted that many-body forces need to be taken into account for conglomerations of nucleons.

The central potential for the  $S = 0$  case is applicable to the low energy proton-proton and neutron-neutron interactions. The attractive part is, however, not strong enough to create a bound state. For  $S = 1$  on the other hand this potential together with the tensor force and the spin-spin interaction is strong enough to present us with a bound state, the deuteron.

## 17.2 The Deuteron

The deuteron is the simplest of all the nucleon bound states i.e., the atomic nuclei. It is therefore particularly suitable for studying the nucleon-nucleon interaction. Experiments have yielded the following data about the deuteron ground state:

Binding energy	$B = 2.225 \text{ MeV}$
Spin and parity	$J^P = 1^+$
Isospin	$I = 0$
Magnetic moment	$\mu = 0.857 \mu_N$
Elec. quadrupole moment	$Q = 0.282 e \cdot \text{fm}^2$ .

The proton-neutron system is mostly made up of an  $\ell = 0$  state. If it were a pure  $\ell = 0$  state then the wave function would be spherically symmetric, the quadrupole moment would vanish and the magnetic dipole moment would be just the sum of the proton and neutron magnetic moments (supposing that the nucleonic magnetic moments are not altered by the binding interaction). This prediction for the deuteron magnetic moment

$$\mu_p + \mu_n = 2.793 \mu_N - 1.913 \mu_N = 0.880 \mu_N \quad (17.9)$$

differs slightly from the measured value of  $0.857 \mu_N$ . Both the magnetic dipole moment and the electric quadrupole moment can be explained by the admixture of a state with the same  $J^P$  quantum numbers

$$|\psi_d\rangle = 0.98 \cdot |^3S_1\rangle + 0.20 \cdot |^3D_1\rangle. \quad (17.10)$$

In other words there is a 4% chance of finding the deuteron in a  $^3D_1$  state. This admixture can be explained from the tensor components of the nucleon-nucleon interaction.

We now want to calculate the nucleon wave function inside a deuteron. Since the system is more or less in an  $\ell = 0$  state, the wave function will be spherically symmetric. We will need the depth  $V$  of the potential well (averaged over the attractive and repulsive parts) and its range,  $a$ . The binding energy of the deuteron alone gives us one parameter – the “volume” of the potential well, i.e.,  $Va^2$ . The solutions of the Schrödinger equation (17.5) are

$$\begin{aligned} \text{if } r < a : u_I(r) &= A \sin kr \quad \text{where } k = \sqrt{2m(E - V)}/\hbar, \quad (V < 0), \\ \text{if } r > a : u_{II}(r) &= Ce^{-\kappa r} \quad \text{where } \kappa = \sqrt{-2mE}/\hbar, \quad (E < 0), \end{aligned} \quad (17.11)$$

and  $m \approx M_p/2$  is the reduced mass of the proton-neutron system.

Continuity of  $u(r)$  and  $du(r)/dr$  at the edge of the well, i.e.,  $r = a$ , implies that [13]

$$k \cot ka = -\kappa \quad ak \approx \frac{\pi}{2} \quad (17.12)$$

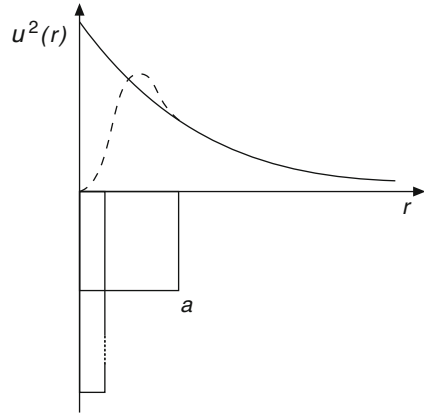
and

$$Va^2 \approx Ba^2 + \frac{\pi^2 (\hbar c)^2}{8 mc^2} \approx 100 \text{ MeV fm}^2. \quad (17.13)$$

Current values for the range of the nuclear force, and hence the effective extension of the potential  $a \approx 1.2 \dots 1.4$  fm, imply that the depth of the potential is  $V \approx 50$  MeV. This is much greater than the deuteron binding energy  $B$  (just



**Fig. 17.5** Radial probability distribution  $u^2(r) = r^2|\psi|^2$  of the nucleons in the deuteron for an attractive potential with range  $a$  (dashed curve) and for the range  $a \rightarrow 0$  with a fixed volume  $Va^2$  for the potential well (continuous curve)



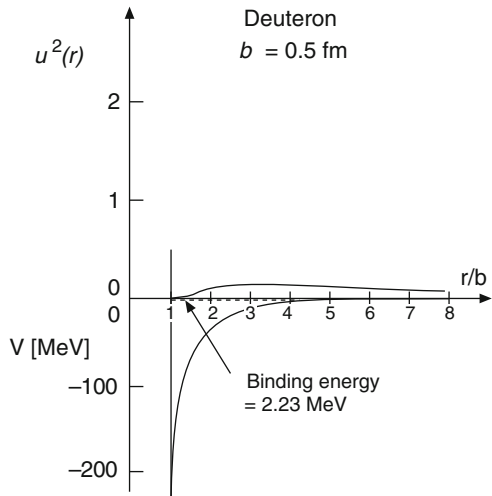
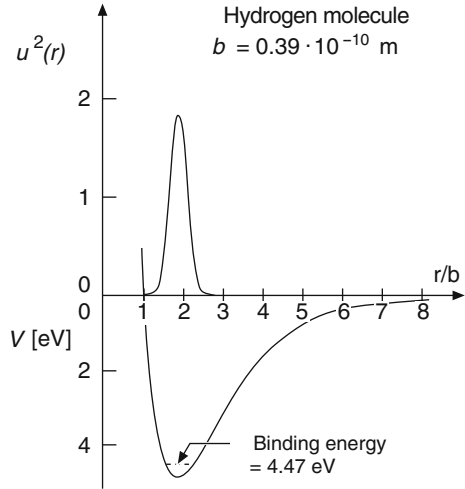
2.25 MeV). The tail of the wave function, which is characterised by  $1/\kappa \approx 4.3$  fm, is large compared to the range of the nuclear force.

The radial probability distribution of the nucleons is sketched in Fig. 17.5 for two values of  $a$  but keeping the volume of the potential well  $Va^2$  constant. Since deuterium is a very weakly bound system the two calculations differ only slightly, especially at larger separations.

A more detailed calculation which takes the repulsive part of the potential into account only changes the above wave function at separations smaller than 1 fm (cf. Fig. 17.5). In Fig. 17.6 the probability distribution of nucleons in deuterium and of hydrogen atoms in a hydrogen molecule are given for comparison. The separations are in both cases plotted in units of the spatial extension  $Rmb$  of the relevant hard core. The hard-core sizes are about  $0.4 \cdot 10^{-10}$  m for the hydrogen molecule and roughly  $0.5 \cdot 10^{-15}$  m for the deuteron. The atoms in the molecule are well localised – the uncertainty in their separation  $\Delta R$  is only about 10% of the separation (cf. Fig. 17.6). The nuclear binding in the deuteron is relatively “weak” and the bound state is much more spread out. This means that *the average kinetic energy is comparable to the average depth of the potential* and so the binding energy, which is just the sum of the kinetic and potential energies, must be very small.

The binding energy of the nucleons in larger nuclei is somewhat greater than that in the deuteron and the density is accordingly larger. Qualitatively we still have the same situation: a relatively weak effective force is just strong enough to hold nuclei together. The properties of the nuclei bear witness to this fact: it is a precondition both for the description of the nucleus as a degenerate Fermi gas and for the great mobility of the nucleons in nuclear matter.

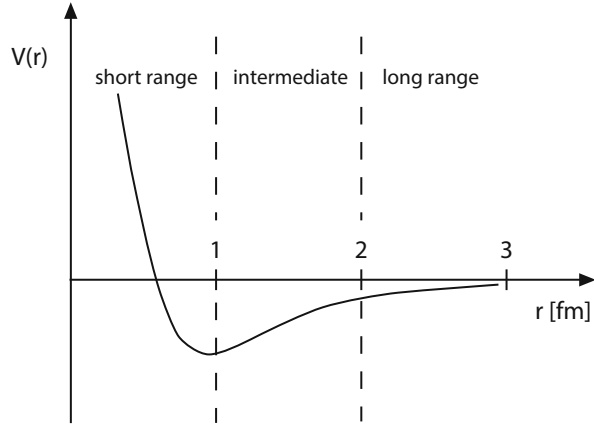
**Fig. 17.6** The radial probability distribution  $u^2(r)$  of the hydrogen atoms in a hydrogen molecule (*top*) [7] and of nucleons in a deuteron (*bottom*) in units of the relevant hard cores (From [1]). The covalent bond strongly localises the H atoms, since the binding energy is comparable to the depth of the potential. The weak nuclear bond, since the potential energy is comparable in size to the kinetic energy, means that the nucleons are delocalised



### 17.3 Nature of the Nuclear Force

We now turn to the task of understanding the strength and the radial dependence of the nuclear force. A sketch of the radial shape of the nucleon-nucleon potential that has been derived from a huge amount of elastic proton-proton and neutron-proton scattering data is shown in Fig. 17.7. It resembles very much the potential between two atoms that is repulsive when the two atoms overlap and attractive at larger distances. Therefore, we will first attempt to describe it by analogies to the atomic case and will employ mainly qualitative arguments.

**Fig. 17.7** Sketch of the nucleon-nucleon potential derived from phase shift analyses of low-energy elastic nucleon-nucleon scattering data



Ideally, we would like to derive the nuclear force between nucleons from QCD, the field theory of the strong interaction between quarks mediated by the exchange of gluons. Such a derivation is, however, not yet possible, one of the reasons being that nucleons are colour-neutral. At distances larger than the confinement scale only colour-neutral objects can be exchanged between them, i.e., only the exchange of two or more gluons, of quark-antiquark pairs or of mesons is possible.

Consequently, one has to rely on simplifications and approximations. Below, we will shortly present some aspects of two different approaches for the description of the nuclear force: quark models and meson-exchange models.

**The nuclear force in the quark model** A consistent theory of the nuclear force, based upon the interaction of quarks and gluons, does not yet exist. But we can explain qualitatively at least part of the nuclear potential in this model. Let us begin with the short-distance repulsive part of the nuclear force and try to construct some analogies to better understood phenomena. That atoms repel each other at short distances is a consequence of the Pauli principle. The electron clouds of both atoms occupy the lowest possible energy levels and if the clouds overlap then some electrons must be elevated into excited states using the kinetic energy of the colliding atoms. Hence we observe a repulsive force at short distances.

The quarks in a system of two nucleons also obey the Pauli principle, i.e., the 6-quark wave function must be totally antisymmetric. It is, however, possible to put as many as 12 quarks into the lowest  $\ell = 0$  state without violating the Pauli principle, since the quarks come in three colours and have two possible spin ( $\uparrow$ ,  $\downarrow$ ) and isospin (u-quark, d-quark) directions. The spin-isospin part of the complete wave function must be symmetric since the colour part is antisymmetric and, for  $\ell = 0$ , the spatial part is symmetric. We thus see that the Pauli principle does not limit the occupation of the lowest quark energy levels in the spatial wave function, and so the fundamental reason for the repulsive core must be sought elsewhere.

The real reason is the spin-spin interaction between the quarks [4]. We have already seen how this makes itself noticeable in the baryon spectrum: the  $\Delta$  baryon,

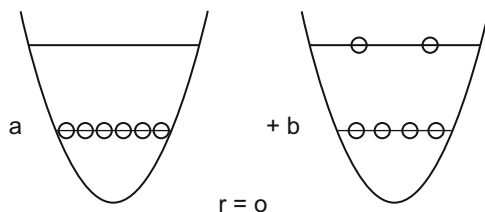


**Fig. 17.8** The quark state for overlapping nucleons. This is composed of a configuration with six quarks in the  $\ell = 0$  state (*left*) and a configuration with two quarks in the  $\ell = 1$  state (*right*). In a non-adiabatic approximation it is found that the latter state dominates at separation  $r = 0$  (probability  $8/9$ ) [5, 14]. For larger distances this state becomes less important and disappears as  $r \rightarrow \infty$

where the three quark spins are parallel to one another, is about  $300 \text{ MeV}/c^2$  heavier than the nucleon. The potential energy then increases if two nucleons overlap and all six quarks remain in the  $\ell = 0$  state since the number of quark pairs with parallel spins is greater than for separated nucleons. For each and every quark pair with parallel spins the potential energy increases by half the  $\Delta$ -nucleon energy difference (16.11).

Of course, the nucleon-nucleon system tries to minimise its “chromomagnetic” energy by maximising the number of antiparallel quark spin pairs. But this is incompatible with remaining in an  $\ell = 0$  state since the spin-flavour part of the wave function must be completely symmetric. The colourmagnetic energy can be reduced if at least two quarks are put into the  $\ell = 1$  state. The necessary excitation energy is comparable to the decrease in the chromomagnetic energy, so the total energy will in any case increase if the nucleons strongly overlap. Hence the effective repulsion at short distances is in equal parts a consequence of an increase in the chromomagnetic and the excitation energies (Fig. 17.8). If the nucleons approach each other very closely ( $r = 0$ ) one finds in a non-adiabatic approximation that there is an  $8/9$  probability of two of the quarks being in a p state [5, 14]. This configuration expresses itself in the relative wave function of the nucleons through a node at 0.4 fm. This together with the chromomagnetic energy causes a strong, short-range repulsion. The nuclear force may be described by a nucleon-nucleon potential which rises sharply at separations less than approximately 0.8 fm.

While the quark model can provide a rather plausible explanation of the repulsive core, the situation is much less satisfactory for the attractive part of the nuclear force. Again we will pursue analogies from atomic physics. As we know, the bonds between atoms are connected to a change in their internal structure and we expect something similar from the nucleons bound in the nucleus. Indeed a change in the quark structure of bound nucleons compared to that of their free brethren has been observed in deep-inelastic scattering off nuclei (EMC effect, see Sect. 8.5).

It is clear upon a moments reflection that the nuclear force is not going to be well described by an *ionic bond*: the confining forces are so strong that it is not possible to lend a quark from one nucleon to another if they do not overlap substantially.

It is often argued that the nuclear forces that are responsible for nuclear binding are residual colour forces, much like the *Van der Waals force* in atomic and molecular physics where the atoms polarise each other and then stick to each other via the resulting dipole-dipole interaction (two-photon exchange) which leads to a potential that decreases with the distance  $r$  between the centres of the atoms like  $1/r^6$ . The analogy in nuclear physics would be a Van der Waals force transmitted by the exchange of two gluons. Explicit calculations have shown, however, that such a force would be too weak to explain the nuclear force at intermediate distances [12].

The only analogy left to us to explain the nuclear force is a *covalent bond*, such as that which is, e.g., responsible for holding the  $H_2$  molecule together. Here the electrons of the two H atoms are continually swapped around and can be ascribed to both atoms. The attractive part of the nuclear force is strongest at distances of around 1 fm, corresponding approximately to the mean square charge radius of the proton. At this distance there is still substantial overlap between the two nucleons. The force could be expressed by the exchange of “single” quarks and indeed reminds us of the atomic covalent bond. Again, model calculations [12] show that the depth of the corresponding potential is much smaller than the experimental value. In fact, quark exchange is less effective than its atomic counterpart of electron exchange. This is partly because to be exchanged the quarks must have the same colour, and there is only a  $1/3$  probability of this. Thus the covalent bond concept, if it is directly transferred from molecules to nuclei, does not give us a good quantitative description of what is going on in nuclei.

Up to now we have neglected the fact that as well as the three quarks in the nucleon there are additional quark-antiquark pairs which are continually being created from gluons and annihilated back into them again. An effective quark-quark exchange may be produced by colour neutral quark-antiquark pairs. This quark-antiquark exchange actually plays a larger role in the nucleon-nucleon interaction than does the simple swapping of two quarks.

**The nuclear force in meson-exchange models** Ever since Yukawa in 1935 first postulated the existence of the pion [16], there have been attempts to describe the inter-nuclear forces in terms of meson exchange [2]. The exchange of mesons with mass  $m$  leads to a potential of the form

$$V = g \cdot \frac{e^{-\frac{mc}{\hbar}r}}{r}, \quad (17.14)$$

where  $g$  is a charge-like constant. This is known as the *Yukawa potential*.

■ To derive the Yukawa potential we first assume that the nucleon acts as a source of virtual mesons in the same way as an electric charge may be viewed as a source of virtual photons.

We start with the wave equation of a free, relativistic particle with mass  $m$ . If we replace the energy  $E$  and momentum  $\mathbf{p}$  in the energy momentum relationship  $E^2 = \mathbf{p}^2c^2 + m^2c^4$  by the

operators  $i\hbar \partial/\partial t$  and  $-i\hbar \nabla$ , as is done in the Schrödinger equation, we obtain the *Klein-Gordon equation*:

$$\frac{1}{c^2} \frac{\partial^2}{\partial t^2} \Psi(\mathbf{x}, t) = \left( \nabla^2 - \mu^2 \right) \Psi(\mathbf{x}, t), \quad \text{where } \mu = \frac{mc}{\hbar}. \quad (17.15)$$

For a massless particle ( $\mu = 0$ ) this equation describes a wave travelling at the speed of light. If we replace  $\Psi$  by the electromagnetic four-potential  $A = (\phi/c, \mathbf{A})$  we obtain the equation for electromagnetic waves in vacuo at a large distance from the source. One may thus interpret  $\Psi(\mathbf{x}, t)$  as the wave function of the photon.

Consider now the static field limit where (17.15) reduces to

$$\left( \nabla^2 - \mu^2 \right) \psi(\mathbf{x}) = 0. \quad (17.16)$$

If we demand a spherically symmetric solution, i.e., one that solely depends upon  $r = |\mathbf{x}|$  we find

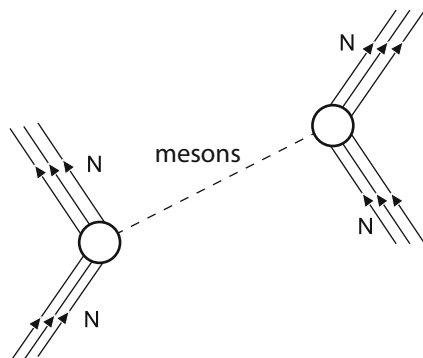
$$\frac{1}{r^2} \frac{d}{dr} \left( r^2 \frac{d\psi(r)}{dr} \right) - \mu^2 \psi(r) = 0. \quad (17.17)$$

A particularly simple ansatz for the potential  $V$  that results from exchanging the particle is  $V(r) = g \cdot \psi(r)$ , where  $g$  is an arbitrary constant. It is clear that this ansatz can make sense if we consider the electromagnetic case: in the limit  $\mu \rightarrow 0$  we obtain the Poisson equation for a space without charges from (17.16), and we obtain from (17.17) the Coulomb potential  $V_C \propto 1/r$ , i.e., the potential of a charged particle at a large separation where the charge density is zero. If we now solve (17.17) for the massive case, we obtain the Yukawa potential (17.14). This potential initially decreases roughly as  $1/r$  and then much more rapidly. The range is of the order of  $1/\mu = \hbar/mc$ , which is also what one would expect from the uncertainty relation. The interaction due to pion exchange has a range of about 1.4 fm.

The above remarks are somewhat naive and not an exact derivation. We have ignored the spin of the particle: the Klein-Gordon equation holds for spinless particles (luckily this is true for the pion). Additionally a virtual meson does not automatically have the rest mass of a free particle. Furthermore these interactions take place in the immediate vicinity of the nucleons and the mesons can strongly interact with them. The wave equation of a free particle can at best be an approximation.

A detailed derivation and discussion of the contributions to the nucleon-nucleon potential by the exchange of the various meson types and their spin and isospin dependences can be found in many reviews, for instance in [8]. Here, we will only summarize the main qualitative features. Nucleon-nucleon interaction by meson exchange is sketched in Fig. 17.9. The range of the corresponding potential decreases as the meson mass increases. At large distances the exchange of single pions dominates. The pion is a pseudoscalar particle and contributes weakly to the central attractive part  $V_0$  and the spin-dependent part  $V_{ss}$  of the nucleon-nucleon potential (17.8), but strongly to the tensor part  $V_T$  that is necessary to describe the deuteron properties. To explain the magnitude of the potential in the intermediate range, one needs to introduce the exchange of a scalar object with quantum numbers  $J^P(I) = 0^+(0)$  and a mass of several times the pion mass. The exchange of this scalar object leads to a strong attractive central force and a contribution to the spin-orbit potential  $V_{LS}$ . This elusive scalar object, originally named “ $\sigma$ ” meson, might possibly be identified with the  $f_0(500)$ , a state with a mass of 400–550 MeV/ $c^2$  and

**Fig. 17.9** At distances between neighbored nucleons larger than 0.5 fm the nuclear force is mediated by the exchange of mesons. At large distances one-pion exchange dominates, the repulsion at small distances is due to the exchange of vector mesons. In the intermediate range the exchange of a scalar object (two-pion exchange) plays an important role



a large width of 400–700 MeV/ $c^2$  decaying dominantly into two pions [11]. For a long time the existence of this particle was very uncertain. Therefore, the exchange of this fictitious particle has been considered to effectively be the exchange of two pions combining to the correct quantum numbers. At distances below approximately 0.8 fm the potential is governed by the exchange of the two lightest vector mesons  $\rho$  and  $\omega$  with masses of  $\sim 780$  MeV/ $c^2$ . For vector particles, one finds a strong repulsive central force (analogous to the repulsion between two like charges caused by one-photon exchange) and a spin-orbit force which has the same sign as in the scalar case but is (for similar masses of scalar and vector particles) by a factor of three stronger. The tensor force has the opposite sign compared to the pseudoscalar case and damps the strong tensor force of one-pion exchange at small distances.

Various potentials based on meson exchange have been developed in the last decades that reproduce the measured cross-sections and phase-shifts with high precision. These models are, however, not fundamental. One neglects, for example, the internal structure of nucleons and mesons and assumes that they are point-particles. The meson-nucleon coupling constants that emerge from experiment must be adapted to take this into account. Altogether more than 30 parameters are needed in these models to describe the potential.

Since mesons are really colour neutral quark-antiquark pairs their exchange and that of colour neutral  $q\bar{q}$  pairs give us, in principle, two equivalent ways of describing the nucleon-nucleon interaction. At short distances, however, where the structure of the nucleons must definitely play a part, a description in terms of meson exchange appears to be inadequate. The coupling constant for the exchange of  $\omega$  mesons, which is responsible for the repulsive part of the potential, has to be given an unrealistically high value – about two or three times the size one would accept from a comparison with the other meson-nucleon couplings. The repulsive part of the potential is better described in a quark picture. On the other hand one-pion exchange models give an excellent fit to the data at larger separations.

The most recent approach to describe the nucleon-nucleon potential and the nuclear force is an effective field theory based on *chiral perturbation theory* [6]. This theory has pions, the nucleon and eventually the  $\Delta$  resonance (all point-like)

as effective fundamental degrees of freedom rather than quarks and gluons. It is nowadays considered by its advocates as the state-of-the-art method for microscopic calculations of interactions at low energies of hadrons and light mesons, of two-nucleon and many-nucleon forces and many aspects of nuclear structure. It is beyond the scope of this book to go into any detail. The interested reader may find derivations and detailed discussions in several reviews like, e.g., [3, 9].

## Problems

### 1. The nuclear force

The nuclear force is transmitted by exchanging mesons. What are the ranges of the forces generated by exchanging the following: a  $\pi$ , two  $\pi$ 's, a  $\rho$ , an  $\omega$ ? Which properties of the nuclear force are determined by the exchange particles?

### 2. Neutron-proton scattering

How large would the total cross-section for neutron-proton scattering be if only the short range repulsion (range,  $b = 0.7$  fm) contributed? Consider the energy regime in which  $\ell = 0$  dominates.

## References

1. A. Bohr, B.R. Mottelson, *Nuclear Structure* (Benjamin, New York, 1969)
2. D.M. Brink, *Nuclear Forces* (Pergamon Press, Oxford, 1965)
3. E. Epelbaum et al., *Rev. Mod. Phys.* **81**, 1773 (2009)
4. A. Faessler, *Prog. Part. Nucl. Phys.* **20**, 151 (1988)
5. A. Faessler et al., *Nucl. Phys.* **A402**, 555 (1982)
6. H. Georgi, *Weak Interactions and Modern Particle Theory* (Dover, Mineola, 2009)
7. G. Herzberg, *Spectra of Diatomic Molecules* (Van Nostrand, New York, 1950)
8. R. Machleidt, *Adv. Nucl. Phys.* **19**, 189 (1989)
9. R. Machleidt, D.R. Entem, *Phys. Rep.* **503**, 1 (2011)
10. M.A. Preston, *Physics of the Nucleus*, 2nd edn. (Addison-Wesley, Wokingham, 1962)
11. Particle Data Group, J. Beringer et al., *Review of Particle Properties*. *Phys. Rev. D* **86**, 010001 (2012)
12. M. Rosina, B. Povh, *Nucl. Phys.* **A572**, 48 (1994)
13. F. Schwabl, *Quantum Mechanics*, 4th edn. (Springer, Berlin/Heidelberg/New York, 2007)
14. U. Straub et al., *Nucl. Phys.* **A483**, 686 (1988)
15. V.A. Telegdi, *Sci. Am.* **206**, 50 (1962)
16. H. Yukawa, *Proc. Phys. Math. Soc. Jpn.* **17**, 48 (1935)



# Chapter 18

## The Structure of Nuclei

Nuclei that are in their ground state or are only slightly excited are examples of degenerate Fermi gases. The nuclear density is determined by the nucleon-nucleon interaction – essentially by the strong repulsion at short distances and the weak attraction between nucleons that are further apart. We have already seen in Sect. 6.2 that nucleons are not localised in the nuclei but rather move around with comparatively large momenta of the order of  $250 \text{ MeV}/c$ . This mobility of the nucleons in the nucleus is a consequence of the fact that, as we have seen for the deuteron, the bonds between nucleons in the nucleus are “weak”. The average distance between the nucleons is much larger than the radius of the nucleon hard core.

The fact that nucleons actually move freely inside the nucleus is not at all obvious and of such great conceptual importance that we shall demonstrate it by considering hypernuclei, i.e., those nuclei containing a hyperon as well as the usual nucleons. We will see that a  $\Lambda$  particle moves inside such nuclei like a free particle inside a potential whose depth is independent of the nucleus under consideration and whose range is the nuclear radius.

The shell model is an improvement upon the Fermi gas model in that it has a more realistic potential and the spin-orbit interaction is now taken into consideration. Not only the nuclear density but also the shapes of the nuclei are fixed by the nucleon-nucleon interaction. A nucleus in equilibrium is not always a sphere; it may be ellipsoidal or even more deformed.

### 18.1 The Fermi Gas Model

We wish to show in this chapter that both the nucleon momentum distribution that we encountered in quasi-elastic electron-nucleus scattering (Sect. 6.2) and the nucleon binding energies can be understood in terms of the Fermi gas model

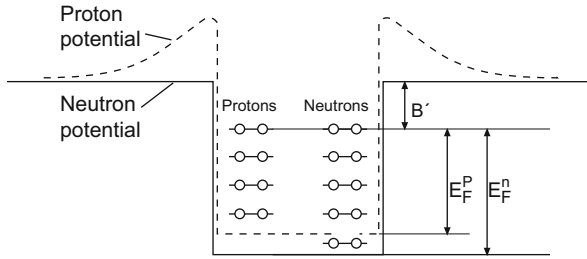


**Fig. 18.1** Sketch of the proton and neutron potentials and states in the Fermi gas model

and that, furthermore, the principal terms of the semi-empirical mass formula (2.8) necessarily emerge from this model. The protons and neutrons that together build up the nucleus are viewed in the Fermi gas model as comprising two independent systems of nucleons. As spin-1/2 particles they naturally obey Fermi-Dirac statistics. It is assumed that the nucleons, inside those constraints imposed by the Pauli principle, can move freely inside the entire nuclear volume.

The potential that every nucleon feels is a superposition of the potentials of the other nucleons. We now assume in our model that this potential has the shape of a well, i.e., that it is constant inside the nucleus and stops sharply at its edge (Fig. 18.1).

The number of possible states available to a nucleon inside a volume  $V$  and a momentum region  $dp$  is given by

$$dn = \frac{4\pi p^2 dp}{(2\pi\hbar)^3} \cdot V. \quad (18.1)$$

At zero temperature, i.e., in the nuclear ground state, the lowest states will all be occupied up to some maximal momentum which we call the *Fermi momentum*  $p_F$ . The number of such states may be found by integrating over (18.1)

$$n = \frac{V p_F^3}{6\pi^2 \hbar^3}. \quad (18.2)$$

Since every state can contain two fermions of the same species, we can have

$$N = \frac{V(p_F^n)^3}{3\pi^2 \hbar^3} \quad \text{and} \quad Z = \frac{V(p_F^p)^3}{3\pi^2 \hbar^3} \quad (18.3)$$

neutrons and protons respectively ( $p_F^n$  and  $p_F^p$  are the Fermi momenta for the neutrons and protons). With a nuclear volume

$$V = \frac{4}{3}\pi R^3 = \frac{4}{3}\pi R_0^3 A \quad (18.4)$$

and the experimental value  $R_0 = 1.21 \text{ fm}$  (5.56), which is obtained from electron scattering, and after assuming that the proton and neutron potential wells have the same radius, we find for a nucleus with  $Z = N = A/2$  the Fermi momentum

$$p_F = p_F^n = p_F^p = \frac{\hbar}{R_0} \left( \frac{9\pi}{8} \right)^{1/3} \approx 250 \text{ MeV}/c. \quad (18.5)$$

The nucleons it seems move freely inside the nucleus with large momenta.

Quasi-elastic electron-nucleus scattering yields a value for the Fermi momentum (6.23) which agrees well with this prediction. For lighter nuclei  $p_F$  tends to be somewhat smaller (Table 6.1, p. 84) and the Fermi gas model is no longer a good approximation in such cases.

The energy of the highest occupied state, the *Fermi energy*  $E_F$ , is

$$E_F = \frac{p_F^2}{2M} \approx 33 \text{ MeV}, \quad (18.6)$$

where  $M$  is the nucleon mass. The difference  $B'$  between the top of the well and the Fermi level is constant for most nuclei and is just the average binding energy per nucleon  $B/A = 7 - 8 \text{ MeV}$ . The depth of the potential and the Fermi energy are to a good extent independent of the mass number  $A$ :

$$V_0 = E_F + B' \approx 40 \text{ MeV}. \quad (18.7)$$

Similarly to the case of a free electron gas in metals, the kinetic energy of the nucleon gas in nuclear matter is comparable to the depth of the potential. This is further evidence that nuclei are rather weakly bound systems.

■ At first sight it might appear as a paradox that on the one hand nucleons occupy energy states between  $-40$  and  $-7 \text{ MeV}$  while on the other hand the average binding energy amounts to  $7 \text{ MeV}$ . One has to realise, however, that the nuclear potential is no given external potential but is generated by the other nucleons. Adding more nucleons to a nucleus does not change the Fermi energy, but the distance of neighbouring energy levels decreases. The constant Fermi energy is a consequence of the constant nuclear density, the increase of the level density a consequence of the increased nuclear volume.

Correspondingly, the removal of nucleons results in an increased distance of the energy levels. By supplying in each case  $7 \text{ MeV}$  to a nucleus one can remove one nucleon after the other but will always find another nucleon at the Fermi level.

Generally speaking heavy nuclei have a surplus of neutrons. Since the Fermi levels of the protons and neutrons in a stable nucleus have to be equal (otherwise the nucleus would enter a more energetically favourable state through  $\beta$ -decay) this implies that the depth of the potential well as it is experienced by the neutron gas has to be greater than of the proton gas (Fig. 18.1). Protons are therefore on

average less strongly bound in nuclei than are neutrons. This may be understood as a consequence of the Coulomb repulsion of the charged protons that leads to an extra term in the potential

$$V_C = (Z - 1) \frac{\alpha \cdot \hbar c}{R}. \quad (18.8)$$

The dependence of the binding energy upon the surplus of neutrons may also be calculated inside the Fermi gas model. First we find the average kinetic energy per nucleon

$$\langle E_{\text{kin}} \rangle = \frac{\int_0^{p_F} E_{\text{kin}} p^2 dp}{\int_0^{p_F} p^2 dp} = \frac{3}{5} \cdot \frac{p_F^2}{2M} \approx 20 \text{ MeV}. \quad (18.9)$$

The total kinetic energy of the nucleus is therefore

$$E_{\text{kin}}(N, Z) = N \langle E_n \rangle + Z \langle E_p \rangle = \frac{3}{10M} (N \cdot (p_F^n)^2 + Z \cdot (p_F^p)^2) \quad (18.10)$$

which may be re-expressed with the help of (18.3) and (18.4) as

$$E_{\text{kin}}(N, Z) = \frac{3}{10M} \frac{\hbar^2}{R_0^2} \left( \frac{9\pi}{4} \right)^{2/3} \frac{N^{5/3} + Z^{5/3}}{A^{2/3}}. \quad (18.11)$$

Note that we have again assumed that the radii of the proton and neutron potential wells are the same. This average kinetic energy has for fixed mass number  $A$  but varying  $N$  or, equivalently,  $Z$  a minimum at  $N = Z$ . Hence the binding energy shrinks for  $N \neq Z$ . If we expand (18.11) in the difference  $N - Z$  we obtain

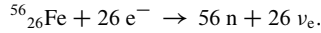
$$E_{\text{kin}}(N, Z) = \frac{3}{10M} \frac{\hbar^2}{R_0^2} \left( \frac{9\pi}{8} \right)^{2/3} \left( A + \frac{5(N - Z)^2}{9A} + \dots \right) \quad (18.12)$$

which gives us the functional dependence upon the neutron surplus. The first term contributes to the volume term in the mass formula while the second describes the correction which results from having  $N \neq Z$ . This so-called *asymmetry energy* grows as the square of the neutron surplus and the binding energy shrinks accordingly. To reproduce the asymmetry term in (2.8) to a reasonable accuracy it is necessary to take the change in the potential for  $N \neq Z$  into account. This additional correction is as important as the change in the kinetic energy.

We thus see that the simple Fermi gas model, where nucleons move freely in an averaged-out potential, can already render the volume and asymmetry terms in the semi-empirical mass formula plausible.

■ The Fermi gas model may also usefully be applied to a very different form of nuclear matter – *neutron stars*. For these no Coulomb energy has to be considered. As well as the attractive nuclear force, which would lead to a density  $\rho_0$ , we also have the gravitational force and the resulting density can be up to ten times larger.

Neutron stars are produced in supernova explosions. The burnt out centre of the star, which is primarily made of iron and whose mass is between one and two solar masses, collapses under the gravitational force. The high density increases the Fermi energy of the electrons so much that the inverse  $\beta$ -decay  $p + e^- \rightarrow n + \nu_e$  takes place, while  $n \rightarrow p + e^- + \bar{\nu}_e$  is forbidden by the Pauli principle. All the protons in the atomic nuclei are step by step converted into neutrons. The Coulomb barrier is thus removed, the nuclei lose their identity and the interior of the star is eventually solely composed of neutrons:



The implosion is only stopped by the Fermi pressure of the neutrons at a density of  $10^{18} \text{ kg/m}^3$ . If the mass of the central core is greater than two solar masses, the Fermi pressure cannot withstand the gravitational force and the star ends up as a black hole.

The best known neutron stars have masses between 1.3 and 1.5 solar masses. The mass of a neutron star which is part of a binary system may be read off from its motion. The radius  $R$  can be measured if enough emission lines can still be measured and a gravitational Doppler shift is observable. This is proportional to  $M/R$ . Typically one finds values like 10 km for the radius.

We only have theoretical information about the internal structure of neutron stars. In the simplest model the innermost core is composed of a degenerate neutron liquid with a constant density. The roughly 1 km thick crust is made out of atoms which despite the high temperature are bound by a strong gravitational pressure in a solid state. It is therefore a good approximation to treat the neutron star as a gigantic nucleus held together by its own gravitational force.

We will assume that the density of the star is constant in the following estimate of the size of a neutron star. We may then neglect any radial dependence of the gravitational pressure and employ an average pressure. Let us consider a typical neutron star with a mass  $M = 3 \cdot 10^{30} \text{ kg}$ , which is about 1.5 solar masses and corresponds to a neutron number of  $N = 1.8 \cdot 10^{57}$ . If we view the neutron star as a cold neutron gas, the Fermi momentum is from (18.5)

$$p_F = \left( \frac{9\pi N}{4} \right)^{1/3} \frac{\hbar}{R}. \quad (18.13)$$

The average kinetic energy per neutron is from (18.9)

$$\langle E_{\text{kin}}/N \rangle = \frac{3}{5} \cdot \frac{p_F^2}{2M_n} = \frac{C}{R^2}, \quad \text{where } C = \frac{3\hbar^2}{10M_n} \left( \frac{9\pi N}{4} \right)^{2/3}. \quad (18.14)$$

The gravitational energy of a star with constant density implies that the average potential energy per neutron is

$$\langle E_{\text{pot}}/N \rangle = -\frac{3}{5} \frac{GNM_n^2}{R}, \quad (18.15)$$

where  $M_n$  is the mass of the neutron and  $G$  is the gravitational constant. The star is in equilibrium if the total energy per nucleon is minimised:

$$\frac{d}{dR} \langle E/N \rangle = \frac{d}{dR} [\langle E_{\text{kin}}/N \rangle + \langle E_{\text{pot}}/N \rangle] = 0. \quad (18.16)$$

and so

$$R = \frac{\hbar^2 (9\pi/4)^{2/3}}{GM_n^3 N^{1/3}}. \quad (18.17)$$

One thus finds a radius of about 12 km for such a neutron star, which is very close to the experimental value, and an average neutron density of  $0.25 \text{ nucleons/fm}^3$ , which is about 1.5 times the density  $\rho_0 = 0.17 \text{ nucleons/fm}^3$  inside an atomic nucleus (5.59).

This good agreement between the predicted and measured values is, however, rather coincidental. In a more exact calculation one must take into account the fact that the density inside a neutron star grows up to  $10\rho_0$  and one then would obtain radii which are much smaller than those measured. On the other hand at a density of  $10\rho_0$ , the inter-neutron separations are only about 0.8 fm, this means that the hard cores of the nucleons touch and a strong repulsion takes place. Taking this into account we can conclude that the gravitational pressure is in equal measure compensated by the Fermi pressure and by nucleon-nucleon repulsion.

We can also expect an admixture of hyperons in equilibrium with the neutrons for such high densities as are found at the centre of neutron stars. It may also be that the overlap of the neutrons, which is largest at the centre of the star, means that the quarks are no longer confined in the individual neutrons. Neutron stars could be also partially composed of *quark matter*.

## 18.2 Hypernuclei

The Fermi gas model is generally employed to describe large scale systems (conduction electrons in metals, nucleons in neutron stars, electrons in a white dwarf, etc.) where the quantisation of angular momentum may be neglected. The system of nucleons inside a nucleus is, by contrast, so small that it possesses discrete energy levels with distinct angular momenta. If one calculates the energy levels in a spherically symmetric potential, one finds states with orbital angular momentum  $\ell = 0, 1, 2, \dots$

At zero temperature the lowest lying states are without exception occupied. The interaction between the nucleons can thus merely cause the individual nucleons to swap their places in the energy level spectrum. As this does not change the total energy of the nucleon it is unobservable. This is why we may talk as though each individual nucleon in the nucleus is in a definite energy and angular momentum state. The wave function that describes such a state is the one-particle wave function. The nuclear wave function is just the product of all the one-particle wave functions.

It would be nice, in order to investigate the energy levels of the individual nucleons, if we could somehow “mark” them. An elegant way to more or less do this in an experiment is to introduce a hyperon into the nucleus, ideally a  $\Lambda$  particle, as a probe. The resulting nucleus is known as a *hypernucleus*.

A  $\Lambda$  particle in the nucleus cannot decay strongly, since strangeness is preserved in strong interactions. Its lifetime is therefore roughly that of a free  $\Lambda$  particle, in other words about  $10^{-10} \text{ s}$ . This is a long enough time to perform a spectroscopic analysis and to investigate the properties of hypernuclei.

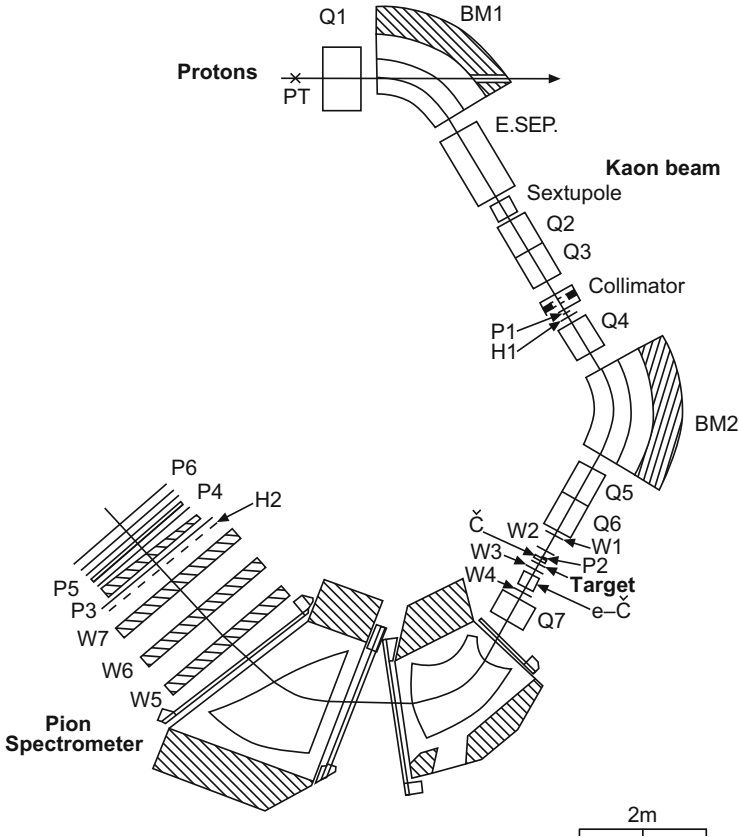
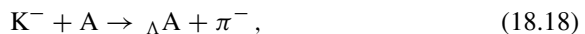


**Fig. 18.2** Experimental apparatus for creating and detecting hypernuclei (From [25]). A beam of  $K^-$  particles hits a 1 cm thick carbon target, generating hypernuclei and  $\pi^-$  mesons. The spectrometer has two stages: initially the momenta of the kaons are measured, then that of the produced pions. The particles are detected and identified with the help of scintillation counters (P), wire chambers (W) and Cherenkov counters ( $\check{C}$ ). The momenta are measured with dipole magnets (BM) while quadrupole lenses (Q) are responsible for the focusing. The excitation energies of the hypernuclei may be read off from the difference in the kaon and pion energies

Hypernuclei are most efficiently produced in the strangeness-exchange reaction



where the index indicates that a neutron in the nucleus is transformed into a  $\Lambda$  by the reaction

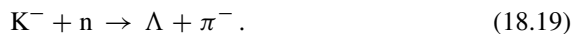


Figure 18.2 shows an apparatus that was used at CERN in the 1970s to generate and detect hypernuclei. The kinematics are particularly convenient if the incident kaon

momentum is  $530 \text{ MeV}/c$  and the final state pions are observed at an angle of  $\theta = 0^\circ$  since in this case no momentum is transferred to the scattered nucleus. In practice one uses kaon beams with momenta between 300 and  $1,000 \text{ MeV}/c$ . The transferred momentum is then still small compared to the Fermi momentum of the nucleons in the nucleus, which can then be to a certain extent considered as undisturbed.

The energy balance of the reaction (18.19) with a free neutron just depends upon the masses of the particles involved. If, however, the neutron is bound inside a nucleus and the  $\Lambda$  also remains inside the nucleus then the energy difference between the  $K^-$  and the  $\pi^-$  yields the difference between the binding energies of the neutron and the  $\Lambda$ :

$$B_\Lambda = B_n + E_\pi - E_K + (M_\Lambda - M_n) \cdot c^2 + \text{recoil}. \tag{18.20}$$

Figure 18.3 shows such a pion spectrum for this reaction for a  $^{12}\text{C}$  nucleus as a function of the  $\Lambda$  binding energy,  $B_\Lambda$ . The experimental value for the neutron separation energy in  $^{12}\text{C}$ , i.e., that needed to pull a neutron out of the nucleus, was taken for  $B_n$ . As well as a clear peak around  $B_\Lambda = 0$  a second, smaller maximum at 11 MeV is observed. This may be interpreted as follows: the transformation of a neutron into a  $\Lambda$  sets free some additional energy which is given to the pion. This energy can only come from the nuclear binding.

We have the following explanation for this. The Pauli principle prevents a proton or a neutron in the nucleus from occupying a lower energy level that is already “taken” – the states in the nucleus get filled “from the bottom up”. If we, however, change a neutron into a  $\Lambda$  particle, then this can occupy any of the states in the nucleus. The  $\Lambda$  does not experience the individual presence of the nucleons, but rather just the potential that they create. This potential is, it should be noted, shallower than that which the nucleons experience. This is because the  $\Lambda$ -nucleon

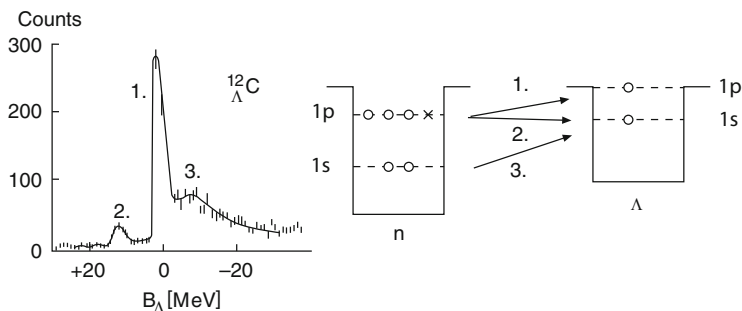


**Fig. 18.3** The pion spectrum from the reaction  $K^- + ^{12}\text{C} \rightarrow \pi^- + ^{12}_\Lambda\text{C}$  for a kaon momentum of  $720 \text{ MeV}/c$  [25]. The pion counting rate at  $0^\circ$  is plotted as a function of the transferred energy  $B_\Lambda$ , which may be interpreted as the binding energy of the  $\Lambda$  in the nucleus. Peak no. 1 corresponds to binding energy  $B_\Lambda = 0$  and peak no. 2, which is the  $^{12}_\Lambda\text{C}$  ground state, has a binding energy of 11 MeV



interaction is weaker than that between the nucleons themselves. That this is the case may also be seen from the lack of any bound state formed from a  $\Lambda$  and a single nucleon.

The spectrum of Fig. 18.3 now makes sense: the protons and neutrons in the  $^{12}\text{C}$  nucleus occupy 1s and 1p energy levels. Should one of the neutrons in a 1p state be transformed into a  $\Lambda$ , then this can also take up a 1p state. In this case the binding energy of the  $\Lambda$  is close to zero. Alternatively it can land in the 1s state and it then has a binding energy of about  $B_\Lambda \approx 11$  MeV.

The smeared out peak with  $B_\Lambda < 0$  can be interpreted as arising from the transformation not of one of the weakly bound neutrons in the 1p state near the Fermi level, but rather of neutrons in the 1s state whose binding energy is larger than the separation energy used for the calculation of  $B_\Lambda$ .

The  $\Lambda$  one-particle states may be seen even more clearly in heavier nuclei. A nice example, the spectrum of  $^{208}_\Lambda\text{Pb}$ , is shown in Fig. 18.4.

Systematic investigations, based upon the reaction

$$\pi^+ + A \rightarrow {}_\Lambda A + \text{K}^+, \quad (18.21)$$

have yielded the binding energies of the 1s states and, furthermore, those of the excited p, d and f states for various nuclei as shown in Fig. 18.5. This shows the dependence of these binding energies upon the mass number  $A$  in the nuclei considered.

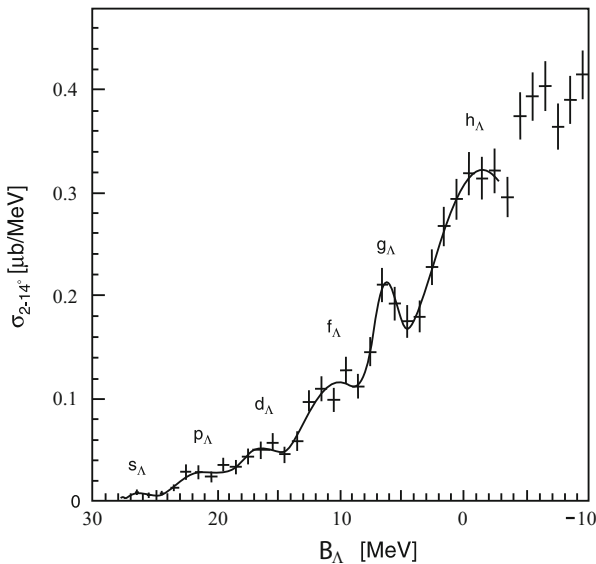


**Fig. 18.4** Excited states of  $^{208}_\Lambda\text{Pb}$  (After [13]). The ground state is labelled as  $s_\Lambda$ , the state at the particle threshold as  $h_\Lambda$

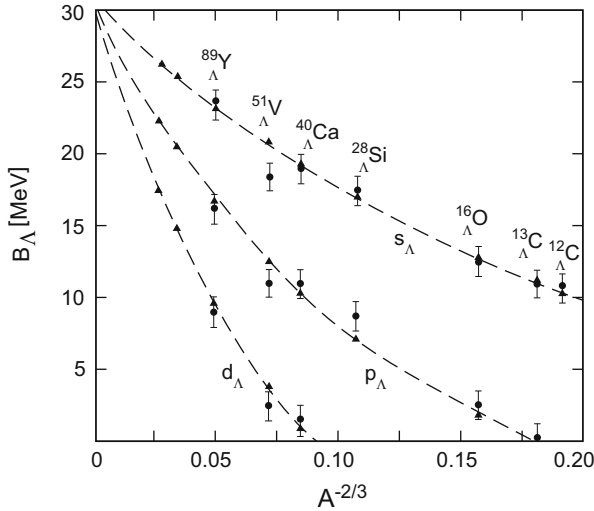


**Fig. 18.5** The binding energy of  $\Lambda$  particles in hypernuclei as a function of the mass number  $A$  [7]. The symbols  $s_{\Lambda}$ ,  $p_{\Lambda}$  and  $d_{\Lambda}$  refer to the state of the  $\Lambda$  in the nucleus. The *triangles* which are connected by the *dashed lines* are theoretical predictions

In this way it is seen that the  $\Lambda$  hyperons occupy *discrete energy levels*, whose binding energies increase with the mass number. The curves shown are the results of calculations assuming both a potential with uniform depth  $V_0 \approx 30$  MeV and a nuclear radius given by  $R = R_0 A^{1/3}$  [7, 25]. The scale  $A^{-2/3}$  corresponds then to  $R^{-2}$  and was chosen because  $B_{\Lambda} R^2$  is almost constant for states with the same quantum numbers, cf. (17.13).

The agreement between the calculated binding energies of the  $\Lambda$  particles and the experimental results is amazing, especially if one considers the simple assumptions made for the potential. The  $\Lambda$  moves as a free particle in the well although the nucleus is composed of densely packed matter.

### 18.3 The Shell Model

The consequences that we have drawn from the spectroscopy of the hypernuclei can be directly applied to the nucleons and we may assume that each nucleon occupies a well-defined energy level.

The existence of these discrete energy levels for the nucleons in the nucleus is reminiscent of the atomic electron cloud. The electrons move in the atom in a central Coulomb potential emanating from the atomic nucleus. In the nucleon, on the other hand, the nucleons move inside a (*mean field*) potential produced by the other

nucleons. In both cases discrete energy levels arise which are filled up according to the dictates of the Pauli principle.

**Magic numbers** In the atomic case we can order the electrons in “shells”. By a shell we mean that several energy levels lie close together clearly separated from the other states. Matters seem to be similar in nuclei.

It is an observed fact that nuclides with certain proton and/or neutron numbers are exceptionally stable (cf. Fig. 2.4) [14]. These numbers (2, 8, 20, 28, 50, 82, 126) are known as *magic numbers*. Nuclei with a magic proton or neutron number possess an unusually large number of stable or very long lived nuclides (cf. Fig. 2.2). If a nucleus has a magic neutron number, then a lot of energy is needed to extract a neutron from it; while if we increase the neutron number by one then the separation energy is much smaller. The same is true of protons. It is also found that a lot of energy is needed to excite such nuclei (Fig. 18.6).

These jumps in the excitation and separation energies for individual nucleons are reminiscent of chemistry: the noble gases, i.e., those with full shells, are particularly attached to their electrons, while the alkali metals, i.e., atoms with just one electron in their outermost shell, have very small separation (ionisation) energies.

The doubly magic nuclei, those with both magic proton and magic neutron numbers, are exceptionally stable. These are the following nuclides:

$${}^4_2\text{He}_2, \quad {}^{16}_8\text{O}_8, \quad {}^{40}_{20}\text{Ca}_{20}, \quad {}^{48}_{20}\text{Ca}_{28}, \quad {}^{208}_{82}\text{Pb}_{126}.$$

The existence of these magic numbers can be explained in terms of the so-called *shell model*. For this we need first to introduce a suitable global nuclear potential.

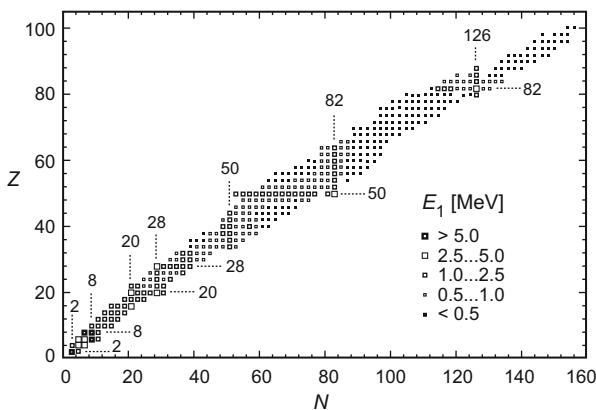


**Fig. 18.6** The energy  $E_1$  of the first excited state of even-even nuclei. Note that this excitation energy is particularly big for nuclei with “magic” proton or neutron number. The excited states generally have the quantum numbers  $J^P = 2^+$ . The following nuclei are exceptions to this rule:  ${}^4_2\text{He}_2$ ,  ${}^{16}_8\text{O}_8$ ,  ${}^{40}_{20}\text{Ca}_{20}$ ,  ${}^{72}_{32}\text{Ge}_{40}$ ,  ${}^{90}_{40}\text{Zr}_{50}$  ( $0^+$ ),  ${}^{132}_{50}\text{Sn}_{82}$ ,  ${}^{208}_{82}\text{Pb}_{126}$  ( $3^-$ ) and  ${}^{14}_6\text{C}_8$ ,  ${}^{14}_8\text{O}_6$  ( $1^-$ ).  $E_1$  is small further away from the “magic” numbers – and is generally smaller for heavier nuclei (Data from [19])

**Eigenstates of the nuclear potential** The wave function of the particles in the nuclear potential can be divided into two parts: a radial one  $R_{n\ell}(r)$ , which only depends upon the radius, and a part  $Y_\ell^m(\theta, \varphi)$  which only depends upon the orientation. The spectroscopic nomenclature used for quarkonium is also employed for the quantum numbers here (see Sect. 14.2):

$$n\ell \quad \text{with} \quad \begin{cases} n = 1, 2, 3, 4, \dots & \text{number of nodes} + 1 \\ \ell = \text{s, p, d, f, g, h, } \dots & \text{orbital angular momentum.} \end{cases}$$

The energy is independent of the  $m$  quantum number, which can assume any integer value between  $+\ell$  and  $-\ell$ . Since nucleons also have two possible spin orientations, this means that the  $n\ell$  levels are in fact  $2 \cdot (2\ell + 1)$  times degenerate. The parity of the wave function is fixed by the spherical wave function  $Y_\ell^m$  and is just  $(-1)^\ell$ .

Since the strong force is so short-ranged, the form of the potential ought to follow the density distribution of the nucleons in the nucleus. For very light nuclei ( $A \lesssim 7$ ) this would mean a Gaussian distribution. The potential can then be approximated by that of a three-dimensional harmonic oscillator. The Schrödinger equation can be solved analytically in this particularly simple case [28]. The energy depends upon the sum  $N$  of the oscillating quanta in all three directions as follows

$$E_{\text{harm. osc.}} = (N + 3/2) \cdot \hbar\omega = (N_x + N_y + N_z + 3/2) \cdot \hbar\omega, \quad (18.22)$$

where  $N$  is related to  $n$  and  $\ell$  by

$$N = 2(n - 1) + \ell. \quad (18.23)$$

Hence states with even  $N$  have positive parity and those with odd  $N$  negative parity.

**Woods-Saxon potential** The density distribution in heavy nuclei can be described by a Fermi distribution, cf. (5.52). The *Woods-Saxon potential* is fitted to this density distribution:

$$V_{\text{centre}}(r) = \frac{-V_0}{1 + e^{(r-R)/a}}. \quad (18.24)$$

States with the same  $N$  but different  $n\ell$  values are no longer degenerate in this potential. Those states with smaller  $n$  and larger  $\ell$  are somewhat lower. The first three magic numbers (2, 8 and 20) can then be understood as nucleon numbers for full shells:

$N$	0	1	2	2	3	3	4	4	4	...
$n\ell$	1s	1p	1d	2s	1f	2p	1g	2d	3s	...
Degeneracy	2	6	10	2	14	6	18	10	2	...
States with $E \leq E_{n\ell}$	2	8	18	20	34	40	58	68	70	...

This simple model does not work for the higher magic numbers. For them it is necessary to include spin-orbit coupling effects which further split the  $n\ell$  shells.

**Spin-orbit coupling** We may formally introduce the coupling of the spin and the orbital angular momentum (17.8) in the same manner as for the (atomic) electromagnetic interaction. We therefore describe it by an additional  $\ell s$  term in the potential:

$$V(r) = V_{\text{centr}}(r) + V_{\ell s}(r) \frac{\langle \ell s \rangle}{\hbar^2}. \quad (18.25)$$

The combination of the orbital angular momentum  $\ell$  and the nucleon spin  $s$  leads to a total angular momenta  $j\hbar = \ell\hbar \pm \hbar/2$  and hence to the expectation values

$$\frac{\langle \ell s \rangle}{\hbar^2} = \frac{j(j+1) - \ell(\ell+1) - s(s+1)}{2} = \begin{cases} \ell/2 & \text{for } j = \ell + 1/2 \\ -(\ell+1)/2 & \text{for } j = \ell - 1/2. \end{cases} \quad (18.26)$$

This leads to an energy splitting  $\Delta E_{\ell s}$  which linearly increases with the angular momentum as

$$\Delta E_{\ell s} = \frac{2\ell + 1}{2} \cdot \langle V_{\ell s}(r) \rangle. \quad (18.27)$$

It is found experimentally that  $V_{\ell s}$  is negative, which means that the  $j = \ell + 1/2$  is always below the  $j = \ell - 1/2$  level, in contrast to the atomic case, where the opposite occurs.

Usually the total angular momentum quantum number  $j = \ell \pm 1/2$  of the nucleon is denoted by an extra index. So, for example, the  $1f$  state is split into a  $1f_{7/2}$  and a  $1f_{5/2}$  state. The  $n\ell_j$  level is  $(2j + 1)$  times degenerate.

Figure 18.7 shows the states obtained from the potential (18.25). The spin-orbit splitting is separately fitted to the data for each  $n\ell$  shell. The lowest shells, i.e.,  $N = 0$ ,  $N = 1$  and  $N = 2$ , make up the lowest levels and are well separated from each other. This, as we would expect, corresponds to the magic numbers 2, 8 and 20. For the  $1f$  shell, however, the spin-orbit splitting is already so large that a sizable gap appears above  $1f_{7/2}$ . This in turn is responsible for the magic number 28. The other magic numbers can be understood in a similar fashion.

This then is the decisive difference between the nucleus and its atomic cloud: the  $\ell s$  coupling in the atom generates the fine structure, small corrections of the order of  $\alpha^2$ , but the spin-orbit term in the nuclear potential leads to sizable splittings of the energy states which are indeed comparable with the gaps between the  $n\ell$  shells themselves. Historically speaking, it was a great surprise that the the nuclear spin-orbit interaction had such important consequences [12, 15].

**One-particle and one-hole states** The shell model is very successful when it comes to explaining the magic numbers and the properties of those nuclei with “one nucleon too many” (or too few).

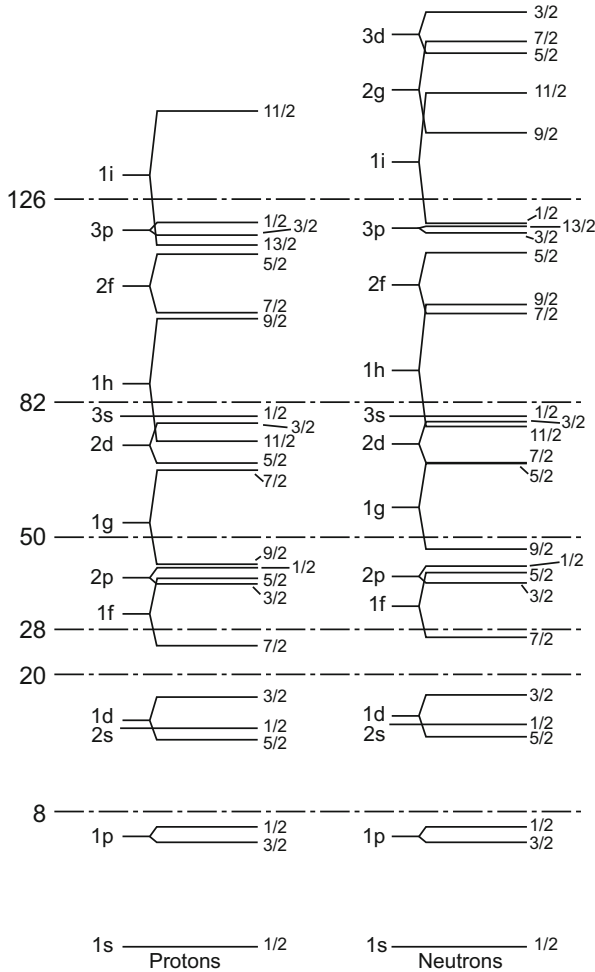


**Fig. 18.7** Single particle energy levels calculated using (18.25) (From [17]). Magic numbers appear when the gaps between successive energy shells are particularly large. This diagram refers to the nucleons in the outermost shells

Those nuclei with mass number between 15 and 17 form a particularly attractive example of this. Their excited states are shown in Fig. 18.8. The  $^{15}\text{N}$  and  $^{15}\text{O}$  nuclei are so-called *mirror nuclei*, i.e., the neutron number of the one is equal to the proton number of the other and vice versa. Their spectra are exceedingly similar, both in terms of where the levels are and also in terms of their spin and parity quantum numbers. This is a consequence of the isospin independence of the nuclear force: if we swap protons and neutrons the strong force essentially does not notice it. The small differences in the spectra can be understood as electromagnetic effects. While the energy levels of  $^{16}\text{O}$  do not resemble those of its neighbours, the  $^{17}\text{O}$  and  $^{17}\text{F}$

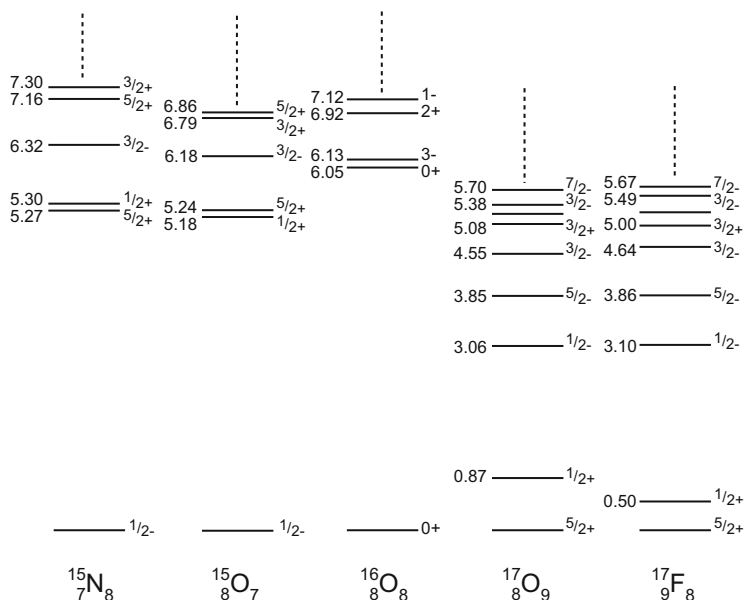


**Fig. 18.8** Energy levels of the  $^{15}\text{N}$ ,  $^{15}\text{O}$ ,  $^{16}\text{O}$ ,  $^{17}\text{O}$  and  $^{17}\text{F}$  nuclei. The vertical axis corresponds to the excitation energy of the states with the various ground states all being set equal, i.e., the differences between the binding energies of these nuclei are not shown

nuclei are, once again, mirror nuclei and have very similar excitation spectra. It is striking that the nuclei with mass numbers 15 and 16 require much more energy to reach their first excited states than do those with mass number 17.

These spectra can be understood inside the shell model. The  $^{16}\text{O}$  nucleus possesses 8 protons and 8 neutrons. In the ground state the  $1s_{1/2}$ ,  $1p_{3/2}$  and  $1p_{1/2}$  proton and neutron shells are fully occupied and the next highest shells,  $1d_{5/2}$ , are empty. Just as in atomic physics the angular momenta of the particles in a full shell add up to zero and the overall parity is positive. The ground state of  $^{16}\text{O}$  has then the quantum numbers  $J^P = 0^+$ . Since the gap between the  $1p_{1/2}$  and  $1d_{5/2}$  energy shells is quite large (about 10 MeV) there are no easily reachable excitation levels.

The two nuclei with  $A = 17$  both have a single extra nucleon in the  $1d_{5/2}$  shell. The spin and parity of the nucleus are completely fixed by this one nucleon. The  $2s_{1/2}$  shell happens to be just a little above the  $1d_{5/2}$  shell and as small an energy as 0.5 MeV suffices to excite this single nucleon to the next shell. The nuclear quantum numbers change from  $5/2^+$  to  $1/2^+$  in this transition. The excited nucleon later decays, through photon emission, into the lowest possible state. Just as we talk of valence electrons in atomic physics, so these nucleons that jump between shells are known as valence nucleons. The  $1d_{3/2}$  shell is about 5 MeV above the  $1d_{5/2}$  one and this amount of energy is required to reach this state.

The  $A = 15$  ground states lack one nucleon in the  $1p_{1/2}$  shell. One speaks of a *hole* and uses the notation  $1p_{1/2}^{-1}$ . The quantum numbers of the hole are those of the nucleus. Thus the ground states of these nuclei have the quantum numbers  $J^P = 1/2^-$ . If a nucleon from the  $1p_{3/2}$  shell is excited into the vacant state in the  $1p_{1/2}$ , and in some sense fills the hole, a hole is then created in the  $1p_{3/2}$  shell. The new nuclear state then has the quantum numbers  $J^P = 3/2^-$ .

**Magnetic moments from the shell model** If in the shell model we associate spin and orbital angular momentum to each individual nucleon, then we can understand the magnetic moment of the nucleus from the sum over the nucleon magnetic moments based upon their spin and orbital angular momenta:

$$\boldsymbol{\mu}_{\text{nucleus}} = \mu_N \cdot \frac{1}{\hbar} \sum_{i=1}^A \{ \boldsymbol{\ell}_i g_\ell + \boldsymbol{s}_i g_s \}. \quad (18.28)$$

Note that

$$g_\ell = \begin{cases} 1 & \text{for protons} \\ 0 & \text{for neutrons} \end{cases} \quad (18.29)$$

and (from (6.7) etc.):

$$g_s = \begin{cases} +5.58 & \text{for protons} \\ -3.82 & \text{for neutrons.} \end{cases} \quad (18.30)$$

Recall our five nuclei with mass numbers from 15 to 17. The magnetic moment of  $^{16}\text{O}$  is zero, which makes perfect sense since in a full shell the spins and angular momenta add up to zero and so the magnetic moment must vanish.

We are in a position to make quantitative predictions for one-particle and one-hole states. We first assume that the nuclear magnetic moment is determined by that of the single nucleon or hole

$$\boldsymbol{\mu}_{\text{nucleus}} = \frac{1}{\hbar} \langle \psi_{\text{nucleus}} | g_\ell \boldsymbol{\ell} + g_s \boldsymbol{s} | \psi_{\text{nucleus}} \rangle \cdot \mu_N. \quad (18.31)$$

The Wigner-Eckart theorem tells us that the expectation value of every vector quantity is equal to its projection onto the total angular momentum, which here means the nuclear spin  $\boldsymbol{J}$ :

$$\boldsymbol{\mu}_{\text{nucleus}} = g_{\text{nucleus}} \cdot \mu_N \cdot \frac{\langle \boldsymbol{J} \rangle}{\hbar}, \quad (18.32)$$

where

$$g_{\text{nucleus}} = \frac{\langle JM_J | g_\ell \boldsymbol{\ell} \boldsymbol{J} + g_s \boldsymbol{s} \boldsymbol{J} | JM_J \rangle}{\langle JM_J | \boldsymbol{J}^2 | JM_J \rangle}. \quad (18.33)$$



Since the nuclear spin  $\mathbf{J}$  in our model is nothing but the total angular momentum of our single nucleon  $\mathbf{j}$  and we have

$$2\ell \mathbf{j} = \mathbf{j}^2 + \ell^2 - \mathbf{s}^2 \quad 2s \mathbf{j} = \mathbf{j}^2 + \mathbf{s}^2 - \ell^2. \quad (18.34)$$

We see that

$$g_{\text{nucleus}} = \frac{g_\ell \{j(j+1) + \ell(\ell+1) - s(s+1)\} + g_s \{j(j+1) + s(s+1) - \ell(\ell+1)\}}{2j(j+1)}. \quad (18.35)$$

The magnetic moment of the nucleus is defined as the value measured when the nuclear spin is maximally aligned, i.e.,  $|M_J| = J$ . The expectation value of  $\langle \mathbf{J} \rangle$  is then  $J\hbar$  and one finds

$$\frac{|\mu_{\text{nucleus}}|}{\mu_N} = g_{\text{nucleus}} \cdot J = \left( g_\ell \pm \frac{g_s - g_\ell}{2\ell + 1} \right) \cdot J \quad \text{for } J = j = \ell \pm \frac{1}{2}. \quad (18.36)$$

There are many different ways to measure nuclear magnetic moments, e.g., in nuclear magnetic spin resonance or from optical hyperfine structure investigations [18]. The experimental values [19] of the magnetic moments can be compared with the predictions of (18.36).

Nucleus	State	$J^P$	$\mu/\mu_N$	
			Model	Expt.
$^{15}\text{N}$	p- $1p_{1/2}^{-1}$	$1/2^-$	-0.264	-0.283
$^{15}\text{O}$	n- $1p_{1/2}^{-1}$	$1/2^-$	+0.638	+0.719
$^{17}\text{O}$	n- $1d_{5/2}$	$5/2^+$	-1.913	-1.894
$^{17}\text{F}$	p- $1d_{5/2}$	$5/2^+$	+4.722	+4.793

The magnetic moments of the  $A = 15$  and  $A = 17$  nuclei can, we see, be understood in a single-particle picture. We should now perhaps admit to having chosen the example with the best agreement between the model and experiment: firstly these nuclei are, up to one single nucleon or hole, doubly magic and secondly they have a relatively small nucleon number which means that effects such as polarisation of the remnant by the valence nucleon are relatively tiny.

We assume for nuclei with odd mass number whose incomplete shells contain more than one nucleon or hole that the total nucleon magnetic moment is due to the one unpaired nucleon [26]. The model then roughly reproduces the experimental trends, but disagreements as big as  $\pm 1\mu_N$  and larger appear for many nuclei. The magnetic moment is, generally speaking, smaller than expected. The polarisation of the rest of the nucleus from the unpaired nucleon tends to explain this [2].

## 18.4 Deformed Nuclei

The shell-model approximation which assumes that nuclei are spherically symmetric objects – plus, of course, the additional spin-orbit interaction – is only good for those nuclei which are close to having doubly magic full shells. For nuclei with half-full shells this is not the case. In such circumstances the nuclei are deformed and the potential is no longer spherically symmetric.

It was already realised in the 1930s, from atomic spectroscopy, that nuclei are not necessarily always spherical [6, 27]. Deviations in the fine structure of the spectra hinted at a non-vanishing electrical quadrupole moment, i.e., that the charge distribution of the nuclei was not spherically symmetric.

**Quadrupole moments** The charge distribution in the nucleus is described in terms of electric multipole moments. Since the odd moments (e.g., the dipole and octupole) have to vanish because of parity conservation, the electric quadrupole moment is the primary measure of in how far the charge distribution, and hence the nucleus, deviates from being spherical.

The classical definition of a quadrupole moment is

$$Q = \int (3z^2 - x^2) \varrho(\mathbf{x}) d^3x. \quad (18.37)$$

An ellipsoid of diameter  $2a$  in the  $z$  direction and diameter  $2b$  in the other two directions (Fig. 3.9), with constant charge density  $\varrho(\mathbf{x})$  has the following quadrupole moment:

$$Q = \frac{2}{5}Ze (a^2 - b^2). \quad (18.38)$$

For small deviations from spherical symmetry, it is common to introduce a measure for the deformation. If the average radius is  $\langle R \rangle = (ab^2)^{1/3}$  and the difference is  $\Delta R = a - b$  then the quadrupole moment is proportional to the *deformation parameter*<sup>1</sup> (cf. Sect. 3.3)

$$\varepsilon = \frac{2}{3} \frac{\Delta R}{\langle R \rangle} \quad (18.39)$$

and we find

$$Q = \frac{6}{5}Ze \langle R \rangle^2 \varepsilon. \quad (18.40)$$

---

<sup>1</sup>We skip over the exact definition of the deformation parameter  $\varepsilon$  here; (18.38) and (18.39) are approximations for small deformations.

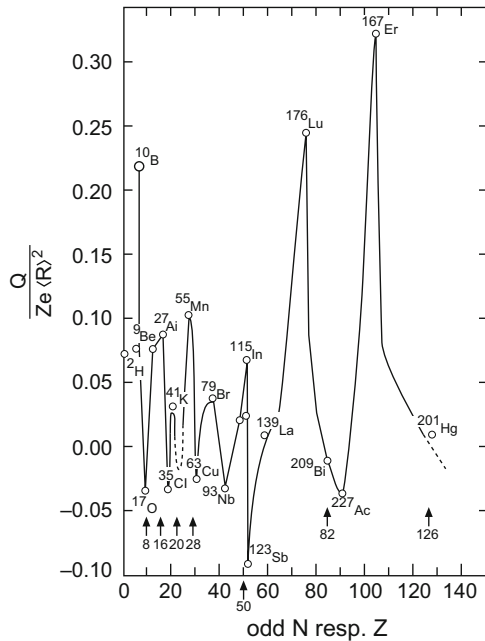
Since the absolute value of a quadrupole moment depends upon the charge and size of the nucleus concerned, we now introduce the concept of the *reduced quadrupole moment* to facilitate the comparison of the deformations of nuclei with different mass numbers. This is a dimensionless quantity and is defined as the quadrupole moment divided by the charge  $Ze$  and the square of the average radius  $\langle R \rangle$ :

$$Q_{\text{red}} = \frac{Q}{Ze\langle R \rangle^2} \quad (18.41)$$

The experimental data for the reduced quadrupole moments are shown in Fig. 18.9. Note that no even-even nuclei are included, as quantum mechanics prevents us from measuring a static quadrupole moment for systems with angular momenta 0 or 1/2. As one sees, the reduced quadrupole moment is small around the magic number nuclei but it is large if the shells are not nearly closed – especially in the lanthanides (e.g.,  $^{176}\text{Lu}$  and  $^{167}\text{Er}$ ). If  $Q$  is positive,  $a > b$ , the nucleus is prolate (shaped like a cigar); if it is negative then the nucleus is oblatelyle deformed (shaped like a lentil). The latter is the rarer case.

The electric quadrupole moments of deformed nuclei are too large to be explained solely in terms of the protons in the outermost, incomplete shell. It is rather the case that the partially occupied proton and neutron shells polarise and deform the nucleus as a whole.

**Fig. 18.9** Reduced quadrupole moments for nuclei with odd proton number  $Z$  or neutron number  $N$  plotted against this number. The quadrupole moments vanish near closed shells and reach their largest values far away from them. It is further clear that prolate nuclei ( $Q > 0$ ) are more common than oblatelyle deformed ones ( $Q < 0$ ). The *solid curves* are based upon the quadrupole moments of very many nuclei, of which only a few are explicitly shown here



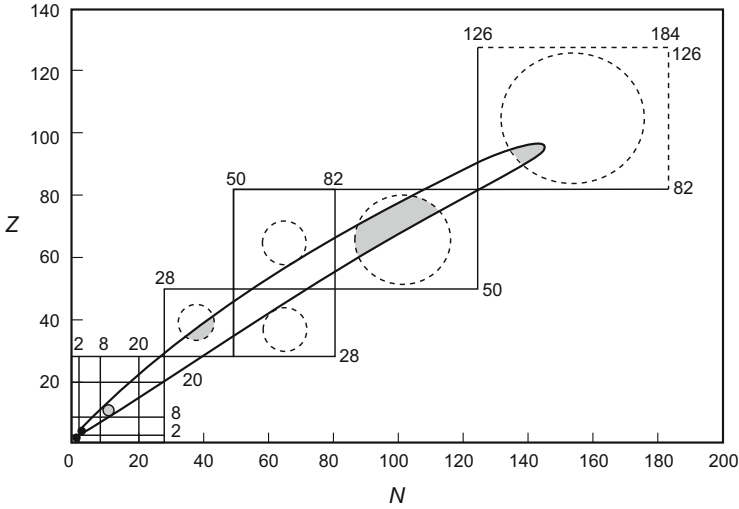


**Fig. 18.10** Deformed nuclei in the  $N$ - $Z$  plane. The *horizontal* and *vertical* lines denote the magic proton and neutron numbers respectively (i.e., they show where the closed shells are). The regions where large nuclear deformations are encountered are *shaded* (From [21])

Figure 18.10 shows in which nuclides such partially full shells have especially strong effects. Stable deformed nuclei are especially common among the rare earths (the lanthanides) and the transuranic elements (the actinides). The light nuclei with partially full shells are also deformed, but, due to their smaller nucleon number, their collective phenomena are less striking.

**Pairing and polarisation energies** We can see why in particular nuclei with half-full shells are deformed if we consider the spatial wave functions of the nucleons. Nucleons in a particular shell have a choice among various spatial and spin states. In atomic physics we have *Hund's rule*: as we fill up an  $n\ell$  subshell with electrons, these initially take up the various hitherto unoccupied orbitals in position space and only when no empty orbitals are left do they start to use the space in every orbital for a further electron with opposite spin. The underlying reason is the electromagnetic repulsion of the electrons, which makes it energetically favourable to have two electrons in spatially separated orbitals rather than having two electrons with opposite spins in the same orbital. Matters are different in nuclear physics, however. The force between the nucleons is, on average, an attractive one. This has two consequences:

- Nuclei become more stable if the nucleons are grouped in pairs with the same spatial wave function and if their angular momenta add to zero, i.e., also:  $\ell_1 = \ell_2$ ,  $m_1 = -m_2$ ,  $\mathbf{j}_1 + \mathbf{j}_2 = \mathbf{0}$ . We talk of a pairing energy. Such pairs have angular momentum and parity,  $J^P = 0^+$ .

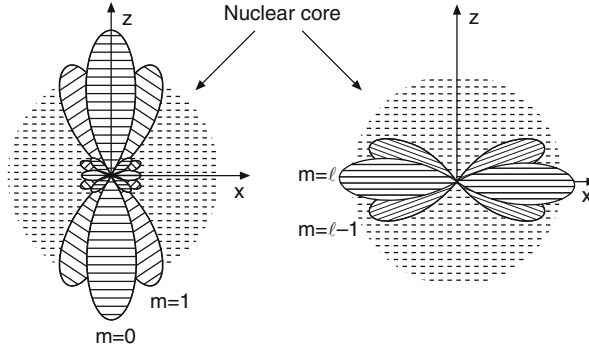


**Fig. 18.11** Overlapping orbitals with adjacent  $m$  quantum numbers. If  $m$  is close to zero the orbitals are parallel to  $z$ , the symmetry axis (*left*). If  $|m|$  is large they are perpendicular to this axis (*right*). The remainder of the nucleus is drawn here as a sphere. This is because nuclear deformations are primarily due to the nucleons in partially filled shells

- Nucleon pairs prefer to occupy neighbouring orbitals (states with adjacent  $m$  values) and this leads, if the nucleus has a half-full shell, to deformations. If the filled orbitals tend to be parallel to the symmetry axis (Fig. 18.11(*left*)) then the nucleus is prolate deformed and if they are perpendicular to this axis (Fig. 18.11(*right*)) the resulting nucleus is oblate.

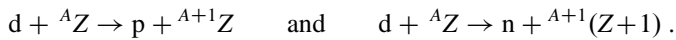
The angular momenta and parity of nuclei are then, not only for almost magic nuclei but quite generally, fixed by individual, unpaired nucleons. Doubly even nuclei will, because of the pairing energy, always have  $J^P = 0^+$  ground states, the  $J^P$  of singly odd nuclei will be determined by their one odd nucleon and, finally, the spin and parity of doubly odd nuclei will depend upon how the quantum numbers of the two unpaired nucleons combine. Experimentally determined ground-state quantum numbers are in excellent agreement with these ideas.

**Single-particle movement of the nucleons** It is necessary, should one want to calculate the energy levels of a deformed nucleus, to recall that the nuclear potential has an ellipsoidal shape. The spin-orbit force is as strong as for the spherically symmetric potential. The one-particle states of deformed nuclei may be found in a conceptionally simple way (the Nilsson model [22]) but the calculations are tedious. The nucleon angular momentum is no longer a conserved quantity in a deformed potential and its place is taken by the projection of the angular momentum onto the symmetry axis of the nucleus. The Nilsson wave functions are therefore composed of shell-model wave functions with the same  $n$  but different  $\ell$ , although their angular momentum projections  $m_j$  must be the same.

## 18.5 Spectroscopy Through Nuclear Reactions

Until now we have mainly concentrated upon experiments using electromagnetic probes (electrons), since the electromagnetic interaction is particularly easily described. It is, however, the case that our modern understanding of nuclear structure, and in particular the quantitative determination of the single-particle properties of low lying nuclear states, comes from analysing reactions where the target and the projectile interact via the nuclear force. Our first quantitative knowledge of the various components of the wave functions goes back to studies of so-called direct reactions. The most prominent examples of these are “stripping” and “pick-up” reactions. In what follows we will restrict ourselves to a qualitative description of these two types of reactions and show how complex the problem becomes when one tries to extract quantitative information.

**Stripping reactions** Stripping reactions are nuclear reactions where one or more of the nucleons from the projectile nucleus are stripped off it and transferred to the target nucleus. The simplest examples of this are the deuteron induced (d, p) and (d, n) reactions:



The following shorthand notation is commonly used to denote such reactions



If the incident deuteron carries a lot of energy, compared to the binding energies of the deuteron and of a neutron in the  $(A+1)$  nucleus, then a quantitative description of the stripping reaction is quite possible. The stripping reaction  ${}^{16}\text{O}(d, p){}^{17}\text{O}$  is depicted in Fig. 18.12.

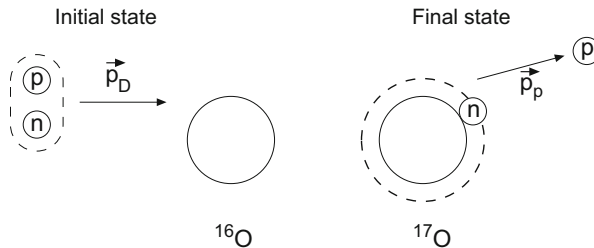


**Fig. 18.12** Sketch of the stripping reaction  ${}^{16}\text{O}(d, p){}^{17}\text{O}$

The cross-section may be calculated from Fermi's golden rule and one finds from (5.22)

$$\frac{d\sigma}{d\Omega} = \frac{2\pi}{\hbar} |\mathcal{M}_{fi}|^2 \frac{p^2 dp V^2}{(2\pi\hbar)^3 v_d dE}. \quad (18.42)$$

We write the matrix element as

$$\mathcal{M}_{fi} = \langle \psi_f | U_{n,p} | \psi_i \rangle, \quad (18.43)$$

where  $\psi_i$  and  $\psi_f$  are the initial and final state wave functions and  $U_{n,p}$  is the interaction that causes the stripping reaction.

**Born approximation** The physical interpretation of the stripping reaction becomes evident when we consider the matrix element in the Born approximation. We assume thereby that the interaction between the deuteron and the nucleus and also that between the proton and the nucleus are both so weak that we may describe the incident deuteron and the outgoing proton by plane waves. In this approximation the initial-state wave function is

$$\psi_i = \phi_A \phi_D \exp(i\mathbf{p}_D \mathbf{x}_D / \hbar). \quad (18.44)$$

Here  $\phi_A$  signifies the ground state of the target nucleus and  $\phi_D$  the internal structure of the deuteron. The incident deuteron plane waves are contained in the function  $\exp(i\mathbf{p}_D \mathbf{x}_D / \hbar)$ . The final-state wave function

$$\psi_f = \phi_{A+1} \exp(i\mathbf{p}_p \mathbf{x}_p / \hbar) \quad (18.45)$$

contains the wave function of the nucleus containing the extra neutron and the outgoing proton's plane waves.

The only likely final states in stripping reactions are those where the nucleon state is not too greatly changed: so we can write the final state to a good approximation as a product of the type

$$\phi_{A+1} = \phi_A \psi_n, \quad (18.46)$$

where  $\phi_A$  describes the internal state of the target nucleus and  $\psi_n$  is a shell-model wave function of the neutron in the potential of the nucleus A.

If the stripping process takes place via a very short-ranged interaction

$$U_{n,p}(\mathbf{x}_n, \mathbf{x}_p) = U_0 \delta(\mathbf{x}_n - \mathbf{x}_p), \quad (18.47)$$

then the matrix element has a very simple form

$$\begin{aligned} \langle \psi_f | U_{n,p} | \psi_i \rangle &= \int \psi_n^*(\mathbf{x}) U_0 \exp(i(\mathbf{p}_D/2 - \mathbf{p}_p)\mathbf{x}/\hbar) \phi_D(\mathbf{x} = \mathbf{0}) d^3x \\ &= U_0 \phi_D(\mathbf{x} = \mathbf{0}) \int \psi_n^*(\mathbf{x}) \exp(i\mathbf{q}\mathbf{x}/\hbar) d^3x. \end{aligned} \quad (18.48)$$

Since  $\mathbf{p}_D/2$  is the average momentum of the proton in the deuteron before the stripping reaction,  $\mathbf{q} = \mathbf{p}_D/2 - \mathbf{p}_p$  is just the average momentum transfer to the nucleus.

The amplitude of the stripping reaction, if we use the Born approximation and a short-ranged interaction, is just the Fourier integral of the wave function of the transferred neutron. The differential cross-section of the (d, p) reaction is proportional to the square of the matrix element and hence to the square of the Fourier integral.

The most important approximation that we have made in calculating the matrix element is the assumption that the interaction which transfers the neutron from the deuteron to the nucleus leaves the motion of the proton basically unchanged. This is a good approximation for deuteron energies greater than 20 MeV or so, since the deuteron binding energy is only 2.225 MeV. The proton will remain on its course even after the neutron is detached.

**Angular momentum** The orbital angular momentum transfer in the stripping reaction is just the orbital angular momentum of the transferred neutron in the state  $|\psi_n\rangle$ . The transfer of  $\ell\hbar$  angular momentum to a nucleus with radius  $R$  requires a momentum transfer of roughly  $|\mathbf{q}| \approx \ell\hbar/R$ . This implies that the first maximum in the angular distribution  $d\sigma/d\Omega$  of the protons will lie at an angle which corresponds to this momentum transfer. Thus the angular distribution of stripping reactions tells us the  $\ell$  quantum number of the single-particle states.

**The reaction  $^{16}\text{O}(\text{d}, \text{p})^{17}\text{O}$**  Figure 18.13 displays the outgoing proton spectrum as measured in the reaction  $^{16}\text{O}(\text{d}, \text{p})^{17}\text{O}$  at a scattering angle of  $\theta = 45^\circ$  and with incident deuteron energies of 24.5 MeV. One recognises 6 peaks which all correspond to different, discrete excitation energies  $E_x$  of  $^{17}\text{O}$ . If one measures at a smaller angle  $\theta$ , and hence smaller momentum transfer, three of these maxima disappear. (The mechanisms which are responsible for the population of these states are more complicated than those of the direct reactions.) The three remaining maxima correspond to the following single-particle states: the  $J^P = 5/2^+$  ( $n-1d_{5/2}^1$ ) ground state, the  $J^P = 1/2^+$  ( $n-2s_{1/2}^1$ ) 0.87 MeV excited state and the  $J^P = 3/2^+$  ( $n-1d_{3/2}^1$ ) 5.08 MeV excited state (cf. Fig. 18.8).

The angular distributions of the protons for these three single-particle states are shown in Fig. 18.14. The maximum of the data for  $E_x = 0.87 = \text{MeV}$  is at  $\theta = 0^\circ$ , i.e., at zero momentum transfer. This implies that the neutron which has been transferred to the nucleus is in a state with zero orbital angular momentum  $\ell$ . And indeed we interpreted this state, with quantum numbers  $J^P = 1/2^+$ , in



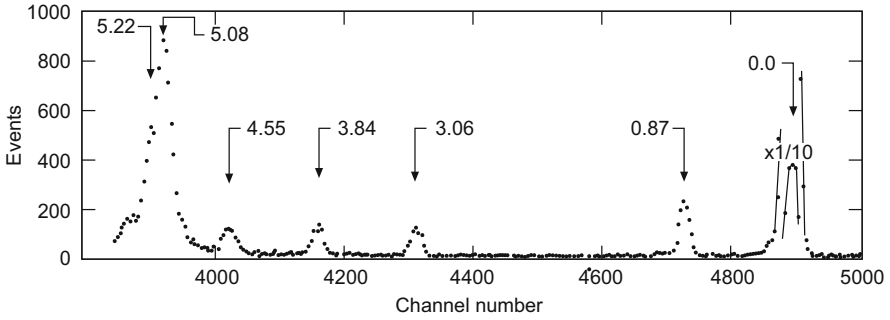


**Fig. 18.13** Proton spectrum of a  $(d, p)$  reaction on  $^{16}\text{O}$ , measured at  $45^\circ$  and projectile energy of 25.4 MeV (From [8]). The channel number is proportional to the proton energy and the excitation energies of  $^{16}\text{O}$  are marked (in MeV) at the various peaks. The ground state and the excited states at 0.87 and 5.08 MeV possess  $J^P = 5/2^+$ ,  $1/2^+$  and  $3/2^+$  quantum numbers respectively and essentially correspond to the  $(n-1d_{5/2}^1)$ ,  $(n-2s_{1/2}^1)$  and  $(n-1d_{3/2}^1)$  single-particle configurations

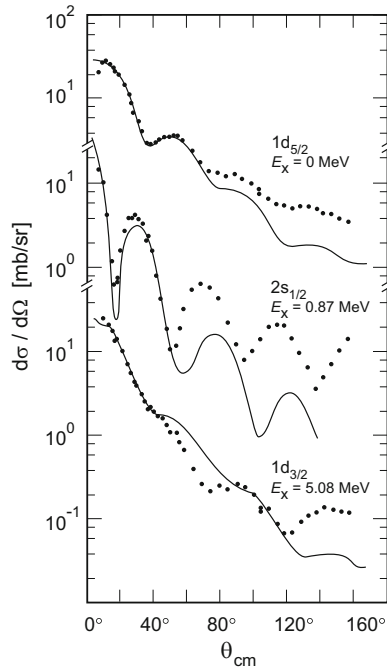


**Fig. 18.14** Angular distributions from the  $^{16}\text{O}(d, p)^{17}\text{O}$  reaction for projectile energies of 25.4 MeV (From [8]). The *continuous curves* are the results of DWBA calculations where the absorption of the deuteron by  $^{16}\text{O}$  was taken into account

the shell model as an  $^{16}\text{O}$  nucleus with an extra neutron in the  $2s_{1/2}$  shell. The two other angular distributions shown have maxima at larger momentum transfers,

which signify  $\ell = 2$ . This is also completely consistent with their quantum numbers. The relative positions of the shells can be determined from such considerations.

**Limits of the Born approximation – DWBA** The results shown in Fig. 18.14 cannot be obtained using the Born approximation, since neither the deflection of the particles in the nuclear field nor absorption effects are taken into account in that approximation. One way to improve the approximation is to use more realistic incident deuteron and outgoing proton wave functions, so that they describe the scattering process as exactly as possible, instead of the plane waves we have employed until now. These wave functions are produced by complicated computer analyses and the results are then compared with our experimental knowledge of elastic proton and deuteron scattering off nuclei. This calculational procedure is known as the *distorted-wave Born approximation (DWBA)*. The continuous lines in Fig. 18.14 are the results of such very tedious calculations. It is obvious that even the best models are only capable of quantitatively reproducing the experimental results at small momentum transfers (small angles).

**Pick-up reactions** Pick-up reactions are complementary to stripping reactions. A proton or neutron is carried away from the target nucleus by a projectile nucleus. Typical examples of this are the (p, d), (n, d), (d,  $^3\text{He}$ ) and (d,  $^3\text{H}$ ) reactions. A (p, d) reaction is shown as an example in Fig. 18.15.

The ideas we used to understand the (d, p) stripping reaction may be directly carried over to the (p, d) pick-up reaction. In the Born approximation, we must only replace the wave function of the transferred neutron  $|\psi_n\rangle$  in (18.48) by that of the  $|\psi_n^{-1}\rangle$  hole state.

**The reaction  $^{16}\text{O}(d, ^3\text{He})^{15}\text{N}$**  It may be clearly seen from Fig. 18.16 that two  $^{15}\text{N}$  states are primarily produced in the reaction  $^{16}\text{O}(d, ^3\text{He})^{15}\text{N}$ . These two states are the  $1p_{1/2}$  and  $1p_{3/2}$  hole states. The other states are rather more complicated configurations (e.g., one particle and two holes) and are much less often excited.

The energy difference between the ground state ( $J^P = 1/2^-$ ) and the  $J^P = 3/2^-$  state is 6.32 MeV (cf. Fig. 18.8). This corresponds to the splitting of the 1p shell in light nuclei due to the  $\ell s$  interaction.

The differential cross-sections for these states are shown in Fig. 18.17. The model calculations are based upon the simple assumption that these states are pure  $p_{1/2}$  and

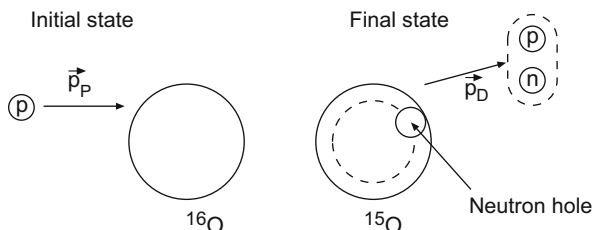


**Fig. 18.15** Sketch of the  $^{16}\text{O}(p, d)^{15}\text{O}$  pick-up reaction

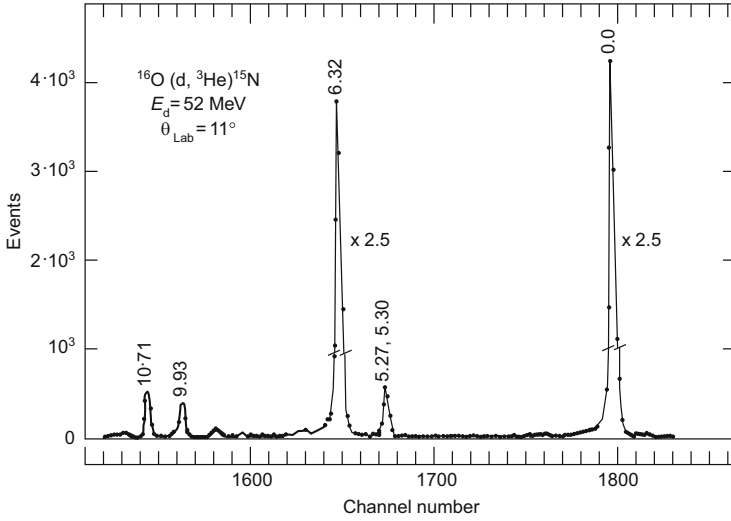


**Fig. 18.16** Spectrum of  $^3\text{He}$  nuclei detected at  $11^\circ$  when 52 MeV deuterons were scattered off  $^{16}\text{O}$  (From [20]). The cross-sections for the production of  $^{15}\text{N}$  in the ground state and in the state with an excitation energy of 6.32 MeV are particularly large (and are scaled down in the diagram by a factor of 2.5)

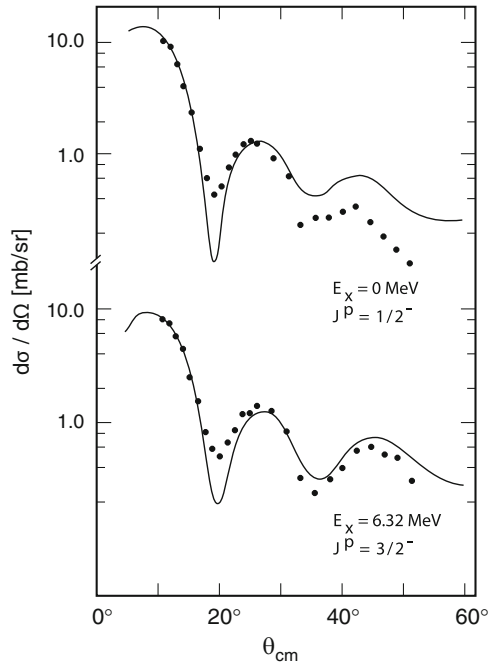


**Fig. 18.17** Differential cross-section  $d\sigma/d\Omega$  for the reaction  $^{16}\text{O}(d, ^3\text{He})^{15}\text{N}$  (From [4]). See also the caption to Fig. 18.14

$p_{3/2}$  hole states. They clearly reproduce the experimental data at small momentum transfers rather well. The admixture of higher configurations must then be tiny. At larger momentum transfers the reaction mechanisms become more complicated and the approximations used here are no longer good enough.

**Direct reactions with heavy nuclei** Stripping and pick-up reactions are well suited for the task of investigating the one-particle properties of both spherical and deformed heavy nuclei. Valence nucleons or valence holes are again excited close to full and nearly empty shells. In those nuclei where there are half-full shells, excited states cannot be described by an excited state of the shell model, rather a mixture of various shell-model states must be used. The properties of the excited states are then determined by the coupling of the valence nucleons.

## 18.6 Beta Decay of the Nucleus

Beta decay provides us with another way to study nuclear structure. The  $\beta$ -decay of individual hadrons was treated in Sect. 16.6 where the example of free neutron decay was handled in more detail. At the quark level this transition corresponds to a d-quark changing into a u-quark. We have already seen that the axial coupling (16.50) is modified in the  $n \rightarrow p$  transition by the internal hadronic structure and the influence of the strong interaction.

If the nucleon is now contained inside a nucleus, further effects need to be considered.

- The matrix element must now contain the overlap of the initial and final-state nuclear wave functions. This means that the matrix element of  $\beta$ -decay lets us glimpse inside the nucleus containing the nucleons.
- The difference between the binding energies of the nuclei before and after the decay defines the type of decay ( $\beta^+$  or  $\beta^-$ ) and fixes the size of the phase space.
- The Coulomb interaction influences the energy spectrum of the emitted electrons or positrons, especially at small velocities, and thus also modifies the phase space.

**Phase space** We calculated in (16.56) the decay rate as a function of the total energy  $E_0$  of the electron and the neutrino. In nuclei the difference between the masses of the initial and final-state nuclei yields  $E_0$ . The integral over the phase space  $f(E_0)$  is now altered by the Coulomb interaction between the charge  $\pm e$  of the emitted electron or positron and that  $Z'e$  of the remaining nucleus. This is described by the so-called *Fermi function*  $F(Z', E_e)$  which is approximately given by

$$F(Z', E_e) \approx \frac{2\pi\eta}{1 - e^{-2\pi\eta}}, \quad \text{where } \eta = \mp \frac{Z'e^2}{4\pi\epsilon_0\hbar v_e} = \mp \frac{Z'\alpha}{v_e/c} \quad \text{for } \beta^\pm, \quad (18.49)$$

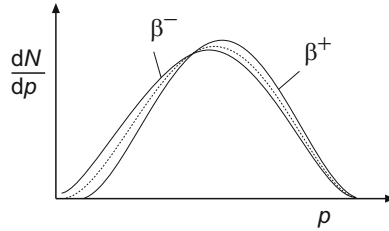


**Fig. 18.18** Schematic appearance of the electron spectrum in  $\beta$ -decay. The phase-space factor from (16.54) produces a spectrum with a parabolic fall off at both ends (dotted line). This is modified by the interaction of the electron/positron with the Coulomb field of the final-state nucleus (continuous lines). These latter curves were calculated from (18.49) for  $Z' = 20$  and  $E_0 = 1$  MeV

where  $v_e$  is the measured final velocity of the electron or positron. The phase-space function  $f(E_0)$  in (16.55) is replaced by

$$f(Z', E_0) = \int_1^{\mathcal{E}_0} \mathcal{E}_e \sqrt{\mathcal{E}_e^2 - 1} \cdot (\mathcal{E}_0 - \mathcal{E}_e)^2 \cdot F(Z', \mathcal{E}_e) d\mathcal{E}_e$$

where  $\mathcal{E} = E/m_e c^2$ ,

(18.50)

which can be calculated to a high precision [5]. The influence of the Coulomb force upon the  $\beta$ -spectrum is shown in Fig. 18.18.

In spectroscopy the information about the structure of the nucleus is contained in the matrix element. The product of the half-life  $t_{1/2}$  and  $f(Z', E_0)$ , which is called the *ft value*, is directly proportional to the inverse square of the matrix element. From (16.56) using  $t_{1/2} = \ln 2 \cdot \tau$  one obtains:

$$f(Z', E_0) \cdot t_{1/2} = ft \text{ value} = \frac{2\pi^3 \hbar^7}{m_e^5 c^4} \cdot \ln 2 \cdot \frac{1}{V^2} \cdot \frac{1}{|\mathcal{M}_{fi}|^2}.$$
(18.51)

The *ft* values vary from as little as  $10^3$  s to as much as  $10^{22}$  s. Normally therefore the logarithm to base ten of its value (in seconds), the *log-ft value*, is quoted.

**The matrix element** The matrix element is influenced not only by the wave function of the nucleon in which the quark transition takes place, but also in turn by the wave function of the nucleus containing the nucleon. In both cases this depends upon how the wave functions before and after the decay overlap.

The ratio of the vector and axial vector parts is determined by the nuclear wave function. Those decays that take place through the vector part of the transition operator are called *Fermi decays*. The spin of the interacting quark does not change here and so the spin of the nucleon is unaffected. The total spin of the electron and the neutrino is thus zero. The decays due to the axial part are called *Gamow-Teller decays*. The lepton spins add up to one here. Generally both Fermi and

Gamow-Teller  $\beta$ -decays are possible. There are, however, cases where only, or nearly only, one of the decays takes place.

Let us attempt to estimate what role is played by orbital angular momentum. The wave function of the electron and the neutrino may be written as a plane wave to a good approximation (cf. (5.18)):

$$\psi(\mathbf{x}) = \frac{e^{i\mathbf{p}\mathbf{x}/\hbar}}{\sqrt{V}} = \frac{1}{\sqrt{V}} \{ 1 + i\mathbf{p}\mathbf{x}/\hbar + \dots \}. \quad (18.52)$$

Since  $\boldsymbol{\ell} = \mathbf{x} \times \mathbf{p}$  this is an expansion in the orbital angular momentum quantum number  $\ell$ . Since the momenta are at most of the order of a few MeV/c and the nuclear radii are a few fm,  $|\mathbf{p}| \cdot R/\hbar$  must be of the order of  $10^{-2}$ . The  $ft$  value contains the square of the matrix element and so we see that every extra unit of  $\ell$  suppresses the decay by a factor of  $10^{-4}$ – $10^{-3}$ . Decays with  $\ell = 0$  are called *allowed*, those with  $\ell = 1$  are then *forbidden* and if  $\ell = 2$  we speak of a *doubly forbidden* decay etc. If  $\ell$  is odd the parity of the nuclear wave function changes, while if it is even parity is conserved.

The following selection rules hold for allowed decays as a result of conservation of angular momentum and parity:

$$\begin{aligned} \Delta P = 0, \quad \Delta J = 0 & \quad \text{for Fermi decays,} \\ \Delta P = 0, \quad \Delta J = 0, \pm 1; (0 \rightarrow 0 \text{ forbidden}) & \quad \text{for Gamow-Teller decays.} \end{aligned}$$

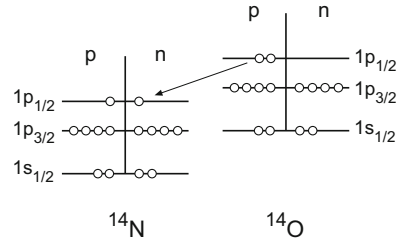
Large  $\ell$  decays only play a role if lower  $\ell$  transitions are ruled out on grounds of angular momentum or parity conservation. Thus for example the decay of a  $1^-$  into a  $0^+$  nucleus is only possible via a (once) forbidden transition and not by an allowed Gamow-Teller transition since the parity of the nucleus changes.

An example of a four times forbidden  $\beta$ -decay is the transition from  $^{115}\text{In}$  ( $J^P = 9/2^+$ ) into  $^{115}\text{Sn}$  ( $J^P = 1/2^+$ ). The  $\log-ft$  value of this decay is 22.7 and its half life is, believe it or not,  $6 \cdot 10^{14}$  years.

**Super allowed decays** If the initial and final state wave functions overlap perfectly then the decay probability is particularly large. This is the case if the created proton and the decayed neutron (or the other way round) have all their quantum numbers in common, i.e., the two nuclear states are in the same isospin multiplet. Such decays are called *super allowed decays*. The  $ft$  values of such transitions are roughly that of the decay of a free neutron (Fig. 18.19).

Super allowed decays are generally  $\beta^+$ -decays. This is because the Coulomb repulsion inside the nucleus slightly splits the states in an isospin multiplet; the excitation energy is higher for those states with more protons and fewer neutrons (cf. Fig. 2.6). Thus the protons in an isospin multiplet decay into neutrons but not the other way round. The  $\beta^-$ -decay of  $^3\text{H}$  into  $^3\text{He}$  is an exception to this rule (another is free neutron decay). This is because the difference between the proton and neutron masses is larger than the decrease in the binding energy of  $^3\text{He}$  from Coulomb repulsion.

**Fig. 18.19** Example of a super allowed  $\beta$  decay



An attractive example of  $\beta$ -decay inside an isospin triplet is provided by the process  $^{14}\text{O} \rightarrow ^{14}\text{N} + e^+ + \nu_e$ , which is a  $0^+ \rightarrow 0^+$  transition (cf. Fig. 2.6) and hence purely a Fermi decay. The three lowest proton shells in the  $^{14}\text{O}$  nucleus, i.e., the  $1s_{1/2}$ ,  $1p_{3/2}$  and  $1p_{1/2}$  shells, are fully occupied as are the two lowest neutron shells, but the  $1p_{1/2}$  neutron shell is empty. Thus one of the two valence nucleons (the protons in the  $1p_{1/2}$  shell) can change into a neutron in the same shell and with the same wave function.

**Allowed decays** Allowed decays are those with  $\ell = 0$ . A familiar example is the  $\beta^-$ -decay of the nuclide  $^{14}\text{C}$ , which is produced by cosmic rays in the upper atmosphere in the reaction  $^{14}\text{N} (n, p) ^{14}\text{C}$ , and is used to determine the age of organic materials. The  $^{14}\text{C}$  ground state belongs, see Fig. 2.6, to an isospin triplet which also includes the 2.31 MeV  $^{14}\text{N}$  state and the ground state of  $^{14}\text{O}$ .

For reasons of energy  $^{14}\text{C}$  is only allowed to decay into the  $^{14}\text{N}$  ground state and this can only happen if the nucleon flips its spin (a Gamow-Teller decay). The half life ( $t_{1/2} = 5,730$  years) and the  $\log-ft$  value (9.04) are much larger than for other allowed decays. This implies that the overlap of the wave functions is extremely small – which is a stroke of luck for archaeology.

**Forbidden decays** Heavy nuclei have an excess of neutrons. If a proton were to decay inside such a nucleus, it would find that the equivalent neutron shell was already full. A super allowed  $\beta^+$ -decay is therefore not possible in heavy nuclei. On the other hand the decay of a neutron into a proton with the same quantum numbers is possible but the resulting nucleus would be in a highly excited state and this is generally ruled out for reasons of energy.

The  $^{40}\text{K}$  nuclide is a good example: it can turn into  $^{40}\text{Ar}$  either through  $\beta^+$ -decay or by a K capture and can also  $\beta^-$ -decay into  $^{40}\text{Ca}$  (cf. Fig. 3.4). The ground state of  $^{40}\text{Ca}$  is a doubly magic nucleus whose  $1d_{3/2}$  (proton and neutron) shells are full while the  $1f_{7/2}$  shells are empty (Fig. 18.20).

The  $^{40}\text{K}$  nuclide has the configuration  $(p-1d_{3/2}^{-1}, n-1f_{7/2}^1)$  and  $^{40}\text{Ar}$  has  $(p-1d_{3/2}^{-2}, n-1f_{7/2}^2)$ . Angular momenta and parity of the unpaired nucleons in  $^{40}\text{K}$  add to  $4^-$ . Hence the decay into the ground states of  $^{40}\text{Ca}$  and  $^{40}\text{Ar}$  are triply forbidden. The decay into the lowest excited state of  $^{40}\text{Ar}$  ( $J^P = 2^+$ ) via K capture is in principle only simply forbidden, but the available phase space is very small since the energy difference is only 0.049 MeV. For these reasons  $^{40}\text{K}$  is extremely long lived ( $t_{1/2} = 1.27 \cdot 10^9$  years) and is still today, billions of years after the birth of the solar system,

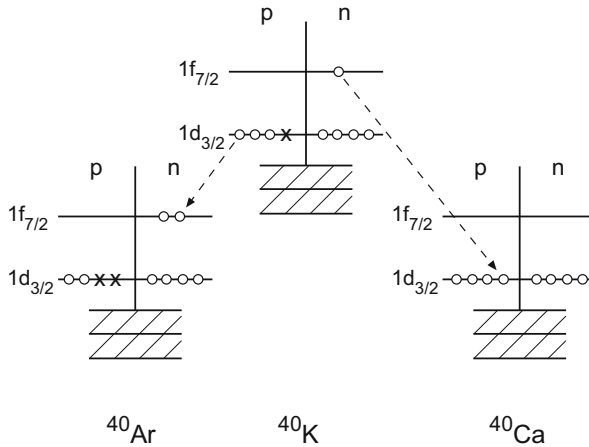


**Fig. 18.20** Sketch of the  $\beta^+$ - and  $\beta^-$ -decays of  $^{40}\text{K}$  in the shell model. The energies are not to scale

around us in substantial quantities. It is the only medium-sized nuclide ( $A < 200$ ) that gives a sizable contribution to the natural background radioactivity.

**Beta decay into highly excited states** The largest excitation energy available to the daughter nucleus in a  $\beta$ -decay is given by the difference in the masses of the nuclei involved. We showed in Sect. 3.1 that the masses of isobars lie on a parabola. Hence the mass difference of neighbouring nuclei inside an isobar spectrum will be particularly large if their charge number  $Z$  sharply differs from that of the stable isobar. The highly neutron-rich nuclei that appear as fission products in nuclear reactors are examples of this.

A lot of energy is available to the  $\beta^-$ -decay of such nuclei. Indeed decays into highly excited states are observed, these can in fact compete with decays into lower levels of the daughter nucleus, despite the smaller phase space available to the former. This is explained by observing that the proton in the daughter nucleus occupies a state in the same shell as the neutron did in the original nucleus. One sees here how well the shell model works even for higher nuclear excitations.

An example of this is shown in Fig. 18.21. In a few per cent of the cases the daughter  $^{99}\text{Y}$  or  $^{99}\text{Zr}$  nucleus is so highly excited that neutron emission is energetically allowed. Since this is a strong process it takes place “at once”. One speaks of *delayed neutron emission* since it only takes place after the  $\beta$ -decay, typically a few seconds after the nuclear fission.

■ These delayed neutrons are of great importance for reactor engineering since the chain reaction can be steered through them. A typical nuclear reactor is made up from fission material (such as  $^{235}\text{U}$  enriched uranium) and a moderator (e.g.,  $\text{H}_2\text{O}$ ,  $\text{D}_2\text{O}$  or  $\text{C}$ ). The absorption cross-section for



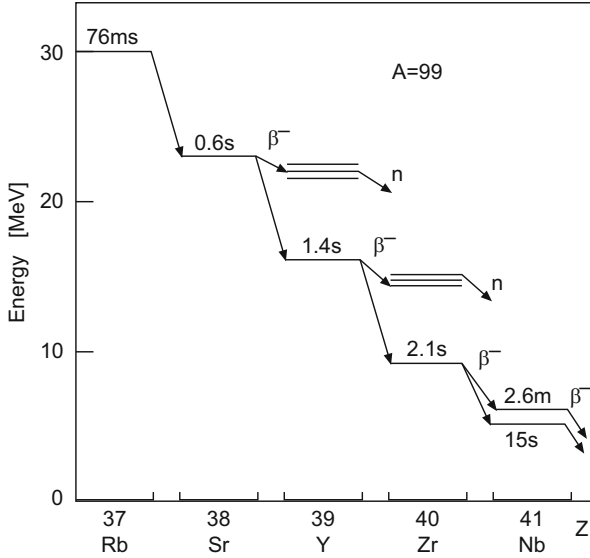


**Fig. 18.21** Successive  $\beta^-$ -decays of neutron-rich isobars with  $A = 99$ . In a few per cent of the decays the  $^{99}\text{Sr}$  and  $^{99}\text{Y}$  nuclides decay into highly excited states of the daughter nuclei, from which neutrons can be emitted (From [19])

$^{235}\text{U}$  is largest for neutron energies below 1 eV. After absorbing a thermal neutron, the resulting  $^{236}\text{U}$  nucleus divides up into two parts (fission) and emits, on average, 2–3 new fast neutrons whose kinetic energies are typically 0.1–1 MeV. These neutrons are now thermalised by the moderator and can then cause further fissions.

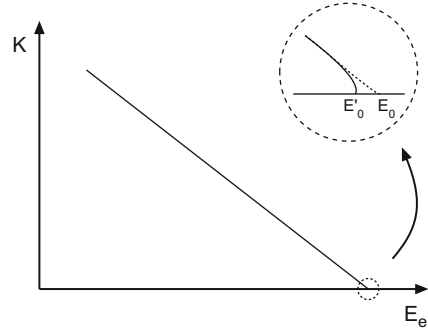
This cycle (neutron absorption – fission – neutron thermalisation) can lead to a self-sustaining chain reaction. Its time constant, which depends on the reactor design, is of the order of 1 ms. This time is much too short to control the chain reaction which for steady operation requires the neutron multiplication factor to be exactly equal to one. In reactor engineering therefore, the multiplication factor due to prompt neutrons is arranged to be slightly less than one. The remainder then is due to delayed neutrons whose time delay is typically of the order of seconds. This fraction, which in practice determines the multiplication rate in the reactor, can be controlled mechanically – by moving absorbing rods in and out of the reactor.

**Measuring the neutrino mass** A direct measurement of the mass is possible from the kinematics of  $\beta$ -decay. The form of the  $\beta$ -spectrum near the end point is highly sensitive to the neutrino mass. This is best seen in a so-called *Kurie plot* where

$$K(E_e) = \sqrt{\frac{dN(E_e)/dE_e}{F(Z', E_e) \cdot E_e \cdot \sqrt{E_e^2 - m_e^2 c^4}}} \tag{18.53}$$

is plotted against the electron energy  $E_e$ . Here,  $dN(E_e)$  is the number of electrons in the energy interval  $[E_e, E_e + dE_e]$ . From (16.51) and (16.54) we have that the distribution function  $K(E_e)$  is a straight line which cuts the abscissa at the maximal

**Fig. 18.22** Kurie plot of the  $\beta$ -spectrum. If the neutrino mass is not zero the *straight line* must bend near the maximum energy and cross the axis vertically at  $E'_0 = E_0 - m_\nu c^2$



energy  $E_0$  – provided the neutrino is massless. If this is not the case then the curve deviates from a straight line at high  $E_e$  and crosses the axis vertically at  $E_0 - m_\nu c^2$  (Fig. 18.22):

$$K(E_e) \propto \sqrt{(E_0 - E_e) \sqrt{(E_0 - E_e)^2 - m_\nu^2 c^4}}. \quad (18.54)$$

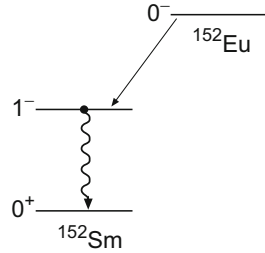
In order to measure the neutrino mass to a good accuracy one needs nuclei where a finite neutrino mass would have a large impact, i.e.,  $E_0$  should only be a few keV. Since atomic effects must be taken into account at low energies, the initial and final atomic states should be as well understood as possible. The most suitable case is the  $\beta^-$ -decay of tritium,  ${}^3\text{H} \rightarrow {}^3\text{He} + e^- + \bar{\nu}_e$ , where  $E_0$  is merely 18.6 keV. The curve crosses the  $E$  axis at  $E_0 - m_\nu c^2$  and  $E_0$  is determined by linearly extrapolating the curve from lower energies.

Actually carrying out such experiments is extremely difficult since the counting rate near the maximal energy is vanishingly small. The spectrum is furthermore smeared by the limited resolution of the spectrometer, the molecular binding of the tritium atom and the energy loss of the electrons in the source itself. It is therefore not possible to directly measure where the curve cuts the axis; rather one simulates the measured curve for various neutrino masses and looks for the best agreement. The very best direct measurements of the neutrino mass give an upper bound of  $2\text{ eV}/c^2$  [24]. In near future, results from the KATRIN experiment are expected which aims for an improvement of this bound by one order of magnitude, or even for a measurement of a non-vanishing value (Fig. 18.23).

This upper bound for the electron-neutrino mass gains a new significance when it is combined with the neutrino mass differences obtained in neutrino oscillation experiments. In the  $\beta$ -decay experiments one measures in fact

$$m_\beta = \sqrt{\sum_k |U_{ek}|^2 m_k^2}, \quad (18.55)$$

**Fig. 18.23** The decay  ${}^{152}_{63}\text{Eu}^m + e^- \rightarrow {}^{152}_{62}\text{Sm} + \gamma + \nu_e$  used in the Goldhaber experiment for the determination of the neutrino helicity

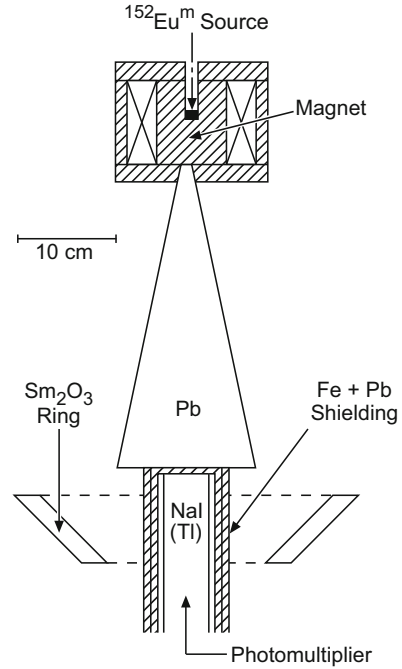


where  $m_k$  are the three individual neutrino masses and  $U_{ek}$  the corresponding elements of the leptonic mixing matrix (cf. Chap. 11). Not only the mass of the electron neutrino but also of those of the muon neutrino and tau neutrino must be smaller than the measured upper bound.

**Measuring the neutrino helicity** The so-called *Goldhaber experiment* is an elegant method to measure the helicity of the  $\nu_e$  from weak nuclear decays [11]. An isomer state of the  ${}^{152}_{63}\text{Eu}^m$  ( $J = 0$ ) nucleus can, via K capture, decay into a  $J = 1$  state of  ${}^{152}_{62}\text{Sm}$  which has an excitation energy of 0.960 MeV. This then emits a photon to enter the  $J = 0$  ground state (Fig. 18.23). This decay is a pure Gamow-Teller transition. Conservation of angular momentum implies that the spin of the  ${}^{152}\text{Sm}$  nucleus must be parallel to that of the captured electron and antiparallel to that of the neutrino. Since the atomic recoil is opposite to the momentum of the neutrino, the helicity of the excited  ${}^{152}\text{Sm}$  nucleus is equal to that of the neutrino. The emitted photon carries the angular momentum of the nucleus. Its spin must be parallel to that of the  ${}^{152}\text{Sm}$  nucleus before the  $\gamma$  was emitted. If the photon is emitted in the recoil direction, then its helicity will be equal to that of the neutrino. To determine the neutrino's helicity one has then to measure the helicity of the photon (which corresponds to a circular polarisation) and at the same time make sure that one is only considering those photons that are emitted in the direction of the recoiling nucleus (the opposite direction to that taken by the neutrino). The experimental apparatus for this experiment is shown in Fig. 18.24. The photons can only reach the detector if they are resonantly scattered in a ring of  $\text{Sm}_2\text{O}_3$ . They are first absorbed and then re-emitted. Resonant absorption, i.e., the reverse of electromagnetic decay, is normally impossible in nuclear physics since the states are narrower than the shift due to the recoil. The photons from the  ${}^{152}\text{Eu}^m$  source are emitted by  ${}^{152}\text{Sm}$  nuclei that are already moving. If a nucleus is moving towards the  $\text{Sm}_2\text{O}_3$  absorber before the  $\gamma$  emission, then the photon has a small amount of extra energy, which is sufficient to allow resonant absorption. In this way one can fix the recoil direction of the  ${}^{152}\text{Sm}$  nucleus and hence that of the neutrino.

The  ${}^{152}\text{Eu}$  source is inside a Fe magnet which the photons must cross to reach the ring of  $\text{Sm}_2\text{O}_3$ . Some of the photons undergo Compton scattering off the electrons in the Fe atoms. Two of the 36 electrons in the iron atom are polarised by the magnetisation. The Compton cross-section is larger if the electrons and photons are polarised in opposite directions. This permits us to determine the photon polarisation

**Fig. 18.24** Set-up of the Goldhaber experiment (From [11]). Photons from the  $^{152}\text{Eu}^m$  source are scattered in the  $\text{Sm}_2\text{O}_3$  ring and detected in a  $\text{NaI}(\text{Tl})$  scintillation detector



by reversing the magnetic fields and comparing the counting rates for the two field orientations.

The helicity of the neutrino was determined from this experiment as being

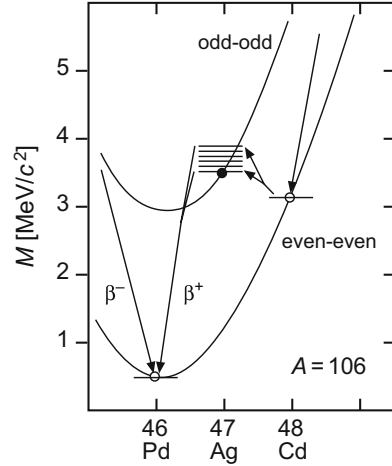
$$h_{\nu_e} = -1.0 \pm 0.3 \quad (18.56)$$

in agreement to the prediction of  $V-A$  theory.

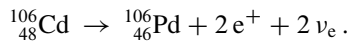
## 18.7 Double Beta Decay

As we mentioned in Sect. 3.1 for the nuclei in the mass range  $A > 70$  there is often more than one  $\beta$ -stable isobar. The isobar with the higher mass may, however, decay into the one with the lower mass via the double  $\beta$ -decay. The straightforward two-neutrino and two-electron decays have been observed experimentally by counter experiments and with the geochemical method by measuring the anomalous isotope abundances of the two isotopes in the common ore. But the main interest in the double  $\beta$ -decay is focused on finding the possible neutrinoless double  $\beta$ -decay. Its existence or nonexistence may give us the answer on the nature of the neutrino, whether it is a Dirac or a Majorana particle.

**Fig. 18.25** Sketch of the double  $\beta$ -decay process for the three  $A = 106$  isobars. The transition occurs via several excited states of the odd-odd nuclide



**Two-neutrino ( $2\nu$ ) double  $\beta$ -decay** In Sect. 3.1 we considered as a possible candidate for the double  $\beta$ -decay the nuclide  $^{106}_{48}\text{Cd}$ :



In Fig. 18.25 we just plot the three nuclides of the  $A = 106$  isobars involved in the double  $\beta$ -decay. The kinetic energy available to the leptons in the final state is 0.728 MeV. Let us make some rough estimate of the lifetime of the two-neutrino double  $\beta$ -decay. To do this it is useful to refer to Sect. 16.6 on neutron beta decay. In the case of double beta decay there are five particles in the final state. The constraints of energy and momentum conservation leave the momentum of the four leptons unconstrained but their summed kinetic energy must add up to the mass difference between the initial and final states. The process is clearly second order in the weak interaction. The formula for the neutron beta decay (16.57) must be modified in two ways. The second-order matrix element involves the product of two transitions through intermediate states divided by the energy of the intermediate state. As there may be more than one intermediate state, the second-order matrix element reads

$$\sum_m \frac{\langle f, 2e^+, 2\nu_e | H_W | m, e^+, \nu_e \rangle \langle m, e^+, \nu_e | H_W | i \rangle}{E_m - \frac{M_i + M_f}{2} c^2}, \quad (18.57)$$

where  $i$  and  $f$  represent the initial and final nuclear states and  $m$  the intermediate states. Let us assume the average excitation of the intermediate states to be  $E_0 \approx (M_i - M_f)c^2$  and we can separate the nuclear matrix element in (18.57) from the leptonic one. In order to get the lower limit of the lifetime we assume that the sum over the intermediate nuclear states has the maximum value, i.e., unity and the matrix element reads  $G_F^2/E_0$ .

The phase space for two particles in the neutron decay (16.57) has to be replaced by one for four particles

$$\frac{(4\pi)^2 E_0^5}{(2\pi)^6 (\hbar c)^6 30} \rightarrow \frac{(4\pi)^4 E_0^{11}}{(2\pi)^{12} (\hbar c)^{12} 2,000}. \quad (18.58)$$

From (18.57) and (18.58) the final result for the lifetime of the two-neutrino  $\beta$ -decay is

$$\frac{1}{\tau_{2\nu}} \approx \frac{2\pi}{\hbar} \cdot \frac{G_F^4}{E_0^2} \cdot \frac{(4\pi)^4}{(2\pi)^{12} (\hbar c)^{12}} \cdot \frac{E_0^{11}}{2,000}. \quad (18.59)$$

In (18.59) we kept the factors of  $\pi$  unchanged in order to show their origin.

For  $E_0 = 2 \text{ MeV}$  one has  $\tau_{2\nu} \approx 10^{20}$  years. Experimentally the lifetimes are of the same order.

**Neutrinoless ( $0\nu$ ) double  $\beta$ -decay** The conjecture that the neutrinos observed in the  $\beta$ -decay are not Dirac but rather Majorana particles is supported mostly by the theorists working on *grand unified theories* (GUT). In these theories it is attempted to merge all three interactions (strong, electromagnetic and weak) into a single superordinate interaction. One of the predictions of GUT is the neutrino's Majorana character, i.e., that the neutrino is identical to its own antiparticle. Obviously, this is impossible for charged leptons or quarks. Only neutral fermions can have this property.

In Fig. 18.26 a ( $2\nu$ ) decay is compared to the ( $0\nu$ ) one. In the ( $2\nu$ ) decay the two protons emit each a positron and a neutrino. In the ( $0\nu$ ) decay a proton emits a positron and a left-handed Majorana neutrino. Because of the finite mass the neutrino is, with a probability  $(1 - \beta_\nu^2)$ , also right-handed and can be absorbed by a proton thus producing the second positron. Conservation of lepton number

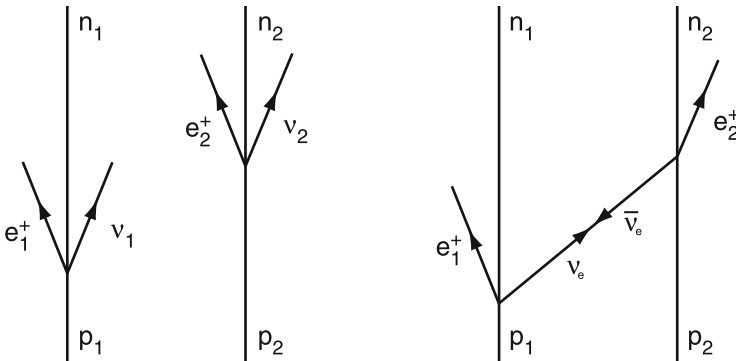


**Fig. 18.26** Comparison between a ( $2\nu$ ) decay (left) and a ( $0\nu$ ) decay (right). In the ( $0\nu$ ) decay, the  $\nu_e$  turns into a  $\bar{\nu}_e$  because of its Majorana character

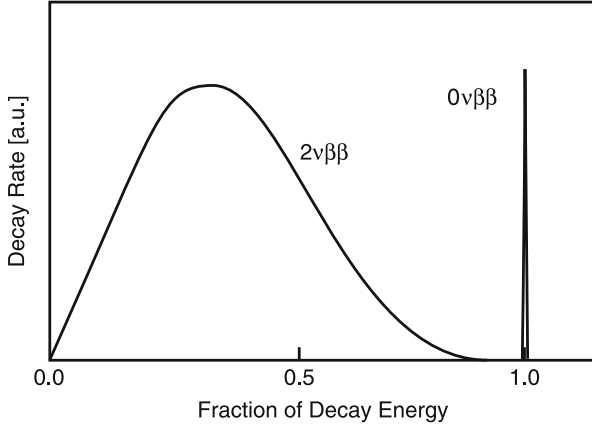


**Fig. 18.27** Hypothetical energy spectrum of double  $\beta$ -decay. The continuum is due to the sum of the two charged-lepton energies in the  $(2\nu)$  decay, the monoenergetic line with the full energy of the transition comes from the  $(0\nu)$  decay. The peak height of the latter is not to scale

is violated by two units in the  $(0\nu)$  decay, a consequence of the neutrino's Majorana character. If the neutrino masses were exactly zero, there would be no experimentally testable difference between Dirac and Majorana neutrinos. But, as the observed neutrino oscillations have shown beyond doubt, they have a finite mass and the double  $\beta$ -decay can provide the answer to the character of the neutrino.

The two processes can be experimentally separated by means of the energy spectrum of the charged leptons. In Fig. 18.27, a hypothetical energy spectrum of the charged particles in the double  $\beta$ -decay is shown. Neutrinoless decay would demonstrate itself in the monoenergetic line with the full energy of the transition, the continuum corresponds to the  $(2\nu)$  decay.

The  $(0\nu)$  process is second-order weak, with just two leptons in the final state. Modifying (16.58) for the  $(0\nu)$  case we obtain

$$\frac{1}{\tau_{0\nu}} \approx \frac{2\pi}{\hbar} \cdot \frac{G_F^4}{R^4} \cdot \frac{(4\pi)^2}{(2\pi)^6(\hbar c)^6} \cdot \frac{E_0^5}{30} \cdot (1 - \beta_\nu^2). \quad (18.60)$$

The  $1/R^4$  dependence comes from two sources. One factor  $1/R^2$  stems from squaring the neutrino propagator  $(p_\nu^2 c^2 + m_\nu^2 c^4)^{-1}$ . For nuclear dimensions, the neutrino can be assumed to be massless and the integration over the momenta gives the  $1/R$  potential like for the Coulomb case. The second  $1/R^2$  originates from the integration over the virtual intermediate nuclear states. The uncertainty principle fixes the neutrino momentum to be  $\approx 1/R$ . For  $R = 5$  fm this corresponds to  $p_\nu \approx 40$  MeV/c. Taking the virtuality to be 40 MeV/c one finds

$$\tau_{0\nu} \approx 4.5 \cdot 10^{11} \cdot (1 - \beta_\nu^2)^{-1} \approx 4.5 \cdot 10^{11} \cdot 2\gamma_\nu^2 \text{ a.} \quad (18.61)$$

One likes to compare the  $(2\nu)$  and the  $(0\nu)$  lifetimes for  $m_\nu = 1 \text{ eV}/c^2$  and  $E_\nu = 40 \text{ MeV}$ . For these values of the neutrino mass we obtain

$$\tau_{0\nu} \approx 8.2 \cdot 10^{25} \text{ a} \quad (18.62)$$

a much longer lifetime than  $\tau_{2\nu}$ . The  $(0\nu)$  decay is favoured by phase space, but suppressed due to the helicity factor  $(1 - \beta_\nu)$ . Already for neutrino masses of  $10^3 \text{ eV}/c^2$  the lifetime of the  $(0\nu)$  decay is larger than that of the  $(2\nu)$  decay. As was said earlier, (18.62) is just a crude estimate and the real value could easily be factors of 10 different. Also  $1 \text{ eV}/c^2$  is certainly an upper bound on the neutrino mass. One problem for the exact calculation of the nuclear matrix elements is the above mentioned large momentum of the exchanged Majorana neutrino. This leads to the occupation of many possible multipole states in the virtual intermediate state of the process while only the  $1^+$  states participate in the  $(2\nu)$  decay. Actual upper limits for the lifetime of the neutrinoless double  $\beta$ -decay are beyond  $10^{25}$  years.

Due to its long lifetime it will be very difficult to verify beyond doubt or to exclude the  $(0\nu)$  decay. However, the larger the neutrino mass the more probable is the  $(0\nu)$  process. Its lifetime decreases quadratically with

$$m_{\beta\beta} = \left| \sum_k U_{ek}^2 m_k \right|. \quad (18.63)$$

This quantity is similar to but not identical with the quantity  $m_\beta$  (18.55) which is measured in single  $\beta$ -decay. It is often denoted as effective neutrino mass. The dependence on the neutrino mass stems from the small contribution with wrong helicity of the Majorana neutrinos with mass  $m_k$ , and for each emitted electron we obtain a factor  $U_{ek}$  of the leptonic mixing matrix. Since all neutrinos contribute, we have to sum over their contributions.

One possibility to investigate double  $\beta$ -decay experimentally is a setup with a well-shielded Germanium counter which serves as source and detector at the same time. One of the Germanium isotopes,  $^{76}\text{Ge}$ , undergoes the double  $\beta$ -decay into  $^{76}\text{Se}$ . Such measurements have been performed by the Heidelberg-Moscow-Collaboration in the Gran Sasso underground laboratory (1,500 m under ground) using Germanium counters enriched in  $^{76}\text{Ge}$  content to 86%. A subgroup of this collaboration claims the observation of  $(0\nu)$  decays corresponding to a lifetime of approximately  $2 \cdot 10^{25}$  years [16]. This would correspond to an effective neutrino mass of  $m_{\beta\beta} \approx 0.5 \pm 0.25 \text{ eV}/c^2$ . The large uncertainty of this result stems both from experiment and theory: the background is very large and the nuclear matrix elements of the decay are insufficiently known. Presently several new experiments with different isotopes and experimental approaches are taking data to verify or disprove this controversial result. In particular, the results of the GERDA experiment [1] which also is performing measurements with  $^{76}\text{Ge}$  let the claimed observation appear to be improbable.



The Majorana character of the neutrino provides a link to the GUT energy scale and the violation of lepton-number conservation would have a number of fundamental consequences also in cosmology. The experimental confirmation of neutrinoless double  $\beta$ -decay beyond any doubt would, therefore, be a ground-breaking discovery.

## Problems

### 1. Fermi gas model

Calculate the dependence of the Fermi pressure upon the nuclear density. How large is this pressure for a density  $\rho_N = 0.17$  nucleons/fm<sup>3</sup>? What is this in macroscopic units (bar)?

### 2. Shell model

- (a) In the following table we present the experimentally determined spins and parities of the ground states and first excited states of some nuclei:

$$\begin{array}{cccccc} {}^7_3\text{Li} & {}^{23}_{11}\text{Na} & {}^{33}_{16}\text{S} & {}^{41}_{21}\text{Sc} & {}^{83}_{36}\text{Kr} & {}^{93}_{41}\text{Nb} \\ J_0^P & 3/2^- & 3/2^+ & 3/2^+ & 7/2^- & 9/2^+ & 9/2^+ \\ J_1^P & 1/2^- & 5/2^+ & 1/2^+ & 3/2^+ & 7/2^+ & 1/2^- \end{array}$$

Find the configurations of the protons and neutrons in the incomplete shells of the one-particle shell model for these nuclei and predict the quantum numbers of their ground states and first excited levels. Compare your results with the table.

- (b) The spins of odd-odd nuclei are generally given by a vector addition of the total angular momenta of the two unpaired nucleons. Which possible nuclear spins and parities should  ${}^6_3\text{Li}$  and  ${}^{40}_{19}\text{K}$  have? Experimentally these nuclei have the quantum numbers  $1^+$  and  $4^-$ .

### 3. Shell model

- (a) Find the gap between the  $1p_{1/2}$  and  $1d_{5/2}$  neutron shells for nuclei with mass number  $A \approx 16$  from the total binding energy of the  ${}^{15}\text{O}$  (111.9556 MeV),  ${}^{16}\text{O}$  (127.6193 MeV) and  ${}^{17}\text{O}$  (131.7627 MeV) atoms [3].
- (b) How does this agree with the energy of the first excited level of  ${}^{16}\text{O}$  (cf. Fig. 18.8)?
- (c) What information does one obtain from the energy of the corresponding state of  ${}^{17}\text{O}$ ?
- (d) How do you interpret the difference in the total binding energies of  ${}^{17}\text{O}$  and  ${}^{17}\text{F}$ ? Estimate the radius of these nuclei.
- (e) The first excited state of  ${}^{17}\text{F}$  is below the equivalent state of  ${}^{17}\text{O}$ . A possible explanation of this is that the unpaired nucleon has a different spatial extension

(smaller?, larger?) in the first excited state than in the ground state. What do you expect from considering the quantum numbers?

#### 4. Shell model

It is conspicuous that many of the nuclei which possess long lived isomer states have  $N$  or  $Z$  in the ranges  $39 \dots 49$  and  $69 \dots 81$  [9, 10, 23]. Why is this?

#### 5. Magnetic moment

The  ${}_{21}^{42}\text{Sc}$  nucleus has a low lying level with  $J^P(I) = 7^+(0)$  and an excitation energy of 618 keV.

- Which shell model configuration would you assign this state to?
- What magnetic moment would you expect?

#### 6. The Goldhaber experiment

${}^{152}\text{Sm}$  possesses a state with excitation energy 0.963 MeV and quantum numbers  $1^-$  which decays via an E1 transition into the ground state.

- How large is the recoil energy of the nucleus?
- Compare this energy with the width of the state which is equivalent to an E1 one particle transition probability. Can a so-emitted photon be absorbed by another nucleus? What happens if we take the influence of thermal motion into account?
- Show that this energy loss is compensated if the excited  ${}^{152}\text{Sm}$  nucleus was produced in an electron capture decay of  ${}^{152}\text{Eu}$  and the photon was emitted in the recoil direction of the  ${}^{152}\text{Sm}$  nucleus.

The energy of the emitted neutrino is 0.950 MeV.

#### 7. Coupling strength of $\beta$ -decay

A maximal energy of  $E_{\text{kin}}^{\text{max}} = 1,810.6 \pm 1.5$  keV is measured in the  $\beta$ -decay  ${}^{14}\text{O} \rightarrow {}^{14}\text{N} + e^+ + \nu_e$  (Fig. 2.6) [30]. A phase space function  $f(Z', E_0)$  of 43.398 is calculated from this [29]. What half-life should  ${}^{14}\text{O}$  have? The experimental value is  $t_{1/2} = 70,606 \pm 18$  ms [30].

## References

- M. Agostini et al., Phys. Rev. Lett. **111**, 122503 (2013)
- A. Arima, H. Horie, Prog. Theor. Phys. **11**, 509 (1954); Prog. Theor. Phys. **12**, 623 (1954)
- G. Audi et al., Nucl. Phys. **A729**, 3 (2003)
- V. Bechtold et al., Phys. Lett. **B72**, 169 (1977)
- H. Behrens, J. Jänecke, *Numerical Tables for Beta-Decay and Electron Capture*. Landolt-Börnstein, New Series, vol. I/4 (Springer, Berlin/Heidelberg, 1969)
- H. Casimir, Physica **2**, 719 (1935)
- R.E. Chrien, C.B. Dover, Annu. Rev. Nucl. Part. Sci. **39**, 113 (1989)
- M.D. Cooper, W.F. Hornyak, P.G. Roos, Nucl. Phys. **A218**, 249 (1974)
- E. Feenberg, K.C. Hammack, Phys. Rev. **75**, 1877 (1949)
- M. Goldhaber, R.D. Hill, Rev. Mod. Phys. **24**, 179 (1952)
- M. Goldhaber et al., Phys. Rev. **109**, 1015 (1958)

12. M. Göppert-Mayer, J.H.D. Jensen, *Elementary Theory of Nuclear Shell Structure* (Wiley, New York, 1955)
13. T. Hasegawa et al., Phys. Rev. **C53**, 31 (1996)
14. O. Haxel, J.H.D. Jensen, H.E. Suess, Die Naturwissensch. **35**, 376 (1948); O. Haxel, J.H.D. Jensen, H.E. Suess, Z. Phys. **128**, 295 (1950)
15. O. Haxel, J.H.D. Jensen, H.E. Suess, Phys. Rev. **75**, 1766 (1949)
16. H.V. Klapdor-Kleingrothaus, A. Dietz, I.V. Krivosheina, Found. Phys. **32**, 1181 (2002); Erratum-ibid. **33**, 679 (2003)
17. P.F.A. Klingenberg, Rev. Mod. Phys. **24**, 63 (1952)
18. H. Kopfermann, *Kernmomente* (Akademische Verlagsgesellschaft, Frankfurt a.M., 1956)
19. C.M. Lederer, V.S. Shirley, *Table of Isotopes*, 7th edn. (Wiley, New York, 1978)
20. G. Mairle, G.J. Wagner, Z. Phys. **258**, 321 (1973)
21. E. Marshalek, L. Person, R. Sheline, Rev. Mod. Phys. **35**, 108 (1963)
22. S.G. Nilsson, Mat. Fys. Medd. Dan. Vid. Selsk. **29**, Nr. 16 (1955)
23. L.W. Nordheim, Phys. Rev. **76**, 1894 (1949)
24. Particle Data Group, J. Beringer et al., *Review of Particle Properties*. Phys. Rev. D **86**, 010001 (2012)
25. B. Povh: Prog. Part. Nucl. Phys. **5**, 245 (1981)
26. T. Schmidt, Z. Phys. **106**, 358 (1937)
27. H. Schüler, T. Schmidt, Z. Phys. **94**, 457 (1935)
28. F. Schwabl, *Quantum Mechanics*, 4th edn. (Springer, Berlin/Heidelberg/New York, 2007)
29. D.H. Wilkinson, B.E.F. Macefield, Nucl. Phys. **A232**, 58 (1974)
30. D.H. Wilkinson, A. Gallmann, D.E. Alburger, Phys. Rev. **C18**, 401 (1978)

## Chapter 19

# Collective Nuclear Excitations

We showed in Sect. 18.3 that the nuclear ground states may be well described if we assume that the nucleons are in the lowest shell-model orbits. The single-particle picture, we further showed for the case of a *single* valence nucleon or nucleon hole, works very well if shells are nearly full or empty. Excited states are then understood as being created by a valence nucleon jumping into a higher shell-model state; a direct analogy to our picture of the atom. As well as such straightforward single-particle excitations, more complicated phenomena can take place in the nucleus. Collective excitations provide some of the most beautiful aspects of nuclear dynamics.

Collective excitations of many-body systems can be phenomenologically understood as fluctuations around a state of equilibrium. These may be fluctuations in density or shape. The type of collective excitation strongly depends upon the composition of the system and the manner in which its components interact with each other. We want now to show the connection between nuclear collective excitations and the forces inside and the structure of the nucleus.

Electromagnetic transitions provide us with the most elegant way to investigate collective excitations in nuclei. We will therefore first consider how electromagnetic transitions in nuclei may be determined, so that we can then say to what extent collective effects are responsible for these transitions.

The first measurements of photon absorption in nuclei led to the discovery that the lion's share of the the absorption is by a *single* state. The first description of this *giant dipole resonance* state was of an oscillation of the protons and neutrons with respect to each other. Later on it was discovered that the transition probability for electric quadrupole transitions of lower energy states was much higher than a single-particle picture of the nucleus predicts. The transition probability for octupole transitions also predominantly stems from single states which we call octupole vibrations.

The single-particle and collective properties of nuclei were regarded for a long time as distinct phenomena. A unified picture first appeared in the 1970s. We want to illustrate this modern framework through the example of giant dipole resonances. What we will discover can be easily extended to quadrupole and octupole oscillations.

Another important collective effect is the rotation of deformed nuclei. Such rotations form a most pleasing chapter, both didactically and aesthetically, in the story of  $\gamma$  spectroscopy.

## 19.1 Electromagnetic Transitions

**Electric dipole transitions** The probability of an electric dipole transition can be somewhat simplistically derived by considering a classical Hertz dipole. The power output emitted by the dipole is proportional to  $\omega^4$ . The rate of photon emission, i.e., the transition probability, may be obtained by dividing the power output by the photon energy  $\hbar\omega$ . One so finds

$$W_{fi} = \frac{1}{\tau} = \frac{e^2}{3\pi\epsilon_0\hbar^4 c^3} E_\gamma^3 \left| \int d^3x \psi_f^* \mathbf{x} \psi_i \right|^2, \quad (19.1)$$

where we have replaced the classical dipole  $e\mathbf{x}$  by the matrix element. This result may also be obtained directly from quantum mechanics.

■ In the following derivation we want to treat the electromagnetic transitions semiclassically, i.e., we will not concern ourselves with quantising the radiation field or spin.

Consider first an excited nuclear state  $\psi_i$  which through  $\gamma$  emission enters a lower lying state,  $\psi_f$ . The golden rule says that the transition probability is

$$dW = \frac{2\pi}{\hbar} |\langle \psi_f | \mathcal{H}_{\text{int}} | \psi_i \rangle|^2 d\rho(E). \quad (19.2)$$

$\mathcal{H}_{\text{int}}$  describes the interaction of the moving charge with the electromagnetic field and  $\rho(E)$  is a phase space factor that describes the final state density at total energy  $E$ . For photon emission we have  $E = E_\gamma$ . Since  $\gamma$  radiation is generally not spherically symmetric, we consider the phase space in a solid angle element  $d\Omega$  around the momentum vector. As in (4.16) we set

$$d\rho(E) = \frac{V |\mathbf{p}|^2 d|\mathbf{p}| d\Omega}{(2\pi\hbar)^3 dE}. \quad (19.3)$$

For the photon we have  $E = c|\mathbf{p}|$  and  $dE = c d|\mathbf{p}|$ , which implies

$$d\rho(E) = \frac{E_\gamma^2 V d\Omega}{(2\pi\hbar c)^3}. \quad (19.4)$$

The  $\mathcal{H}_{\text{int}}$  operator can be obtained by considering the classical Hamiltonian for the interaction between a charge  $e$ , which emits the photon, and the electromagnetic field  $A = (\phi/c, \mathbf{A})$  [10]:

$$\mathcal{H} = \frac{1}{2m} (\mathbf{p} - e\mathbf{A})^2 + e\phi. \quad (19.5)$$

Note that we have here assumed a point-like charge. The term quadratic in  $A$  is negligible and we may write

$$\mathcal{H} = \frac{\mathbf{p}^2}{2m} - \frac{e}{m} \mathbf{p}\mathbf{A} + e\phi. \quad (19.6)$$

The first term corresponds to free movement of the charged particle and the last two describe the interaction

$$\mathcal{H}_{\text{int}} = -\frac{e}{m} \mathbf{p}\mathbf{A} + e\phi, \quad (19.7)$$

which, for a point-like particle, is just given by the scalar product of the electric four-current

$$\mathbf{j} = (e \cdot c, e\mathbf{v}) \quad (19.8)$$

and the electromagnetic field

$$A = (\phi/c, \mathbf{A}). \quad (19.9)$$

In an electromagnetic decay  $e\phi$  does not contribute to the transition probability, since real photons are transversely polarised and monopole transitions are hence forbidden.

If one replaces the momentum  $\mathbf{p}$  by the operator  $\mathbf{p} = -i\hbar\nabla$  and interprets the vector  $\mathbf{A}$  as the wave function of the photon, one obtains the matrix element

$$\langle \psi_f | \mathcal{H}_{\text{int}} | \psi_i \rangle = -\frac{ie\hbar}{m} \int d^3x \psi_f^* (\nabla \psi_i) \mathbf{A}. \quad (19.10)$$

The gradient  $\nabla$  may be replaced by the commutator of the coordinate  $\mathbf{x}$  with the Hamilton operator, since for stationary states

$$\mathcal{H}_0 = \frac{\mathbf{p}^2}{2m} + V(\mathbf{x}) \quad (19.11)$$

we have the following relation:

$$\mathbf{x} \mathcal{H}_0 - \mathcal{H}_0 \mathbf{x} = \frac{i\hbar}{m} \mathbf{p} = \frac{\hbar^2}{m} \nabla. \quad (19.12)$$

In this way we have

$$-\frac{ie}{\hbar} \int d^3x \psi_f^* (\mathbf{x} \mathcal{H}_0 - \mathcal{H}_0 \mathbf{x}) \psi_i \mathbf{A} = \frac{ie}{\hbar} (E_i - E_f) \int d^3x \psi_f^* \mathbf{x} \psi_i \mathbf{A}, \quad (19.13)$$

and the matrix element has the standard form for multipole radiation.

In the semiclassical derivation of  $\gamma$  emission, one writes the photon wave function as

$$\mathbf{A} = \sqrt{\frac{\hbar}{2\varepsilon_0\omega V}} \boldsymbol{\varepsilon} \cos(\mathbf{k}\mathbf{x} - \omega t), \quad (19.14)$$

where  $\boldsymbol{\varepsilon}$  is the polarisation vector of the photon,  $E_\gamma = \hbar\omega = E_i - E_f$  is its energy and  $\mathbf{k}$  the wave vector. That this is indeed correct may be easily checked by calculating the electromagnetic radiation energy in a volume  $V$  using  $\mathbf{A}$  from (19.14):

$$\hbar\omega = V \cdot \left( \frac{1}{2} \varepsilon_0 \overline{\mathbf{E}^2} + \frac{1}{2} \frac{1}{\mu_0} \overline{\mathbf{B}^2} \right) = V \varepsilon_0 \overline{\mathbf{E}^2} \quad \text{with} \quad \mathbf{E} = -\frac{\partial \mathbf{A}}{\partial t}, \quad (19.15)$$

where the bar represents time averaging. With this result we now may write the transition probability as:

$$\begin{aligned} dW_{fi} &= \frac{2\pi}{\hbar} \frac{\hbar}{2\varepsilon_0\omega V} \frac{e^2 E_\gamma^2}{\hbar^2} \left| \boldsymbol{\varepsilon} \int d^3x \psi_f^* \mathbf{x} \psi_i e^{i\mathbf{k}\mathbf{x}} \right|^2 \frac{E_\gamma^2 V d\Omega}{(2\pi\hbar c)^3} \\ &= \frac{e^2}{8\pi^2 \varepsilon_0 \hbar^4 c^3} E_\gamma^3 \left| \boldsymbol{\varepsilon} \int d^3x \psi_f^* \mathbf{x} e^{i\mathbf{k}\mathbf{x}} \psi_i \right|^2 d\Omega. \end{aligned} \quad (19.16)$$

The wavelengths of the gamma rays are large compared to a nuclear radius. The multipole expansion

$$e^{i\mathbf{k}\mathbf{x}} = 1 + i\mathbf{k}\mathbf{x} + \dots \quad (19.17)$$

is very useful, since, generally speaking, only the lowest transition that the quantum numbers allow needs to be taken into account. Only very occasionally are two multipoles of equal strength in a transition. If one now sets  $e^{i\mathbf{k}\mathbf{x}} \approx 1$ , integrates (19.16) over the solid angle  $d\Omega$  and the polarisation one obtains (19.1).

Electric dipole (E1) transitions always connect states with different parities. The photon carries away angular momentum  $|\ell| = 1\hbar$  and so the angular momenta of the initial and final states may at most differ by one unit.

Since transitions from one shell into the one immediately above play the most important role in collective excitations, we now introduce the standard notation for the wave function. A closed shell shall be denoted by the symbol  $|0\rangle$  ("vacuum wave function"). If a particle in the state  $\phi_{j_1}$  of the closed shell jumps into the state  $\phi_{j_2}$  of the next shell a particle-hole state is created, which we symbolise by  $|\phi_{j_1}^{-1}\phi_{j_2}\rangle$ . The dipole matrix element

$$\langle \phi_{j_1}^{-1}\phi_{j_2} | e\mathbf{x} | 0 \rangle = e \int d^3x \phi_{j_2}^* \mathbf{x} \phi_{j_1} \quad (19.18)$$

describes the transition of a nucleon from the state  $\phi_{j_1}$  to the state  $\phi_{j_2}$ . Since  $|0\rangle$  is a full shell state it must have spin and parity  $J^P = 0^+$ , hence the excited particle-hole state after the electric dipole transition must have the quantum numbers  $J^P = 1^-$ .

**Magnetic dipole transitions** The transition probability of a magnetic dipole (M1) transition is obtained by replacing the electric dipole in (19.1) by a magnetic one:

$$W_{fi} = \frac{1}{\tau} = \frac{\mu_0}{3\pi\hbar^4 c^3} E_\gamma^3 \left| \int d^3x \psi_f^* \boldsymbol{\mu} \psi_i \right|^2, \quad \text{where } \boldsymbol{\mu} = \frac{e}{2m} (\mathbf{L} + g\mathbf{s}). \quad (19.19)$$

Here  $\mathbf{L}$  is the orbital angular momentum operator and  $\mathbf{s}$  is the spin operator.

**Higher multipoles** If the electric dipole transition is forbidden, in other words if both states have the same parity or the vectorial addition of the angular momenta is inconsistent, then only higher multipole radiation can be emitted. The next highest multipoles in the transition probability hierarchy are the above magnetic dipole (M1) transition and the electric quadrupole (E2) transition [7]. Both are second order in the expansion (19.17). The parity of the initial and final states must be identical in electric quadrupole transitions and the triangle inequality  $|j_f - j_i| \leq 2 \leq j_f + j_i$  must be fulfilled by the angular momenta. While the transition probability for dipole radiation is, from (19.1), proportional to  $E_\gamma^3$ , for electric quadrupole radiation it goes as  $E_\gamma^5$ . This is because there is a new factor of  $i\mathbf{k}\mathbf{x}$  in the matrix element and  $|\mathbf{k}|$  is proportional to  $E_\gamma$ . The energy-independent part of the matrix element has the form  $r^2 Y_2^m(\theta, \varphi)$ .

## 19.2 Dipole Oscillations

**Photon absorption in nuclei** A broad resonance, which was already known in the 1950s, dominates the absorption of gamma rays by nuclei. The experimental techniques for investigating this resonance were rather awkward since no variable energy gamma sources existed.

The method of in flight positron annihilation, which was developed in the 1960s, first permitted detailed measurements of the gamma cross-sections. Positrons, which have been produced through pair creation from a strong bremsstrahlung source, are selected according to their energy and focused upon a target. They then partially annihilate with the target electrons and produce bremsstrahlung as an unwanted by-product (Fig. 19.1).

Such a gamma spectrum is shown in Fig. 19.2. A peak can be clearly distinguished from the bremsstrahlung at the maximal possible energy and this is presumed to come from the  $e^+e^-$  annihilation. The energy dependence of  $\gamma$ -induced cross-sections can be thoroughly investigated by varying the energy of the positrons.



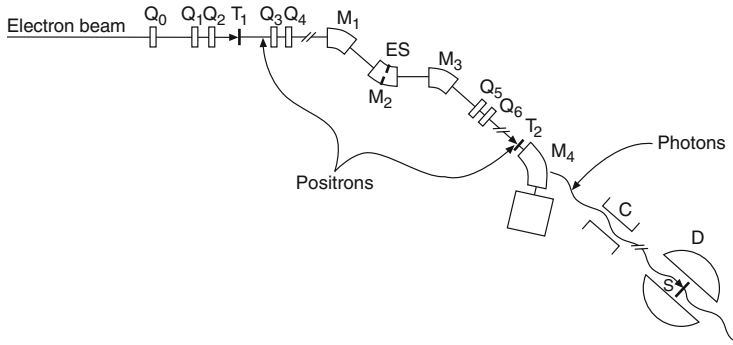


**Fig. 19.1** Experimental set-up for in flight positron annihilation (From [2]). An electron beam hits a target ( $T_1$ ). The bremsstrahlung that is produced converts into electron-positron pairs. The positrons are then selected according to their energy by three dipole magnets ( $M_1$ ,  $M_2$ ,  $M_3$ ) before hitting a second target ( $T_2$ ). Some of them annihilate in flight with target electrons. A further magnet ( $M_4$ ) deflects all charged particles and only photons arrive at the experimenter's real target (S)

As well as the total cross-section, the cross-section for the photoproduction of neutrons (*nuclear photoeffect*)

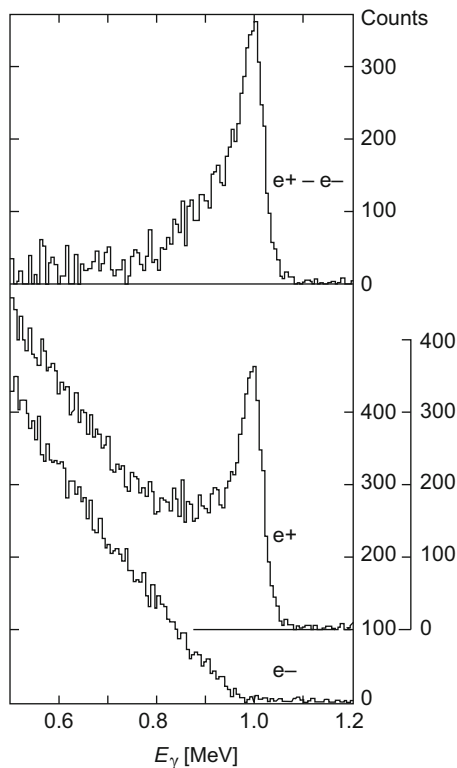
$${}^A\text{X}(\gamma, n){}^{A-1}\text{X} \quad (19.20)$$

is of special importance. This is in fact the major part of the total cross-section. The photoproduction of protons is, by contrast, suppressed by the Coulomb barrier. In what follows we will limit ourselves to the  $(\gamma, n)$  reaction.

We have chosen  $\sigma(\gamma, n)$  for neodymium isotopes as an example (Fig. 19.3). Various observations may be made:

- The absorption probability is centred in a resonance which we call a *giant resonance*.
- The excitation energy of the giant resonance is roughly twice the separation between neighbouring shells. This is astounding since, for reasons of parity and angular momentum conservation, many more single-particle transitions are possible between one shell and the next than between a shell and the next but one.
- While a narrow resonance is observed in absorption by  ${}^{142}\text{Nd}$ , this splits into two resonances as the mass number increases.
- The integrated cross-section is about as big as the sum over all expected cross-sections for the transition of a single nucleon from the last closed shell. This means that all the protons and neutrons of the outermost shell contribute coherently to this resonance.

**Fig. 19.2** The photon spectrum from in-flight electron positron annihilation [2]. This is later used for  $(\gamma, n)$  reactions. The background of bremsstrahlung from positrons hitting the target is determined by aiming a monoenergetic beam of electrons at the target. The cross-section for fixed photon energies is found by performing experiments with the two different photon beams and subtracting the counting rates



A qualitative explanation of the giant resonances comes from the oscillation of protons and neutrons with respect to each other (Fig. 19.4). The  $^{150}\text{Nd}$  is deformed and has a cigar-like shape. The two maxima for this nucleus correspond to oscillations along the symmetry axis (lower peak) and orthogonal to it (higher peak).

We will attempt to justify this intuitive picture of giant resonances and their excitation energies in the framework of the shell model.

**The giant dipole resonance** Consider once again the example of the doubly magic  $^{16}\text{O}$  nucleus. Let us assume that photon absorption leads to a nucleon in the  $1p_{3/2}$  or  $1p_{1/2}$  shell being excited into the  $1d_{5/2}$ ,  $1d_{3/2}$  or  $2s_{1/2}$  shell. If this nucleon drops back into the  $1p$  shell, it can pass on its excitation energy through recoils to other nucleons, which may then, for example, be themselves excited out of the  $1p$  shell into the  $1d$  or  $2s$  shell. If the nuclear states that are produced by the excitation of a nucleon into a higher level were degenerate, then the probability of generating all of these states must be equal and a simple single-particle picture would be doomed to failure from the start. In reality this is almost the case; the excited states are almost degenerate.

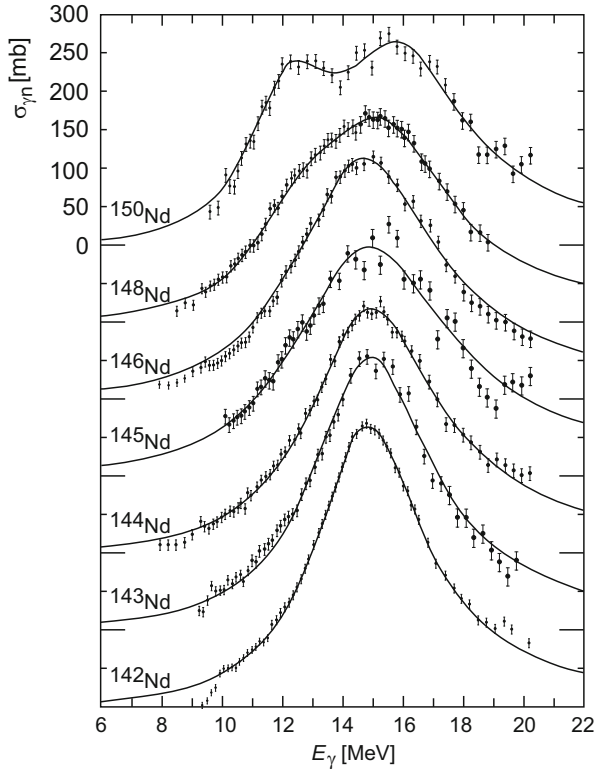


**Fig. 19.3** Cross-section for  $\gamma$ -induced emission of neutrons in neodymium isotopes [2]. The curves have been shifted vertically for the sake of clarity. Neodymium isotopes progress from being spherically symmetric to being deformed nuclei. The giant resonance of the spherically symmetric  $^{142}\text{Nd}$  nucleus is narrow, while that of the deformed  $^{150}\text{Nd}$  nucleus shows a double peak

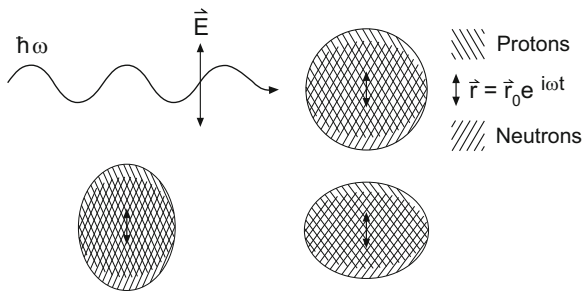


**Fig. 19.4** The giant dipole resonance as oscillations of the protons and neutrons against each other. In deformed nuclei (*below*) two oscillation modes are available

One can understand these states as a combination of a hole in the remaining nucleus and a particle in a higher shell, and the interaction between the particle and all the nucleons of the now incomplete shell may be viewed as an interaction between the particle and the hole. This interaction depends upon the spin and isospin of the particle-hole system and causes the states to mix strongly. Below we want to use a greatly simplified model to show how the transition strengths of all one particle-one hole states combine through this mixing into a single state.

We use  $\mathcal{H}_0$  to denote the Hamiltonian operator of a nucleon in the central potential of the single-particle shell model. In the transition of the particle from a full shell to the one above, we must also take the particle-hole interaction into account; the Hamiltonian operator must then be written as

$$\mathcal{H} = \mathcal{H}_0 + \mathcal{V}. \quad (19.21)$$

Collective excitations appear just because of the mixing generated by this particle-hole interaction  $\mathcal{V}$ .

Consider now all particle-hole states with  $1^-$  spin and parity. These can only be particle-hole combinations such that the angular momenta  $\mathbf{j}_1$  and  $\mathbf{j}_2$  add vectorially to  $1\hbar$  and the sum of the orbital angular momentum quantum numbers  $\ell_1 + \ell_2$  is odd (so that the parity is negative). If we restrict ourselves to the excitation of a nucleon from the  $1p$  into the  $1d$  or  $2s$  shell, then we have the following possible particle-hole states:

$$\begin{aligned} & \left| \phi_{1p_{3/2}}^{-1} \phi_{1d_{5/2}} \right\rangle, \left| \phi_{1p_{3/2}}^{-1} \phi_{2s_{1/2}} \right\rangle, \left| \phi_{1p_{3/2}}^{-1} \phi_{1d_{3/2}} \right\rangle, \\ & \left| \phi_{1p_{1/2}}^{-1} \phi_{2s_{1/2}} \right\rangle, \left| \phi_{1p_{1/2}}^{-1} \phi_{1d_{3/2}} \right\rangle. \end{aligned}$$

Since both the proton and neutron shells are full in the  $^{16}\text{O}$  nucleus, such states exist for both proton and neutron excitations. They have all got roughly the same energy and may be viewed as approximately degenerate.

The number of nucleons per shell is larger in heavy nuclei, and the number of nearly degenerate particle-hole  $J^P = 1^-$  states is accordingly greater. The number of particle-hole states,  $N$ , is between 10 to 20 for medium-sized nuclei.

The connection between one-particle and collective excitation can be clarified by a simple model [4]. We denote particle-hole states by  $|\psi_i\rangle$ :

$$|\psi_i\rangle = \left| \phi_{j_1}^{-1} \phi_{j_2} \right\rangle, \quad \text{where } i = 1 \dots N. \quad (19.22)$$

The  $|\psi_i\rangle$  are, by definition, eigenstates of the unperturbed Hamiltonian

$$\mathcal{H}_0 |\psi_i\rangle = E_i |\psi_i\rangle. \quad (19.23)$$

The solution to the Schrödinger equation with the full Hamiltonian operator

$$\mathcal{H}|\Psi\rangle = (\mathcal{H}_0 + \mathcal{V})|\Psi\rangle = E|\Psi\rangle, \quad (19.24)$$

is  $|\Psi\rangle$ . This wave function  $|\Psi\rangle$  projected out upon the space spanned by  $|\psi_i\rangle$  in (19.22) may be written as

$$|\Psi\rangle = \sum_{i=1}^N c_i |\psi_i\rangle, \quad (19.25)$$

where the coefficients  $c_i$  fulfil the secular equation

$$\begin{pmatrix} E_1 + V_{11} & V_{12} & V_{13} & \cdots \\ V_{21} & E_2 + V_{22} & V_{23} & \cdots \\ V_{31} & V_{32} & E_3 + V_{33} & \cdots \\ \vdots & \vdots & \vdots & \ddots \end{pmatrix} \cdot \begin{pmatrix} c_1 \\ c_2 \\ c_3 \\ \vdots \end{pmatrix} = E \cdot \begin{pmatrix} c_1 \\ c_2 \\ c_3 \\ \vdots \end{pmatrix}. \quad (19.26)$$

We assume for simplicity that all the  $V_{ij}$  are the same

$$\langle \psi_i | V | \psi_j \rangle = V_{ij} = V_0. \quad (19.27)$$

The solution of the secular equation is then rather simple: the coefficients  $c_i$  may be written as

$$c_i = \frac{V_0}{E - E_i} \sum_{j=1}^N c_j, \quad (19.28)$$

where  $\sum_j c_j$  is a constant. Summing over all  $N$  particle-hole states on both sides and bearing in mind that  $\sum_i c_i = \sum_j c_j$ , we obtain the relation

$$1 = \sum_{i=1}^N \frac{V_0}{E - E_i}, \quad (19.29)$$

as the solution of the secular equation.

The solutions of this equation are most easily understood graphically (Fig. 19.5). The right-hand side of the equation has poles at  $E = E_i$  where  $i = 1 \dots N$ . The solutions  $E'_i$  to (19.29) are to be found where the right-hand side is unity. The new energies are marked by circles on the abscissa;  $N - 1$  eigenvalues (3 in the diagram) are “squeezed in” between the unperturbed energies  $E_1 \dots E_n$ . The exception, denoted by  $E_C$ , is the collective state, as we will show in the following. A repulsive ( $V_0 > 0$ ) interaction, as is assumed in the diagram, has its collective state above the particle-hole state.

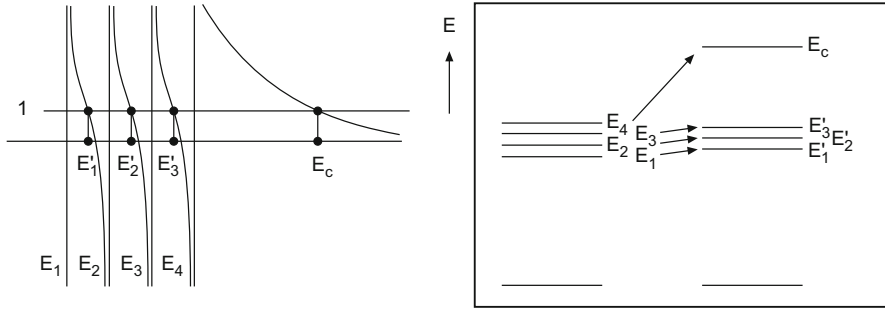


**Fig. 19.5** Graphical representation of the solution to the secular equation (19.26) and a picture of how the energy levels are shifted

To obtain a quantitative estimate of the energy shift, we now assume that  $E_i = E_0$  for all  $i$ . Equation (19.29) then becomes

$$1 = \sum_{i=1}^N \frac{V_0}{E_C - E_i} = \frac{NV_0}{E_C - E_0}, \tag{19.30}$$

from which

$$E_C = E_0 + N \cdot V_0 \tag{19.31}$$

follows. The energy shift of the collective state is proportional to the number of degenerate states. From experiment we know that the energy of the giant resonance is roughly twice the separation between two shells, i.e.,  $NV_0 \approx E_0$ . The effective interaction decreases for heavier nuclei but this is compensated by the increased number of states which can enter the collective motion.

The expansion coefficients for the collective state

$$c_i^{(C)} = \frac{V_0}{E_C - E_i} \sum_j c_j^{(C)} \tag{19.32}$$

are nearly independent of  $i$  so long as the energy of the collective state  $E_C$  is well separated from the  $E_i$ . The collective state has the following configuration:

$$|\psi_C\rangle = \frac{1}{\sqrt{N}} \sum_{j_1 j_2 \dots j_N} |\phi_{j_1}^{-1} \phi_{j_2} \dots \phi_{j_N}\rangle. \tag{19.33}$$

This state is singled out by the fact that the amplitudes of each and every particle-hole state add with the same sign (constructively), since  $E_C > E_i$  for all  $i$ . For the other  $N - 1$  diagonal states only one of the  $c_j$  is large and the others are small and have different signs. The superposition of the amplitudes is therefore destructive.

The coherent superposition of the amplitudes means that the transition probability is large for the collective case and otherwise small as we will show in what follows.

If we do not assume as in (19.27) that all the  $V_{ij}$  are equal, then the calculation becomes more tedious but the general conclusion remains the same: as long as the  $V_{ij}$  are of the same order of magnitude the highest state is shifted well above the others and manifests itself as a coherent sum of all the particle-hole states.

**Estimating the transition probability** The operator for the electric dipole transition is

$$\mathbf{D} = e \sum_{p=1}^Z \mathbf{x}_p, \quad (19.34)$$

where  $\mathbf{x}_p$  is the coordinate of a proton. This must be modified slightly, since it is not yet clear which coordinate system  $\mathbf{x}_p$  refers to. The most natural coordinate system is the centre-of-mass system and we therefore write

$$\mathbf{D} = e \sum_{p=1}^Z (\mathbf{x}_p - \mathbf{X}), \quad \text{where} \quad \mathbf{X} = \frac{1}{A} \left( \sum_{p=1}^Z \mathbf{x}_p + \sum_{n=1}^N \mathbf{x}_n \right). \quad (19.35)$$

This may be recast as

$$\mathbf{D} = e \frac{N}{A} \sum_{p=1}^Z \mathbf{x}_p - e \frac{Z}{A} \sum_{n=1}^N \mathbf{x}_n. \quad (19.36)$$

We interpret this expression as meaning that

$$\begin{aligned} e_p &= +eN/A \text{ is the effective proton charge} \quad \text{and} \\ e_n &= -eZ/A \text{ is the effective neutron charge.} \end{aligned} \quad (19.37)$$

A photon ‘‘pulls’’ the protons in one direction and the neutrons in the opposite one. The neutrons and protons always move oppositely to each other under the influence of the photon in such a way that the centre-of-mass stays in the same place.

If we replace  $\psi_i$  and  $\psi_f$  in (19.1) by the nucleon wave functions in the one-particle shell model before and after the  $\gamma$  emission, we find the so-called one-particle transition probability. This, weighted with the square of the effective charge, may be used to estimate the collective nature of transitions.

We need to use the wave function (19.33) to calculate the matrix element

$$\mathcal{M}_{fi} = \int d^3x \psi_f^* D_z \psi_i, \quad (19.38)$$

where  $D_z$  is the  $z$  component of the dipole operator (19.34), if we want to calculate the transition probability. In our case  $\psi_i$  is just  $|0\rangle$ , the wave function of the ground state with closed shells and  $\psi_f$  is the wave function (19.33) of the collective excitation. Thus we have

$$\mathcal{M}_{C0} = \frac{1}{\sqrt{N}} \int d^3x \left\{ \left\langle \phi_{j_i}^{-1} \phi_{j_k} \right| + \left\langle \phi_{j_i}^{-1} \phi_{j_m} \right| + \dots \right\} D_z |0\rangle. \quad (19.39)$$

The matrix element between the ground state and the particle-hole excitation can be identified with the dipole transition of a particle from a closed shell into a higher one. The integrals

$$A_n = \int d^3x \phi_{j_k}^* D_z \phi_{j_i} \quad (19.40)$$

represent the amplitude for the transition of a particle from the  $j_i$  shell into the  $j_k$  one. Here  $n$  is an index which denotes each of the total  $N$  particle-hole states. The phases of the transition amplitudes  $A_n$  that contribute to the collective state are the phases of the differences of the magnetic substates. In the square of the amplitudes an equal number of mixed terms with positive and negative signs occur; they therefore average out to zero. If we assume for simplicity that the moduli  $|A_n|$  are also identical, then the squared matrix element becomes

$$|\mathcal{M}_{C0}|^2 = \frac{1}{N} \left| \sum_{n=1}^N A_n \right|^2 = \frac{N^2}{N} |A|^2 = N |M_{1\text{-particle}}|^2. \quad (19.41)$$

The transition probabilities are then rearranged. Because the states mix, we no longer have  $N$  different states each excited with probability  $|A|^2$ , but rather the total transition probability  $N|A|^2$  is taken up by the collective state.

These ideas apply equally to both protons and neutrons. But, since the proton and neutron effective charges (19.37) are of opposite signs, protons and neutrons oscillate inside the nucleus with opposite phases. This is the semiclassical interpretation of the giant dipole resonance.<sup>1</sup> The oscillation in deformed nuclei can take place along or orthogonal to the symmetry axis. This leads to two peaks in the excitation curve, as is seen in Fig. 19.3 for the case of  $^{150}\text{Nd}$ .

This treatment of the collective dipole resonance in a shell model, where we limited ourselves to just a few particle-hole states and then actually only solved it schematically, explains why the dipole transition strength is essentially restricted to one state. The resonance lies above the neutron threshold, i.e., in the continuum, and primarily mixes with neutron scattering states. Thus the cross-section for photon absorption displays a broad structure instead of a narrow state.

---

<sup>1</sup>There is an attractive analogy to the giant dipole resonance in plasma physics: electromagnetic radiation directed at a plasma is absorbed over a broad band around the so-called plasma frequency. At this frequency the totality of the free electrons oscillate against the ions.



### 19.3 Shape Oscillations

**Quadrupole oscillations** Other nuclear collective states have also been observed in experiments. To keep things simple, we will limit ourselves in what follows to doubly even nuclei. Their ground and first excited states always have quantum numbers  $J^P = 0^+$  and  $J^P = 2^+$ , with the exception of doubly magic nuclei and a very few others (Figs. 18.6 and 19.6). The simplest explanation for these excited levels would be that a nucleon pair has been broken apart to produce the second lowest energy level,  $J^P = 2^+$ . Measurements of the lifetimes of such states show, however, that the transition probability for the electric quadrupole transition is up to two orders of magnitude larger than a one-particle transition would suggest. The lowest  $2^+$  states are in fact, for nuclei with enough particles outside closed shells, our first encounter with the ground-state rotational band which we will treat in Sect. 19.4. If the configuration has only a few particles outside closed shells, then we describe these states as oscillations of the geometric shape of the nucleus around its equilibrium form, which last is approximately spherically symmetric. For such  $2^+$  states it seems likely that these vibrations are of the quadrupole type (Fig. 19.7a).

Near the giant dipole resonance, and so at much higher excitation energies, further collective states with  $J^P = 2^+$  are observed in electron scattering. These are called giant quadrupole resonances.

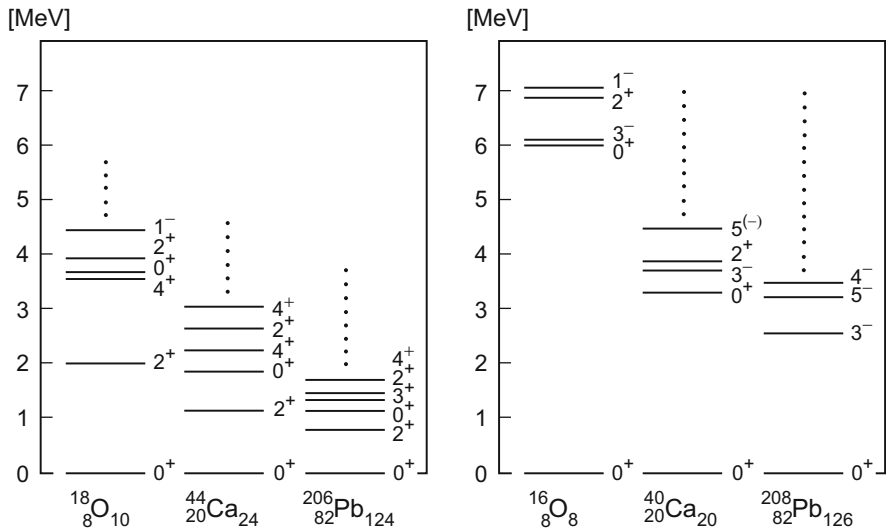
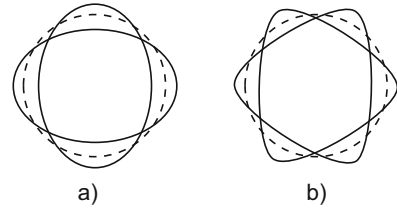


**Fig. 19.6** Energy levels of three simply magic even-even nuclei,  $^{18}\text{O}$ ,  $^{44}\text{Ca}$  and  $^{206}\text{Pb}$  (left), and three doubly magic ones,  $^{16}\text{O}$ ,  $^{40}\text{Ca}$  and  $^{208}\text{Pb}$  (right). The excited states in the first case have  $J^P = 2^+$ . This state is lacking in the three doubly magic nuclei, which instead have a lower lying  $3^-$  state. The transition probability into the ground state is high compared with what we would expect from a single-particle excitation. These states are interpreted as collective quadrupole or octupole vibrations

**Fig. 19.7** (a) Quadrupole vibrations; (b) Octupole vibrations



This illustrative discussion of quadrupole oscillations needs to be explained, in a similar fashion to our treatment of the giant dipole resonance, in terms of the shell model and the nature of the nuclear force. In a single-particle picture collective excitations only arise if the particles in a shell are excited with correlated phases. For the giant dipole resonances we saw that this took place through coherent addition of all particle-hole excitations. To now create  $J^P = 2^+$  states we need to either promote one particle into the next but one shell, or into the next level inside the same shell. This is a consequence of the spin and parity of the shell states. Shells below  $^{48}\text{Ca}$  have alternating  $+1$  and  $-1$  parity and in heavier nuclei at least states with similar  $j$  will have opposite parities in successive shells. The particle-hole states are in this case nearly degenerate which can lead to collective states. Exciting particles inside the same shell leads to low lying quadrupole vibrations, exciting them into the next but one shell generates giant quadrupole resonances.

While the semiclassical picture of a giant dipole resonance has the protons and neutrons oscillating against each other, the protons and neutrons in nuclear quadrupole oscillations can move either with the same or opposite phase. If they move in phase the isospin is unchanged, if oppositely it is changed by unity. We will only consider the first case here. The interaction between particle-hole states which causes this in-phase motion is, obviously, of an attractive type. If we were to solve the secular equation for a collective  $2^+$  state, we would see that the attractive interaction shifts the energy levels downwards. The lowest energy state is built up out of a coherent superposition of particle-hole states with  $J^P = 2^+$  and is collectively shifted down.

The various collective excitations in the framework of the shell model are depicted in Fig. 19.8. The giant quadrupole resonance splits into two parts. That with  $\Delta I = 1$ , which comes from proton-neutron repulsion, is, similarly to the giant dipole resonance, shifted up to higher energies. The giant quadrupole resonance which has  $\Delta I = 0$  corresponds to shape oscillations and is shifted down. In both cases, however, the shift is smaller than was the case for the giant dipole resonance, which implies that the collective nature of these excitations is less pronounced. This may be explained as follows: the one-particle-one-hole excitations which build up the giant dipole resonance can only, for reasons of energy, enter a few other states, which themselves are one-particle-one-hole excitations in the same shell combinations. This state made up of single-particle-hole excitations is thus long lived and displays a strongly coherent nature. This is all no longer true for excitations into the next shell but one, such as those which comprise the quadrupole

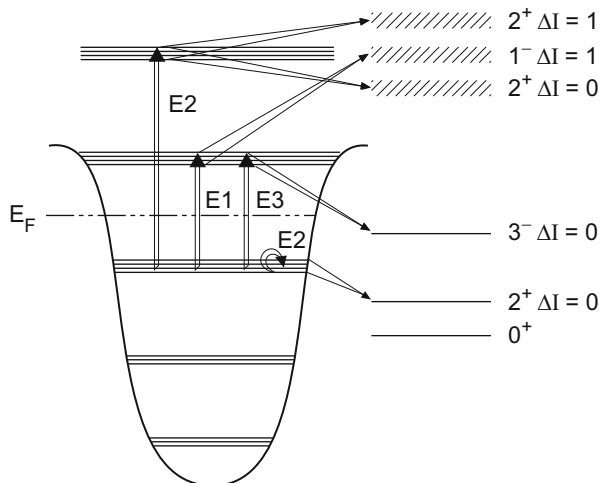


**Fig. 19.8** Collective excitations in the framework of the shell model. Shape oscillations are denoted by  $\Delta I = 0$ . Those collective states where the protons and neutrons oscillate in phase are shifted downwards. States where they oscillate with opposite phases ( $\Delta I = 1$ ) are pushed up to higher energies. Shells below the Fermi energy  $E_F$  are occupied by nucleons. The ground state lies at a position below the single-particle excitations given by the pairing energy

resonance. The single-particle-hole excitations of the next shell but one can decay into two-particle-hole states. Hence they have shorter lifetimes, are less coherent and less collective.

If the protons and neutrons move in phase this appears as a change in the shape of the nucleus. This alteration can hardly be quantitatively described in the shell model, since its particle wave functions were obtained using a spherically symmetric potential. Shape oscillations change the form of the potential and the nucleonic motion has to alter itself accordingly. Quantitative treatments of nuclei with large quadrupole oscillations are then of a hybrid form, where the total wave function has both vibrational and single-particle parts.

**Octupole oscillations** Nuclei with doubly closed shells, like  $^{16}\text{O}$ ,  $^{40}\text{Ca}$  and  $^{208}\text{Pb}$ , possess a low-lying  $3^-$  state (Fig. 19.6) whose transition probability can be up to two orders of magnitude higher than the single-particle prediction. This state can be interpreted as an octupole vibration (Fig. 19.7b). The collective  $3^-$  states can, like the giant dipole resonance, be built up out of particle-hole excitations in neighbouring shells. Since the protons and neutrons oscillate in phase in such shape vibrations, the particle-hole interaction must be attractive. The collective octupole excitations are shifted to lower energies.

**Summary** The picture of collective excitations which we have here attempted to explain is the following: since the shell energies in the nucleus are distinctly separated from each other, those particle-hole states which are created when a

nucleon is excited into a higher shell are nearly degenerate. Coherent superposition of these particle-hole states then form a collective excitation. Shape oscillations can be interpreted as coherent superpositions of the movement of single particles, but a quantitative description is only possible in terms of collective variables.

## 19.4 Rotational States

Nuclei with sufficiently many nucleons outside of closed shells display a characteristic excitation pattern: a series of states with increasing total angular momentum, the separation between whose energies increases linearly. These excitations are interpreted as corresponding to the nucleus rotating and, in analogy to molecular physics, the series are called *rotational bands*. Electric quadrupole transitions between the states of a rotational band display a markedly collective nature. The excitation pattern, and also the collective character of the quadrupole transitions, are understood as consequences of these nuclei being highly deformed [3]. Generally speaking the spin of the nuclear ground state is coupled to the angular momentum of the collective excitations. We will bypass this complication by only considering even-even nuclei, since these have spin zero in the ground state.

Rotational energy in classical mechanics depends upon the angular momentum  $\mathbf{J}$  and the moment of inertia  $\Theta$ :

$$E_{\text{rot}} = \frac{|\mathbf{J}_{\text{rot}}|^2}{2\Theta}. \quad (19.42)$$

In quantum mechanics rotation is described by a Hamiltonian operator

$$\mathcal{H}_{\text{rot}} = \frac{\mathbf{J}^2}{2\Theta}. \quad (19.43)$$

In such a quantum mechanical system the rotation must be perpendicular to the symmetry axis. The eigenstates of the angular momentum operator  $\mathbf{J}$  are the spherical harmonic functions  $Y_J^m$ , which describe the angular distribution of the wave function. The associated eigenvalues are:

$$E_J = J(J+1) \frac{\hbar^2}{2\Theta}. \quad (19.44)$$

The gaps between successive states increase linearly because of  $E_{J+1} - E_J = 2(J+1)\hbar^2/2\Theta$ . This is typical of rotating states. Only even values of  $J$  are attainable, for reasons of symmetry, for those nuclei which have  $J^P = 0^+$  in the ground state. The moment of inertia  $\Theta$  can be found from the spins and excitation energies.

We want to discuss the experimental data through two examples which we have chosen out of the range of masses where highly deformed nuclei occur: the lanthanides and the actinides.

**Coulomb excitation** Coulomb excitations in heavy ion reactions are often used to produce highly excited rotating states. To ensure that the interaction only takes place via Coulomb excitation, both partners must remain further apart than the range of the nuclear force. The projectile energy must then be chosen such that the *Coulomb threshold*

$$E_C = \frac{Z_1 Z_2 e^2}{4\pi\epsilon_0} \frac{1}{R_1 + R_2} = \frac{Z_1 Z_2 \alpha \cdot \hbar c}{R_1 + R_2} \quad (19.45)$$

of the partners is not crossed. Larger values for the radii  $R_1$  and  $R_2$  of the reacting particles than in (5.56), say  $R = 1.68 \text{ fm} \cdot A^{1/3}$  are then assumed to make sure that the tails of the nuclear wave functions do not have any effects [5].

Consider now the example of the Coulomb scattering of a  $^{90}_{40}\text{Zr}$  projectile off a  $^{232}_{90}\text{Th}$  target nucleus. The  $^{90}\text{Zr}$  ion is accelerated in a Tandem Van de Graaff accelerator up to a kinetic energy of  $E_{\text{Zr}} = 415 \text{ MeV}$ . The centre-of-mass energy which is then available to the colliding particles is

$$E_{\text{cm}} = \frac{A_{\text{Th}}}{A_{\text{Zr}} + A_{\text{Th}}} E_{\text{Zr}} \approx 299 \text{ MeV}. \quad (19.46)$$

If we insert the charge numbers and radii of these two nuclei into (19.45), we find that  $E_C \approx 300 \text{ MeV}$ . The centre-of-mass energy is, in other words, just below the limit where the first non-electromagnetic effects would make themselves felt.

The  $^{90}\text{Zr}$  projectile nucleus follows a hyperbolic path in the field of the target nucleus (Fig. 19.9a) and exposes the  $^{232}\text{Th}$  nucleus to a rapidly changing electric field. The path of the ion is so sharply curved that frequencies in the time-dependent electric field are generated that are high enough to produce individual excitations with energies up to about 1 MeV.

There is not just a quantitative but also a qualitative difference between Coulomb excitation and electron scattering off nuclei:

- The principal distinction is that the interaction is much stronger with a projectile charge which is  $Z$  times that of the electron. One must replace  $\alpha$  by  $Z\alpha$  in the matrix element (5.31). This means that the cross-section increases as  $Z^2$ .
- If we are not to cross the Coulomb threshold, the projectile energy must be so low that its velocity obeys  $v \lesssim 0.05 c$ . Magnetic forces are hence of little importance.
- The ion orbit may be calculated classically, even for inelastic collisions. The kinetic energy of the projectile in Coulomb excitation changes by less than 1 % and thus its path is practically the same. The frequency distribution of the virtual photons is very well known and the transition amplitudes can be worked out to a high degree of accuracy.

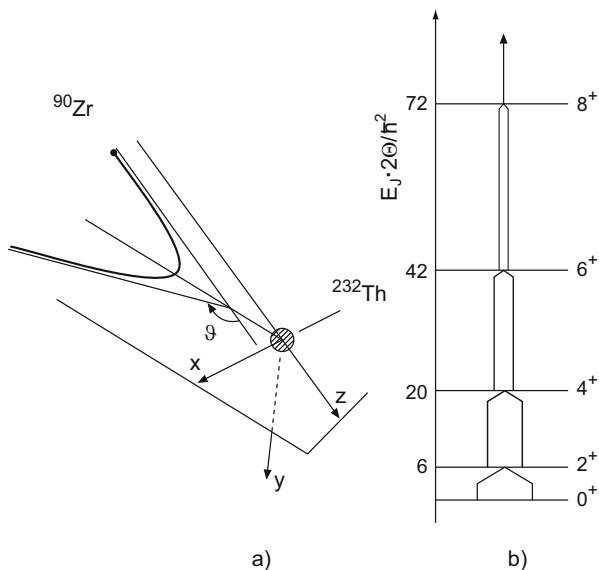


**Fig. 19.9** (a) Kinematics of a heavy ion collision (here  $^{90}\text{Zr} + ^{232}\text{Th}$ ). The projectile follows a hyperbolic orbit in the Coulomb field of the target nucleus. (b) Sketch of multiple Coulomb excitation of a rotational band. Successive quadrupole excitations lead to the  $2^+$ ,  $4^+$ ,  $6^+$ ,  $8^+$ , ... states being populated (with decreasing intensity)

The large coupling strength means that successive excitation from one level to the next is now possible. This is sketched in Fig. 19.9b: the quadrupole excitation reproduces itself inside a rotational band from the  $2^+$  state via the  $4^+$  to the  $6^+$ .

The popularity of Coulomb excitation in gamma spectroscopy is well founded. In such reactions we primarily produce states inside rotational bands. The cross-sections into the excited states give us, through the transition probabilities, the most important information about the collective nature of the rotational bands. Measurements of the cross-sections into the various states simultaneously determine the transition probability for the electric quadrupole transition inside the rotational band.

The introduction of germanium semiconductor detectors has marked a very significant step forward in nuclear-gamma spectroscopy. The low energy part of the gamma spectrum of Coulomb excitation of  $^{232}\text{Th}$  from scattering with  $^{90}\text{Zr}$  ions is shown in Fig. 19.10. This gamma spectrum was recorded with a Ge-semiconductor counter and a coincidence condition for the backwardly scattered  $^{90}\text{Zr}$  ions, which were measured with a Si-semiconductor detector (Fig. 19.11).

Excellent energy resolution makes it possible to see individual transitions inside rotational bands. Three series of lines can be recognised. The strongest are transitions inside the ground state rotational band ( $J_g \rightarrow (J - 2)_g$ ). According to (19.42) these lines should be equidistantly spaced out. This is only approximately the case. This may be explained by noting that the moment of inertia increases with

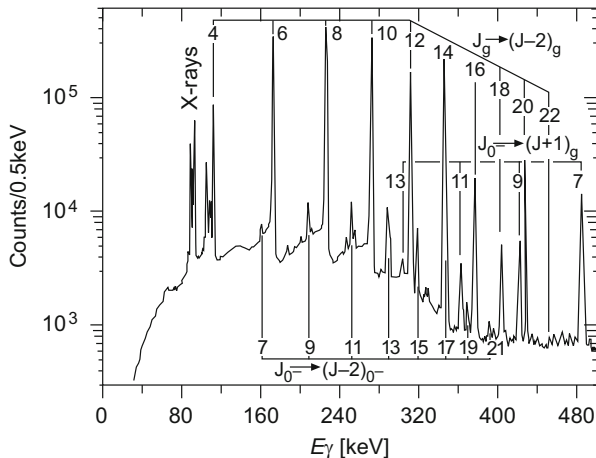


**Fig. 19.10** Photon spectrum of a Coulomb excited  $^{232}\text{Th}$  nucleus. Three series of matching lines may be seen. The strongest lines correspond to transitions in the ground state rotational band  $J_g \rightarrow (J - 2)_g$ . The other two bands are strongly suppressed and are the results of excited states (cf. Fig. 19.12) [8]

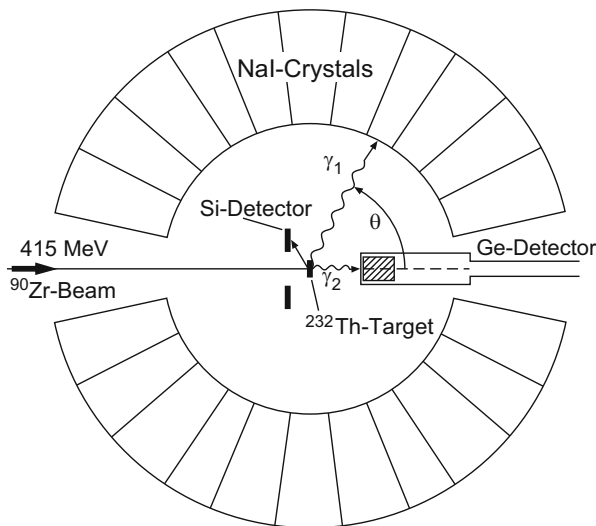


**Fig. 19.11** Experimental apparatus for investigating Coulomb excitation in heavy ion collisions. In the example shown a  $^{90}\text{Zr}$  beam hits a  $^{232}\text{Th}$  target. The backwardly scattered Zr projectiles are detected in a silicon detector. A germanium detector, with which the  $\gamma$  cascades inside the rotational bands can be finely resolved, gives a precise measurement of the  $\gamma$  spectrum. These photons are additionally measured by a crystal ball of NaI crystals with a poorer resolution. A coincidence condition between the silicon detector and the NaI crystals can be used to single out an energy window inside which one may study the nuclear rotational states with the germanium detector (From [8])

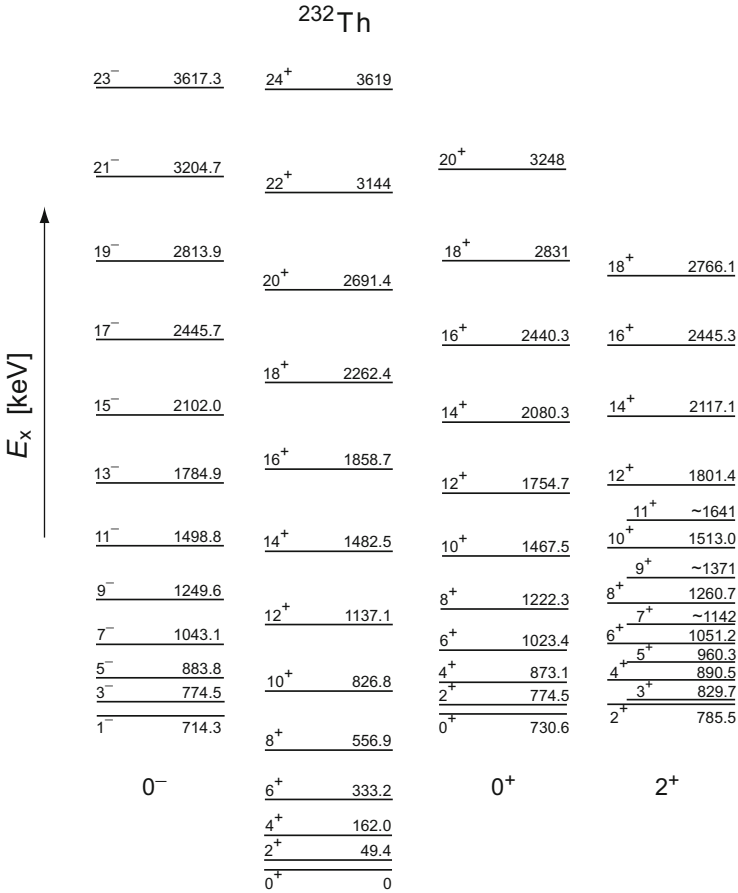
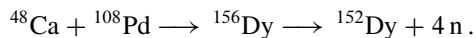


**Fig. 19.12** Spectrum of the  $^{232}\text{Th}$  nucleus. The excitation energies are in keV. As well as the ground state rotational band, which may be excited up to  $J^P = 24^+$ , other rotational bands have been observed which are built upon vibrational excitations (From [8]). The quantum numbers of the vibrational states are given below the bands. For reasons of symmetry, the only rotational states which can be constructed upon the  $J^P = 0^-$  vibrational state are those with odd angular momenta

the spin. Events with scattering angles around  $180^\circ$  are chosen because the projectile must then have gotten very close to the target and at the moment of closest approach have experienced a strong acceleration. The virtual-photon spectrum which the projectile emits contains high frequencies which are important for the excitation of the high spin states. The spectrum which emerges from this sort of measurement is shown in Fig. 19.12: as well as the ground state rotational band, there are other rotational bands which are built upon excited states. In this case the excitations may be understood as vibrational states.



**Fusion reactions** Records in high spin excitations may be obtained with the help of fusion reactions such as



Only  ${}^{48}\text{Ca}$  nuclei with a kinetic energy of 200 MeV can just overcome the Coulomb barrier. If the fusion process takes place when the nuclei just touch, then the  ${}^{156}\text{Dy}$  fusion product receives angular momentum

$$\ell\hbar \approx (R_1 + R_2)\sqrt{2mE}, \quad (19.47)$$

where  $m$  is the reduced mass of the  ${}^{48}\text{Ca}$ - ${}^{108}\text{Pd}$  system;  $R_1$  and  $R_2$  are of course the correct nuclear radii from (5.56). The calculation thus yields  $\ell \approx 180$ . In practice the fusion reaction only takes place if the projectile and target overlap, so this number should be understood as an upper limit on the accessible angular momentum. Experimentally states up to  $J^P = 60^+$  have been reached in this reaction (Fig. 19.14).

**The moment of inertia** The size of the moment of inertia can with the aid of (19.44) be extracted from the measured energy levels of the rotational bands. The deformation  $\varepsilon$  can be obtained from the transition probability for electric quadrupole radiation inside the rotational band. The matrix element for the quadrupole radiation is proportional to the quadrupole moment of the nucleus, which, for collective states, is given by (18.40). The observed connection between the moment of inertia and the deformation parameter is displayed in Fig. 19.13. Note that the nuclear moments of

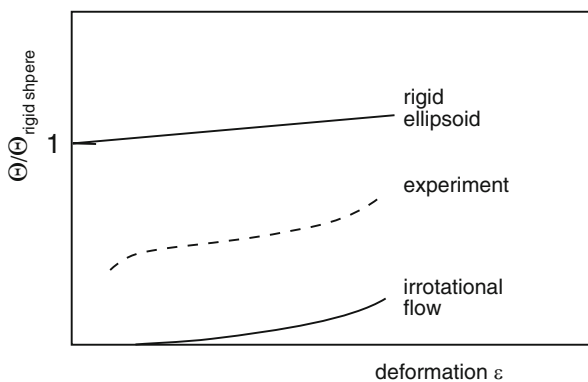


**Fig. 19.13** Moments of inertia of deformed nuclei compared with a rigid sphere as a function of the deformation parameter  $\varepsilon$ . The extreme cases of a rigid ellipsoid and an irrotational liquid are given for comparison

inertia are normalised to those of a rigid sphere with radius  $R_0$

$$\Theta_{\text{rigid sphere}} = \frac{2}{5}MR_0^2. \quad (19.48)$$

The moment of inertia increases with the deformation and is about half that of a rigid sphere.<sup>2</sup>

Two extreme cases are also shown in Fig. 19.13. The moment of inertia is maximised if the deformed nucleus behaves like a rigid body. In this case we have (for small deformations  $\varepsilon$ )  $\Theta \approx (1 + \varepsilon/2) \cdot \Theta_{\text{rigid sphere}}$ .

The other limit is reached if the nucleus behaves like an irrotational liquid. Superfluid  $^4\text{He}$  is an example of an ideal fluid, incompressible and frictionless. Currents in a frictionless liquid are irrotational. A rotating massless eggshell filled with superfluid helium would have the moment of inertia of an irrotational current. Only the bulge of the egg, and not the interior, would contribute to the moment of inertia. The moment of inertia for such an object is

$$\Theta = \frac{405\varepsilon^2}{64\pi} \cdot \Theta_{\text{rigid sphere}}, \quad (19.49)$$

where  $\varepsilon$  is the deformation parameter from (18.39).

Let us return to the example of the  $^{232}\text{Th}$  nucleus. The transition probabilities yield a deformation parameter of  $\varepsilon = 0.17$ . If the rotation of the nucleus could be described as that of an irrotational current, then its moment of inertia would, from (19.49), have to be 6% of that of a rigid sphere. The level spacings of the ground-state band yield, however

$$\frac{\Theta_{^{232}\text{Th}}}{\Theta_{\text{rigid sphere}}} \approx 0.3. \quad (19.50)$$

This implies that the experimentally determined moment of inertia lies between the two extremes (Fig. 19.13).

This result may be understood at a qualitative level rather easily. We mentioned in Sect. 18.4 that nuclear deformation is a consequence of an accumulation of mutually attractive orbitals either parallel to the symmetry axis (prolate shape) or perpendicular to it (oblate shape). The deformation is associated with the orbitals and one would expect deformed nuclei to rotate like rigid ellipsoids; but this clearly does not happen. This deviation from the rotation of a rigid rotator implies that nuclear matter must have a superfluid component. Indeed nuclei behave like eggshells that are filled with a mixture of a normal fluid and a superfluid.

---

<sup>2</sup>The comparison with a rigid sphere is, of course, purely classical; a spherically symmetric quantum mechanical system cannot rotate.

The superfluid components of nuclear matter are presumably generated by the pairing force. Nucleons with opposite angular momenta combine to form pairs with spin zero (cf. p. 322). Such zero spin systems are spherically symmetric and cannot contribute to the rotation. The pair formation may be understood analogously to the binding of electrons in *Cooper pairs* in superconductors [1, 6]. The paired nucleons represent, at least as far as rotation is concerned, the superfluid component of nuclear matter. This means on the other hand that not all nucleons can be paired off in deformed nuclei; the larger the deformation, the more nucleons must remain unpaired. This explains why the moment of inertia increases with the deformation (Fig. 19.13).

A similar dependence of the moment of inertia upon the unpaired nucleons can be seen in the rotational bands. The speed of rotation of the nucleus, and hence the centrifugal force upon the nucleons, increases with angular momentum. This causes nucleon pairs to break apart. Thus for large angular momenta the moment of inertia approaches that of a rigid rotator, as one can vividly demonstrate in  $^{152}\text{Dy}$ .

The excitation spectrum of  $^{152}\text{Dy}$  (Fig. 19.14) is more than a little exotic. The ground state of  $^{152}\text{Dy}$  is not strongly deformed, as one sees from the fact that the levels in the ground state rotational band do not strictly follow the  $E \propto J(J + 1)$  law and that transition probabilities are small. This band, in which the  $0^+$  until  $46^+$  states have been observed, first shows a genuine rotational character for high spins. The band which goes up to  $J^P = 60^+$  is particularly interesting [12]. The moment of inertia of this band is that of a rigid ellipsoid whose axes have the ratios 2 : 1 : 1 [9]. The transition probabilities inside this band are of the order of 2000 single-particle probabilities. Additionally to these two rotational bands, which have a prolate character, states have been found which may be interpreted as those of an oblately deformed nucleus. Evidently  $^{152}\text{Dy}$  has two energy minima near to its ground state, a prolate and an oblate shape. This example shows very nicely that for nuclei with incomplete shells a deformed shape is more stable than a sphere. Tiny changes in the configuration of the nucleus decide whether the prolate or oblate form is energetically favoured (Fig. 18.11).

**Further excitations of deformed nuclei** We have here only treated the collective aspects of rotation. Generally, however, excitations occur where, as well as rotation, an oscillation around either the equilibrium shape of the deformed nucleus or single-particle excitations are seen. (The latter case may be particularly clearly seen in odd nuclei.) The single-particle excitations may be, as described in Sect. 18.4, calculated from the movement of nucleons in a deformed potential. Deformed nuclei may be described, similarly to their vibrating brethren, in a hybrid model which employs collective variables for the rotational and vibrational degrees of freedom. The single-particle motion is coupled to these collective variables. The names of Bohr and Mottelson in particular are associated with the work that showed that a consistent description of nuclear excitations is possible in such hybrid models.

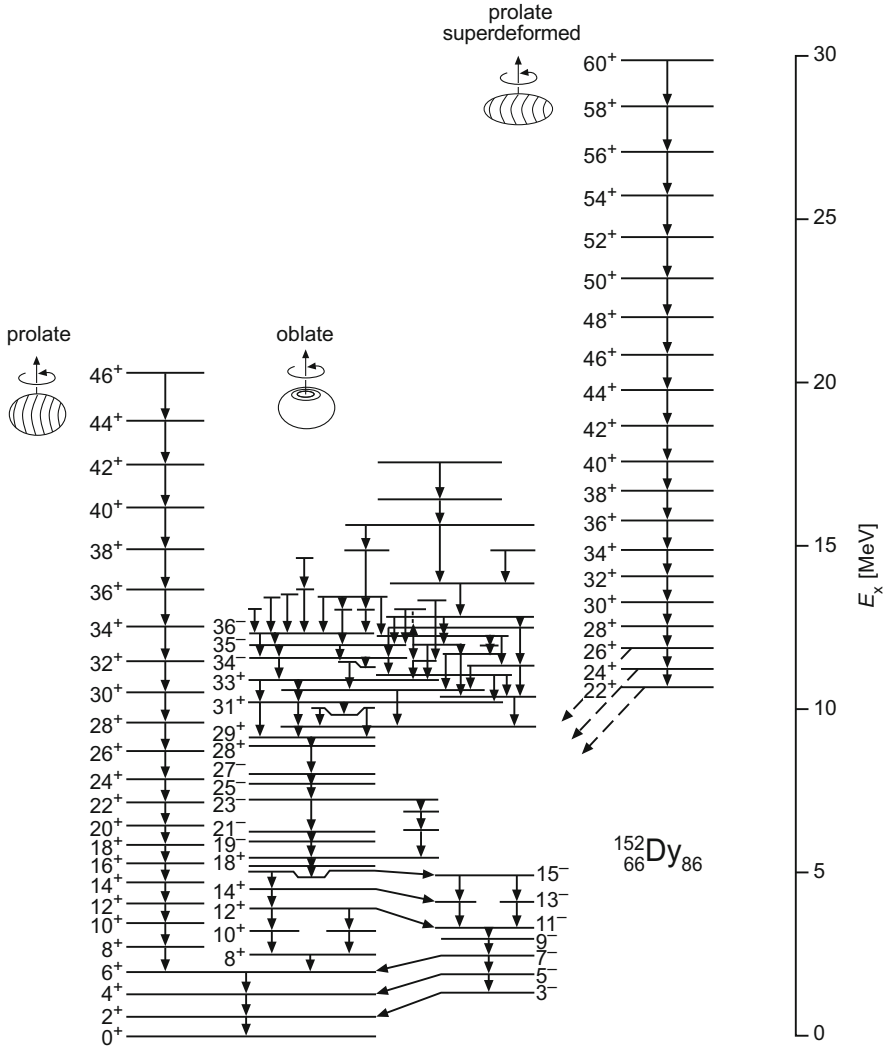


**Fig. 19.14** Energy levels of  $^{152}\text{Dy}$  [11]. Although the low energy levels do not display typical rotational bands, these are seen in the higher excitations, which implies that the nucleus is then highly deformed

## Problems

### 1. The electric dipole giant resonance

- (a) How large is the average deviation between the centres-of-mass of the protons and neutrons in giant dipole resonances for nuclei with  $Z = N = A/2$ ?

The  $A$  dependence of the resonance energy is very well described by  $\hbar\omega \approx 80 \text{ MeV}/A^{1/3}$ . Give the numerical value for  $^{40}\text{Ca}$ .

- (b) Calculate the squared matrix element for the dipole transition in this model.
- (c) Calculate the matrix element for a proton or neutron dipole transition (19.36) in the shell model with a harmonic oscillator potential. Use the fact that single particle excitations are about half the size of those of the giant resonance.

## 2. Deformation

The deformation parameter of the  $^{176}_{71}\text{Lu}$  nucleus is  $\varepsilon = +0.21$ . Find the semi-axes  $a$  and  $b$  of the rotational ellipsoid, describe its shape and calculate the quadrupole moment of this nucleus.

## 3. Rotational bands

The rotational band of  $^{152}\text{Dy}$  in Fig. 19.14 which extends up to  $J^P = 60^+$  corresponds to the rotation of an ellipsoid the ratio of whose axes is 2 : 1 : 1. What would be the velocity of the nucleons at the “tip” of the ellipsoid if this was a rotating rigid body? Compare this velocity with the *average* speed of nucleons in a Fermi gas with  $p = p_F = 250 \text{ MeV}/c$ .

## References

1. J. Bardeen, L.N. Cooper, J.R. Schrieffer, Phys. Rev. **108**, 1157 (1957)
2. B.L. Berman, S.C. Fultz, Rev. Mod. Phys. **47**, 713 (1975)
3. A. Bohr, B.R. Mottelson, Mat. Fys. Medd. Dan. Vid. Selsk. **27**, no 16 (1953)
4. G.E. Brown, *Unified Theory of Nuclear Models and Forces* (North Holland, Amsterdam, 1967)
5. P.R. Christensen et al., Nucl. Phys. **A207**, 33 (1973)
6. L.N. Cooper, Phys. Rev. **104**, 1186 (1956)
7. E. Fermi, *Nuclear Physics*, 5th edn. (University of Chicago Press, Chicago, 1953)
8. W. Korten, ‘Suche nach Mehr - Phonon Banden in  $^{232}\text{Th}$ ’ (in german), Dissertation, Heidelberg (1988)
9. I. Ragnarsson, S. Åberg, Phys. Lett. **B180**, 191 (1986)
10. F. Schwabl, *Quantum Mechanics*, 4th edn. (Springer, Berlin/Heidelberg/New York, 2007)
11. J. Sharpey-Schafer, Phys. World **3**(Nr. 9), 31 (1990)
12. P.J. Twin et al., Phys. Rev. Lett. **57**, 811 (1986)

## Chapter 20

# Nuclear Thermodynamics

So far we have concerned ourselves with the properties of nuclei in the ground state or the lower lying excited states. We have seen that the observed phenomena are characterised, on the one hand, by the properties of a degenerate fermion system and, on the other, by the limited number of the constituents. The nuclear force generates, to a good approximation, an overall mean field in which the nucleons move like free particles. In the shell model the finite size of nuclei is taken into account and the states of the individual nucleons are classified according to radial excitations and angular momenta. Thermodynamically speaking, we assign such systems zero temperature.

In the first part of this chapter we want to concern ourselves with highly excited nuclei. At high excitation energies the mean free path of the nucleon inside the nucleus is reduced; it is only about 1 fm. The nucleus is then no longer a degenerate fermionic system, but rather resembles, ever more closely for increasing excitations, the state of a normal liquid. It is natural to use statistical methods in the description of such systems. A clear description may be gained by employing thermodynamical quantities. The excitation of the nucleus is characterised by the temperature. We should not forget that strictly speaking one can only associate a temperature to large systems in thermal equilibrium and even heavy nuclei do not quite correspond to such a system. As well as this, excited nuclei are not in thermal equilibrium, but rather rapidly cool down via the emission of nucleons and photons. In any thermodynamical interpretation of experimental results we must take these deficiencies into account. In connection with nuclear thermodynamics one prefers to speak about *nuclear matter* rather than nuclei, which implies that many experimental results from nuclear physics may be extrapolated to large systems of nucleons. As an example of this we showed, when we considered the nuclear binding energy, that by taking the surface and Coulomb energies into account one can calculate the binding energy of a nucleon in nuclear matter. This is just the volume term of the mass formula (2.8).

Heavy ion reactions have proven themselves especially useful in the investigation of the thermodynamical properties of nuclear matter. In nucleus-nucleus collisions the nuclei melt together to form for a brief time a nuclear-matter system with increased density and temperature. We will try below to describe the phase diagram of nuclear matter using experimental and theoretical results about these reactions.

The results of nuclear thermodynamics are also of great importance for cosmology and astrophysics. According to our current understanding, the universe in the early stages of its existence went through phases where its temperature and density were many orders of magnitude higher than in the universe of today. These conditions cannot be reconstructed in the laboratory. Many events in the history of the universe have, however, left lasting traces. With the help of this circumstantial evidence one can try to draw up a model of the development of the universe.

## 20.1 Thermodynamical Description of Nuclei

We have already in Sect. 3.4 (Fig. 3.10) distinguished between three sorts of excitations in nuclei:

- The ground state and the low-lying states can be described in terms of single-particle excitations or via collective motion. This was treated in Chaps. 18 and 19.
- Far above the particle threshold there are no discrete states but only a continuum.
- In the transition region below and barely above the particle threshold there are lots of narrow resonances. These states do not, however, contain any information about the structure of the nucleus. The phenomena in this energy range in nuclei are widely referred to as *quantum chaos*.

In the following we shall concern ourselves with the last two of these domains. Their description involves statistical methods and so we will initially turn our attention to the concept of *nuclear temperature*.

**Temperature** We want to introduce the idea of temperature in nuclear physics through the example of the spontaneous fission of  $^{252}\text{Cf}$ . The half-life of  $^{252}\text{Cf}$  is 2.6 years and it has a 3.1 % probability of decaying via spontaneous fission. There is some friction in the separation of the fission fragments. Therefore, not all of the available energy from the fission process is converted into kinetic energy for the fragments. Rather the internal energy of the fragments is increased: the two fragments heat up.

The cooling-down process undergone by the fission fragments is shown schematically in Fig. 20.1. Initially cooling down takes place via the emission of slow neutrons. Typically 4 neutrons are emitted, each of them carrying off, on average, 2.1 MeV. Once the fragments have cooled below the threshold for neutron emission, they can only cool further by photon emission.

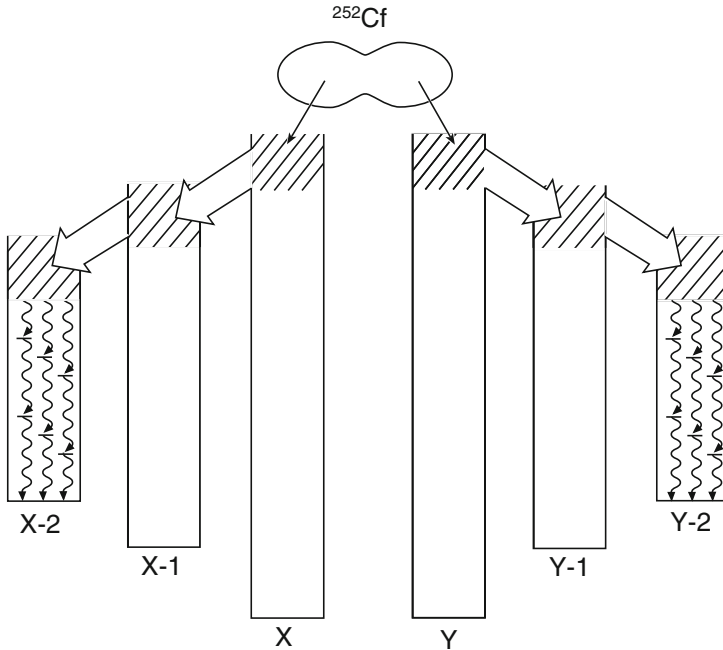


**Fig. 20.1** Cooling of fission fragments (schematic). A  $^{252}\text{Cf}$  nucleus splits into two parts with mass numbers  $X$  and  $Y$  which then cool down by emitting first neutrons and later photons

The energy spectrum of the emitted neutrons has the form of an evaporation spectrum. It may be described by a Maxwell distribution:

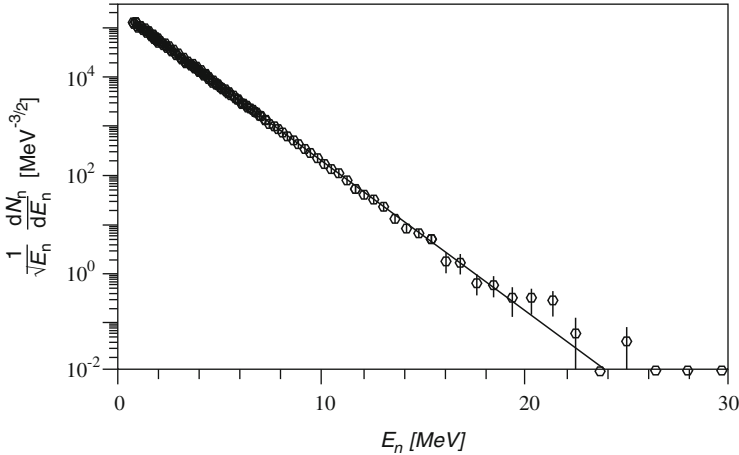
$$N_n(E_n) \sim \sqrt{E_n} \cdot e^{-E_n/kT}. \quad (20.1)$$

Figure 20.2 shows the experimental spectrum normalised by a factor of  $\sqrt{E_n}$ . The exponential fall-off is characterised by the temperature  $T$  of the system, in this case  $kT = 1.41$  MeV. Fission fragments from different nuclei are found to have different temperatures. One finds, e.g., a smaller value in the fission of  $^{236}\text{U}$ , namely  $kT = 1.29$  MeV.

Figure 20.3 displays the energy spectrum of the photons emitted in the de-excitation of the produced daughter nuclei. On average about 20 photons are set free for each spontaneous fission, and 80% of these photons have energies of less than 1 MeV. This spectrum also closely resembles an evaporation spectrum. The stronger fall-off of the photon spectrum compared to the neutron spectrum signals that the temperature in the photon emission phase, which takes place for lower nuclear excitations, is significantly lower.

Our successful statistical interpretation of these neutron and photon spectra leads to the important conclusion that the states in the neighbourhood of the particle threshold, which may be understood as a reflection of the corresponding transitions,





**Fig. 20.2** Energy spectrum of neutrons emitted in the spontaneous fission of  $^{252}\text{Cf}$  (From [6]). The distribution is divided by  $\sqrt{E_n}$  and then fitted to the exponential behaviour of a Maxwell distribution (*solid line*)

can also be described with statistical methods. Indeed the observed form of the spectrum may be formally derived from a statistical study of the density of states of a degenerate Fermi gas.

## 20.2 Compound Nuclei and Quantum Chaos

Many narrow resonances may be found in the transition region below and just above the particle threshold of a heavy nucleus. The states below the particle threshold are discrete and each one of these states possesses definite quantum numbers. The same is true for the states immediately above the threshold. Decays into these states are only described statistically through the density of these states. These states therefore do not contain any specific information about the structure of the nucleus.

**Compound nuclei** In neutron capture by heavy nuclei a multitude of resonances is observed. An example of such a measurement is seen in Fig. 20.4 where the cross-section for neutron scattering off thorium displays very many resonances. One should note that the energy scale is in eV, the separation of these resonances is thus six orders of magnitude smaller than the gaps in energy separating lower lying states. This observation was already explained in the thirties by Niels Bohr in the so-called compound-nucleus model. Neutrons in the nucleus have a very short free path due to the strong interaction and they very rapidly distribute their energy among the nucleons in the nucleus. The probability that all the energy supplied is held by one single nucleon is small. Therefore, the nucleons cannot escape from the nucleus

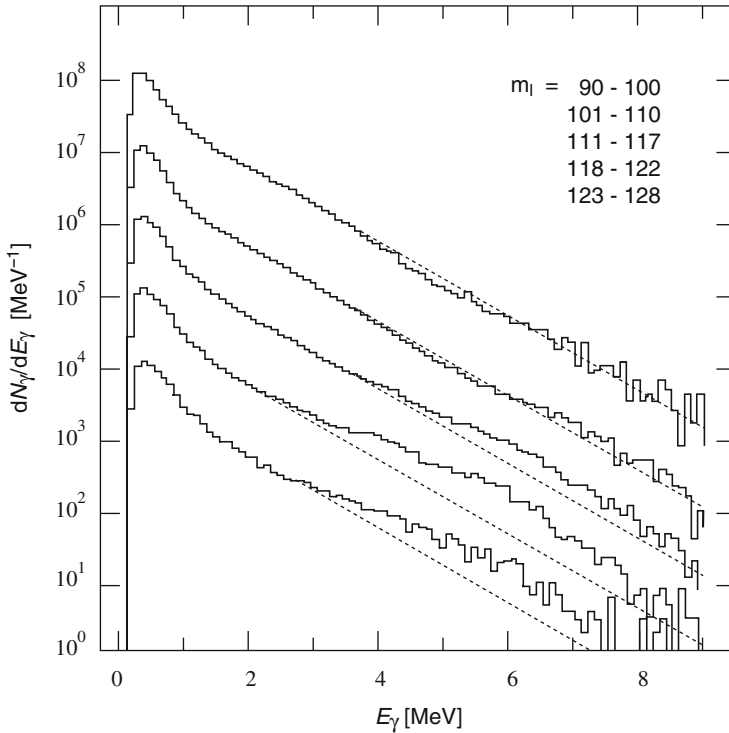


**Fig. 20.3** Photon emission energy spectra in the spontaneous fission of  $^{252}\text{Cf}$ . The various spectra correspond to different mass numbers,  $m_1$ , of the lighter fission products (from top to bottom). The dotted line is a common fit of an exponential function (From [11])

and this leads to a long lifetime for the compound-nucleus states. This lifetime is mirrored in the narrow widths of the resonances.

This picture has been greatly refined in the intervening decades. Thus the compound-nucleus state is not reached immediately, but rather the system, via successive collisions, passes through a series of intermediate states. The compound-nucleus state is the limiting case in which the nucleons are in thermal equilibrium.

**Quantum chaos in nuclei** In the theory of classical deterministic systems we distinguish between regular and chaotic orbits. Regular orbits are stable orbits which are not greatly affected by small external perturbations. The particles undergo periodic motion and the entire configuration of the system thus repeats itself. Chaotic orbits are very different. They are not periodic and infinitesimally small perturbations lead to big changes. While predictions for the development of regular systems may be made to an arbitrary accuracy, the uncertainties associated with predicting chaotic systems increase exponentially.

In quantum mechanics regular orbits correspond to states whose wave functions may be calculated with the help of the Schrödinger equation in some model, e.g.,

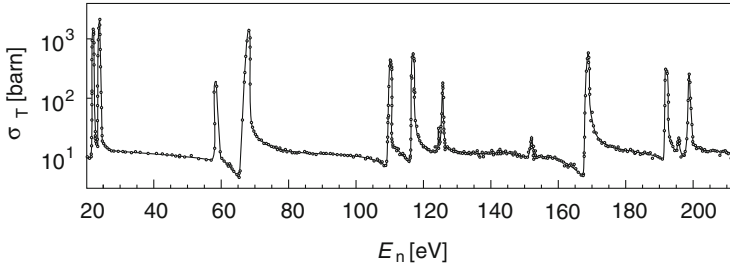


**Fig. 20.4** Total cross-section for the reaction  $^{232}\text{Th} + n$  as a function of the neutron energy. The sharp peaks correspond to resonances with orbital angular momentum  $\ell = 0$  (From [5])

for nuclei the shell model. The quantum mechanical equivalent of classical chaotic motion are states which are stochastically made up of single-particle wave functions. In both the classical and quantum mechanical cases a system in a chaotic state does not contain any information about the interactions between the particles.

The stochastic composition of chaotic states can be experimentally demonstrated by measuring the energy separations between these states. For this one considers resonance spectra such as that of Fig. 20.4. In the excitation region of the compound nucleus the states are very dense, so a statistical approach is justified.

It is apparent here that states with the same spin and parity (in Fig. 20.4 all the sharp resonances) attempt to keep as far apart as possible. The most likely separation of these states is significantly greater than the most likely separation of the energy levels of states if they were, for the same state density, distributed in a statistical fashion, according to a Poisson distribution independently of each other. This behaviour of the chaotic states is just what one expects if they are made up from a mixture of single-particle states with the same quantum numbers. Such quantum mechanical mixed states attempt to repel each other, i.e., their energy levels arrange themselves as far apart from each other as possible.

The existence of collective states, such as, e.g., the giant dipole resonance, for excitations above the particle threshold, i.e., in the region where the behaviour of the states is chaotic, is a very pretty example of the coexistence of regular and chaotic nuclear dynamics. Excitation of the collective state of the giant resonance takes place through photon absorption. The collective state couples to the many chaotic states via the nucleon-nucleon interaction. These partially destroy the coherence and thus reduce the lifetime of the collective state.

**The continuum** The continuum is by no means flat, rather strong fluctuations are seen in the cross-section. The reason for this is that, on the one hand, at higher energies the widths of the resonances increase because more decay channels stand open to them, but on the other hand the density of states also increases. Resonances with the same quantum numbers thus interfere with each other which leads to fluctuations in the total cross-section. These fluctuations do not correspond to single resonances but to the interference of many resonances. The size of the fluctuations

and their average separation can be quantitatively calculated from the known state density [9].

## 20.3 The Phases of Nuclear Matter

**The liquid-gas phase transition** Peripheral heavy ion reactions have proven themselves most useful as a way to heat up nuclei in a controlled way. In a glancing collision of two nuclei (Fig. 20.5) two main fragments are produced which are heated up by friction during the reaction. In such reactions one can measure rather well both the temperature of the fragments and also the energy supplied to the system. The temperature of the fragments is found from the Maxwell distribution of the decay products, while the total energy supplied to the system is determined

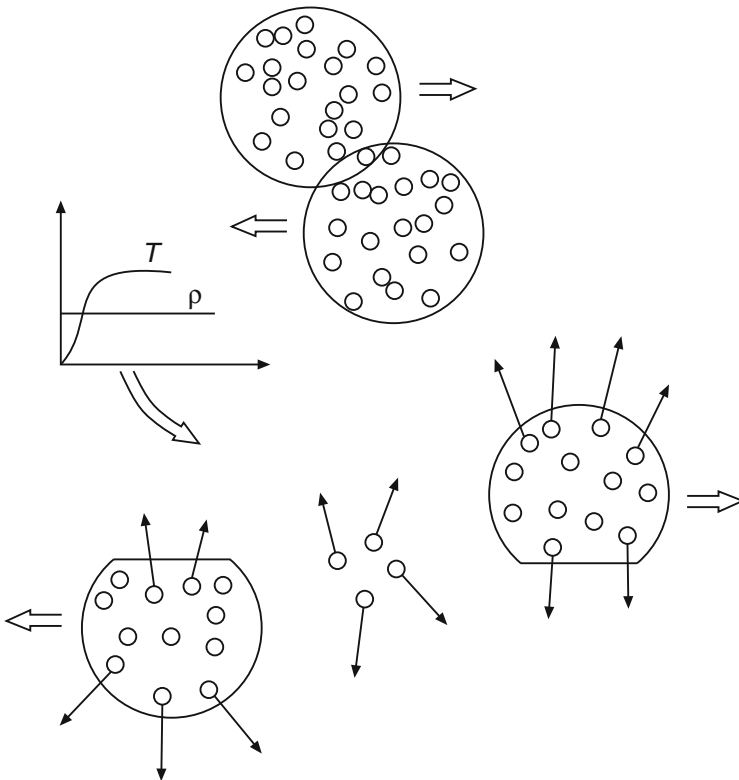


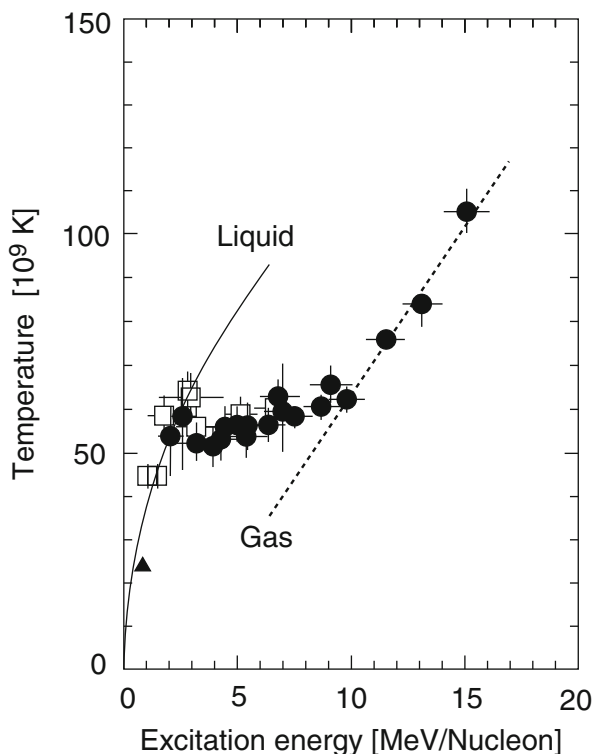
**Fig. 20.5** A peripheral nuclear collision. The large fragments are heated up by friction. As well as this, individual nucleons and smaller nuclear fragments are also produced in the collision. The diagram describes the time evolution of the density  $\rho$  and temperature  $T$  of the fragments during the collision

by detecting all of the particles produced in the final state. Since the fragment which came from the projectile moves off in the direction of the projectile, its decay products will also move in that direction and may be thus kinematically distinguished both from the decay products of the target fragments and also from the frictionally induced evaporative nucleons. The contributions from the energy supplied to the fragments and from the energy lost to friction during the glancing collision may thus be separated from one another.

Let us take as an example an experiment where gold nuclei with an energy of 600 MeV/nucleon were fired at a gold target. The reaction products were then tracked down using a detector which spanned almost the entire solid angle (a  $4\pi$  detector).

The dependence of the fragments' temperature on the energy supplied to the system is shown in Fig. 20.6. For excitation energies  $E/A$  up to about 4 MeV/nucleon one observes that the temperature sharply increases. In the region  $4 \text{ MeV} < E/A < 10 \text{ MeV}$  the temperature hardly varies at all, while at higher energies it again grows rapidly. This behaviour is reminiscent of the process of water evaporation where, around the boiling point, at the phase transition from liquid into steam, the temperature remains constant, even though energy is added to the system, until the entire liquid has been converted into a gaseous state. It is therefore natural to

**Fig. 20.6** Temperature of the fragments in a peripheral collision of two  $^{197}\text{Au}$  nuclei as a function of the excitation energy per nucleon (From [17]). The behaviour of the temperature can be understood as a phase transition in nuclear matter



interpret the temperature dependence described above as a nuclear matter phase transition from a liquid to a gas-like state.

The terms which we have used come from equilibrium thermodynamics. For such conditions a logical interpretation of the phase transition would be the following: at a temperature of about  $kT \sim 4 \text{ MeV}$  a layer of nucleons in a gaseous phase forms around the nucleus. This does not evaporate away but remains in equilibrium with the liquid nucleus and exchanges nucleons with it. The nucleon gas can only be further heated up after the whole of the nucleon liquid has evaporated.

**Hadronic matter** If we wish to investigate central, and not peripheral, collisions in gold-gold collisions, we have to select in the experiment those events in which many charged and neutral pions are emitted (Fig. 20.7). To keep the discussion simple, we will choose projectile energies of  $10 \text{ GeV/nucleon}$  or more for which a large number of pions is created.

At such energies the nucleonic excitation  $N + N \rightarrow \Delta + N$  has a cross-section of  $\sigma = 40 \text{ mb}$ . The corresponding path length  $\lambda \approx 1/\sigma\rho_N$  in the nucleus is of the order of  $1 \text{ fm}$ . This means that multiple collisions take place in heavy ion collisions and that for sufficiently high energies every nucleon will on average be excited once or more into a  $\Delta$  baryon. In the language of thermodynamics this excitation corresponds to the opening up of a new degree of freedom.

The  $\Delta$  baryons decay rapidly but they are continually being reformed through the inverse reaction  $\pi N \rightarrow \Delta$ . Creation and decay via  $\pi N \leftrightarrow \Delta$  thus stand in a dynamical equilibrium. This mix of nucleons,  $\Delta$  baryons, pions and, in significantly smaller amounts, other mesons is called *hadronic matter*.

Pions, since they are much lighter than the other hadrons, are primarily responsible for energy exchange inside hadronic matter. The energy density and temperature of hadronic matter produced in a collision of two atomic nuclei can be experimentally determined with the help of these pions. The temperature is found from the energy distribution of those pions which are emitted orthogonally to the beam direction. Their energy spectrum has the exponential behaviour expected of a Boltzmann distribution:

$$\frac{dN}{dE_{\text{kin}}} \propto e^{-E_{\text{kin}}/kT}, \quad (20.2)$$

where  $E_{\text{kin}}$  is the kinetic energy of the pion. One finds experimentally that the temperature of the pionic radiation is never greater than  $kT \approx 150 \text{ MeV}$ , no matter how high the energies of the colliding nuclei are. This may be understood as follows: hot nuclear matter expands and in doing so cools down. Below a temperature  $kT \approx 150 \text{ MeV}$ , the hadronic interaction probability of the pions, and thus energy exchange between them and other particles, decreases sharply. This process is referred to as the pions *freezing out*.<sup>1</sup>

---

<sup>1</sup>A similar process takes place in stars: the electromagnetic radiation in the interior of the Sun is at many millions of K. On its way out it cools down via interactions with matter. What we observe is

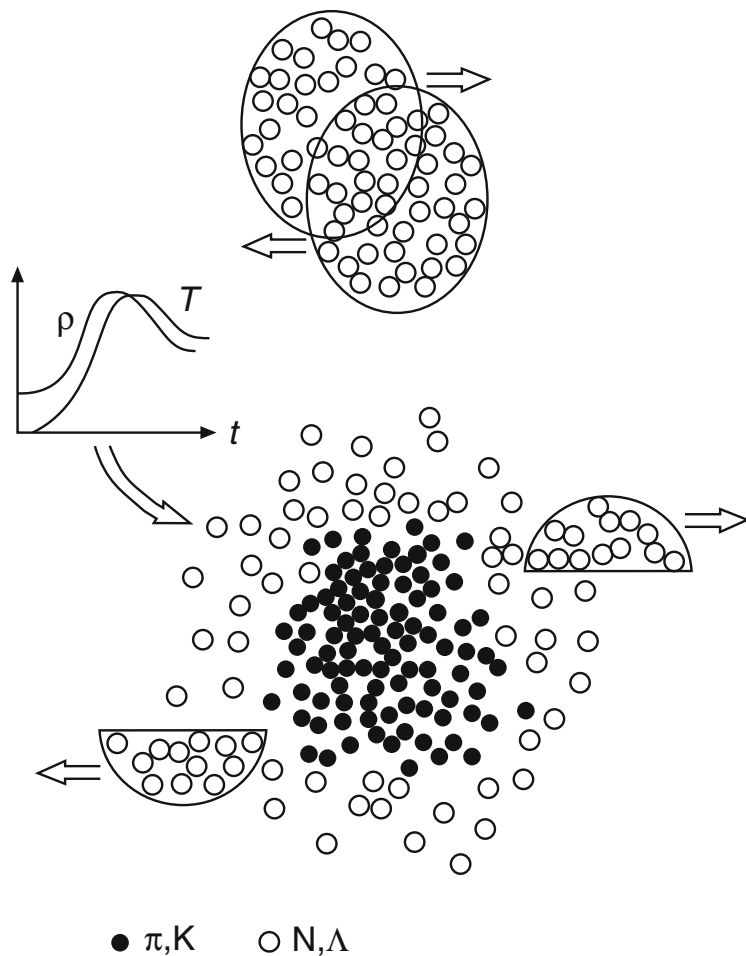


**Fig. 20.7** Central collision of two heavy nuclei at high energies. A large number of pions is produced here. The curves show the increase of density,  $\rho$ , and temperature,  $T$ , in the central region of the collision

**Phase diagram for nuclear matter** The various phases of nuclear matter are summarised in Fig. 20.8. We want to clarify this phase diagram by comparing nuclear matter with usual matter (that composed of atoms or molecules). Cold nuclei have density  $\rho_N$  and temperature  $kT = 0$ . A neutron star corresponds to a state with  $kT = 0$ , however, its density is about 3–10 times as big as that of nuclei.

---

white light whose spectrum corresponds to the temperature of the solar surface. In contrast to hot nuclear matter, the Sun is of course in equilibrium and is not expanding.

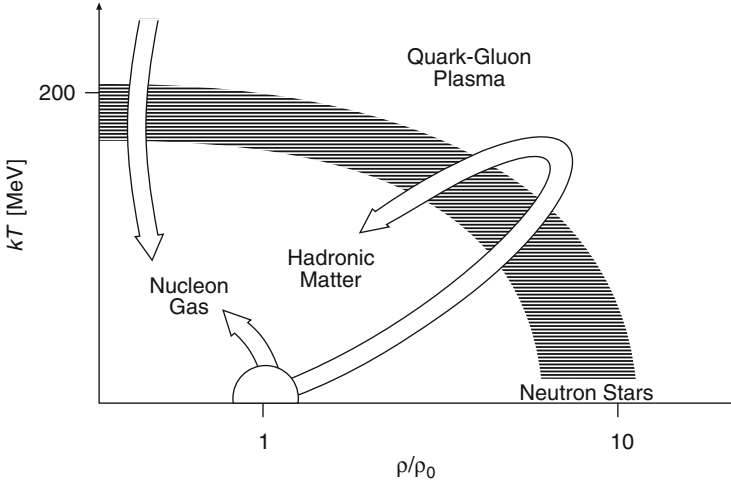


**Fig. 20.8** Phase diagram for nuclear matter. Normal nuclei have  $\rho = \rho_0$  ( $= \rho_N$ ) and temperature  $T = 0$ . The *arrows* show the paths followed by nuclei in various heavy ion reactions. The *short arrow* symbolises the heating up of nuclei in peripheral collisions; the *long arrow* corresponds to relativistic heavy ion collisions, in which nuclear matter possibly crosses the quark-gluon plasma phase. The cooling of the universe at a time of  $\approx 1 \mu\text{s}$  after the big bang is represented by the *downwards pointing arrow*

If one supplies energy to a normal nucleus, it heats up and emits nucleons or small nuclei, mainly  $\alpha$ -clusters, just as a liquid droplet evaporates atoms or molecules. If, however, one confines the material, increasing the energy supplied leads to the excitation of internal degrees of freedom. In a molecular gas these are rotational and vibrational excitations. In nuclei nucleons can be excited into  $\Delta(1,232)$  resonances or to still higher nucleon states. We have called the mish-mash of nucleons and pions, which are then created by decays, *hadronic matter*.

**Quark-gluon plasma** The complete dissociation of atoms into electrons and atomic nuclei (a plasma) has its equivalent in the disintegration of nucleons and pions into quarks and gluons. Qualitatively the positions of the phase boundary in the temperature-density diagram (Fig. 20.8) may be understood as follows: at normal nuclear densities each nucleon occupies a volume of about  $6 \text{ fm}^3$ , whereas the actual volume of a nucleon itself is only about a third of this. If one then were to compress a cold nucleus ( $T = 0$ ) to many times its usual density, the individual nucleons would overlap and cease to exist as individual particles. Quarks and gluons would then be able to move “freely” in the entire nuclear volume. If on the other hand one were to follow a path along the temperature axis, i.e., increase the temperature without thereby altering the nucleon density in the nucleus, then at a temperature of  $kT \approx 200 \text{ MeV}$  enough energy would be available to the individual nucleon-nucleon interactions to increase, via pion production, the



hadronic density and the frequency of the collisions between them so much that it would be impossible to assign a quark or gluon to any particular hadron.

This state is referred to as a *quark-gluon plasma*. As we have already mentioned, this state, where the hadrons are dissolved, cannot be observed through the study of emitted hadrons. There are attempts to detect a quark-gluon plasma state via electromagnetic radiation. The coupling of photons to quarks is about two orders of magnitude smaller than that of strongly interacting matter is. Thus any electromagnetic radiation produced in any potential creation of a quark-gluon plasma, e.g., in relativistic heavy ion collisions, could be directly observed. It would not be cooled down in the expansion of the system.<sup>2</sup>

There is a great deal of interest in detecting a quark-gluon plasma because it would mean an experimental confirmation of our ideas of the structure of strongly interacting matter. Therefore, it is searched for intensively in collisions of ultra-relativistic heavy ions, e.g., in experiments at RHIC (*Relativistic Heavy Ion Collider*) at Brookhaven/USA or the experiment ALICE (*A Large Ion Collider Experiment*) at the LHC. If the assignment of quarks and gluons to individual hadrons were removed, the constituent quarks would lose their masses and turn into partonic quarks; one would be able to simulate the state of the universe at a very early stage in its history.

## 20.4 Particle Physics and Thermodynamics in the Early Universe

*In all societies men have constructed myths about the origins of the universe and of man. The aim of these myths is to define man's place in nature, and thus give him a sense of purpose and value.*

John Maynard Smith [20]

The interplay between cosmology and particle physics during the last few decades has lead to surprising insights for both areas. In what follows we want to depict current ideas about the evolution of the universe and show what consequences this evolution has had for our modern picture of particle physics. We will here make use of the standard cosmological model, the big bang model, according to which the universe began as an infinitely hot and dense state. This fireball then expanded explosively and its temperature and density have continued to decrease till the present day. This expansion of an initially hot plasma of elementary particles was the origin of all nowadays known macroscopic and microscopic forms of matter:

---

<sup>2</sup>The above analogy from astrophysics is also applicable here: the neutrinos which are created in fusion reactions in the solar interior are almost unhindered in their escape from the Sun. Their energy spectrum thus corresponds to the temperature at their production point and not to that of the surface.

stars and galaxies; leptons, quarks, nucleons and nuclei. This model for the time development of the universe was motivated and then confirmed by two important experimental observations: the continuous expansion of the universe and the cosmic background radiation.

**The expanding universe** The greatest part of the mass of the universe is located in galaxies. These spatially concentrated star systems are held together by the force of gravity and, depending upon their size, have masses of between  $10^7$  and  $10^{13}$  solar masses. It is believed that there are about  $10^{23}$  stars in the universe – a number comparable to the number of molecules in a mole.

With the help of large telescopes it is possible to measure the distance to and the velocities of galaxies which are very far away from the Earth. The velocity of a galaxy relative to the Earth can be determined from the Doppler shift of atomic spectral lines, which are known from laboratory measurements. One so finds a shift of the observed lines into the red, i.e., the longer wavelength region. This corresponds to a motion of the galaxies away from us. This observation holds no matter what direction in the heavenly sphere the galaxy under observation is in. A determination of the distance to the galaxy is carried out by measuring its light intensity and estimating its luminosity; these quantities are related by the well-known  $1/r^2$  law. Such distance estimates are particularly imprecise for very distant galaxies.

The measured velocities  $v$  of the observed galaxies are roughly linearly proportional to their separation  $d$  from the Earth

$$v = H_0 \cdot d, \quad (20.3)$$

where  $H_0$  is called the *Hubble constant* after the discoverer of this relationship. The measurements of  $H_0$  have been improved appreciably in recent years. Its present value from a combination of data of various experiments is [13]:

$$H_0 = 69.32 \pm 0.88 \text{ km s}^{-1}/\text{Mpc} \quad (1 \text{ Pc} = 3.1 \cdot 10^{13} \text{ km} = 3.3 \text{ light years}).$$

These observations taken together are interpreted as implying an isotropic expansion of the universe.

According to the big bang theory, the initial hot plasma filled the universe with extremely short wavelength electromagnetic radiation, which, though, increased its wavelength as the universe expanded and cooled. The observation, by Penzias and Wilson [16], of this radiation in the microwave-length region, which we now call the *cosmic background radiation*, was therefore a very important confirmation of the big bang model. This microwave radiation corresponds to black body radiation at a temperature

$$T = (2.7255 \pm 0.0006) \text{ K}.$$

It was measured, e.g., by the COBE satellite [10], in every direction of the universe as being extraordinarily isotropic. This isotropy is, however, not exact. Tiny temperature fluctuations with an amplitude of  $\Delta T/T \approx 10^{-5}$  have been observed. They are supposed to have been generated from small density perturbations in the early universe giving rise to seeds of galaxies and clusters. The anisotropy in the cosmic microwave background contains, therefore, important information about cosmological parameters. Presently such fluctuations are being searched for and studied with high precision by satellite experiments like WMAP [13] or Planck [1].

A relation between the age and the size of the universe can be derived with the help of general relativity theory and the observed expansion of the universe. In the simplest model, the *Friedman model* of the expanding universe, one distinguishes between three cases which depend upon the average mass density of the universe: if the average density is greater than a critical density, then the mutual attraction of the galaxies will slow the expansion of the universe down and eventually produce a contraction. The universe will then collapse into a point (*closed universe*). If the average density is smaller than the critical density, gravitation cannot reverse the expansion. In such a case the universe will expand forever (*open universe*). If the average and critical densities are approximately the same, the universe would asymptotically approach a limiting radius and not expand further (*flat universe*). Present observations point to a flat universe with critical density.

The consequences for the future expansion of the universe that we discussed so far are only valid when we neglect the mysterious *dark energy*. This is a contribution to the critical density aggregating to 70 %, but its origin is currently not understood at all. For instance, in a flat universe it would cause an accelerated expansion as opposed to an eventual standstill. Roughly speaking, the effect of dark energy on the evolution of the universe is inverse to the one of gravity. The latter tends to slow down the expansion, which is easy to understand, as it causes mutual attracts of all matter. A large number of cosmological observations can only be explained if dark energy is present.

Furthermore, the density measured with optical methods (about 4 % of the critical density) is smaller than the density obtained from observations based on gravitational effects. This means that there exists at least one type of *dark matter*, contributing with 23 % to the critical density. Obvious candidates would be massive neutrinos, which would, even though their mass is small, contribute strongly to the density, because of their huge number in the universe. However, particles with small masses such as neutrinos (at most  $2 \text{ eV}/c^2$ , see Sect. 18.6 for experiments determining neutrino mass) are unfortunately no suitable dark matter candidates. Namely, observations of the distribution of galaxies are compatible only with heavy neutral dark matter particles ( $10\text{--}1,000 \text{ GeV}/c^2$ ) whose interactions are of the order of the weak interaction. Such *WIMPs* (*Weakly Interacting Massive Particles*) show up typically in so-called supersymmetric theories, which are the most popular extension of the Standard Model. The contribution of dark matter to the critical density corresponds for a WIMP with mass  $100 \text{ GeV}/c^2$  about 3,000 particles per cubic metre. Direct detection of dark matter can take place in very sensitive experiments that search for the elastic scattering of dark matter particles

with nuclei. The recoil of the nucleus results, depending on the material, in phonons, scintillation light or an ionisation signal. One also hopes to produce dark matter particles in collider experiments at the LHC. A modern overview about properties and candidates for dark matter is [3]. A general introduction to cosmology can be found in [2, 19].

Since the universe is still in an early stage of its expansion the previous history of our universe would be similar in all three cases. The age of a universe with a sub-critical density is given by the inverse Hubble constant

$$t_0 = \frac{1}{H_0}, \quad (20.4)$$

and is about 14 billion years.

**The first three minutes of the universe** In the initial phase of the universe all the (anti)particles and the gauge bosons were in thermodynamical equilibrium, i.e., there was so much thermal, and thus kinematical, energy available that all the (anti)particles could transform into each other at will. There was therefore no difference between quarks and leptons, which means that the strength of all the interactions was the same.

After about  $10^{-35}$  s the temperature had decreased so much due to the expansion that a phase transition took place and the strong interaction decoupled from the electroweak interaction, i.e., the strongly interacting quarks barely interacted with the leptons any more. At this stage the ratio between the numbers of quarks and photons was fixed at about  $10^{-9}$ .

After about  $10^{-11}$  s, at a temperature  $kT \approx 100$  GeV, a further phase transition took place in which the weak interaction decoupled from the electromagnetic interaction. We will discuss this process below.

When, after about  $10^{-6}$  s, the continuous expansion of the universe had lowered its temperature down to  $kT \approx 100$  MeV, which is the typical energy scale for hadronic excitations, the quarks formed bound states in the shape of baryons and mesons. The protons and neutrons so-produced were in thermal equilibrium due to weak processes.

After about 1 s and at a temperature  $kT \approx 1$  MeV, the difference between the neutron and proton masses, the neutrinos had too little energy to maintain the state of equilibrium between the protons and neutrons. They decoupled from matter, i.e., they henceforth essentially no longer interacted at all and propagated freely through the universe. Meanwhile the ratio of protons to neutrons increased up to a value of 7.

After about 3 min of expansion the temperature had fallen to  $kT \approx 100$  keV. From this moment the thermal equilibrium between nucleons and photons was broken, since the photon energies were no longer sufficient to break up the light nuclei, through photofission processes, into their constituents at the same pace as they were produced by nucleon fusion. In this phase the big bang nucleosynthesis of deuterium, helium and lithium nuclei took place.

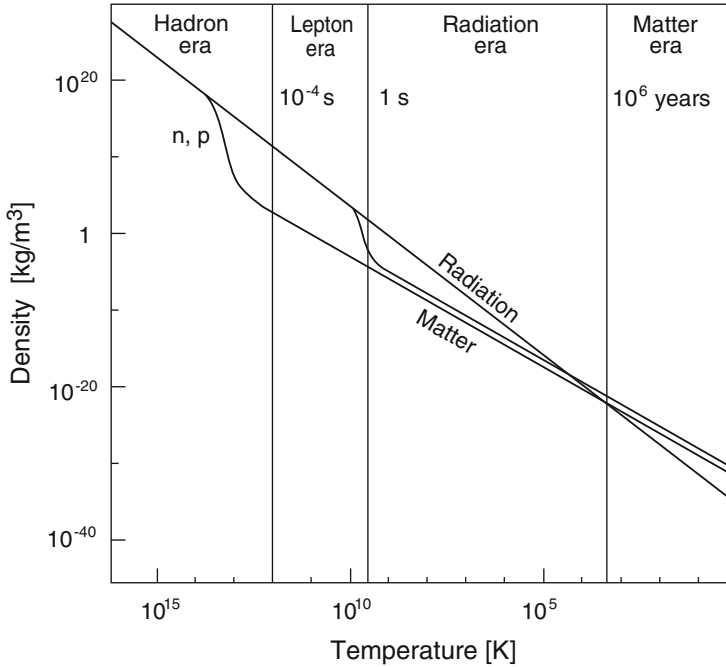


**Fig. 20.9** The evolution of the energy density of the universe, as a function of temperature, after the electroweak phase transition ( $T \approx 10^{15}$  K). In the early development of the universe radiation was in thermal equilibrium with matter and antimatter. Over a period of time matter decoupled from radiation and the matter and radiation energy densities developed different temperature dependencies, so that the universe finally became matter dominated

Figure 20.9 schematically shows the early history of the universe from the electroweak phase transition on. The curves represent the time (or temperature) dependent evolution of the energy density of radiation and matter. One can see the sharp drop in the energy density caused by the expansion of the universe. At temperatures of  $10^{13}$  K the hadrons, and later the leptons, decouple from the radiation. At  $T \approx 10^4$  K a matter dominated universe takes over from a previously radiation dominated universe. The current temperature of the universe is 2.73 K, the temperature of the cosmic background radiation.

Below we want to delve further into some important events from this early history of the universe.

**Matter-antimatter asymmetry** All observations show that the present universe is made up solely of matter and there is no evidence for some parts of the universe being composed of antimatter. Since according to our ideas all (anti)particles at a very early stage of the universe were in thermal equilibrium, i.e., fermion-antifermion creation from gauge bosons was just as frequent as fermion-antifermion annihilation into gauge bosons, then if this symmetry had survived the development

of the universe, there ought to be just as many fermions as antifermions or, more especially, as many quarks as antiquarks (which means as many baryons and antibaryons) in the universe. Furthermore there ought to be free photons which were produced in fermion-antifermion annihilation, but which due to the expansion and cooling of the universe could not go through the reverse reaction. One finds today that the ratio of baryons to photons is  $6 \cdot 10^{-10}$ . If all of these photons came from quark-antiquark annihilation, then a quark-antiquark asymmetry in the hot plasma of the early universe of

$$\Delta N_q = \frac{N_q - N_{\bar{q}}}{N_q + N_{\bar{q}}} = 6 \cdot 10^{-10} \quad (20.5)$$

would be sufficient to explain the current observed matter-antimatter asymmetry. The question is how did this small but decisive surplus of quarks arise in the early universe?

To generate a matter-antimatter asymmetry we have to fulfil three conditions: CP violation, baryon number violation and thermal non-equilibrium. In the framework of *grand unified theories*, GUTs, one can imagine that all of these conditions could be fulfilled.<sup>3</sup> Consider the situation of the universe at time  $t < 10^{-35}$  s. At this moment all (anti)fermions were equivalent, so they could be transformed into each other which could in certain reactions lead to a violation of baryon number. A hypothetical exchange particle, which mediates such a transition, is the X boson whose mass would be about  $10^{14}$  GeV/ $c^2$ . These X bosons could be produced as real particles at sufficiently high energies and would decay into a quark and an electron, similarly the  $\bar{X}$  boson decays into an antiquark and a positron. CP violation in the decay of the X boson would mean that the decay rates of the X and  $\bar{X}$  bosons would not be exactly equal. In thermal equilibrium, i.e., at temperatures or energies above the mass of the X boson, the effect of CP violation on the baryon number would be eliminated since the creation and decay of the X and  $\bar{X}$  bosons would be in equilibrium. This equilibrium would first be destroyed by the cooling of the universe and the asymmetry of the CP violating decay of the X boson would lead to a quark surplus, which eventually would be responsible for the matter-antimatter asymmetry we observe in the universe around us. The creation of a baryon excess from an initially baryon-antibaryon symmetric situation is called *baryogenesis*.

There are searches in progress for evidence of the existence of systems with CP violation and baryon number violation in the present universe. As discussed in Sects. 15.4 and 15.5, CP violation has been detected in  $K^0$  and  $B^0$  decays, but the observed effect is not sufficient to explain the matter-antimatter asymmetry. Experiments looking for proton decay have so far not yielded any evidence for baryon number violation.

---

<sup>3</sup>In principle the standard model of particle physics fulfils the three conditions, but predicts a matter-antimatter asymmetry that is smaller than the observed one (20.5) by ten orders of magnitude.

The discovery of small but non-zero neutrino mass receives in this context an important significance: in Sect. 11.4 we have outlined the seesaw mechanism as an explanation for the smallness of neutrino mass. The heavy Majorana neutrinos that were introduced, having masses of typically  $10^{15}$ – $10^9$  GeV/ $c^2$  can be produced in the hot early universe. If their interactions, which lead in particular to decay into leptons, violate the CP symmetry, then due to their Majorana nature more leptons than antileptons are generated. The necessary departure from thermal equilibrium would be caused by the cooling of the universe. Non-perturbative standard model processes, which we will not discuss in detail here, transform this lepton asymmetry into a baryon asymmetry. The generation of a baryon excess via a lepton excess is called *leptogenesis*. Therefore, the search for CP violation in the lepton sector, and the proof that lepton number conservation is indeed violated, is conceptually of great importance (see Sect. 11.4).

**Electroweak phase transition** Let us now consider the universe at the age of just  $10^{-11}$  s when it had a temperature of  $kT \approx 100$  GeV. It is believed that one can reconstruct the development of the universe from what is now known of elementary particle physics back to this stage. Extrapolations further back into the past may be based on plausible assumptions but they are in no way proven.

It is believed that the *electroweak phase transition* took place at this stage. Only after this phase transition did the now known properties of the elementary particles establish themselves. A loss of symmetry and an increase in order is characteristic of a phase transition of this type; just as in the phase transition from the paramagnetic to the ferromagnetic phase in iron when it drops below the Curie temperature. For temperatures equivalent to energies  $>100$  GeV, in other words before the phase transition, the photon, W and Z gauge bosons had similar properties and the distinction between the electromagnetic and weak forces was removed. In this state there was also no significant difference between electrons and neutrinos. Below the critical temperature this symmetry was, however, destroyed. This phenomenon, known in the standard model of elementary particle physics as *spontaneous symmetry breaking*, caused the W and Z bosons to acquire their large masses from so-called Higgs fields and the elementary particles took on the properties that we are now familiar with (cf. Sect. 12.4).

Although today elementary particles may be accelerated up to energies of a few TeV and the W and Z bosons have been experimentally produced and detected, it will not be possible to reproduce in the laboratory the high energy-densities of  $10^8$  times the nuclear density which existed at the electroweak phase transition. We can therefore only try to reproduce and to demonstrate the traces left by the phase transition, i.e., the W, Z and Higgs bosons, so as to use them as witnesses of what went on in the initial stages of the universe.

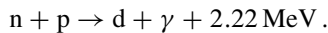
**Hadron formation** An additional phase transition took place when the universe was about  $1 \mu\text{s}$  old. At this stage the universe had an equilibrium temperature  $kT \approx 100$  MeV. The hadrons constituted themselves in this phase from the previously free quarks and gluons (*quark-gluon plasma*). Mostly nucleons were formed in this way.

Since the masses of the u- and d-quarks are very similar, they first formed roughly the same numbers of protons and neutrons, which initially existed as free nucleons since the temperature was too high to permit the formation of nuclei. These protons and neutrons were in thermal equilibrium until the temperature of the universe had sunk so much that the reaction rates for neutron creation processes (e.g.,  $\bar{\nu}_e p \rightarrow e^+ n$ ) were, as a consequence of the greater mass of the neutron, significantly less than that of the inverse processes of proton formation (e.g.,  $\bar{\nu}_e p \leftarrow e^+ n$ ). Thenceforth the numerical ratio of neutrons to protons decreased.

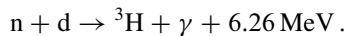
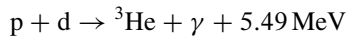
There are currently attempts to simulate this transition from a quark-gluon plasma to a hadronic phase in heavy ion reactions. In these reactions one tries to first create a quark-gluon plasma through highly energetic collisions of ions, in which the matter density is briefly increased to a multiple of the usual nuclear density. In such a state the quarks should only feel the short-range and not the long-range part of the strong potential, since this last should be screened by their tightly packed neighbours. In such a situation the quarks may be viewed as quasi-free and form a quark-gluon plasma. Such a quark-gluon plasma has, however, not yet been indubitably generated and a study of the transition to the hadronic phase is thus only possible in a rather limited fashion.

In the universe the transition from a quark-gluon plasma to the hadronic phase took place via the equilibrium temperature dropping at low matter densities. In the laboratory it is attempted to fleetingly create this transition by varying the matter density at high temperature (cf. Fig. 20.8 and Sect. 20.3).

**Primordial synthesis of the elements** At  $t = 200$  s in the cosmological calendar, the composition of baryonic matter was 88 % protons and 12 % neutrons. The creation of deuterium nuclei by the fusion of neutrons and protons was, until this stage, in equilibrium with the inverse reaction, the photodisintegration of the deuteron into a proton and a neutron, and the lifetime of the deuterons was extremely short. But now the temperature dropped below the level where the energy of the electromagnetic radiation sufficed to maintain the photodisintegration of the deuterons. Now long-lived deuterons were created by the reaction



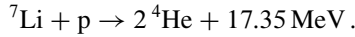
The lifetime of these deuterons was now limited by its fusion with protons and neutrons



Finally the particularly stable  ${}^4\text{He}$  nucleus was created in reactions like  ${}^3\text{H} + p$ ,  ${}^3\text{He} + n$ ,  ${}^3\text{He} + d$  and  $d + d$ . The Li nuclei created by  ${}^4\text{He} + {}^3\text{H} \rightarrow {}^7\text{Li} + \gamma + 2.47 \text{ MeV}$



were on the other hand immediately destroyed again by the highly exothermic reaction



Essentially all of the neutrons ended the primordial nucleosynthesis phase inside  ${}^4\text{He}$ , which thus constitutes about 24 % of the mass of the universe.

Only traces of deuterium,  ${}^3\text{He}$  and  ${}^7\text{Li}$  are still present, so at that moment the greatest part of the baryonic mass must have been in the form of protons. Since there are no stable nuclei with masses  $A = 5$  and  $A = 8$  it was not possible at that stage of the universe's development to build up nuclei heavier than  ${}^7\text{Li}$  through fusion processes. Such nuclei could only be produced much later in stellar interiors.

The primordial element-synthesis phase ended after about 10 min when the temperature had dropped so far that the Coulomb barrier prevented further fusion processes. The much later synthesis of heavy nuclei inside stars has not altered the composition of baryonic matter significantly. The ratio of hydrogen to helium which is observed in the present universe (cf. Fig. 2.2) is in excellent agreement with the theoretically calculated value. This is a strong argument in favour of the big bang model.

**Cosmic microwave background** The expanding universe, the helium to hydrogen ratio as the signature of the primordial synthesis of the elements and the cosmic microwave background (CMB) are the three most important experimental observations supporting the big bang model of the universe.

After the “first ten minutes”, the universe was composed of a plasma of fully ionised hydrogen and helium and about  $10^{10}$  times as many photons. The energy density in the universe was radiation dominated. The main mechanism for energy transport in this period was Compton scattering. The photon mean free path was small at the cosmic scale and the universe opaque.

One would expect that the decoupling of radiation from matter started when the temperature became too low to keep the thermal equilibrium via the reaction



If this process took place under equilibrium conditions the decoupling temperature would be  $kT_{\text{dec}} = 0.32 \text{ eV}$  ( $T_{\text{dec}} \approx 3,700 \text{ K}$ ).

However, the recombination of hydrogen actually started later, at somewhat lower temperatures than  $kT = 0.32 \text{ eV}$ . The reason is as follows. Hydrogen can be ionised by multiple absorption of low-energy photons from  $2S$  or  $2P$  excited states. Later recombination by a cascade passing through the  $2P$  state can produce a photon of the correct energy (Lyman- $\alpha$  line), which in turn can excite another atom to the same state which then can be ionised by abundant low-energy photons. As photons from the  $2P \rightarrow 1S$  transitions are confined in the universe, recombination is not possible via a direct cascade through the  $2P$  level. The only leakage of the Lyman- $\alpha$  photons passes through the two-photon decay of the  $2S$  state. The lifetime of this

state is  $\approx 0.1$  s; therefore, hydrogen recombination is a non-equilibrium process. The transition from an opaque to a transparent universe took place at  $T \approx 3,000$  K. Although the mean free path of photons increased dramatically at this temperature, photons still interacted with free electrons via Thomson scattering to a significant extent. Therefore, the photon background that we observe comes from the so-called last scattering surface, where Thomson scattering did not play a role any longer. This was the case about  $4 \times 10^5$  years after the big bang. At present the decoupled radiation is a perfect black body spectrum, with temperature  $T \approx 2.7$  K.

The cosmic background radiation is a rich source of information about the universe before the decoupling of the photons. The temperature fluctuations in order of  $10^{-5}$  have been interpreted as quantum fluctuations in the early universe. They were the seeds from which the galaxies later developed. The fact that the fluctuations have not been smeared out is seen as a proof for the universe to be flat, i.e., its density has the critical value [12].

## 20.5 Stellar Evolution and Element Synthesis

The close weave linking nuclear physics and astrophysics stretches back to the thirties when Bethe, Weizsäcker and others tried to draw a quantitative balance between the energy emitted by the Sun and the energy that could be released by the known nuclear reactions. It was, though, Eddington who in 1920 had recognised that nuclear fusion is the source of energy production in stars.

The basis for modern astrophysics was, however, laid by Fred Hoyle [14, 15] at the end of the forties. The research programme he proposed required a consistent treatment of astronomical observations, study of the plasma dynamics of stellar interiors and calculations of the sources of energy using the cross-sections for nuclear reactions measured in laboratories. Stellar evolution and the creation of the elements had to be treated together. The observed abundance of the elements around us had to be explicable from element synthesis in the early stages of the universe and from nuclear reactions in stars and this would thus be a decisive test of the consistency of stellar evolution models. The results of this programme were presented by E. Burbidge, G. Burbidge, Fowler and Hoyle [7].

Stars are produced by the contraction of interstellar gas and dust. This matter is almost solely composed of primordial hydrogen and helium. The contraction heats up the centre of the star. When the temperature and pressure are sufficiently large to render nuclear fusion possible, radiation is produced whose pressure prevents a further contraction of the star. The virial theorem for the gravitational force law implies a fall-off in the temperature of stars from their centres to their exteriors. This means that at any separation from the centre of a star the average kinetic energy of an atom is half the size of its potential energy. The energy produced in nuclear reactions is primarily transported by radiation to the surface. The matter in the star is not greatly mixed up in the process. During the life of the star its chemical composition

changes in the regions where the nuclear reactions take place, in other words most of all in the core of the star.

**Fusion reactions** A star in equilibrium produces as much energy through nuclear reactions as it radiates. The equilibrium state is thus highly dependent upon the rate of the fusion reactions. Energy may be released by fusing light nuclei together. It is especially effective to fuse hydrogen isotopes together to form  ${}^4\text{He}$ , since the difference between its binding energy per nucleon, 7.07 MeV, and that of its neighbours is especially large (cf. Fig. 2.4). We will treat this reaction in more detail below. Fusion processes require a sufficiently high temperature, or energy, for the reaction partners to surmount the Coulomb barrier. It is not necessary that the energy of the nuclei involved is actually above the barrier, rather what really matters, in analogy to  $\alpha$ -decay, is the probability,  $e^{-2G}$ , that the Coulomb barrier may be tunnelled through. The Gamow factor,  $G$ , depends upon the relative velocities and the charge numbers of the reaction partners. It is given by (see Sect. 3.15)

$$G = \frac{\pi\alpha Z_1 Z_2}{v/c} \propto \frac{1}{\sqrt{E}}. \quad (20.7)$$

Fusion reactions in stars normally take place below the Coulomb barrier and through the tunnel effect.

The reaction rate per unit volume is according to (4.3) and (4.4) given by

$$\dot{N} = n_1 n_2 \langle \sigma v \rangle, \quad (20.8)$$

where  $n_1$  and  $n_2$  are the particle densities of the two fusion partners. We have written the average value  $\langle \sigma v \rangle$  since the velocity distribution in a hot stellar plasma is given by a Maxwell-Boltzmann distribution

$$n(v) \propto e^{-mv^2/2kT} = e^{-E/kT} \quad (20.9)$$

and the cross-section  $\sigma$  of the fusion reaction depends strongly, through the Gamow factor, upon the relative velocity of the reaction partners. This average value must be calculated by integration over  $v$ . Figure 20.10 schematically shows the convolution of the Gamow factor with a Maxwell distribution. The overlap of the distributions fixes the reaction rate and the energy range for which fusion reactions are possible. This depends upon the plasma temperature and the charges of the fusion partners. The higher the charge numbers, the higher the necessary temperatures at which fusion reactions become possible.

In this way the lightest nuclide in the star's interior, hydrogen, is burnt up, i.e., fused together. When this is used up, the temperature has to increase drastically for helium and, later, other heavier elements to be able to fuse together. The length of the various burn-phases depends upon the mass of the star in question. For heavier stars the pressure and thus the density of the plasma at the centre is higher and so

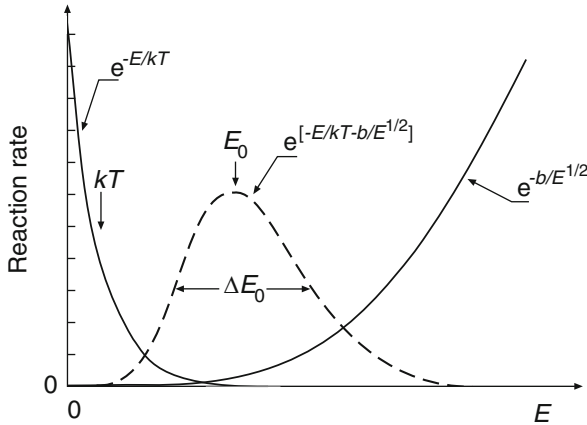
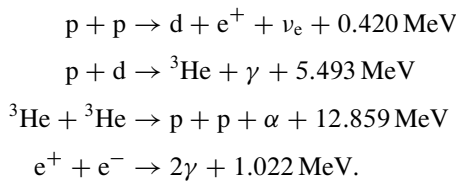


**Fig. 20.10** Schematic representation of the convolution of a Maxwell distribution  $\exp\{-E/kT\}$  with a Gamow factor  $\exp\{-b/E^{1/2}\}$  as used to calculate the rate of fusion reactions. The product of the curves is proportional to the fusion probability (dashed curve). Fusion essentially takes place in a very narrow energy interval with width  $\Delta E_0$ . The integral over this curve is proportional to the total reaction rate

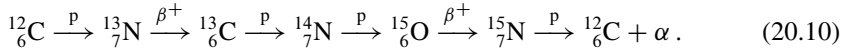
the reaction rate is higher compared to lighter stars. Thus heavier stars are shorter lived than heavy ones.

**Hydrogen burning** In the formation phase of stars with masses greater than about one tenth of a solar mass, the temperatures inside the stars reach values of  $T > 10^7$  K, and thus the first nuclear fusion processes are possible. In the early part of their lives stars gain their energy by burning hydrogen into helium in the *proton-proton cycle*:



All in all, in the net reaction  $4p \rightarrow \alpha + 2e^+ + 2\nu_e$ , 24.69 MeV of energy is released. The total released energy is 26.73 MeV when also the contribution from  $e^+e^-$  pair annihilation is taken into account. Of this  $\approx 0.3$  MeV is on average taken by neutrinos and thus lost to the star. The first reaction is the slowest in the cycle since it requires not only the fusion of two protons but also the simultaneous transformation of a proton into a neutron via a weak interaction process. This reaction thus determines the lifetime of the star in the first stage of its evolution. There are various possible branches to the proton-proton cycle, but they are of little importance for energy production in stars.

As long as the supplies of hydrogen are adequate the star remains stable. For our Sun this period will last about  $10^{10}$  years, of which about half are already gone. Larger stars with higher central densities and temperatures burn faster. If in such stars  $^{12}\text{C}$  is already present, then the *carbon cycle* can take place:



The amount of carbon which was transformed at the beginning of the cycle is again available for further use at the end and thus it acts as a catalyst. The net reaction is as in the proton-proton cycle,  $4\text{p} \rightarrow \alpha + 2\text{e}^+ + 2\nu_{\text{e}}$ , and the amount of energy released is also 24.69 or 26.73 MeV, respectively. The carbon cycle can take place much faster than the proton-proton cycle. But this new cycle only starts at higher temperatures due to the greater Coulomb barrier. In the Sun this cycle contributes by about 1.6 % to the energy production.

**Helium burning** Once the hydrogen supplies have dried up, the core of the star, which is now composed of helium, cannot withstand the pressure and collapses. For stars much smaller than the Sun the gravitational pressure is not great enough to ignite further fusion reactions. Without the radiative pressure, the star collapses under its own gravity to a planet-sized sphere. Fermi pressure is the first thing to stop the collapse and the star becomes a white dwarf.

Heavier stars heat up until they reach a temperature of about  $10^8$  K and a density of  $10^8$  kg/m<sup>3</sup>. Helium burning then starts up. There is still some hydrogen in the outermost regions of the star, which is heated up by the helium burning in the hot central region until in this layer hydrogen burning commences. The outer mantle swells up through the radiation pressure. Since the surface area increases the surface temperature drops, even though the energy production is increasing in this stage. The colour of the star turns red and it becomes a red giant.

A synthesis of nuclei heavier than  $^4\text{He}$  appears to be impossible because there are no stable nuclei with  $A = 5$  and  $A = 8$ .  $^8\text{Be}$  has a lifetime of only  $10^{-16}$  s, and  $^5\text{He}$  and  $^5\text{Li}$  are still less stable. But in 1952 E. Salpeter showed how heavy nuclei could be produced by helium fusion [18].

At high temperatures around  $10^8$  K, which are present in stellar interiors, the unstable  $^8\text{Be}$  nucleus can be formed from helium-helium fusion and equilibrium for the reaction  $^4\text{He} + ^4\text{He} \leftrightarrow ^8\text{Be}$  is created. This reaction is only possible in sufficient amounts at such high temperatures, since as well as the Coulomb barrier an energy level difference of 92 keV must be overcome (Fig. 20.11). At a density of  $10^8$  kg/m<sup>3</sup> in the interior of the star an equilibrium concentration of one  $^8\text{Be}$  nucleus for  $10^9$   $^4\text{He}$  nuclei is produced. This minuscule proportion would be enough to produce sizable amounts of carbon via  $^4\text{He} + ^8\text{Be} \rightarrow ^{12}\text{C}^*$  if there were a  $0^+$  state in  $^{12}\text{C}$  a little above the production threshold over which a resonant reaction can take place. Shortly after this suggestion was made such a state at an excitation energy of 7.654 MeV was indeed found [8]. This state decays with a probability of  $4 \cdot 10^{-4}$  into the  $^{12}\text{C}$  ground state (Fig. 20.11). Although this state is 287 keV above the  $^8\text{Be} + \alpha$  threshold, it can indeed be populated by reaction partners from the high-energy tail

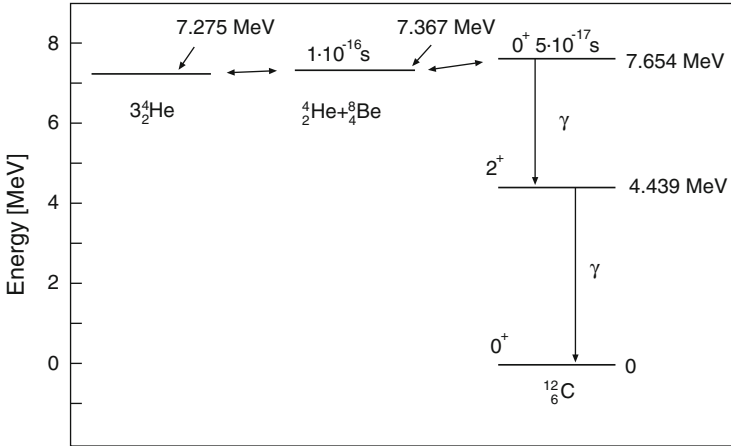
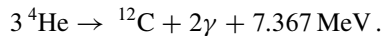


**Fig. 20.11** Energy levels of the system:  $3\alpha$ ,  $\alpha + {}^8\text{Be}$  and  ${}^{12}\text{C}$ . Just above the ground states of the  $3\alpha$  system and of the  $\alpha + {}^8\text{Be}$  system there is a  $0^+$  state in the  ${}^{12}\text{C}$  nucleus, which can be created through resonant fusion of  ${}^4\text{He}$  nuclei. This excited state decays with a 0.04 % probability into the  ${}^{12}\text{C}$  ground state

of the Maxwell velocity distribution. The net reaction of helium fusion into carbon is thus

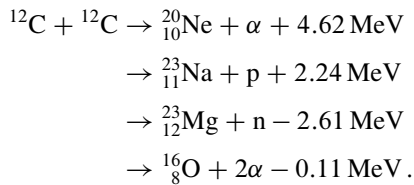


This so-called triple- $\alpha$  reaction plays a key role in building up the heavier elements of the universe. Approximately 1 % of all the nuclei in the universe are heavier than helium and they were practically all created in the triple- $\alpha$  process.

**Burning into iron** When the helium supplies have been used up and the star is primarily made up of  ${}^{12}\text{C}$ , then stars with masses of the order of the solar mass turn into white dwarfs.

More massive stars go through further phases of development. According to the temperature  $\alpha$ -particles can fuse with  ${}^{12}\text{C}$ ,  ${}^{16}\text{O}$ ,  ${}^{20}\text{Ne}$  etc., or carbon, oxygen, neon and silicon can simply fuse with each other.

As an example let us mention the reactions



Other reactions follow the same pattern and populate all the elements between carbon and iron.

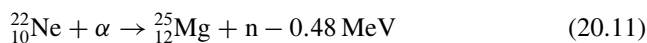
The heavier the fusing nuclei are, the greater is the Coulomb repulsion and so the temperature must then be higher for fusion to take place. Since the temperature is greatest at the centre and falls off towards the surface, an onion-like stellar structure is formed. At the centre of the star iron is synthesised, towards the edges ever lighter elements are made. In the outermost layers the remnants of hydrogen and helium are burnt off.

The burning of the heavier nuclei takes place at ever shorter time scales, since the centre of the star needs to be ever hotter, but simultaneously the energy gained per nucleon-fusion decreases as the mass number increases (Fig. 2.4). The final phase, the fusion of silicon to form iron, lasts for only a matter of days [4]. The process of nuclear fusion in stars concludes with the formation of iron since iron has the largest binding energy per nucleon.

When the centre of the star is made of iron, there is no further source of energy available. There is neither radiative pressure nor thermal motion to withstand gravity. The star collapses. The outer material of the star collapses as if in free fall to the centre. Through this implosion the nuclear matter at the centre reaches a tremendous density and temperature which leads to an enormous explosion. The star emits at a stroke more energy, typically about  $10^{47}$  J, than it has previously created in its entire life. This is called a supernova. The greater part of the stellar matter is then flung out into interstellar space and can later be used as building material for new stars. If the mass of the remaining stellar core is smaller than the mass of the Sun, the star ends its life as a white dwarf. If it is between one and two solar masses a neutron star is born. The matter from still heavier remnants ends up as a black hole. It is interesting to note that such an explosion of a star as supernova is a neutrino source of extremely high intensity. These neutrinos are produced, e.g., via the reaction  $p + e \rightarrow n + \nu_e$  at the beginning of the collapse and carry about 99% of the vast amount of energy released in a supernova explosion.

**Synthesis of heavier nuclei** Nuclei heavier than iron are synthesised by neutron accumulation. We distinguish between two processes.

*The slow process (s-process).* In the burning phase of the star neutrons are produced in nuclear reactions such as, e.g.,



or



Through repeated neutron captures, neutron-rich isotopes are produced. If the isotopes are unstable under  $\beta$ -decay, they decay into their most stable isobar (Figs. 3.2 and 3.3). Thus the synthesis of heavier and heavier elements can proceed along a stability valley (Fig. 3.1). A limit is, however, reached at lead. Nuclei above lead are  $\alpha$ -unstable. Isotopes built up by the slow process then decay again into  $\alpha$ -particles and lead.

*The rapid process (r-process).* This process takes place during a supernova explosion when neutron fluxes of  $10^{32} \text{ m}^{-2} \text{ s}^{-1}$  can be reached and the successive accumulation of many neutrons is much quicker than  $\beta$ - or  $\alpha$ -decay processes. Elements heavier than lead can be produced in this process. The upper limit for the creation of transuranic elements is determined by spontaneous fission.

All the elements (apart from hydrogen and helium) which make up the Earth and ourselves came originally from the interior of stars and were (probably several times in fact) released through supernova explosions. Even the absolute amounts as well as the distribution of the elements which are heavier than helium may be calculated from the age of the universe and from cross-sections measured in laboratories. The results are in excellent agreement with the measured values of the abundance of the elements (Fig. 2.2). This is definitely one of the great triumphs of the joint efforts of nuclear and astrophysicists.

## Problems

### 1. Sun

The solar mass is  $M_{\odot} \approx 2 \cdot 10^{30} \text{ kg}$  ( $3.3 \cdot 10^5$  times the mass of the Earth). The chemical composition of the solar surface is 71 % hydrogen, 27 % helium and 2 % heavier elements (expressed as parts by mass). The luminosity of the Sun is  $4 \cdot 10^{26} \text{ W}$ .

- How much hydrogen is converted into helium every second?
- How much mass does the Sun lose in the same period?
- What fraction of the original hydrogen content has been converted into helium since the creation of the Sun ( $5 \cdot 10^9$  years)?
- How large was the loss of mass in the same period?
- Model calculations indicate that the Sun will burn hydrogen at a similar rate for a further  $5 \cdot 10^9$  years. A shortage of hydrogen will then force it into a red giant state. Motivate this time scale.

### 2. Supernova

A neutron star with mass,  $M = 1.5 M_{\odot}$  ( $\approx 3.0 \cdot 10^{30} \text{ kg}$ ), and radius  $R \approx 10 \text{ km}$  is the remnant of a supernova. The stellar material originates from the iron core ( $R \gg 10 \text{ km}$ ) of the supernova.

- How much energy was released during the lifetime of the original star by converting hydrogen into iron? (The binding energy of  $^{56}\text{Fe}$  is  $B = 8.79 \text{ MeV/nucleon}$ .) *NB:* Since after the implosion only a part of the original iron core remains in the neutron star, the calculation should be performed only for this mass.
- How much energy was released during the implosion of the iron core into a neutron star?
- In what form was the energy radiated off?



## References

1. P.A.R. Ade et al., arXiv:1303.5076
2. L. Bergström, A. Goobar, *Cosmology and Particle Astrophysics*, 2nd edn. (Springer, Berlin/Heidelberg/New York/Tokyo, 2006)
3. G. Bertone, *Particle Dark Matter* (Cambridge University Press, Cambridge, 2010)
4. H.A. Bethe, G. Brown, *Sci. Am.* **252**, 40 (1985)
5. A. Bohr, B.R. Mottelson, *Nuclear Structure* (Benjamin, New York, 1969)
6. C. Budtz-Jorgensen, H.-H. Knitter, *Nucl. Phys.* **A490**, 307 (1988)
7. E.M. Burbidge et al., *Rev. Mod. Phys.* **29**, 547 (1957)
8. C.W. Cook et al., *Phys. Rev.* **107**, 508 (1957)
9. T. Ericson, T. Mayer-Kuckuk, *Annu. Rev. Nucl. Sci.* **16**, 183 (1966)
10. D.J. Fixsen et al., *Astrophys. J.* **473**, 576 (1996)
11. P. Glässel et al., *Nucl. Phys.* **A502**, 315c (1989)
12. G. Hinshaw et al., *Astrophys. J. Suppl.* **170**, 288 (2007)
13. G. Hinshaw et al., *Astrophys. J. Suppl.* **208**, 19 (2013)
14. F. Hoyle. *Mon. Not. R. Astro. Soc.* **106**, 343 (1946)
15. F. Hoyle, *Astrophys. J. Suppl.* **1**, 121 (1954)
16. A.A. Penzias, R.W. Wilson, *Astrophys. J.* **142**, 419 (1965)
17. J. Pochodzalla et al., *Phys. Rev. Lett.* **75**, 1040 (1995)
18. E.E. Salpeter, *Astrophys. J.* **115**, 326 (1952)
19. S. Serjeant, *Observational Cosmology* (Cambridge University Press, Cambridge, 2010)
20. J.M. Smith, *Did Darwin Get It Right?* (Chapman & Hall, New York/London, 1989)

# Chapter 21

## Many-Body Systems in the Strong Interaction

*How many bodies are required before we have a problem? G. E. Brown points out that this can be answered by a look at history. In eighteenth-century Newtonian mechanics, the three-body problem was insoluble. With the birth of relativity around 1910 and quantum electrodynamics in 1930, the two- and one-body problems became insoluble. And within modern quantum field theory, the problem of zero bodies (vacuum) is insoluble. So, if we are out after exact solutions, no bodies at all is already too many!*

R. D. Mattuck [1]

In the second part of this book we have described how many-body systems may be built out of quarks. The strong interaction is responsible for the binding of these systems, which should be contrasted with the binding of atoms, molecules and solids which are held together by the electromagnetic interaction.

The systems which are built out of quarks – hadrons and nuclei – are complex quantum-mechanical systems. This complexity manifests itself in the systems’ many, apparently mutually incompatible facets. Some aspects of these systems may be understood in a single-particle picture, while some indicate the existence of large sub-structures and others are explained as collective effects of the entire system and finally some are chaotic and only amenable to a statistical description. Each of these concepts, however, only describes a single aspect of these systems.

**Quasi-particles** At sufficiently low excitation energies, many-body systems, even if they possess a complicated internal structure, may often be described as systems of so-called *quasi-particles*: instead of treating the elementary building blocks, together with their vast variety of mutual interactions, one works with “effective particles” (e.g., electrons and holes in semi-conductors). A large part of the interactions of the fundamental constituents with each other is thus incorporated into the internal structure of the quasi-particles which then, in consequence, only weakly interact with each other.

**Collective states** Another group of elementary low-energy excitations are the so-called collective states, where many building blocks of a system interfere coherently. Examples of this are lattice vibrations in a crystal (phonons) and waves on the surface of an atomic nucleus.

**Chaotic phenomena** For greater excitation energies all many-particle systems become more and more complex, until they can no longer be described quantitatively in terms of elementary excitations. Statistical phenomena, which have a universal character, and are thus independent of the details of the interaction, are observed.

**Hadrons** Little is so far known about the structure of hadrons. Their elementary constituents are gluons and quarks. However, in order to actually observe these experimentally, measurements at “infinitely” large momentum transfers would be necessary. Therefore even in deep-inelastic scattering one only ever observes effective quarks, i.e., many-particle systems. The success of QCD lies in the fact that it is able to quantitatively explain the dependence of the structure functions on the resolution. However, the absolute shape of the structure functions, i.e., hadronic structure, cannot yet be predicted even at large momentum transfers.

The structure of the nucleons depends, however, on the behaviour of quarks at relatively small momenta, since the energies of the excited states are only a few hundred MeV. At such low momentum transfers the coupling constant  $\alpha_s$  is so large that the standard QCD perturbative expansion is no longer applicable and we have to deal with a genuine many-particle system.

It has been seen that the spectroscopic properties of hadrons can be described simply in terms of constituent quarks and that one does not need to take the gluons into account. Constituent quarks are complex objects and not elementary particles: we have to understand them as *quasi-particles*. Their properties (e.g., their masses, sizes and magnetic moments) are distinctly different from those of the elementary quarks. It seems that a certain order in hadronic spectroscopy can be obtained by introducing these quasi-particles. The group-theoretical classification of excited states is in fact very successful, but the dynamics are not well understood. It is also not evident whether complex hadronic excitations can be described in the constituent-quark model.

Excited states of hadrons made out of light quarks are known only up to about 3 GeV. The resonances get broader and are more closely packed together as their energy increases. At energies  $\gtrsim 3$  GeV, no further resonance structures can be recognised. This could perhaps be a region where chaotic phenomena might be expected. However, they cannot be observed because of the large widths of the resonances.

Collective phenomena have also not yet been observed in hadrons. This may be due to the fact that the number of effective constituents is too small to produce coherent phenomena.

**Forces of the strong interaction** *Elementary* particles (quarks and leptons) interact through *elementary* forces which are mediated by the exchange of gluons, photons and the W and Z bosons. The forces between systems with internal structure (atoms, nucleons, constituent quarks) are of a more complicated nature and are themselves many-particle phenomena (e.g., the Van der Waals force or covalent binding forces).

To a first approximation the forces of the strong interaction between nucleons or between constituent quarks may be parametrised by effective forces. These are short-ranged and may be, depending upon spin and isospin, either attractive or repulsive. For constituent quarks the short distance interaction seems to be adequately described by one-gluon exchange with an effective coupling constant  $\alpha_s$  while at large distances many-gluon exchange is parametrised by a confinement potential. Two-gluon exchange (Van der Waals force) and two-quark exchange (covalent bond) presumably play a minor role in the interaction between two nucleons.

The short-range repulsion is, on the one hand, a consequence of the symmetry of the quark wave function of the nucleon, and, on the other hand, of chromomagnetic repulsion. The dominant part of the attractive nuclear force is mediated by the exchange of  $q\bar{q}$  pairs. It is not surprising that these pairs can be identified with the light mesons.

Within the nucleus, this force is also strongly modified by many-body effects (e.g., the Pauli principle). Hence in nuclear physics calculations, phenomenological forces, whose forms and parameters have to be fitted to experimental results, are frequently employed.

**Nuclei** The idea that nuclei are composed of nucleons is somewhat naive. It is more realistic to conceive of the constituents of the nucleus as quasi-nucleons. The properties of these quasi-particles are similar to those of the nucleons if they are close to the Fermi surface. Some low-energy nuclear phenomena (spin, magnetic moments, excitation energies) can be described by the properties of individual, weakly bound nucleons in the outermost shells or by holes in an otherwise closed shell.

Strongly bound nucleons cannot be assigned to individual states of the shell model. This can be seen, for example, in the very broad states observed in quasi-elastic scattering. In contradistinction, a strongly bound  $\Lambda$  particle inside the nucleus can, it seems, be adequately described as a quasi-particle even in deeply bound states.

Even larger structures in the nucleus may behave like quasi-particles. Pairs of neutrons or protons can couple in the nucleus to form  $J^P = 0^+$  pairs, i.e., quasi-particles with boson properties. This pairing is suspected to lead to superfluid phenomena in nuclei, analogous to Cooper pairs in superconductors and atomic pairs in superfluid  $^3\text{He}$ . As we have seen, the moments of inertia of rotational states can be qualitatively described in a two-fluid model composed of a normal and of a superfluid phase.

Some nuclear properties can be understood as collective excitations. Such effects can most clearly be observed in heavy nuclei. For example, giant dipole resonances can be interpreted as density oscillations. A nucleus, since it is a finite system, may also undergo shape oscillations. In analogy to solid state physics, quadrupole excitations are described in terms of phonons. The rotational bands of deformed nuclei have an especially collective nature.

At higher energies the collective and quasi-particle character of the excitations is lost. This is the start of the domain of configuration admixtures, where states are built from superpositions of collective and/or particle-hole wave functions. At even higher excitation energies the nuclear level density increases exponentially with the excitation energy and a quantitative description of the individual levels becomes impossible. The great complexity of the levels makes a new description using statistical methods possible.

**Digestive** In our approach to complex systems we have tried to let ourselves be guided by our understanding of more elementary systems. This helped us to gain a deeper insight into the architecture of more complex systems, and yet we had to introduce new *effective* building blocks, which mutually interact via effective forces, to obtain a *quantitative* treatment of complex phenomena.

Thus in hadron spectroscopy, we used constituent quarks, and not the quarks from the underlying theory of QCD; the interactions between nucleons are best described in terms of meson exchange, not by the exchange of gluons and quarks; in the nucleus effective forces are usually employed instead of the forces known from the nucleon-nucleon interaction and the richness of collective states in nuclei are, even though we have sketched the connection to the shell model, quantitatively better described in terms of collective variables and not in terms of single-particle excitations. This all means that the best description always seems to come from the framework of an “effective theory” chosen according to our experimental resolution. This is by no means a peculiarity of the complex systems of the strong interactions, but is a general property of many-body systems.

Our modern struggles to improve our understanding are fought on two frontiers: physicists are testing whether the modern standard model of elementary particle physics is indeed fundamental or itself “just” an effective theory, and are simultaneously trying to improve our understanding of the regularities of the complex systems of the strong interaction.

*And it shall be, when thou hast made an end of reading this book, that thou shalt bind a stone to it, and cast it into the midst of Euphrates.*

Jeremiah 51. 63

## Reference

1. R.D. Mattuck, *A Guide to Feynman Diagrams in the Many-Body Problem*, 2nd edn. (McGraw-Hill, New York, 1976)

# Appendix A

In the main body of this book we have described particle and nuclear physics and the underlying interactions concisely and in context. We have here and there elucidated the basic principles and methods of the experiments that have led us to this knowledge. We now want to briefly describe the individual tools of experimental physics – the particle accelerators and detectors – whose invention and development have often been a sine qua non for the discoveries discussed here. More detailed discussions may be found in the literature [4, 7, 11, 15–17].

## A.1 Accelerators

Particle accelerators provide us with different types of particle beams whose energies (at the time of writing) can be anything up to a few TeV ( $10^6$  MeV). These beams serve on the one hand as “sources” of energy which if used to bombard nuclei can generate a variety of excited states or indeed new particles. On the other hand they can act as “probes” with which we may investigate the structure of the target particle.

The most important quantity, whether we want to generate new particles or excite a system into a higher state, is the centre-of-mass energy  $\sqrt{s}$  of the reaction under investigation. In the reaction of a beam particle a with total energy  $E_a$  with a target particle b which is at rest this is

$$\sqrt{s} = \sqrt{2E_a m_b c^2 + (m_a^2 + m_b^2)c^4}. \quad (\text{A.1})$$

In high energy experiments where the particle masses may be neglected in comparison to the beam energy this simplifies to

$$\sqrt{s} = \sqrt{2E_a m_b c^2}. \quad (\text{A.2})$$

The centre-of-mass energy for a stationary target only, we see, grows with the square root of the beam particle's energy.

If a beam particle with momentum  $p$  is used to investigate the structure of a stationary target, then the best possible resolution is characterised by its reduced de Broglie wavelength  $\lambda = \hbar/p$ . This is related to the energy  $E$  through (4.1).

All accelerators essentially consist of the following: a particle source, a structure to actually do the accelerating and an evacuated beam pipe. It should also be possible to focus and deflect the particle beam. The accelerating principle is always the same: charged particles are accelerated if they are exposed to an electric field. A particle with charge  $Ze$  which traverses a potential difference  $U$  receives an amount of energy,  $E = ZeU$ . In the following we wish to briefly present the three most important types of accelerators.

**Electrostatic accelerators** In these accelerators the relation  $E = ZeU$  is directly exploited. The main components of an electrostatic accelerator are a high voltage generator, a terminal and an evacuated beam pipe. In the most common sort, the *Van de Graaff accelerator*, the terminal is usually a metallic sphere which acts as a capacitor with capacitance  $C$ . The terminal is charged by a rotating, insulated band and this creates a high electric field. From a grounded potential positive charges are brought onto the band and then stripped off onto the terminal. The entire set up is placed inside an grounded tank which is filled with an insulating gas (e.g.,  $\text{SF}_6$ ) to prevent premature discharge. The voltage  $U = Q/C$  which may be built up in this way can be as much as 15 MV. Positive ions, produced in an ion source, at the terminal potential now traverse inside the beam pipe the entire potential difference between the terminal and the tank. Protons can in this way reach kinetic energies up to 15 MeV.

Energies twice as high may be attained in tandem Van de Graaff accelerators (Fig. A.1). Here the accelerating potential is used twice over. Negative ions are first produced at ground potential and then accelerated along a beam pipe towards the terminal. A thin foil, or similar, placed there strips some of the electrons off the ions and leaves them positively charged. The accelerating voltage now enters the game again and protons may in this way attain kinetic energies of up to 30 MeV. Heavy ions may lose several electrons at once and consequently reach even higher kinetic energies.

Van de Graaff accelerators can provide reliable, continuous particle beams with currents of up to  $100\ \mu\text{A}$ . They are very important workhorses for nuclear physics. Protons and both light and heavy ions may be accelerated in them up to energies at which nuclear reactions and nuclear spectroscopy may be systematically investigated.

**Linear accelerators** GeV-type energies may only be attained by repeatedly accelerating the particle. Linear accelerators, which are based upon this principle, are made up of many accelerating tubes laid out in a straight line and the particles progress along their central axis. Every pair of neighbouring tubes have oppositely arranged potentials such that the particles between them are accelerated, while the interior of the tubes is essentially field free (Wideröe type). A high frequency

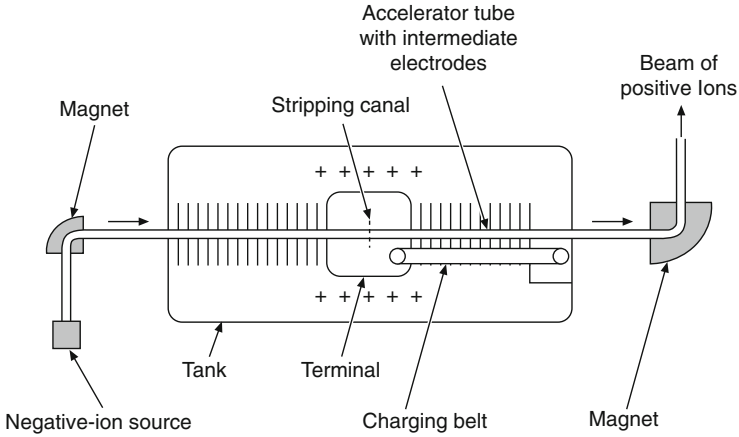


**Fig. A.1** Sketch of a tandem Van de Graaff accelerator. Negative ions are accelerated from the left towards the terminal where some of their electrons are stripped off and they become positively charged. This causes them to now be accelerated away from the terminal and the potential difference between the terminal and the tank is traversed for a second time

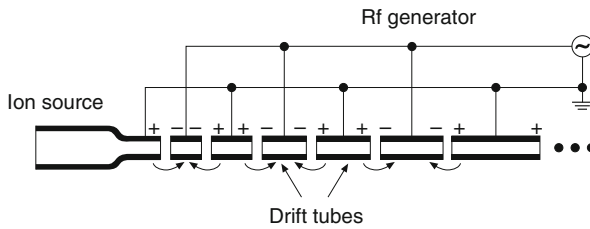


**Fig. A.2** Sketch of the fundamentals of a (Wideröe type) linear accelerator. The potentials of the tubes shown are for one particular moment in time. The particles are accelerated from the source to the first drift tube. The lengths  $L_i$  of the tubes and the generator frequency  $\omega$  must be adjusted to each other so that we have  $L_i = v_i \pi / \omega$  where  $v_i$  is the particle velocity at the  $i$ th tube. This depends both upon the generator voltage and the type of particle being accelerated

generator changes the potentials with a period such that the particles between the tubes always feel an accelerating force. After passing through  $n$  tubes the particles will have kinetic energy  $E = nZe U$ . Such accelerators cannot produce continuous particle beams; they accelerate packets of particles which are in phase with the generator frequency.

Since the generator frequency is fixed, the lengths of the various stages need to be adjusted to fit the speed of the particles as they pass through (Fig. A.2). If we have an electron beam this last subtlety is only relevant for the first few acceleration steps, since the small electron mass means that their velocity is very soon nearly equal to the speed of light. On the other hand the tube lengths generally need to be continually altered along the entire length of proton linear accelerators. The final



energy of a linear accelerator is determined by the number of tubes and the maximal potential difference between them.

At present the largest linear accelerator in the world, where many important experiments on deep inelastic scattering off nucleons have been carried out, was the roughly 3 km long electron linear accelerator at the Stanford Linear Accelerator Center (SLAC). Here electrons passed through around 100,000 accelerating stages to reach energies of about 50 GeV.

**Synchrotrons** While particles pass through each stage of a linear accelerator just once, synchrotrons, which have a circular form, may be used to accelerate particles to high energies by passing them many times through the same accelerating structures.

The particles are kept on their circular orbits by magnetic fields. The accelerating stages are mostly only placed at a few positions upon the circuit. The principle of the synchrotron is to synchronously change the generator frequency  $\omega$  of the accelerating stages together with the magnetic field  $B$  in such a way that the particles, whose orbital frequencies and momenta  $p$  are increasing as a result of the acceleration, always feel an accelerating force and are simultaneously kept on their assigned orbits inside the vacuum pipe. This means that the following constraints must be simultaneously fulfilled:

$$\omega = n \cdot \frac{c}{R} \cdot \frac{pc}{E} \quad n = \text{positive integer} \quad (\text{A.3})$$

$$B = \frac{p}{ZeR}, \quad (\text{A.4})$$

where  $R$  is the radius of curvature of the synchrotron ring. Technical limitations upon the  $B$  and  $\omega$  available mean that one has to inject preaccelerated particles into synchrotron rings whereupon they can be brought up to their preassigned final energy. Linear accelerators or smaller synchrotrons are used in the preacceleration stage. Synchrotrons also only produce packets of particles and do not deliver continuous beams.

High particle intensities require well focused beams close to the ideal orbit. Focusing is also of great importance in the transport of the beam from the preaccelerator to the main stage and from there to the experiment (injection and extraction). Magnetic lenses, made from quadrupole magnets, are used to focus the beam in high energy accelerators. The field of a quadrupole magnet focuses charged particles in one plane on its central axis and defocuses them on the other plane perpendicular to it. An overall focusing in both planes may be achieved by putting a second quadrupole magnet, whose poles are rotated relative to those of the first one through  $90^\circ$ , after the first magnet. This principle of *strong focusing* is similar to the optical combination of thin diverging and converging lenses which always effectively focuses. Figure A.3 depicts the essentials of a synchrotron and the focusing effects of such quadrupole doublets.

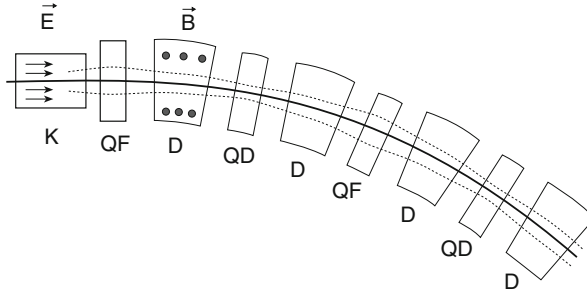


**Fig. A.3** Section (to scale) of a synchrotron from above. The essential accelerating and magnetic structures are shown together with the beam pipe (*continuous line*). High frequency accelerator tubes (K) are usually only placed at a few positions around the synchrotron. The fields of the dipole magnets (D), which keep the particles on their circular paths, are perpendicular to the page. Pairs of quadrupole magnets form doublets which focus the beam. This is indicated by the *dotted lines* which (exaggeratedly) show the shape of the beam envelope. The quadrupoles marked QF have a focusing effect in the plane of the page and the QD quadrupoles a defocusing effect

Particles accelerated in synchrotrons lose some of their energy to *synchrotron radiation*. This refers to the emission of photons by any charged particle which is forced onto a circular path and is thus radially accelerated. The energy lost to synchrotron radiation must be compensated by the accelerating stages. This loss is for highly relativistic particles

$$-\Delta E = \frac{4\pi\alpha\hbar c}{3R}\beta^3\gamma^4, \quad \text{where } \beta = \frac{v}{c} \approx 1 \quad \text{and} \quad \gamma = \frac{E}{mc^2}, \quad (\text{A.5})$$

per orbit – it increases in other words with the fourth power of the particle energy  $E$ . The mass dependence means that this rate of energy loss is about  $10^{13}$  times larger for electrons than for protons of the same energy. The maximal energy in modern electron synchrotrons is thus about 100 GeV. Synchrotron radiation does not play an important role for proton beams. The limit on their final energy is set by the available field strengths of the dipole magnets which keep the protons in the orbit. Proton energies up to a few TeV may be achieved with superconducting magnets.

There are two types of experiment which use particles accelerated in synchrotrons. The beam may, after it has reached its final energy, be deflected out of the ring and led off towards a stationary target. Alternatively the beam may be stored in the synchrotron until it is either loosed upon a thin, internal target or collided with another beam.

**Storage rings** The centre-of-mass energy of a reaction involving a stationary target only grows with the square root of the beam energy (A.2). Much higher centre-of-mass energies may be obtained for the same beam energies if we employ colliding particle beams. The centre-of-mass energy for a head on collision of two particle beams with energy  $E$  is  $\sqrt{s} = 2E$  – i.e., it increases linearly with the beam energy.

The particle density in particle beams, and hence the reaction rate for the collision of two beams, is very tiny; thus they need to be repeatedly collided in any experiment with reasonable event rates. High collision rates may, e.g., be obtained by continuously operating two linear accelerators and colliding the particle beams they produce. Another possibility is to store particle beams, which were accelerated in a synchrotron, at their final energy and at the accelerating stages just top up the energy they lose to synchrotron radiation. These stored particle beams may be then used for collision experiments.

Consider as an example the HERA ring at the Deutsche Elektronen-Synchrotron (German Electron Synchrotron, DESY) in Hamburg that was operated during the years 1992–2007. This was made up of two separate storage rings of the same diameter which run parallel to each other at about 1 m separation. Electrons were accelerated up to about 27.6 GeV and protons to about 920 GeV before storage. The beam tubes came together at two points, where the detectors were positioned, and the oppositely circling beams were allowed to collide there.

Construction is rather simpler if one wants to collide particles with their antiparticles (e.g., electrons and positrons or protons and antiprotons). In such cases only one storage ring is needed and these equal mass but oppositely charged particles can simultaneously run around the ring in opposite directions and may be brought to collision at various interaction points. Examples of these are the LEP ring (Large Electron Positron Ring) at CERN where electrons and positrons with energies up to 104.6 GeV collided and the Sp $\bar{p}$ S (Super Proton Antiproton Synchrotron) where 310 GeV protons and antiprotons were brought violently together. Both of these machines were to be found at the European Nuclear Research Centre CERN near Geneva.

An example of a research complex of accelerators is shown in Fig. A.4; that of DESY. A total of seven preaccelerators service the DORIS and HERA storage rings where experiments with electrons, positrons and protons take place. Two preaccelerator stages are needed for the electron-positron ring DORIS where the beams each have a maximal energy of 5.6 GeV. Three such stages are required for the electron-proton ring HERA (27.6 GeV electrons and 920 GeV protons). DORIS also served as an source of intensive synchrotron radiation and was used as a research instrument in surface physics, chemistry, biology and medicine.

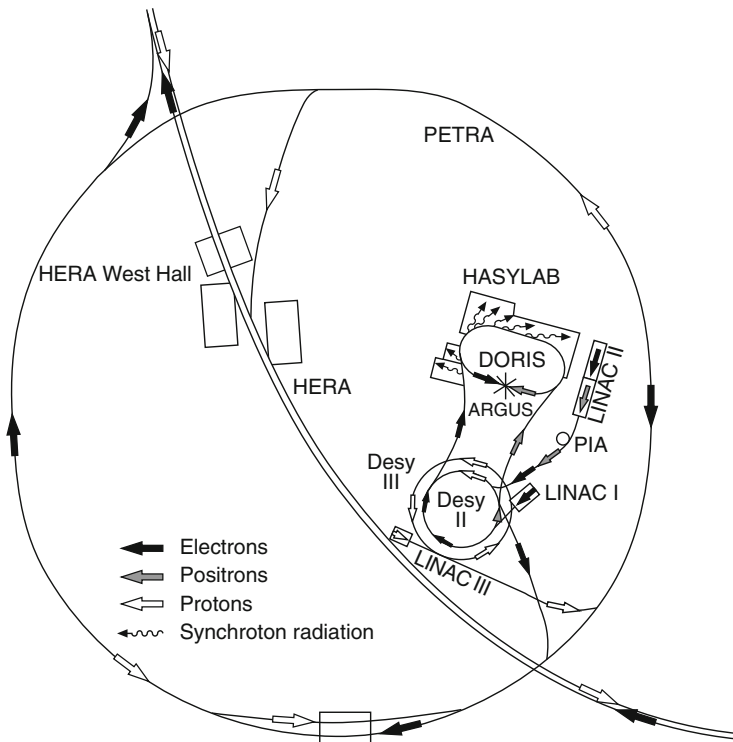


**Fig. A.4** The accelerator complex at the German Electron Synchrotron, DESY, in Hamburg. The DORIS and HERA storage rings are serviced by a chain of preaccelerators. Electrons are accelerated up to 450 MeV in the LINAC I or LINAC II linear accelerators before being injected into the DESY II synchrotron, where they may reach up to 9 GeV. Thence they either pass into DORIS or the PETRA synchrotron. PETRA acts as a final preaccelerator for HERA and electron energies of up to 14 GeV may be attained there. Before HERA was commissioned PETRA worked as an electron-positron storage ring with a beam energy of up to 23.5 GeV. Positrons are produced with the help of electrons accelerated in LINAC II and are then accumulated in the PIA storage ring before their injection into DESY II where they are further accelerated and then led off to DORIS. Protons are accelerated in LINAC III up to 50 MeV and then preaccelerated in the proton synchrotron DESY III up to 7.5 GeV before being injected into PETRA. There they attain 40 GeV before being injected into HERA. The HERA ring, which is only partially shown here, has a circumference of 6,336 m, while the circumference of PETRA is 2,300 m and that of DESY II(III) is around 300 m (*Courtesy of DESY*)

## A.2 Detectors

The construction and development of detectors for particle and nuclear physics has, as with accelerator physics, developed into an almost independent branch of science. The demands upon the quality and complexity of these detectors increase with the ever higher particle energies and currents involved. This has necessarily led to a strong specialisation among the detectors. There are now detectors to measure times,

particle positions, momenta and energies and to identify the particles involved. The principles underlying the detectors are mostly based upon the electromagnetic interactions of particles with matter, e.g., ionisation processes. We will therefore first briefly delineate these processes before showing how they are applied in the individual detectors.

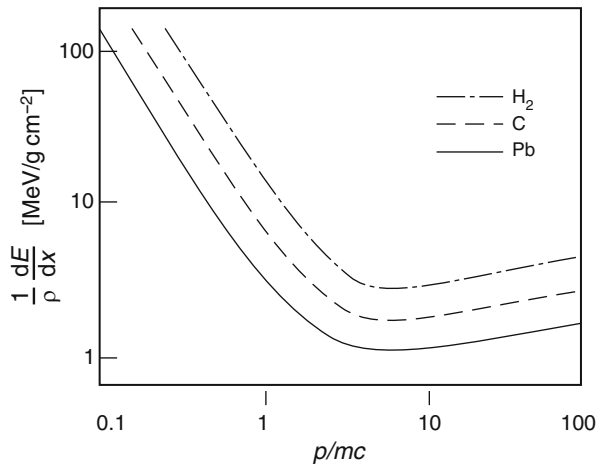
**Interaction of particles with matter** If charged particles pass through matter they lose energy through collisions with the medium. A large part of this corresponds to interactions with the atomic electron clouds which lead to the atoms being excited or ionised. The energy lost to ionisation is described by the *Bethe-Bloch formula* [1, 2]. Approximately we have [12]

$$-\frac{dE}{dx} = \frac{4\pi}{m_e c^2} \frac{n z^2}{\beta^2} \left( \frac{e^2}{4\pi\epsilon_0} \right)^2 \left[ \ln \frac{2m_e c^2 \beta^2}{I \cdot (1 - \beta^2)} - \beta^2 \right], \tag{A.6}$$

where  $\beta = v/c$ ,  $ze$  and  $v$  are the charge and speed of the particle,  $n$  is the electron density and  $I$  is the average excitation potential of the atoms (typically  $16 \text{ eV} \cdot Z^{0.9}$  for nuclear charge numbers  $Z > 1$ ). The energy loss thus depends upon the charge and speed of the particle (Fig. A.5) but not upon its mass. It decreases for small velocities as  $1/v^2$ , reaches a minimum around  $p/mc \approx 4$  and then increases only logarithmically for relativistic velocities. The energy loss to ionisation per length  $dx$  traversed normalised to the density  $\rho$  of the matter at the ionisation minimum, and also for higher particle energies, is roughly  $1/\rho \cdot dE/dx \approx 2 \text{ MeV}/(\text{g cm}^{-2})$ .

Electrons and positrons lose energy not just to ionisation but also to a further important process: *bremsstrahlung*. Electrons braking in the field of a nucleus radiate energy in the form of photons. This process strongly depends upon the material and the energy: it increases roughly linearly with energy and quadratically with the charge number  $Z$  of the medium. Above a critical energy  $E_c$ , which may

**Fig. A.5** Rough sketch of the average energy loss of charged particles to ionisation processes in hydrogen, carbon and lead. The energy loss divided by the density of the material is plotted against  $p/mc = \beta\gamma$  for the particle in a log-log plot. The specific energy loss is greater for lighter elements than for heavy ones



be coarsely parametrised by  $E_c \approx 600 \text{ MeV}/Z$ , bremsstrahlung energy loss is more important for electrons than is ionisation. For such high energy electrons an important material parameter is the *radiation length*  $X_0$ . This describes the distance over which the electron energy decreases due to bremsstrahlung by a factor of  $e$ . High energy electrons are best absorbed in materials with high charge numbers  $Z$ , e.g., lead, where the radiation length is just 0.56 cm.

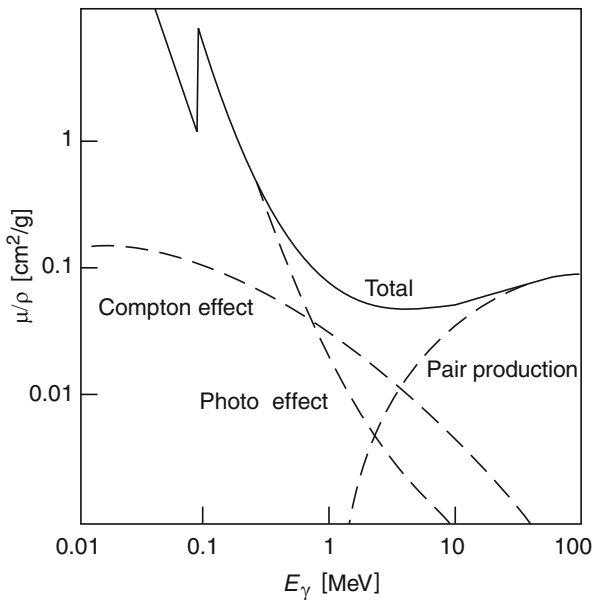
While charged particles traversing matter lose energy slowly to electromagnetic interactions before finally being absorbed, the interaction of a photon with matter takes place at a point. The intensity  $I$  of a photon beam therefore decreases exponentially with the thickness  $\ell$  of the matter traversed:

$$I = I_0 \cdot e^{-\mu \ell} . \tag{A.7}$$

The absorption coefficient  $\mu$  depends upon the photon energy and the type of matter.

The interaction of photons with matter essentially takes place via one of three processes: the *photoelectric effect*, the *Compton effect* and *pair production*. These processes depend strongly upon the medium and the energy involved. The photoelectric effect dominates at low energies in the keV range, the Compton effect for energies from several 100 keV to a few MeV while in high energy experiments only pair production is of any importance. Here the photon is converted inside the nuclear field to an electron-positron pair. This is the dominant process above several MeV. In this energy range the photon can also be described by the radiation length  $X_0$ : the conversion length  $\lambda$  of a high energy photon is  $\lambda = 9/7 \cdot X_0$ . The energy dependence of these three processes in lead is illustrated in Fig. A.6.

**Fig. A.6** The photon absorption coefficient  $\mu$  in lead divided by the density plotted against the photon energy. The *dashed lines* are the contributions of the individual processes; the photoelectric effect, the Compton effect and pair production. Above a few MeV pair production plays the dominant role



We wish to briefly mention two further processes which are useful in particle identification: the radiation of Cherenkov light and nuclear reactions. *Cherenkov radiation* is photon emission from charged particles that cross through a medium with a velocity greater than the speed of light in that medium. These photons are radiated in a cone with angle

$$\theta = \arccos \frac{1}{\beta n} \quad (\text{A.8})$$

around the path of the charged particle ( $n$  is the refractive index of the medium). The energy loss to Cherenkov radiation is small compared to that through ionisation.

*Nuclear reactions* are important for detecting neutral hadrons such as neutrons that do not participate in any of the above processes. Possible reactions are nuclear fission and neutron capture (eV-keV range), elastic and inelastic scattering (MeV range) and hadron production (high energies).

**Measuring positions** The ability to measure the positions and momenta of particles is important in order to reconstruct the kinematics of reactions. The most common detectors of the paths of particles exploit the energy lost by charged particles to ionisation.

*Bubble chambers, spark chambers, and streamer chambers* show us where particles pass through by making their tracks visible so that they may be photographed. These pictures have a high illustrative value and possess a certain aesthetic appeal. Many new particles were discovered in bubble chambers in particular in the 1950s and 1960s. These detectors are nowadays only used for special applications.

*Proportional counters* consist of flat, gas-filled forms in which many thin, parallel wires ( $r \approx 10 \mu\text{m}$ ) are arranged. The wires are maintained at a positive potential of a few kV and are typically arranged at separations of about 2 mm. Charged particles passing through the gas ionise the gas atoms in their paths and the so-released electrons drift off to the anode wires (Fig. A.7). The electric field strengths around the thin wires are very high and so the primary electrons are accelerated and reach kinetic energies such that they themselves start to ionise the gas atoms. A charge avalanche is let loose which leads to a measurable voltage pulse on the wire. The arrival time and amplitude of the pulse are registered electronically. The known position of the wire tells us where the particle passed by. The spatial resolution in the direction perpendicular to the wires is of the order of half the wire separation. An improved resolution and a reconstruction of the path in all three spatial coordinates is in practice obtained by using several layers of proportional counters with the wires pointing in different directions.

*Drift chambers* function similarly to proportional chambers. The wires are, however, at a few centimetres separation. The position of the particle's path  $x$  is now obtained from the time of the voltage pulse  $t_{\text{wire}}$  on the wire relative to the time  $t_0$  that the particle crossed through the detector. This latter time has to be measured in

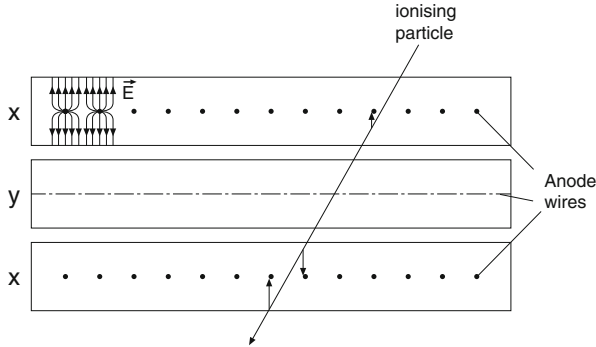


**Fig. A.7** Group of three proportional chambers. The anode wires of the layers marked x point into the page, while those of the y layer run at right angles to these (*dashed line*). The cathodes are the edges of the chambers. A positive voltage applied to the anode wires generates a field like the one sketched in the *upper left hand corner*. A particle crossing through the chamber ionises the gas in its path and the electrons drift along the field lines to the anode wire. In the example shown a signal would be obtained from one wire in the upper x plane and from two in the lower x layer

another detector. Ideally we should have the linear relation

$$x = x_{\text{wire}} + v_{\text{drift}} \cdot (t_{\text{wire}} - t_0), \tag{A.9}$$

if the electric field due to additional electrodes, and hence the drift velocity  $v_{\text{drift}}$  of the released electrons in the gas, are very homogeneous. Drift chambers’ spatial resolution can be as good as  $50 \mu\text{m}$ . Several layers are again required for a three dimensional reconstruction. Wire chambers are very useful for reconstructing paths over large areas. They may be made to cover several square metres.

*Silicon strip detectors* are made out of silicon crystals with very thin electrodes attached to them at separations of about, e.g.,  $20 \mu\text{m}$ . A charged particle crossing the wafer produces electron-hole pairs, in silicon this only requires  $3.6 \text{ eV}$  per pair. An external voltage collects the charge at the electrodes where it is registered. Spatial resolutions less than  $10 \mu\text{m}$  may be reached in this way.

**Measuring momenta** The momenta of charged particles may be determined with the help of strong magnetic fields. The Lorentz force causes these particles to follow circular orbits which may then be, e.g., measured in bubble chamber photographs or reconstructed from several planes of wire chambers. A “rule of thumb” for the momentum component  $p_{\perp}$  perpendicular to the magnetic field may be obtained from the measured radius of curvature of the particle path  $R$  and the known, homogeneous magnetic field  $B$ :

$$p_{\perp} \approx 0.3 \cdot B \cdot R \left[ \frac{\text{GeV}/c}{\text{T m}} \right]. \tag{A.10}$$



*Magnetic spectrometers* are used to indirectly determine the radius of curvature from the angle which the particle is deflected through in the magnetic field; one measures the particle's path before and after the magnets. This method of measuring the momenta actually has smaller errors than a direct determination of the radius of curvature would have. The relative accuracy of these measurements typically decreases with increasing momenta as  $\delta(p)/p \propto p$ . This is because the particle path becomes straighter at high momenta.

**Measuring energies** A measurement of the energy of a particle usually requires the particle to be completely absorbed by some medium. The absorbed energy is transformed into ionisation, atomic excitations or perhaps Cherenkov light. This signal which may, with the help of suitable devices, be transformed into a measurable one is proportional to the original energy of the particle. The energy resolution depends upon the statistical fluctuations of the transformation process.

*Semiconductor detectors* are of great importance in nuclear physics. Electron-hole pairs created by charged particles are separated by an external voltage and then detected as voltage pulses. In germanium only 2.8 eV is required to produce an electron-hole pair. In silicon 3.6 eV is needed. Semiconductor detectors are typically a few millimetres thick and can absorb light nuclei with energies up to a few tens of MeV. Photon energies are determined through the photoelectric effect – one measures the signal of the absorbed photoelectron. The large number  $N$  of electron-hole pairs that are produced means that the energy resolution of such semiconductor counters is excellent,  $\delta E/E \propto \sqrt{N}/N$ . For 1 MeV particles it is between  $10^{-3}$  and  $10^{-4}$ .

*Electromagnetic calorimeters* may be used to measure the energies of electrons, positrons and photons above about 100 MeV. One exploits the cascade of secondary particles that these particles produce via repeated bremsstrahlung and pair production processes inside the material of the calorimeter. The production of such a measurable ionisation or visible signal is illustrated in Fig. A.8. The complete absorption of such a shower in a calorimeter takes place, depending upon the energy involved, over a distance of about 15–25 times the radiation length  $X_0$ . We will consider the example of homogeneous calorimeters made of NaI(Tl) crystals or lead glass.

NaI doped with small amounts of thallium is an inorganic scintillator in which charged particles produce visible wavelength photons. These photons may then be converted into an electric pulse with the help of photomultipliers. Calorimeters are made from large crystals of NaI(Tl) with photomultipliers attached to their backs (see Fig. 14.5). The relative energy resolution typically has values of the order of  $\delta E/E \approx 1\text{--}2\% / \sqrt[4]{E [\text{GeV}]}$ . NaI(Tl) is also of great importance for nuclear-gamma spectroscopy, and hence for energies  $\lesssim 1$  MeV, since it has a large photon absorption coefficient, particularly for the photoelectric effect.

Cascade particles in lead glass produce Cherenkov light which may also be registered with the help of photomultipliers. Lead glass calorimeters may be built up from a few thousand lead glass blocks, which can cover several square metres. The transverse dimension of these blocks is adjusted to the transverse extension of

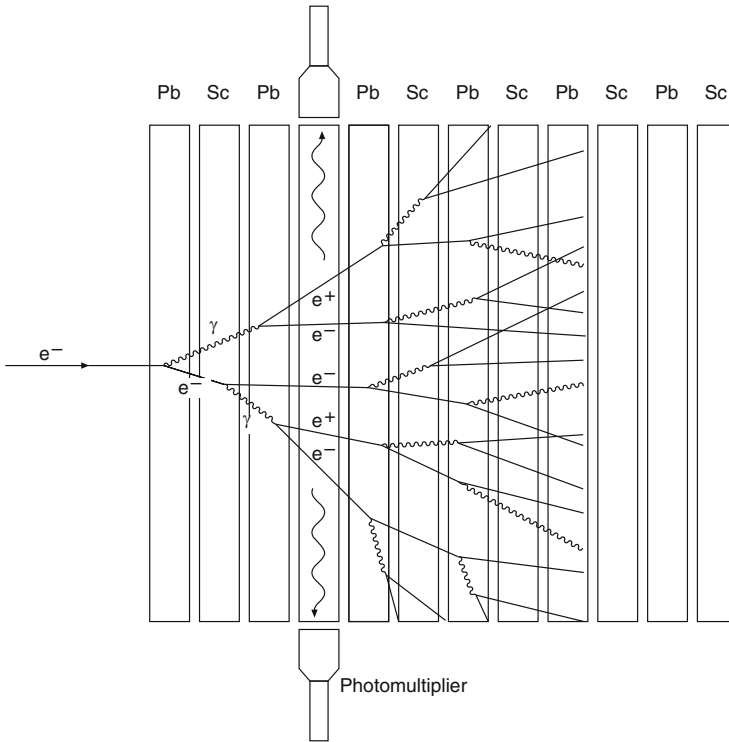


**Fig. A.8** Sketch of particle cascade formation inside a calorimeter. An electromagnetic cascade inside a sampling calorimeter made out of layers of lead and scintillator is depicted. The lead acts as an absorber material where the bremsstrahlung and pair production processes primarily take place. The opening angles are, for purposes of clarity, exaggerated in the diagram. The particle tracks are for the same reason not continued on into the rearmost layers of the detector. Electrons and positrons in the scintillator produce visible scintillation light, which through total reflection inside the scintillator is led off to the sides (*large wavy lines*) where it is detected by photomultipliers. The total amount of scintillator light measured is proportional to the energy of the incoming electron

electromagnetic showers, typically a few centimetres. Energy resolution is typically around  $\delta E/E \approx 3-5\% / \sqrt{E [\text{GeV}]}$ .

*Hadronic calorimeters* may be used to measure hadronic energies. These produce a shower of secondary particles (mostly further hadrons) in inelastic reactions. Such hadronic showers have, compared to electromagnetic showers, a larger spatial extension and display much larger fluctuations in both the number and type of secondary particles involved. *Sampling calorimeters* made up of alternating layers of a pure absorber material (e.g., iron, uranium) and a detector material (e.g., an organic scintillator) are used to measure hadron energies. Only a small fraction of the original particle's energy is deposited in the detector material. The energy resolution of hadronic calorimeters is, both for this reason and because of the

large fluctuations in the number of secondary particles, only about  $\delta E/E \approx 30 - 80\% / \sqrt{E} [\text{GeV}]$ .

Momentum and energy measurements are interchangeable for highly relativistic particles (5.6). The accuracy of momentum measurements in magnetic spectrometers decreases linearly with particle momentum, while the precision of energy measurements in calorimeters increases as  $1/\sqrt{E}$ . Depending upon the particle type and the particular detector configuration it can make sense for particles with momenta above 50–100 GeV to measure momenta indirectly through a more accurate energy measurement in a calorimeter.

**Identifying particles** The mass and the charge of a particle generally suffice to identify it. The sign of a particle's charge may be easily read off from the particle's deflection in a magnetic field, but a direct measurement of the particle's mass is mostly impossible. There is therefore no general particle identification recipe; rather lots of different methods, which often use other particle properties, are available. Subsequently, we will briefly list those methods which are used in particle physics for particles with momenta above about 100 MeV/c.

- Short lived particles may be identified from their decay products with the help of the method of invariant masses (cf. Sect. 16.1).
- The presence of neutrinos is usually only detected by measuring a deficit of energy or momentum in a reaction.
- Electrons and photons are recognised through their characteristic electromagnetic showers in calorimeters. We may distinguish between them by putting an ionisation detector (e.g., a scintillator or a wire chamber) in front of the calorimeter – of the two only an electron will leave an ionisation trail.
- Muons are identified by their exceptional penetrative powers. They primarily lose energy to ionisation and may be detected with the help of ionisation chambers placed behind lead plates, which will absorb all other charged particles.
- Charged hadrons, such as pions, kaons and protons, are the most difficult particles to distinguish. For them not only a momentum measurement is required but also a further independent measurement is needed – which one is best suited depends upon the particle's momentum.
  - The time of flight between two ionisation detectors may be measured for momenta below 1 GeV/c, since the velocity depends for a fixed momentum upon the mass. A further possibility is to measure the loss of energy to ionisation – this depends upon the particle velocity. In this range it varies as  $1/v^2$ .
  - This latter approach may be extended to 1.5–50 GeV/c momenta (where the energy loss only increases logarithmically as  $\beta = v/c$ ) if the measurements are performed repeatedly.

- Various sorts of *Cherenkov counters* may be used in the range up to about 100 GeV/c. Threshold Cherenkov counters require a material with a refractive index  $n$  so arranged that only specific particles with a particular momentum can produce Cherenkov light (cf. A.8). In ring imaging Cherenkov counters (RICH) the opening angle of the Cherenkov photons is measured for all the particles and their speed may be calculated from this. If their momentum is known then this determines their identity.
  - *Transition radiation detectors* may be used for  $\gamma = E/mc^2 \gtrsim 100$ . Transition radiation is produced when charged particles cross from one material to another which has a different dielectric constant. The intensity of the radiation depends upon  $\gamma$ . Thus an intensity measurement can enable us to distinguish between different hadrons with the same momenta. This is in fact the only way to identify such particles if the energy of the hadron is above 100 GeV. Transition radiation may also be employed to distinguish between electrons and pions. The tiny mass of the electrons means that this is already possible for energies around 1 GeV.
- Neutron detection is a special case;  $(n, \alpha)$  and  $(n, p)$  nuclear reactions are used to identify neutrons – from those with thermal energies to those with momenta up to around 20 MeV/c. The charged reaction products have fixed kinetic energies and these may be measured in scintillation counters or gas ionisation counters. For momenta between 20 MeV/c and 1 GeV/c one looks for protons from elastic neutron-proton scattering. The proton target is generally part of the material of the detector itself (plastic scintillator, counter gas). At higher momenta only hadron calorimeter measurements are available to us. The identification is then, however, as a rule not unambiguous.

**A detector system** We wish to present as an example of a system of detectors the ZEUS detector at the HERA storage ring. This detector measured the reaction products in high energy electron-proton collisions with centre-of-mass energies up to about 320 GeV (Fig. A.9). It was so arranged that apart from the beam pipe region the reaction zone was hermetically covered. Many different detectors, chosen to optimise the measurement of energy and momentum and the identification of the reaction products, made up the whole. The most important components are the wire chambers, which were arranged directly around the reaction point, and, just outside these, a uranium-scintillator calorimeter where the energies of electrons and hadrons were measured to a high precision.

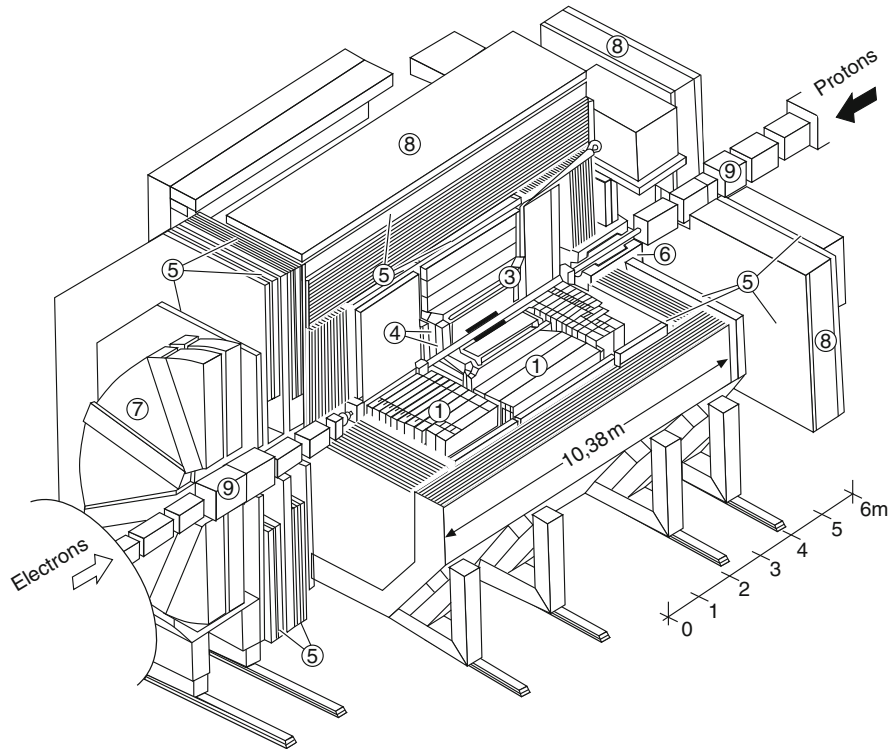


**Fig. A.9** The ZEUS detector at the HERA storage ring in DESY. The electrons and protons are focused with the help of magnetic lenses (9) before they are made to collide at the interaction point in the centre of the detector. The tracks of charged reaction products are registered in the vertex chamber (3) which surrounds the reaction point and also in the central track chamber (4). These drift chambers are surrounded by a superconducting coil which produces a magnetic field of up to 1.8 T. The influence of this magnetic field on the electron beam which passes through it must be compensated by additional magnets (6). The next layer is a uranium-scintillator calorimeter (1) where the energies of electrons, photons and also of hadrons may be measured to a great accuracy. The iron yoke of the detector (2), into which the magnetic flux of the central solenoid returns, also acts as an absorber for the backwards calorimeter, where the energy of those high energy particle showers that are not fully absorbed in the central uranium calorimeter may be measured. Large area wire chambers (5), positioned behind the iron yoke, surround the whole detector and are used to betray the passage of any muons. These chambers may be used to measure the muons' momenta since they are inside either the magnetic field of the iron yoke or an additional 1.7 T toroidal field (7). Finally a thick reinforced concrete wall (8) screens off the experimental hall as far as is possible from the radiation produced in the reactions (*Courtesy of DESY*)

### A.3 Combining Angular Momenta

The combination of two angular momenta  $|j_1 m_1\rangle$  and  $|j_2 m_2\rangle$  to form a total angular momentum  $|JM\rangle$  must obey the following selection rules:

$$|j_1 - j_2| \leq J \leq j_1 + j_2, \quad (\text{A.11})$$

$$M = m_1 + m_2, \quad (\text{A.12})$$

$$J \geq |M|. \quad (\text{A.13})$$

The coupled states may be expanded with the help of the *Clebsch-Gordan coefficients* (CGC)  $(j_1 j_2 m_1 m_2 | JM)$  in the  $|j_1 j_2 JM\rangle$  basis:

$$|j_1 m_1\rangle \otimes |j_2 m_2\rangle = \sum_{\substack{J=j_1+j_2 \\ J=|j_1-j_2| \\ M=m_1+m_2}} (j_1 j_2 m_1 m_2 | JM) \cdot |j_1 j_2 JM\rangle. \quad (\text{A.14})$$

The probability that the combination of two angular momenta  $|j_1 m_1\rangle$  and  $|j_2 m_2\rangle$  produces a system with total angular momentum  $|JM\rangle$  is thus the square of the corresponding CGC's.

The corollary

$$|j_1 j_2 JM\rangle = \sum_{\substack{m_1=+j_1 \\ m_1=-j_1 \\ m_2=M-m_1}} (j_1 j_2 m_1 m_2 | JM) \cdot |j_1 m_1\rangle \otimes |j_2 m_2\rangle, \quad (\text{A.15})$$

also holds. For a system  $|JM\rangle$ , which has been produced from a combination of two angular momenta  $j_1$  and  $j_2$ , the square of the CGC's gives the probability that the individual angular momenta may be found in the states  $|j_1 m_1\rangle$  and  $|j_2 m_2\rangle$ .

Equations (A.14) and (A.15) may also be applied to isospin. Consider, for example, the  $\Delta^+$  baryon ( $I = 3/2, I_3 = +1/2$ ) which can decay into  $p + \pi^0$  or  $n + \pi^+$ . The branching ratio can be found to be

$$\frac{B(\Delta^+ \rightarrow p + \pi^0)}{B(\Delta^+ \rightarrow n + \pi^+)} = \frac{|\langle \frac{1}{2} \ 1 + \frac{1}{2} \ 0 \mid \frac{3}{2} \ +\frac{1}{2} \rangle|^2}{|\langle \frac{1}{2} \ 1 \ -\frac{1}{2} \ +1 \mid \frac{3}{2} \ +\frac{1}{2} \rangle|^2} = \frac{\left(\sqrt{\frac{2}{3}}\right)^2}{\left(\sqrt{\frac{1}{3}}\right)^2} = 2. \quad (\text{A.16})$$

The CGC's are listed for combinations of low angular momenta. The values for  $j_1 = 1/2$  and  $j_2 = 1$  may be found with the help of the general phase relation

$$(j_2 j_1 m_2 m_1 | JM) = (-1)^{j_1+j_2-J} \cdot (j_1 j_2 m_1 m_2 | JM). \quad (\text{A.17})$$

$j_1 = 1/2$		$j_2 = 1/2$		
$m_1$	$m_2$	$J$	$M$	CGC
1/2	1/2	1	1	+1
1/2	-1/2	1	0	$+\sqrt{1/2}$
1/2	-1/2	0	0	$+\sqrt{1/2}$
-1/2	1/2	1	0	$+\sqrt{1/2}$
-1/2	1/2	0	0	$-\sqrt{1/2}$
-1/2	-1/2	1	-1	+1

$j_1 = 1$		$j_2 = 1$		
$m_1$	$m_2$	$J$	$M$	CGC
1	1	2	2	+1
1	0	2	1	$+\sqrt{1/2}$
1	0	1	1	$+\sqrt{1/2}$
1	-1	2	0	$+\sqrt{1/6}$
1	-1	1	0	$+\sqrt{1/2}$
1	-1	0	0	$+\sqrt{1/3}$
0	1	2	1	$+\sqrt{1/2}$
0	1	1	1	$-\sqrt{1/2}$
0	0	2	0	$+\sqrt{2/3}$
0	0	1	0	0
0	0	0	0	$-\sqrt{1/3}$
0	-1	2	-1	$+\sqrt{1/2}$
0	-1	1	-1	$+\sqrt{1/2}$
-1	1	2	0	$+\sqrt{1/6}$
-1	1	1	0	$-\sqrt{1/2}$
-1	1	0	0	$-\sqrt{1/3}$
-1	0	2	-1	$+\sqrt{1/2}$
-1	0	1	-1	$-\sqrt{1/2}$
-1	-1	2	-2	+1

$j_1 = 1$		$j_2 = 1/2$		
$m_1$	$m_2$	$J$	$M$	CGC
1	1/2	3/2	3/2	+1
1	-1/2	3/2	1/2	$+\sqrt{1/3}$
1	-1/2	1/2	1/2	$+\sqrt{2/3}$
0	1/2	3/2	1/2	$+\sqrt{2/3}$
0	1/2	1/2	1/2	$-\sqrt{1/3}$
0	-1/2	3/2	-1/2	$+\sqrt{2/3}$
0	-1/2	1/2	-1/2	$+\sqrt{1/3}$
-1	1/2	3/2	-1/2	$+\sqrt{1/3}$
-1	1/2	1/2	-1/2	$-\sqrt{2/3}$
-1	-1/2	3/2	-3/2	+1

### A.4 Physical Constants

**Table A.1** Physical constants [3, 8, 12]. The numbers in brackets signify the uncertainty in the last decimal places. The sizes of  $c$ ,  $\mu_0$  (and hence  $\epsilon_0$ ) are defined by the units “metre” and “ampere” [13]. These constants are therefore error free

Constants	Symbol	Value
Speed of light	$c$	$2.997\,924\,58 \cdot 10^8 \text{ m s}^{-1}$
Planck’s constant	$h$	$6.626\,069\,57 (29) \cdot 10^{-34} \text{ J s}$
	$\hbar = h/2\pi$	$1.054\,571\,726 (47) \cdot 10^{-34} \text{ J s}$
		$= 6.582\,119\,28 (15) \cdot 10^{-22} \text{ MeV s}$
	$\hbar c$	$197.326\,9718 (44) \text{ MeV fm}$
	$(\hbar c)^2$	$0.389\,379\,338 (17) \text{ GeV}^2 \text{ mbarn}$
Atomic mass unit	$u = M_{12C}/12$	$931.494\,061 (21) \text{ MeV}/c^2$
Mass of the proton	$M_p$	$938.272\,046 (21) \text{ MeV}/c^2$

(continued)

**Table A.1** (continued)

Constants	Symbol	Value
Mass of the neutron	$M_n$	939.565 379 (21) MeV/c <sup>2</sup>
Mass of the electron	$m_e$	0.510 998 928 (11) MeV/c <sup>2</sup>
Elementary charge	$e$	1.602 176 565 (35) · 10 <sup>-19</sup> A s
Dielectric constant	$\epsilon_0 = 1/\mu_0 c^2$	8.854 187 817 · 10 <sup>-12</sup> A s/V m
Permeability of vacuum	$\mu_0$	4 $\pi$ · 10 <sup>-7</sup> V s/A m
Fine structure constant	$\alpha = e^2/4\pi\epsilon_0\hbar c$	1/137.035 999 074 (44)
Class. electron radius	$r_e = \alpha\hbar c/m_e c^2$	2.817 940 3267 (27) · 10 <sup>-15</sup> m
Compton wavelength	$\lambda_e = r_e/\alpha$	3.861 592 6800 (25) · 10 <sup>-13</sup> m
Bohr radius	$a_0 = r_e/\alpha^2$	5.291 772 1092 (17) · 10 <sup>-11</sup> m
Bohr magneton	$\mu_B = e\hbar/2m_e$	5.788 381 8066 (38) · 10 <sup>-11</sup> MeV T <sup>-1</sup>
Nuclear magneton	$\mu_N = e\hbar/2m_p$	3.152 451 2605 (22) · 10 <sup>-14</sup> MeV T <sup>-1</sup>
Magnetic moment	$\mu_e$	1.001 159 652 180 76 (27) $\mu_B$
	$\mu_p$	2.792 847 356 (23) $\mu_N$
	$\mu_n$	-1.913 042 72 (45) $\mu_N$
Avogadro's number	$N_A$	6.022 141 29 (27) · 10 <sup>23</sup> mol <sup>-1</sup>
Boltzmann's constant	$k$	1.380 6488 (13) · 10 <sup>-23</sup> J K <sup>-1</sup>
		= 8.617 3324 (78) · 10 <sup>-5</sup> eV K <sup>-1</sup>
Gravitational constant	$G$	6.673 84 (80) · 10 <sup>-11</sup> N m <sup>2</sup> kg <sup>-2</sup>
	$G/\hbar c$	6.708 37 (80) · 10 <sup>-39</sup> (GeV/c <sup>2</sup> ) <sup>-2</sup>
Fermi constant	$G_F/(\hbar c)^3$	1.166 378 7 (6) · 10 <sup>-5</sup> GeV <sup>-2</sup>
Weinberg angle	$\sin^2 \theta_W$	0.231 16 (12)
Mass of the W <sup>±</sup>	$M_W$	80.385 (15) GeV/c <sup>2</sup>
Mass of the Z <sup>0</sup>	$M_Z$	91.1876 (21) GeV/c <sup>2</sup>
Strong coupling const.	$\alpha_s(M_Z^2 c^2)$	0.1184 (7)



# Solutions to Problems

## Chapter 2

1. Proton repulsion in  ${}^3\text{He}$ :

$$\begin{aligned} V_C &= \frac{-\hbar c \alpha}{R} = (M_{{}^3\text{He}} - M_{{}^3\text{H}}) \cdot c^2 - (M_n - M_p) \cdot c^2 \\ &= E_\beta^{\text{max}} - (M_n - M_p - m_e) \cdot c^2. \end{aligned}$$

This yields  $R = 1.88 \text{ fm}$ . The  $\beta$ -decay recoil and the difference between the atomic binding energies may be neglected.

## Chapter 3

1. (a) At Saturn we have  $t/\tau = 4 \text{ years}/127 \text{ years}$  and we require

$$N_0 \frac{1}{\tau} e^{-t/\tau} \cdot 5.49 \text{ MeV} \cdot 0.055 = 395 \text{ W}$$

power to be available. This implies  $N_0 = 3.4 \cdot 10^{25}$  nuclei, which means  $13.4 \text{ kg } {}^{238}\text{Pu}$ .

- (b) At Neptune (after 12 years) 371 W would be available.  
(c) The power available from radiation decreases as  $1/r^2$ . Hence at Saturn 395 W power would require an area of  $2.5 \cdot 10^3 \text{ m}^2$  and 371 W at Neptune could be produced by an area of  $2.3 \cdot 10^4 \text{ m}^2$ . This would presumably lead to construction and weight problems.

2. (a) Applying the formula  $N = N_0 e^{-\lambda t}$  to both uranium isotopes leads to

$$\frac{99.28}{0.72} = \frac{e^{-\lambda_{238}t}}{e^{-\lambda_{235}t}} \quad \text{which yields: } t = 5.9 \cdot 10^9 \text{ years.}$$

Uranium isotopes, like all heavy ( $A \gtrsim 56$ ) elements, are produced in supernova explosions. The material which is so ejected is used to build up new stars. The isotopic analysis of meteorites leads to the age of the solar system being  $4.55 \cdot 10^9$  years.

- (b) After  $2.5 \cdot 10^9$  years,  $(1 - e^{-\lambda t})$  of the nuclei will have decayed. This is 32 %.  
 (c) Equation (2.8) yields that a total of 51 MeV is released in the  $^{238}\text{U} \rightarrow ^{206}\text{Pb}$  decay chain. In spontaneous fission 190 MeV is set free.
3. (a)

$$A_2(t) = N_{0,1} \cdot \lambda_1 \cdot \frac{\lambda_2}{\lambda_2 - \lambda_1} (e^{-\lambda_1 t} - e^{-\lambda_2 t})$$

for large times  $t$ , because of  $\lambda_1 \ll \lambda_2$ :

$$A_2(t) = N_{0,1} \cdot \lambda_1.$$

- (b) The concentration of  $^{238}\text{U}$  in concrete can thus be found to be

$$\begin{array}{l} \text{room volume} \\ \text{eff. concrete volume} \end{array} \quad \begin{array}{l} V: 400 \text{ m}^3 \\ V_B: 5.4 \text{ m}^3 \end{array} \implies \varrho_U = \frac{V \cdot A}{V_B \cdot \lambda_{238}} = 1.5 \cdot 10^{21} \frac{\text{atoms}}{\text{m}^3}.$$

4. Nuclear masses for fixed  $A$  depend quadratically upon  $Z$ . From the definitions in (3.6) the minimum of the parabola is at  $Z_0 = \beta/2\gamma$ . The constant  $a_a$  in  $\beta$  and  $\gamma$  is part of the asymmetry term in the mass formula (2.8) and, according to (18.12), does not depend upon the electromagnetic coupling constant  $\alpha$ . The “constant”  $a_c$ , which describes the Coulomb repulsion and enters the definition of  $\gamma$ , is on the other hand proportional to  $\alpha$  and may be written as:  $a_c = \kappa\alpha$ . Inserting this into  $Z_0 = \beta/2\gamma$  yields

$$Z_0 = \frac{\beta}{2(a_a/A + \kappa\alpha/A^{1/3})} \implies \frac{1}{\alpha} = \frac{2\kappa AZ_0}{A^{1/3}(A\beta - 2a_a Z_0)}.$$

Assuming that the minimum of the mass formula is exactly at the given  $Z$  one finds  $1/\alpha$  values of 128, 238 and 522 for the  $^{186}_{74}\text{W}$ ,  $^{186}_{82}\text{Pb}$  and  $^{186}_{88}\text{Ra}$  nuclides. Stable  $^{186}_{94}\text{Pu}$  cannot be obtained just by “twiddling”  $\alpha$ .

5. The energy  $E$  released in  $^A_Z X \rightarrow ^{A-4}_{Z-2} Y + \alpha$  is

$$E = B(\alpha) - \delta B \quad \text{where } \delta B = B(X) - B(Y).$$

Note that we have here neglected the difference in the atomic binding energies. If we further ignore the pairing energy, which only slightly changes, we obtain

$$\begin{aligned} E &= B(\alpha) - \frac{\partial B}{\partial Z} \delta Z - \frac{\partial B}{\partial A} \delta A = B(\alpha) - 2 \frac{\partial B}{\partial Z} - 4 \frac{\partial B}{\partial A} \\ &= B(\alpha) - 4a_v + \frac{8}{3} a_s \frac{1}{3A^{1/3}} + 4a_c \frac{Z}{A^{1/3}} \left(1 - \frac{Z}{3A}\right) - a_a \left(1 - \frac{2Z}{A}\right)^2. \end{aligned}$$

Putting in the parameters yields  $E > 0$  if  $A \gtrsim 150$ . Natural  $\alpha$ -activity is only significant for  $A \gtrsim 200$ , since the lifetime is extremely long for smaller mass numbers.

6. The mother nucleus and the  $\alpha$  particle are both  $0^+$  systems which implies that the spin  $J$  and parity  $P$  of a daughter nucleus with orbital angular momentum  $L$  and spatial wave function parity  $(-1)^L$  must combine to  $0^+$ . This means that  $J^P = 0^+, 1^-, 2^+, 3^-, \dots$  are allowed.

## Chapter 4

1. (a) In analogy to (4.5) the reaction rate must obey  $\dot{N} = \sigma \dot{N}_d n_t$ , where  $\dot{N}_d$  signifies the deuteron particle current and  $n_t$  is the particle areal density of the tritium target. The neutron rate found in any solid angle element  $d\Omega$  must then obey

$$d\dot{N} = \frac{d\sigma}{d\Omega} d\Omega \dot{N}_d n_t = \frac{d\sigma}{d\Omega} \frac{F}{R^2} \frac{I_d}{e} \frac{\mu_t}{m_t} N_A,$$

where  $e$  is the elementary electric charge,  $m_t$  is the molar mass of tritium and  $N_A$  is Avogadro's number.

Inserting the numbers yields  $d\dot{N} = 1,444$  neutrons/s.

- (b) Rotating the target away from the orthogonal increases the effective particle area density "seen" by the beam by a factor of  $1/\cos\theta$ . A rotation through  $10^\circ$  thus increases the reaction rate by 1.5%.
2. The number  $N$  of beam particles decreases according to (4.5) with the distance  $x$  covered as  $e^{-x/\lambda}$  where  $\lambda = 1/\sigma n$  is the absorption length.

- (a) Thermal neutrons in cadmium: We have

$$n_{\text{Cd}} = \rho_{\text{Cd}} \frac{N_A}{A_{\text{Cd}}},$$

where the atomic mass of cadmium is given by  $A_{\text{Cd}} = 112.40 \text{ g mol}^{-1}$ . We thus obtain

$$\lambda_{\text{n,Cd}} = 9 \mu\text{m}.$$

- (b) For highly energetic photons in lead one may find in an analogous manner ( $A_{\text{Pb}} = 207.19 \text{ g mol}^{-1}$ )

$$\lambda_{\gamma, \text{Pb}} = 2.0 \text{ cm}.$$

- (c) Antineutrinos predominantly react with the electrons in the Earth. Their density is

$$n_{e, \text{Earth}} = \rho_{\text{Earth}} \left( \frac{Z}{A} \right)_{\text{Earth}} N_A.$$

We therefore obtain

$$\lambda_{\bar{\nu}/\text{Earth}} = 6.7 \cdot 10^{16} \text{ m},$$

which is about  $5 \cdot 10^9$  times the diameter of the planet.

Note: the number of beam particles only decreases exponentially with distance if *one* reaction leads to the beam particles being absorbed; a criterion which is fulfilled in the above examples. The situation is different if  $k \gg 1$  reactions are needed (e.g.,  $\alpha$  particles in air). In such cases the range is almost constant  $L = k/\sigma n$ .

## Chapter 5

1. (a) From  $Q^2 = -(p - p')^2$  and (5.13) one finds

$$Q^2 = 2M(E - E'),$$

with  $M$  the mass of the heavy nucleus. This implies that  $Q^2$  is largest at the smallest value of  $E'$ , i.e.,  $\theta = 180^\circ$ . The maximal momentum transfer is then from (5.15)

$$Q_{\text{max}}^2 = \frac{4E^2M}{Mc^2 + 2E},$$

- (b) From (5.15) we find for  $\theta = 180^\circ$  that the energy transfer  $\nu = E - E'$  is

$$\nu = E \left( 1 - \frac{1}{1 + 2\frac{E}{Mc^2}} \right) = \frac{2E^2}{Mc^2 + 2E}.$$

The energy of the backwardly scattered nucleus is then

$$E'_{\text{nucleus}} = Mc^2 + \nu = Mc^2 + \frac{2E^2}{Mc^2 + 2E}$$

and its momentum is

$$|\mathbf{P}'| = \sqrt{Q_{\text{max}}^2 + \frac{\nu^2}{c^2}} = \sqrt{\frac{4ME^2}{Mc^2 + 2E} + \frac{4E^4}{c^2(Mc^2 + 2E)^2}}.$$

- (c) The nuclear Compton effect may be calculated with the help of  $\Delta\lambda = \frac{h}{Mc}(1 - \cos\theta)$ . The same result as for electron scattering is obtained since we have neglected the electron rest mass in (a) and (b) above.
2. Those  $\alpha$  particles which directly impinge upon the  $^{56}\text{Fe}$  nucleus are absorbed. Elastically scattered  $\alpha$  particles correspond to a “shadow scattering” which may be described as Fraunhofer diffraction upon a disc. The diameter  $D$  of the disc is found to be

$$D = 2(\sqrt[3]{4} + \sqrt[3]{56}) \cdot 0.94 \text{ fm} \approx 10 \text{ fm}.$$

In the literature  $D$  is mostly parametrised by the formula  $D = 2\sqrt[3]{A} \cdot 1.3 \text{ fm}$ , which gives the same result. The wavelength of the  $\alpha$  particles is  $\lambda = h/p$ , where  $p$  is to be understood as that in the centre-of-mass system of the reaction. Using  $pc = 840 \text{ MeV}$  one finds  $\lambda = 1.5 \text{ fm}$ .

The first minimum is at  $\theta = 1.22\lambda/D \approx 0.18 \approx 10.2^\circ$ . The intensity distribution of the diffraction is given by the Bessel function  $j_0$ . The further minima correspond to the nodes of this Bessel function.

The scattering angle ought, however, to be given in the laboratory frame and is given by  $\theta_{\text{lab}} \approx 9.6^\circ$ .

3. The smallest separation of the  $\alpha$  particles from the nucleus is  $s(\theta) = a + \frac{a}{\sin\theta/2}$  for the scattering angle  $\theta$ . The parameter  $a$  is obtained from  $180^\circ$  scattering, since the kinetic energy is then equal to the potential energy:

$$E_{\text{kin}} = \left| \frac{zZe^2\hbar c}{4\pi\epsilon_0\hbar c 2a} \right|.$$

For 6 MeV  $\alpha$  scattering off gold, we have  $a = 19 \text{ fm}$  and  $s = 38 \text{ fm}$ . For deviations from Rutherford scattering to occur, the  $\alpha$  particles must manage to get close to the nuclear forces, which can first happen at a separation  $R = R_\alpha + R_{\text{Au}} \approx 9 \text{ fm}$ . A more detailed discussion is given in Sect. 19.4. Since  $s \gg R$  no nuclear reactions are possible between 6 MeV  $\alpha$  particles and gold and no deviation from the Rutherford cross-section should therefore be expected. This would only be possible for much lighter nuclei.

4. The kinetic energy of the electrons may be found as follows:

$$\frac{\hbar}{\sqrt{2M_\alpha E_\alpha^{\text{kin}}}} \approx \lambda_\alpha \stackrel{!}{=} \lambda_e \approx \frac{\hbar c}{E_e^{\text{kin}}} \implies E_e^{\text{kin}} \approx \sqrt{2M_\alpha c^2 E_\alpha^{\text{kin}}} = 211 \text{ MeV}.$$

The momentum transfer is maximal for scattering through  $180^\circ$ . Neglecting the recoil we have

$$|\mathbf{q}|_{\text{max}} = 2|\mathbf{p}_e| = \frac{2\hbar}{\lambda_e} \approx 2\sqrt{2M_\alpha E_\alpha^{\text{kin}}} = 423 \text{ MeV}/c,$$

and the variable  $\alpha$  in Table 5.1 may be found with the help of (5.56) to be

$$\alpha_{\text{max}} = \frac{|\mathbf{q}|_{\text{max}} R}{\hbar} = \frac{423 \text{ MeV} \cdot 1.21 \cdot \sqrt[3]{197} \text{ fm}}{197 \text{ MeV fm}} = 15.1.$$

The behaviour of the function  $3\alpha^{-3}(\sin\alpha - \alpha\cos\alpha)$  from Table 5.1 is such that it has 4 zero points in the range  $0 < \alpha \leq 15.1$ .

- Electrons oscillate most in the field of the X-rays since  $M_{\text{nuclear}} \gg m_e$ . As in the H atom, the radial wave function of the electrons also falls off exponentially in He. Hence, just as for electromagnetic electron scattering off nucleons, a dipole form factor is observed.
- If a 511 keV photon is Compton scattered through  $30^\circ$  off an electron at rest, the electron receives momentum,  $p_e = 0.26 \text{ MeV}/c$ . From the virial theorem an electron bound in a helium atom must have kinetic energy  $E_{\text{kin}} = -E_{\text{pot}}/2 = -E_{\text{tot}} = 24 \text{ eV}$ , which implies that the momentum of the Compton electron is smeared out with  $\Delta p \approx \pm 5 \cdot 10^{-3} \text{ MeV}/c$  which corresponds to an angular smearing of  $\Delta\theta_e \approx \Delta p/p = \pm 20 \text{ mrad} \approx \pm 1^\circ$ .

## Chapter 6

- The form factor of the electron must be measured up to  $|\mathbf{q}| \approx \hbar/r_0 = 200 \text{ GeV}/c$ . One thus needs  $\sqrt{s} = 200 \text{ GeV}$ , i.e., 100 GeV colliding beams. For a target at rest,  $2m_e c^2 E = s$  implies that  $4 \cdot 10^7 \text{ GeV}$  (!) would be needed.
- Since the pion has spin zero, the magnetic form factor vanishes and we have (6.10):

$$\frac{d\sigma(e\pi \rightarrow e\pi)}{d\Omega} = \left( \frac{d\sigma}{d\Omega} \right)_{\text{Mott}} G_{E,\pi}^2(Q^2)$$

$$G_{E,\pi}^2(Q^2) \approx \left( 1 - \frac{Q^2 \langle r^2 \rangle_\pi}{6\hbar^2} \right)^2 = 1 - 3.7 \frac{Q^2}{\text{GeV}^2/c^2}.$$

## Chapter 7

1. Comparing the coefficients in (6.5) and (7.8) yields

$$\frac{2W_1}{W_2} = 2\tau, \quad \text{where} \quad \tau = \frac{Q^2}{4m^2c^2},$$

and  $m$  is the mass of the target. Replacing  $W_1$  by  $F_1/Mc^2$  and  $W_2$  by  $F_2/v$  means that we can write

$$\frac{v}{Mc^2} \cdot \frac{F_1}{F_2} = \frac{Q^2}{4m^2c^2}.$$

Since we consider elastic scattering off a particle with mass  $m$  we have  $Q^2 = 2mv$  and thus

$$m = \frac{Q^2}{2v} = x \cdot M \quad \text{since} \quad x = \frac{Q^2}{2Mv}.$$

Inserting this mass into the above equation yields (7.11).

2. The squared four momentum of the scattered parton is  $(q + \xi P)^2 = m^2c^2$ , where  $m$  is the mass of the parton. Expanding and multiplying with  $x^2/Q^2$  yields

$$\frac{x^2M^2c^2}{Q^2}\xi^2 + x\xi - x^2 \left( 1 + \frac{m^2c^2}{Q^2} \right) = 0.$$

Solving the quadratic equation for  $\xi$  and employing the approximate formula given in the question yields the result we were asked to obtain. For  $m = xM$  we have  $x = \xi$ . In a rapidly moving frame of reference we also have  $x = \xi$ , since the masses  $m$  and  $M$  can then be neglected.

## Chapter 8

1. (a) From  $x = Q^2/2Mv$  we obtain  $x \gtrsim 0.003$ .  
 (b) The average number of resolved partons is given by the integral over the parton distributions from  $x_{\min}$  to 1. The normalisation constant,  $A$ , has to be chosen such that the number of valence quarks is exactly 3. One finds:

	Sea quarks	Gluons
$x > 0.3$	0.005	0.12
$x > 0.03$	0.4	4.9

2. (a) The centre-of-mass energy of the electron-proton collision calculated from

$$s = (p_p c + p c)^2 = M^2 c^4 + m^2 c^4 + 2(E_p E - \mathbf{p}_p \cdot \mathbf{p} c^2) \approx 4E_p E$$

is

$$\sqrt{s} = 319 \text{ GeV},$$

if we neglect the electron and proton masses. For a stationary proton target ( $E_p = Mc^2$ ;  $\mathbf{p}_p = \mathbf{0}$ ) the squared centre-of-mass energy of the electron-proton collision is found to be  $s \approx 2EMc^2$ . The electron beam energy would have to be

$$E = \frac{s}{2Mc^2} = 54.1 \text{ TeV}$$

to attain a centre-of-mass energy  $\sqrt{s} = 319 \text{ GeV}$ .

- (b) Consider the underlying electron-quark scattering reaction  $e(E) + q(xE_p) \rightarrow e(E') + q(E'_q)$ , where the bracketed quantities are the particle energies. Energy and momentum conservation yield the following three relations:

$$\begin{aligned} (1) \quad E + xE_p &= E' + E'_q && \text{overall energy} \\ (2) \quad E' \sin \theta / c &= E'_q \sin \gamma / c && \text{transverse momentum} \\ (3) \quad (xE_p - E) / c &= (E'_q \cos \gamma - E' \cos \theta) / c && \text{longitudinal momentum.} \end{aligned}$$

$Q^2$  may be expressed in terms of the electron parameters  $E$ ,  $E'$  and  $\theta$  as (6.2)

$$Q^2 = 2EE'(1 - \cos \theta) / c^2.$$

We now want to replace  $E'$  with the help of (1)-(3) by  $E$ ,  $\theta$  and  $\gamma$ . After some work we obtain

$$E' = \frac{2E \sin \gamma}{\sin \theta + \sin \gamma - \sin(\theta - \gamma)}$$

and thus

$$Q^2 = \frac{4E^2 \sin \gamma (1 - \cos \gamma)}{[\sin \theta + \sin \gamma - \sin(\theta - \gamma)] c^2}.$$

Experimentally the scattering angle  $\gamma$  of the scattered quark may be expressed in terms of the energy-weighted average angle of the hadronisation products

$$\cos \gamma = \frac{\sum_i E_i \cos \gamma_i}{\sum_i E_i}.$$



- (c) The greatest possible value of  $Q^2$  is  $Q_{\max}^2 = s/c^2$ . This occurs for electrons scattering through  $\theta = 180^\circ$  (backward scattering) when the energy is completely transferred from the proton to the electron,  $E' = E_p$ . At HERA  $Q_{\max}^2 = 10^5$  (GeV/c)<sup>2</sup>, while for experiments with a static target and beam energy  $E = 300$  GeV we have  $Q_{\max}^2 = 2EM \approx 560$  (GeV/c)<sup>2</sup>. The spatial resolution is  $\Delta x \simeq \hbar/Q$  which for the cases at hand is  $0.62 \cdot 10^{-3}$  fm and  $8.3 \cdot 10^{-3}$  fm respectively, i.e., a thousandth or a hundredth of the proton radius. In practice the fact that the cross-section falls off very rapidly at large  $Q^2$  means that measurements are only possible up to about  $Q_{\max}^2/2$ .
- (d) The minimal value of  $Q^2$  is obtained at the minimal scattering angle ( $7^\circ$ ) and for the minimal energy of the scattered electron (5 GeV). From (6.2) we obtain  $Q_{\min}^2 \approx 2.1$  GeV<sup>2</sup>/c<sup>2</sup>. The maximal value of  $Q^2$  is obtained at the largest scattering angle ( $178^\circ$ ) and maximal scattering energy (820 GeV). This yields  $Q_{\max}^2 = 10^5$  (GeV/c)<sup>2</sup>. The corresponding values of  $x$  are obtained from  $x = Q^2/2Pq$ , where we have to substitute the four-momentum transfer  $q$  by the four-momenta of the incoming and scattered electron. This gives us  $x_{\min} \approx 2.7 \cdot 10^{-5}$  and  $x_{\max} \approx 1$ .
- (e) The transition matrix element and hence the cross-section of a reaction depend essentially upon the coupling constants and the propagator (4.23), (10.3). We have

$$\sigma_{\text{em}} \propto \frac{e^2}{Q^4}, \quad \sigma_{\text{weak}} \propto \frac{g^2}{(Q^2 + M_W^2 c^2)^2}.$$

Equating these expressions and using  $e = g \sin \theta_W$  implies that the strengths of the electromagnetic and weak interactions will be of the same order of magnitude for  $Q^2 \approx M_W^2 c^2 \approx 10^4$  GeV<sup>2</sup>/c<sup>2</sup>.

## Chapter 9

1. (a) The relation between the event rate  $\dot{N}$ , the cross-section  $\sigma$  and the luminosity  $\mathcal{L}$  is from (4.13):  $\dot{N} = \sigma \cdot \mathcal{L}$ . Therefore using (9.5)

$$\dot{N}_{\mu^+\mu^-} = \frac{4\pi\alpha^2\hbar^2c^2}{3 \cdot 4E^2} \cdot \mathcal{L} = 0.14/\text{s}.$$

At this centre-of-mass energy,  $\sqrt{s} = 8$  GeV, it is possible to produce pairs of u-, d-, s- and c-quarks. The ratio  $R$  defined in (9.10) can therefore be calculated using (9.11) and we so obtain  $R = 10/3$ . This implies

$$\dot{N}_{\text{hadrons}} = \frac{10}{3} \cdot \dot{N}_{\mu^+\mu^-} = 0.46/\text{s}.$$

- (b) At  $\sqrt{s} = 500 \text{ GeV}$  pair creation of all 6 quark flavours is possible. The ratio is thus  $R = 5$ . To reach a statistical accuracy of 10% one would need to detect 100 events with hadronic final states. From  $N_{\text{hadrons}} = 5 \cdot \sigma_{\mu^+\mu^-} \cdot \mathcal{L} \cdot t$  we obtain  $\mathcal{L} = 8 \cdot 10^{33} \text{ cm}^{-2} \text{ s}^{-1}$ . Since the cross-section falls off sharply with increasing centre-of-mass energies, future  $e^+e^-$ -accelerators will need to have luminosities of an order 100 times larger than present day storage rings.
2. (a) From the supplied parameters we obtain  $\delta E = 1.9 \text{ MeV}$  and thus  $\delta W = \sqrt{2} \delta E = 2.7 \text{ MeV}$ . Assuming that the natural decay width of the  $\Upsilon$  is smaller than  $\delta W$ , the measured decay width, i.e., the energy dependence of the cross-section, merely reflects the uncertainty in the beam energy (and the detector resolution). This is the case here.
- (b) Using  $\lambda = \hbar/|p| \approx (\hbar c)/E$  we may re-express (9.8) as

$$\sigma_f(W) = \frac{3\pi\hbar^2 c^2 \Gamma_{e^+e^-} \Gamma_f}{4E^2 [(W - M_\Upsilon c^2)^2 + \Gamma^2/4]}.$$

In the neighbourhood of the (sharp) resonance we have  $4E^2 \approx M_\Upsilon^2 c^4$ . From this we obtain

$$\int \sigma_f(W) dW = \frac{6\pi\hbar^2 c^2 \Gamma_{e^+e^-} \Gamma_f}{M_\Upsilon^2 c^4 \Gamma}.$$

The measured quantity was  $\int \sigma_f(W) dW$  for  $\Gamma_f = \Gamma_{\text{had}}$ . Using  $\Gamma_{\text{had}} = \Gamma - 3\Gamma_{\ell^+\ell^-} = 0.925\Gamma$  we find  $\Gamma = 0.051 \text{ MeV}$  for the total natural decay width of the  $\Upsilon$ . The true height of the resonance ought therefore to be  $\sigma(W = M_\Upsilon) \approx 4,100 \text{ nb}$  (with  $\Gamma_f = \Gamma$ ). The experimentally observed peak was, as a result of the uncertainty in the beam energy, less than this by a factor of over 100 (see Part a).

## Chapter 10

1.  $p + \bar{p} \rightarrow \dots$  strong interaction.  
 $p + K^- \rightarrow \dots$  strong interaction.  
 $p + \pi^- \rightarrow \dots$  baryon number not conserved, so reaction impossible.  
 $\bar{\nu}_\mu + p \rightarrow \dots$  weak interaction, since neutrino participates.  
 $\nu_e + p \rightarrow \dots$  lepton number not conserved, so reaction impossible  
 $\Sigma^0 \rightarrow \dots$  electromagnetic interaction, since photon radiated off.
2. (a) •  $\mathcal{C}|\gamma\rangle = -1|\gamma\rangle$ . The photon is its own antiparticle. Its  $\mathcal{C}$ -parity is  $-1$  since it couples to electric charges which change their sign under the  $\mathcal{C}$ -parity transformation.

- $\mathcal{C}|\pi^0\rangle = +1|\pi^0\rangle$ , since  $\pi_0 \rightarrow 2\gamma$  and C-parity is conserved in the electromagnetic interaction.
  - $\mathcal{C}|\pi^+\rangle = |\pi^-\rangle$ , not a C-eigenstate.
  - $\mathcal{C}|\pi^-\rangle = |\pi^+\rangle$ , not a C-eigenstate.
  - $\mathcal{C}(|\pi^+\rangle - |\pi^-\rangle) = (|\pi^-\rangle - |\pi^+\rangle) = -1(|\pi^-\rangle - |\pi^+\rangle)$ , C-eigenstate.
  - $\mathcal{C}|\nu_e\rangle = |\bar{\nu}_e\rangle$ , not a C-eigenstate.
  - $\mathcal{C}|\Sigma^0\rangle = |\bar{\Sigma}^0\rangle$ , not a C-eigenstate.
- (b) •  $\mathcal{P}\mathbf{r} = -\mathbf{r}$
- $\mathcal{P}\mathbf{p} = -\mathbf{p}$
  - $\mathcal{P}\mathbf{L} = \mathbf{L}$  since  $\mathbf{L} = \mathbf{r} \times \mathbf{p}$
  - $\mathcal{P}\boldsymbol{\sigma} = \boldsymbol{\sigma}$ , since  $\boldsymbol{\sigma}$  is also angular momentum;
  - $\mathcal{P}\mathbf{E} = -\mathbf{E}$ , positive and negative charges are (spatially) flipped by  $\mathcal{P}$  the field vector thus changes its direction;
  - $\mathcal{P}\mathbf{B} = \mathbf{B}$ , magnetic fields are created by moving charges, the sign of the direction of motion and of the position vector are both flipped (cf. Biot-Savart law:  $\mathbf{B} \propto q\mathbf{r} \times \mathbf{v} / |\mathbf{r}|^3$ ).
  - $\mathcal{P}(\boldsymbol{\sigma} \cdot \mathbf{E}) = -\boldsymbol{\sigma} \cdot \mathbf{E}$
  - $\mathcal{P}(\boldsymbol{\sigma} \cdot \mathbf{B}) = \boldsymbol{\sigma} \cdot \mathbf{B}$
  - $\mathcal{P}(\boldsymbol{\sigma} \cdot \mathbf{p}) = -\boldsymbol{\sigma} \cdot \mathbf{p}$
  - $\mathcal{P}(\boldsymbol{\sigma} \cdot (\mathbf{p}_1 \times \mathbf{p}_2)) = \boldsymbol{\sigma} \cdot (\mathbf{p}_1 \times \mathbf{p}_2)$
3. (a) Since pions have spin 0, the spin of the  $f_2$ -meson must be transferred into orbital angular momentum for the pions, i.e.,  $\ell = 2$ . Since  $P = (-1)^\ell$ , the parity of the  $f_2$ -meson is  $P = (-1)^2 * P_\pi^2 = +1$ . Since the parity and C-parity transformations of the  $f_2$ -decay both lead to the same state (spatial exchange of  $\pi^+/\pi^-$  and exchange of the  $\pi$ -charge states) we have  $C = P = +1$  for the  $f_2$ -meson.
- (b) A decay is only possible if  $P$  and  $C$  are conserved by it. Since  $\mathcal{C}|\pi^0\rangle|\pi^0\rangle = +1|\pi^0\rangle|\pi^0\rangle$  and the angular momentum argument of (a) remains valid ( $\ell = 2 \rightarrow P = +1$ ), the decay  $f_2 \rightarrow \pi^0\pi^0$  is allowed. For the decay into two photons we have:  $\mathcal{C}|\gamma\rangle|\gamma\rangle = +1$ . The total spin of the two photons must be  $2\hbar$  and the  $z$ -component  $S_z = \pm 2$ . Therefore one of the two photons must be left-handed and the other right-handed. (Sketch the decay in the centre-of-mass system and draw in the momenta and spins of the photons!) Only a linear combination of  $S_z = +2$  and  $S_z = -2$  can fulfil the requirement of parity conservation, e.g., the state  $(|S_z = +2\rangle + |S_z = -2\rangle)$ . Applying the parity operator to this state yields the eigenvalue  $+1$ . This means that the decay into two photons is also possible.
- 4.(a) The pion decays in the centre-of-mass frame into a charged lepton with momentum  $\mathbf{p}$  and a neutrino with momentum  $-\mathbf{p}$ . Energy conservation supplies  $m_\pi c^2 = \sqrt{m_\ell^2 c^4 + |\mathbf{p}|^2 c^2} + |\mathbf{p}|c$ . For the charged lepton we have

$E_\ell^2 = m_\ell^2 c^4 + |\mathbf{p}|^2 c^2$ . Taking  $v/c = |\mathbf{p}|c/E_\ell$  one obtains from the above relations

$$1 - \frac{v}{c} = \frac{2m_\ell^2}{m_\pi^2 + m_\ell^2} = \begin{cases} 0.73 & \text{for } \mu^+ \\ 0.27 \cdot 10^{-4} & \text{for } e^+ . \end{cases}$$

(b) The ratio of the squared matrix elements is

$$\frac{|\mathcal{M}_{\pi e}|^2}{|\mathcal{M}_{\pi \mu}|^2} = \frac{1 - v_e/c}{1 - v_\mu/c} = \frac{m_e^2}{m_\mu^2} \frac{m_\pi^2 + m_\mu^2}{m_\pi^2 + m_e^2} = 0.37 \cdot 10^{-4} .$$

(c) We need to calculate  $\varrho(E_0) = dn/dE_0 = dn/d|\mathbf{p}| \cdot d|\mathbf{p}|/dE_0 \propto |\mathbf{p}|^2 d|\mathbf{p}|/dE_0$ . From the energy conservation equation (see Part a) we find  $d|\mathbf{p}|/dE_0 = 1 + v/c = 2m_\pi^2/(m_\pi^2 + m_\ell^2)$  and  $|\mathbf{p}_\ell| = c(m_\pi^2 - m_\ell^2)/(2m_\pi)$ . Putting it together we get

$$\frac{\varrho_e(E_0)}{\varrho_\mu(E_0)} = \frac{(m_\pi^2 - m_e^2)^2}{(m_\pi^2 - m_\mu^2)^2} \frac{(m_\pi^2 + m_e^2)^2}{(m_\pi^2 + m_\mu^2)^2} = 3.49 .$$

Therefore the phase space factor for the decay into the positron is larger.

(d) The ratio of the partial decay widths now only depends upon the masses of the particles involved and turns out to be

$$\frac{\Gamma(\pi^+ \rightarrow e^+ \nu)}{\Gamma(\pi^+ \rightarrow \mu^+ \nu)} = \frac{m_e^2}{m_\mu^2} \frac{(m_\pi^2 - m_e^2)^2}{(m_\pi^2 - m_\mu^2)^2} = 1.28 \cdot 10^{-4} .$$

This value is in good agreement with the experimental result.

5. (a) The decay is isotropic in the pion's centre-of-mass frame (marked by a circumflex) and we have  $\hat{\mathbf{p}}_\mu = -\hat{\mathbf{p}}_\nu$ . Four-momentum conservation  $p_\pi^2 = (p_\mu + p_\nu)^2$  implies

$$|\hat{\mathbf{p}}_\mu| = \frac{m_\pi^2 - m_\mu^2}{2m_\pi} c \approx 30 \text{ MeV}/c \quad \text{and thus}$$

$$\hat{E}_\mu = \sqrt{\hat{\mathbf{p}}_\mu^2 c^2 + m_\mu^2 c^4} \approx 110 \text{ MeV} .$$

Using  $\beta \approx 1$  and  $\gamma = E_\pi/m_\pi c^2$ , the Lorentz transformations of  $\hat{E}_\mu$  into the laboratory frame for muons emitted in the direction of the pion's flight ("forwards") and for those emitted in the opposite direction ("backwards") are

$$E_\mu = \gamma \left( \hat{E}_\mu \pm \beta |\hat{\mathbf{p}}_\mu| c \right) \implies \begin{cases} E_{\mu, \max} \approx E_\pi , \\ E_{\mu, \min} \approx E_\pi (m_\mu/m_\pi)^2 . \end{cases}$$

The muon energies are therefore:  $200 \text{ GeV} \lesssim E_\mu \lesssim 350 \text{ GeV}$ .

- (b) In the pion centre-of-mass frame the muons are 100% longitudinally polarised because of the parity violating nature of the decay (Sect. 10.5). This polarisation must now be transformed into the laboratory frame. Consider initially just the “forwards” decays: the pion and muon momenta are parallel to the direction of the transformation. Such a Lorentz transformation will leave the spin unaffected and we see that these muons will also be 100% longitudinally polarised, i.e.,  $P_{\text{long}} = 1.0$ . Similarly for decays in the “backwards” direction we have  $P_{\text{long}} = -1.0$ . The extremes of the muon energies thus lead to extreme values of the polarisation. If we select at intermediate muon energies we automatically vary the longitudinal polarisation of the muon beam. For example 260 GeV muon beams have  $P_{\text{long}} = 0$ . The general case is given in [9].  $P_{\text{long}}$  depends upon the muon energy as

$$P_{\text{long}} = \frac{u - \left[ (m_{\mu}^2/m_{\pi}^2)(1-u) \right]}{u + \left[ (m_{\mu}^2/m_{\pi}^2)(1-u) \right]}, \quad \text{where} \quad u = \frac{E_{\mu} - E_{\mu,\text{min}}}{E_{\mu,\text{max}} - E_{\mu,\text{min}}}.$$

6. (a) The photon energy in the electron rest frame is obtained through a Lorentz transformation with dilatation factor  $\gamma = 26.67 \text{ GeV}/m_e c^2$ . This yields  $E_i = 2\gamma E_{\gamma} = 251.6 \text{ keV}$  for  $E_{\gamma} = 2\pi\hbar c/\lambda = 2.41 \text{ eV}$ .
- (b) Photon scattering off a stationary electron is governed by the Compton scattering formula:

$$E_f(\theta) = \left( \frac{1 - \cos \theta}{mc^2} + \frac{1}{E_i} \right)^{-1},$$

where  $E_f(\theta)$  is the energy of the photon after the scattering and  $\theta$  is the scattering angle. Scattering through  $90^\circ$  ( $180^\circ$ ) leads to  $E_f = 168.8$  ( $126.8$ ) keV. After the reverse transformation into the laboratory system, we have the energy  $E'_\gamma$ :

$$E'_\gamma(\theta) = \gamma E_f(\theta) (1 - \cos \theta) = \gamma \left( \frac{1}{mc^2} + \frac{1}{E_i(1 - \cos \theta)} \right)^{-1}.$$

For the two cases of this example,  $E'_\gamma$  takes on the values 8.80 (13.24) GeV. The scattering angle in the laboratory frame  $\theta_{\text{lab}}$  is also  $180^\circ$ , i.e., the outgoing photon flies exactly in the direction of the electron beam. Generally we have

$$\theta_{\text{lab}} = \pi - \frac{1}{\gamma \tan \frac{\theta}{2}}.$$

- (c) For  $\theta = 90^\circ$  this yields  $\theta_{\text{lab}} = \pi - 1/\gamma = \pi - 19.16 \mu\text{rad}$ . The spatial resolution of the calorimeter must therefore be better than 1.22 mm.

## Chapter 11

1. The neutrino flux is  $\Phi_\nu = 6 \cdot 10^{10} \text{ cm}^{-2} \text{ s}^{-1}$ . The number of  $^{71}\text{Ga}$  nuclei is then

$$\begin{aligned} N_{^{71}\text{Ga}} &= \frac{\text{total Gallium mass}}{\text{mean mass per atom}} \cdot \text{fraction } ^{71}\text{Ga} \\ &= \frac{3 \cdot 10^4 \text{ kg}}{(0.40 \cdot 71 + 0.60 \cdot 69) \cdot 931.5 \cdot 1.6 \cdot 10^{-13} \text{ J}/c^2} \cdot 0.40 \\ &= 1.0 \cdot 10^{29}, \end{aligned}$$

from which the reaction rate can be calculated:

$$\begin{aligned} \dot{N}_{\text{reaction}} &= N_{^{71}\text{Ga}} \cdot \sigma_{\nu\text{Ge}} \cdot \Phi_\nu \cdot \varepsilon \\ &= 1.0 \cdot 10^{29} \cdot 2.5 \cdot 10^{-45} \text{ cm}^2 \cdot 6.0 \cdot 10^{10} \text{ cm}^{-2} \text{ s}^{-1} \cdot 0.5 \\ &= 0.7/\text{day}. \end{aligned}$$

Since  $N(t) = \dot{N}_{\text{reaction}} \tau (1 - e^{-t/\tau})$  one expects after three weeks 8 Ge atoms and after a very long time 11 atoms.

*Note:* The cross-section is highly energy-dependent. The quoted value is an average one that takes into account the energy spectrum of the solar neutrinos.

2. The solutions can be easily confirmed by inserting them in the expressions. The mixing angle in matter is maximal for  $\sin^2 2\theta_M = 1$ , or  $\frac{c^4 \Delta m^2}{2E} \cos 2\theta = \sqrt{2} G_F N_e$ . Remarkably this can occur for arbitrarily small, but different from zero, values of the mixing angle in vacuum,  $\theta$ . Also, this resonance is only possible for  $\Delta m^2 > 0$ . For antineutrinos the additional term in  $H_M$  changes its sign, and the resonance can only occur for negative  $\Delta m^2$ . One can therefore distinguish the normal from the inverted mass ordering. Matter effects are discussed in detail in [5].
3. The CP-transformed channel is  $P_{\bar{\nu}_\alpha \rightarrow \bar{\nu}_\beta}$ , since CP transforms left-handed neutrinos into right-handed antineutrinos. The T-transformed channel is  $P_{\nu_\beta \rightarrow \nu_\alpha}$ . Therefore the effect of CPT is  $P_{\nu_\alpha \rightarrow \nu_\beta} \rightarrow P_{\bar{\nu}_\beta \rightarrow \bar{\nu}_\alpha}$ , and since CPT is conserved it follows  $P_{\nu_\alpha \rightarrow \nu_\beta} = P_{\bar{\nu}_\beta \rightarrow \bar{\nu}_\alpha}$ . Survival probabilities have  $\alpha = \beta$ , and hence  $P_{\nu_\alpha \rightarrow \nu_\alpha} = P_{\bar{\nu}_\alpha \rightarrow \bar{\nu}_\alpha}$ .
4. In case of an inverted hierarchy we have  $m_2 \approx m_1 \approx \sqrt{|\Delta m_{31}^2|}$ , and we can neglect  $\sin^2 \theta_{13} m_3$  with respect to the other two terms in  $m_{\beta\beta}$ . Thus we have

$$m_{\beta\beta} \approx \cos^2 \theta_{13} \sqrt{|\Delta m_{31}^2|} |\cos^2 \theta_{12} + \sin^2 \theta_{12} e^{i\gamma}|.$$

The minimal value occurs for  $e^{i\gamma} = -1$ , and is given by

$$m_{\beta\beta}^{\min} \approx \cos^2 \theta_{13} \cos 2\theta_{12} \sqrt{|\Delta m_{31}^2|} \approx 0.018 \text{ eV}/c^2.$$

We can now rule out the Majorana character of the neutrinos as follows: assume that a future neutrino oscillation experiment shows that the inverted mass ordering is realised. Hence  $m_{\beta\beta}$  must be larger than  $0.018 \text{ eV}/c^2$ . If experiments that look for neutrinoless double beta decay obtain a limit on  $m_{\beta\beta}$  that is smaller than this value, neutrinos must be Dirac particles.

## Chapter 12

1. The total width  $\Gamma_{\text{tot}}$  of  $Z^0$  may be written as

$$\Gamma_{\text{tot}} = \Gamma_{\text{had}} + 3\Gamma_{\ell} + N_{\nu}\Gamma_{\nu}$$

and  $\Gamma_{\nu}/\Gamma_{\ell} = 1.99$  (see text). From (12.9) it follows that

$$\sigma_{\text{had}}^{\text{max}} = \frac{12\pi(\hbar c)^2}{M_Z^2} \frac{\Gamma_e \Gamma_{\text{had}}}{\Gamma_{\text{tot}}}.$$

Solving for  $\Gamma_{\text{tot}}$  and inserting it into the above formula yields from the experimental results  $N_{\nu} = 2.96$ . Varying the experimental results inside the errors only changes the calculated value of  $N_{\nu}$  by about  $\pm 0.1$ .

## Chapter 14

1. The reduced mass of positronium is  $m_e/2$ . From (14.4) we thus find the ground state ( $n = 1$ ) radius to be

$$a_0 = \frac{2\hbar}{\alpha m_e c} = 1.1 \cdot 10^{-10} \text{ m}.$$

The range of the weak force may be estimated from Heisenberg's uncertainty relation:

$$R \approx \frac{\hbar}{M_W c} = 2.5 \cdot 10^{-3} \text{ fm}.$$

At this separation the weak and electromagnetic couplings are of the same order of magnitude. The masses of the two particles, whose bound state would have the Bohr radius  $R$ , would then be

$$M \approx \frac{2\hbar}{\alpha R c} \approx 2 \cdot 10^4 \text{ GeV}/c^2.$$

This is equivalent to the mass of  $4 \cdot 10^7$  electrons or  $2 \cdot 10^4$  protons. This vividly shows just how weak the weak force is.

- From (19.1) the transition probability obeys  $1/\tau \propto E_\gamma^3 |\langle r_{fi} \rangle|^2$ . If  $m$  is the reduced mass of the atomic system, we have  $|\langle r_{fi} \rangle| \propto 1/m$  and  $E_\gamma \propto m$ .  $1/\tau = m/m_e \cdot 1/\tau_H$  implies  $\tau = \tau_H/940$  for protonium.
- The transition frequency in positronium  $f_{e^+e^-}$  is given by

$$\frac{f_{e^+e^-}}{f_H} = \frac{7 g_e m_p}{4 g_p m_e} \frac{|\psi(0)|_{e^+e^-}^2}{|\psi(0)|_H^2}.$$

Using (14.4) one finds  $|\psi(0)|^2 \propto m_{\text{red}}^3 = [(m_1 \cdot m_2)/(m_1 + m_2)]^3$ . One so obtains  $f_{e^+e^-} = 204.5$  GHz. One can analogously find  $f_{\mu^+e^-} = 4.579$  GHz. The deviations from the measured values (0.5 % and 2.6 % respectively) are due to higher order QED corrections to the level splitting. These are suppressed by a factor of the order  $\alpha \approx 0.007$ .

## Chapter 15

- Angular momentum conservation requires  $\ell = 1$ , since pions are spin-0. In the ( $\ell = 1$ ) state, the wave function is antisymmetric, but two identical bosons must have a totally symmetric wave function.
- The branch in the denominator is Cabibbo-suppressed and from (10.21) we thus expect:  $R \approx 20$ .
- (a) From the decay law  $N(t) = N_0 e^{-t/\tau}$  we obtain the fraction of the decaying particles to be  $F = (N_0 - N)/N_0 = 1 - e^{-t/\tau}$ . In the laboratory frame we have  $t_{\text{lab}} = d/(\beta c)$  and  $\tau_{\text{lab}} = \gamma \tau^*$ , where  $\tau^*$  is the usual lifetime in the rest frame of the particle. We thus obtain

$$F = 1 - \exp\left(-\frac{d}{\beta c \gamma \tau^*}\right) = 1 - \exp\left(-\frac{d}{\sqrt{1 - \frac{m^2 c^4}{E^2}} c \frac{E}{m c^2} \tau^*}\right),$$

and from this we find  $F_\pi = 0.9\%$  and  $F_K = 6.7\%$ .

- From four momentum conservation we obtain, e.g., for pion decay  $p_\mu^2 = (p_\pi - p_\nu)^2$  and upon solving for the neutrino energy get

$$E_\nu = \frac{m_\pi^2 c^4 - m_\mu^2 c^4}{2(E_\pi - |\mathbf{p}_\pi| c \cos \theta)}.$$

At  $\cos \theta = 1$  we have maximal  $E_\nu$ , while for  $\cos \theta = -1$  it is minimal. We can so obtain  $E_\nu^{\text{max}} \approx 87.5$  GeV and  $E_\nu^{\text{min}} \approx 0$  GeV (more precisely: 11 keV)



in pion decay. In the case of kaon decay, we obtain  $E_v^{\max} \approx 191 \text{ GeV}$  and  $E_v^{\min} \approx 0 \text{ GeV}$  (more precisely: 291 keV).

4. (a) The average decay length is  $s = v\tau_{\text{lab}} = c\beta\gamma\tau$  where  $\gamma = E_B/m_Bc^2 = 0.5 m_\gamma/m_B$  and  $\beta\gamma = \sqrt{\gamma^2 - 1}$ . One thus obtains  $s = 0.028 \text{ mm}$ .
- (b) From  $0.2 \text{ mm} = c\beta\gamma\tau = \tau \cdot |\mathbf{p}_B|/m_B$  we obtain  $|\mathbf{p}_B| = 2.3 \text{ GeV}/c$ .
- (c) From the assumption,  $m_B = 5.29 \text{ GeV}/c^2 = m_\gamma/2$ , the B-mesons do not have any momentum in the centre-of-mass frame. In the laboratory frame,  $|\mathbf{p}_B| = 2.3 \text{ GeV}/c$  and thus  $|\mathbf{p}_\gamma| = 2|\mathbf{p}_B|$ . We obtain from this  $E_\gamma = \sqrt{m_\gamma^2 c^4 + \mathbf{p}_\gamma^2 c^4} = 11.6 \text{ GeV}$ .
- (d) From four-momentum conservation  $p_\gamma = p_{e^+} + p_{e^-}$  we obtain (setting  $m_e = 0$ )  $E_\gamma = E_{e^+} + E_{e^-}$  and  $\mathbf{p}_\gamma c = E_{e^+} + E_{e^-}$  from this we get  $E_{e^+} = 8.12 \text{ GeV}$  and  $E_{e^-} = 3.44 \text{ GeV}$  (or vice-versa).

## Chapter 16

1. (b) All of the neutral mesons made out of u- and d-quarks (and similarly the  $s\bar{s}$  ( $\phi$ ) meson) are very short lived;  $c\tau < 100 \text{ nm}$ . The dilatation factor  $\gamma$  that they would need to have in order to traverse a distance of several centimetres in the laboratory frame is simply not available at these beam energies. Since mesons with heavy quarks (c, b) cannot be produced, as not enough energy is available, the only possible mesonic decay candidate is the  $K_S^0$ . Similarly the only baryons that come into question are the  $\Lambda^0$  and the  $\bar{\Lambda}^0$ . The primary decay modes of these particles are  $K_S^0 \rightarrow \pi^+\pi^-$ ,  $\Lambda^0 \rightarrow p\pi^-$  and  $\bar{\Lambda}^0 \rightarrow \bar{p}\pi^+$ .
- (c) We have for the mass  $M_X$  of the decayed particle from (16.1)

$$M_X^2 = m_+^2 + m_-^2 + 2\sqrt{\mathbf{p}_+^2/c^2 + m_+^2}\sqrt{\mathbf{p}_-^2/c^2 + m_-^2} - \frac{2}{c^2}|\mathbf{p}_+||\mathbf{p}_-|\cos\angle(\mathbf{p}_+, \mathbf{p}_-),$$

where the masses and momenta of the decay products are denoted by  $m_\pm$  and  $\mathbf{p}_\pm$  respectively. Consider the first pair of decay products: the hypothesis that we have a  $K_S^0 \rightarrow \pi^+\pi^-$  ( $m_\pm = m_{\pi^\pm}$ ) decay leads to  $M_X = 0.32 \text{ GeV}/c^2$  which is inconsistent with the true  $K^0$  mass ( $0.498 \text{ GeV}/c^2$ ). The hypothesis  $\Lambda^0 \rightarrow p\pi^-$  ( $m_+ = m_p$ ,  $m_- = m_{\pi^-}$ ) leads to  $M_X = 1.11 \text{ GeV}/c^2$  which is in very good agreement with the mass of the  $\Lambda^0$ . The  $\bar{\Lambda}^0$  possibility can, as with the  $K^0$  hypothesis, be confidently excluded. Considering the second pair of decay particles we similarly find:  $K^0$  hypothesis,  $M_X = 0.49 \text{ GeV}/c^2$ ;  $\Lambda^0$  hypothesis,  $M_X = 2.0 \text{ GeV}/c^2$ ; the  $\bar{\Lambda}^0$  hypothesis also leads to a contradiction. In this case we are dealing with the decay of a  $K^0$ .

- (d) Conservation of strangeness in the strong interaction means that as well as the  $\Lambda^0$ , which is made up of a uds quark combination, a further hadron with an  $\bar{s}$ -quark must be produced. The observed  $K_S^0$  decay means that this was

a  $K^0$  ( $\bar{s}d$ ).<sup>1</sup> Charge and baryon number conservation now combine to imply that the most likely total reaction was

$$p + p \rightarrow K^0 + \Lambda^0 + p + \pi^+.$$

We cannot, however, exclude additional, unobserved neutral particles or very short lived intermediate states (such as a  $\Delta^{++}$ ).

2. Let us consider the positively charged  $\Sigma$  particles  $|\Sigma^+\rangle = |u^\uparrow u^\uparrow s^\downarrow\rangle$  and  $|\Sigma^{+*}\rangle = |u^\uparrow u^\uparrow s^\uparrow\rangle$ . Since the spins of the two u-quarks are parallel, we have

$$\sum_{\substack{i,j=1 \\ i < j}}^3 \frac{\sigma_i \cdot \sigma_j}{m_i m_j} = \frac{\sigma_u \cdot \sigma_u}{m_u^2} + 2 \frac{\sigma_u \cdot \sigma_s}{m_u m_s}.$$

We first inspect

$$2 \sigma_u \cdot \sigma_s = \sum_{\substack{i,j=1 \\ i < j}}^3 \sigma_i \cdot \sigma_j - \sigma_u \cdot \sigma_u.$$

We already know the first term on the r.h.s. from (16.10). It is  $-3$  for  $S = 1/2$  baryons and  $+3$  for  $S = 3/2$  baryons. The second term is  $+1$ . This yields

$$\Delta M_{ss} = \begin{cases} \frac{4 \hbar^3}{9 c^3} \pi \alpha_s |\psi(0)|^2 \left( \frac{1}{m_{u,d}^2} - \frac{4}{m_{u,d} m_s} \right) & \text{for the } \Sigma \text{ states,} \\ \frac{4 \hbar^3}{9 c^3} \pi \alpha_s |\psi(0)|^2 \left( \frac{1}{m_{u,d}^2} + \frac{2}{m_{u,d} m_s} \right) & \text{for the } \Sigma^* \text{ states.} \end{cases}$$

The average mass difference between the  $\Sigma$  and  $\Sigma^*$  baryons is about  $200 \text{ MeV}/c^2$ . With the mass formula (16.12) we have

$$M_{\Sigma^*} - M_{\Sigma} = \Delta M_{ss}(\Sigma^*) - \Delta M_{ss}(\Sigma) = \frac{4 \hbar^3}{9 c^3} \pi \alpha_s |\psi(0)|^2 \frac{6}{m_{u,d} m_s} \approx 200 \text{ MeV}/c^2,$$

where we assume that  $\psi(0)$  is the same for both states. We thus obtain ( $m_{u,d} = 363 \text{ MeV}/c^2$ ,  $m_s = 538 \text{ MeV}/c^2$ )

$$\alpha_s |\psi(0)|^2 = 0.61 \text{ fm}^{-3}.$$

<sup>1</sup>Both the  $K^0$  and the  $\bar{K}^0$  can decay as  $K_S^0$  (cf. Sect. 15.4).

Inserting a hydrogen atom-type wave function,  $|\psi(0)|^2 = 3/4\pi r^3$ , and  $\alpha_s \approx 1$ , yields a rough approximation for the average separation  $r$  of the quarks in such baryons:  $r \approx 0.8$  fm.

3. The  $\Lambda$  is an isospin singlet ( $I = 0$ ). To a first approximation the decay is just the quark transition  $s \rightarrow u$ , which changes the isospin by  $1/2$ . Thus the pion-nucleon system must be a  $I = 1/2$  state. Charge conservation implies that the third component is  $I_3^N + I_3^\pi = -1/2$ . The matrix elements of the decay of the  $\Lambda^0$  are proportional to the squares of the Clebsch-Gordan coefficients:

$$\frac{\sigma(\Lambda^0 \rightarrow \pi^- + p)}{\sigma(\Lambda^0 \rightarrow \pi^0 + n)} = \frac{(1 \frac{1}{2} -1 + \frac{1}{2} | \frac{1}{2} -\frac{1}{2})^2}{(1 \frac{1}{2} 0 -\frac{1}{2} | \frac{1}{2} -\frac{1}{2})^2} = \frac{(-\sqrt{2/3})^2}{(\sqrt{1/3})^2} = 2.$$

4. The probability that a muon be captured from a  $1s$  state into a  $^{12}\text{C}$  nucleus is

$$\frac{1}{\tau_{\mu\text{C}}} = \frac{2\pi}{\hbar} \left| \langle ^{12}\text{B} e^{ip_\nu r} | \sum_i g_A \sigma_i I_- | ^{12}\text{C} \psi_\mu(r) \rangle_{(r=0)} \right|^2 \int \frac{p_\nu^2 dp_\nu d\Omega}{(2\pi\hbar)^3 dE_\nu}.$$

Since carbon has  $J^P = 0^+$  and boron  $J^P = 1^+$ , this is a purely axial vector transition. We further have  $dp_\nu/dE_\nu = 1/c$ ,  $\int d\Omega = 4\pi$  and  $|\psi_\mu(r=0)|^2 = 3/(4\pi r_\mu^3)$ . The radius of the  $^{12}\text{C}$  muonic atomic is found to be

$$r_\mu = \frac{a_{\text{Bohr}} m_e}{Z m_\mu} = 42.3 \text{ fm},$$

and the energy is

$$E_\nu = m_\mu c^2 - 13.3 \text{ MeV} \approx 90 \text{ MeV}.$$

This yields the absorption probability

$$\frac{1}{\tau_{\mu\text{C}}} = \frac{2\pi}{\hbar c} \frac{4\pi c E_\nu^2}{(2\pi)^3 (\hbar c)^3} \left| \langle ^{12}\text{B} | \sum_i g_A \sigma_i I_- | ^{12}\text{C} \rangle \right|^2 |\psi(0)|^2.$$

These are all known quantities except for the matrix element. This may be extracted from the known lifetime of the  $^{12}\text{B} \rightarrow ^{12}\text{C} + e^- + \bar{\nu}_e$  decay:

$$\frac{1}{\tau_{^{12}\text{B}}} = \frac{1}{2\pi^3 \hbar^7 c^6} \left| \langle ^{12}\text{C} | \sum_i g_A \sigma_i I_+ | ^{12}\text{B} \rangle \right|^2 E_{\text{max}}^5.$$

We thus finally obtain

$$\frac{1}{\tau_{\mu\text{C}}} \approx 1.5 \cdot 10^4 \text{ s}^{-1}.$$

The total decay probability of the muon decay in  $^{12}\text{C}$  is the sum of the probabilities of the free muon decaying and of its being captured by the nucleus:

$$\frac{1}{\tau} = \frac{1}{\tau_\mu} + \frac{1}{\tau_{\mu\text{C}}}.$$

5. These branching ratios depend primarily upon two things: (a) the phase space and (b) the fact that the strangeness changes in the first case (Cabibbo suppression) but not in the latter. A rough estimate may be obtained by assuming that the matrix elements are, apart from Cabibbo suppression, identical. From (10.21) and (16.58) one finds

$$\frac{W(\Sigma^- \rightarrow n)}{W(\Sigma^- \rightarrow \Lambda^0)} \approx \frac{\sin^2 \theta_C}{\cos^2 \theta_C} \cdot \left(\frac{E_1}{E_2}\right)^5 = \frac{1}{20} \cdot \left(\frac{257 \text{ MeV}}{81 \text{ MeV}}\right)^5 \approx 16.$$

This agreement is not bad at all, considering the coarseness of our approximation. In the decay  $\Sigma^+ \rightarrow n + e^+ + \nu_e$  we would need two quarks to change their flavours; (suu)  $\rightarrow$  (ddu).

6. (a) Baryon number conservation means that baryons can neither be annihilated nor created but rather only transformed into each other. Hence only the relative parities of the baryons have any physical meaning.
- (b) The deuteron is a ground state p-n system, i.e.,  $\ell = 0$ . Its parity is therefore  $\eta_d = \eta_p \eta_n (-1)^0 = +1$ . Since quarks have zero orbital angular momentum in nucleons, the quark intrinsic parities must be positive.
- (c) The downwards cascade of pions into the ground state may be seen from the characteristic X-rays.
- (d) Since the deuteron has spin 1, the d- $\pi$  system is in a state with total angular momentum  $J = 1$ . The two final state neutrons are identical fermions and so must have an antisymmetric spin-orbit wave function. Only  ${}^3\text{P}_1$  of the four possible states with  $J = 1$ ,  ${}^3\text{S}_1$ ,  ${}^1\text{P}_1$ ,  ${}^3\text{P}_1$  and  ${}^3\text{D}_1$  fulfils this requirement.
- (e) From  $\ell_m = 1$ , we see that the pion parity must be  $\eta_\pi = \eta_n^2 (-1)^1 / \eta_d = -1$ .
- (f) The number of quarks of each individual flavour ( $N_q - N_{\bar{q}}$ ) is separately conserved in parity conserving interactions. The quark parities can therefore be separately chosen. One could thus choose, e.g.,  $\eta_u = -1, \eta_d = +1$ , giving the proton a positive and the neutron a negative parity. The deuteron would then have a negative parity and the charged pions a positive one. The  $\pi^0$  as a  $u\bar{u}/d\bar{d}$  mixed state would though keep its negative parity. Particles like  $(\pi^+, \pi^0, \pi^-)$  or (p, n) although inside the same isospin multiplets would then have distinct parities – a rather unhelpful convention. For  $\eta_n = \eta_p = -1$ , on the other hand, isospin symmetry would be fulfilled. The parities of nucleons and odd nuclei would then be the opposite of the standard convention, while those of mesons and even nuclei would be unchanged. The  $\Lambda$  and  $\Lambda_c$  parities are just those of the s- and c-quarks and may be chosen to be positive.

## Chapter 17

1. The ranges,  $\lambda \approx \hbar c/mc^2$ , are: 1.4 fm ( $1\pi$ ), 0.7 fm ( $2\pi$ ), 0.3 fm ( $\rho$ ,  $\omega$ ). Two pion exchange with vacuum quantum numbers,  $J^P = 0^+$ ,  $I = 0$ , generates a scalar potential which is responsible for nuclear binding. Because of its negative parity, the pion is emitted with an angular momentum,  $\ell = 1$ . The spin dependence of this component of the nuclear force is determined by this. Similar properties hold for the  $\rho$  and  $\omega$ . The isospin dependence is determined by the isospin of the exchange particle;  $I = 1$  for the  $\pi$  and  $\rho$  and  $I = 0$  for the  $\omega$ . Since isospin is conserved in the strong interaction, the isospin of interacting particles is coupled, just as is the case with angular momentum.
2. Taking (17.1), (17.2) and (17.6) into account we obtain

$$\sigma = 4\pi \left( \frac{\sin kb}{k} \right)^2.$$

At low energies, where the  $\ell = 0$  partial wave dominates, we obtain in the  $k \rightarrow 0$  limit, the total cross-section,  $\sigma = 4\pi b^2$ .

## Chapter 18

1. At constant entropy  $S$  the pressure obeys

$$p = - \left( \frac{\partial U}{\partial V} \right)_S,$$

where  $V$  is the volume and  $U$  is the internal energy of the system. In the Fermi gas model we have from (18.9):

$$U = \frac{3}{5}AE_F \quad \text{and hence} \quad p = -\frac{3}{5}A \frac{\partial E_F}{\partial V}.$$

From (18.3) we find for  $N = Z = A/2$ :

$$A = 2 \frac{V p_F^3}{3\pi^2 \hbar^3} = 2 \frac{V (2ME_F)^{3/2}}{3\pi^2 \hbar^3} \implies \frac{\partial E_F}{\partial V} = -\frac{2E_F}{3V}.$$

The Fermi pressure is then

$$p = \frac{2A}{5V} E_F = \frac{2}{5} \rho_N E_F,$$

where  $\rho_N$  is the nucleon density. This implies for  $\rho_N = 0.17$  nucleons/fm<sup>3</sup> and  $E_F \approx 33$  MeV

$$p = 2.2 \text{ MeV/fm}^3 = 3.6 \cdot 10^{27} \text{ bar}.$$

2. (a) We only consider the odd nucleons. The even ones are all paired off in the ground state. The first excited state is produced either by (I) the excitation of the unpaired nucleon into the next subshell or (II) by the pairing of this nucleon with another which is excited from a lower lying subshell.

	<sup>7</sup> Li	<sup>23</sup> Na	<sup>33</sup> S	<sup>41</sup> Sc	<sup>83</sup> Kr	<sup>93</sup> Nb
Ground state	1p <sub>3/2</sub> <sup>1</sup>	1d <sub>5/2</sub> <sup>3</sup>	1d <sub>3/2</sub> <sup>1</sup>	1f <sub>7/2</sub> <sup>1</sup>	1g <sub>9/2</sub> <sup>-3</sup>	1g <sub>9/2</sub> <sup>1</sup>
Excited (I)	1p <sub>1/2</sub> <sup>1</sup>	2s <sub>1/2</sub> <sup>1</sup>	(1f <sub>7/2</sub> <sup>1</sup> )	(2p <sub>3/2</sub> <sup>1</sup> )	(1g <sub>7/2</sub> <sup>1</sup> )	(1g <sub>7/2</sub> <sup>1</sup> )
Excited (II)	(1s <sub>1/2</sub> <sup>-1</sup> )	1p <sub>1/2</sub> <sup>-1</sup>	2s <sub>1/2</sub> <sup>-1</sup>	1d <sub>3/2</sub> <sup>-1</sup>	2p <sub>1/2</sub> <sup>-1</sup>	2p <sub>1/2</sub> <sup>-1</sup>
$J_0^P$ experiment	3/2 <sup>-</sup>	3/2 <sup>+</sup>	3/2 <sup>+</sup>	7/2 <sup>-</sup>	9/2 <sup>+</sup>	9/2 <sup>+</sup>
$J_0^P$ model	3/2 <sup>-</sup>	5/2 <sup>+</sup>	3/2 <sup>+</sup>	7/2 <sup>-</sup>	9/2 <sup>+</sup>	9/2 <sup>+</sup>
$J_1^P$ experiment	1/2 <sup>-</sup>	5/2 <sup>+</sup>	1/2 <sup>+</sup>	3/2 <sup>+</sup>	7/2 <sup>+</sup>	1/2 <sup>-</sup>
$J_1^P$ case (I)	1/2 <sup>-</sup>	1/2 <sup>+</sup>	(7/2 <sup>-</sup> )	(3/2 <sup>-</sup> )	(7/2 <sup>+</sup> )	(7/2 <sup>+</sup> )
$J_1^P$ case (II)	(1/2 <sup>+</sup> )	1/2 <sup>-</sup>	1/2 <sup>+</sup>	3/2 <sup>+</sup>	1/2 <sup>-</sup>	1/2 <sup>-</sup>

Those states whose excitation would be beyond a “magic” boundary are shown here in brackets. This requires a lot of energy and so is only to be expected for higher excitations. As one sees, the predictive powers of the shell model are good for those nuclei where the unfilled subshell is only occupied by a single nucleon.

- (b) The  $(p - 1p_{3/2}^1; n - 1p_{3/2}^1)$  in <sup>6</sup>Li implies  $J^P = 0^+, 1^+, 2^+, 3^+$ . <sup>40</sup>K has from  $(p - 1d_{3/2}^{-1}; n - 1f_{7/2}^1)$  a possible coupling to  $2^-, 3^-, 4^-, 5^-$ .
3. (a) An <sup>17</sup>O nucleus may be viewed as being an <sup>16</sup>O nucleus with an additional neutron in the 1f<sub>5/2</sub> shell. The energy of this level is thus  $B(^{16}\text{O}) - B(^{17}\text{O})$ . The 1p<sub>1/2</sub> shell is correspondingly at  $B(^{15}\text{O}) - B(^{16}\text{O})$ . The gap between the shells is thus

$$E(1f_{5/2}) - E(1p_{1/2}) = 2B(^{16}\text{O}) - B(^{15}\text{O}) - B(^{17}\text{O}) = 11.5 \text{ MeV}.$$

- (b) One would expect the lowest excitation level with the “right” quantum numbers to be produced by exciting a nucleon from the topmost, occupied shell into the one above. For <sup>16</sup>O this would be the  $J^P = 3^-$  state, which is at 6.13 MeV, and could be interpreted as  $(1p_{1/2}^{-1}, 1d_{5/2})$ . The excitation energy is, however, significantly smaller than the theoretical result of 11.5 MeV. It seems that collective effects (state mixing) are making themselves felt. This is confirmed by the octupole radiation transition probability, which is an order of magnitude above what one would expect for a single particle excitation.
- (c) The  $1/2^+$  quantum numbers make it natural to interpret the first excited state of <sup>17</sup>O as  $2s_{1/2}$ . The excitation energy is then the gap between the shells.
- (d) Assuming (more than a little naively) that the nuclei are homogeneous spheres with identical radii, one finds from (2.11) that the difference in the

binding energies implies the radius is  $(3/5) \cdot 16\hbar\alpha c/3.54 \text{ MeV} = 3.90 \text{ fm}$ , which is much larger than the value of  $3.1 \text{ fm}$ , which follows from (5.56). In the shell model one may interpret each of these nuclei as an  $^{16}\text{O}$  nucleus with an additional nucleon. The valence nucleon in the  $d_{5/2}$  shell thus has a larger radius than one would expect from the above simple formula which does not take shell effects into account.

- (e) The larger Coulomb repulsion means that the potential well felt by the protons in  $^{17}\text{F}$  is shallower than that of the neutrons in  $^{17}\text{O}$ . As a result the wave function of the excited, “additional” proton in  $^{17}\text{F}$  is more spread out than that of the equivalent “additional” neutron in  $^{17}\text{O}$  and the nuclear force felt by the neutron is stronger than that acting upon the proton. This difference is negligible for the ground state since the nucleon is more strongly bound.
4. At the upper edge of the closed shells which correspond to the magic numbers 50 and 82 we find the closely adjacent  $2p_{1/2}$ ,  $1g_{9/2}$  and the  $2d_{3/2}$ ,  $1h_{11/2}$ ,  $3s_{1/2}$  levels respectively. It is thus natural that for nuclei with nucleon numbers just below 50 or 82 the transition between the ground state and the first excited state is a single particle transition ( $g_{9/2} \leftrightarrow p_{1/2}$  and  $h_{11/2} \leftrightarrow d_{3/2}, s_{1/2}$  respectively). Such processes are 5th order (M4 or E5) and hence extremely unlikely [6].
5. (a) The spin of the state is given by the combination of the unpaired nucleons which are in the  $(p - 1f_{7/2}, n - 1f_{7/2})$  state.
- (b) The nuclear magnetic moment is just the sum of the magnetic moments of the neutron in the  $f_{7/2}$  shell  $-1.91 \mu_N$  and of the proton in the  $f_{7/2}$  shell  $+5.58 \mu_N$ . From (18.36) we would expect a  $g$  factor of 1.1.
6. (a) In the de-excitation  $i \rightarrow f$  of an Sm nucleus *at rest* the atom receives a recoil energy of  $\mathbf{p}_{\text{Sm}}^2/2M$  where  $|\mathbf{p}_{\text{Sm}}| = |\mathbf{p}_\gamma| \approx (E_i - E_f)/c$ . In the case at hand this is  $3.3 \text{ eV}$ . The same amount of energy is lost when the photon is absorbed by another Sm nucleus.
- (b) If we set the matrix element in (19.1) to one, this implies a lifetime of  $\tau = 0.008 \text{ ps}$ , which is equivalent to  $\Gamma = 80 \text{ MeV}$ . In actual measurements one finds  $\tau = 0.03 \text{ ps}$ , i.e.,  $\Gamma = 20 \text{ MeV}$  [10], which is of a similar size. Since the width of the state is much smaller than the energy shift of  $2 \cdot 3.3 \text{ eV}$ , no absorption can take place. Thermal motion will change  $|\mathbf{p}_{\text{Sm}}|$  by roughly  $\pm\sqrt{M \cdot kT}$ . At room temperature this corresponds to smearing the energy by  $\pm 0.35 \text{ eV}$ , which is also insufficient.
- (c) If the Sm atom emits a neutrino before the deexcitation, then  $|\mathbf{p}_{\text{Sm}}|$  is changed by  $\pm|\mathbf{p}_\nu| = \pm E_\nu/c$ . If the emission directions of the neutrino and of the photon are opposite to each other, then the energy of the radiated photon is  $3.12 \text{ eV}$  larger than the excitation energy  $E_i - E_f$ . This corresponds to the classical Doppler effect. In this case resonant fluorescence is possible for the  $\gamma$  radiation. The momentum direction of the neutrino can be determined in this fashion.
7. The three lowest proton shells in the  $^{14}\text{O}$  nucleus, the  $1s_{1/2}$ ,  $1p_{3/2}$  and  $1p_{1/2}$ , are fully occupied as are the two lowest neutron shells. The  $1p_{1/2}$  shell is, however, empty (sketched on p. 333). Thus one of the two valence nucleons (one of

the protons in their  $1p_{1/2}$  shell) can transform into a neutron at the equivalent level and with the same wave function (super allowed  $\beta$ -decay). We thus have  $\int \psi_n^* \psi_p = 1$ . This is a  $0^+ \rightarrow 0^+$  transition, i.e., a pure Fermi decay. Each of the two protons contributes a term to the matrix element equal to the vector part of (16.48). The total is therefore  $|\mathcal{M}_{fi}|^2 = 2g_V^2/V^2$ . Equation (16.56) now becomes

$$\frac{\ln 2}{t_{1/2}} = \frac{1}{\tau} = \frac{m_e^5 c^4}{2\pi^3 \hbar^7} \cdot 2g_V^2 \cdot f(E_0).$$

Using the vectorial coupling (16.65) one finds the half-life is 70.373 s – which is remarkably close to the experimental value. Note: the quantum numbers and definite shell structure here means that this is one of the few cases where a nuclear  $\beta$ -decay can be calculated exactly. In practice this decay is used to determine the strength of the vectorial coupling.

## Chapter 19

- (a) In the collective model of giant resonances we consider  $Z$  protons and  $N$  neutrons whose mutual vibrations are described by a harmonic oscillator. The Hamiltonian may be written as

$$\mathcal{H} = \frac{p^2}{2m} + \frac{m\omega^2}{2}x^2, \quad \text{where} \quad \hbar\omega = 80A^{-1/3} \text{ MeV},$$

and  $m = A/2M_N$  is the reduced mass. The solution of the Schrödinger equation yields the lowest lying oscillator states [14]

$$\psi_0 = \frac{1}{\sqrt[4]{\pi} \sqrt{x_0}} \cdot e^{-(x/x_0)^2/2}, \quad \text{where} \quad x_0 = \sqrt{\hbar/m\omega},$$

$$\psi_1 = \frac{1}{\sqrt[4]{\pi} \sqrt{x_0}} \cdot \sqrt{2} \left(\frac{x}{x_0}\right) e^{-(x/x_0)^2/2}.$$

The average deviation is

$$x_{01} := \langle \psi_0 | x | \psi_1 \rangle = \frac{\sqrt{2}}{\sqrt{\pi}} x_0 \int \left(\frac{x}{x_0}\right)^2 e^{-(x/x_0)^2} d\frac{x}{x_0} = \frac{\sqrt{2}}{\sqrt{\pi}} x_0.$$

For  $^{40}\text{Ca}$  we have  $x_0 = 0.3$  fm and  $x_{01} = 0.24$  fm.

- The matrix element is  $Zx_{01}$ . Its square is therefore 23 fm<sup>2</sup>.
- The single particle excitations have about half the energy of the giant resonance, i.e.,  $\hbar\omega \approx 40A^{-1/3}$  MeV. The reduced mass in this case is approximately the nucleon mass, since the nucleon moves in the mean field



of the heavy nucleus. This increases  $x_0$ , and thus  $x_{01}$ , by a factor of  $\sqrt{40}$ . The 24 nucleons in the outermost shell each contribute to the square of the matrix element with an effective charge  $e/2$ . The square of the matrix element is so seen to be  $27.6 \text{ fm}^2$ . The agreement with the result of (b), i.e., the model where the protons and neutrons oscillate collectively, is very good.

2. Using the definitions in Chap. 18.4, we obtain for small deformations

$$\varepsilon \approx \frac{3}{2} \cdot \frac{a-b}{\langle R \rangle}, \quad \langle R \rangle = (ab^2)^{1/3}.$$

- (a) From this we get  $a = (1 + \varepsilon)\langle R \rangle$ ,  $b = \langle R \rangle/\sqrt{1 + \varepsilon} \approx (1 - \varepsilon/2)\langle R \rangle$  and  $Q = \frac{6}{5}Ze\langle R \rangle^2\varepsilon$ . With the central nuclear density  $\rho_N \approx 0.17 \text{ nucleons/fm}^3$  (5.59), we obtain  $a \approx 7.6 \text{ fm}$ ,  $b \approx 5.7 \text{ fm}$ ,  $Q \approx 710 \cdot e \text{ fm}^2$ . The nucleus is prolately deformed.
- (b) For a rotation of a rigid ellipsoid transverse to its symmetry axis, the moment of inertia is

$$\Theta_{\text{rigid ellipsoid}} = \frac{1}{5}M(a^2 + b^2).$$

For small deformations we have

$$\Theta_{\text{rigid ellipsoid}} \approx \left(1 + \frac{\varepsilon}{2} + \varepsilon^2\right) \cdot \Theta_{\text{rigid sphere}},$$

and we obtain  $\Theta_{\text{rigid ellipsoid}} \approx 1.15 \cdot \Theta_{\text{rigid sphere}}$ , with  $\Theta_{\text{rigid sphere}} = \frac{2}{5}M\langle R \rangle^2 \approx 2.6 \cdot 10^6 \text{ MeV}/c^2 \text{ fm}^2$  being the moment of inertia of a rigid sphere.

If the nucleus would behave as an ideal fluid, then it would have a moment of inertia  $\Theta_{\text{ideal fluid}} \approx 0.086 \cdot \Theta_{\text{rigid sphere}} \approx 2.2 \cdot 10^5 \text{ MeV}/c^2 \text{ fm}^2$ .

3. The Fermi velocity is  $v_F = p_F/\sqrt{M_N^2 + p_F^2/c^2} = 0.26 c$ . The angular velocity is

$$\omega = \frac{|\mathbf{L}|}{\Theta} \approx \frac{60\hbar}{AM_N(a^2 + b^2)^2/5} = 0.95 \cdot 10^{21} \text{ s}^{-1},$$

where  $a = 2b = \sqrt[3]{4R}$ , and we have employed the value of  $R$  from (5.56). The speed is  $v = a \cdot \omega$  and is about  $0.03 c$  or around 12 % of the Fermi velocity. The high rotational velocity causes a Coriolis force which is responsible for breaking up the nucleon pairs.

## Chapter 20

1. (a) In the reaction  $4p \rightarrow \alpha + e^+ + 2\nu_e$ , 26.72 MeV of energy is released. The neutrinos carry off 0.52 MeV, and so 26.2 MeV remains to heat up the Sun. The number of hydrogen atoms which are converted into helium every second is:

$$\dot{N}_p = 4 \cdot \frac{4 \cdot 10^{26} \text{ W}}{26.4 \times 1.6 \cdot 10^{-13} \text{ Ws}} \approx 0.4 \cdot 10^{39} \text{ atoms/s} .$$

- (b)  $0.4 \cdot 10^{10} \text{ kg/s}$   
 (c)  $\approx 7\%$   
 (d)  $\approx 130$  terrestrial masses  
 (e) Nuclear reactions take place in the interior of the Sun, primarily at radii  $r < R_\odot/4$ . By burning off 7% of the hydrogen the helium concentration in the interior of the Sun is increased by about 50%. Doubling this concentration means that hydrogen burning is no longer efficient: helium burning starts up and the Sun swells into a red giant.
2. (a) The number of neutrons in the neutron star is  $N_n = 1.8 \cdot 10^{57}$ . The energy released by fusing  $N_n$  protons into  ${}^{56}\text{Fe}$  is  $2.6 \cdot 10^{45} \text{ J}$ .
- (b) We neglect the gravitational energy of the iron core in the original star, (since  $R \gg 10 \text{ km}$ ). Thus the energy released during the implosion is the gravitational energy of the neutron star minus the energy needed to transform the iron into free neutrons (this last is the energy which was originally released during the fusion of hydrogen into iron):

$$E_{\text{Implosion}} \approx \frac{3GM^2}{5R} - 2.6 \cdot 10^{45} \text{ J} = 3.3 \cdot 10^{46} \text{ J} .$$

The energy released via the implosion during the supernova explosion is more than ten times larger than the fusion energy. Although only about 20-50% of the matter of the original star ends up in the neutron star, the fusion energy released during the entire lifetime of the star is slightly less than the energy released in the supernova explosion.

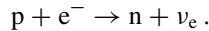
- (c) Most of the energy is radiated off as neutrino emission:

$$e^+ + e^- \rightarrow \bar{\nu}_e + \nu_e, \bar{\nu}_\mu + \nu_\mu, \bar{\nu}_\tau + \nu_\tau .$$

The positrons in this process are generated in the reaction:

$$p + \bar{\nu}_e \rightarrow e^+ + n .$$

Neutrinos can, however, also be directly produced in:



The last two processes are responsible for the transformation of the protons in  $^{56}\text{Fe}$ .

## References

1. H.A. Bethe, *Ann. Physik* **5**, 325 (1930)
2. F. Bloch, *Ann. Physik* **16**, 285 (1933)
3. E.R. Cohen, B.N. Taylor, *Rev. Mod. Phys.* **59**, 1121 (1987)
4. T. Ferbel, *Experimental Techniques in High Energy Physics* (Addison-Wesley, Menlo Park, 1987)
5. C. Giunti, C.W. Kim, *Fundamentals of Neutrino Physics and Astrophysics* (Oxford University Press, Oxford, 2007)
6. M. Goldhaber, A.W. Sunyar, *Phys. Rev.* **83**, 906 (1951)
7. C. Grupen, B.A. Schwarz, *Particle Detectors*, 2nd edn. (Cambridge University Press, Cambridge, 2008)
8. P. Langacker, in *Precision Tests of the Standard Electroweak Model*, ed. by P. Langacker (World Scientific, Singapur, 1995)
9. L.M. Lederman, M.J. Tannenbaum, in *Advances in Particle Physics*, ed. by R.L. Cool, R.E. Marshak, vol. 1 (Interscience, New York, 1968)
10. C.M. Lederer, V.S. Shirley, *Table of Isotopes*, 7th edn. (Wiley, New York, 1978)
11. W.R. Leo, *Techniques for Nuclear and Particle Physics Experiments*, 2nd edn. (Springer, Berlin/Heidelberg/New York, 1994)
12. Particle Data Group, J. Beringer et al., *Review of Particle Properties*. *Phys. Rev. D* **86**, 010001 (2012)
13. P.W. Petley, *Nature* **303**, 373 (1983)
14. F. Schwabl, *Quantum Mechanics*, 4th edn. (Springer, Berlin/Heidelberg/New York, 2007)
15. K. Wille, *The Physics of Particle Accelerators* (Oxford University Press, Oxford, 2000)
16. E. Wilson, E.J.N. Wilson, *An Introduction to Particle Accelerators* (Oxford University Press, Oxford, 2001)
17. H. Wiedemann, *Particle Accelerator Physics*, 3rd edn. (Springer, Berlin/Heidelberg/New York, 2007)

# Index

- Absorption coefficient, 413
- Activity, 26
- Alpha decay, 25, 31
- Antiproton, 186
- Asymmetry
  - energy, 20, 306
  - term, 20
- Asymptotic freedom, 110, 222
- ATLAS experiment, 202
- Atomic number, 13
- Axial vector current, 155, 280, 331
  
- BaBar experiment, 154, 245, 248
- Baryon, 103, 104, 253–255
  - number conservation, 104
- Beauty oscillations, 245, 249
- Belle experiment, 154, 245, 248
- Beta decay, 25, 27–29, 274–277, 281, 330, 332
  - allowed, 332
  - double, 29, 338
  - forbidden, 332
  - inverse, 144, 307
  - neutrinoless double, 180, 340
  - super allowed, 332
- Bethe-Bloch formula, 412
- Bhabha scattering, 127
- Big bang, 204
- Binding energy, 19, 20, 25, 294, 305, 306, 310, 311
  - of deuteron, 17, 292–294
  - of hypernuclei, 310
- Bjorken scaling variable, 89
- Bohr magneton, 423
- Bohr radius, 216, 217, 423
  
- Born approximation, 59, 325, 326
- Boson
  - gluons, 3, 4
  - Goldstone, 198
  - Higgs particle, 197–200, 202
  - photon, 3, 4
  - W, 3, 4, 143, 144, 146, 187
  - Z<sup>0</sup>, 3, 4, 123, 133, 143, 186, 187, 189
- Bottomium, 226
  - decays, 229
- Breit frame, 94, 119
- Breit-Wigner formula, 129, 190
- Bremsstrahlung, 412
- Bubble chamber, 414
  
- C-Parity, 5, 156
- Cabibbo angle, 152, 276
- Cabibbo-Kobayashi-Maskawa matrix, see CKM matrix, 153
- Callan-Gross relation, 92
- Calorimeter, 416
- Carbon cycle, 396
- Central potential, 292, 312
- CERN, 42, 87, 186, 187, 410
- Chaos, 401, 402
- Charge
  - colour, 4, 104–106, 108
  - conjugation, 5, 156
  - distribution, 67, 70, 80
  - electric, 4
  - weak, 4, 146, 147
- Charge radius, 70
  - of kaons, 85
  - of neutron, 81

- of nuclei, 71
- of pions, 85
- of proton, 79, 80
- Charmonium, 218–220
- Cherenkov counter, 419
- Cherenkov radiation, 173, 414
- Chiral perturbation theory, 300
- Chirality, 154
- Chromomagnetic interaction, 225, 226, 263, 297
- CKM matrix, 153, 246
  - Wolfenstein parametrisation, 246
- Clebsch-Gordan coefficients, 262, 421, 422
- CLEO experiment, 154
- COBE satellite, 386
- Colour, 104–106, 133–135, 151
  - wave function, 260
- Compound nucleus, 378
- Compact Muon Solenoid (CMS) experiment, 202
- Compton effect, 413
- Confinement, 106, 110, 222
- Conservation laws, 208
- Constituent quarks, 108, 226, 233, 270, 282, 402
- Cooper pairs, 197, 199, 370
- Coriolis force, 449
- Coulomb
  - barrier, 32
  - excitation, 364, 365
  - potential, 31, 215
  - term, 20, 34
  - threshold, 364
- Coupling constant
  - electromagnetic, 7, 108, 109, 216
  - strong, 106, 109, 115, 135, 137
  - weak, 147, 151, 192
- Covalent bond, 298, 402
- CP violation, 153, 157, 244–247, 249
  - in  $B^0$  decays, 247, 249
  - CKM matrix, 246
  - direct, 244
  - in  $K^0$  decays, 244
  - indirect, 244
- Critical density, 386
- Cross-section, 44
  - differential, 48
  - geometric, 45
  - total, 46
- Crystal ball, 219
- Current quarks, 108
- Dark energy, 386
- Dark matter, 386
- Daya Bay experiment, 177
- De Broglie wavelength, 43
- Decay
  - chain, 33
  - constant, 26
  - width, 129
- Deformation, 35, 320, 321, 323, 369, 370
- Delayed neutron emission, 334
- $\Delta$  resonance, 89, 253, 254, 260
- Deuteron, 97, 292
  - binding energy, 17, 292–294
  - dipole moment, 293
  - magnetic moment, 292, 293
  - quadrupole moment, 292
- Deutsche Elektronen-Synchrotron (DESY), 42, 87, 410, 411
- DGLAP equations, 113, 114
- Dipole
  - form factor, 78
  - oscillator, 351ff
  - transition, electric, 36, 219, 350
  - transition, magnetic, 36, 220
- Dirac particle, 180, 266
- Direct nuclear reaction, 324
- Distorted-wave Born approximation (DWBA), 328
- Doppler shift, 385
- Double beta decay, 338
  - neutrinoless, 180, 340
- Double Chooz experiment, 177
- Drell-Yan process, 116
- Drift chamber, 414
- DWBA. *See* Distorted-wave Born approximation (DWBA)
- Electron
  - capture, 29
  - charge, 11, 13
  - discovery, 11
  - magnetic moment, 76
  - mass, 12, 14
  - volt, 6
- EMC effect, 117, 118, 297
- Exclusive measurement, 44
- Fermi
  - constant, 146, 147, 275
  - decay, 275, 331

- energy, 305
- function, 330
- gas, 84, 303, 304
- momentum, 84, 304, 307, 310
- motion, 83, 97
- pressure, 308
- Feynman diagrams, 50
- Fine structure, 216, 217
- Fine structure constant, 7
- Flavour, 96, 143
- Flux, 44
- FNAL, 42, 87, 133
- Form factor, 61, 64, 66, 67, 80, 81
  - dipole, 78
  - electric, 77, 80
  - of kaons, 85
  - magnetic, 77, 80
  - monopole, 85
  - of neutron, 77, 80
  - of nuclei, 66–68
  - of nucleons, 81
  - of pions, 85
  - of proton, 77
- Formation experiments, 255
- Four-momentum, 55, 56
  - transfer, 75, 76
- Four-vector, 55
- Friedman model, 386
- $ft$  value, 331
- Fusion reactions, 368
  
- g-factor, 76
  - of electron, 76
  - of neutron, 77
  - of nuclei, 319
  - of proton, 77
- G-parity, 240
- Gamma decay, 36–38
- Gamow factor, 32, 33
- Gamow-Teller decay, 276, 331–333
- Gauss system, 7
- Giant dipole resonance, 38, 347, 348, 352, 353, 359
- Gluon, 101, 105–108, 119, 135, 137
  - distribution, 114, 116–118
- Golden rule, 49, 50, 147, 275, 325
- Goldhaber experiment, 337
- Gottfried sum rule, 100, 116
- Grand unified theory (GUT), 204
- Gravitational Doppler shift, 307
  
- H1 detector, 110
- H1 experiment, 110, 112, 162, 193
  
- Hadronic matter, 381, 383
- Hadronisation, 134, 136, 224
- Hadrons, 103
- Half life, 26
- Hard core, 290, 308
- Heavyside-Lorentz system, 7
- Helicity, 63, 154, 156, 271
- HERA, 42, 87, 161, 272, 410, 411
- HERMES experiment, 272
- Higgs boson, 197, 198, 200, 202
  - mass, 200–203
  - production, 201, 202
- Higgs potential, 197
- Hubble constant, 385
- Hund rule, 322
- Hyperfine structure, 216, 217, 319
- Hypernuclei, 308, 309
- Hyperon, 253, 255, 308
  - magnetic moment, 268
  - semileptonic decays, 280, 281
  
- Impulse approximation, 82, 93
- Inclusive measurement, 44
- Internal conversion, 37, 38
- Invariant mass, 257, 258
- Ionisation, 412, 414, 416
- Isobars, 14
- Isomers, 38
- Isospin, 5, 22, 234, 288
  - strong, 5, 275
  - weak, 5, 274, 276
- Isotones, 14
- Isotopes, 14
  
- Jacobian peak, 188
- Jets, 136
- JLab, 79
  
- K capture, 29, 144, 333, 337
- KamLAND detector, 177
- Kaon, 85, 131, 239
  - $K_S^0$  regeneration, 243
  - charge radius, 85
- KATRIN experiment, 180
- Klein-Gordon equation, 299
- Kurie plot, 335
  
- Large Electron Positron (LEP), 41, 133, 185, 410
- Large Hadron Collider (LHC), 42, 199, 202

- Larmor frequency, 269
- Leptogenesis, 390
- Lepton, 125, 126, 128, 141
  - families, 141, 168
  - family number, 142
  - number, 142
  - number conservation, 142
  - number violation, 181
  - universality, 128
- Leptonic processes, 144
- Lifetime, 26, 31, 38
- Linear accelerator, 406
- Liquid drop model, 20
- log-*ft* value, 331
- Luminosity, 47
  
- Magic numbers, 313, 314
- Magnetic moment, 76
  - of deuteron, 292
  - of electron, 76
  - of hyperons, 268
  - of neutron, 76
  - of nuclei, 318, 319
  - of nucleons, 76, 266, 267
  - of proton, 76
  - in the quark model, 266
- Magnetic spectrometer, 64, 416
- Majorana neutrino, 180, 340, 390
- Mass
  - defect, 13
  - formula, 19, 306
  - invariant, 56
  - number, 14
- Meissner effect, 196, 197, 199
- Meson(s), 103, 104, 233–235
  - B, 230
  - D, 229
  - exchange of, 298
  - $\Upsilon$ , 133, 226, 229
  - $J/\psi$ , 132, 218, 228–231
  - pseudoscalar, 234, 236
  - vector, 130
- Mirror nuclei, 21, 316, 317
- Moment of inertia, 363, 365, 368–370
- Momentum transfer, 60–62, 67, 76
- Moseley's law, 13
- Mott cross-section, 63, 75
- Muon, 139
  - beam, 87
  - decay, 140, 147, 155
  - experiments, 161
  - lifetime, 147
  
- Neutrino, 140–142
  - atmospheric, 175
  - electron-, 141
  - experiments, 161
  - helicity, 155, 156, 337, 338
  - mass, 167, 178, 180, 335, 336, 342, 390
  - mass ordering, 176, 178
  - mass-squared difference, 175, 176
  - muon-, 141
  - oscillations, 167, 168, 171
  - reactor, 176
  - scattering, 157, 158
  - solar, 171
  - tau-, 141
- Neutron
  - capture, 17, 35, 38
  - charge radius, 81
  - decay, 275, 278, 279
  - lifetime, 279
  - magnetic moment, 77, 267
  - mass, 14
  - scattering, 38
  - star, 307, 308
- Nilsson model, 323
- Non-leptonic processes, 145
- Nuclear
  - fission (*see* Nuclear fission)
  - force, 287–289
  - magneton, 77, 266, 423
  - matter, 373, 374
  - photoelectric effect, 38, 352
  - spin resonance, 319
  - temperature, 374
- Nuclear fission
  - barrier, 34, 35
  - induced, 35
  - spontaneous, 25, 34
- Nucleon resonances, 88, 254
- Nuclides, 14
  
- Oscillations
  - beauty-, 245, 249
  - neutrino, 167, 168, 171, 175, 176, 178
  - strangeness-, 243
  
- Pair production, 413
- Pairing
  - force, 322, 370
  - term, 20, 21
- Parity, 5, 314, 332
  - intrinsic, 5, 234
  - of nuclear levels, 314

- of quarkonia, 219
  - violation, 154–157
- Partial waves, 288, 289
- Partial width, 129
- Parton distributions, 116
- Parton model, 93, 96–98, 100
- Phase space, 49
- Phase transition, electroweak, 390
- Photoelectric effect, 413
- Pick-up reaction, 328
- Pion, 85, 104, 239, 310
  - charge radius, 85
  - decay, 141, 156
  - parity, 240
- Pions, 298
- Planck constant, 7
- Planck experiment, 386
- PMNS matrix, 168
- Point interaction, 146–148, 225
- Poisson equation, 299
- Polarisation experiments, 81, 161, 272
- Polarised beams, 81, 161, 271
- Polarised targets, 81, 272
- Pontecorvo, 168
- Positronium, 215, 217
- Potential well, 304, 305
- Principal quantum number, 215, 218
- Probability amplitude, 48
- Production experiments, 255, 280
- Propagator, 52, 62, 146
- Proportional counter, 414
- Proton
  - anti-, 186
  - charge, 13
  - charge radius, 79
  - decay, 104
  - magnetic moment, 77, 266
  - mass, 14
- Proton-proton cycle, 395
  
- Quadrupole moment
  - of deuteron, 292, 293
  - of nuclei, 320, 321
- Quadrupole oscillations, 360, 361
- Quadrupole transition, 36, 351
- Quantum chaos, 374
- Quantum chromodynamics, 50, 87, 105–107, 109, 221
- Quantum electrodynamics, 50, 55
- Quark, 95, 96
  - charge, 95, 100
  - distribution, 96, 114, 116–118
  - families, 96
  - helicity distributions, 271
  - isospin, 95
  - mass, 96, 133
  - matter, 308
  - sea quark, 96, 98, 119
  - spin, 95
  - top, 133
- Quark-gluon plasma, 384, 390, 391
- Quarkonia, 215
- Quasi-particles, 401, 402
  
- r-process, 399
- Radiation length, 413
- Recoil polarisation, 80
- Renormalisation, 193
- Resonances, 88, 129, 255
- Resonant absorption, 337
- Rosenbluth formula, 77
- Rotational bands, 363, 365–368, 370
- Rutherford scattering, 12
  - cross-section, 58
  
- s-process, 398
- s-waves, 289
- Sampling calorimeter, 417
- Sargent's rule, 278, 280
- Scaling violations, 110, 112–115
- Scattering
  - angle, 57
  - deep-inelastic, 92, 157, 158, 161
  - elastic, 42, 58–61
  - experiments, 41
  - inelastic, 43, 72, 88, 89
  - neutrino-electron, 192
  - of neutrinos, 157, 158
  - of neutrons, 376
  - phase, 288–290
  - polarised, 80, 81
  - quasi-elastic, 82, 403
  - Rutherford, 12
- Scintillator, 416, 417, 419
- Sea quark, 96, 98, 160, 186
- Seesaw mechanism, 182
- Self similarity, 116
- Semiconductor detector, 416
- Semileptonic processes, 144
- Separation energy, 38, 310
- Shadowing, 120
- Shell model, 303, 312–314, 403
- Silicon strip detector, 415
- Spark chamber, 414
- Spin dependence, of nuclear force, 292



- Spin structure functions, 271
- Spin structure of the nucleon, 270
- Spin-orbit interaction, 216, 292, 320
- Spin-spin interaction, 237, 263, 296
- Splitting function, 114
- Spontaneous symmetry breaking, 196
- Standard model, 207, 208, 210
- Stanford Linear Accelerator Center (SLAC), 79, 87, 91
- Stanford Linear Collider (SLC), 185
- Storage ring, 110, 123, 410
- Strange particles, 131
- Strangeness, 131, 234, 253
- Strangeness oscillations, 243
- Streamer chamber, 414
- Stripping reaction, 324, 326
- Structure function, 90, 91, 96
  - of the deuteron, 97, 100, 111
  - of the neutron, 97, 98, 100
  - nuclear effects, 117–119
  - polarised, 271
  - of the proton, 97, 98, 100, 112
- Sudbury Neutrino Observatory (SNO)
  - experiment, 173
- Superconductivity, 196, 197, 199, 370
- Superfluidity, 369, 370
- SuperKamiokande experiment, 173, 175
- Supernova, 398
- Surface term, 20, 34
- Surface thickness, 71
- Symmetry breaking, 197
- Synchrotron, 408
  - radiation, 409
- Tau lepton, 126, 140
  - decay, 140, 144, 151
- Tensor force, 292, 293
- Tevatron, 42
- Thomson model, 12
- Top quark, 133, 227
- Transition matrix element, 48
- Transition radiation detector, 419
- Transmission, 32
- Transverse mass, 188
- Transverse momentum, 187
- Tunnel effect, 32, 34
- Unitarity triangle, 247, 249, 250
- Universe
  - closed, 386
  - critical density, 386
  - flat, 386
  - open, 386
- V–A theory, 155, 274
- Vacuum expectation value, 198
- Valence nucleon, 317, 330
- Valence quark, 95, 96, 160, 186
- Van de Graaff accelerator, 406
- Van der Waals force, 298, 402
- Vector current, 155, 280, 331
- Vector meson, 130, 234–236
- Vertex, 51
- Virtual particles, 51
- Volume term, 19, 20
- Weak interaction
  - charged currents, 143–145, 157, 162, 173, 193
  - neutral currents, 143, 150, 174, 193
- Weak isospin, 191
- Weinberg angle, 192
- Weizsäcker formula, 19
- White dwarf, 308, 396, 397
- WMAP experiment, 386
- Woods-Saxon potential, 314
- Yukawa potential, 298, 299
- ZEUS detector, 419
- ZEUS experiment, 110, 112, 162
- Zweig rule, 132, 229, 240